AD 684065

Bulletin 39
Part 3
(of 6 Parts)

THE SHOCK AND VIBRATION BULLETIN

JANUARY 1969

A Publication of
THE SHOCK AND VIBRATION
INFORMATION CENTER
Naval Research Laboratory, Washington, D.C.



DDC
RECEIVED
MAR 21 1969
C

Office of
The Director of Defense
Research and Engineering

Reproduced by the
CLEARINGHOUSE
for Federal Scientific & Technical
Information Springfield Va. 22151

This document has been approved for public release and sale; its distribution is unlimited.

ACCESSION for
CFSTI WHITE SECTION
DDC BUFF SECTION
UNANNOUNCED
JUSTIFICATION
BY
DISTRIBUTION/AVAILABILITY CODES
DIST. AVAIL. and/or SPECIAL
1

SYMPOSIUM MANAGEMENT

THE SHOCK AND VIBRATION INFORMATION CENTER

William W. Mutch, Director
Henry C. Pusey, Coordinator
Rudolph H. Volin, Coordinator
Katherine G. Jahnel, Administrative Secretary

Bulletin Production

Graphic Arts Branch, Technical Information Division,
Naval Research Laboratory

Bulletin 39
Part 3
(of 6 Parts)

THE SHOCK AND VIBRATION BULLETIN

JANUARY 1969

A Publication of
THE SHOCK AND VIBRATION
INFORMATION CENTER
Naval Research Laboratory, Washington, D.C.

The 39th Symposium on Shock and Vibration was held in Pacific Grove, California, on 22-24 October 1968. The U.S. Army was host.

Office of
The Director of Defense
Research and Engineering

CONTENTS

PART 3

Structural Analysis

MODAL DENSITIES OF SANDWICH PANELS: THEORY AND EXPERIMENT 1
Larry L. Erickson, NASA Ames Research Center, Moffett Field, California

TURBINE ENGINE DYNAMIC COMPATIBILITY WITH HELICOPTER AIRFRAMES 17
Kenneth C. Mard and Paul W. von Hardenberg, Sikorsky Aircraft Division of United Aircraft Corporation, Stratford, Connecticut

SYNTHESIS OF RIGID FRAMES BASED ON DYNAMIC CRITERIA 31
Henry N. Christiansen, Associate Professor, Department of Civil Engineering Science, Brigham Young University, Provo, Utah, and E. Alan Pettit, Jr., Engineer, Humble Oil Company, Benicia, California

DYNAMIC RESPONSE OF PLASTIC AND METAL SPIDER BEAMS FOR 1/9TH SCALE SATURN MODEL 39
L. V. Kulasa, KPA Computer Techniques, Inc., Pittsburgh, Pennsylvania, and W. M. Laird, University of New York, Fredonia, New York

*CHARTS FOR ESTIMATING THE EFFECT OF SHEAR DEFORMATION AND ROTARY INERTIA ON THE NATURAL FREQUENCIES OF UNIFORM BEAMS 49
F. F. Rudder, Jr., Aerospace Sciences Research Laboratory, Lockheed-Georgia Company, Marietta, Georgia

ACOUSTIC RESPONSE ANALYSIS OF LARGE STRUCTURES 55
F. A. Smith, Martin Marietta Corporation, Denver Division, Denver, Colorado, and R. E. Jewell, NASA Marshall Space Flight Center, Huntsville, Alabama

*ESTIMATION OF PROBABILITY OF STRUCTURAL DAMAGE FROM COMBINED BLAST AND FINITE-DURATION ACOUSTIC LOADING 65
Eric E. Ungar and Yoram Kadman, Bolt Beranek and Newman Inc., Cambridge, Massachusetts

*THE RESPONSE OF MECHANICAL SYSTEMS TO BANDS OF RANDOM EXCITATION 73
L. J. Pulgrano and M. Ablowitz, Grumman Aircraft Engineering Corporation, Bethpage, New York

*PREDICTION OF STRESS AND FATIGUE LIFE OF ACOUSTICALLY-EXCITED AIRCRAFT STRUCTURES 87
Noe Arcas, Grumman Aircraft Engineering Corporation, Bethpage, New York

VIBRATION ANALYSIS OF COMPLEX STRUCTURAL SYSTEMS BY MODAL SUBSTITUTION 99
R. L. Bajan, C. C. Feng, University of Colorado, Boulder, Colorado, and I. J. Jaszlics, Martin Marietta Corporation, Denver, Colorado

THE APPLICATION OF THE KENNEDY-PANCU METHOD TO EXPERIMENTAL VIBRATION STUDIES OF COMPLEX SHELL STRUCTURES 107
John D. Ray, Charles W. Bert and Davis M. Egle, School of Aerospace and Mechanical Engineering, University of Oklahoma, Norman, Oklahoma

*NORMAL MODE STRUCTURAL ANALYSIS CALCULATIONS VERSUS RESULTS 117
Culver J. Floyd, Raytheon Company, Submarine Signal Division, Portsmouth, Rhode Island

COMPARISONS OF CONSISTENT MASS MATRIX SCHEMES 129
R. M. Mains, Department of Civil and Environmental Engineering, Washington University, St. Louis, Missouri

*This paper not presented at Symposium.

MEASUREMENT OF A STRUCTURE'S MODAL EFFECTIVE MASS 143
G. J. O'Hara and G. M. Remmers, Naval Research Laboratory, Washington, D.C.

SIMPLIFYING A LUMPED PARAMETER MODEL 153
Martin T. Soifer and Arlen W. Bell, Dynamic Science, a Division of Marshall Industries, Monrovia, California

STEADY STATE BEHAVIOR OF TWO DEGREE OF FREEDOM NONLINEAR SYSTEMS . . 161
J. A. Padovan and J. R. Curreri, Polytechnic Institute of Brooklyn, Brooklyn, New York, and M. B. Electronics, New Haven, Connecticut

THE FLUTTER OR GALLOPING OF CERTAIN STRUCTURES IN A FLUID STREAM 171
Raymond C. Binder, University of Southern California, Los Angeles, California

*AIRCRAFT LANDING GEAR BRAKE SQUEAL AND STRUT CHATTER INVESTIGATION . . 179
F. A. Biehl, McDonnell Douglas Corporation, Long Beach, California

EXPERIMENTAL INVESTIGATION OF NONLINEAR VIBRATIONS OF LAMINATED ANISOTROPIC PANELS 191
Bryor L. Mayberry and Charles W. Bert, School of Aerospace and Mechanical Engineering, University of Oklahoma, Norman, Oklahoma

*STRUCTURAL DYNAMICS ANALYSIS OF AN ANISOTROPIC MATERIAL 201
S. K. Lee, General Electric Company, Syracuse, New York

*EXPERIMENTS ON THE LARGE AMPLITUDE PARAMETRIC RESPONSE OF RECTANGULAR PLATES UNDER IN-PLANE RANDOM LOADS 205
R. L. Silver and J. H. Somerset, Department of Mechanical and Aerospace Engineering, Syracuse University, Syracuse, New York

*RESPONSE OF STIFFENED PLATES TO MOVING SPRUNG MASS LOADS 233
Ganpat M. Singhvi, Schutte Mochon, Inc., Milwaukee, Wisconsin, and Larry J. Feeser, University of Colorado, Boulder, Colorado

*PARAMETRIC RESPONSE SPECTRA FOR IMPERFECT COLUMNS 247
Martin L. Moody, University of Colorado, Boulder, Colorado

PAPERS APPEARING IN PART 1
Part 1 - Classified
(Unclassified Titles)

AN INTRODUCTION TO THE BASIC SHOCK PROBLEM
F. Weinberger and R. Heise, Jr., Naval Ship Research and Development Center, Washington, D.C.

DESIGN INPUT DERIVATION AND VALIDATION
R. O. Belsheim, G. J. O'Hara and R. L. Bort, Naval Research Laboratory, Washington, D.C.

SHOCK DESIGN OF NAVAL BOILERS
D. M. Gray, Combustion Engineering, Inc., Windsor, Connecticut

MACHINERY DESIGN FOR SHIPBOARD UNDERWATER SHOCK
G. W. Bishop, Bishop Engineering Company, Princeton, New Jersey

SHOCK DESIGN OF SHIPBOARD STRUCTURES
R. J. Della Rocca and N. R. Addonizio, Gibbs and Cox, Inc., New York, New York

REVIEW AND APPROVAL OF DYNAMIC ANALYSIS
M. J. Macy and L. A. Gordon, Supervisor of Shipbuilding, Conversion and Repair, USN, Brooklyn, New York

COMPUTER AIDED DESIGN - ANALYSIS FOR SHIPBOARD UNDERWATER SHOCK
M. Pakstys, Jr., General Dynamics, Electric Boat Division, Groton, Connecticut

CURRENT NAVY SHOCK HARDENING REQUIREMENTS AND POLICY
J. R. Sullivan, H. H. Ward and D. M. Lund, Department of the Navy, Naval Ship Systems Command Headquarters, Washington, D.C.

*This paper not presented at Symposium.

SHOCK DESIGN AND TEST QUALIFICATION OF SHIPBOARD SYSTEMS/COMPONENTS -- PANEL SESSION

*HARDENING OF SURFACE SHIPS AND SUBMARINES FOR ADVANCED SEABASED DETERRENCE
H. L. Rich, Naval Ship Research and Development Center, Washington, D.C.

TOWARD A MORE RATIONAL BLAST-HARDENED DECKHOUSE DESIGN
Shou-ling Wang, Naval Ship Research and Development Center, Washington, D.C.

COMPUTATION OF THE MOBILITY PROPERTIES OF A UNIFORM BEAM FOUNDATION
J. E. Smith and R. J. Hanners, Naval Ship Research and Development Center, Annapolis, Maryland

AN ANALYTICAL INVESTIGATION OF THE DAMPING OF RADIAL VIBRATIONS OF A PIPE BY CONSTRAINED VISCOELASTIC LAYERS USING AXIAL STAVES
R. A. DiTaranto, PMC Colleges, Chester, Pennsylvania, and W. Blasingame, Naval Ship Research and Development Center, Annapolis, Maryland

*DAMPED CYLINDRICAL SHELLS AND DYNAMIC SYSTEMS EFFECTS
B. E. Douglas and E. V. Thomas, Naval Ship Research and Development Center, Annapolis, Maryland

APPLICATION OF SPACED DAMPING TO MACHINERY FOUNDATIONS
J. R. Hupton, General Dynamics, Electric Boat Division, Groton, Connecticut, H. T. Miller and G. E. Warnaka, Lord Manufacturing Company, Erie, Pennsylvania

*ROCKET SLED TESTS OF THE AGM-12 "BULLPUP" MISSILE
Robert D. Kimsey, Naval Missile Center, Point Mugu, California

AIM-4D FLIGHT MEASUREMENT PROGRAM
R. P. Mandich and W. G. Spalthoff, Hughes Aircraft Company, Canoga Park, California

*AEROELASTIC ANALYSIS OF A FLEXIBLE RE-ENTRY VEHICLE
H. Saunders and A. Kirsch, General Electric Company, Re-Entry Systems Department, Philadelphia, Pennsylvania

PAPERS APPEARING IN PART 2

Vibration

ELECTRICAL GENERATION OF MOTION IN ELASTOMERS
S. Edelman, S. C. Roth and L. R. Grisham, National Bureau of Standards, Washington, D.C.

CONTROLLED DECELERATION SPECIMEN PROTECTION SYSTEMS FOR ELECTRODYNAMIC VIBRATION SYSTEMS
Lawrence L. Cook, Jr., NASA Goddard Space Flight Center, Greenbelt, Maryland

CONTROL TECHNIQUES FOR SIMULTANEOUS THREE-DEGREE-OF-FREEDOM HYDRAULIC VIBRATION SYSTEM
H. D. Cyphers and J. F. Sutton, NASA Goddard Space Flight Center, Greenbelt, Maryland

*INITIAL REPORT ON EQUIVALENT DAMAGE MEASUREMENT BY UTILIZING S/N FATIGUE GAGES
Thomas B. Cost, Naval Weapons Center, China Lake, California

HOLOGRAM INTERFEROMETRY AS A PRACTICAL VIBRATION MEASUREMENT TECHNIQUE
Cameron D. Johnson and Gerald M. Mayer, Navy Underwater Sound Laboratory, Fort Trumbull, New London, Connecticut

RESPONSE OF AN ELASTIC STRUCTURE INVOLVING CROSS CORRELATIONS BETWEEN TWO RANDOMLY VARYING EXCITATION FORCES
A. Razzaque, Grumman Aircraft Engineering Corporation, Bethpage, New York, and J. R. Curreri, Polytechnic Institute of Brooklyn, Brooklyn, New York

AUTOMATIC NORMALIZATION OF STRUCTURAL MODE SHAPES
C. C. Isaacson and R. W. Merkel, Engineering Laboratories, McDonnell Aircraft Company, St. Louis, Missouri

*This paper not presented at Symposium.

*RESONANT BEAM HIGH "G" VIBRATION TESTING
B. A. Kohler, International Business Machines Corporation, Federal Systems Division, Owego, New York

THE USE OF LIQUID SQUEEZE-FILMS TO SUPPORT VIBRATING LOADS
Brantley R. Hanks, NASA Langley Research Center, Langley Station, Hampton, Virginia

POINT-TO-POINT CORRELATION OF SOUND PRESSURES IN REVERBERATION CHAMBERS
Charles T. Morrow, LTV Research Center, Western Division, Anaheim, California

ENVIRONMENTAL LABORATORY MISSILE FAILURE RATE TEST WITH AERODYNAMIC FUNCTION SIMULATION
Raymond C. Binder and Gerald E. Berge, Naval Missile Center, Point Mugu, California

APOLLO CSM DYNAMIC TEST PROGRAM
A. E. Chirby, R. A. Stevens and W. R. Wood, Jr., North American Rockwell Corporation, Downey, California

MODAL SURVEY RESULTS FROM THE MARINER MARS 1969 SPACECRAFT
R. E. Freeland, Jet Propulsion Laboratory, California Institute of Technology, Pasadena, California, and W. J. Gaugh, Northrop Systems Laboratories, Northrop Corporation, Hawthorne, California

UPRATED SATURN I FULL SCALE DYNAMIC TEST CORRELATION
Charles R. Wells and John E. Hord, Chrysler Corporation Space Division, New Orleans, Louisiana

AN APPROACH FOR DUPLICATING SPACECRAFT FLIGHT-INDUCED BODY FORCES IN A LABORATORY
S. M. Kaplan and A. J. Soroka, General Electric Company, Philadelphia, Pennsylvania

FLEXURE GUIDES FOR VIBRATION TESTING
Alexander Yorgiadis and Stanley Barrett, North American Rockwell Corporation, Downey, California

A COMPRESSION-FASTENED GENERAL-PURPOSE VIBRATION AND SHOCK FIXTURE
Warren C. Beecher, Instrument Division, Lear Siegler, Inc., Grand Rapids, Michigan

VIBRATION EQUIVALENCE: FACT OR FICTION?
LaVerne Root, Collins Radio Company, Cedar Rapids, Iowa

PROVIDING REALISTIC VIBRATION TEST ENVIRONMENTS TO TACTICAL GUIDED MISSILES
K. R. Jackman and H. L. Holt, General Dynamics, Pomona, California

*THE REDUCTION OF THE VIBRATION LEVEL OF A CIRCULAR SHAFT MOVING TRANSVERSELY THROUGH WATER AT THE CRITICAL REYNOLDS NUMBER
Irvin F. Gerks, Honeywell, Inc., Seattle, Washington

*ANALYSIS AND DESIGN OF RESONANT FIXTURES TO AMPLIFY VIBRATOR OUTPUT
J. Verga, Hazeltine Corporation, Little Neck, New York

PAPERS APPEARING IN PART 4

Damping

*APPLICATION OF A SINGLE-PARTICLE IMPACT DAMPER TO AN ANTENNA STRUCTURE
R. D. Rocke, Hughes Aircraft Company, Fullerton, California, and S. F. Masri, University of Southern California, Los Angeles, California

A PROPOSED EXPERIMENTAL METHOD FOR ACCURATE MEASUREMENTS OF THE DYNAMIC PROPERTIES OF VISCOELASTIC MATERIALS
Kenneth G. McConnell, Associate Professor of Engineering Mechanics, Iowa State University, Ames, Iowa

DAMPING OF BLADE-LIKE STRUCTURES
David I. G. Jones, Air Force Materials Laboratory, Wright-Patterson Air Force Base, Ohio, and Ahid D. Nashif, University of Dayton, Dayton, Ohio

*This paper not presented at Symposium.

MULTI-LAYER ALTERNATELY ANCHORED TREATMENT FOR DAMPING OF SKIN-STRINGER STRUCTURES
Captain D. R. Simmons, Air Force Institute of Technology, Wright-Patterson Air Force Base, Ohio, J. P. Henderson, D. I. G. Jones, Air Force Materials Laboratory, Wright-Patterson Air Force Base, Ohio, and C. M. Cannon, University of Dayton, Dayton, Ohio

AN ANALYTICAL AND EXPERIMENTAL INVESTIGATION OF A TWO-LAYER DAMPING TREATMENT
A. D. Nashif, University of Dayton, Dayton, Ohio, and T. Nicholas, Air Force Materials Laboratory, Wright-Patterson Air Force Base, Ohio

DAMPING OF PLATE VIBRATIONS BY MEANS OF ATTACHED VISCOELASTIC MATERIAL
I. W. Jones, Applied Technology Associates, Inc., Ramsey, New Jersey

VIBRATIONS OF SANDWICH PLATES WITH ORTHOTROPIC FACES AND CORES
Fakhruddin Abdulhadi, Reliability Engineering, IBM Systems Development Division, Rochester, Minnesota, and Lee P. Sapetta, Department of Mechanical Engineering, University of Minnesota, Minneapolis, Minnesota

THE NATURAL MODES OF VIBRATION OF BORON-EPOXY PLATES
J. E. Ashton and J. D. Anderson, General Dynamics, Fort Worth, Texas

*NATURAL MODES OF FREE-FREE ANISOTROPIC PLATES
J. E. Ashton, General Dynamics, Fort Worth, Texas

ACOUSTIC TEST OF BORON FIBER REINFORCED COMPOSITE PANELS CONDUCTED IN THE AIR FORCE FLIGHT DYNAMICS LABORATORY'S SONIC FATIGUE TEST FACILITY
Carl L. Rupert, Air Force Flight Dynamics Laboratory, Wright-Patterson Air Force Base, Ohio

STRENGTH CHARACTERISTICS OF JOINTS INCORPORATING VISCOELASTIC MATERIALS
W. L. LaBarge and M. D. Lamoree, Lockheed-California Company, Burbank, California

Isolation

RECENT ADVANCES IN ELECTROHYDRAULIC VIBRATION ISOLATION
Jerome E. Ruzicka and Dale W. Schubert, Barry Controls, Division of Barry Wright Corporation, Watertown, Massachusetts

ACTIVE ISOLATION OF HUMAN SUBJECTS FROM SEVERE AIRCRAFT DYNAMIC ENVIRONMENTS
Peter C. Calcaterra and Dale W. Schubert, Barry Controls, Division of Barry Wright Corporation, Watertown, Massachusetts

ELASTIC SKIDMOUNTS FOR MOBILE EQUIPMENT SHELTERS
R. W. Doll and R. L. Laier, Barry Controls, Division Barry Wright Corporation, Burbank, California

COMPUTER-AIDED DESIGN OF OPTIMUM SHOCK-ISOLATION SYSTEMS
E. Sevin, W. D. Pilkey and A. J. Kalinowski, IIT Research Institute, Chicago, Illinois

ANALYTIC INVESTIGATION OF BELOWGROUND SHOCK-ISOLATING SYSTEMS SUBJECTED TO DYNAMIC DISTURBANCES
J. Neils Thompson, Ervin S. Perry and Suresh C. Arya, The University of Texas at Austin, Austin, Texas

GAS DYNAMICS OF ANNULAR CONFIGURED SHOCK MOUNTS
W. F. Andersen, Westinghouse Electric Corporation, Sunnyvale, California

A SCALE MODEL STUDY OF CRASH ENERGY DISSIPATING VEHICLE STRUCTURES
D. J. Bozich and G. C. Kao, Research Staff, Wyle Laboratories, Huntsville, Alabama

DESIGN OF RECOIL ADAPTERS FOR ARMAMENT SYSTEMS
A. S. Whitehill and T. L. Quinn, Lord Manufacturing Company, Erie, Pennsylvania

*A DYNAMIC VIBRATION ABSORBER FOR TRANSIENTS
Dirse W. Sallet, University of Maryland, College Park, Maryland and Naval Ordnance Laboratory, White Oak, Silver Spring, Maryland

*This paper not presented at Symposium.

PAPERS APPEARING IN PART 5

Shock

DYNAMIC RESPONSE OF A SINGLE-DEGREE-OF-FREEDOM ELASTIC-PLASTIC SYSTEM SUBJECTED TO A SAWTOOTH PULSE
Martin Wohltmann, Structures and Mechanics Department, Martin Marietta Corporation, Orlando, Florida

*TRANSIENT DYNAMIC RESPONSES IN ELASTIC MEDIUM GENERATED BY SUDDENLY APPLIED FORCE
Dr. James Chi-Dian Go, The Boeing Company, Seattle, Washington

IMPACT FAILURE CRITERION FOR CYLINDRICAL AND SPHERICAL SHELLS
Donald F. Haskell, Hittman Associates, Inc., Columbia, Maryland

*THE EXCITATION OF SPHERICAL OBJECTS BY THE PASSAGE OF PRESSURE WAVES
Gordon E. Strickland, Jr., Lockheed Missiles and Space Company, Palo Alto, California

THE PERFORMANCE CHARACTERISTICS OF CONCENTRATED-CHARGE, EXPLOSIVE-DRIVEN SHOCK TUBES
L. W. Bickle and M. G. Vigil, Sandia Laboratories, Albuquerque, New Mexico

*PRIMACORD EXPLOSIVE-DRIVEN SHOCK TUBES AND BLAST WAVE PARAMETERS IN AIR, SULFURHEXAFLUORIDE AND OCTOFLUOROCYCLOBUTANE (FREON-C318)
M. G. Vigil, Sandia Laboratories, Albuquerque, New Mexico

ZERO IMPEDANCE SHOCK TESTS, A CASE FOR SPECIFYING THE MACHINE
Charles T. Morrow, LTV Research Center, Western Division, Anaheim, California

SHOCK TESTING WITH AN ELECTRODYNAMIC EXCITER AND WAVEFORM SYNTHESIZER
Dana A. Regillo, Massachusetts Institute of Technology, Lincoln Laboratory, Lexington, Massachusetts

SLINGSHOT SHOCK TESTING
LaVerne Root and Carl Bohs, Collins Radio Company, Cedar Rapids, Iowa

SHOCK TESTING AND ANALYSIS: A NEW LABORATORY TECHNIQUE
J. Fagan and J. Sincavage, RCA Astro-Electronics Division, Princeton, New Jersey

*INSTRUMENTATION FOR A HUMAN OCCUPANT SIMULATION SYSTEM
W. I. Kipp, Monterey Research Laboratory, Inc., Monterey, California

PAPERS APPEARING IN PART 6

Introductory Papers

THE IMPACT OF A DYNAMIC ENVIRONMENT ON FIELD EXPERIMENTATION
Walter W. Hollis, U.S. Army Combat Developments Command, Experimentation Command, Fort Ord, California

TRANSCRIPT OF PANEL DISCUSSION ON PROPOSED USASI STANDARD ON METHODS FOR ANALYSIS AND PRESENTATION OF SHOCK AND VIBRATION DATA
Julius S. Bendat, Measurement Analysis Corporation, Los Angeles, California, and Allen J. Curtis, Hughes Aircraft Corporation, Culver City, California

Transportation and Packaging

THE BUMP TESTING OF MILITARY SIGNALS EQUIPMENT IN THE UNITED KINGDOM
W. Childs, Signals Research and Development Establishment, Ministry of Technology, United Kingdom

NLABS SHIPPING HAZARDS RECORDER STATUS AND FUTURE PLANS
Dennis J. O'Sullivan, Jr., U.S. Army Natick Laboratories, Natick, Massachusetts

*This paper not presented at Symposium.

NORMAL AND ABNORMAL DYNAMIC ENVIRONMENTS ENCOUNTERED IN TRUCK TRANSPORTATION
J. T. Foley, Sandia Laboratories, Albuquerque, New Mexico

DEVELOPMENT OF A RAILROAD ROUGHNESS INDEXING AND SIMULATION PROCEDURE
L. J. Pursifull and B. E. Prothro, U.S. Army Transportation Engineering Agency, Military Traffic Management and Terminal Service, Fort Eustis, Virginia

AN APPROXIMATE METHOD OF DYNAMIC ANALYSIS FOR MISSILE CONTAINER SYSTEMS
Mario Paz, Associate Professor, and Ergin Citipitioglu, Associate Professor, University of Louisville, Louisville, Kentucky

SIMULATED MECHANICAL IMPACT TEST EQUIPMENT
D. R. Agnew, Naval Air Development Center, Johnsville, Warminster, Pennsylvania

Environmental Measurements

SUCCESS AND FAILURE WITH PREDICTION AND SIMULATION OF AIRCRAFT VIBRATION
A. J. Curtis and N. G. Tinling, Hughes Aircraft Company, Culver City, California

PHOENIX ENVIRONMENTAL MEASUREMENTS IN F-111B WEAPONS BAY
T. M. Kiwior, R. P. Mandich and R. J. Oedy, Hughes Aircraft Company, Canoga Park, California

LUNAR ORBITER FLIGHT VIBRATIONS WITH COMPARISONS TO FLIGHT ACCEPTANCE REQUIREMENTS AND PREDICTIONS BASED ON A NEW GENERALIZED REGRESSION ANALYSIS
Sherman A. Clevenson, NASA Langley Research Center, Langley Station, Hampton, Virginia

VIBRATION AND ACOUSTIC ENVIRONMENT CHARACTERISTICS OF THE SATURN V LAUNCH VEHICLE
Clark J. Beck, Jr. and Donald W. Caba, The Boeing Company, Huntsville, Alabama

THE BLAST FIELD ABOUT THE MUZZLE OF GUNS
Peter S. Westine, Southwest Research Institute, San Antonio, Texas

SPECIFICATIONS: A VIEW FROM THE MIDDLE
T. B. Delchamps, Bell Telephone Laboratories, Inc., Whippany, New Jersey

STRUCTURAL ANALYSIS

MODAL DENSITIES OF SANDWICH PANELS: THEORY AND EXPERIMENT

Larry L. Erickson
Ames Research Center, NASA
Moffett Field, California 94035

Formulas are presented that can be used to estimate the average modal densities of sandwich beams and flat or cylindrically curved sandwich panels. Numerical results, presented in terms of general parameters, indicate the relative importance of transverse shear flexibility, orthotropic shear moduli of the core, face-bending stiffness, rotary inertia, and panel curvature over a wide frequency range. Modal densities determined experimentally from resonance tests of flat rectangular sandwich panels having orthotropic cores are close to the modal densities estimated by theory except at frequencies near that of the fundamental mode. In this low-frequency range, the theoretical estimates are not valid.

INTRODUCTION

There has been an effort during the past few years to develop a new approach to multimodal vibration problems that avoids the problem of expanding the response in terms of the mode shapes [1,2]. In this approach, sometimes referred to as "statistical energy analysis," average response levels in various frequency bands are estimated without knowledge of the mode shapes and resonance frequencies. Instead, what is required is a knowledge of the type (e.g., flexural) and number of structural vibration modes occurring in a given frequency interval. This quantity, the number of modes per unit frequency, is called the "modal density" of the structure.

Because the modal density of a structure is relatively independent of the boundary conditions, statistical energy analysis shows promise of becoming a useful tool for estimating average response levels of multimodal structural vibrations. For example, one of the more useful response quantities is acceleration spectral density, which is directly proportional to modal density.

Equations have been derived for the modal densities of several structural elements and can be found in Refs. [3] and [4]. A portion of the results in Ref. [4] pertains to flat and doubly curved sandwich panels, and it is shown that the transverse shear flexibility of such panels can have a significant effect on the modal density of the panel. However, the results of Ref. [4] apply only to sandwich panels with isotropic cores, whose faces behave as membranes (i.e., the face-bending stiffness is neglected). Since lightweight sandwich panels often have cores with orthotropic shear moduli (e.g., honeycomb), there is a practical need for being able to account for the effect of these moduli on the modal density. In addition, it is known from sandwich panel buckling theory that for small wavelengths of deformation the face-bending stiffness can become important [5].

In the present investigation, modal density estimates are obtained analytically for sandwich beams and for flat or cylindrically curved sandwich panels. The effects of the transverse shear flexibility of the core, including orthotropic shear moduli parallel to the faces, face-bending stiffness, and rotary inertia, are examined. Numerical results are presented in graphical form.

In addition, experimental results obtained from resonance tests of flat rectangular sandwich panels with orthotropic honeycomb cores are presented. In these tests, up to 80 consecutive vibration modes per panel were excited and identified. The experimentally determined modal densities are compared with the modal densities predicted by theory.

SYMBOLS

a	axial length of panel, in.
b	circumferential width of panel, in.

C curvature parameter, $\frac{1}{R}\frac{b^2}{\pi^2}\sqrt{\frac{E'}{D}}$

C_{eff} $\frac{C}{(\gamma)^{0.15}}$

D bending stiffness of panel, in.-lb, $\frac{E_f t_f h_c^2\left(1+\frac{t_f}{h_c}\right)^2}{2(1-\mu^2)}$

D_{Q_x}, D_{Q_y} transverse shear stiffnesses of panel, lb/in., $G_{c_x} h_c\left(1+\frac{t_f}{h_c}\right)^2$, $G_{c_y} h_c\left(1+\frac{t_f}{h_c}\right)^2$

$D_{Q_{eff}}$ $\sqrt{D_{Q_x} D_{Q_y}}$, lb/in.

E_f Young's modulus for isotropic faces of sandwich panel, lb/in.^{2}

E' extensional stiffness, lb/in., $2t_f E_f$

G_{c_x}, G_{c_y} orthotropic shear modulus of sandwich core in x and y directions, respectively, lb/in.^{2}

h_c thickness of sandwich core, in.

I mass density moment of inertia per unit width about the middle surface of the panel, lb-sec^2/in.

M mass density per unit area of panel, lb-sec^2/in.^{3}

N cumulative number of modes occurring below a specified frequency

R constant radius of curvature of panel, in.

r_x, r_y orthotropic shear-flexibility parameters; $\frac{\pi^2}{b^2}\frac{D}{D_{Q_x}}$, $\frac{\pi^2}{b^2}\frac{D}{D_{Q_y}}$

r_{eff} $\frac{\pi^2}{b^2}\frac{D}{D_{Q_{eff}}}$

t_f thickness of sandwich face sheets, in.

γ $\frac{D_{Q_x}}{D_{Q_y}} = \frac{G_{c_x}}{G_{c_y}}$

μ Poisson's ratio of face sheet material

ρ^2 $\left(\frac{m}{a/b}\right)^2 + n^2$

ρ_c mass density of core, lb-sec^2/in.^{4}

ρ_f mass density of face, lb-sec^2/in.^{4}

τ $\frac{1}{3}\left(\frac{\frac{t_f}{h_c}}{1+\frac{t_f}{h_c}}\right)^2$

χ rotary inertia parameter, $\frac{\pi^2}{b^2}\frac{I}{M}$

ω frequency, rad/sec

ω_o fundamental frequency of an infinitely long, simply supported flat panel as predicted by classical plate theory, rad/sec, $\frac{\pi^2}{b^2}\sqrt{D/M}$

Subscripts

c core of sandwich panel

eff effective value or quantity

f face of sandwich panel

THEORY AND ASSUMPTIONS

Panel

The coordinate system and geometry of the curved sandwich panel are shown in Fig. 1. The

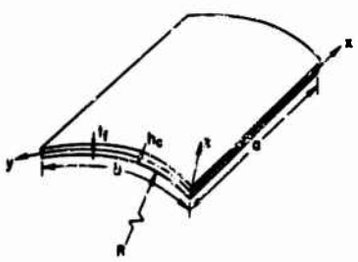


Fig. 1.- Panel geometry and coordinate system.

panel is of length a, circumferential width b, and has constant radius of curvature R. The two face sheets are of the same isotropic, homogeneous material and have equal uniform thicknesses t_f. The core may possess orthotropic shear moduli (G_{c_x}, G_{c_y}) and is of uniform thickness h_c.

The modal density estimates obtained herein are based on two frequency equations that relate

the panel natural frequencies (ω rad/sec) to various physical characteristics of the panel and to the number of half-waves m and n that form in the x and y directions, respectively. The first of these equations, derived from the theory of Ref. [6] (see appendix), is

$$\left[\left(\frac{\omega}{\omega_o}\right)^2 - \left(\frac{C}{\rho^2}\right)^2\left(\frac{m}{a/b}\right)^4\right]\left\{\left\{1 + r_x\left[\frac{1-\mu}{2}\rho^2 - \chi\left(\frac{\omega}{\omega_o}\right)^2\right]\right\}\left\{1 + r_y\left[\frac{1-\mu}{2}\rho^2 - \chi\left(\frac{\omega}{\omega_o}\right)^2\right]\right\} + \left(\frac{1+\mu}{2}\right)\left\{\left[\frac{1-\mu}{2}\rho^2 - \chi\left(\frac{\omega}{\omega_o}\right)^2\right]r_x r_y \mu^2 + r_x\left(\frac{m}{a/b}\right)^2 + r_y n^2\right\}\right] - \left[\rho^2 - \chi\left(\frac{\omega}{\omega_o}\right)^2\right] \times \left\{\rho^2 + \left[\frac{1-\mu}{2}\rho^2 - \chi\left(\frac{\omega}{\omega_o}\right)^2\right]\left[r_y\left(\frac{m}{a/b}\right)^2 + r_x n^2\right]\right\} = 0 \quad (1)$$

where $\rho^2 = [m/(a/b)]^2 + n^2$. In this equation, the physical and geometric properties of the panel are described by the following dimensionless quantities:

(a) the length-width ratio a/b,
(b) the curvature parameter C, which is proportional to $1/R$,
(c) the rotary inertia parameter χ, which is proportional to the mass density moment of inertia of the panel,
(d) the shear flexibility parameters r_x and r_y, which are proportional to $1/G_{c_x}$ and $1/G_{c_y}$, respectively.

The reference frequency ω_o is the fundamental frequency of a flat, simply supported panel with an infinite length ($a/b = \infty$) as predicted by classical plate theory (shoar and rotary inertia neglected) and μ is Poisson's ratio of the faces.

In Eq. (1), the bending stiffness of the faces about their middle surfaces has been neglected. The second frequency equation accounts for the face-bending stiffness but does not incorporate the effects of rotary inertia or curvature. This equation, obtained from Ref. [7], is

$$\left(\frac{\omega}{\omega_o}\right)^2 = \left[\left(\frac{m}{a/b}\right)^2 + n^2\right]^2\left[\tau + \frac{1}{1+\zeta}\right] \quad (2)$$

where

$$\tau = \frac{1}{3}\left(\frac{t_f/h_c}{1 + (t_f/h_c)}\right)^2 \quad (3)$$

and

$$\zeta = \frac{r_y}{\gamma}\left[\left(\frac{m}{a/b}\right)^2 + \gamma n^2\right]\frac{\left\{1 + \left(\frac{1-\mu}{2}\right)r_y\frac{\left[\left(\frac{m}{a/b}\right)^2 + n^2\right]^2}{\left(\frac{m}{a/b}\right)^2 + \gamma n^2}\right\}}{\left\{1 + \left(\frac{1-\mu}{2}\right)r_y\left[\left(\frac{m}{a/b}\right)^2 + \frac{n^2}{\gamma}\right]\right\}} \quad (4)$$

The quantity τ is due to the face-bending stiffness and ζ is due to the orthotropic shear flexibilities of the core, characterized by the ratio $\gamma = G_{c_x}/G_{c_y}$. It should be noted that Eqs. (1) and (2) are identical when the effects of rotary inertia, curvature, and face-bending stiffness are simultaneously neglected ($\chi = C = \tau = 0$).

The basic assumptions made in the theories upon which Eqs. (1) and (2) are based are:

(a) linear, elastic behavior of core and faces,
(b) the transverse deflection of the panel is comprised of deformations due to both transverse shearing forces and bending moments,
(c) the bending stiffness of the core is negligible compared to the overall bending stiffness of the panel. This allows the panel's flexural deformations to be described by an isotropic bending stiffness D,
(d) transverse shear strains in the faces and all normal strains in the z direction are neglected,
(e) the cores are homogeneous. Thus, for cellular-type cores such as honeycomb, the wavelengths of vibration must be at least several times the cell size.

Although the natural frequencies predicted by Eqs. (1) and (2) are valid only for simply supported panels, the equations for modal density are applicable to panels having other boundary conditions, because once the frequency range of the lowest several modes is exceeded the boundary conditions generally have a negligible effect on the number of modes existing in a given frequency interval. This has been observed experimentally for flat panels and cylindrical shells that were essentially rigid in shear.[8-10] For mathematical arguments, see Refs. [11] and [12].

Modal Density Formulation

For a given panel configuration (a/b, C, χ, r_x, r_y, τ, and ω_o fixed), Eq. (1) or (2) represents a set of constant frequency curves in the $[m/(a/b)] - n$ plane. A typical curve is

illustrated in Fig. 2. Each combination of m and n represents the only mode that occurs in

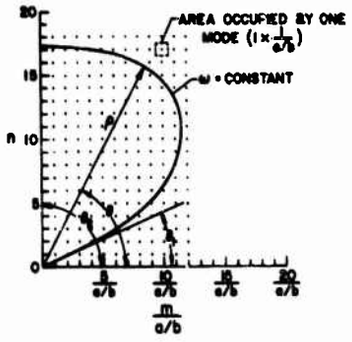


Fig. 2.- Modes bounded by a constant frequency curve.

an area $1[1/(a/b)]$ in the first quadrant of the $[m/(a/b)]$ - n plane. The total area occupied by the N modes bounded by the curve ω = constant is approximately $N[1/(a/b)]$. This area is also given approximately by $(1/2)\int_{\theta_1}^{\theta_2} \rho^2(\omega,\theta)d\theta$, where θ is defined in Fig. 2 and $\rho^2 = [m/(a/b)]^2 + n^2$ is determined in terms of ω and θ from Eq. (1) or (2). The limits of integration are such that ρ^2 is real and positive. The approximate number of modes existing below the specified frequency ω = constant is then expected to be asymptotically equal to [11]

$$N = \frac{1}{2}\frac{a}{b}\int_{\theta_1}^{\theta_2} \rho^2(\omega,\theta)d\theta$$

The average number of modes ΔN existing in a frequency band $\Delta\omega$, about the center frequency ω, defines the average modal density, which is

$$\frac{\Delta N}{\Delta\omega} = \frac{dN}{d\omega} = \frac{1}{2}\frac{a}{b}\left[\int_{\theta_1}^{\theta_2} \frac{\partial\rho^2(\omega,\theta)}{\partial\omega}\,d\theta + \rho^2(\omega,\theta_2)\frac{d\theta_2}{d\omega} - \rho^2(\omega,\theta_1)\frac{d\theta_1}{d\omega}\right] \qquad (5)$$

For the panel configurations considered herein, the last two terms in Eq. (5) are zero. For comparison with the frequency-independent flat-plate modal density predicted by classical plate theory, i.e., $dN/d(\omega/\omega_o) = (\pi/4)(a/b)$ [12], the estimates of sandwich panel modal density presented here are expressed in the form

$$\frac{1}{\frac{\pi}{4}\frac{a}{b}}\frac{dN}{d\left(\frac{\omega}{\omega_o}\right)} = \frac{2}{\pi}\int_{\theta_1}^{\theta_2} \frac{\partial\rho^2\left(\frac{\omega}{\omega_o},\theta\right)}{\partial\left(\frac{\omega}{\omega_o}\right)}\,d\theta \qquad (6)$$

From the results that follow, it can be noted that the right-hand side of Eq. (6) is independent of the panel length and width. These lateral dimensions appear only on the left-hand side of the equation, and since the term $(a/b)(1/\omega_o)$ is proportional to the product (ab) the modal density is directly proportional to the surface area of the panel. Although Eqs. (1) and (2) were derived on the basis of a rectangular planform, the modal densities obtained from them can apparently be applied to panels with other shapes, having a surface area S, by replacing the rectangular area (ab) with the area S [12].

ANALYSIS

To calculate the modal density from Eq. (6) requires that $\partial\rho^2/\partial(\omega/\omega_o)$ be expressed analytically as a function of ω and θ. Unfortunately, ρ^2 appears as a cubic and a quartic term in Eqs. (1) and (2), respectively, and is not readily obtained analytically. However, for the isotropic core ($r_x = r_y = r$), Eqs. (1) and (2) can be solved exactly for $\partial\rho^2/\partial(\omega/\omega_o)$. This is done in the following sections. It is then shown, by neglecting the face-bending stiffness, that the isotropic results can be applied to panels with moderately orthotropic cores by use of "effective" shear flexibility and curvature parameters. Finally, an approximate solution is obtained for a flat panel, which gives the combined effect of orthotropic shear moduli and face-bending stiffness.

Flat Panel With Isotropic Core

Combined Effect of Shear Flexibility and Rotary Inertia - This case is obtained from Eq. (1) by setting $\chi = 0$ and $r_x = r_y = r$, which results in

$$2\rho^2 = (r+\chi)\left(\frac{\omega}{\omega_o}\right)^2 + \sqrt{\left[(r+\chi)\left(\frac{\omega}{\omega_o}\right)^2\right]^2 + 4\left(\frac{\omega}{\omega_o}\right)^2\left[1 - r\chi\left(\frac{\omega}{\omega_o}\right)^2\right]} \qquad (7)$$

For the bending set of modes. Since ρ^2 is independent of θ (i.e., ω = constant is a circle in the $[m/(a/b)]$ - n plane), the limits of integration in Eq. (6) are $\theta_1 = 0$ and $\theta_2 = \pi/2$. Performing the integration yields the following estimate for the modal density of a flat sandwich panel with an isotropic core:

$$\frac{1}{\frac{\pi}{4}\frac{a}{b}}\frac{dN}{d\left(\frac{\omega}{\omega_o}\right)} = \left(1+\frac{\chi}{r}\right)\left(r\,\frac{\omega}{\omega_o}\right) + \frac{1+\frac{1}{2}\left(1-\frac{\chi}{r}\right)^2\left(r\,\frac{\omega}{\omega_o}\right)^2}{\sqrt{1+\frac{1}{4}\left(1-\frac{\chi}{r}\right)^2\left(r\,\frac{\omega}{\omega_o}\right)^2}} \qquad (8)$$

The variation in modal density with $r(\omega/\omega_o)$, as given by Eq. (8), is shown in Fig. 3

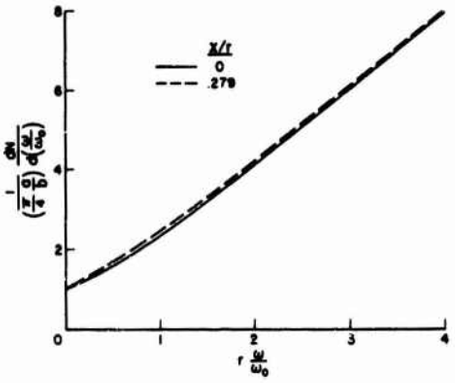


Fig. 3.- Effect of shear flexibility and rotary inertia on the modal density of a flat sandwich panel; isotropic core, face-bending stiffness neglected.

for $\gamma = 0$ (i.e., rotary inertia neglected) and $\chi/r = 0.279$. For $r = 0$ (infinite shear stiffness), the frequency-independent, classical plate value for modal density is obtained. When shear flexibility is not neglected ($r > 0$), the modal density increases with increasing frequency and with increasing shear flexibility. The value $\chi/r = 0.279$ corresponds to the extreme case of a solid panel, whereas $\chi/r < 0.1$ is more typical of sandwich panel construction. Since the two curves in Fig. 3 differ at most by about 6 percent, it is concluded that for the small values of χ/r usually encountered in sandwich panels the effect of rotary inertia on the modal density is negligible in comparison to the effect of shear flexibility.

The curves given by Eq. (8) are asymptotic to the curve

$$\frac{1}{\frac{\pi}{4}\frac{a}{b}}\frac{dN}{d\left(\frac{\omega}{\omega_o}\right)} = 2\left(r\,\frac{\omega}{\omega_o}\right) \qquad (9)$$

and for $r(\omega/\omega_o) \geq 3$ this straight line approximates the solid curve of Fig. 3 to within 1 percent. However, Eq. (9) implies that the modal density ($\Delta N/\Delta\omega$) becomes independent of the face material properties at large values of $r(\omega/\omega_o)$. This physically unrealistic result arises because Eq. (8) does not account for the bending stiffness of the panel faces.

Combined Effect of Shear Flexibility and Face-Bending Stiffness - In view of the results of the previous section, it is assumed here that rotary inertia can be neglected. Eq. (2) can then be used to determine the effect of face-bending stiffness on the modal density. For an isotropic core, Eq. (2) can be written as

$$r\,\frac{\omega}{\omega_o} = r\rho^2\sqrt{\tau + \frac{1}{1 + r\rho^2}} \qquad (10)$$

which is independent of θ. Use of Eq. (6) yields

$$\frac{1}{\frac{\pi}{4}\frac{a}{b}}\frac{dN}{d\left(\frac{\omega}{\omega_o}\right)} = \frac{1}{\left[\frac{\partial\,(\omega/\omega_o)}{\partial\rho^2}\right]}$$

$$= \frac{\sqrt{1 + r\rho^2}}{\sqrt{1 + \tau(1 + r\rho^2)}\left\{1 - \frac{r\rho^2}{2(1 + r\rho^2)[1 + \tau(1 + r\rho^2)]}\right\}} \qquad (11)$$

for the estimate of modal density. The variation in modal density with $r(\omega/\omega_o)$ is obtained from Eqs. (10) and (11) by treating the face-to-core-thickness ratio t_f/h_c as a parameter and the quantity $r\rho^2$ as a variable. This variation is shown in Fig. 4 for various values of

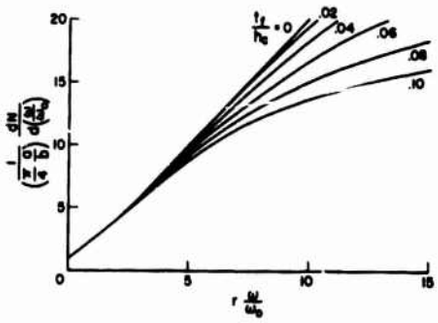


Fig. 4.- Effect of shear flexibility and face-bending stiffness on the modal density of a flat sandwich panel; isotropic core, rotary inertia neglected.

t_f/h_c. Neglecting the face-bending stiffness ($t_f/h_c = 0$ curve) leads to an overestimate of the modal density by an amount that increases with increasing frequency and with increasing ratios of face-to-core thickness. However, for many sandwich configurations, t_f/h_c is on the order of 0.1 or less and often the quantity r/ω_o is so small that a frequency of several thousand Hertz is required to produce a value of $r(\omega/\omega_o)$ on the order of 1.0. Thus, there are many practical situations where the face-bending stiffness can be neglected when computing the modal density.

For those cases where the face-bending stiffness should be taken into account, the following simple equation is useful:

$$\frac{1}{\frac{\pi}{4}\frac{a}{b}}\frac{dN}{d\left(\frac{\omega}{\omega_o}\right)} = \frac{2r\,\frac{\omega}{\omega_o}}{\sqrt{1+\frac{1}{3}\left[\frac{t_f/h_c}{1+(t_f/h_c)}\right]^2\left(2r\,\frac{\omega}{\omega_o}\right)^2}} \qquad (12)$$

For $r(\omega/\omega_o) \geq 3$ and $t_f/h_c \leq 0.2$, this result predicts values of the modal density within about 1 percent of the values given by the exact solution. (Eq. (12) is obtained from Eqs. (10) and (11) by taking $rp^2 >> 1$.)

Sandwich Beam

The bending set of modes for a beam can be obtained from the equations describing the bending modes of the panel by setting the $m/(a/b)$ terms equal to zero. The modal density is then simply obtained from $dN/d(\omega/\omega_o) = dn/d(\omega/\omega_o)$.

Combined Effect of Shear Flexibility and Rotary Inertia - This case is obtained by setting $m/(a/b) = 0$ in Eq. (7). Differentiating with respect to ω/ω_o yields

$$\frac{dN}{d\left(\frac{\omega}{\omega_o}\right)} = \frac{\left(1+\frac{\chi}{r}\right)\left(r\,\frac{\omega}{\omega_o}\right) + \frac{2+\left(1-\frac{\chi}{r}\right)^2\left(r\,\frac{\omega}{\omega_o}\right)^2}{\sqrt{4+\left(1-\frac{\chi}{r}\right)^2\left(r\,\frac{\omega}{\omega_o}\right)^2}}}{\sqrt{2\left(\frac{\omega}{\omega_o}\right)}\sqrt{\left(1+\frac{\chi}{r}\right)\left(r\,\frac{\omega}{\omega_o}\right)+\sqrt{4+\left(1-\frac{\chi}{r}\right)^2\left(r\,\frac{\omega}{\omega_o}\right)^2}}} \qquad (13)$$

The variation in modal density with frequency, given by Eq. (13), is shown in Fig. 5

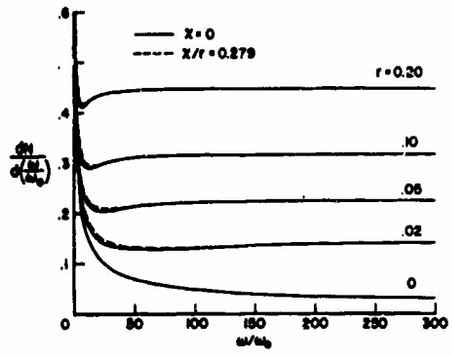


Fig. 5.- Effect of shear flexibility and rotary inertia on the modal density of a sandwich beam; face-bending stiffness neglected.

for various values of the shear flexibility parameter, r, and for two values of χ/r. As for panels, realistic values of χ/r give essentially the same results as $\chi = 0$ (rotary inertia neglected). The $r = \chi = 0$ curve corresponds to classical beam theory, which predicts that modal density decreases with increasing frequency. When shear flexibility is accounted for ($r > 0$), Eq. (13) predicts that the beam modal density is nearly constant over a wide frequency range. However, this result is valid only for conditions where the face-bending stiffness is unimportant.

Combined Effect of Shear Flexibility and Face-Bending Stiffness - If rotary inertia is neglected, Eq. (10) can be used to determine the effect of the face-bending stiffness on the modal density of a beam by letting $m/(a/b) = 0$. The result is

$$\frac{\omega}{\omega_o} = n^2\sqrt{\tau + \frac{1}{1+rn^2}} \qquad (14)$$

$$\frac{dN}{d\left(\frac{\omega}{\omega_o}\right)} = \frac{1}{\frac{d(\omega/\omega_o)}{dn}} = \frac{\sqrt{1+rn^2}}{2n\sqrt{1+\tau(1+rn^2)}\left\{1-\frac{rn^2}{2(1+rn^2)[1+\tau(1+rn^2)]}\right\}} \qquad (15)$$

The variation in modal density with frequency as given by Eqs. (14) and (15) is shown in Fig. 6 for several values of r and

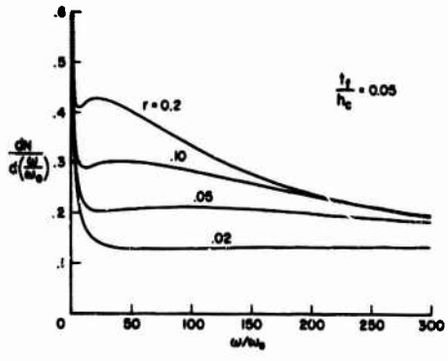


Fig. 6.- Effect of shear flexibility and face-bending stiffness on the modal density of a sandwich beam; rotary inertia neglected.

with a face-to-core-thickness ratio of 0.05. Comparison of the curves in Fig. 6 with the corresponding curves in Fig. 5 reveals that neglecting the face-bending stiffness again leads to an overestimate of the modal density by an amount that increases with increasing frequency. The face-bending stiffness is also seen to have a

smaller effect on beams with stiff cores (small r) than on beams with more flexible cores (larger r).

Figs. 5 and 6 both indicate a large rise in modal density as ω/ω_o approaches zero. However, it must be remembered that the equations presented for modal density are estimates that have been obtained by representing the number of modes by a continuous function of frequency. This representation is not really meaningful at frequencies near that of the fundamental mode ($\omega/\omega_o \approx 1$) as there are usually too few modes involved. Thus, the large rise in modal density as $\omega/\omega_o \to 0$ is physically unrealistic. A similar situation occurs in the modal density estimates for curved panels.

Curved Sandwich Panel With Isotropic Core

If the parameter C is retained in Eq. (1), the effects of panel curvature can be determined. For an isotropic core ($r = r_x = r_y$), the bending set of modes is described by

$$2\rho^2 = (r + \chi)\left(\frac{\omega}{\omega_o}\right)^2 - rC^2\cos^4(\theta) + \sqrt{\left[(r-\chi)\left(\frac{\omega}{\omega_o}\right)^2 - rC^2\cos^4(\theta)\right]^2 + 4\left[\left(\frac{\omega}{\omega_o}\right)^2 - C^2\cos^4(\theta)\right]} \qquad (16)$$

The modal density is then given by

$$\frac{1}{\frac{\pi}{4}\frac{a}{b}}\frac{dN}{d\left(\frac{\omega}{\omega_o}\right)} = \frac{2}{\pi}\left[\left(1 + \frac{\chi}{r}\right)\left(r\,\frac{\omega}{\omega_o}\right)\left(\frac{\pi}{2} - \theta_1\right) + \int_{\theta_1}^{\pi/2} \frac{2 + \left(\alpha - \frac{\chi}{r}\right)\left(1 - \frac{\chi}{r}\right)\left(r\,\frac{\omega}{\omega_o}\right)^2}{\sqrt{4\alpha + \left(\alpha - \frac{\chi}{r}\right)^2\left(r\,\frac{\omega}{\omega_o}\right)^2}}\,d\theta\right] \qquad (17)$$

where

$$\alpha = 1 - [C/(\omega/\omega_o)]^2\cos^4(\theta)$$

with

$$\theta_1 = \cos^{-1}\left\{\left(\frac{\frac{\omega}{\omega_o}}{C}\right)^2\left(1 - \frac{\chi}{r}\right) + \frac{2}{(rC)^2}\left[1 - \sqrt{1 - \left(r\,\frac{\omega}{\omega_o}\sqrt{\frac{\chi}{r}}\right)^2}\right]\right\}^{1/4}$$

if

$$r\,\frac{\omega}{\omega_o}\sqrt{\frac{\chi}{r}} \le 1$$

and

$$\left(\frac{\frac{\omega}{\omega_o}}{C}\right)^2\left(1 - \frac{\chi}{r}\right) + \frac{2}{(rC)^2}\left[1 - \sqrt{1 - \left(r\,\frac{\omega}{\omega_o}\sqrt{\frac{\chi}{r}}\right)^2}\right] \le 1$$

are both satisfied; otherwise $\theta_1 = 0$.

When $\chi = r = 0$ (rotary inertia and shear flexibility neglected) Eq. (17) can be expressed in terms of the complete elliptic integral of the first kind [11]. For nonzero values of χ and r, Eq. (17) can be expressed as a hyperelliptic integral. Although some hyperelliptic integrals can be reduced to the sum of elliptic integrals, no such attempt was made here; instead, the results presented here were obtained by numerically integrating Eq. (17). These results are presented in Fig. 7 where the

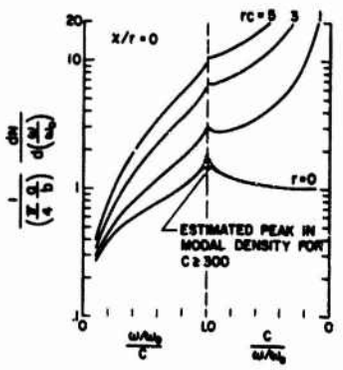


Fig. 7.- Modal densities of cylindrically curved sandwich panels; isotropic core, face-bending stiffness neglected.

variation in modal density with $(\omega/\omega_o)/C$ is shown for various values of the product rC. The numerical results shown in Fig. 7 are all for $\chi = 0$ (rotary inertia neglected). However, in view of the relatively insignificant effect of rotary inertia on the modal densities of the beam and flat panel, it is likely that the curves in Fig. 7 would be only slightly altered by realistic values of χ/r.

Since Eq. (17) does not account for the face-bending stiffness, it undoubtedly overestimates the modal density at the larger values of $r(\omega/\omega_o)$. (The curves in Fig. 7 correspond to $0 \le r(\omega/\omega_o) \le 10$.) To gain an idea of the error involved for various combinations of $r(\omega/\omega_o)$ and t_f/h_c, Fig. 4 should be examined.

Except for $r = 0$, Fig. 7 obscures the fact that when ω/ω_o exceeds C the curved panel modal density becomes asymptotic to that of the corresponding flat panel ($C = 0$). This behavior can be seen more clearly by replotting Fig. 7 in terms of ω/ω_o for a fixed value of r and for various values of $C \ge 0$ or by comparing Eqs. (8) and (17).

The peaks in modal density about $\omega/\omega_c = C$ (the so-called ring frequency) are due to a concentration of modes occurring near this frequency and is most pronounced for $r = 0$. However, the sharp spike is due to the singularity in Eq. (17) at $\omega/\omega_o = C$ (when $\chi = 0$) and is physically unrealistic. A truer estimate for the peaks in modal density about the ring frequency can be obtained by directly calculating the number of curved panel modes, ΔN_C, occurring there from the frequency equation:

$$\left(\frac{\omega}{\omega_o}\right)^2 = \frac{\left[\left(\frac{m}{a/b}\right)^2 + n^2\right]^2}{1 + r\left[\left(\frac{m}{a/b}\right)^2 + n^2\right]} + \frac{C^2\left(\frac{m}{a/b}\right)^4}{\left[\left(\frac{m}{a/b}\right)^2 + n^2\right]^2} \tag{18}$$

(Eq. (18) is obtained from Eq. (16).)

For $r = 0$, the results of such calculations for the interval $0.95\ C < \omega/\omega_o < 1.05\ C$ are presented in Table 1 for various degrees of curvature (a/b was taken equal to $4/\pi$). The number of modes ΔN_F that the corresponding flat panel has in the same frequency interval is also shown for comparison. For $300 \leq C \leq 1000$, the actual peak in curved panel modal density is about 1-1/2 times that of the flat panel value (indicated in Fig. 7 by the dashed curve). For $75 \leq C < 300$, a somewhat smaller increase is evident. For C less than about 50, the effect of curvature is so small that the panel essentially behaves as if it were flat.

Effect of Orthotropic Core Shear Moduli

If the effects of rotary inertia and face-bending stiffness are neglected, the equation governing ρ^2 for a curved sandwich panel having an orthotropic core is obtained from Eq. (1) by setting $\chi = 0$. This yields

$$\left[1 + \frac{1-\mu}{2}\frac{r_y}{\gamma}\rho^2\right]\left\{\rho^4 - \left[\left(\frac{\omega}{\omega_o}\right)^2 - C^2\cos^4(\theta)\right]\left(1 + r_y\rho^2\right)\right\}$$

$$+ r_y\left(\frac{\gamma-1}{\gamma}\right)\left\{\frac{1-\mu}{2}\rho^4 + \left[\left(\frac{\omega}{\omega_o}\right)^2\right.\right.$$

$$\left.\left. - C^2\cos^4(\theta)\right]\left[1 - \frac{1-\mu}{2}\right]\right\}\rho^2\cos^2(\theta) = 0 \tag{19}$$

Except when $\gamma = 1$ (isotropic core), Eq. (19) is cubic in ρ^2 and no attempt is made to solve it in this form. However, a clue to the effect of γ can be obtained by considering the conditions

$$\left.\begin{aligned} \frac{r_y\rho^2}{\gamma} &>> 1 \quad \text{for } \gamma > 1 \\ r_y\rho^2 &>> 1 \quad \text{for } \gamma < 1 \end{aligned}\right\} \tag{20}$$

which imply that

$$\left(\frac{r_y}{\sqrt{\gamma}}\frac{\omega}{\omega_o}\right)^2\left\{1 - [C/(\omega/\omega_o)]^2\cos^4(\theta)\right\} >> 1$$

Under these conditions,

$$\rho^2 = \frac{r_y\left[\left(\frac{\omega}{\omega_o}\right)^2 - C^2\cos^4(\theta)\right]}{\gamma\left(1 - \frac{\gamma-1}{\gamma}\sin^2(\theta)\right)} \tag{21}$$

Substituting into Eq. (6) and noting that $\theta_1 = 0$ and $\theta_2 = \pi/2$ yields

$$\frac{1}{\frac{\pi}{4}\frac{a}{b}}\frac{dN}{d\left(\frac{\omega}{\omega_o}\right)} = 2\left(\frac{r_y}{\sqrt{\gamma}}\right)\left(\frac{\omega}{\omega_o}\right) \tag{22}$$

which is valid only for the conditions stated just prior to Eq. (21). Comparison of this result with Eq. (9) suggests that the isotropic results can perhaps be applied to panels with orthotropic cores by replacing r with an effective shear-flexibility parameter $r_{eff} = r_y/\sqrt{\gamma}$. However, it is also likely that C will have to be replaced with an effective curvature parameter since Eq. (22) is not valid where the effects of curvature are most pronounced ($\omega/\omega_o \leq C$).

This idea was examined by solving Eq. (19) for ω/ω_o in terms of m and n.

$$\left(\frac{\omega}{\omega_c}\right)^2 = \frac{\left[\left(\frac{m}{a/b}\right)^2 + n^2\right]^2}{1 + \zeta} + \frac{C^2\left(\frac{m}{a/b}\right)^4}{\left[\left(\frac{m}{a/b}\right)^2 + n^2\right]^2} \tag{23}$$

where ζ is the same as in Eq. (4). For specified values of a/b, r_y, γ, and C, the number of modes N existing below any frequency ω/ω_o can be calculated and a plot of N vs. ω/ω_o is readily constructed. The possibility of duplicating this plot (and hence the modal density) by calculating N from the isotropic frequency equation (Eq. (18)) with r replaced by some r_{eff} and with C replaced by some C_{eff} was then considered, i.e., from

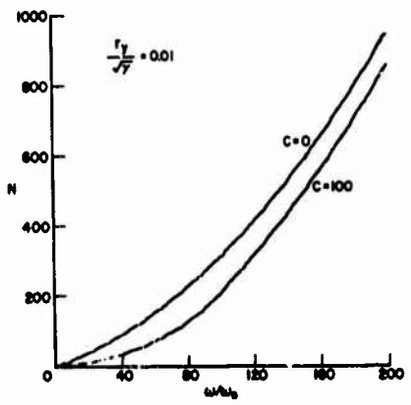
$$\left(\frac{\omega}{\omega_o}\right)^2 = \frac{\left[\left(\frac{m}{a/b}\right)^2 + n^2\right]^2}{1 + r_{eff}\left[\left(\frac{m}{a/b}\right)^2 + n^2\right]} + \frac{C_{eff}^2\left(\frac{m}{a/b}\right)^4}{\left[\left(\frac{m}{a/b}\right)^2 + n^2\right]^2} \tag{24}$$

Values for γ from 0.4 to 2.5 (representative of honeycomb cores) were considered for $1 \leq a/b \leq 2.55$, $r_y/\sqrt{\gamma}$ up to 0.125, and C up

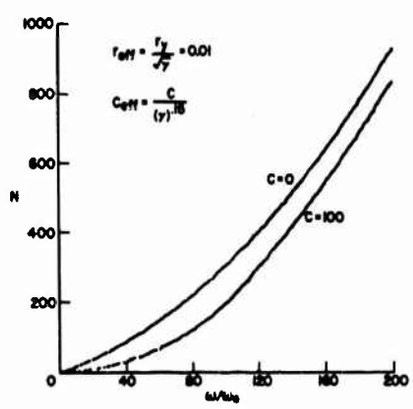
to 400. In each case, the plots of N vs. ω/ω_o obtained from Eq (23) were duplicated, within about 5 percent or less, by Eq. (24) if r_{eff} and C_{eff} were taken as

$$\left.\begin{aligned} r_{eff} &= \frac{r_y}{\sqrt{\gamma}} = \frac{\pi^2}{b^2}\frac{D}{\sqrt{D_{Q_x} D_{Q_y}}} \\ C_{eff} &= \frac{C}{(\gamma)^{0.15}} \end{aligned}\right\} \qquad (25)$$

Typical results are shown in Figs. 8(a) and 8(b). Fig. 8(a) shows exact plots of N vs. ω/ω_o for C = 0 and 100 with $r_y = 0.00707$, $\gamma = 1/2$, and a/b = 2.55. The corresponding plots obtained from Eq. (24) with r_{eff} and C_{eff} defined by Eqs. (25) are shown in Fig. 8(b).



(a) Exact; Eq. (23).

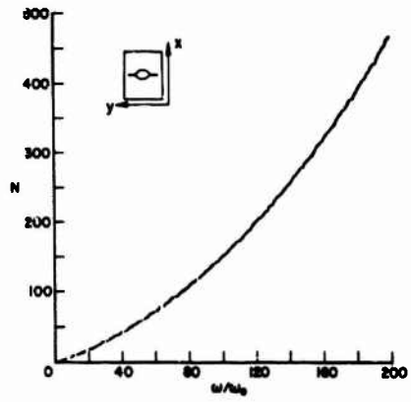


(b) Empirical; Eq. (24).

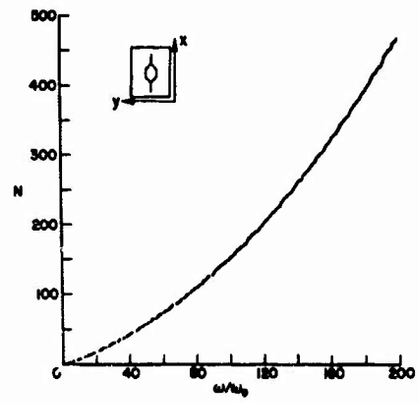
Fig. 8.- Comparison of cumulative number of modes for sandwich panels having orthotropic cores as predicted by exact and empirical frequency equations; rotary inertia and face-bending stiffness neglected, a/b = 2.55, $\gamma = 0.5$.

The form of Eq. (24) is exactly the same as Eq. (18). Thus, when the effects of rotary inertia and face-bending stiffness are small, the modal density estimates obtained for panels with isotropic cores appear to be applicable to panels with orthotropic cores such as honeycomb by simply replacing r and C with the quantities r_{eff} and C_{eff}, respectively, defined by Eqs. (25). Note that the "effective" shear stiffness is the geometric mean of the two orthotropic stiffnesses.

Another check on the validity of this empirical approach is that for a flat panel, Eqs. (24) and (25) predict that the variation in N with ω/ω_o is unaffected by a 90° core rotation. This is verified by using Eq. (23) (the exact equation) to show that, for $0.4 \leq \gamma \leq 2.5$, plots of N vs. ω/ω_o are indeed unaffected by such a rotation. A typical example is shown in Figs. 9(a) and 9(b). Fig. 9(a) is for a flat



(a) $\gamma = 0.5$



(b) $\gamma = 2.0$

Fig. 9.- Comparison of cumulative number of modes for two flat sandwich panels which have orthotropic cores differing in orientation by 90°; rotary inertia and face-bending stiffness neglected, a/b = 1.27, $r_y/\sqrt{\gamma} = 0.01$.

panel (C = 0) with $r_y = 0.00707$, $\gamma = 1/2$, and $a/b = 1.27$. Fig. 9(b) corresponds to the same flat panel but with the core rotated 90° ($r_y = 0.01414$, $\gamma = 2$). The resulting curves of N vs. ω/ω_o are virtually identical.

In the case of a flat panel, an approximate solution giving the combined effect of orthotropic core shear moduli and face-bending stiffness on the modal density can be obtained by neglecting certain terms in Eq. (2). For $[r_{eff}(\omega/\omega_o)]^2 >> 1$, the conditions given by Eqs. (20) are satisfied and by order of magnitude considerations Eq. (2) then simplifies to

$$r_y \tau \rho^4 + [1 + (\gamma - 1)\cos^2(\theta)]\rho^2 - r_y\left(\frac{\omega}{\omega_o}\right)^2 = 0 \tag{26}$$

Solving for ρ^2 and substituting into Eq. (6) leads to the following approximate equation for the modal density:

$$\frac{1}{\frac{\pi}{4}\frac{a}{b}} \frac{dN}{d\left(\frac{\omega}{\omega_o}\right)} = \left(2r_{eff}\frac{\omega}{\omega_o}\right)\beta^{1/4}\frac{K(k)}{\frac{\pi}{2}} \tag{27}$$

where

$$\beta = \frac{\gamma}{\left[1 + \gamma\tau\left(2r_{eff}\frac{\omega}{\omega_o}\right)^2\right]\left[\gamma + \tau\left(2r_{eff}\frac{\omega}{\omega_o}\right)^2\right]}$$

$$2k^2 = 1 - \left[1 + \tau\left(2r_{eff}\frac{\omega}{\omega_o}\right)^2\right]\sqrt{\beta}$$

and K(k) is the complete elliptic integral of the first kind.

The only terms in Eq. (27) that involve the orthotropic shear moduli are β and r_{eff}. Both terms, and therefore the modal density given by Eq. (27), are unaffected by a 90° rotation of the core. This is shown in Fig. 10 by the

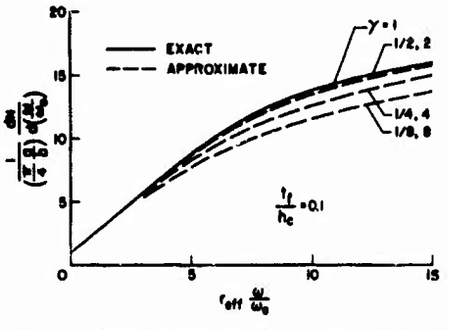


Fig. 10.- Combined effect of orthotropic core shear moduli and face-bending stiffness on the modal density of a flat sandwich panel; rotary inertia neglected.

dashed curves labeled $\gamma = 1/2$ or 2, $\gamma = 1/4$ or 4, and $\gamma = 1/3$ or 8. The solid curve is for an isotropic core ($\gamma = 1$) and is obtained from the exact solution (Eq. (11)). All the curves shown in Fig. 10 are for a face-to-core-thickness ratio of $t_f/h_c = 1/10$.

Note that Eq. (27) depends on both $\sqrt{D_{Q_x}D_{Q_y}}$ and $\gamma = D_{Q_x}/D_{Q_y}$. Only when the face-bending stiffness is negligible can the effect of an orthotropic core on the modal density of a flat panel be described solely in terms of the effective shear stiffness:

$$D_{Q_{eff}} = \sqrt{D_{Q_x}D_{Q_y}}$$

For $\gamma = 1$ (isotropic core), Eq. (27) reduces to Eq. (12). This suggests that for the moderately small range of γ usually encountered in honeycomb cores ($0.4 < \gamma < 2.5$), Eq. (27) should be fairly accurate if $t_f/h_c \leq 0.2$ and $r_{eff}(\omega/\omega_o) \geq 3$ are both satisfied.

EXPERIMENT

Very little experimental data are available in the literature on the mode shapes and natural frequencies of vibrating sandwich panels, especially for frequencies substantially above that of the fundamental mode. Although about 35 modes were excited in each of the two panels tested in Ref. [7], the panel configurations and frequency range were such that the maximum value obtained for $r_{eff}(\omega/\omega_o)$ was about 0.25. At this small value of $r_{eff}(\omega/\omega_o)$, the shear flexibility of the core has a relatively small effect, theoretically, on the modal density (see Fig. 3). Thus, it was necessary to conduct some experiments that would cover a higher range in $r_{eff}(\omega/\omega_o)$ for obtaining results that could be compared with theory.

Apparatus

Sandwich Panels - The specimens tested consisted of four flat, rectangular sandwich panels of aluminum honeycomb cores bonded to stainless-steel face sheets with a structural adhesive. The effective length and width of each panel (measured between the boundaries of the panel support fixture) was a = 28.5 in. and b = 24.0 in., respectively. Table 2 lists the pertinent core and face properties along with the resulting panel parameters. The weight of the bonding material was lumped with the weight of the faces to produce an effective face density called $(\rho_f)_{eff}$. Values of the core shear moduli were calculated from the theoretical equations of Ref. [13].

Support and Excitation System - The panel mounting fixture consisted of two aluminum frames bolted to the outer 3 inches of the panel perimeter to provide a partially clamped edge condition. To prevent crushing of the [illegible], the outer 3 inches of the honeycomb cells was filled with a liquid aluminum potting material. The panel was excited from below by a small (25-lb force) permanent magnet shaker. The shaker was

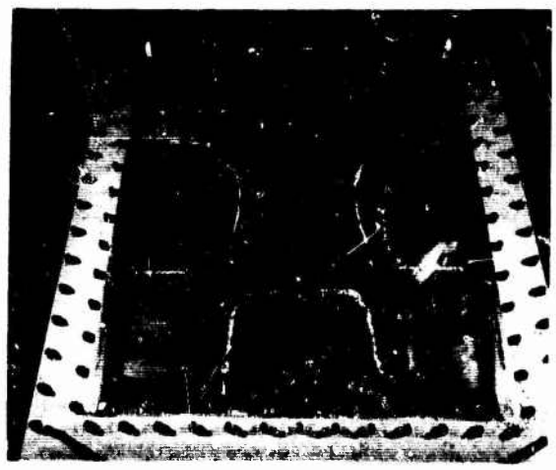
coupled to the panel surface by means of a small vacuum attachment to avoid the fastening of attachment points to the panel. This arrangement proved to be quite satisfactory for transmitting motion to the panel and it allowed the excitation point to be easily changed.

Test Procedure

For each panel, between 70 and 80 consecutive modes of vibration were excited by varying the frequency and location of the applied excitation. The mode shape at each resonance was visualized by the formation of Chladni figures produced by the collection of sand particles along node lines. A few of these sand patterns are shown in Fig. 11.

Test Results

Frequencies are given in Table 3 for the four test panels, corresponding to the maximum resonance response for the modes listed. The mode number m in the x direction (n in the y direction) indicates m - 1 (n - 1) lines of zero deflection between the panel boundaries x = 0 (y = 0) and x = a (y = b).



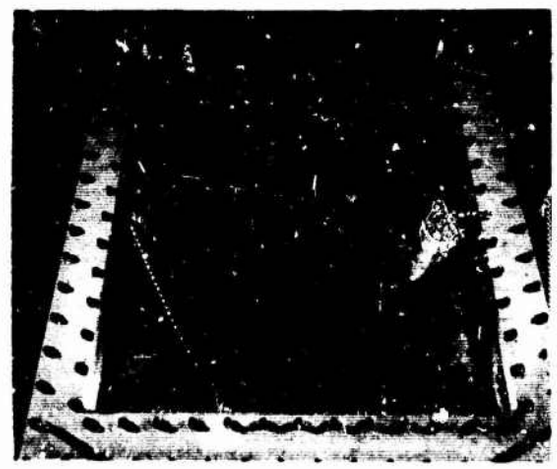
(a) Mode (3,3) - 1260 Hz.



(c) Mode (5,6) - 2630 Hz.



(b) Mode (4,4) - 1780 Hz.

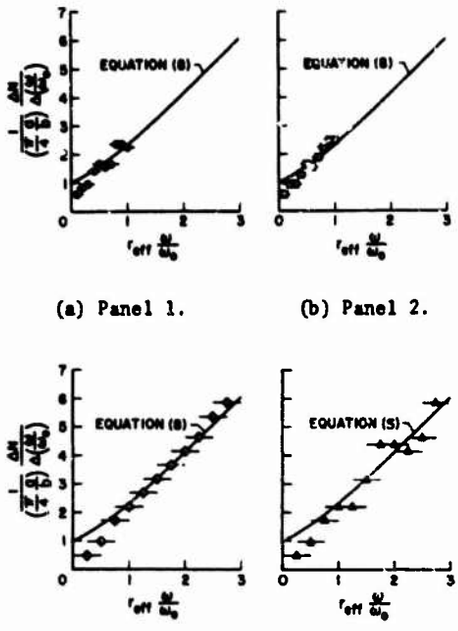


(d) Mode (8,6) - 3240 Hz.

Fig. 11.- Some Chladni figures on panel number 4 showing modes (m,n).

COMPARISON OF THEORY AND EXPERIMENT

The experimental values of $\frac{1}{\frac{\pi}{4}\frac{a}{b}} \frac{\Delta N}{\Delta\left(\frac{\omega}{\omega_0}\right)}$ and their variation with $r_{eff}(\omega/\omega_0)$ are shown in Figs. 12(a) and 12(b) for panels 1 and 2, respectively, and in Figs. 12(c) and 12(d) for panels 3 and 4, respectively. The horizontal lines indicate the intervals of $r_{eff}(\omega/\omega_0)$ used to compute the corresponding data points. The solid curve in each figure is the theoretical estimate for modal density given by Eq. (8) with r replaced by r_{eff}. For all four panels, the quantity χ/r_{eff} is much less than 1 so, theoretically, the effect of rotary inertia is negligible. For the range of $r_{eff}(\omega/\omega_0)$ and t_f/h_c covered by the experiments, the theoretical effect of the face-bending stiffness is also negligible.



(a) Panel 1. (b) Panel 2.

(c) Panel 3. (d) Panel 4.

Fig. 12.- Comparison of theoretical and experimental modal densities.

A comparison of the results presented in Figs. 12 indicates that the theory gives a fairly good estimate of the average modal density except at the smaller values of $r_{eff}(\omega/\omega_0)$. The values of $r_{eff}(\omega/\omega_0)$ at which the comparison becomes poor correspond to the frequency range in the vicinity of the fundamental mode where relatively few modes occur. As mentioned earlier, the continuous frequency representation of a discrete number of modes is unrealistic in this frequency range.

Panels 3 and 4 are nominally identical, the major difference being about a 20-percent variation in γ. However, comparison of Figs. 12(c) and 12(d) shows that the experimental results obtained from panel 3 fall very close to the theoretical curve at nearly every point while the results from panel 4 are more scattered. This is due to a "clumping" of more than the average number of modes (as predicted by theory) in one frequency interval while an adjacent frequency interval has fewer than the average number of modes. (This clumping effect is also seen in Figs. 9(a) and 9(b), for example, at $170 < \omega/\omega_0 < 180$.) Depending on the size of frequency interval chosen, this clumping may or may not produce noticeable variations in modal density from the average. The theory gives only the average modal density and does not predict variations from this average.

It should also be noted that the test panels were fastened in a semiclamped configuration, while the theory was based on simple support boundary conditions. The fairly good agreement between the experimental and theoretical results lends support to the implicit assumption that the modal density of sandwich panels, like single-layered panels, is relatively independent of the boundary conditions.

CONCLUSIONS

Theoretical estimates are obtained for the modal densities of sandwich beams and flat or cylindrically curved sandwich panels. The relative importance of transverse shear flexibility and orthotropic shear moduli of the core, bending stiffness of the faces, rotary inertia, and panel curvature as they affect modal density is judged. Experimental values of modal density were obtained from resonance tests of flat rectangular panels with orthotropic cores. From the results of the investigation, the following conclusions are noted:

1. Failure to account for the transverse shear flexibility of the core can lead to a significant underestimation of the modal density.

2. The effect of rotary inertia is generally negligible compared to the effect of transverse shear flexibility.

3. For many practical sandwich configurations and frequency ranges, the effect of the face-bending stiffness can be neglected.

4. For flat rectangular panels with orthotropic cores, a 90° rotation of the core material with respect to the faces has no effect on the average modal density.

5. Where face-bending effects are small, the results obtained for flat and cylindrically curved sandwich panels with isotropic cores can be applied to panels with orthotropic cores such as honeycomb by introducing an effective shear modulus and an effective curvature parameter.

The effective shear modulus is simply the geometric mean of the two face parallel shear moduli.

6. The agreement between modal densities predicted by theory and modal densities determined from experiment was generally good except at frequencies near that of the fundamental mode, where the theory is not applicable.

APPENDIX

Derivation of Equation (1)

The differential equations governing the panel vibrations are obtained from the small deflection theory of Ref. [6] by adding transverse and rotary inertia terms:

$$\left.\begin{aligned}
&\frac{\partial Q_x}{\partial x} + \frac{\partial Q_y}{\partial y} - \frac{E'}{R^2}\nabla^{-4}\left(\frac{\partial^4 w}{\partial x^4}\right) - M\frac{\partial^2 w}{\partial t^2} = 0 \\
&-\frac{\partial^3 w}{\partial x \partial y^2} - \frac{\partial^3 w}{\partial x^3} - \frac{Q_x}{D} + \frac{1}{DQ_x}\left(\frac{\partial^2 Q_x}{\partial x^2} + \frac{1-\mu}{2}\frac{\partial^2 Q_x}{\partial y^2}\right) \\
&\quad + \frac{1}{DQ_y}\left(\frac{1+\mu}{2}\right)\frac{\partial^2 Q_y}{\partial x \partial y} + \frac{I}{D}\frac{\partial^2}{\partial t^2}\left(\frac{\partial w}{\partial x} - \frac{Q_x}{DQ_x}\right) = 0 \\
&-\frac{\partial^3 w}{\partial x^2 \partial y} - \frac{\partial^3 w}{\partial y^3} - \frac{Q_y}{D} + \frac{1}{DQ_y}\left(\frac{\partial^2 Q_y}{\partial y^2} + \frac{1-\mu}{2}\frac{\partial^2 Q_y}{\partial x^2}\right) \\
&\quad + \frac{1}{DQ_x}\left(\frac{1+\mu}{2}\right)\frac{\partial^2 Q_x}{\partial x \partial y} + \frac{I}{D}\frac{\partial^2}{\partial t^2}\left(\frac{\partial w}{\partial y} - \frac{Q_y}{DQ_y}\right) = 0
\end{aligned}\right\} \qquad (A1)$$

In Eqs. (A1), x and y specify the coordinates of a point in the middle surface of the panel (Fig. 1) and t denotes time. The operator ∇^{-4} is defined by $\nabla^{-4}(\nabla^4 w) = \nabla^4(\nabla^{-4} w) = w$, where $\nabla^4 = (\partial^4/\partial x^4) + 2(\partial^4/\partial x^2 \partial y^2) + (\partial^4/\partial y^4)$.

The motion described by these equations is that a straight line perpendicular to the undeformed middle surface ($z = 0$) remains straight and of constant length after deformation but not necessarily perpendicular to the deformed middle surface. This inclination in the x (or y) direction from a right angle is the average shear angle Q_x/DQ_x (or Q_y/DQ_y) produced by the resultant transverse shear force Q_x (or Q_y) per unit width.

For simply supported edges parallel to the x axis at which the support is applied over the entire thickness, the boundary conditions are [14]

$$w = M_y = \frac{Q_x}{DQ_x} = 0 \qquad (A2)$$

where the moment M_y (acting about the x axis) is given by

$$M_y = -D\left[\frac{\partial^2 w}{\partial y^2} - \frac{1}{DQ_y}\frac{\partial Q_y}{\partial y} + \mu\left(\frac{\partial^2 w}{\partial x^2} - \frac{1}{DQ_x}\frac{\partial Q_x}{\partial x}\right)\right] \qquad (A3)$$

The boundary conditions along the edges parallel to the y axis are obtained by interchanging y and x.

Expressions for the lateral deflection and shear angles that satisfy the boundary conditions are

$$\left.\begin{aligned}
w(x,y,t) &= A' \sin\frac{m\pi x}{a}\sin\frac{n\pi y}{b}\, e^{i\omega t} \\
\frac{Q_x}{DQ_x}(x,y,t) &= \frac{B'}{DQ_x}\cos\frac{m\pi x}{a}\sin\frac{n\pi y}{b}\, e^{i\omega t} \\
\frac{Q_y}{DQ_y}(x,y,t) &= \frac{C}{DQ_y}\sin\frac{m\pi x}{a}\cos\frac{n\pi y}{b}\, e^{i\omega t}
\end{aligned}\right\} \qquad (A4)$$

where m and n are integers designating the number of sinusoidal half-waves in the x and y directions, respectively, and ω is the panel frequency (rad/sec).

The differential Eqs. (A1) are also satisfied by the above forms for w, Q_x/DQ_x, and Q_y/DQ_y provided

$$\begin{vmatrix}
\left(\frac{C}{\rho^2}\right)^2\left(\frac{m}{a/b}\right)^4 - \left(\frac{\omega}{\omega_o}\right)^2 & \frac{m}{a/b} & n \\
\left(\frac{m}{a/b}\right)\left[\rho^2 - \chi\left(\frac{\omega}{\omega_o}\right)^2\right] & -\left(1+r_x\left[\left(\frac{m}{a/b}\right)^2 + \left(\frac{1-\mu}{2}\right)n^2 - \chi\left(\frac{\omega}{\omega_o}\right)^2\right]\right) & -\left(\frac{1+\mu}{2}\right)\left(\frac{m}{a/b}\right)nr_y \\
n\left[\rho^2 - \chi\left(\frac{\omega}{\omega_o}\right)^2\right] & -\left(\frac{1+\mu}{2}\right)\left(\frac{m}{a/b}\right)nr_x & -\left(1+r_y\left[n^2 + \left(\frac{1-\mu}{2}\right)\left(\frac{m}{a/b}\right)^2 - \chi\left(\frac{\omega}{\omega_o}\right)^2\right]\right)
\end{vmatrix} = 0 \qquad (A5)$$

Expanding the determinant yields Eq. (1).

REFERENCES

1. Ira Dyer, "Statistical Vibration Analysis," Intl. Sci. and Tech., No. 20, pp. 35-41; Discussion, pp. 85-86, Aug. 1963

2. Preston W. Smith, Jr., and Richard H. Lyon, "Sound and Structural Vibration," NASA CR-160, 1965

3. Eric E. Ungar, "Fundamentals of Statistical Energy Analysis of Vibrating Systems," Rept. 1350 (AFFDL-TR-66-52), Bolt Beranek and Newman Inc., May 1966

4. J. P. D. Wilkinson, "Modal Densities of Certain Shallow Structural Elements," J. Acoustical Soc. of Am., Vol. 43, No. 2, pp. 245-251, Feb. 1968

5. A. S. Benson, and J. Mayers, "General Instability and Face Wrinkling of Sandwich Plates - Unified Theory and Applications," AIAA, Vol. 5, No. 4, pp. 729-739, April 1967

6. Manuel Stein, and J. Mayers, "A Small-Deflection Theory for Curved Sandwich Plates," NACA Rept. 1008, 1951

7. M. E. Raville, and C. E. S. Ueng, "Determination of Natural Frequencies of Vibration of a Sandwich Plate," Vol. XXIV, No. 2, B. E. Rossi, ed., Soc. for Exptl. Stress Anal., pp. 490-493, 1967

8. Gideon Maidanik, "Response of Ribbed Panels to Reverberant Acoustic Fields," J. Acoustical Soc. of Am., Vol. 34, No. 6, pp. 809-826, June 1962

9. Manfred Heckl, "Vibrations of Point Driven Cylindrical Shells," J. Acoustical Soc. of Am., Vol. 34, No. 10, pp. 1553-1557, Oct. 1962

10. David K. Millar, and Franklin D. Hart, "Modal Densities of Thin Circular Cylinders," NASA CR-897, 1967

11. V. V. Bolotin, "On the Density of the Distribution of Natural Frequencies of Thin Elastic Shells," J. Appl. Math. and Mech., Vol. 27, No. 2, pp. 538-543, Oct. 1963

12. R. Courant, and D. Hilbert, "Methods of Mathematical Physics," Vol. I, Chap. VI, Interscience Publishers Inc., 1953

13. S. Kelsey, R. A. Gellatly, and B. W. Clark, "The Shear Modulus of Foil Honeycomb Cores," Aircraft Engineering, pp. 294-302, Oct. 1958

14. Charles Libove, and S. B. Batdorf, "A General Small-Deflection Theory for Flat Sandwich Plates," NACA Rept. 899, 1948 (Supersedes NACA TN 1526)

TABLE 1
Comparison of Curved and Flat Panel Modal Densities at the Ring Frequency $r = \chi = 0$

Curvature Parameter C	Frequency Interval $0.95C < \omega/\omega_o < 1.05C$	Number of Modes in Frequency Interval		$\frac{\Delta N_C}{\Delta N_F}$
		Flat Panel ΔN_F	Curved Panel ΔN_C	
50	47.5 → 52.5	5	5	1.0
75	71.25 → 78.75	6	8	1.33
100	95 → 105	10	13	1.30
200	190 → 210	21	27	1.29
300	285 → 315	29	43	1.48
400	380 → 420	39	55	1.41
500	475 → 525	49	76	1.55
750	712.5 → 787.5	76	115	1.51
1000	950 → 1050	101	155	1.53

TABLE 2
Description of Test Panels
[All superscripts are powers of ten]

Length of panel: a = 28.5 in.
Width of panel: b = 24.0 in.

Materials

Panels 1 and 2: Faces of 302 stainless steel sheet
Cores of 1/8-5052 - 0.002 aluminum honeycomb

Panels 3 and 4: Faces of 321 stainless steel sheet
Cores of OX-3/16-5052 - 0.0007 overexpanded aluminum honeycomb

	Core Properties				Face Properties				Panel Parameters					
Panel	ρ_c, $\frac{\text{lb-sec}^2}{\text{in.}^4}$	G_{cx}, lb/in.^{2}	G_{cy}, lb/in.^{2}	h_c, in.	$(\rho f)_{eff}$, $\frac{\text{lb-sec}^2}{\text{in.}^4}$	E_f, lb/in.^{2}	μ	t_f, in.	$\frac{a}{b}$	$\frac{t_f}{h_c}$	ω_o, $\frac{\text{rad}}{\text{sec}}$	r_{eff}	$\frac{\chi}{r_{eff}}$	γ
1	1.21^{-5}	131,000	53,000	0.502	80.3^{-5}	26^{+6}	0.245	0.0154	1.19	0.0307	738	0.0221	0.0449	2.47
2	1.21^{-5}	53,000	131,000	0.502	81.4^{-5}	26^{+6}	0.245	0.0154	1.19	0.0307	734	0.0221	0.0450	0.405
3	0.316^{-5}	21,700	23,900	0.503	80.3^{-5}	28^{+6}	0.245	0.0203	1.19	0.0404	843	0.114	0.00993	0.908
4	0.316^{-5}	23,900	21,700	0.503	81.1^{-5}	28^{+6}	0.245	0.0203	1.19	0.0404	840	0.114	0.00993	1.10

TABLE 3
Experimental Resonance Frequencies, Hz
[Panels 1 and 2; heavy line encloses modes for which $r_{eff}(\omega/\omega_o) < 1.1$]

	m \ n	1	2	3	4	5	6	7	8	9	10	11
Panel 1	1	294	713	1130	1890	2470	3070	3720	4360	5020	5660	6330
	2	615	950	1425	1960	2590	3230	3850	4460	5140	5770	
	3	1018	1360	1750	2280	2780	3390	3950	4610	5280	5910	
	4	1600	1840	2200	2620	3180	3790	4310	4920	5520		
	5	2162	2460	2815	3130	3630	4130	4750	5300	5900		
	6	2980	3170	3440	3750	4200	4720	5220	5740			
	7	3716	3870	4010	4370	4780	5230	5750	6220			
	8	4470	4660	4930	5090	5460	5890					
	9	5260	5430	5630	5820	6160						
	10	6070										
Panel 2	1	300	726	1180	2260	3060	3960	4900	5940			
	2	530	991	1560	2350	3170	3990	4970				
	3	940	1300	1780	2450	3270	4120	5080				
	4	1340	1690	2120	2700	3530	4360	5150				
	5	1870	2020	2520	3080	3790	4570	5370				
	6	2290	2510	2890	3440	4090	4820	5630				
	7	2750	2930	3360	3840	4470	5150	5980				
	8	3220	3420	3800	4250	4800	5540					
	9	3710	3960	4240	4610	5220	5870					
	10	4200	4421	4680	5170	5630						
	11	4610	4910	5070	5640	6070						
	12	5130	5360	5590	6080							
	13	5700	5800	6100								

TABLE 3

Experimental Resonance Frequencies, Hz - Concluded

[Panels 3 and 4; heavy line encloses modes for which $r_{eff}(\omega/\omega_o) < 3.0$]

	m \ n	1	2	3	4	5	6	7	8	9	10
Panel 3	1	280	674	940	1360	1760	2140	2520	2910	3290	3640
	2	443	760	1070	1430	1810	2200	2630	3020	3360	
	3	810	990	1300	1570	1930	2310	2700	3080	3430	
	4	1010	1230	1500	1770	2110	2440	2800	3140	3500	
	5	1330	1530	1750	1980	2310	2580	2930	3280		
	6	1760	1830	2020	2220	2500	2780	3130	3440		
	7	2000	2140	2290	2490	2700	3000	3350			
	8	2360	2440	2560	2750	2960	3210	3540			
	9	2650	2710	2890	3060	3230	3540				
	10	2950	3050	3200	3300	3500					
	11	3300	3390	3460							
	12	3590									
Panel 4	1	288	638	951	1380	1780	2140	2540	2910	3310	3670
	2	437	754	1060	1430	1820	2200	2620	3060	3380	
	3	784	990	1260	1580	1940	2300	2700	3100	3460	
	4	981	1220	1480	1780	2100	2450	2800	3130	3590	
	5	1310	1540	1720	2010	2310	2630	2940	3310		
	6	1780	1820	2000	2230	2530	2810	3140	3480		
	7	2030	2130	2290	2490	2720	3010	3360			
	8	2340	2430	2580	2760	2970	3240	3530			
	9	2630	2700	2870	3030	3260	3500				
	10	2930	3050	3210	3340	3540	3730				
	11	3270	3390	3460	3620						
	12	3650	3700								

DISCUSSION

Voice: How were the panels excited?

Mr. Erickson: In each case, the panel is excited by a relatively small permanent magnet, 25 lbs force shaker. It was attached by means of a vacuum cup so that the point of excitation could be readily moved without adding any mass to the panel.

TURBINE ENGINE DYNAMIC COMPATIBILITY WITH HELICOPTER AIRFRAMES

Kenneth C. Mard and Paul W. on Hardenberg
© Sikorsky Aircraft Division of United Aircraft Corporation
Stratford, Connecticut, U.S.A. 1968
All Rights Reserved

During the development of the U. S. Marines CH53A transport helicopter, Sikorsky Aircraft was funded to conduct an intensive investigation into the dynamic characteristics of the CH53A/T64-6 engine installation. The purpose was to gain assurance that the turbine engine and helicopter airframe dynamic characteristics were compatible and that unanticipated dynamic problems would not occur during service life.

The program was unique because: (a) it was an extensive dynamic compatibility study implemented during a helicopter design phase and went far beyond current design and substantiation specifications; (b) it paves the way for future specification requirements for helicopter/turbine installations; and (c) it gave greater technical capability to the airframe manufacturer to meet his responsibilities for the engine/airframe installation design and substantiation.

This program, conducted with the cooperation of General Electric's Small Aircraft Engine Division, included an analysis of engine and airframe induced vibration characteristics, ground shake tests with and without the engine operating, and flight test verification of the installation. Data gathered on natural modes, forced response and the procedures developed in evaluating the effects of interface impedance provided a high degree of confidence that future changes to the airframe or engine would not result in unanticipated problems.

INTRODUCTION

The reciprocating engine stands at a high level of development today. It took the talents of two generations of engineers to mitigate the effects of torque pulsations caused by each cylinder firing and the inertia forces from the unbalanced reciprocating elements. The introduction of gas turbines to the helicopter industry was welcomed not only because of the greatly improved power to weight ratio, but also because the smooth process of continuous combustion and simple rotating elements promised freedom from engine vibration which is fatigue-inducing and annoying.

Flight tests on two T-58 General Electric gas turbine installations, the Sikorsky HSS-1F helicopter and the S-62 helicopter, confirmed that the vibration and dynamic forces emanating from the turbines did not require the added complication of isolation to protect the airframe. On the basis of this experience the Navy's SH-3A anti-submarine helicopter was designed and produced without further consideration of the interface between the airframe and engine.

For nearly three years the development and production of this aircraft proceeded without serious engine installation problems. Then, rather suddenly, an almost exponential increase in the number of engine installation discrepancies were reported, the majority of

Reproduced with permission.

which were fatigue cracks in the nonrotating engine structure. Fig. 1 shows the removal rate as a function of accumulated flight time.

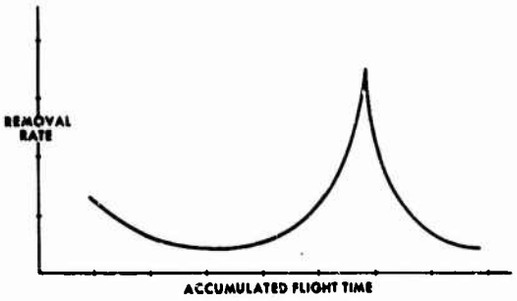


FIG. 1 SH3A/T58 ENGINE REMOVAL RATE VS. ACCUMULATED FLIGHT TIME

The impact of the sharp increase was a drain on the spare part reserve and a reduction of aircraft availability to a seriously low level with an unpredictable amount of unscheduled maintenance.

The most frequently reported discrepancy was cracking of the flange of the power turbine bearing housing. This housing provided the structural path which supported the rear of the engine on the airframe. It also housed the bearing which supported the free turbine wheel and drive shaft. Vibration measurements taken on this part revealed a high amplitude resonance excited by imbalance of the free turbine and drive shaft as shown in Fig. 2.

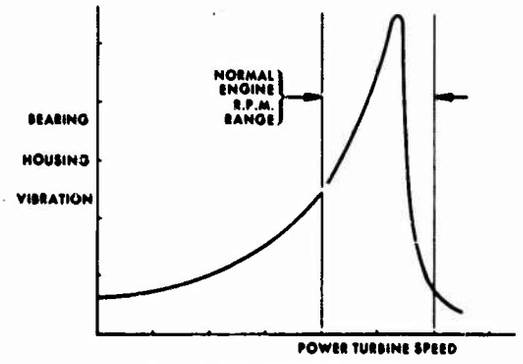


FIG. 2 SH3A/T58 ENGINE TURBINE BEARING HOUSING VIBRATION VS. TURBINE SPEED

The significant fact here is that there was no requirement from the engine manufacturer nor any motive for the airframe manufacturer to examine this area prior to the sharp rise in fatigue cracking of this component. In fact, measurements made at locations recommended by the engine manufacturer were within specified limits.

The resonance was successfully detuned by the addition of a 13 lb weight adjacent to the bearing housing, but the disturbing question still remained as to why this resonance revealed itself so far along the life cycle of the aircraft. Further investigation, coupled with a detailed dynamic analysis developed by the engine manufacturer, pinpointed the cause to be a change in impedance at the interface between the aircraft and engine. This subtle change, merely the change in material in a bushing which exhibited poor life characteristics, had an unusually strong effect on this resonance.

Subsequent to the initial development of the SH-3A, a commercial derivative called the S-61L was introduced. Although the dynamic system on this model was the same as the SH-3A, the fuselage was stretched to adapt it to its commercial role. The front frame of the engine is mounted directly to the airframe and, even though the mount was unchanged from the SH-3A, the airframe dynamic characteristics were sufficiently different to cause another serious structural integrity problem with the engine. Main rotor excitation of the helicopter at 17 cps was transmitted through the airframe in sufficient magnitude to excite the first bending mode of the engine. Vibratory amplitudes of this mode were enough to cause a high stress problem in the power turbine bearing housing structure. This did not occur in the SH-3A because the front frame of the engine was mounted near a node in the airframe. The solution to the problem was to change the interface impedance between the front frame of the engine and airframe so as to alter the resonant frequency of the first bending mode. This problem was not recognized initially because of insufficient knowledge of the structural dynamic characteristics of the engine installation.

Neither of these problems were anticipated by the engine or airframe manufacturer. This experience made it imperative that in future installations the definition and control of compatible interface characteristics be given high priority.

The award to Sikorsky Aircraft by the U. S. Marines for development of the CH53A

transport helicopter presented a new challenge in achieving a reliable turbine engine installation in a helicopter airframe. It was recognized by the Bureau of Naval Weapons, the engine manufacturer (General Electric), and Sikorsky (the weapons system contractor) that a gap existed in the definition of, and the responsibility for, the engine/airframe interface impedance characteristics. The weapons system contractor, by definition is responsible for the total performance and effectiveness of the system in the field. Since the engine subsystem dynamic characteristics were not available, technical cognizance of the engine installation had been delegated to the engine manufacturer by BuWeps, causing a discontinuity in total system responsibility.

In recognition of this, BuWeps funded Sikorsky to conduct an intensive investigation into the dynamic characteristics of the CH53A/T64-6 engine installation. This program of beefing up the technical capability of the weapons system contractor gave added assurance that the initial installation on the CH53A would be free of structural dynamic problems and that future developments would receive positive and competent guidance. The strong technical support and cooperative attitude of General Electric's Small Aircraft Engine Division, Lynn, Mass., is largely responsible for the success of this program and is gratefully acknowledged.

CH53A/T64-6 ENGINE DYNAMICS PROGRAM

Development costs of an engine usually exceed, by several times, the development cost of the helicopter that receives it. In addition, the concept and design of the engine precedes the application so that in any use the engine must be adapted with little or no change.

The basic philosophy behind the CH53A/T64-6 Engine Dynamics Program was to extrapolate from the experience already developed by the engine manufacturer rather than to establish the integrity of the installation on an absolute basis. The engine had already completed its 150 hour qualification run and was starting to be used in other applications when this Engine Dynamics Program was proposed. Initial development problems had been resolved and it was rational to believe that the fewest new problems would arise if changes in the engine dynamic response characteristics between the other installations and the CH53A were minimized.

There is only one variable that can be used to achieve this objective. This is the interface impedance between the engine and airframe or other hardware used to adapt the engine. A mathematical model must be used to assess the interplay between this variable and the baseline configuration used by the engine manufacturer during his development and qualification phase. This constituted Phase I of the program.

A dynamic analysis of a turbine engine is complicated by the high frequency modes that must be considered and the uncertainty of important parameters. The mathematical model must be correlated with shake tests and forced response tests of the engine installation. The second phase of the Engine Dynamics Program included shake tests of the installation using external excitation to determine response of natural modes and frequencies, and a second test was conducted with the engine running under power using calibrated unbalance of its own rotating elements to determine forced response characteristics. The final phase included flight tests to verify the conclusions of the analytical and ground test phases. Fig. 3 summarizes the principle elements of the program.

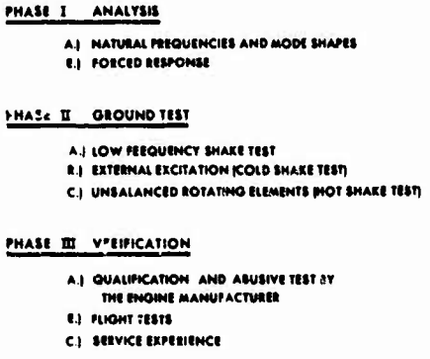


FIG. 3 CH53A/T64-6 ENGINE DYNAMICS PROGRAM

DESCRIPTION OF THE CH53A/T64-6 ENGINE INSTALLATION

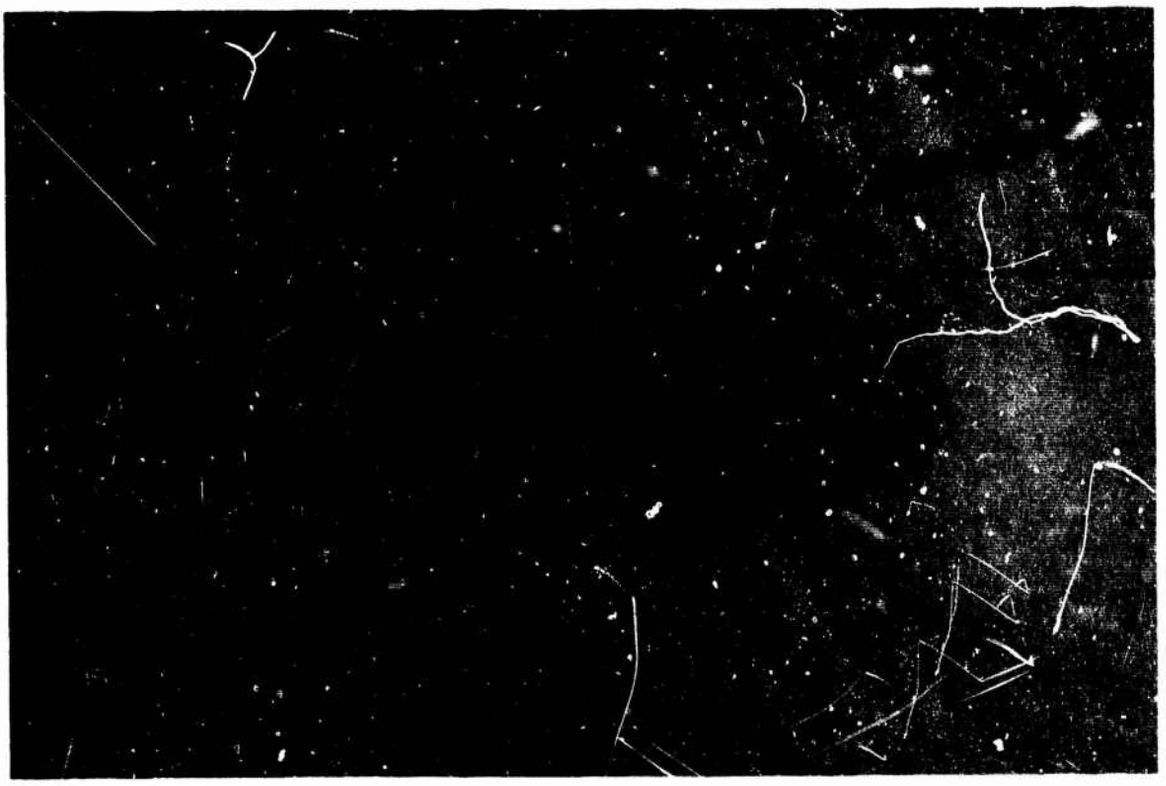


Fig. 4 CH53A helicopter with T64-6 engines

The CH53A transport helicopter, shown in Fig. 4 was designed to carry a payload of 8000 lbs, a radius of 100 nautical miles at speeds in excess of 150 knots. It is powered by two T64-6 General Electric turbine engines, each producing up to 2850 shaft horsepower. Fig. 5, a schematic of the engine installation, shows that it is attached to the airframe at two points. The rear mount under the gas turbine is only capable of vertical and lateral reactions. The forward mount under the nose gear box provides vertical, lateral, longitudinal and torsional restraint. The power output shaft is at the front of the engine, concentric with the compressor air intake, and is routed through a torque tube to the nose gear box and then to the main transmission of the helicopter. Restraint by the output drive shaft from the nose gear box to the main transmission is minimized by flexible couplings.

Fig. 5 also shows the schematic of the internal configuration of the engine. A unique feature is the concentric shaft of the power turbine and gas generator. The tail pipe and nose gear box as well as the mount characteristics, constitute the impedance variable under the airframe manufacturer's control.

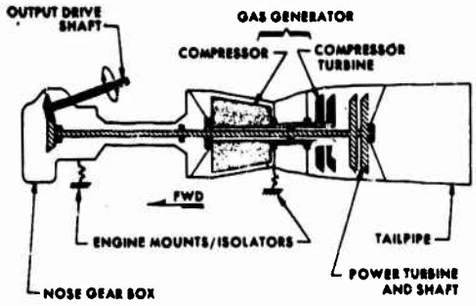


FIG. 5 CH53A/T64-6 ENGINE INSTALLATION SCHEMATIC

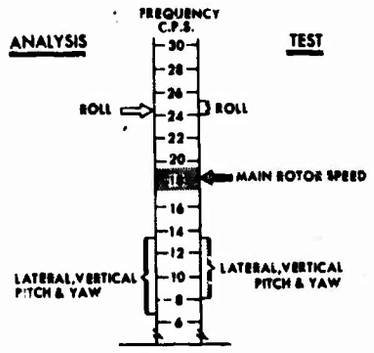


FIG. 6 RIGID BODY NATURAL FREQUENCIES CH53A/T64-6 ENGINE INSTALLATION

The engine mount characteristics were selected early in the design phase of the CH53A and before the start of the Engine Dynamics Program. The design requirements, however, were established with the objective of dis-associating the airframe from the engine. A natural frequency of 10 cps was selected for the translational and pitching modes. This effectively decoupled airframe excitation from the first bending mode of the engine by a frequency ratio of two to one. It was necessary to compromise the transmissibility to the torsional or roll mode because of the requirement to react the engine output torque with a minimum of deflection. This was accomplished with the cooperation of the Lord. Mfg. Co. who fabricated a unique forward mount incorporating high vertical and lateral flexibility while retaining stiffness in the roll and longitudinal direction. Fig. 6 shows the results of analysis and test of this installation. As shown, resulting natural frequencies were sufficiently removed from the principal airframe excitation to preclude any significant response.

ENGINE DYNAMIC ANALYSIS

An essential ingredient to understanding the fundamental characteristics which make up the dynamic response of a complex structure such as an engine is a definitive analysis. The General Electric Co. had made significant progress with their development of the VAST (System Vibration and Static Analysis) analysis Ref. (1). This analysis is based upon the Prohl method Ref. (2). This method analyzes a beam or span by dividing it into a series of discreet stations where the lumped mass of the station is considered to act. Spans are selected on the basis of being a uniform beam with boundary conditions such as a bearing or a major change in structural properties. The structural characteristics are determined for the station between the discreet masses. Equations relating the inertia and elastic forces are written for each station in the span. By algebraic elimination the boundary condition at the end of the span can be expressed in terms of the boundary conditions at the beginning of the span. Boundary conditions at either end of the span can include the equilibrium requirement of another span which joins it at that point. Relative motion between the coordinate systems of each span are accounted for by a set of compatibility equations. Natural frequencies are determined by finding a

frequency which satisfies the boundary conditions at the free ends of the engine. Forced responses are determined by calculating a response amplitude that will put the exciting forces in equilibrium. A limitation of this analysis is that it did not include damping. Altogether 20 spans, which included 225 stations, were used to describe the installation. This detail was necessary because the exciting frequencies went up to 300 cps.

Ten transverse natural frequencies of the system in the vertical plane were located in the range from 0 to 330 cps, two of which were rigid body modes. These modes are shown relative to the gas generator, power turbine and gear box output shaft rotating frequencies in Fig. 7.

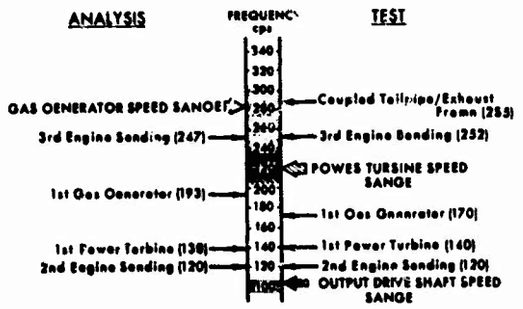


FIG. 7 CH53A/T64-6 ENGINE INSTALLATION FLEXURAL NATURAL FREQUENCIES

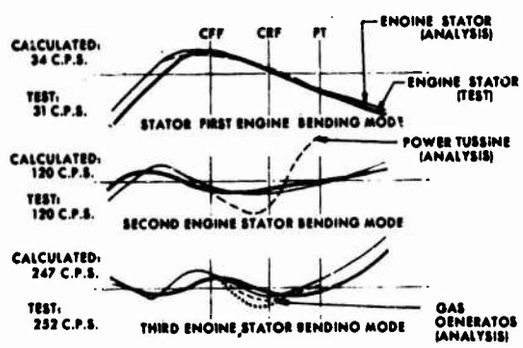


FIG. 8 CH53A/T64-6 ENGINE INSTALLATION CALCULATED MODE SHAPES AND TEST MEASUREMENTS

Fig. 8 illustrates the mode shapes that were calculated and shows the relative motion that can exist between the rotors and external shell (stator) bending response. A similar analysis was conducted to determine the torsional modes involved.

Fig. 7 shows that the two ranges of exciting frequencies that are of most concern in exciting the natural modes are the power turbine rotating frequency, which is 227 cps, and the gas generator rotating frequency which varies, depending on the power required, between 217 and 300 cps. It is observed that several modes are coincident with the gas generator frequencies and may be excited such as the third engine bending mode. From this it may be predicted that gas generator frequency should be the principle response seen in operation.

Forced response shapes for specific unbalances of the rotating components were calculated also to give better insight into the response characteristics of the engine. Fig. 9 shows two calculated response shapes to an unbalance of 60 gram inches located at the power turbine rotor.

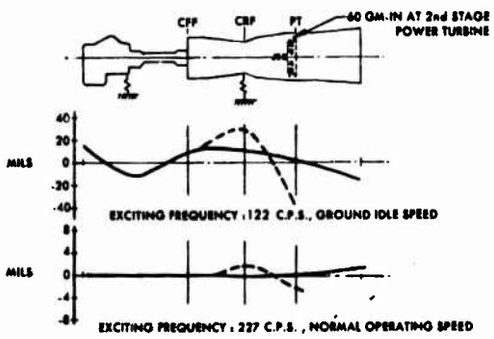


FIG. 9 CH53A/T64-6 ENGINE INSTALLATION CALCULATED FORCED RESPONSE SHAPES

The forced response shape at 122 cps was chosen as a near resonant, low power turbine speed condition used occasionally for engine warm-up. As expected, the response shape is primarily the second engine bending mode shape and the amplitudes are elevated because no damping is considered in the analysis. The interesting aspect of this condition is that the amplitude of the power turbine is considerably greater than the amplitude of the engine shell.

Therefore, low vibration measurements at the power turbine frame and compressor frame locations would not necessarily indicate freedom from problems. As a result, strain gage measurements of the power turbine rotating system should be carefully reviewed during low speed transient conditions. The second response shape is at 227 cps, the normal operating speed of the power turbine. It shows only a modest amplitude of the power turbine and shaft and little engine stator response, considering the amount of unbalance. Similar calculations were made with unbalances at several planes of the gas generator and excitation at the airframe interface.

The results of this study stressed the value of forced response analysis as a means of exposing potential problem areas not easily uncovered in testing. Study of these data provided guidance for the planning and conduct of the subsequent shake test program.

GROUND VIBRATION TESTS

It was shown in Fig. 6 that natural frequencies were sufficiently removed from the principle airframe exciting frequency to minimize rigid mode response. In successfully developing an installation with relatively low rigid body natural frequencies, the objective of eliminating any influence that the airframe might have on the engine dynamic response was also achieved since the first flexural engine mode was well above these frequencies. The engine rigid body response was measured with the aircraft in simulated flight by suspending the aircraft from the main rotor head and exciting it at the main rotor blade passage frequency with a shaker force of representative magnitudes. See Fig. 10.

Two test installations were utilized in the conduct of the higher frequency portion of the ground test program. These were the Sikorsky turbine test bed, Fig. 11, and the tie-down test aircraft, shown in Fig. 12. On both installations, tests were conducted on engine installations complete with nose gear boxes, tail pipes, suspension systems, and other interfacing hardware provided by the airframe manufacturer. Although the airframe structure was substantially different between these installations, this was not considered a significant factor because the low impedance of the isolator between the engine and airframe minimized coupling influences in the higher frequency portion of the test program. Fig. 13 shows a close-up photo of the shake test set up.

It was realized that shake test data obtained as a result of a single source of excitation could not yield data that would provide correlatable results with the dynamic analysis that was conducted in Phase I. See Ref. (3). Damping masks natural frequencies and mode shapes of complex structure and care must be taken in identifying high forced response to a natural mode of vibration. The analysis, however, did provide excellent guidance in identifying these modes. The engine structure is composed of several loosely coupled beam structures, the power turbine rotor, the gas generator rotor, and the engine stator, connected by bearings. The easily interpreted results of the analysis made it possible to examine their relative responses and draw conclusions as to their contribution at other frequencies. A forced response vs. frequency plot showed that the internal modes could not be identified since they did not show up as a significant response to the external excitation.

Response shapes of the external shell were measured and considered to be close approximations of the calculated shell modes. Fig. 8 shows a correlation of the measured and calculated shell modes. The natural frequencies were predicted reasonably well, but more important, the correlation with the shell mode shapes gave some assurance that the response of the internal components was reasonable, also.

"Hot" shake tests were the final phase of the ground test program. These tests were conducted with the engine operating normally under power and with excitations from the source they were most expected; unbalance in the compressor section, the gas generator turbine, the power turbine, and the output drive shaft. There were two purposes for this test; the first was to determine the sensitivity of the engine to self-excitation, particularly when operating in close proximity to known resonances; the second was to determine if there were other effects not covered by the analysis.

Clipping blades a small amount caused internal imbalances in the compressor or turbine section, ranging from 17 gram inches in the power turbine to 27 gram inches at the first stage of the compressor. See Fig. 14. The imbalances were thought to be significantly greater than the inherent unbalance in a new engine.

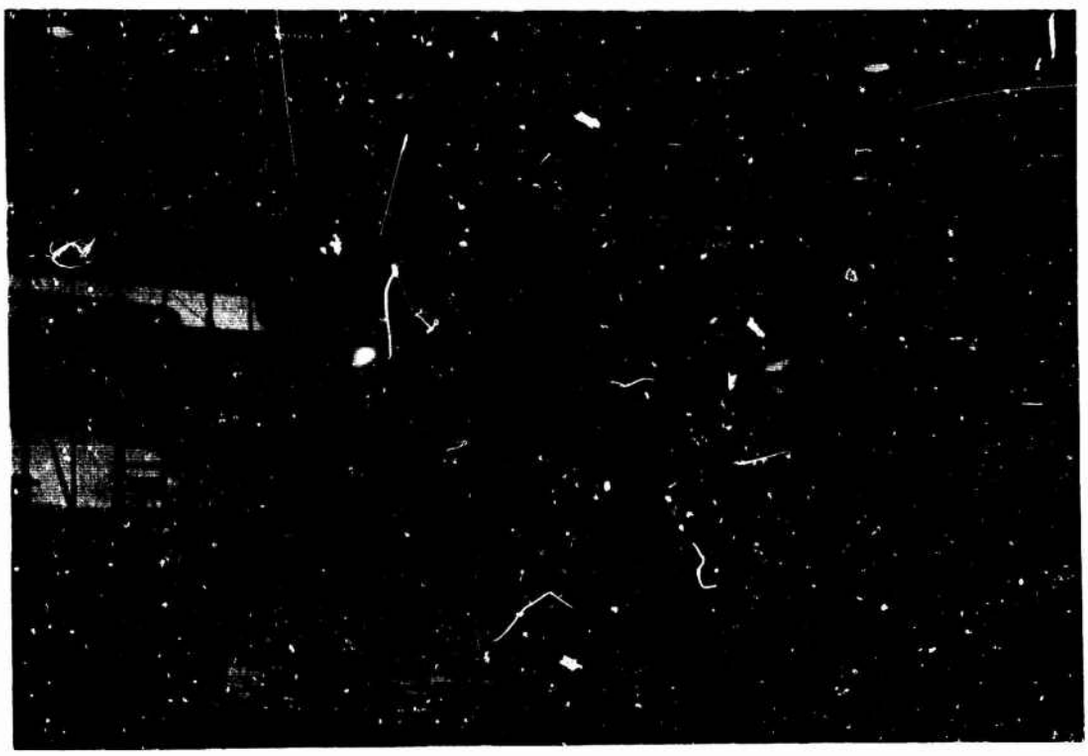


Fig. 10 CH53A/T64-6 low frequency engine vibration test

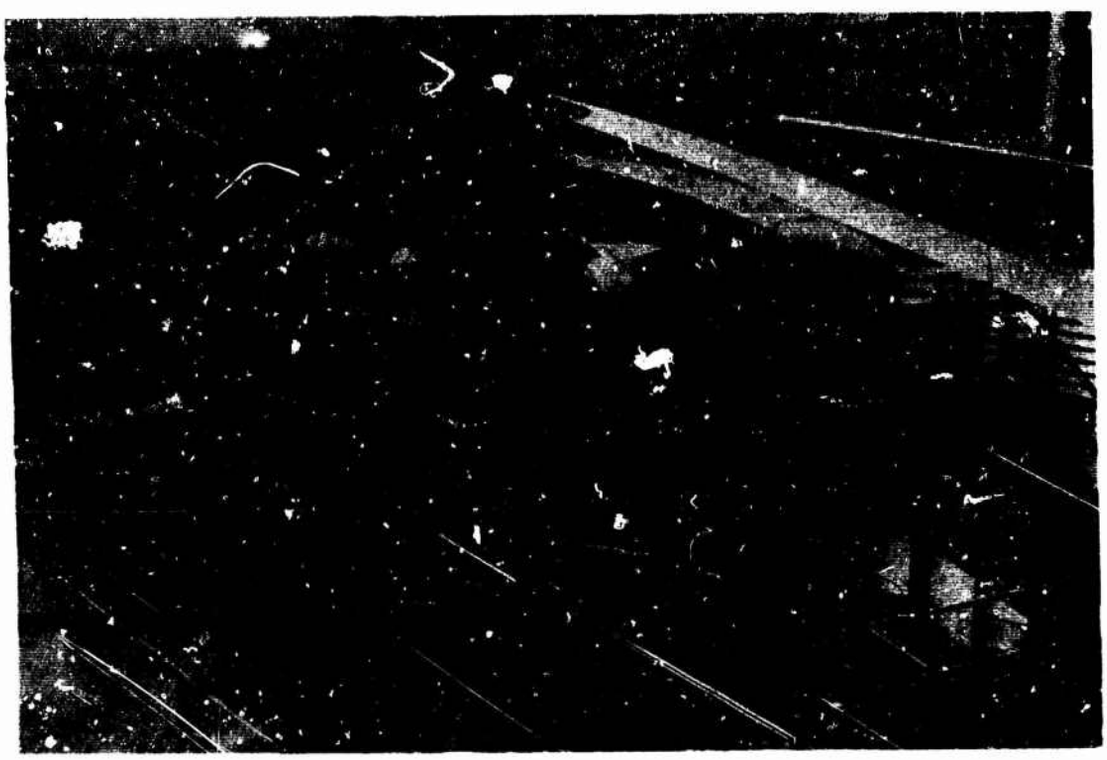


Fig. 11 Sikorsky CH53A test-bed installation

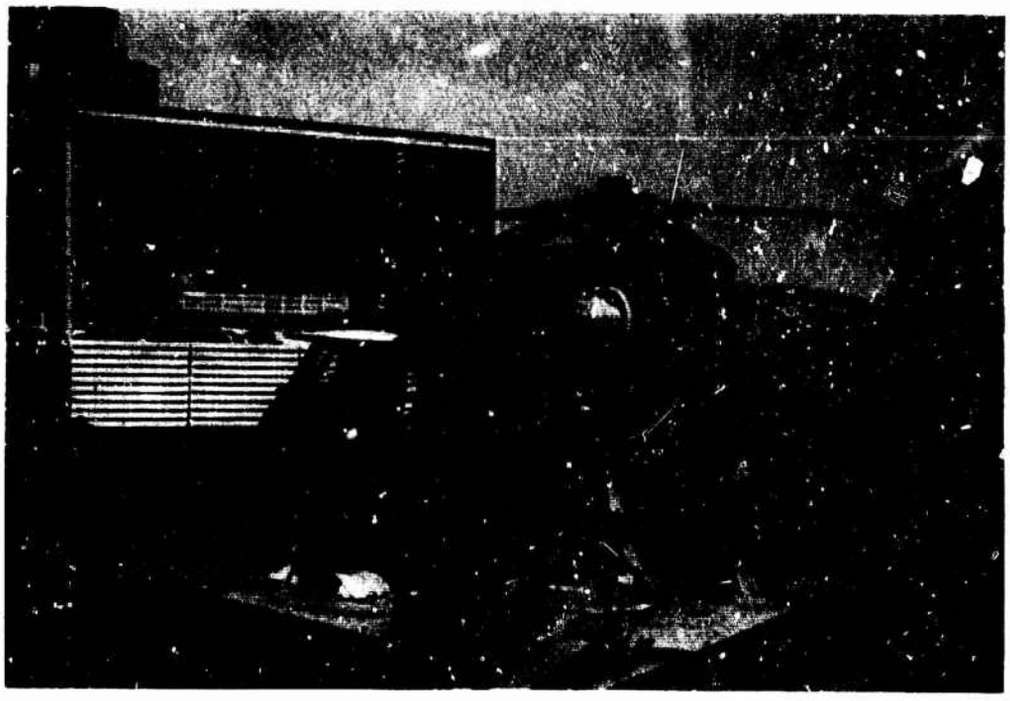


Fig. 12 Sikorsky CH53A tie-down aircraft installation



Fig. 13 Sikorsky CH53A test-bed installation "cold" shake test set-up

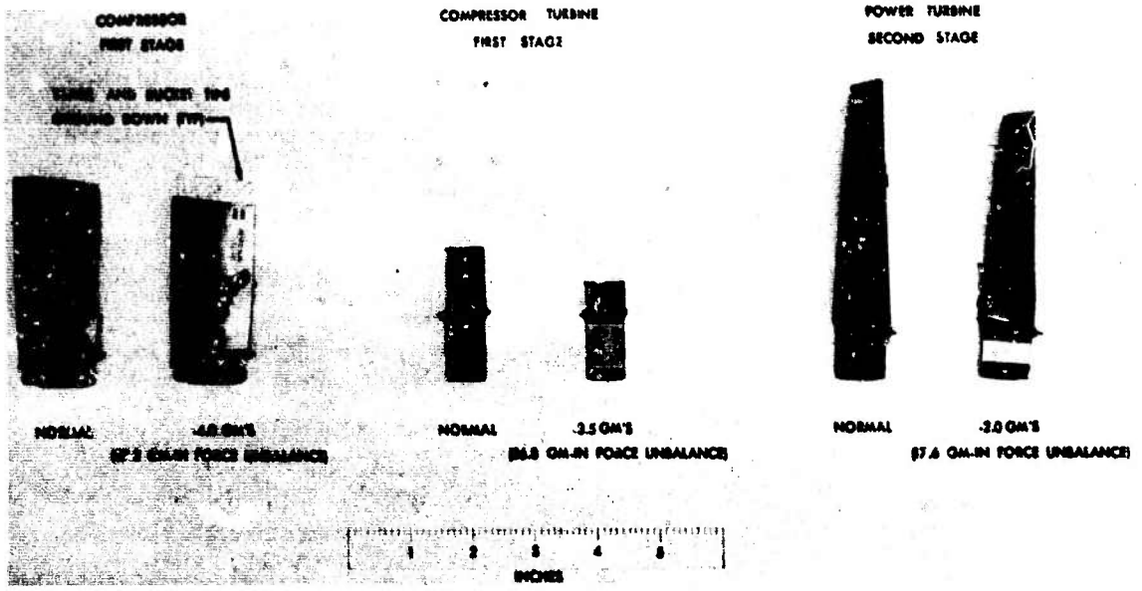


Fig. 14 Unbalanced blades for the CH53A/T64-6 hot run-up test

Nominal subassembly imbalance limits are reported to be kept within 1.0 to 1.5 gram inches. Abusive tests conducted by the engine manufacturer exposed the engine to imbalances in the order of 60 gram inches and appears to be very conservative. Data obtained from engines run with known added imbalances were used to produce the results shown in Fig. 15.

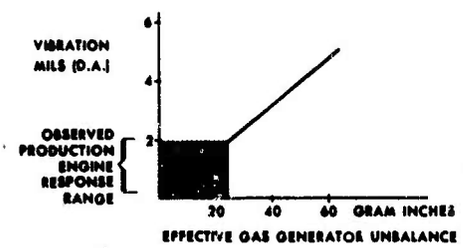


FIG. 15 CH53A/T64-6 ENGINE INSTALLATION RESPONSE TO UNBALANCE

This curve relates the vibration measured on the power turbine frame at a specific operating condition to effective gas generator unbalance; that is, imbalance necessary to be added to the compressor at the forward end and at the compressor turbine to achieve a similar vibration level. The measured vibration levels taken from production engines indicate that effective inherent imbalance as high as 25 gram inches exist with an average of 10 to 15 gram inches. This is in order of magnitude greater than component balance tolerances used by the engine manufacturer and is probably caused by thermal effects, assembly stack up, bearing clearances, etc. This finding makes the results of the engine manufacturer's abusive test less conservative.

Calculating the structural properties of a thin wall structure is difficult. Analytically, the tail pipe was treated as a cone shaped beam in bending, but it was not possible to determine its radial degrees of freedom in sufficient detail to understand the higher frequency modes. It was not surprising, then, to discover a mode which seems to predominate in tail pipe response at a frequency where no other mode was calculated. Fig. 16 shows the response of the power turbine frame with and without the tail pipe installed.

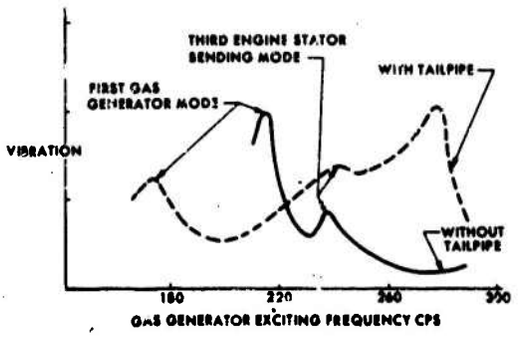


FIG. 16 CH53A/T64-6 ENGINE INSTALLATION EFFECT OF TAILPIPE

Note that the response level in the 240 to 280 cps range was significantly affected by the tail pipe which constitutes less than 2% of the weight of the installation. Observe also that this effect is probably responsible for the poor correlation of the first gas generator mode frequency with that predicted by the analysis.

Another important result of the "hot" shake test was to confirm that gas generator imbalance would be the principal source of engine vibration at operating conditions. Fig. 17 shows engine response to gas generator, power turbine, and output drive shaft imbalance. As shown, the principal response of the engine was to gas generator imbalance and maximum response would be measured at the power turbine frame location. The results further confirm that engine response in the 120 cps range is relatively insensitive to power turbine imbalance and increasingly sensitive to output drive shaft imbalance above the operating speed range. This latter result illustrates the importance of keeping the second engine bending mode frequency well above the output drive shaft operating speed range.

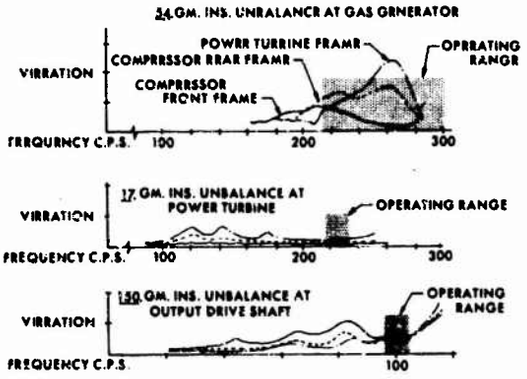


FIG. 17 CH53A/T64-6 ENGINE INSTALLATION CHARACTERISTIC VIBRATION SIGNATURE

SUMMARY OF ANALYSIS AND GROUND TEST RESULTS

After an intensive exposure to the structural dynamics of the T64-6 turbine engine installed in the CH53A helicopter both in analysis and shake test, it was possible to anticipate its response characteristics and to develop a high degree of confidence that concurrent qualification and abusive testing by the engine manufacturers and subsequent flight testing by the airframe manufacturer would expose any significant potential problem. It was realized that the torque tube/nose gear box interface was important since it controlled the second engine bending mode and thereby the response to output drive shaft unbalance. It was known that gas generator imbalance would be significant and that deterioration in its balance such as that caused by ingestion of foreign objects could prove serious. It was also determined that the most sensitive place to observe this deterioration was at the power turbine frame. In addition, tail pipe structural characteristics, a part under the control of the airframe manufacturer, could have a dramatic effect on the response of the rest of the engine. Much was learned also of the relationship between the external shell and the internal rotors which could not be visually observed.

Although it was not expected that an engine structural reliability problem would be uncovered during the design and development phase of the CH53A, it required favorable comparison of flight test results with operational limits established through qualification and abusive testing by the engine manufacturer to make this assurance.

OPERATIONAL VIBRATORY RESPONSE LIMITS

The validity of operational vibratory response limits set by an engine manufacturer depends largely on their applicability to a specific installation. Abusive tests, that is, tests conducted by the engine manufacturer by exposing their engine to unbalance or external excitation substantially in excess of that normally expected, are used to develop an envelope within which vibration is considered acceptable. (See Ref. (4) for a discussion on the development of abusive test philosophy by the engine manufacturer.) This assumes, however, that airframe interface impedance does not alter the relative response between the required point of measurement and some other part of the engine where a critical stress may occur. The knowledge gained by both the airframe and engine manufacturers in this program helped to preclude this possibility. While the resonance of the power turbine bearing housing was not discovered in the SH3A/T58 installation, there was little possibility of that happening with the CH53A/T64 installation. Abusive tests were either carefully designed to account for the airframe impedance or allowance was made for any differences through use of the analytical and test data. As a result, the engine manufacturer was able to specify

vibration limits as a function of frequency, Fig. 18, with reasonable assurance that a high degree of structural integrity would be achieved if these limits were not exceeded.

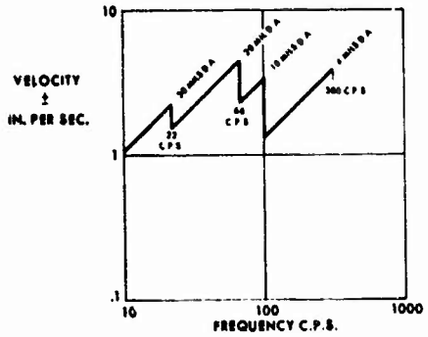


FIG. 18 CH53A/T64-6 ENGINE INSTALLATION RECOMMENDED VIBRATION LIMITS

FLIGHT TEST RESULTS

Flight tests were conducted to obtain both low frequency rigid body response and higher frequency response in a production aircraft. In addition, high temperature strain gages were added to obtain stress information on specific internal parts. Typical data, shown in Fig. 19 shows that the installation is well within the recommended limits of the engine manufacturer.

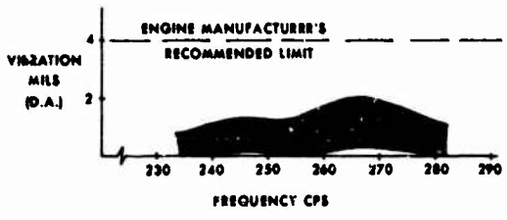


FIG. 19 CH53A/T64-6 ENGINE INSTALLATION PRODUCTION ENGINE MEASUREMENTS

Test data taken on a number of production aircraft confirm that there is only a nominal variation in response. A more important factor is the number of engine removals per flight hour. Fig. 20 shows this removal rate for all causes as a function of flight hours compared to the T58/S61 history. The T64-6 installation reflects a higher degree of engine reliability from the outset, and has not experienced a major structural integrity problem.

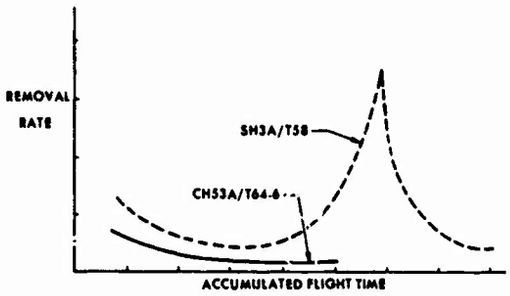


FIG. 20 CH53A/T64-6 AND SH3A/T58 ENGINE REMOVAL RATES VS ACCUMULATED FLIGHT TIMES

CONCLUSIONS

The CH53A/T64-6 Engine Dynamics Program developed a strong working relationship between the airframe and engine manufacturers. In addition, this program was unique in that it was the first extensive dynamic compatibility study implemented during a helicopter design phase and went far beyond current engine installation design and substantiation specifications. In doing so it paves the way for future specification requirements for helicopter/turbine engine installations.

Much credit goes to the Navy for realizing the need for this program. It is recommended that a similar program be an intimate part of the development of any advanced VTOL system so that the prime contractor can exercise the proper technical control and judgment in achieving a compatible turbine engine installation.

REFERENCES

(1) J. K. Sevcik, "System Vibration and Static Analysis (VAST Program)," A.S.M.E. Paper Number 63-AHGT-57, March 3-7, 1963

(2) M. A. Prohl, "A General Method for Calculating Critical Speeds of Flexible Rotors," Journal of Applied Mechanics, Trans. A.S.M.E., Sept. 1945

(3) C. C. Kennedy and C. D. P. Pancu, "Use of Vectors in Vibration Measurement and Analysis," Journal of the Aeronautical Sciences, Volume 14, Number 11, pp. 603-625, Nov. 1947

(4) G. Sonder, "Abusive Testing of Turboshaft Engines," A.H.S., Proc. of 21st Annual Nat. Forum, pp. 240-243, May 12-14, 1965

DISCUSSION

Voice: What do you mean by the removal rates?

Mr. Mard: This is the number of engine removals per hour of flight time. This is for all causes, not just failures of structural integrity. We felt that the high amplitude response of an engine would cause other problems and deterioration of other components so this removal rate was for all causes.

Dr. Mains (Washington University, St. Louis): You have had an opportunity here to compare your calculations with two different kinds of tests. What was the correlation in results between your predictions and your measurements?

Mr. Mard: The correlation was primarily with frequency. The force response using the unbalanced engine during the hot shake test will produce responses from a number of modes. When we were operating very close to a resonance, we were able, from past experience from analysis of cold shake tests to identify the mode with which we were dealing. The cold shake tests were the ones in which we were able to get the best correlation, because we could take detailed measurements along the engines and parts internally and identify our analytical modes with those we found responding from our cold shake test. The hot shake tests were more difficult to perform in that it was more difficult to make measurements. We could not get anybody to go near the engine to put a hand probe on, for instance. For this reason it was a little more difficult to get correlation, but we do feel that there was not very much change between what we have seen in the cold shake and in the hot.

Dr. Mains: You answered my next question by your answer now in that my next question was going to be how did you handle the combination of modes in the calculation when you do not know the phase. But obviously that was the reason why your predictions in your measurements of amplitudes for example under forced response would not necessarily agree.

Mr. Mard: That is right. And there are other modes present, too, that confuse things, like this radial mode of the tail pipe which was not accounted for in our analysis.

Mr. Mustain (McDonnel Douglas): We had a problem on the DC-9 and we went through quite an extensive program. The frequencies you mentioned are above 31 hertz, around 100 and 200, in this area. You worked out fine. In our case we had a problem in the same range. But we had hoped to isolate it with a vibration isolator. They really did not do us any good at all. We were using isolators at various frequencies around 15 hertz and in that range. If they had worked ideally they would have probably solved our problem. We had to go to vibration absorbers to solve our problem. My question is: what type of isolator did you use? What frequencies did you have? Did you have any problems at all in that area? Did the isolators work better for you than they did for us?

Mr. Mard: Well, the kind of isolators we had were developed by a combined effort between Lord Manufacturing Co. and Sikorsky. They were low frequency for all but one mode. The natural frequencies range in the order of 7 to 10 hertz. The principal exciting frequency I might add is around 18 hertz from the airplane and we had to avoid this frequency. The torsional mode – the one reacting the torque of the engine – was placed higher so as to preclude large static deflections. This was in the order of 23-24 hertz. We did not encounter any problems with this isolator. I think you have to give more specific information about your problem to determine whether or not an isolator would buy you anything or hurt you. Here we did not have a problem which we were trying to solve except that we knew the engine was developed in an environment which was similar to that which we

achieve with these isolators. Now if we had made a rigid attachment to the airframe, and we probably could have done so, we would have destroyed this transfer of development information. We were anxious not to do this – we were anxious to depend or extrapolate as much as we could from the engine manufacturers source of knowledge. This is the reason why we isolated. We did not have a problem to avoid. We tried to utilize his development skills.

Dr. Dreher (Air Force Flight Dynamics Laboratory): It was not clear to me how your natural frequencies varied, or differed from taking the engine by itself as compared to the engine when installed in the airframe. Was there a sizeable difference in the natural frequencies?

Mr. Mard: Oh yes, there was a considerable difference. Because the nose gear box that was a sizeable mass. Initially, we did quite a bit of work on the impedance between this nose gear box and the torque tube which was supplied by the engine manufacturer. This produced a rather flexible plate.

Dr. Dreher: What was the frequency of that?

Mr. Mard: This was close to the output shaft frequency – 100 hertz. We were able to place it just above the output shaft speed and avoid a problem here. This was the first one we were confronted with when we adapted this engine to our installation. There were quite a few tests run by the engine manufacturer with our installation. There were quite a few tests run by the engine manufacturer with our assistance in developing a compatible impedance between these elements. This is really the point. The engine manufacturer has a wealth of experience but it is on dynamic conditions. The mathematical model of the engine installation is quite different than we see. By having a good mathematical model we can examine his knowledge – what he has learned – and transfer it to the models that we have created.

Dr. Dreher: Do you feel that the difference in vibration of natural frequencies was primarily caused by this shaft that connected to the rotor, and one might not find as great a difference in a normal jet engine aircraft where there is no direct link to the airframe itself?

Mr. Mard: I think the difference lies in how much mass you hang on either end of the engine – the tailpipe had a very dramatic effect. I think this has to be looked at quite individually and each case would be unique, I'm sure.

Dr. Dreher: My thought here was just how much can the engine manufacturer do ahead of time – that is, when he originally develops the engine. It seems reasonable that he should compute the natural frequencies of the armature and so on, that is, the bending modes and the radial modes, and that he could obviate a lot of built-in vibration in his engine if he thought about the dynamics before he built the engine.

Mr. Mard: Well, first he did not have this capability initially. It was through working with him that he did develop an analysis which would help with the installation problem such as the one we had. But you have to remember that when you start hanging the kind of hardware that we are talking about on the engine it becomes a specific installation – and there are specific frequencies which you are trying to avoid.

Dr. Dreher: I guess we have some frequencies in which the engine can be at fault all by itself, but there are some peculiar installation problems.

Mr. Mard: They are highly coupled. I guess what I am trying to say is that the influence of these other elements which you hang on the engine can change the response of the engine radically.

Dr. Dreher: You indicate now that there is no firm military specification that defines the effort that should be accomplished.

Mr. Mard: No. There has been very little communication in the past between engine manufacturers and airframe manufacturers.

Dr. Dreher: Seems like this might be a good subject for a panel discussion next year.

SYNTHESIS OF RIGID FRAMES BASED ON DYNAMIC CRITERIA

Henry N. Christiansen, Associate Professor
Department of Civil Engineering Science
Brigham Young University
Provo, Utah

and

E. Alan Pettit, Jr., Engineer
Humble Oil Company
Benicia, California
Formerly Graduate Student, Department of Civil Engineering Science
Brigham Young University
Provo, Utah

This paper describes the development of an automated structural design procedure for sizing the members of three-dimensional rigid-joint frames subject to resonant frequency requirements. The procedure seeks a minimum cost structure for which the lowest natural frequency is specified. The development includes a mathematical formulation of the problem, the organization of an iterative design procedure, and the presentation of an example problem.

DESIGN REQUIREMENTS

This investigation in the field of automated structural synthesis is directed toward structures that are designed on the basis of stiffness rather than strength criteria. The stiffness requirement in this instance is expressed in terms of the undamped natural frequencies of vibration of the structural model. The particular problem considered here is the minimum cost design of three-dimensional rigid-joint frames subject to the requirement that the lowest resonant frequency of the structure be above a specified level. A procedure is developed for the sizing of the members of the structure while changes in geometry which might also improve the dynamic performance are not considered.

Such a design requirement occurs in the case of auto-track microwave antenna structures. The operation of this type of instrument requires accurate positioning of the reflector while tracking a target. This accuracy requirement is met by an automatic control system, but the response of the system is limited by the lowest natural frequency of vibration of the structure. Thus it is necessary to have a certain level of structural stiffness such that the free vibrations of the antenna are not amplified by the feed-back control system. It is, of course, desirable to satisfy this requirement with a minimum cost structure.

Often the manufacturers of such equipment will receive an invitation to bid on the development of an antenna system for which the tracking rates and accuracy are specified. Consideration of the automatic control problem yields a lower bound on the natural frequency of vibration of the antenna, but the company seldom has the time (or money) to develop accurate costs for an appropriate structure. The system described here provides a quick reaction design capability which is suited to this problem.

A similar situation occurs in the design of vibration test fixtures. The fixture serves as a structural link between the shaker and the specimen. Since both the specimen and fixture respond as a coupled system to the moving boundary imposed by the shaker, it is desirable, although not always essential, for the natural frequencies of the fixture to be considerably above the upper level of the

forcing frequency. If the connection between the fixture and specimen allows a single degree of freedom at the connection, control may be based upon this motion and stiffness requirements for the fixture may be circumvented. However, if this connection is not dominated by a single motion or the connection takes place at several locations on the flexible specimen, the moving boundary problem, as seen by the specimen, is complex unless the fixture is "stiff." In such a situation, providing the fixture is a space frame, the design system may be utilized to provide adequate stiffness.

FUNDAMENTALS OF STRUCTURAL SYNTHESIS

In 1900, F.H. Cilley [1] demonstrated that for a hyperstatic truss under a single loading system, the minimum weight structure will be a statically determinant substructure in which the truss members are selected to achieve allowable stress. It may be demonstrated that, for a single material statically determinant truss subject to a single loading system and measuring the stiffness as the reciprocal of the strain energy, the weight-to-stiffness ratio is minimized by a member area distribution which results in uniform stress.

For a hyperstatic structure under multiple loading, the above conclusions do not necessarily apply. As a result, research in structural design has proceeded along two lines, the fully-stressed method, and the method of steepest descent.

For multiple loadings, Cilley [1] used the fully stressed design concept in which each member reaches its allowable stress under at least one of the alternate load systems. This concept may be extended to include stiffness criteria under multiple loads by assigning a uniform-design stress level to each alternative loading. Then, each member is sized so that its maximum stress is equal to the design stress level for at least one loading.

Since the member forces in a hyperstatic structure are a function of the member properties, several iterations of analysis and redesign may be required to achieve a suitable design. During these iterations the stress levels are adjusted to satisfy the required stiffness criteria. L.C. Schmidt [2], in 1958, explored the fully-stressed concept and concluded that, for an indeterminant structure, there will be a number of fully-stressed designs. He decided that the optimum structure will be the least weight structure of all the fully-stressed designs.

L.A. Schmidt [3,4] (1960) has formulated the synthesis of an optimum minimum-weight structure under alternate loads based upon the method of steepest descents. This approach is quite general and does lead to optimum designs but is mathematically complex. His studies, based upon three-bar trusses, have shown that considerable computational effort is required. The minimum weight structures identified by Schmidt [3,4] are not all fully-stressed designs. Later R. Razani [5] (1956) compared fully-stressed and steepest descent methods. If the fully-stressed design does not minimize weight, a procedure is outlined for determining the minimum weight design.

In 1964, J.W. Young and H.N. Christiansen [6] applied the fully stressed method to the design of three-dimensional trussas which were subject to lower bounds on resonant frequency. In particular, their routine was applied to the design of a satellite dispenser structure. Very good designs (on the basis of minimum weight) were obtained for rather large hyperstatic trussas. In 1966, C.H. Lu [7] studied the adaptation of this procedure to rigid joint frames. The work presented here is an extension of Lu's efforts where the merit function involves costs instead of weight.

PROBLEM FORMULATION

The basic design premise is that the amplitude of the strain energy should be minimized for a given cost. The cost is concurrently adjusted to produce the desired resonant frequency characteristics. It is assumed that this premise will result in a minimization of the ratio of cost to natural frequency. The design procedure, while accepting hyperstatic configurations, proceeds as though the structure is determinant. For this reason only "good" designs and not optimum designs may be expected. Because the member properties, the mode shapes at resonance, the inertial loads, the design stress levels, and the cost are initially unknown, the procedure must iterate on all of these parameters as it converges toward an acceptable design.

The structural cost is approximated by

$$\text{Cost} = \sum_{m=1}^{N} (B_{1m} + B_{2m} l_m) \qquad (1)$$

where B_{1m} are arbitrarily specified and l_m is a characteristic section property (i.e. other section properties are related by known functions to l_m) of the m^{th} member. This function was chosen for mathematical simplification and to allow a linearized approximation of more complex relationships. If "large" changes in the design are indicated, the constants B_{1m} are reevaluated and the design process is repeated.

The strain energy of the structure is represented by

$$U = U_A + U_B + U_T \qquad (2)$$

where U_A, U_B, and U_T represent the strain energy associated with axial elongation, bending, and torsion respectively. Strain energy due to

shear deformation is neglected. Restricting the design to thin-wall tubular members (again for simplification) these energies are expressed in terms of the member forces and moments as follows.

$$U_A = \frac{1}{2}\sum_{m=1}^{N}\frac{F_{1m}^2 L_m}{A_m E_m}$$

$$U = \frac{1}{6}\sum_{m=1}^{N}\frac{L_m}{E_m I_m}\sum_{j=2}^{3}\left(M_{j1m}^2 + M_{j1m}M_{j2m} + M_{j2m}^2\right)$$

$$U_T = \frac{1}{4}\sum_{m=1}^{N}\frac{M_{1m}^2 L_m}{G_m I_m} \qquad (3)$$

where for the m^{th} member F_{1m} is the axial force, M_{jkm} is the bending moment about the j^{th} local axis at the k^{th} end of the beam (see figure 1), M_{1m} is the torque, and L_m, A_m, I_m, E_m, G_m are the length, cross-sectional area, moment of inertia of the cross-section, modulus of elasticity, and shear modulus respectively. These formulas preclude distributed loadings along the element.

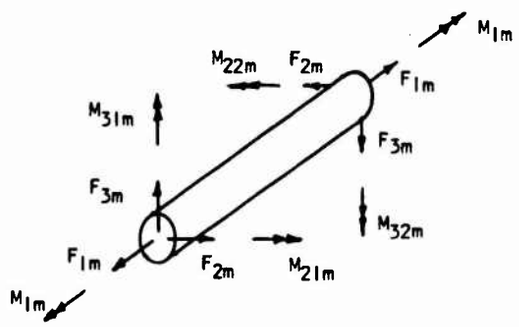


Fig. 1 - Member Force Components

To minimize the strain energy subject to the constraint of a constant cost, the Lagrange Multiplier method is utilized. This allows the unconstrained minimization of a new function

$$Y = U - \lambda\left\{\sum_{m=1}^{N}\left(B_{1m} + B_{2m}I_m\right) - Cost\right\} \qquad (4)$$

where λ is the Lagrange Multiplier, as yet unknown. Therefore, it is required that

$$\frac{\partial Y}{\partial I_l} = 0; \text{ for } l = 1,2,\ldots N$$

and (5)

$$\frac{\partial Y}{\partial \lambda} = 0$$

In order to obtain a constrained minimum for the strain energy. Performing the indicated differentiation, according to Eq.s 3 for the strain energy terms, these requirements yield the following set of coupled simultaneous equations.

$$-\frac{F_{1l}^2 L_l}{2A_l^2 E_l}\left(\frac{\partial A_l}{\partial I_l}\right) + \frac{1}{2}\sum_{m=1}^{N}\left\{\frac{L_m}{A_m E_m}\frac{\partial}{\partial I_l}\left(F_{1m}^2\right)\right\}$$

$$-\frac{L_l}{6E_l I_l^2}\sum_{j=2}^{3}\left(M_{j1l}^2 + M_{j1l}M_{j2l} + M_{j2l}^2\right)$$

$$+\frac{1}{6}\sum_{m=1}^{N}\frac{L_m}{E_m I_m}\frac{\partial}{\partial I_l}\left\{\sum_{j=2}^{3}\left(M_{j1m}^2 + M_{j1m}M_{j2m} + M_{j2m}^2\right)\right\}$$

$$-\frac{M_{1l}^2 L_l}{4G_l I_l^2} + \sum_{m=1}^{N}\left\{\frac{L_m}{G_m I_m}\frac{\partial}{\partial I_l}\left(M_{1m}^2\right)\right\} + \lambda B_{2l} = 0$$

for $l = 1,2,\ldots N$

and

$$\sum_{m=1}^{N}\left(B_{1m} + B_{2m}I_m\right) - Cost = 0 \qquad (6)$$

The even-numbered groups of terms in the first set of the above equations involve rates of change in member forces with respect to changes in section properties. For a statically determinant structure these derivatives are zero. While this is not true for hyperstatic structures, it is consistent with the concepts of the fully stressed method to neglect these terms. Thus, assuming these derivatives to be zero, the governing equations reduce to

$$-\frac{F_{1l}^2 L_l}{2A_l^2 E_l}\left(\frac{\partial A_l}{\partial I_l}\right) - \frac{L_l}{6E_l I_l^2}\sum_{j=2}^{3}\left(M_{j1l}^2 + M_{j1l}M_{j2l}\right.$$

$$\left. + M_{j2l}^2\right) - \frac{M_{1l}^2 L_l}{4G_l I_l^2} + \lambda B_{2l} = 0 \quad \text{for } l = 1.2,\ldots N$$

and

$$\sum_{m=1}^{N}\left(B_{1m} + B_{2m}I_m\right) - Cost = 0 \qquad (7)$$

The evaluation of the rate of change of cross-sectional area with respect to a change in the moment of inertia of the cross-section requires a decision as to the manner in which the section is allowed to change (i.e. in diameter and/or wall thickness). It is convenient to assume a constant diameter and to allow only variations in wall thickness. Then, using the following approximate formulas for a thin-walled tube,

$$A_l = 2\pi r_l t_l$$

$$I_i = \pi r_i^3 t_i \tag{8}$$

where r_i is the nominal radius and t_i is the wall thickness for the i^{th} member, one easily obtains

$$\frac{\partial A_i}{\partial I_i} = 2/r_i^2 \tag{9}$$

With this substitution, the governing equations may be solved for I_i, with the result

$$I_i = \left\{ \frac{L_i}{2\lambda B_{2i}} \left[\frac{F_{1i}^2 r_i^2}{2E_i} + \frac{1}{3E_i} \sum_{j=2}^{3} (M_{ji}^2 + M_{j1i} M_{j2i} + M_{j2i}^2) + \frac{M_{1i}^2}{2G_i} \right] \right\}^{1/2} \tag{10}$$

It should be observed that with the exception of λ, the formula for moment of inertia, I_i, depends only upon the properties and member forces of the i^{th} member. It is also noted that variations in λ serve to scale all moment of inertia calculations in the same manner. Thus λ may be adjusted to yield the desired natural frequencies.

An approximate initial value for λ, useful in improving the rate of convergence, may be obtained in several ways. For example, each equation may be solved for λ with the initial value given for I_i used in place of the predicted value. These N values for λ may be averaged simply, or weighted by member volume or member cost. The resulting value is deemed appropriate to the calculated natural frequency and, thus, must be adjusted to produce the required frequency. Since I_i is a reciprocal square root function of λ and the natural frequency is itself a square root function of stiffness, the appropriate correction for λ is given by

$$\lambda_{k+1} = \lambda_k \left(\frac{W_k}{W_o} \right)^4 \tag{11}$$

where k is the iteration cycle number, and W_k and W_o are the calculated and required natural frequencies respectively.

STATIC AND DYNAMIC MATHEMATICAL MODELS

The design procedure uses two mathematical models of the structure: 1) a static model, which is used to predict stiffness and member forces; and 2) a dynamic model, which is used to predict resonant frequencies and mode shapes. The models are developed for three-dimensional rigid joint frames subject to the usual limitations of small displacements, elastic behavior, and the absence of damping.

The static model includes, where possible, every member and joint in the structure to be modeled. Specification of the model includes a list of the joint coordinates and restraints, and for each member the section properties, and shear and elastic modulus. The model may also include the flexibilities of non-frame elements which may be needed for an accurate model, but which are not allowed to change during the design process. The governing equations—widely available [8]—for the static model are

$$[K]\{U\} = \{P\} \tag{12}$$

In which $[K]$ is the stiffness matrix, $\{U\}$ are the joint displacements and rotations, and $\{P\}$ are the corresponding applied joint forces and moments. Solving for the joint displacements and rotations gives

$$\{U\} = [K]^{-1}\{P\} \tag{13}$$

In which $[K]^{-1}$ is the flexibility matrix for the static model. Member forces and moments, $\{F\}_i$, are given by

$$\{F\}_i = [S]_i \{U\}_i \tag{14}$$

where $[S]_i$ is the stress matrix for the i^{th} member, and $\{U\}_i$ is a subset of $\{U\}$ consisting of the joint displacements and rotations at each end of the member.

The dynamic model consists of a definition of the dynamic displacements—or degrees of freedom—to be used for predicting mode shapes and frequencies. The displacements of the dynamic model, $\{q\}$, are linearly related to the joint displacements in the form

$$\{q\} = [C]\{U\} \tag{15}$$

The corresponding relationship between the forces and moments of the dynamic model, $\{Q\}$, and the applied joint loads of the static model is

$$\{P\} = [C]^T\{Q\} \tag{16}$$

Thus, $[C]$ specifies the transformation between the dynamic and static models. This transformation, which is specified as part of the input data, is a result of the manner in which the mass is modeled. In general, not all of the joints in the static model will be assigned mass nor will all the dynamic displacements be located at joints.

The relationship between the displacements and forces of the dynamic model is

$$\{q\} = [A]\{Q\} \tag{17}$$

In which $[A]$ is the flexibility matrix for the dynamic model. This matrix is obtained from the flexibility matrix of the static model by the expression

$$[A] = [C][K]^{-1}[C]^T \tag{18}$$

which may be achieved by combining Eqs. 15 and

16, with the aid of Eq. 13 and comparing the result to Eq. 17.

During vibration, the effective forces acting on the structure are given by D'Alembert's Principle, namely,

$$\{Q\} = -[M]\{\ddot{q}\} \tag{19}$$

in which $[M]$ is the mass matrix, specified by the analyst. Substitution of Eq. 19 into Eq. 17 yields

$$\{q\} = -[A][M]\{\ddot{q}\} \tag{20}$$

which governs the motion of the dynamic model. This equation can be reduced, by standard techniques, to an eigenvalue problem, the solution of which provides the resonant frequencies, ω_j, and corresponding mode shapes $\{\phi\}_j$.

DESIGN PROCEDURE

A block diagram illustrating the major steps in the procedure is shown in Fig. 2. It begins, at block 1, with an input description of the models and design requirements. This consists of: a) joint coordinates and restraints; b) member properties including, for each member, an initial estimate of the moment of inertia, minimum allowable moment of inertia, nominal radius, shear modulus and elastic modulus, and an indication of whether or not the moment of inertia is allowed to change during the design process; c) mass matrix and supplementary flexibilities not modeled by frame members; d) the transformation between the static and dynamic model; and e) the design requirements consisting of the design frequency and frequency tolerance, the allowable tolerance for the convergence of the member moments of inertia, and the maximum number of design cycles permitted.

The initial step in the analysis, block 2 of Fig. 2, is the formulation of the stiffness matrix for the static model, followed by the calculation, Eq. 18, of the flexibility matrix of the dynamic model. The dynamic model is then used, Eq. 20, to obtain frequencies and mode shapes. Finally, member forces and moments, for each mode shape, are determined from the expression

$$\{F\}_{ij} = \omega_j^2 [S]_i [K]^{-1} [C]^T [M] \{\phi\}_j \tag{21}$$

which is obtained by combining Eqs. 13, 14, 16, and 19 and assuming simple harmonic motion.

The next operation, block 3 of Fig. 2, is to predict improved member areas and moments of inertia. With the Lagrange Multiplier updated, Eq. 11, the moments of inertia are calculated according to Eq. 10. These calculations are repeated for each mode shape with the maximum value being selected for the next iteration. Member cross-sectional areas are then computed from

$$A_i = 2I_i / r_i^2 \tag{22}$$

The final step in the design cycle, block 4 of Fig. 2, is the test to determine if the design requirements are satisfied. If the resonant frequencies and member moments of inertia satisfy the inequalities

$$1 - \Delta_f \le \frac{\omega_j}{\omega_o} \le 1 + \Delta_f$$

and (23)

$$1 - \Delta_I \le \frac{(I_i)_{new}}{(I_i)_{old}} \le 1 + \Delta_I$$

the procedure is judged to have converged and the design process is stopped. In these expressions Δ_f and Δ_I are the allowable tolerances on the resonant frequencies and member moments of inertia. If the above inequalities are not satisfied the design cycle is repeated using the newly predicted member sections. The iteration is continued until the design requirements are met, the number of iterations equals the prescribed maximum, or until all members have realized their minimum moment of inertia.

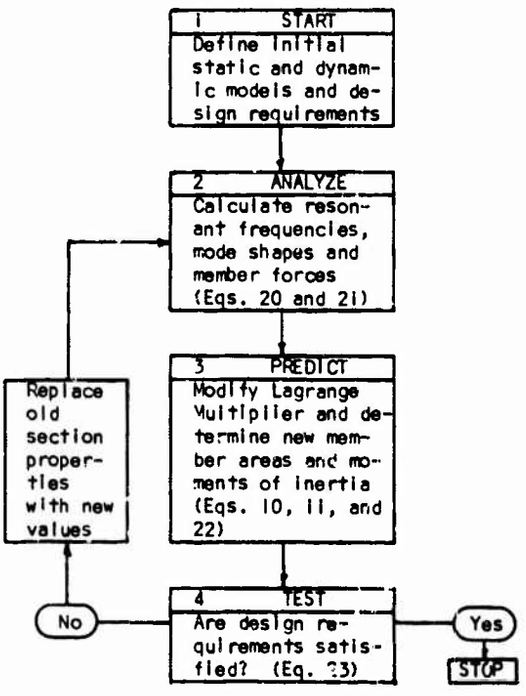


Fig. 2 - Block Diagram of Design Procedure

EXAMPLE PROBLEM

The example problem is a hypothetical 40 foot "x-y" auto-track antenna structure. The basic components (see Fig. 3) are the steel

framework, counterweights, and reflector and feed system.

The parabolic reflector and feed system are assumed fixed in design and are modeled as a six degree of freedom rigid body with a weight of 4000 pounds and a radius of gyration of 10 and 6 feet about the vertical and horizontal axes respectively. The 10,000 pound counterweights provide static balance about the x and y axes and are modeled here as three degree of freedom point masses. The larger members as shown in Fig. 3 are 16 inches in diameter. The mass of the framework is neglected. The required lowest natural frequency is 2 c.p.s. Figs. 4, 5, 6 and 7 illustrate the rapid convergence character of the system. On Figs. 4, 5 and 7 the results shown are for the cost function,

$$\text{Cost} = \sum_{i=1}^{28} (1.0 + l_i) \qquad (24)$$

while on Fig. 6 the results for the function

$$\text{Cost} = \sum_{i=1}^{28} (1.0 + L_i A_i) \qquad (25)$$

are shown in addition. This latter function being proportional to weights yields a "minimum weight" design. For the first cost function above it may be interesting to note that for the first iteration, the design was governed by the lowest frequency mode (bending x axis) for 10 of the 28 members. The next lowest mode (bending y axis) governed the design of the other 18 members. By the ninth iteration each mode (which had remained in the same order) governed the design of 14 members. The third mode is a torsion mode but remains non-critical. By the ninth iteration the ratio of the largest moment of inertia to the smallest is 250 and only the very small members are changing by 10%. Running time for this problem is approximately 50 seconds per iteration on an IBM 360 Model 50 Digital Computer. Core storage required for data for this problem was about 2000 locations.

CONCLUDING REMARKS

Experience to date indicates rapid convergence and good design behavior for the procedure. Symmetry is maintained during the redesign process to four significant figures using

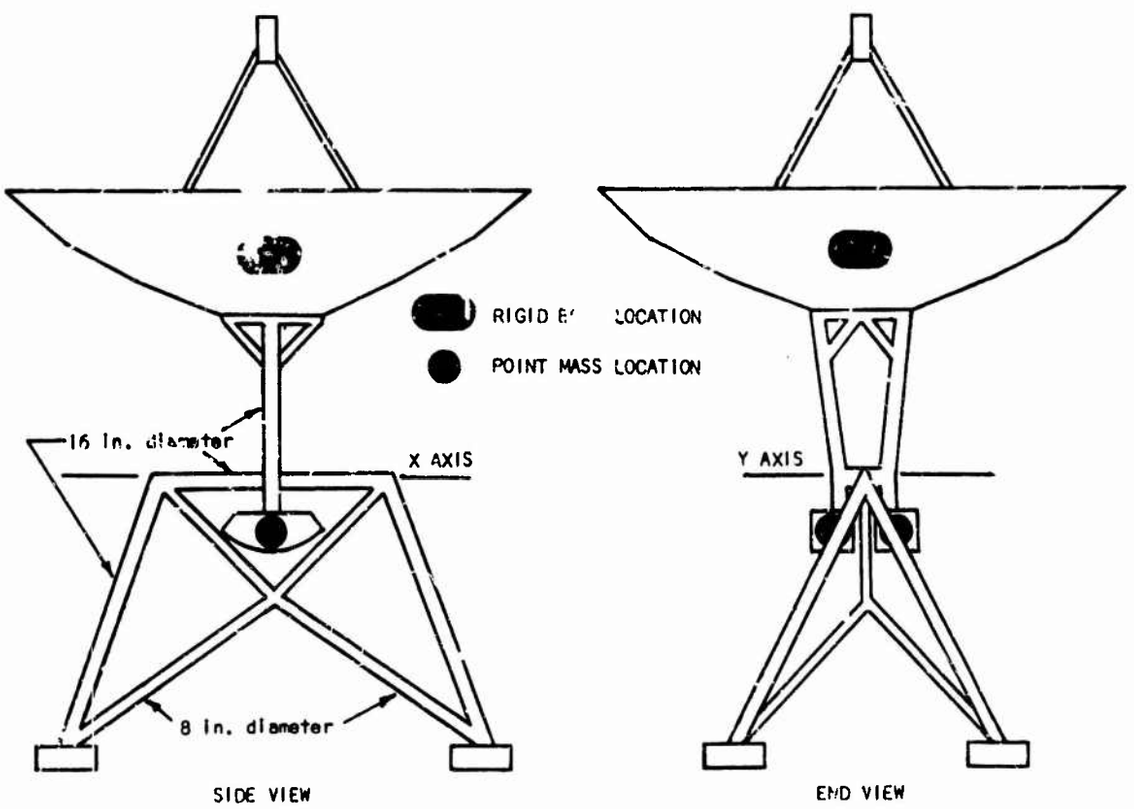


FIG. 3 XY AUTO-TRACK ANTENNA CONFIGURATION

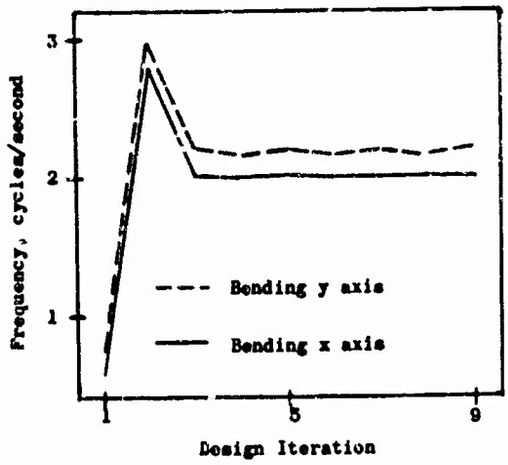


FIGURE 4 - CONVERGENCE OF RESONANT FREQUENCY

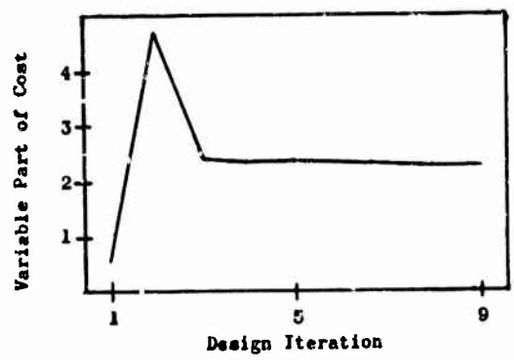


FIGURE 5 - CONVERGENCE OF COST

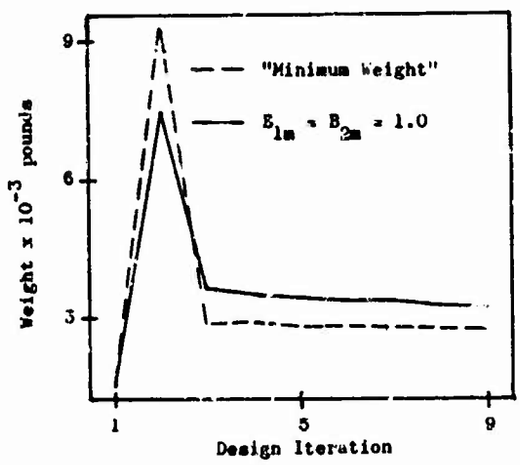


FIGURE 6 - CONVERGENCE OF WEIGHT

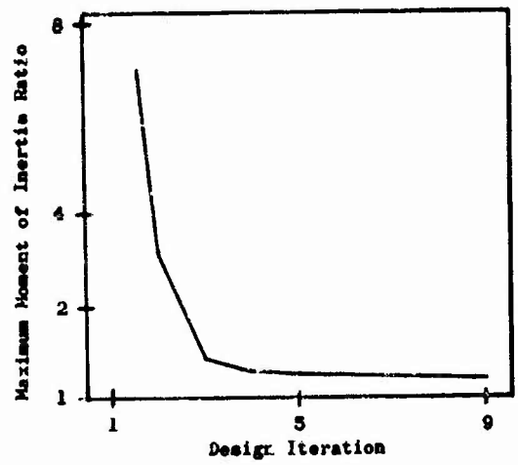


FIGURE 7 - CONVERGENCE OF MEMBER MOMENTS OF INERTIA

single precision and a 32 bit storage word. The asymmetry is no greater after 20 cycles than after the first - indicating good stability. Computer running times are relatively modest. It would seem reasonable to apply the procedure to problems where the static and dynamic models had as many as 400 and 40 degrees of freedom respectively. The two major limitations - tubular members and linear cost functions - which restrict the scope of application of the present program will be removed in future work.

REFERENCES

1. Cilley, F.H., "The Exact Design of Statically Indeterminent Frameworks, An Exposition of its Possibility, but Futility," Transactions, ASCE, Vol. 42, June 1900, pp. 353-407.

2. Schmidt, L.C., "Fully Stressed Design of Elastic Redundant Trusses under Alternative Loading Systems," Australian Journal of Applied Science, East Melbourne, Australia, Vol. 9, 1958, pp. 337-348.

3. Schmidt, L.A., Jr., "Structural Design by Systematic Synthesis," Proceedings, 2nd ASCE Conference on Electronic Computation, Pittsburgh, Pennsylvania, September 8-9, 1960, pp. 105-132.

4. Schmidt, L.A., and R.H. Mallet, "Structural Synthesis and Design Parameter Hierarchy," Journal of the Structural Division, ASCE, Vol. 89, No. ST4, Proc. Paper 3599, August 1963, pp. 269-300

5. Razani, R., "The Behavior of the Fully Stressed Design of Structures and Its Relationship to Minimum-Weight Design," AIAA Journal, American Institute of

Aeronautics and Astronautics, New York, New York, Vol. 3, No. 12, December 1965, pp. 2262-2268.

6. Young, J.W., and H.N. Christiansen, "Synthesis of a Space Truss Based on Dynamic Criteria." Journal of the Structural Division, ASCE, Vol. 92, No. ST6, Proc. Paper 5021, December 1966, pp. 425-442.

7. Lu, C.H., "Synthesis of Rigid Frames Subject to Dynamic Design Requirements," Unpublished Master's Thesis, Brigham Young University, Provo, Utah.

8. Pestel, E.C. and Leckie, F.A., "Matrix Methods in Elastomechanics," McGraw-Hill Book Co., Inc., New York, N.Y., 1963.

DISCUSSION

Robert B. McCalley (General Electric Co.): Would you elaborate briefly on this strain energy concept used to predict the changes that you want in the structure?

Dr. Christiansen: Yes. We add up the strain energy during the bending deformations, torsional and axial deformations – sheer deformations are neglected. We then look at the variation of the strain energy with respect to changes in moment of inertia or primary variables of the cross sectional properties, we do not need to include all. Of course, if you have a relationship between moment of inertia and cross-sectional area you simply look at the variation with respect to moment of inertia and then the drift of moment of inertia with respect to cross-sectional area when you are looking at the axial deformation. We had this strain energy function which was constrained to constant cost – so we have a set of equations which are the derivatives of the strain energy with respect to changes in moments of inertia, and a derivative with respect to the Lagrange multiplier. Assume that the structure is determinate, and based upon that assumption, although these are not determinate structures – the equations uncouple, and except for the Lagrange multiplier which is approximated in the iteration procedure, proceeds from that point. The design procedure, of course, converges still in one or two iterations with the determinate structure – but highly indeterminate structures show about the same behavior. We get – because of these approximations – only what we hope to be good designs, not truly optimum designs.

Mr. McCalley: Is this the strain energy in the whole structure or just in a specific mode that you may want to get away from?

Dr. Christiansen: We repeat this procedure for each mode, and we look at the worst case for each individual member. In the initial cycles particular members may be dependent upon 3 or 4 modes but finally the lowest mode will be controlling after a large number of cycles. If you don't do this – if you look just at what you think is the lowest mode you get the structure jumping, and you get bouncing back and forth. So you have to look at several modes – in this case it was only necessary to look at 2 modes.

DYNAMIC RESPONSE OF PLASTIC AND METAL SPIDER BEAMS FOR 1/9th SCALE SATURN MODEL

L. V. Kulasa
KPA Computer Techniques, Inc.
Pittsburgh, Pennsylvania

and

W. M. Laird
University of New York
Fredonia, New York

Plastic and metal spider beams for a 1/9th scale Saturn model were vibration tested in a simulated free-free condition, to determine the vibration characteristics and to demonstrate the advantages of using plastics for dynamic model testing. Frequencies were measured by using accelerometers bonded to the beam and to the electrodynamic shaker which provided the vibratory excitation. Mode shapes were visually observed with a stroboscope and were recorded using a Fastax camera operating at approximately 2,000 frames per second. A motion picture, illustrating the test apparatus and recorded mode shapes, is available from the University of Pittsburgh - Mechanical Engineering Department.

INTRODUCTION

Dynamically scaled models have long been used for wind tunnel, towing-tank and structural tests to predict the full-scale, or "prototype" phenomena [1, 2, 3, 4, 5]. It is generally recognized that to be dynamically similar, such models should be scaled with respect to geometry, material properties and loading parameters. The art which is concerned with the quantitative theory of dynamic scaling is commonly referred to as "Dimensional Analysis" [1, 2, 3, 4]. In the application of dimensional analysis to the field of experimental engineering, exact dynamic scaling is usually impossible because of the unavailability of suitable materials and the practical complications of exact geometric scaling. This requires the use of "distorted" models, i.e., proper scaling does not exist for the model. However, distorted models may be used successfully by applying suitable "prediction factors" to the test results. Correction factors, or "prediction factors," may be estimated theoretically, but are usually determined from the experience gained as prototypes are constructed and tested.

The advent of large nuclear and aerospace structures has complicated model testing techniques in that reasonably sized metal models require excessive geometric scale ratios. For example, a 10:1 model of the C-5 Saturn launch vehicle would be 40 feet high, a large heavy structure. If higher geometric scale ratios are used to reduce the weight and size of the model, inaccuracies are introduced in measuring prediction factors for the dynamic response. Therefore, plastic models provide the advantage of a lightweight, reasonable scale model test.

Metal models can be used in the study of a prototype system, however, plastic models can be used in many cases and demonstrate several relative advantages.

The purpose of the test described herein was to evaluate the feasibility of using a plastic model to predict the dynamic response of a metal model. To do this the theoretical correlation factor was calculated and compared with the experimentally measured correlation factor.

This report describes the results obtained from testing two 1/9th scale Saturn model spider beams. A metal spider beam and the plastic spider beam were used for vibration tests to determine the principal frequencies and mode shapes of both beams in a simulated free-free condition.

PLASTICS AND DYNAMICALLY SIMILAR MODELS

A dimensional analysis of structural models develops as one of the governing dimensionless ratios:

$$\pi = \frac{E}{\gamma L} \qquad (1)$$

where

π = dimensionless ratio;

E = modulus of elasticitity, $lb/in.^2$;

γ = weight density of material, $lb/in.^3$;

L = representative length, in.

For a model to be dynamically similar (undistorted), this and other dimensionless ratios must be equal to those for the prototype. Equation (1) is a measure of the elastic forces compared to the inertia forces. Since the value of E/γ is dependent only on the material involved, undistorted dynamic similarity can be achieved only by proper selection of geometric scale ratios and the relative E/γ value for the given material. Table 1 is a tabulation of typical values of E/γ for a variety of materials. Inspection of Table 1 indicates that even with a model scale ratio as high as 10:1, a dynamically similar model having a value of E/γ equal to that of the prototype could be achieved by constructing the model from a suitable plastic.

Questions then arise concerning the behavior of the mechanical properties of plastics. Creep, aging and other non-linear effects may invalidate the advantages of achieving dynamic similarity with some plastics. However, it has been established that many plastic materials exhibit

TABLE 1

Typical Values of E/γ For Various Materials [6, 7, 8]

Material	Modulus of Elasticity 10^6 lb/in.^{2}	Material Density γ, lb/in.^{3}	$\frac{E}{\gamma} \times 10^{-6}$
Aluminum	10.0	0.098	102.04
Lead	2.4	0.410	5.85
Iridium	75.0	0.810	92.59
Gold	11.4	0.699	16.31
Tin	4.0	0.264	15.15
Steel	30.0	0.283	106.01
Wood	1.1	0.013	84.62
Brass	15.0	0.308	48.70
Homopolymer	0.410	0.051	8.04
Acetal, Copolymer	0.375	0.051	7.35
Acetal, Implex A	0.220	0.041	5.37
Acrylic, Implex B	0.270	0.039	6.92
Chlorinated Polyethers	0.150	0.051	2.94
Polycarbonate	0.320	0.043	7.44
Polypropylene	0.160	0.034	4.71
Poly-Styrene	0.100 to 0.500	0.040	2.50 to 12.50
Tenite II*	0.200 to 0.500	0.043	4.65 to 11.63

* Material used for the plastic spider beam.

reasonably linear characteristics. Figures 1 and 2 show typical static and dynamic characteristics obtained by tests on tensile and cantilever beam specimens of cellulose acetate butyrate (trade name Tenite II). These tests were conducted because the properties of many materials can vary from sample to sample and therefore, for application, specific values for material properties should be determined by testing coupons from the material used for the model.

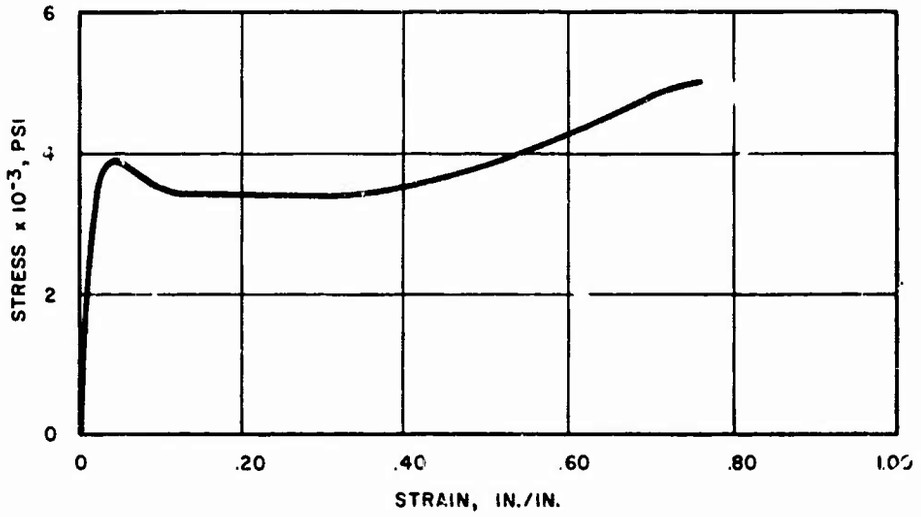


Figure 1. Typical stress-strain curve at room temperature for cellulose acetate butyrate

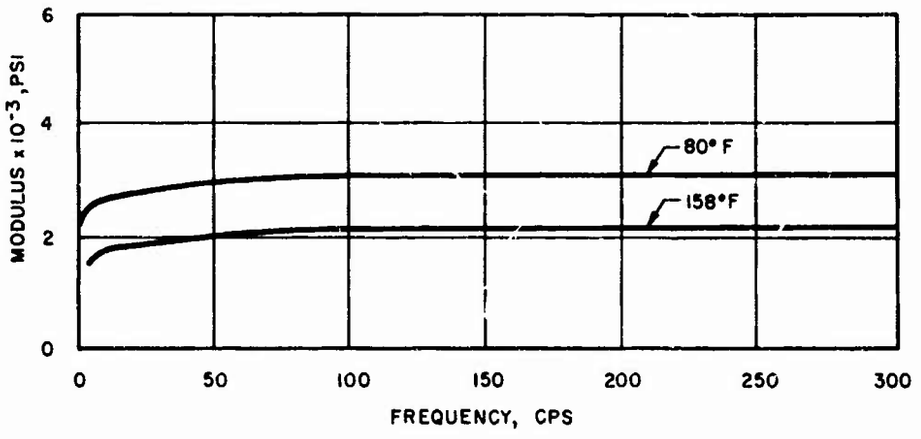


Figure 2. Dynamic modulus of elasticity vs. frequency for cellulose acetate butyrate

Sankey [9] also reports on the use of plastic models. He found excellent correlation between the vibration response of a plastic model compared to the response of a steel prototype.

THEORETICAL CORRELATION FOR NATURAL FREQUENCIES

To properly assess the performance of the plastic model, the theoretical correlation factor relating the plastic model natural frequencies to those of the metal model was calculated and compared with that obtained by experiment. In this investigation the plastic model and the metal model were geometrically identical. Being of different materials, the plastic model is therefore considered a "distorted" model [1, 2, 3].

For a plastic model and metal model which are geometrically similar although not identical, the theory of models assumes that

$$\frac{\omega_p}{\omega_m} = \frac{\ell_m}{\ell_p}\sqrt{\frac{(E/\gamma)_p}{(E/\gamma)_m}} \qquad (2)$$

where

ω = natural frequency, rad/sec.;

ℓ = representative length, in.;

E = modulus of elasticity, lb/in.^{2};

γ = weight density of material, lb/in.^{3};

m = subscript referring to metal model;

p = subscript referring to plastic model.

The material properties for 6061-T6 aluminum alloy (metal model) and cellulose acetate butyrate (plastic model) were:

$E_p = 2.9 \times 10^5$ lb/in.^{2}

$E_m = 10.7 \times 10^6$ lb/in.^{2}

$\gamma_p = .043$ lb/in.^{3}

$\gamma_m = .098$ lb/in.^{3}

Since the metal model and plastic model are geometrically identical,

$$\frac{\ell_m}{\ell_p} = 1$$

Therefore, Eq. (2) reduced to

$$\frac{\omega_p}{\omega_m} = \sqrt{\frac{(E/\gamma)_p}{(E/\gamma)_m}} \qquad (3)$$

or the theoretical correlation factor is:

$$\frac{\omega_p}{\omega_m} = 0.248 \qquad (4)$$

EXPERIMENTAL PROCEDURE

The metal model, made available by the NASA Langley Research Center, was a built-up spider beam assembly approximately 28 inches in diameter constructed of 6061-T6 aluminum alloy. Figures 3 and 4 illustrate a drawing and photograph of the physical spider beam. The plastic model was constructed of cellulose acetate butyrate (Tenite II) and consisted of glued sections which duplicated the geometrical system of the metal model.

Figure 5 is an illustration of the test apparatus used for testing. The plastic model and metal model were each forced into oscillation by an electrodynamic shaker. A connecting arm was used to transmit the excitation to the spider beam from the shaker. The spider beam was attached to a wire suspended from a height sufficient to allow the beam to maintain a free-free simulation. Response amplitudes were obtained with a Columbia Research Laboratory Accelerometer model 606-3 bonded to a radial arm of the spider beam with back-to-back adhesive tape. Input amplitudes were measured by a similar accelerometer mounted on the armature of the electrodynamic shaker. This provided data from which the magnification factor (output amplitude/input amplitude) as a function of the driving frequency was calculated.

Mode shapes were determined by visual observation using a stroboscope and recorded by high-speed motion pictures using a Fastax high-speed camera operating at approximately 2,000 frames per second.

EXPERIMENTAL RESULTS

Figures 6 and 7 are frequency spectra obtained for the plastic model and metal model. The peaks of the curves in these figures represent the natural frequencies for the first several models of vibration.

Table 2 lists the natural frequencies of the plastic model and the metal model and the experimentally calculated correlation factor which can be compared with the

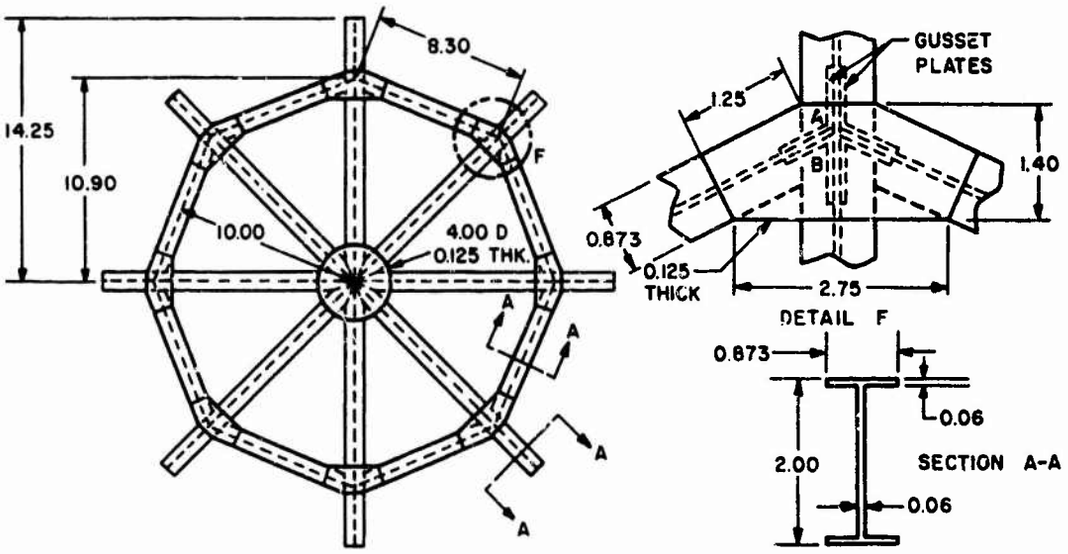


Figure 3. Spider beam wsembly



Figure 4. Photograph of spider beam

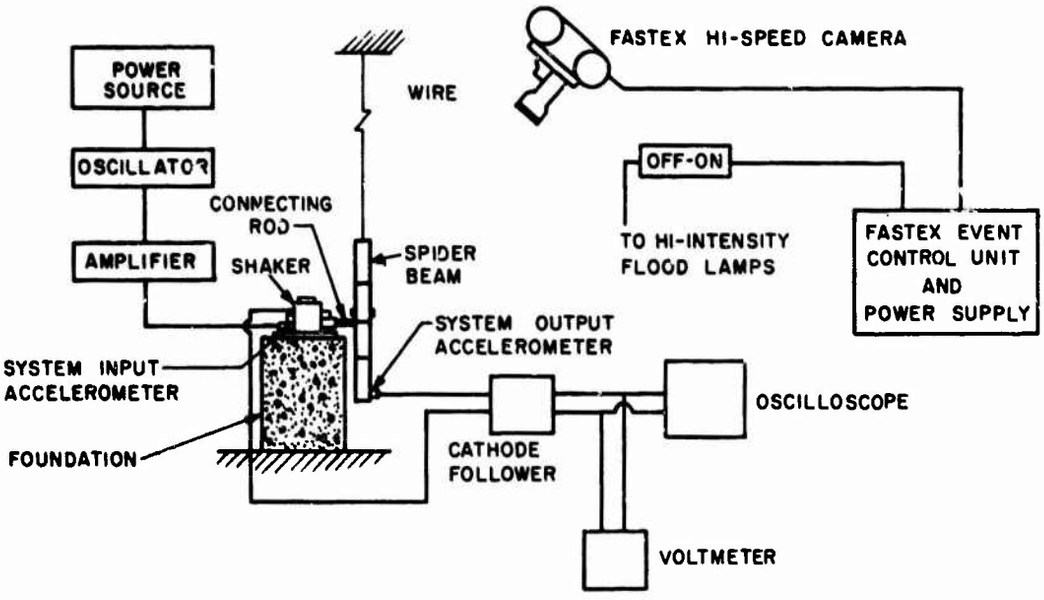


Figure 5. Test apparatus

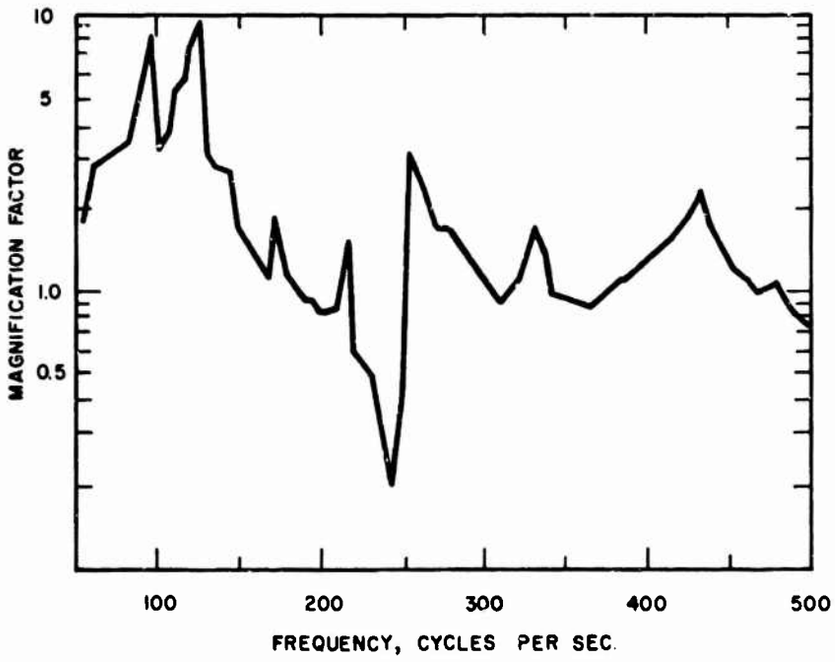


Figure 6. Vibration response of cellulose acetate butyrate spider beam

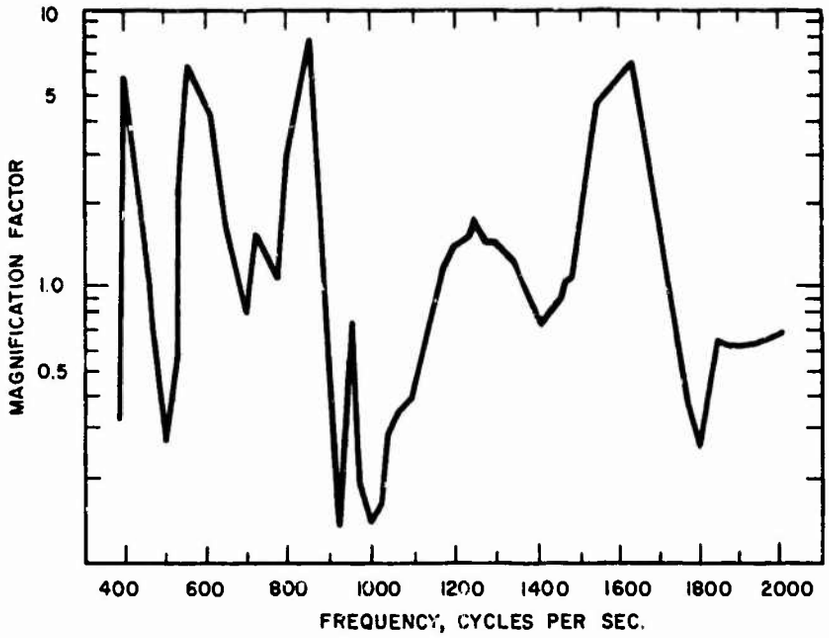


Figure 7. Vibration response of aluminum spider beams

TABLE 2

Natural Frequencies

(Theoretical Correlation Factor $\omega_p/\omega_m = 0.248$)

Mode	Metal Model ω_m, cps	Plastic Model ω_p, cps	Experimental Correlation Factor (ω_p/ω_m)	Correlation Factor Percent Error
1	405	96	.237	4.6
2	555	127	.229	8.2
3	725	175	.241	2.9
4	850	217	.255	2.8
5	950	254	.267	7.7
6	1,250	331	.265	6.9
7	1,625	435	.268	8.1
8	1,850	480	.259	4.4

theoretical correlation factor of Eq. (4), $\omega_p/\omega_m = 0.248$.

Figures 8 and 9 are illustrations of the first and second modes of vibration of both the plastic model and metal model. The mode shapes for all observed modes of vibration were similar for both the plastic and metal spider beams. In the first mode of vibration, radial members oscillate symmetrically with respect to two perpendicular diametral members as shown in Figure 8. The second mode of vibration can best be described as the shape resembling an "umbrella".

The higher modes of vibration were observed for both models and were similar in all distinquishable cases. There are high-speed motion pictures of the first and second mode shapes.

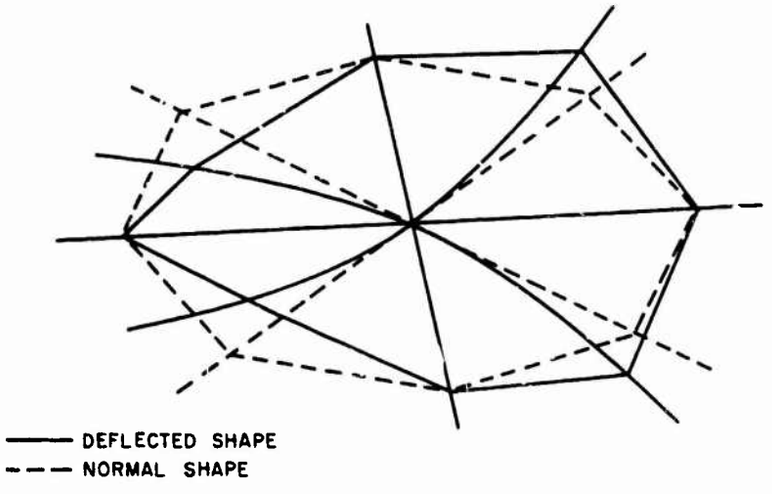


Figure 8. First mode of vibration, mode shape

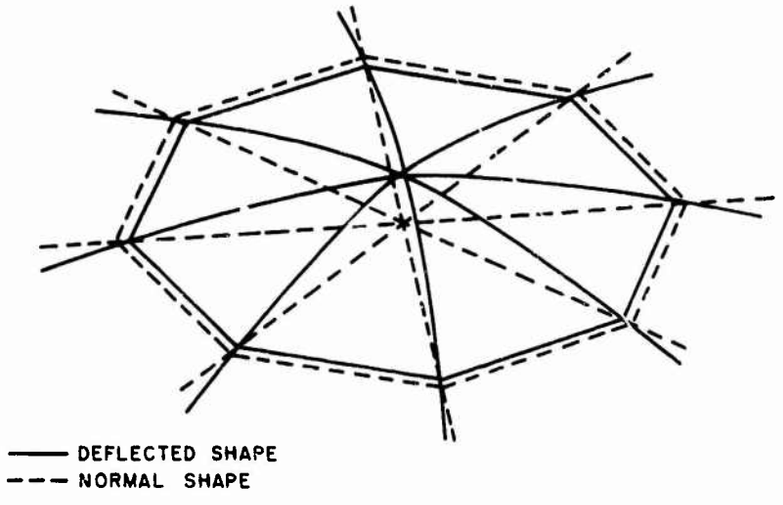


Figure 9. Second mode of vibration, mode shape

CONCLUSION

It appears that scaled plastic models can be used to provide a good representation of the vibration characteristics of a metal model (prototype). In addition to large aerospace structures such as the spider beam, reports of plastic model tests of a nuclear reactor vessel and analysis and vibration tests of a plastic model of a radial drill press, References 10 and 11, show good results.

Examination of Table 2 shows that the error for predicted frequencies of the metal model, based on the plastic model test, range from 2.8 to 8.2 percent for the first eight modes of vibration. The predicted frequencies were obtained using the plastic model results and the theoretical correlation factor of $\omega_p/\omega_m = 0.248$.

The mode shapes for the first and second modes of vibration were shown in Figures 8 and 9 respectively. These and the higher modes of vibration were observed visually. The advantage of the plastic model is evident from observing the movement of the plastic and metal spider beams that result from a vibratory excitation. The plastic, being more flexible, results in a greater amplitude for a given input force thus allowing for a clearly defined mode shape. The use of transparent plastic models is also highly desirable for the present application because the motion of the members is not obscured by intervening members of the structure. This is particularly valuable in determining the mode shapes. Another advantage of using plastics is that it is possible to achieve complete dynamic similarity at the scale ratio of 10:1.

The flexible, lightweight and transparent features of most plastics represent advantages that can allow for an economic accurate prediction of the dynamic response of a prototype system. However, the essential material properties and their characteristic behavior must be investigated thoroughly to insure that the test data is understood and results in an accurate representation of the dynamic response of a given structure.

REFERENCES

1. G. Murphy, "Similitude in Engineering," The Ronald Press, New York, 1950.
2. H. E. Huntley, "Dimensional Analysis," Rinehart and Company, Inc., New York, 1951.
3. L. I. Sedov, "Similarity and Dimensional Methods in Mechanics," Academic Press, New York, 1959. (Translated from the Russian by M. Holt and Morris Friedman.)
4. J. K. Vennard, "Elementary Fluid Mechanics," John Wiley and Sons, Inc., New York.
5. "Proceedings," NASA-University Conference on the Science and Technology of Space Exploration, V-2, Chicago, Illinois, November, 1962.
6. O. W. Eshbach, "Handbook of Engineering Fundamentals," John Wiley and Sons, Inc., New York, 1952.
7. "Machine Design," September 20, 1962.
8. "Modern Plastics," Encyclopedia Issue, 1965.
9. G. O. Sankey, "Plastic Models for Vibration Analysis," Proceedings, Society for Experimental Stress Analysis, Vol. XI, No. 2, 1953.
10. H. E. Sheets, "Natural Frequencies and Mode Shapes of a Westinghouse 1/4 Scale Lucite Model of the S5N578 Reactor Vessel," Electric Boat Division, General Dynamics Corporation, Groton, Connecticut, September, 1958.
11. S. Taylor and S. A. Tobias, "Lumped-Constants Method for the Prediction of the Vibrstion Characteristics of Machine Tool Structures," Proceedings of the 5th International Machine Tool Design and Research Conference, University of Birmingham, September, 1964.
12. A. A. Tomkins, "How Engineers View Plastics," Chemistry and Industry, February 27, 1965.

DISCUSSION

Mr. Perelman (Esso Production Research Co.): Did you do any experimental work to determine stresses in models such as these:

Dr. Laird: No. We made no attempt to obtain stresses. We were trying to predict natural frequencies and take moving pictures.

Mr. Perelman: We have had some experience with large scale structures of this type and our results have been very unsatisfactory with respect to stress work.

Dr. Laird: I would hesitate to venture a comment on trying to analyze these things dimensionally and their dynamic similitude as far as stresses are concerned. I think there will be creep and similar effects.

CHARTS FOR ESTIMATING THE EFFECT OF SHEAR DEFORMATION AND ROTARY INERTIA ON THE NATURAL FREQUENCIES OF UNIFORM BEAMS*

F. F. Rudder, Jr.
Aerospace Sciences Research Laboratory, Lockheed-Georgia Company
Marietta, Georgia

The effect of shear deformation and rotary inertia on the natural frequencies of a uniform beam are presented in the form of design charts. These charts represent the eigenvalues obtained using Timoshenko beam theory for several sets of boundary conditions of interest to engineers. In particular, the charts illustrate the manner in which the Timoshenko theory asymptotically approaches elementary beam theory.

INTRODUCTION

The dynamics engineer is often required to estimate the vibration characteristics of beams or beam-like structures. The frequencies and mode shapes of Bernoulli-Euler beams have been well documented in the literature [1,2]. These beams are basically characterized as "slender"; however, it is not always obvious that a beam-like structure can be considered "slender" especially from a dynamics standpoint. This paper considers the effect of shear deformation and rotary inertia on the natural frequencies of beams according to Timoshenko's theory [3]. In particular, the effect on the fundamental and first harmonic frequencies for simply-supported, cantilever, and clamped-clamped uniform beams is presented in the form of design charts. The range of parameters considered is broad enough to include situations encountered in aircraft and ship design.

NOMENCLATURE

The theoretical development and solutions to the equations of motion have been discussed by many authors [4,5,6]. However, these papers have either considered a very limited range of parameters or specialized problems. The purpose here is simply to discuss the results obtained without recourse to lengthy theoretical developments.

For specified boundary conditions the dynamic characteristics of an elementary or Bernoulli-Euler beam are contained in the single frequency parameter

$$\zeta^2 = \frac{mL^4}{EI}\omega^2 \tag{1}$$

whereas Timoshenko's theory introduces two additional parameters to include shear deformation and rotary inertia. The shear deformation parameter is

$$\alpha^2 = \frac{EI}{\kappa AGL^2} \tag{2}$$

and the rotary inertia parameter is

$$\beta^2 = \frac{I}{AL^2} \tag{3}$$

where m is the mass per unit length

E, G are Young's modulus and the shear modulus of the material, respectively

I is the second area moment of the beam cross-section

L is the length of the beam

κ is the cross-section shape factor (Reference 7 gives an especially good account of this number)

A is the cross-section area

ω is the undamped circular frequency (rad./sec.)

For the elementary or "slender" beam, values of the frequency parameter, ζ, for the fundamental and first four harmonic frequencies and the boundary conditions under consideration are presented in Table 1.

For the Timoshenko beam, the values of the frequency parameter, ζ, which satisfy the equations of motion and the appropriate boundary conditions are functions of the parameters α and β. The difficulty of presenting a generalized parameter study is that α and β are not independent and are related according to

$$\alpha = \sqrt{\frac{E}{\kappa G}}\,\beta \tag{4}$$

*Paper not presented at Symposium.

TABLE 1
Volues af for an Elementary Beom for the First Five Modes of Vibration

Simply Supported Ends	Clamped Free Ends	Clamped-Clamped Ends
9.8646	3.1586	22.3681
39.4584	22.0540	61.7008
88.5928	61.7008	120.6371
158.3361	120.6376	199.8051
247.5573	199.8051	298.4511

However, in the theoretical development another parameter

$$\zeta = 1/(\alpha\beta) \tag{5}$$

appears which allows one to separate the parameters α and β. The relation expressed by Equation (5) is presented graphically in Figure 1, where the range of values for α and β have been limited to numbers encountered in practice.

Volues of the frequency parameter, ζ, for the Timoshenko beam theory form o surfoce in the three-dimensional space defined by points (α, ζ, ζ). The values of the frequency parameter, ζ, for the elementary beam appear as o plane (i.e., ζ = constant) in this space. The surface, $\zeta(\alpha,\zeta)$, for values of ζ corresponding to the fundamentol frequency of o cantilever Timoshenko beam is illustrated in Figure 2. The plane $\zeta = 3.5186$ corresponds to the elementary solution (see Table 1). The dashed lines in the foreground illustrate the asymptotic naturn of the Timoshenko theory to the siementory theory. Basicolly, the effect of shear deformation and rotary inertio on the natural frequency of o beam is to cause o frequency decrease relative to the elementary solution for the corresponding mode. The magnitude of this decrease depends upon the value of α and ζ or olternotely α and β. If α is smoll and β is lorge, rotary inertio effects predominate as illustrated by the spike in the upper left of Figure 2. If α is large (i.e., if there is significant shear flexibility), the value of ζ is independent of ζ as exhibited by the portion of the surface on the right-hand side of Figure 2.. The percentage decrease from the elementary solution for various points an the surface of Figure 2 is so indicated in the figure.

DESIGN CHARTS

Results presented in the form illustrated in Figure 2 are not suitable for design use. Figures 3 through 8 have been constructed so that the frequency parameter, $\zeta(\alpha, \zeta)$, can be determined approximately once α and ζ are known. These charts are plots of $\zeta(\alpha, \zeta)$ vs. ζ with curves of α = constant. One must use the parameters of the beam to compute α and β using Equations 2 and 3. (The parameter κ con be calculoted using the results of Reference 7). Then, from Equation 5 or Figure 1, the parameter ζ is computed. Depending upon the boundary conditions of the problem, the appropriate design chart is entered using the values af α and ζ and the corresponding frequency parameter, ζ, is determine approximotely. It should be noted that if $\alpha < 0.02$ and $\zeta > 5000.0$ the values af ζ given in Table 1 are to be considered accurate (i.e., elementary beam theory applies to the problem at hand) at least for the first two modes of vibration.

CONCLUSIONS

The design charts presented in Figures 3 through 8 allow rough estimates of the effect of shear deformotion and rotary inertia an the fundamental and first harmonic frequency of simply supported, cantilevered, and clamped-clamped beams. The range af parameters considered in these charts covers all situations encountered in practice.

REFERENCES

1. Grover L. Rogers, An Introduction to the Dynamics af Framed Structures, p. 176, John Wiley & Sons, Inc., New York, N. Y., 1959.

2. D. Young and R. P. Felgar, Jr., "Tables of Characteristic Functions Representing Narmal Modes of Vibration of o Beam," Engineering Research Bulletin No. 4913, Bureau of Engineering Research, University of Texos, Austin, 1949.

3. S. P. Timoshenko and D. H. Young, Vibration Problems in Engineering, 3rd Edition, pp. 329-331, D. Van Nostrand Company, Inc., New York, N. Y., 1954.

4. R. W. Leonard, "On the Salutian for the Transient Response of Beams," NACA TR-R-21, 1958.

5. T. C. Huang, "The Effect of Rotary Inertio and af Shear Deformation on the Frequency and Normal Mode Equations of Uniform Beams with Simple End Conditions," Journol of Applied Mechanics, pp. 579-584, December 1961.

6. F. F. Rudder, "Effect of Shear Deformation and Rotary Inertia on the Dynamic Characteristics of a Beam," Lockheed-Georgia Co. Rept. ER-9715, 1968.

7. G. R. Cowper, "The Shear Coefficient in Timoshenko's Beom Theory," Journal of Applied Mechanics, pp. 335-340, June 1966.

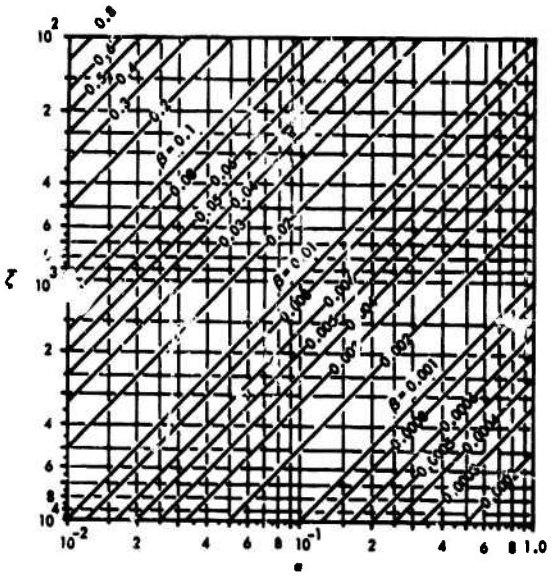


Fig. 1 Plot of $\bar{\zeta}$ vs a in the range of practical interest

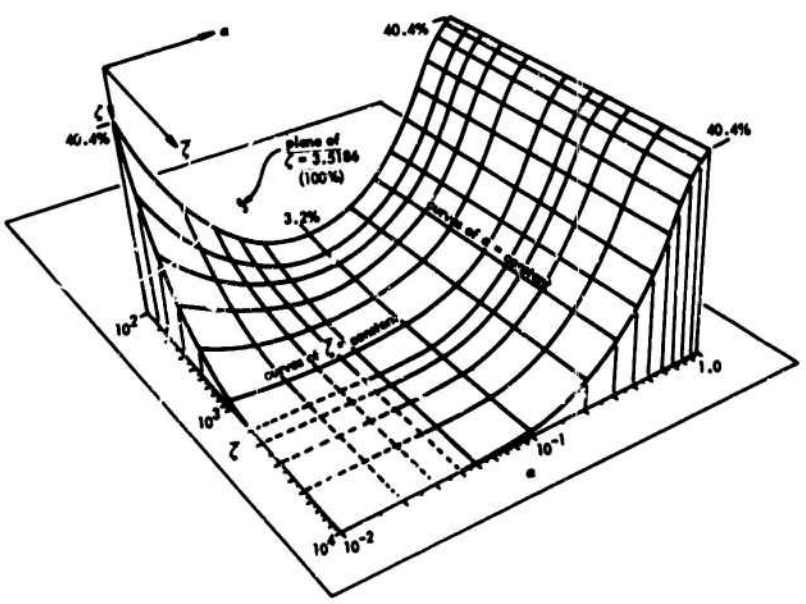


Fig. 2 The solution surface $\zeta(a,\bar{\zeta})$ for a cantilever Timoshenko beam (fundamental mode)

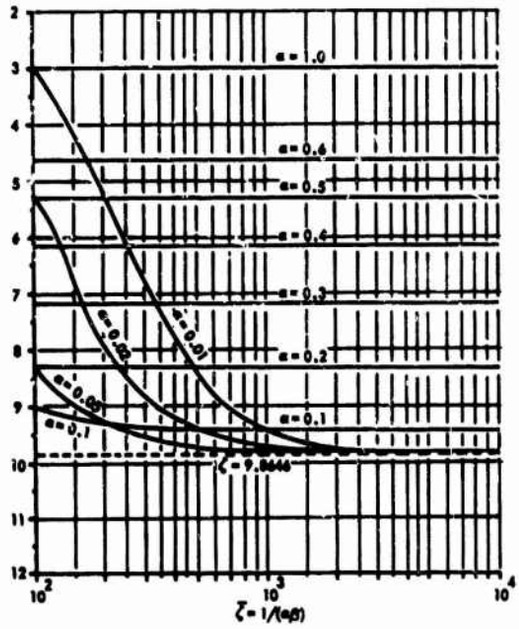


Fig. 3 Simply supported Timoshenko beam: fundamental frequency

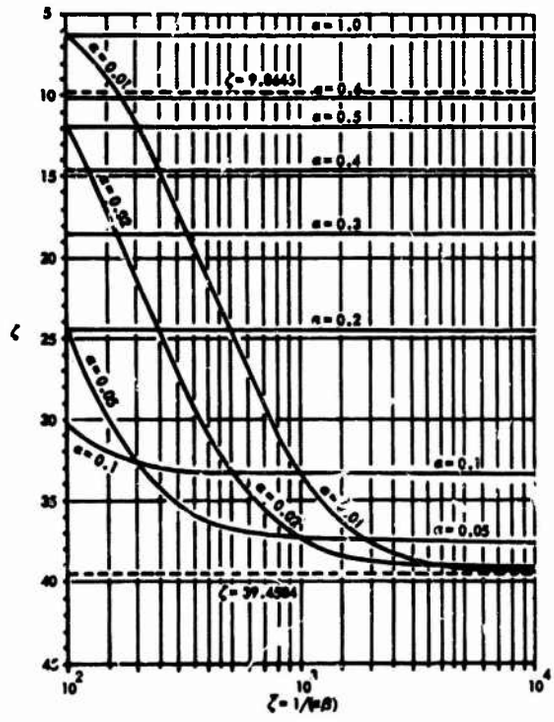


Fig. 4 Simply supported Timoshenko beam: first harmonic frequency

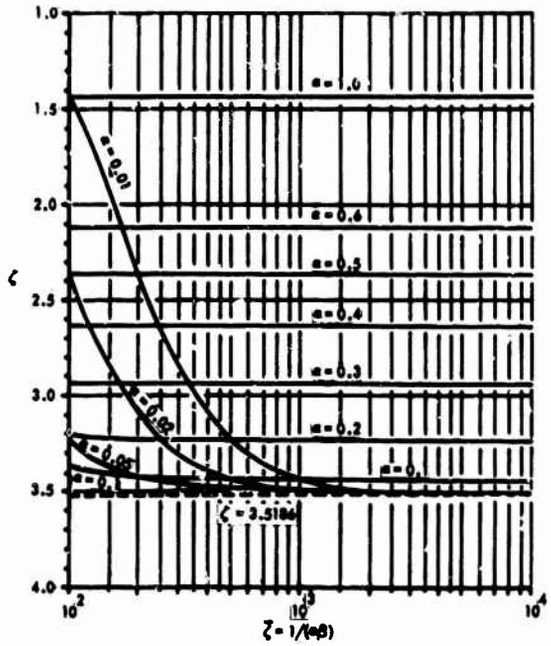


Fig. 5 Cantilever Timoshenko beam: fundamental frequency

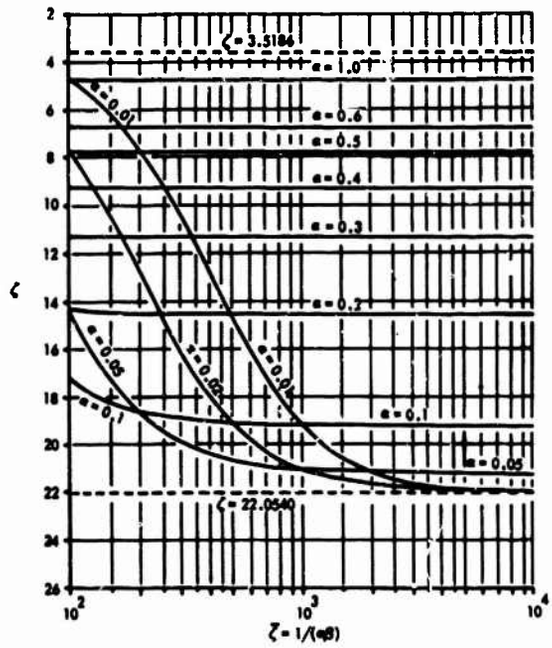


Fig. 6 Cantilever Timoshenko beam: first harmonic frequency

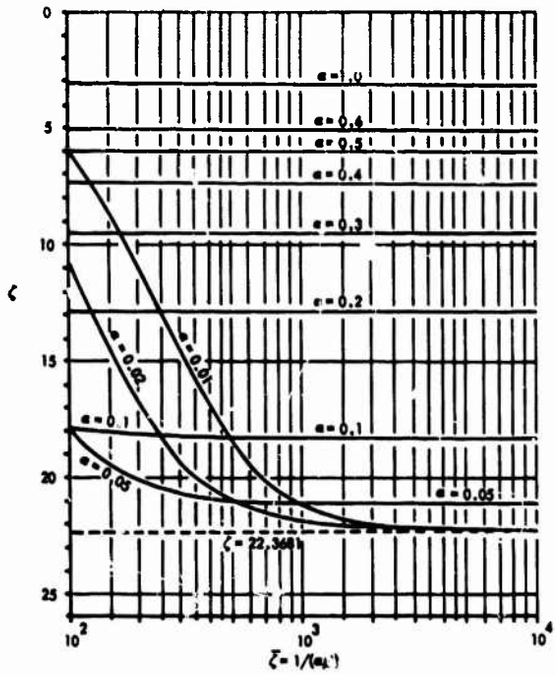


Fig. 7 Clamped-clamped Timoshenko beam: fundamental frequency

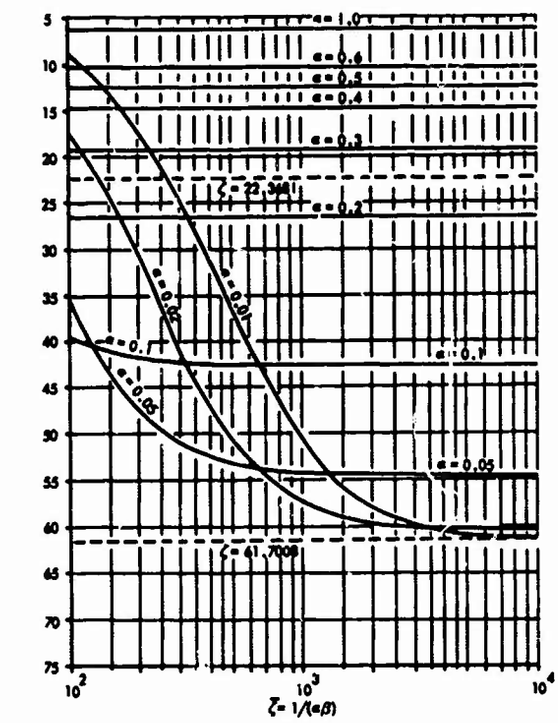


Fig. 8 Clamped-clamped Timoshenko beam: first harmonic frequency

ACOUSTIC RESPONSE ANALYSIS OF LARGE STRUCTURES

F. A. Smith
Martin Marietta Corporation
Denver Division
Denver, Colorado 80201

and

R. E. Jewell
The National Aeronautics and Space Administration
Marshall Space Flight Center
Huntsville, Alabama

Following is a summary of the technical approach and the results of an acoustic response analysis performed on a large complex payload. The purpose of the analysis was to evaluate the feasibility of calculating the acoustic response of complex structures to at least 200 Hz including considerations of the structural properties of the payload. The technical approach used to obtain the modal representation of the payload and the payload configuration is presented. Because of the required frequency response of the complex structure, the final model used in the response analysis represents over 3,000 degrees of freedom. The method for applying the acoustic pressures is discussed as well as the results of the analysis.

CONFIGURATION

The analysis was performed on a payload planned for the Saturn 1B (S-1B) vehicle as a part of the Apollo Applications Program (AAP). An over-all view of the payload installed within the S-1B structure is shown in Figure 1. The payload consisted of three major elements; the rack structure, the Apollo Telescope Mount (ATM) and the Lunar Module (LM). The rack structure supported miscellaneous equipment, the ATM, and the LM, and in turn was supported by the S-1B Structural Payload Adapter (SLA) at four points. The payload weighed approximately 30,000 pounds, was 30 feet long and 23 feet in diameter. The SLA was an eight-degree conical frustum (16° included angle at the apex) made of aluminum honeycomb. The SLA was attached to an Instrumentation Unit (IU) that mated to the upper stage of the S-1B. The analysis included the payload plus the SLA. No other portion of the S-1B was considered.

INTRODUCTION

The determination of random response vibration levels of a complex structure forced by acoustics was required. The structure to be evaluated was a payload planned for flight by the Apollo Applications Program (AAP). The boost vehicle for this payload was the Saturn 1B.

Historically, definition of random vibration levels for the frequency range above 30 to 50 Hz is based on previously measured data acquired on similar configurations during flight. Various "scaling laws" are applied to these empirical data to account for small differences in configuration and mass. However, these scaling techniques do not include considerations of basic structural properties or local dynamic response characteristics. When no measured data are available for the configuration of interest, these scaling techniques become order-of-magnitude estimates.

The majority of equipment trusses and local support structure have their fundamental resonances above 30 Hz, with many occurring up to 200 Hz. Consequently, design loads must consider the frequency range to at least 200 Hz.

A response analysis for the AAP payload was performed by classical methods, which inherently include considerations of structural properties.[1] The structure was modeled using the direct stiffness approach in generating the stiffness matrices. The mass was lumped at

LM/ATM Mounted in SLA of S-IB

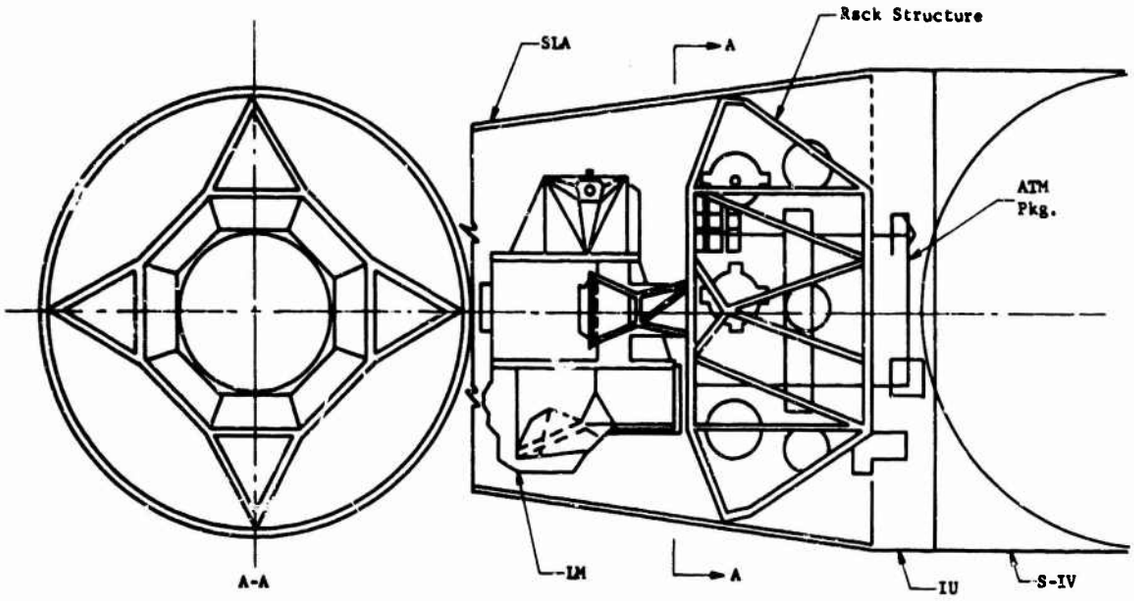


Figure 1. Peyloed Configuration

propar collocation points. The acoustics ware represented as pressure spactral daneitiae and applied on tha extarnel surface of the peyloed support structure. Response celculetione ware in terms of accelaration spactrel dansitiee.

The techniquae ueed are discussed in the following paragraphe and demonetrete the feseibility of responsa celculetione in the criticel fraquancy renga of interest. Comparisons with one flight-measurad date point ere made; celculetad valuas compare favorebly.

BASIS OF ANALYSIS

The analysis was based on e set of equetions written in matrix notation that definee the response of eny structura to fluctuating pressura. For eny arbitrary eystam, the equetions of motion cen be expreeeed by:

$$[M]\{\ddot{\delta}\} + [C]\{\dot{\delta}\} + [K]\{\delta\} = \{F_o\} \qquad (1)$$

whara M is the mass matrix, C is the demping matrix, K is tha stiffnaca matrix, and F ie tha forca matrix. By substitution of the modal coordinata trensformation,

$$\{\delta\} = [\Phi]\{q\} \qquad (2)$$

tha abova equation can ba expreesed ee:

$$\left[M_{EQ}\right]\{\ddot{q}\} + \left[2\zeta\omega M_{EQ}\right]\{\dot{q}\} + \left[\omega^2 M_{EQ}\right]\{q\} = [\Phi]'\{F_o\} \qquad (3)$$

This equation is obtained by the above substitution end by premultiplying by Φ'. This can be further manipuleted to yield:

$$\left[\omega^2 - \Omega^2 + 2j\zeta\omega\Omega\right]\{q_{(\Omega)}\} = [\Phi]'\{F_o\};$$

$$M_{EQ} = [1] \qquad (4)$$

It wee desired to exprees the forcing function es the product of the pressura end the area over which it ects. By computing the area in the system coordinete exee for ell collocstion points, an eree metrix and e pressure were substituted for the force matrix to obtain:

$$\left[\omega^2 - \Omega^2 + 2j\zeta\omega\Omega\right]\{q_{(\Omega)}\} = [\Phi]'\left\{\frac{A}{0}\right\} P_o \qquad (5)$$

Solving for q end trensforming beck to discrete coordinates yields:

$$\{\delta\} = [\Phi]\left[\frac{1}{\omega^2 - \Omega^2 + 2j\zeta\omega\Omega}\right][\Phi]'\left\{\frac{A}{0}\right\} P_o \qquad (6)$$

eubetituting the eecond time derivative $\ddot{\delta} = \Omega^2\delta$ yielde

$$\frac{\{\ddot{\delta}\}}{P_o} = [\Phi]\left[\frac{\Omega^2}{\omega^2 - \Omega^2 + 2j\zeta\omega\Omega}\right][\Phi]'\left\{\frac{A}{0}\right\} \qquad (7)$$

The eystem trenefer function wes obteined by teking the absolute velue of the above equetion. By expreesing the fluctueting preesura in the form of e spectrel deneity, the reeponee epectrel deneity wee formuleted ee follows:

$$S_n(\Omega) = |H(\Omega)|^2_n \, S_{input}(\Omega) \qquad (8)$$

Where $S_{input}(\Omega)$ has units of psi^2/Hz, $|H(\Omega)|^2_n$ has units of $(in./sec^2/psi)^2$ and $S_n(\Omega)$ has units of $(in./sec^2)^2/Hz$. These are the input pressure spectral density, the transfer function squared, and the response power spectral density at degree-of-freedom "n" and frequency "Ω."

These equations were the basis for the acoustic response analysis. Two simplifying assumptions were made when applying these equations. The first was to assume that the fluctuating pressures act in a correlated manner over the individual elements of areas for a single quadrant. The second was to assume that the pressures act in an uncorrelated manner between the four quadrants (payload attachment points).

The first assumption was justified by the following rationale. Consider an element of area of the SLA exposed to the fluctuating pressures. By making the element geometrically small compared to the half wavelength of the highest frequency of interest, lower frequencies will appear well correlated. This is particularly true for panel fatigue analysis.

The second assumption was reasoned as follows. The diameter of the SLA at the attachment points of the payload was approximately 23 feet. Therefore, the circumferential distance between two adjacent attachments was approximately 18 feet. This spatial distance was considered sufficient to assume uncorrelated pressures. Consequently, forces (product of pressures and areas) were considered correlated for one quadrant, but uncorrelated between quadrants.

TECHNIQUE FOR ESTABLISHING MODEL

The approach used to obtain representative mode shapes and frequencies of the SLA and payload does not represent new technology. However, it may be somewhat unique.

It was considered necessary to model the structure to a fine degree of detail in order to obtain accuracy in the high frequency range. This detailed representation of the payload required the use of axial members, beams, plates, and torsional elements to define the structural properties. This representation resulted in a model containing over 3,000 degrees of freedom; however, the maximum size that could be used in available eigenvalue routines was 200 degrees of freedom. The problem was to establish a final model with characteristics of the detailed 3,000 degrees of freedom and accomplish this using the existing 200-degree-of-freedom eigenvalue routines.

To obtain the desired model the payload was divideo into segments, eigenvalue solutions were performed on the segments then the individual results combined into one model using modal stiffness coupling techniques.[2,3,4,5,6,7] The segments were the SLA, the rack structure, the ATM, and the LM.

The SLA shell structure was idealized by rectangular plates for both in-plane and out-of-plane stresses using the direct stiffness approach as shown in flat pattern in Figure 2. In addition, eight beams were used to represent a ring circumferentially from collocation point 25 to 32. The SLA structure was detailed as 288 degrees of freedom; six degrees of freedom at 48 collocation points. The resulting stiffness matrix was restrained at collocation points 41 through 48 by deleting the associated rows and columns from the stiffness matrix, thereby representing a cantilevered condition for the SLA. The rotational degrees of freedom were then removed from the influence coefficient matrix by deleting appropriate rows and columns, leaving three displacement degrees of freedom at each collocation point. The resulting matrix was 120 degrees of freedom representing 40 collocation points.

The total weight of the SLA was 3950 pounds. This mass was apportioned at each collocation point to obtain a lumped mass representation. An eigenvalue solution was performed on this payload element to obtain cantilevered mode shapes and frequencies of the SLA. The resulting eigenvalues started at 14 Hz.

The support rack was idealized using axial and torsional elements, straight and curved beams, rectangular and triangular plates. The rack was detailed as 1932 degrees of freedom. Collocation points representative of equipment locations were selected and the remaining ones were reduced as was done on the SLA. Three degrees of freedom was retained for each mass collocation point. The final reduced matrix was 90 degrees of freedom. The total weight of the rack and equipment was 13,165 pounds. The eigenvalue solution for the free rack condition had a total of 84 elastic modes beginning at 16.8 Hz.

The ATM structure was idealized by rectangular plates, axial members, and straight and curved beams. The structure was detailed as 160 degrees of freedom. The influence coefficient matrix was subsequently reduced to 87 degrees of freedom. The total weight of the ATM including equipment was 4880 pounds. Again, a lumped mass representation was used. The resulting free-condition eigenvalues started at 7.8 Hz.

The LM structure was represented as a rigid member due to lack of stiffness definition. However, the six rigid body modes were included. The total weight of the LM was 10,500 pounds.

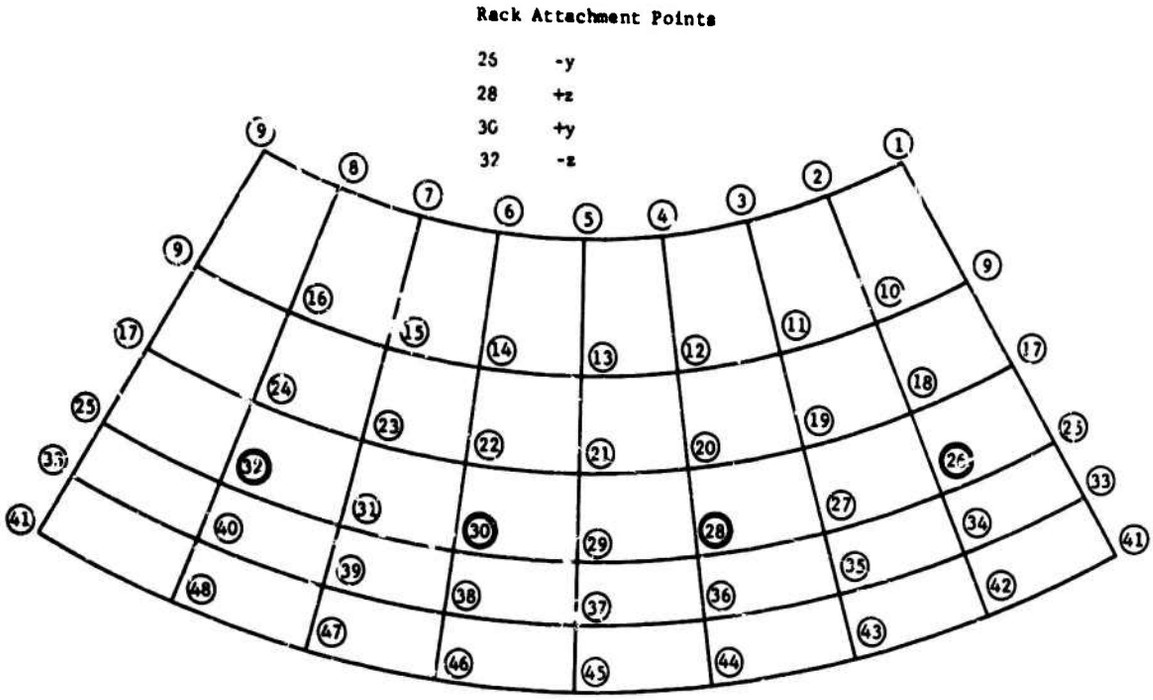


Figure 2. SLA Structural Model (Points 41 through 48 restrained)

For each payload element (rack, ATM, LM, and SLA) the structural members connecting the elements were used as the discrete coupling mechanism. As mentioned previously, only the lower modes of the free elements were used in obtaining the final model.

Table 1 contains the coupled frequencies of the final model and identifies the major uncoupled contributing mode for each frequency. The final model contains 124 modes with frequencies ranging from 6.4 Hz to 624 Hz. However, only 122 modes were considered usable in the acoustic response analysis covering the frequency range to 204 Hz.

Table 1. Identification of the Coupled Modes

MODE	MAJOR UNCOUPLED CONTRIBUTING MODE	NROW	MEQ CONTRIB	COUPLED FREQUENCY	UNCOUPLED FREQUENCY
1	MODE 3 LM A/S	121	.6414	6.403	0.
2	MODE 2 LM A/S	120	.5609	7.196	0.
3	MODE 7 TELESCOPE	1	.9903	7.592	7.588
4	MODE 7 TELESCOPE	2	.9997	7.924	7.923
5	MODE 2 RACK	4	.6039	9.699	9.306
6	MODE 5 LM A/S	124	.4791	10.825	0.
7	MODE 3 RACK	3	.3890	11.359	9.015
8	MODE 50 SLA	119	.4068	14.413	0.
9	MODE 2 SLA	5	.9922	15.061	14.986
10	MODE 1 SLA	6	.7292	16.468	15.515
11	MODE 3 SLA	8	.7209	17.574	17.461
12	MODE 4 SLA	9	.7235	17.856	17.522
13	MODE 5 TELESCOPE	7	.2932	18.251	16.611
14	MODE 6 TELESCOPE	10	.5277	18.956	19.142
15	MODE 5 SLA	11	.5396	22.086	19.501
16	MODE 5 SLA	12	.8051	22.926	23.030
17	MODE 4 RACK	13	.3534	24.057	24.097
18	MODE 4 RACK	13	.3407	27.004	24.097
19	MODE 12 RACK	14	.5376	29.258	28.818

Table 1. (Continued)

20	MODE 10 SLA	16	.5277	31.709	29.834
21	MODE 9 SLA	17	.3060	31.770	32.623
22	MODE 6 SLA	19	.9853	33.791	33.790
23	MODE 9 SLA	17	.2660	34.547	32.623
24	MODE 9 SLA	20	.6446	34.829	34.651
25	MODE 9 SLA	20	.2205	34.893	34.651
26	MODE 2 TELESCOPE	21	.8666	36.420	36.044
27	MODE 9 RACK	23	.5092	41.008	41.256
28	MODE 11 SLA	24	.2511	43.671	42.523
29	MODE 8 RACK	27	.2706	45.013	45.226
30	MODE 11 SLA	25	.3651	45.346	43.277
31	MODE 8 RACK	27	.3526	46.812	45.226
32	MODE 9 TELESCOPE	30	.9447	47.342	47.538
33	MODE 11 SLA	29	.2966	49.556	47.324
34	MODE 8 RACK	28	.1575	50.434	46.168
35	MODE 10 TELESCOPE	32	.8192	50.845	50.737
36	MODE 15 RACK	31	.3755	51.429	49.027
37	MODE 15 RACK	35	.2817	53.891	57.059
38	MODE 11 TELESCOPE	33	.7197	54.381	54.220
39	MODE 11 RACK	34	.3232	57.448	54.694
40	MODE 14 SLA	36	.4537	58.514	58.729
41	MODE 12 TELESCOPE	37	.6452	59.700	59.441
42	MODE 13 SLA	40	.8695	63.709	63.731
43	MODE 13 TELESCOPE	39	.7709	63.828	63.607
44	MODE 14 TELESCOPE	41	.7262	64.813	64.665
45	MODE 16 SLA	43	.9077	66.381	66.410
46	MODE 15 SLA	44	.5650	66.684	67.106
47	MODE 16 TELESCOPE	46	.2198	67.445	69.512
48	MODE 14 TELESCOPE	45	.4292	67.685	68.168
49	MODE 14 TELESCOPE	45	.3102	69.643	68.168
50	MODE 17 SLA	49	.2528	70.746	72.262
51	MODE 16 TELESCOPE	46	.2920	71.546	69.512
52	MODE 17 SLA	49	.3163	72.650	72.262
53	MODE 25 RACK	48	.5522	72.850	72.158
54	MODE 18 TELESCOPE	51	.3467	73.631	73.918
55	MODE 18 TELESCOPE	51	.1833	74.783	73.918
56	MODE 20 SLA	53	.4306	77.413	77.452
57	MODE 20 SLA	53	.3594	77.498	77.452
58	MODE 24 RACK	54	.3517	80.328	79.677
59	MODE 24 RACK	54	.4005	81.961	79.677
60	MODE 21 SLA	56	.9109	82.572	82.517
61	MODE 29 SLA	57	.9187	83.185	83.168
62	MODE 25 SLA	63	.1614	84.809	89.665
63	MODE 19 TELESCOPE	58	.3038	85.444	85.909
64	MODE 19 TELESCOPE	58	.4328	86.513	85.909
65	MODE 22 SLA	59	.5834	87.114	86.644
66	MODE 24 SLA	60	.7697	88.197	87.745
67	MODE 25 SLA	61	.5545	88.660	88.295
68	MODE 28 SLA	64	.9935	91.404	91.400
69	MODE 31 SLA	65	.5607	92.844	92.728
70	MODE 30 SLA	66	.5580	92.988	93.479
71	MODE 29 RACK	67	.3480	93.815	95.886
72	MODE 20 TELESCOPE	68	.7875	96.802	96.740
73	MODE 32 SLA	69	.9294	97.661	97.727
74	MODE 25 SLA	62	.1777	99.815	89.085
75	MODE 19 TELESCOPE	70	.7708	100.901	100.445
76	MODE 29 RACK	67	.1927	102.250	95.886
77	MODE 33 SLA	72	.4703	104.176	103.563
78	MODE 34 SLA	71	.5106	104.502	103.453
79	MODE 35 SLA	73	.8302	106.202	105.690
80	MODE 35 SLA	74	.7845	108.605	107.504
81	MODE 36 SLA	75	.9337	110.033	109.899
82	MODE 37 SLA	78	.5168	112.759	112.860
83	MODE 37 SLA	78	.3995	113.782	112.860
84	MODE 33 RACK	80	.2772	115.638	118.258
85	MODE 33 RACK	79	.4183	118.937	116.068

Table 1. (Concluded)

86	MODE 33 RACK	80	.4501	120.899	118.258
87	MODE 41 SLA	83	.5577	122.916	122.806
88	MODE 32 RACK	81	.2080	123.608	118.979
89	MODE 40 SLA	84	.6434	123.969	123.609
90	MODE 32 RACK	82	.3188	127.014	120.996
91	MODE 36 SLA	87	.3892	129.226	129.463
92	MODE 40 SLA	88	.6990	129.800	129.780
93	MODE 34 RACK	86	.5589	131.118	127.396
94	MODE 34 RACK	85	.2505	131.939	125.581
95	MODE 37 RACK	91	.4961	135.391	135.558
96	MODE 36 RACK	92	.4130	136.918	137.100
97	MODE 37 RACK	91	.3255	138.998	135.558
98	MODE 44 SLA	93	.5993	139.529	139.231
99	MODE 22 TELESCOPE	94	.5063	141.074	140.476
100	MODE 24 TELESCOPE	96	.7218	142.516	142.479
101	MODE 23 TELESCOPE	95	.3371	145.346	141.115
102	MODE 41 RACK	98	.2714	146.965	148.469
103	MODE 41 RACK	98	.5060	148.600	148.469
104	MODE 42 RACK	100	.5265	152.214	152.118
105	MODE 26 RACK	99	.4672	152.274	148.923
106	MODE 42 RACK	101	.6499	159.004	157.635
107	MODE 41 RACK	102	.6534	160.602	159.378
108	MODE 45 SLA	105	.9902	166.461	166.405
109	MODE 39 RACK	104	.4950	168.768	164.649
110	MODE 43 RACK	106	.8158	170.594	169.756
111	MODE 46 SLA	107	.4726	174.463	173.014
112	MODE 44 RACK	108	.4684	176.301	175.979
113	MODE 44 RACK	109	.6762	178.653	176.851
114	MODE 50 SLA	112	.4594	180.333	182.069
115	MODE 26 TELESCOPE	110	.5298	181.163	180.744
116	MODE 26 TELESCOPE	111	.4854	182.756	181.408
117	MODE 47 RACK	113	.5234	184.115	183.659
118	MODE 27 TELESCOPE	114	.7637	185.353	184.616
119	MODE 50 RACK	115	.9357	187.448	187.211
120	MODE 50 RACK	117	.3803	190.369	192.862
121	MODE 50 SLA	118	.3839	193.461	195.450
122	MODE 50 SLA	118	.5512	204.341	195.450
123	MODE 36 RACK	89	.1323	530.593	132.230
124	MODE 39 RACK	103	.1906	824.130	162.613

Application of Acoustics

The maximum acoustic environment at the payload attachment location occurred during the vehicle lift-off event. Therefore, the lift-off environment was used in the response analysis. The magnitude and energy distribution defining the acoustic environment used is shown in Figure 3. The pressure spectral density of this environment is shown in Figure 4.

Because the acoustic levels are nearly equal along the SLA length during lift-off, the pressure spectral density was considered constant for each area of application. The force spectral density was established by producting the pressure spectral density with the proportioned area for each collocation point. It was assumed that the pressure spectral density acted perpendicular to the SLA surface.

As discussed previously, the applied forces were assumed correlated in each quadrant but uncorrelated between quadrants. The technique employed was to apply the forces at all collocation points lying within one quadrant (Figure 5) and compute the vibration response for all equipment locations. This same computation was performed on each of the remaining three quadrants. The total uncorrelated response was then determined by root-sum-squaring the four individual quadrant responses.

The response in terms of accelerstion spectral densities was determined in each of three axes at all equipment locations and at the SLA areas close to the payload attachment points.

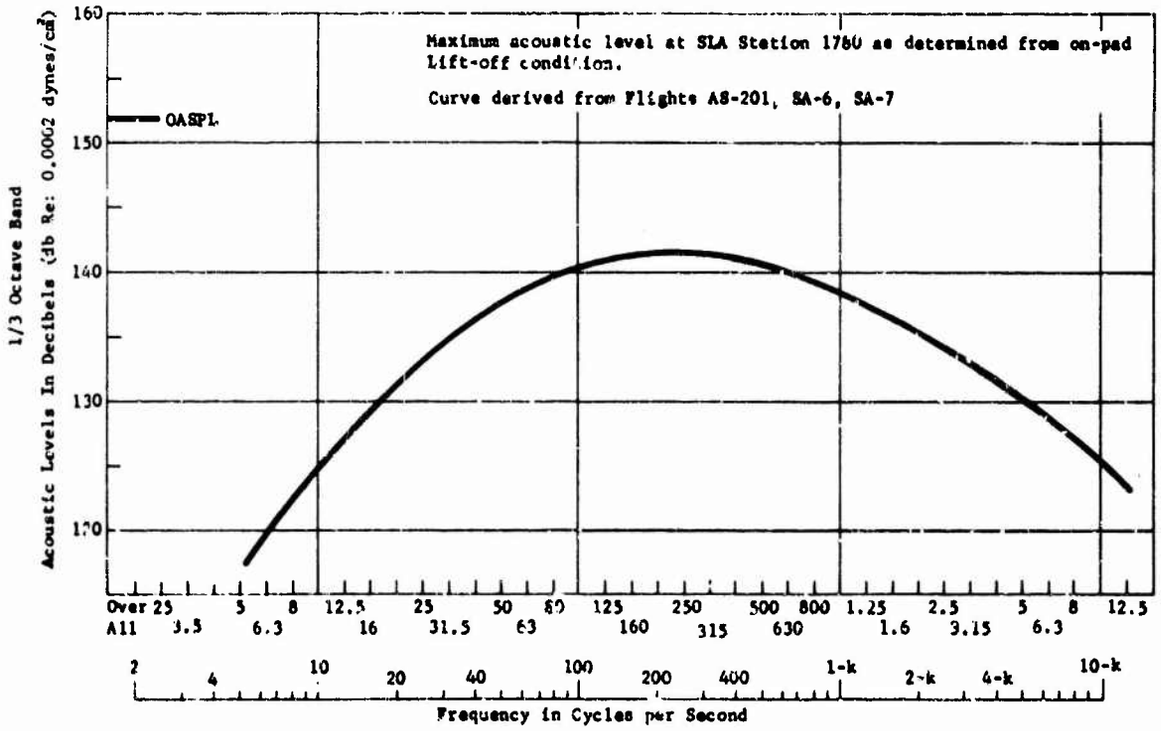


Figure 3. Acoustic Environment

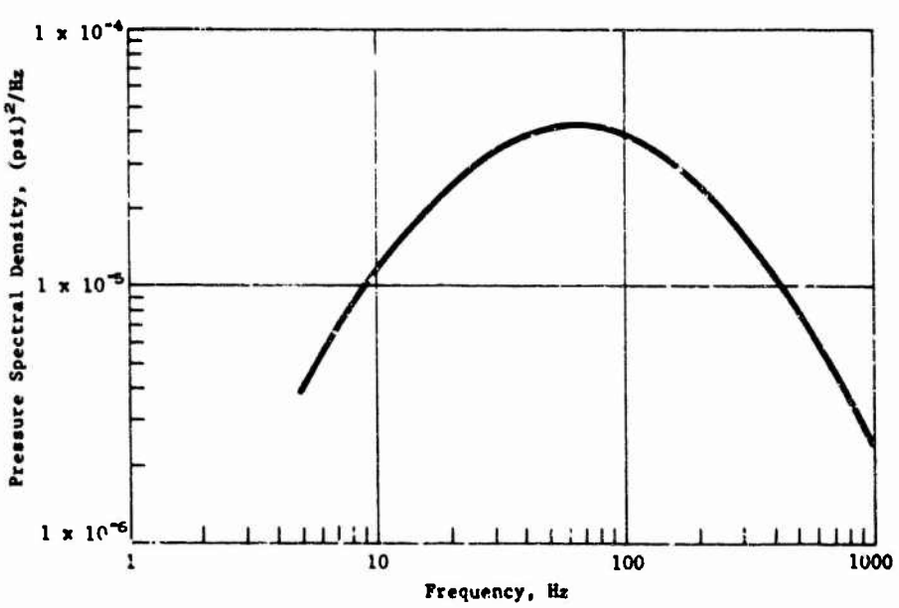


Figure 4. PSD of Acoustics

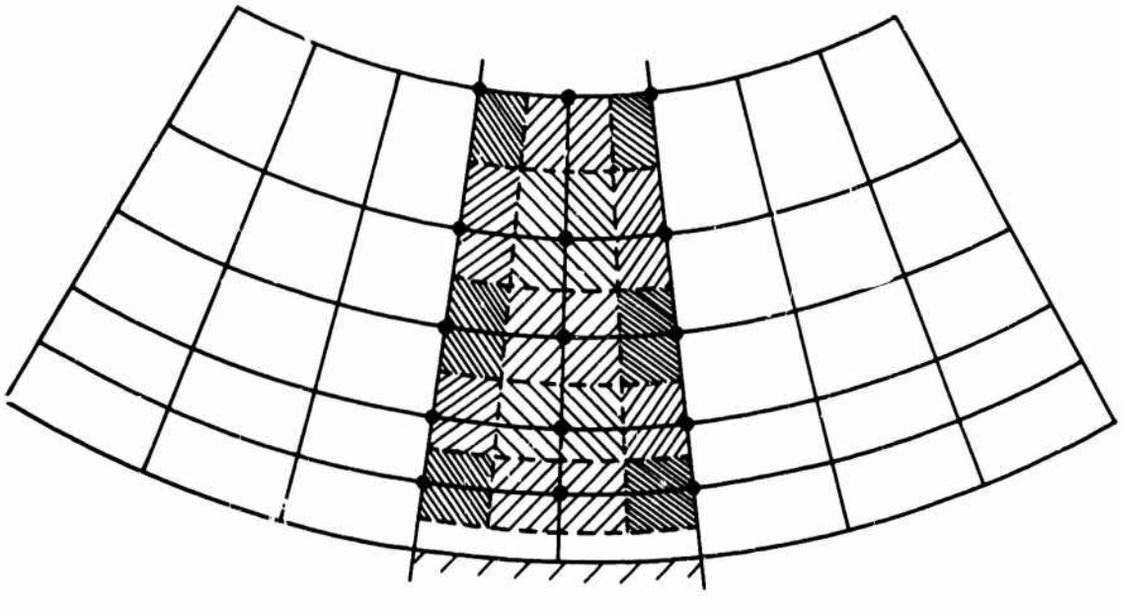


Figure 5. SLA Mass and Force Collocation Points (one quadrant)

Summary of Results

The following items of the analysis by necessity were based on engineering judgment and could have an appreciable effect on results:

a. Modal damping of one percent;

b. Forces associated with one attachment point assumed to act in one direction (normal to the SLA);

c. Forces associated with the four attachment points assumed to be uncorrelated;

d. SLA model restrained at the bottom, free at the top.

The opinion was that one percent modal damping would produce reasonable results because ground vibration survey tests of other payloads have produced similar damping.

The assumption that forces at the four attachment points are uncorrelated is considered reasonable due to the spatial separation of the points.

Items b and d combined to produce the most questionable phase of the analysis. It was noted that toward the top of the SLA the response was excessive. In retrospect, this is considered due to the top of the SLA being free. However, the large distance (21 feet) from the top of the SLA to the payload attachment points may result in little effect on payload response.

Because the payload analyzed has not yet flown, one cannot evaluate the accuracy of the analytical technique. However, the S-1B has flown with other heavy payloads and measurements were made on the shell supporting the payload (SLA). A comparison of the measured and calculated values is shown in Figure 6.

Of primary interest is the similar spectrum shape of the calculated response with the measured one. This indicates that structural properties of the SLA were closely simulated. No data point (measurement) exists for other internal equipment locations. It is interesting that the calculated magnitudes were nearly equal to the measured ones, indicating that the assumed damping and pressure correlation values are realistic.

FUTURE DEVELOPMENT

The analytical approach used in the analysis discussed is written in general terms and, therefore, does not apply to one program or configuration only. The methods can be applied to the class of vehicles generating significant acoustic levels such as the Saturn. Test data are sorely needed to validate the existing analytical techniques discussed. More detailed knowledge of the forcing function and its interaction with various structure geometries is needed.

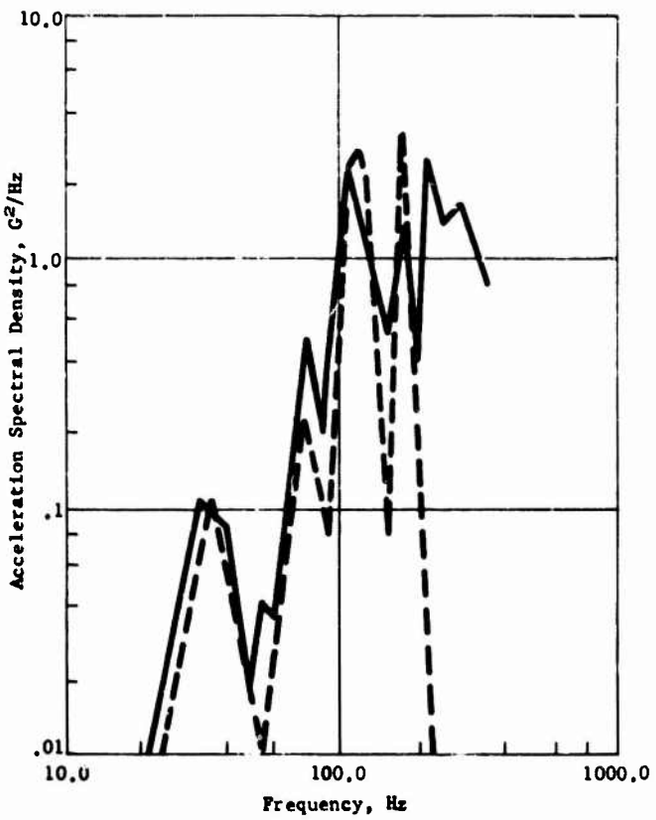


Figure 6. Comparison of Analytical and Test Data

Specifically, the method discussed should be modified to include pressure correlation coefficients and structural joint acceptance parameters. This modification should be made in conjunction with a test program to establish pressure correlation coefficients for various phases of flight. Analytical predictions should be made and compared with test results under controlled conditions to determine the limitations of existing methodology.

REFERENCES

1. Martin Marietta Report ED-2002-329, "Load Environment Analysis for Flight AAP-4 Configuration," dated 21 December 1967, Contract NAS8-21004.

2. R. Bajan and C. C. Feng, "Free Vibration Analysis by the Modal Substitution Method," Proceedings of 2nd AIAA-AAS Symposium Space Projections from the Rocky Mountains, June 16, 1968.

3. B. A. Hunn, "A Method of Calculating the Space Free Resonant Modes of an Aircraft," Journal of the Royal Aeronautical Society, Vol. 57, June, 1953, pp. 420-422.

4. W. C. Hurty, "A Criterion for Selecting Realistic Natural Modes of a Structure," Technical Memorandum 33-364, Jet Propulsion Laboratory, Pasadena, California, November 1967.

5. W. C. Hurty, "Dynamic Analysis of Structural Systems by Component Mode Synthesis," Technical Report 32-350, January 1964.

6. W. C. Hurty, "Dynamic Analysis of Structural Systems Using Component Modes," AIAA Journal, Vol. 3, No. 4, April 1965, pp. 678-685.

7. G. M. L. Gladwell, "The Vibration of Frames," Journal of Sound and Vibration, Vol. 1, Pt. 4, July 1964, pp. 402-425.

DISCUSSION

Mr. Mallgren (McDonnell Douglas): Did you attempt to correlate the shell measurement with some of the empirical techniques such as Barrett or Mahaffey-Smith or Franklin?

Mr. Smith: No, we did not. As you know if you use the Mahaffey-Smith or Franklin or any of the other classical approaches, what you really get is based primarily on the mass law. This does not give the kind of detailed frequency response for which we were looking. That check has not been made however.

Mr. Pakstys (General Dynamics/Electric Boat): I assume that for the math modeling to represent the shell structure, you were using a plate finite element of some sort. Could you give the details – what kind of an element it was?

Mr. Smith: Yes, we had planned on using a triangular element and at the time we did not have a triangular element in use. So we approximated this with a rectangular element. Now because the cone is very, very shallow in angle – it is an 8 degree conical section – we did not have exact conditions on the plate edges but they were fairly close. We represented both the in-plane and the out-of-plane stress conditions with rectangular plates.

Mr. Pakstys: Is there any name for this particular finite element that you used?

Mr. Smith: No. The technique is a finite element direct stiffness approach. I have references on it in the paper.

Mr. Kapur (Aerospace Corp.): What kind of pressure cross correlation were you using within a given quadrant?

Mr. Smith: No, had I had the capability for cross correlation then I could have represented the entire shell structure and computed the response in one fell swoop. As it was we approximated the correlation by assuming that it was well correlated in one quadrant and we applied all the forces simultaneously for that one quadrant and computed the response on the first quadrant and did likewise on the remaining three and then root-sum-squared the results, so we did not have a cross pressure correlation.

ESTIMATION OF PROBABILITY OF STRUCTURAL DAMAGE FROM COMBINED BLAST AND FINITE-DURATION ACOUSTIC LOADING*

Eric E. Ungar and Yoram Kadman
Bolt Beranek and Newman Inc.
Cambridge, Massachusetts

Results are summarized that permit one to estimate the probability that the response of a structure to random acoustic excitation will exceed a specified level during a time interval of given duration. Characteristics of responses to explosion pressure-pulses are described in simplified terms. Means are presented for obtaining engineering estimates of the probability that the response of a structure to a pressure pulse, which occurs at a given time during the action of the acoustic excitation, will exceed a prescribed value.

INTRODUCTION

In addition to experiencing rocket-noise excitation, structures that are located near rocket testing or launching facilities may occasionally be exposed to blast loads due to explosions. The analyst or designer of such structures needs to evaluate the probability of structural damage due to the combined acoustic and blast-pressure excitation associated with a given test or launch. It is the purpose of this paper to present an approach for obtaining engineering estimates of this damage probability.

The structural deformations and stresses associated with the response of a structure to a given explosion blast may be estimated relatively simply. If these deformations and/or stresses are large enough to lead to damage even in the absence of simultaneous acoustic excitation, then the probability of failure due to combined acoustic and blast loading obviously is unity. If, on the other hand, blast effects are relatively insignificant, then one may calculate the failure probability on the basis of only the structural response to acoustic excitation. However, the situations of greatest practical interest generally tend to lie between these two extremes and to be more difficult to analyze.

This paper first summarizes some results that permit one to estimate the probability that a structural response (e.g., a stress or displacement) to acoustic excitation of finite duration will exceed some "safe" value. The paper then discusses the characteristics of responses to pressure pulses, and thereafter presents an approach for estimating the probability of failure due to combined acoustic and pulse loading. Illustrative calculations appear in the final section.

PROBABILITY OF FAILURE DUE TO RANDOM EXCITATION OF FINITE DURATION

Dominance of Linear Behavior of Fundamental Mode

The stresses and deformations associated with the fundamental flexural modes of plate-like and beam-like structures exposed to acoustic pressures generally predominate over those associated with the higher modes. Specifically, fundamental-mode predominance occurs if the acoustic pressure (at frequencies above the structural fundamental) increases less rapidly than with the first power of frequency [1] (i.e., if the sound-pressure-spectrum level increases at less than 6dB per octave, or if the sound pressure level in proportional frequency bands increases at less than 12dB per octave). Thus, in most practical cases, only the response of the fundamental mode need be considered.

*This paper was not presented in full at the Symposium.

The mathematically linear behavior of structures is generally of greatest practical interest. If structural damage is defined as exceedance of a yield stress, then the stress-strain characteristics of the undamaged structure are linear by definition; although other sources of nonlinearity may exist (e.g., support friction), these are usually insignificant. Even where the damage process itself is associated with extreme nonlinearities (such as fracture or post-buckling deformation), linear analysis usually yields a good first approximation to the actual motions before damage. The general applicability of linear results is fortunate since only linear problems have been solved extensively in general terms. Linear structural behavior will be postulated henceforth in this paper.

Modeling of Mode as Simple Oscillator

It is well known that the response of a mode may be described in terms of that of a corresponding single-degree-of-freedom system [2]. For structures that behave linearly, the corresponding single-degree-of-freedom oscillator is also linear. Therefore, one may derive much of the structural response information of interest here by drawing upon the extensive existing literature pertaining to the responses of simple linear oscillators (which generally are represented by the familiar mass-spring-dashpot combinations).

Thus, in order to evaluate the probability that the (stress or displacement) response of a given structure to a prescribed random acoustic excitation (acting during a time interval T) will exceed some specified safe value b, one may study the equivalent problem for a linear oscillator. This equivalent problem consists of determining the probability that the oscillator, which represents the fundamental structural mode, will experience an excursion that exceeds a specified "threshold" value b (in response to a random force acting over a time interval T).

Probability of Threshold Exceedance

Problems like those described in the for foregoing paragraph have been studied extensively, and although no exact solutions have been found, much useful data is available from analytic approximations [3], digital simulations [4,5] and analog simulations [6,7].

Where the excitation (and therefore also the response) is a Gaussian random process, one may approximate the probability P that the absolute value of the displacement of a linear oscillator will exceed a threshold value b within a time interval T by the simple expression [4,5].

$$P(b,T) \approx 1 - A \exp[-\alpha f_n T]. \qquad (1)$$

Here f_n represents the natural frequency of the oscillator; A and α are functions of the threshold level b, of the conditions of motion at the beginning of the time interval T, and of the damping of the oscillator, as discussed subsequently. The approximation given in Eq. (1) holds only for time intervals $T > T_c$, where T_c denotes the time interval required for the response autocorrelation function to decay to a small value.* For most practical purposes one may take

$$T_c = 1/2\pi\zeta f_n, \qquad (2)$$

where ζ denotes the damping ratio of the oscillator (i.e., the ratio of the oscillator's viscous damping coefficient to its critical damping coefficient).

Figure 1, which has been extracted

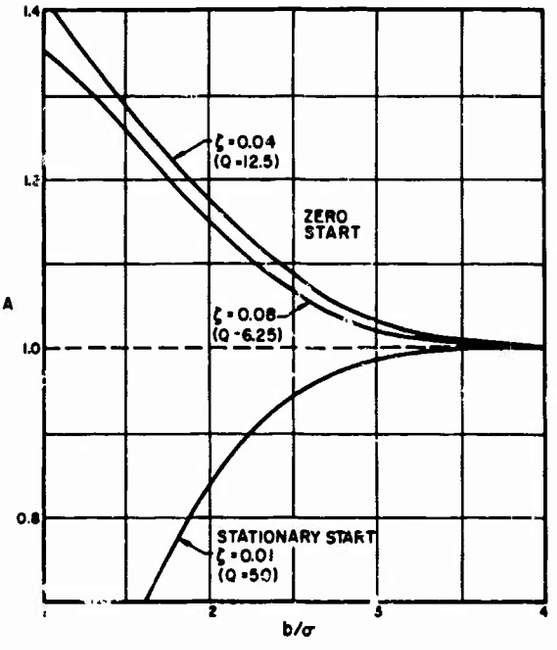


Fig. 1 Dependence of the parameter A on threshold/rms ratio.

* Note that P(b,T) approaches unity as T increases. This result agrees with what one expects intuitively: the longer the exposure interval, the more likely one is to obtain an excursion that exceeds a given threshold value.

from Ref. 4, indicates how the parameter A varies with the ratio b/σ, where σ represents the root-mean-square displacement. The parameter A depends on the threshold value b, on the motion conditions at the beginning of the time interval of concern, and only slightly on the damping of the oscillator. The upper curves, labeled "zero start", pertain to an oscillator that is at rest and at equilibrium (zero displacement and velocity) at the beginning of the time interval of interest. The lower curve, labeled "stationary start", pertains to the situation where stationary random oscillation conditions exist before the time interval. The two upper curves correspond to two different damping ratios ζ and indicate that ζ has only a minor effect on the value of A; hence, only one lower curve is given.

As is evident from Fig. 1, A approaches unity for large b/σ. Also, for a given value of b/σ, one obtains a larger value of A for zero-start than for stationary-start conditions; threshold exceedance within the time interval T thus is more likely with stationary than with zero starts - as one would expect intuitively since a finite time is required for the response to build up from the zero to the stationary level.

Values of the parameter α that correspond to given values of the ratio b/σ may be obtained from Fig. 2, which also has been extracted from Ref. 4. Values of α for damping ratios other than those to which Fig. 2 pertains may be obtained by interpolation or extrapolation.

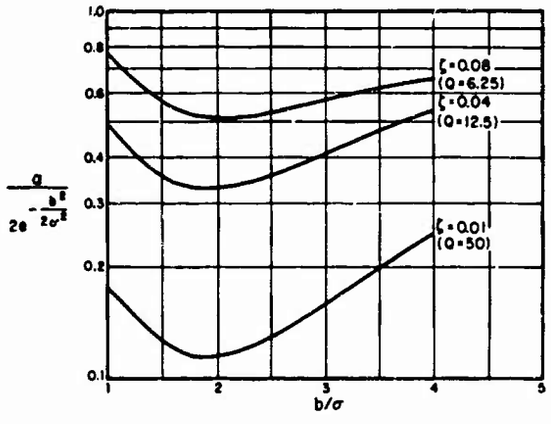


Fig. 2 Dependence of the parameter α on threshold/rms value.

PROBABILITY OF FAILURE DUE TO PULSE LOADING SUPERPOSED ON RANDOM EXCITATION

Pulse Response

Pressure-vs-time curves corresponding to explosions typically rise very sharply and decay slowly. [8,9] The contribution of the fundamental mode again dominates the response of most common structural elements to such pressure pulses [8], whose decay process may be approximated by an exponential function. If one models the fundamental mode of a given structure as a simple oscillator with mass M and stiffness k, one may readily determine that the displacement response x(t) of that mode to an exponentially decaying force spike $F\exp(-\beta t)$ obeys

$$\frac{x(t)}{X_s}\left[1+\left(\frac{\beta}{\omega}\right)^2\right]=e^{-\beta t}-\cos\omega t+\frac{\beta}{\omega}\sin\omega t. \quad (3)$$

where $\omega=\sqrt{k/M}$ denotes the circular natural frequency of the oscillator and $X_s=F/k$ represents its static deflection under a force of magnitude F. In the derivation of Eq. (3), the oscillator was assumed to be at rest and at equilibrium at time t=0 and damping was neglected. Although the response of a damped system may be derived readily, damping is not considered here explicitly, in order not to complicate the present discussion - and since most practical structures are lightly enough damped so that Eq. (3) provides a reasonable approximation.

It is instructive to examine the behavior of Eq. (3), particularly for extreme values of the decay exponent β. If the oscillator executes many cycles of vibration before the pressure spike decays considerably - i.e., if $\beta/\omega\ll 1$, - then the right-hand side of Eq. (3) may be approximated by 1-cos ωt, at least for the first few cycles. On the other hand, for a very rapidly decaying pulse i.e., for $\beta/\omega\gg 1$-the right-hand side is very nearly equal to $(\beta/\omega)\sin\omega t$. Thus, for very large and for very small values of β/ω, the right-hand side of Eq. (3) may be approximated by a sinusoid.

Failure Due to Combined Loading

If the maximum response one obtains from Eq. (3) exceeds the prescribed limit, then failure as a result of the pressure pulse will occur even in the absence of additional acoustic loading. This case is trivial and will not be discussed further; the remainder of this paper deals with the case where the pressure pulse by itself is insufficient to cause failure.

In order to obtain a simple method for estimating the probability of damage due to the superposition of pressure-pulse on random vibration effects, it is convenient to replace the sinusoids that approximate the right-hand side of Eq. (3) by the square waves sketched in Fig. 3. The motion of a lightly damped

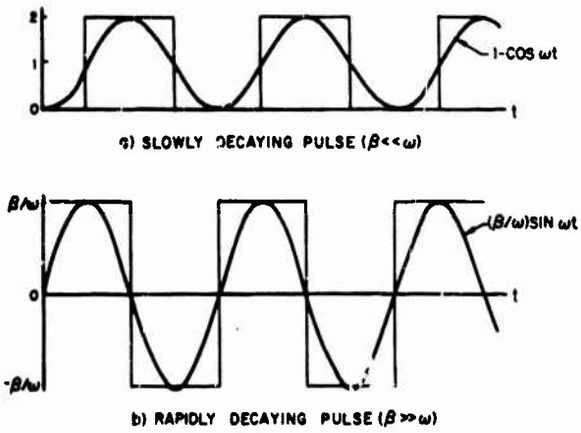


Fig. 3 Square-Wave Approximations to Sinusoids Representing Pulse Responses

structure after application of a slowly decaying pulse ($\beta<<\omega$) when may be taken to be at the maximum value x_m for half of the time and at zero for half of the time.

The probability that the response due to combined loading will exceed the threshold value b during the time that the pulse response is at x_m is the same as the probability that the positive portion of the acoustic response will exceed the reduced threshold value $b_m=b-x_m$. This probability may be calculated directly from Eq. (1); however, one must account for the fact that Eq. (1) represents the probability that the absolute value of the response exceeds b. Since for a zero-mean random process, +x is as likely to exceed +b as -x is to exceed -b, one must divide the expression of Eq. (1) by 2 in order to determine the probability of positive exceedances only. (During the time that the pulse response is at $+x_m$, failure may also occur if the acoustic response takes on a negative value whose magnitude exceeds $b + x_m$. However, the probability of a large excursion of this sort is much smaller than that of a smaller excursion and may be neglected within the degree of the present approximation.)

The probability of failure due to combined loading during the time that the pulse response is at 0 is given directly by Eq. (1). If one notes that failure may occur either when the pulse response is at x_m (which occurs with a probability of 1/2), or when the pulse response is at 0 (which also occurs with a probability of 1/2), one finds that the probability of failure due to combined acoustic and slowly decaying pulse loading ($\beta<<\omega$) may be written as

$$P_{cs} = \tfrac{1}{2}P(b_m,T) + \tfrac{1}{2}P(b,T), \qquad (4)$$

where

$$b_m = b - x_m, \quad x_m = 2F/k. \qquad (5)$$

By similar reasoning one may obtain the probability of failure due to combined acoustic loading of finite duration T and a rapidly decaying pulse ($\beta>>\omega$) as

$$P_{cr} = \tfrac{1}{2}P(b_r, T), \qquad (6)$$

where

$$b_r = b - x_r, \quad x_r = (\omega/\beta)\cdot(F/k). \qquad (7)$$

Failure due to Blast after Acoustic Loading

In the course of a rocket launch (or test), a structure near the launch site is exposed initially only to rocket noise (for some time interval T_1). If the launch (or test) is terminated by an explosion, then the structure will be subject to a pressure pulse in addition to continuation of the rocket noise* (for some time interval T_2). The probability of failure during the first time interval may be calculated from Eq. (1), and that for failure during the second interval from Eqs. (4) or (7). However, failure during the second interval can occur only if the structure survives the first; hence, the probability P_t of failure during the total exposure time T_1+T_2 is given by

$$P_t(b,T_1+T_2)=P(b,T_1)+[1-P(b,T_1)]P_c(b,T_2), \qquad (8)$$

where P_c represents a probability calculated either from Eq. (4) or from Eq. (7), whichever is appropriate for the

* Since shock waves associated with explosions travel faster than sound, one may perceive the noise from rockets at a position far from the launch pad for some time after the explosion pressure pulse from a vehicle destruct has arrived at that position.

specific case under consideration.

ILLUSTRATIVE ANALYSIS AND CALCULATION

Problem Formulation

Consider a 5x4 ft pane of 3/4 in. thick laminated glass, made up of five equally thick laminations. This pane is to be used in a structure from which the launching of large rockets may be observed. From calculations or experimental measurements one finds that the glass pane has a fundamental resonance frequency* of 10Hz and damping at that frequency (including edge support contributions) which corresponds to $\zeta=0.01$. The maximum allowable stress in the glass is 6000 psi. (This relatively low value applies for glass that may have surface scratches obtained by exposure to sand storms.)

The octave-band sound pressure levels expected at the site of the observation structure during testing of a certain rocket are

Octave-band center frequency	4	8	16	31.5	63
SPL (dB re 2×10^{-4} μ bar)	136	136	135	134	121

Assume that this acoustic excitation persists for 20 sec., that then a blast occurs with a peak over-pressure of 0.2 psi and a decay constant $\beta=2.0$ sec^{-1}, and that the acoustic excitation continues to be sensed at the observation site for 2.5 sec. after arrival of the blast pulse. What is the probability of damage to the pane?

Modal Properties

If one assumes the pane to be a simply supported plate, then the fundamental mode shape is given by [2,10]

$$\phi(y,z) = \sin(\pi y/a)\cdot\sin(\pi z/c) , \qquad (9)$$

where a and c denote the pane edge lengths, and where y and z are coordinates along axes parallel to the pane edges. For a pressure distribution p(t) that is uniform over the surface of the pane, the modal force F(t) is found to obey [2,10]

$$F(t) = \int_0^a\int_0^c p(t)\phi(y,z)dy.dz=\frac{4ac}{\pi^2}\,p(t), \qquad (10)$$

and the modal mass M is given by

$$M=\int_0^a\int_0^c \mu\,\phi^2(y,z)\,dy\,dz=\frac{\mu ac}{4} , \qquad (11)$$

where μ represents the mass per unit area of the pane. (The modal mass here is seen to be equal to one quarter of the total mass of the pane.) The modal stiffness k may be calculated from

$$k = M\omega^2 , \qquad (12)$$

where ω represents the fundamental natural frequency.

The modal displacement x here corresponds to the displacement of the plate center. With such a displacement there is associated a maximum stress s, which obeys [11]

$$s = \pi^2 Ehx/2a \qquad (13)$$

where E represents the Young's modulus and h the thickness of the plate, and where a is the length of the shorter plate edge.

Modal Response to Noise

The root-mean-square displacement σ of a classical single-degree-of-freedom system excited by Gaussian noise whose spectrum is flat in the vicinity of the resonance of the system is given by [12]

$$2k\cdot\sigma = \sqrt{\pi W_f\cdot f_n/\zeta}. \qquad (14)$$

Here W_f represents the spectral density of the excitation force, and is related to the root-mean-square value F_{rms} of that force in a frequency band of width Δf as

$$W_f = F_{rms}^2/\Delta f. \qquad (15)$$

Probability of Failure due to Acoustic Excitation

The sound pressure level in the band encompassing the 10Hz natural frequency is 136dB, which corresponds to a root-mean-square pressure P_{rms} = 2.6psf. From Eq. (10), the corresponding rms modal force in the octave band centered on 8Hz is found to be F_{rms} = 21 lb. From Eq. (15) and by noting that for octave bands the center frequency is equal to $\sqrt{2}$ times the bandwidth, one obtains $W_f f_n$ = 780 lb^2. For a glass density of 170 lb/ft^3, the surface weight of the pane is 10.6 lb/ft^2. Eq. (11) then yields M=53 lb., and Eq. (12) gives k= 540 lb/in. From Eq. (14) one

*This frequency corresponds to the case where the adhesive between the laminations transfers no shear stress.

then finds $\sigma = 0.46$ in.

If one takes the Young's modulus $E = 10^7$ psi for glass and a plate thickness $h = 0.15$ (for one lamination), then one may calculate from Eq. (13) the maximum allowable displacement b that corresponds to the specified allowable stress of 6000 psi. One obtains $b = 1.85$ in., and therefore $b/\sigma = 4.0$.

From Eq. (2), one may calculate $T_c = 1.6$ sec. Since all time intervals of concern here exceed 1.6 sec., Eq. (1) and relations derived from it apply to the present problem. From Fig. 1, one finds that for zero start (i.e., for the pane undeflected and at rest before the sound acts on it) $A = 1.00$. From Fig. 2 one obtains

$$\alpha/2 \cdot \exp[-b^2/2\sigma^2] = 0.23, \text{ from}$$

which $\alpha = 1.55 \times 10^{-5}$. Substitution in Eq. (1) then yields $P(b,T_1) = 0.03$; that is, the probability that the 6000 psi "safe" stress will be exceeded during a 20 sec. exposure of the pane to the previously specified sound pressures is 3%.

Probability of Failure due to Combined Blast and Acoustic Loading

Since $\omega = 2\pi f_n = 63$ sec^{-1}, one finds that $\beta/\omega = 0.032 \ll 1$, and that Eqs. (4) and (5) apply. For the 0.2 psi peak pressure, Eq. (10) gives the modal force as $F = 230$ lb. From Eq. (5), one then finds that the maximum displacement x_m due to the shock is $x_m = 0.85$ in., and that the reduced threshold displacement value $b_m = 1.0$ in. then $b_m/\sigma = 2.2$. For this value, and assuming stationary start conditions, since the structure has been in motion for many cycles before the blast occurs, Figs. 1 and 2 yield $A = 0.88$ and $\alpha = .021$. Then, for the 2.5 sec interval following the arrival of the pressure pulse, one finds from Eq. (4) that the failure probability is

$$P_{cs} = \tfrac{1}{2}P(1.0\text{in}, 2.5\text{ sec}) + \tfrac{1}{2}P(1.85\text{in}, 2.5\text{sec})$$

$$= \tfrac{1}{2}\{1-0.88\exp[-.021(10)(2.5)]\} + \tfrac{1}{2}\{1-1.00\exp[-1.55\times10^{-5}(10)(2.5)]\}$$

$$= \tfrac{1}{2}(.480)+\tfrac{1}{2}(.004) = 0.12 .$$

Finally, from Eq. (8) one finds that the probability of failure for the entire 22.5 sec time interval is

$$P_t = 0.03 + (0.97)(0.12) = 0.15 .$$

REFERENCES

1. E.E. Ungar, "Maximum Stress in Beams and Plates Vibrating at Resonance," Trans. ASME, Ser. B (J. Eng. Ind.) Vol. 84, pp. 149-155, Feb. 1962

2. K.N. Tong, Theory of Mechanical Vibrations. Wiley, New York, 1960

3. W.D. Mark, "On False Alarm Probabilities of Filtered Noise," Proc. IEEE, Vol. 54, No. 2, pp. 316-317 (L), 1966

4. K.L. Chandiramani, "First Passage Probabilities for a Linear Oscillator," Doctoral Thesis, Massachusetts Institute of Technology, Dept. of Mechanical Engineering, 1965

5. S.H. Crandall, K.L. Chandiramani, and R.G. Cook, "Some First Passage Problems in Random Vibrations," Trans. ASME, Ser. E (J. Appl. Mech.) pp. 532-538, Sept. 1966

6. R.L. Barnoski, "The Maximum Response of a Linear Mechanical Oscillator to Stationary and Nonstationary Random Excitation," NASA Rept. CR-340, 1965

7. R.L. Barnoski, "The Maximum Response to Random Excitation of Distributed Structures with Rectangular Geometry," J. Sound Vib., Vol. 1, No. 3, pp. 330-350, 1968

8. "Fundamentals of Protective Design (Non-Nuclear)," U.S. Army Rept. TM 5-855-1, July 1965

9. Effects of Atomic Weapons, U.S.Atomic Energy Commission, Washington, D.C., 1962. Revised Ed., Reprinted 1964, edited by S. Glasstone

10. E.E. Ungar, "Mechanical Vibrations," Chap. 6 of Mechanical Design and Systems Handbook, McGraw-Hill Book Co., Inc., New York, 1964, edited by H.A. Rothbart

11. S. Timoshenko, Theory of Plates and Shells, Chap. V, McGraw-Hill Book Co., Inc., New York, 1940

12. S.H. Crandall and W.D. Mark, Random Vibrations in Mechanical Systems, Academic Press, New York, 1963

DISCUSSION

Mr. Swanson (MTS Systems Corp): I have worked for a while on the earthquake simulation problem which is very similar to the one you described. It has the characteristic of the intensity going from zero up to some peak value and dropping off again over a finite length of time. Do you assume that you are dealing with a Gaussian disturbance, or is this generalized to some sort of other general distribution of events?

Dr. Ungar: The analysis indeed is Gaussian and the systems we deal with are linear. The only solutions that are known are for Gaussian and linear systems.

Mr. Swanson: I guess you are familiar with the work of Freudenthal and his colleagues at Columbia who have investigated the upper and lower bounds of non-stationary random processes. They have a good paper on that.

Dr. Ungar: There is a great deal of work on non-stationary random processes. The earthquake problem of course is an interesting one and the real problem with practical applications has to do with the lack of information on the statistics of the earthquake process itself.

Mr. Swanson: That is true except that there is a growing literature of continuous recordings of earthquake motions, and from this PSD analyses an RMS analyses can be obtained.

Dr. Ungar: Unfortunately, I think the large events about which we are mostly concerned are rare and one can not use a usual type of analysis or approximation because there is no information about details of distributions.

Dr. Bouche (Endevco Corp): The shock wave portion of the excitation reminds me of the effect of sonic booms on structures. In the shock analysis here, can you, or do you take into account the shock excitation of the structure insofar as it excites resonances in the structure?

Dr. Ungar: Indeed we do take these excitations into account I glossed over the answer rather quickly. These wiggly curves that I have drawn here are supposed to represent the response of a structure to the shock which is superposed on the random response.

THE RESPONSE OF MECHANICAL SYSTEMS TO BANDS OF RANDOM EXCITATION*

L. J. Pulgrano and M. Ablowitz†
Grumman Aircraft Engineering Corporation
Bethpage, New York

The mean square response of a single-degree-of-freedom system has been determined for both band-limited white noise excitation and a band of excitation having a constant db/octave change in level. Solutions are given for those input-output combinations that are of greatest interest, such as force or acceleration excitations and acceleration or displacement responses. The results include exact analytical expressions for all cases, and both approximate expressions and graphical presentations for use in making quick calculations in most practical cases.

LIST OF SYMBOLS

a	$2\sqrt{1-\zeta^2}$
b	exponent controlling rate of change of spectrum (see equation 12)
C	viscous damping coefficient
$f(t)$	normalized exciting force = F/M
$F(t)$	exciting force (see Figure 1)
$H(\omega)$	transfer function (output/input)
$H_{0,1,2,3}$	see equations (7) to (10)
$I_b(\Omega)$	function defined by equation (22a)
K	spring constant
ℓ	$2(1-2\zeta^2)$
ln	logarithm to the base e
M	mass
n	number of octaves between two frequencies
N	db/octave variation in spectrum
$S(\omega)$	spectral density (one-sided, radians/time units)
S_R	response spectral density
S_i	input spectral density
t	time
u	absolute input displacement (see Figure 1)
x	absolute response displacement (see Figure 1)
y	relative displacement = $x-u$ (see Figure 1)
$z_{1,2,3}$	general response variable associated with transfer function $H_{1,2,3}$
ω	circular frequency (radians/time)
ω_n	natural frequency $\sqrt{K/M}$
Ω	normalized frequency = ω/ω_n
ζ	critical damping ratio = $C/2M\omega_n$
$\langle\ \rangle$	average value of bracketed quantity

INTRODUCTION

The calculation of the mean square response of a randomly-excited vibrating system usually involves the evaluation of a relatively complicated integral. Results are widely available for the case of a single-degree-of-freedom system excited by white noise (e.g., see Reference 1), and the white noise results can often be used with good approximation for lightly damped systems having resonances within the band of excitation. However, if the system is heavily damped, or if the excitation is largely nonresonant, or if the spectral density is changing rapidly in the vicinity of resonance, the use of a white noise approximation may lead to serious error. It is necessary for these cases to have solutions for the response to bands of excitation, if accurate results are to be obtained in a relatively short time.

*Paper not presented at Symposium.
†Currently at Massachusetts Institute of Technology.

Some results are available for band limited white noise excitation [1], but these are restricted to the case of displacement response to force or acceleration excitation. In this report these results are extended to other commonly used input-output parameters, such as acceleration response to force or acceleration excitation. In addition, the response to bands of excitation having spectra that change at a constant db/octave rate are investigated. Such spectra usually are encountered in vibration design and test specifications. By superimposing results for various bands of excitation, the response to any spectrum can be quite closely approximated.

All the results presented are for single-degree-of-freedom systems. However, such results have application to a wider range of problems, since normal mode techniques [2] can be used to reduce multi-modal systems to a series of single-degree-of-freedom systems, provided damping coupling is negligible and the responses of the modes can be assumed uncorrelated.

BASIC EQUATIONS

The basic input-output relationship for a randomly-excited linear system is [1]

$$S_R(\omega) = S_I(\omega)|H(\omega)|^2 \qquad (1)$$

where

$S_R(\omega)$ = response spectral density

$S_I(\omega)$ = input spectral density

$H(\omega)$ = transfer function relating response to input for sinusoidal excitation

The mean square response $\langle z^2 \rangle$ is obtained by integration

$$\langle z^2 \rangle = \int_{\omega_1}^{\omega_2} S_R(\omega)\, d\omega$$

$$= \int_{\omega_1}^{\omega_2} S_I(\omega)|H(\omega)|^2 d\omega \qquad (2)$$

The integral must be evaluated for the specific case at hand. The plan here is to select the most common forms for $S_I(\omega)$ and $H(\omega)$, to perform the required integrations, and then to present the results in the form of plots or tabulations for easy usage.

TRANSFER FUNCTIONS

Figure 1 shows a single-degree-of-freedom system which may be excited by either base motion or an applied force. The general equation of motion for the system is

$$M\ddot{x} + C\dot{y} + Ky = F(t) \qquad (3)$$

where the meaning of the symbols is evident from Figure 1. In terms of the relative coordinate $y = x-u$, equation (3) can be written

$$\ddot{y} + 2\zeta\omega_n\dot{y} + \omega_n^2 y = f(t) - \ddot{u}(t) \qquad (4)$$

where

$$\omega_n^2 = K/M$$

$$\zeta = C/2M\omega_n$$

$$f(t) = F(t)/M$$

Equation (4) can now be used to find any desired transfer function for the single-degree-of-freedom system. For example, consider the displacement response $x(t)$ for an applied force excitation. Then

$$\ddot{u} = u = 0$$

$$y = x-u = x$$

and (4) becomes

$$\ddot{x} + 2\zeta\omega_n\dot{x} + \omega_n^2 x = f(t) \qquad (5)$$

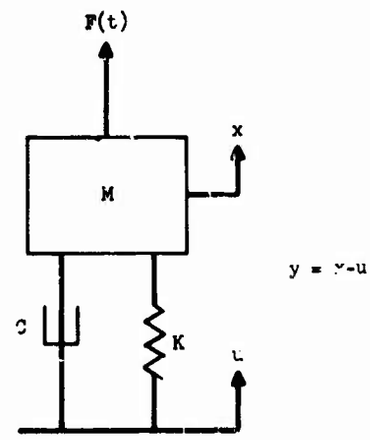


Figure 1 Analytical Model

The transfer function is determined by assuming a harmonic excitation; thus, using phasor notation, the exciting force is

$$f(t) = f_o e^{i\omega t}$$

$$x(t) = x_o e^{i\omega t}$$

Then (5) becomes

$$(-\omega^2 + 2i\zeta\omega_n\omega + \omega_n^2)x_o = f_o$$

and the transfer function is given by

$$H_{x,f}(\omega) = \frac{x_o}{f_o} = \frac{1/\omega_n^2}{(1-\Omega^2) + 2i\zeta\Omega} \qquad (6)$$

where $\Omega = \omega/\omega_n$, a non-dimensional frequency parameter that will be used throughout the discussion. It is important to bear in mind that f in (6) is a normalized force $f = F/M$, and not the applied force F.

In a similar manner, the transfer functions relating other parameters can be determined. The analyses have been carried out for the combinations of greatest interest, and the results are shown in Table I. The transfer functions are all seen to be quite similar, the only differences being in the numerators. The last column of the Table shows the squares of the magnitudes of the transfer functions (which are required in equation (2) for the mean square response) in terms of a basic function, H_o^2, where

$$H_o^2 = \frac{1}{(1-\Omega^2)^2 + 4\zeta^2\Omega^2} \qquad (7)$$

Only three transfer functions are needed to describe the five input-output combinations in the Table. It will be convenient to give a specific designation to each of the three functions, as follows:

$$H_1^2 = (1/\omega_n^4)H_o^2 \qquad (8)$$

$$H_2^2 = (1 + 4\zeta^2\Omega^2)H_o^2 \qquad (9)$$

$$H_3^2 = \Omega^4 H_o^2 \qquad (10)$$

These relations are also shown in the last column of the Table, so that the appropriate transfer function for any of the input-output combinations can be readily determined.

EXCITATION SPECTRAL DENSITIES

Excitation spectral densities, S_I, are typically smoothed into spectra that appear as a series of straight lines on log-log plots. The slopes in regions of varying spectral density are generally given in terms of decibels per octave. Mathematically, the straight line log-log plots are governed by an equation of the form

$$\log S = \log S_o + b \log \Omega \qquad (11)$$

which means that the variables are related by

$$S(\Omega) = S_o\Omega^b \qquad (12)$$

Thus, S_o represents the spectral density at $\Omega = 1$ (i.e., at $\omega = \omega_n$) and b controls the rate at which the spectrum varies. The case of $b = 0$ corresponds to white noise excitation of $S(\Omega) = S_o$.

The exponent b must now be related to the db/octave variation in level if it is to be useful. If two frequencies Ω_2 and Ω_1 are n octaves apart, then

$$\frac{\Omega_2}{\Omega_1} = 2^n \qquad (13)$$

or

$$n = \frac{\log (\Omega_2/\Omega_1)}{\log 2} \qquad (14)$$

$$\doteq 3.32 \log_{10}(\Omega_2/\Omega_1) \qquad (14a)$$

the decibel difference between the spectral densities at the two frequencies is

$$db = 10 \log_{10}\left(\frac{S(\Omega_2)}{S(\Omega_1)}\right) \qquad (15)$$

From (12)

$$\frac{S(\Omega_2)}{S(\Omega_1)} = \left(\frac{\Omega_2}{\Omega_1}\right)^b \qquad (16)$$

Thus

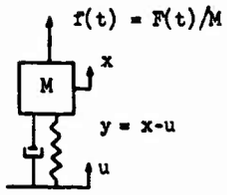
$$db = 10b \log_{10}\left(\frac{\Omega_2}{\Omega_1}\right) \qquad (17)$$

The db/octave variation, N, is obtained from (17) and (14):

$$N = \frac{db}{n} = 3.01b \doteq 3b \qquad (18)$$

Table I

Transfer Functions For Single-Degree-of-Freedom Systems



$$\ddot{y}+2\zeta\omega_n\dot{y}+\omega_n^2 y = f-\ddot{u}$$

input	output	$H(\Omega)$	$\lvert H(\Omega)\rvert^2$
$\ddot{u}$	y	$-\dfrac{1/\omega_n^2}{1-\Omega^2+2i\zeta\Omega}$	$\dfrac{1}{\omega_n^4} H_o^2 = H_1^2$
$\ddot{u}$	$\ddot{x}$	$\dfrac{1+2i\zeta\Omega}{1-\Omega^2+2i\zeta\Omega}$	$(1+4\zeta^2\Omega^2)H_o^2 = H_2^2$
u	x	$\dfrac{1+2i\zeta\Omega}{1-\Omega^2+2i\zeta\Omega}$	$(1+4\zeta^2\Omega^2)H_o^2 = H_2^2$
f	x	$\dfrac{1/\omega_n^2}{1-\Omega^2+2i\zeta\Omega}$	$\dfrac{1}{\omega_n^4} H_o^2 = H_1^2$
f	$\ddot{x}$	$-\dfrac{\Omega^2}{1-\Omega^2+2i\zeta\Omega}$	$\Omega^4 H_o^2 = H_3^2$

Note: $\Omega = \omega/\omega_n$

$$H_o^2 = \frac{1}{(1-\Omega^2)^2+4\zeta^2\Omega^2}$$

A useful relation between the spectral densities at two frequencies is evident from (12). For the two frequencies Ω_2 and Ω_1

$$S(\Omega_2) = S_o\Omega_2^b$$

$$S(\Omega_1) = S_o\Omega_1^b$$

Dividing one equation by the other and rearranging results in

$$S(\Omega_2) = S(\Omega_1)\left(\frac{\Omega_2}{\Omega_1}\right)^b \qquad (19)$$

The spectral density S_o is in radians/time units and is a one-sided spectral density. Design requirements are generally in cycles/time units. To convert from a cycles/time spectral density to a radians/time spectral density divide by 2π.

MEAN SQUARE RESPONSE

The mean square response, as given by (2), can now be expressed in terms of a spectral density of the form of (12) and the three transfer functions of (8), (9) and (10). Consider first the function H_1^2:

$$\langle z_1^2 \rangle = \int_{\omega_1}^{\omega_2} S_I(\omega)\, H_1^2\, d\omega$$

$$= \int_{\Omega_1}^{\Omega_2} \frac{S_o \Omega^b}{\omega_n^3}\, H_c^2\, d\Omega \qquad (20)$$

where $d\Omega = d\omega/\omega_n$ and the subscript on z indicates the transfer function being used. Equation (20) can be rewritten as follows:

$$\langle z_1^2 \rangle = \frac{\pi S_o}{4\zeta\omega_n^3} \left[I_b(\Omega_2) - I_b(\Omega_1) \right] \qquad (21)$$

where

$$I_b(\Omega) = \frac{4\zeta}{\pi} \int \Omega^b H_o^2\, d\Omega \qquad (22)$$

$$= \frac{4\zeta}{\pi} \int \frac{\Omega^b}{(1-\Omega^2)^2 + 4\zeta^2\Omega^2}\, d\Omega \qquad (22a)$$

$I_b(\Omega)$ will turn out to be an important function, in terms of which the mean square responses for all the transfer functions under consideration can be expressed. It actually is a generalization of the function used by Crandall and Mark [1] for the special case of b = 0 and $|H(\Omega)|^2 = H_1^2$. The constants in front of the integral in $I_b(\Omega)$ were chosen to make the coefficient in (21) equal to the white noise response of the system. (See Reference 1, bearing in mind that their $S(\omega)$ is a two-sided spectral density, which has a value of half the $S(\omega)$ used herein.)

For the second transfer function, H_2, there results

$$\langle z_2^2 \rangle = \int_{\Omega_1}^{\Omega_2} S_o\, \Omega^b (1 + 4\zeta^2\Omega^2)\, H_o^2\, \omega_n\, d\Omega$$

$$= \frac{\pi\omega_n S_o}{4\zeta} \left[I_b(\Omega) + 4\zeta^2 I_{b+2}(\Omega) \right]_{\Omega_1}^{\Omega_2} \qquad (23)$$

The coefficient in this case is approximately the white noise result for small damping, the actual white noise result being

$$\langle z_2^2 \rangle_{WN} = \frac{\pi\omega_n S_o}{4\zeta} (1 + 4\zeta^2) \qquad (24)$$

Finally, the response for the third transfer function is

$$\langle z_3^2 \rangle = \int_{\Omega_1}^{\Omega_2} S_o \Omega^b \Omega^4 H_o^2 \omega_n\, d\Omega$$

$$= \frac{\pi\omega_n S_o}{4\zeta} \left[I_{b+4}(\Omega_2) - I_{b+4}(\Omega_1) \right] \qquad (25)$$

The coefficient in this case does not represent the white noise response, because the white noise response is infinite.

RECURSION RELATION FOR $I_b(\Omega)$

The results of (21), (23), and (25) give the mean square response in terms of the functions $I_b(\Omega)$; the problem now is to evaluate $I_b(\Omega)$. There are a large number of values of b in the range of interest, making it unwieldy to evaluate and plot the I_b functions over the entire range. Fortunately, there exists a simple recursion relation between the functions.

From (22a) I_b is defined as

$$I_b(\Omega) = \frac{4\zeta}{\pi} \int \frac{\Omega^b}{(1-\Omega^2)^2 + 4\zeta^2\Omega^2}\, d\Omega \qquad (22a)$$

The denominator of the integrand can be expanded to obtain

$$\text{den} = \Omega^4 - 2(1-2\zeta^2)\Omega^2 + 1 \qquad (26)$$

$$= \Omega^4 - \ell\,\Omega^2 + 1 \qquad (26a)$$

where $\ell = 2(1-2\zeta^2)$ (27)

Division of the numerator of the integrand by the denominator yields

$$\frac{\Omega^b}{\Omega^4 - \ell\Omega^2 + 1} = \Omega^{b-4} + \frac{\ell\Omega^{b-2} - \Omega^{b-4}}{\Omega^4 - \ell\Omega^2 + 1} \qquad (28)$$

Then I_b becomes

$$I_b = \frac{4\zeta}{\pi} \frac{\Omega^{b-3}}{b-3} + \ell\, I_{b-2} - I_{b-4} \qquad (29)$$

for $b \neq 3$. When $b = 3$ the result is

$$I_3 = \frac{4\zeta}{\pi} \ln \Omega + \ell\, I_1 - I_{-1} \qquad (30)$$

Equations (29) and (30) are the desired recursion relations. They enable all I_b functions to be obtained in terms of only four, such as I_0, I_1, I_2 and I_3. The details have been worked out for the range of b values from -6 to 9, using the above four I_b's as the basic functions. The results are shown in Table II.

EVALUATION OF BASIC I_b FUNCTIONS

It remains now to evaluate the basic functions I_0 to I_3, since once they are known all others can be readily determined. The evaluation involves an integration which is effected using a partial fraction expansion. The details will only be shown for I_0 to illustrate the technique; the other I_b's are determined in a similar manner, but only the results will be given.

From equation (22a) I_0 is given by

$$I_0 = \frac{4\zeta}{\pi} \int \frac{1}{(1-\Omega^2)^2 + 4\zeta^2\Omega^2}\, d\Omega \qquad (31)$$

The denominator of the integrand can be factored into two quadratics to obtain.

$$I_0 = \frac{4\zeta}{\pi} \int \frac{1}{(1 + a\Omega + \Omega^2)(1-a\Omega + \Omega^2)}\, d\Omega \qquad (32)$$

where $a = 2\sqrt{1-\zeta^2}$. By using a partial fraction expansion the integrand can be written in a more convenient form:

$$I_0 = \frac{4\zeta}{\pi} \int \frac{1}{2}\left[\frac{1+\Omega/a}{1+a\Omega+\Omega^2} + \frac{1-\Omega/a}{1-a\Omega+\Omega^2}\right] d\Omega \qquad (33)$$

The integrand now consists of terms that can be found in integral tables. Upon integration there results

$$I_0 = \frac{1}{\pi}\left[\tan^{-1}\left(\frac{2\Omega+a}{2\zeta}\right) + \tan^{-1}\left(\frac{2\Omega-a}{2\zeta}\right)\right] + \frac{\zeta}{\pi a} \ln\left(\frac{1+a\,\Omega+\Omega^2}{1-a\,\Omega+\Omega^2}\right) \qquad (34)$$

The arctangent terms can be combined using the trigonometric identity

$$\tan^{-1}x + \tan^{-1}y = \tan^{-1}\left(\frac{x+y}{1-xy}\right) \qquad (35)$$

to obtain

$$I_0 = \frac{1}{\pi} \tan^{-1}\left(\frac{2\zeta\Omega}{1-\Omega^2}\right) + \frac{\zeta}{\pi a} \ln\left(\frac{1+a\Omega+\Omega^2}{1-a\Omega+\Omega^2}\right) \qquad (36)$$

The expressions for I_1 to I_3 can be obtained in a similar manner. The results are

$$I_1 = \frac{2}{\pi a} \tan^{-1}\left(\frac{a\zeta}{1-2\zeta^2-\Omega^2}\right) \qquad (37)$$

$$I_2 = \frac{1}{\pi} \tan^{-1}\left(\frac{2\zeta\Omega}{1-\Omega^2}\right) - \frac{\zeta}{\pi a} \ln\left(\frac{1+a\Omega+\Omega^2}{1-a\Omega+\Omega^2}\right) \qquad (38)$$

$$I_3 = \frac{2(1-2\zeta^2)}{\pi a} \tan^{-1}\left(\frac{a\zeta}{1-2\zeta^2-\Omega^2}\right) + \frac{\zeta}{\pi} \ln\left[(1-\Omega^2)^2+4\zeta^2\Omega^2\right] \qquad (39)$$

For completeness these results are also included in Table II.

It is worth noting that the result for I_0 is the same as that given by Crandall and Mark (Reference 1, equation 2.51) for band-limited white noise.

INTERPRETATION OF RESULTS

With the function I_b completely determined, it remains to interpret the results, to consider the general trends and to develop working curves that can be used to facilitate numerical calculations.

The results of a previous section showed that the mean square response to a band of excitation is directly related to the difference in the I_b function evaluated at the limits of the band (see equations 21, 23, and 25). It should be stressed that it is the <u>difference</u> in the function I_b at two frequencies that determines the response, and not the value at any one frequency.

The general shape of I_b is shown in Figure 2 as a function of Ω for several values of b and one value of ζ. The band-limited noise function, I_0, is seen to increase from zero to one as Ω increases from zero. The largest contribution to the response occurs in the vicinity of resonance, where the slope $dI_b/d\Omega$ is a maximum. For white noise excitation, the response within the resonant bandwidth accounts for approximately half of the total response. The total response to white noise for the transfer function H_1 reduces, as it should, to just the coefficient term in (21) since $I_0(\infty) - I_0(0) = 1$.

Table II

Expressions For I_b For The Range
From b = -6 To +9

$$I_{-6} = -\frac{4\zeta}{\pi}\left(\frac{1}{5\Omega^5} + \frac{\ell}{3\Omega^3} + \frac{(\ell^2-1)}{\Omega} + \ell(\ell^2-2)I_o - (\ell^2-1)I_2\right)$$

$$I_{-5} = -\frac{4\zeta}{\pi}\left(\frac{1}{4\Omega^4} + \frac{\ell}{2\Omega^2} - (\ell^2-1)\ln\Omega\right) + \ell(\ell^2-2)I_1 - (\ell^2-1)I_3$$

$$I_{-4} = -\frac{4\zeta}{\pi}\left(\frac{1}{3\Omega^3} + \frac{\ell}{\Omega}\right) + (\ell^2-1)I_o - \ell I_2$$

$$I_{-3} = -\frac{4\zeta}{\pi}\left(\frac{1}{2\Omega^2} - \ell\ln\Omega\right) + (\ell^2-1)I_1 - \ell I_3$$

$$I_{-2} = -\frac{4\zeta}{\pi}\left(\frac{1}{\Omega}\right) + \ell I_o - I_2$$

$$I_{-1} = \frac{4\zeta}{\pi}\ln\Omega + \ell I_1 - I_3$$

$$I_o = \frac{1}{\pi}\tan^{-1}\left(\frac{2\zeta\Omega}{1-\Omega^2}\right) + \frac{\zeta}{\pi a}\ln\left(\frac{1+a\Omega+\Omega^2}{1-a\Omega+\Omega^2}\right)$$

$$I_1 = \frac{2}{\pi a}\tan^{-1}\left(\frac{a\zeta}{1-2\zeta^2-\Omega^2}\right)$$

$$I_2 = \frac{1}{\pi}\tan^{-1}\left(\frac{2\zeta\Omega}{1-\Omega^2}\right) - \frac{\zeta}{\pi a}\ln\left(\frac{1+a\Omega+\Omega^2}{1-a\Omega+\Omega^2}\right)$$

$$I_3 = \frac{\zeta}{\pi}\ln\left((1-\Omega^2)^2 + 4\zeta^2\Omega^2\right) + \frac{2(1-2\zeta^2)}{\pi a}\tan^{-1}\left(\frac{a\zeta}{1-2\zeta^2-\Omega^2}\right)$$

$$I_4 = \frac{4\zeta}{\pi}\Omega + \ell I_2 - I_o$$

$$I_5 = \frac{4\zeta}{\pi}\frac{\Omega^2}{2} + \ell I_3 - I_1$$

$$I_6 = \frac{4\zeta}{\pi}\frac{\Omega^3}{3} + \ell I_4 - I_2$$

$$= \frac{4\zeta}{\pi}\left(\frac{\Omega^3}{3} + \ell\Omega\right) + (\ell^2-1)I_2 - \ell I_o$$

$$I_7 = \frac{4\zeta}{\pi}\left(\frac{\Omega^4}{4} + \frac{\ell\Omega^2}{2}\right) + (\ell^2-1)I_3 - \ell I_1$$

$$I_8 = \frac{4\zeta}{\pi}\left(\frac{\Omega^5}{5} + \frac{\ell\Omega^3}{3}\right) + (\ell^2-1)I_4 - \ell I_2$$

$$= \frac{4\zeta}{\pi}\left[\frac{\Omega^5}{5} + \frac{\ell\Omega^3}{3} + (\ell^2-1)\Omega\right] + \ell(\ell^2-2)I_2 - (\ell^2-1)I_o$$

$$I_9 = \frac{4\zeta}{\pi}\left[\frac{\Omega^6}{6} + \frac{\ell\Omega^4}{4} + (\ell^2-1)\frac{\Omega^2}{2}\right] + \ell(\ell^2-2)I_3 - (\ell^2-1)I_1$$

General Recursion Relation:

$$I_b = \frac{4\zeta}{\pi}\frac{\Omega^{b-3}}{b-3} + \ell I_{b-2} - I_{b-4} \quad \text{for } b \neq 3$$

Note: $\ell = 2(1-2\zeta^2)$

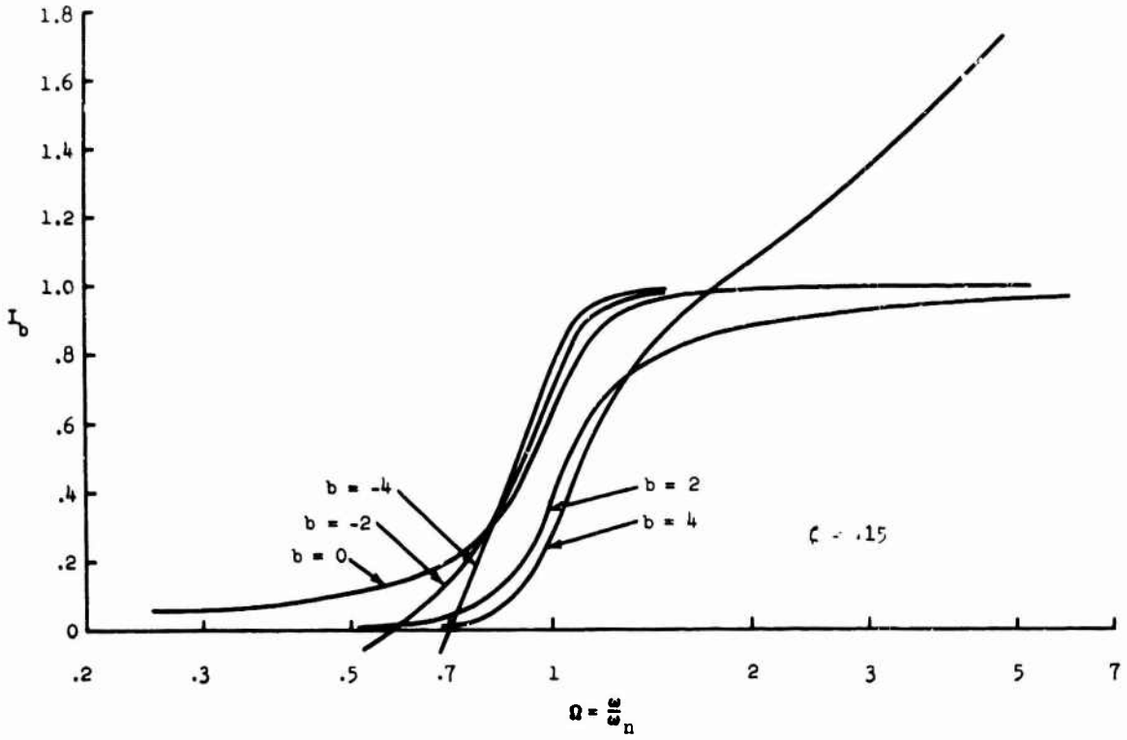


Figure 2 Variation of I_b With Ω

The response for negative values of b or for $b \geq 4$ does not converge to a finite value as the excitation bandwidth becomes large. Thus, an infinite bandwidth approximation, analogeous to the white noise approximation for b = 0, cannot be used in these cases. For positive values of b the region above resonance is seen to contribute more to the total response than the region below resonance; for negative values of b the opposite is true. This is an expected result, since the region that contributes most to the response is that in which the excitation spectral density is highest.

It is of interest to know what effect a sloping spectrum will have on the resonant response of a system whose resonant bandwidth lies within the band of excitation. For purposes of this comparison the resonant bandwidth is taken as the effective random bandwidth, which is simply $\pi/2$ times the half power bandwidth, or $\pi\zeta$. Figure 3 shows plots of normalized resonant response as a function of b for various damping values. The minimum resonant response occurs for b = 2, the value that makes the response spectral density most nearly symmetric about $\Omega = 1$. For light damping ($\zeta \leq .05$) the resonant response remains within 7% of the white noise result for all values of b between ± 8 (i.e., up to 24 db/octave slope). However, for heavy damping significant differences in response occur for even moderate values of b. For example, a difference of about 23% exists for b = -4 and $\zeta = .15$.

From these curves it would appear that in many cases a white noise approximation can provide quick and reasonably accurate results even for cases in which the excitation is steeply sloped. However, it must be emphasized that these curves represent only the resonant response. In cases where the excitation is steeply sloped the spectral density may reach values that are far higher than the resonant value, and the nonresonant response may then become much more significant, or even dominant.

Figures 4 to 8 show plots of the functions I_0 to I_4 vs. Ω for a family of ζ's. These Figures are intended as "working curves" which can be used to facilitate calculation of the basic I_b functions. Figure 8, which gives I_4, actually was not needed since I_4 is not one of the basic functions; however, since it represents a commonly-encountered 12 db/octave slope, it was included for convenience.

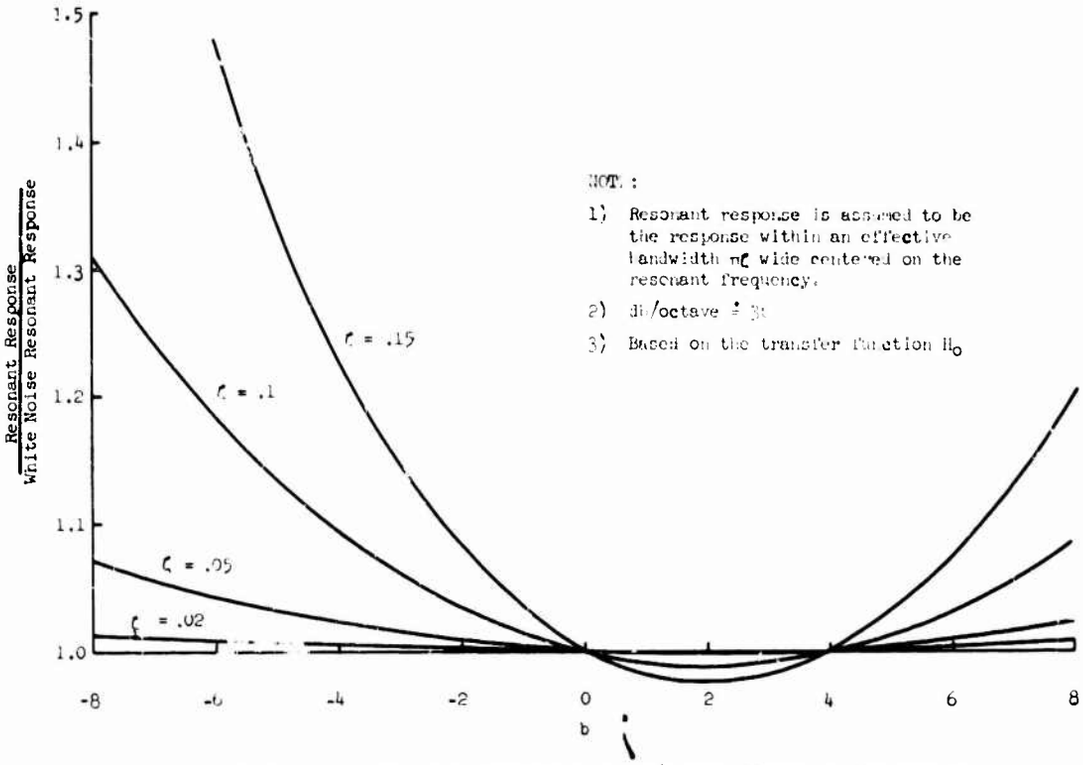


Figure 3 Variation in Resonant Response with db/Octave Change in Excitation

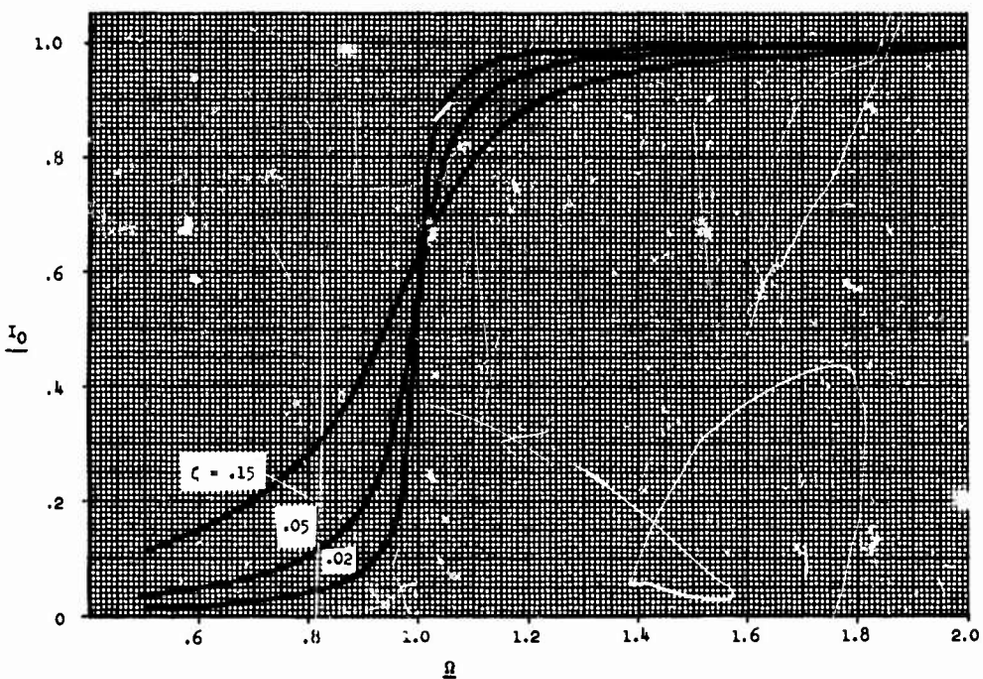


Figure 4 I_0 vs Ω

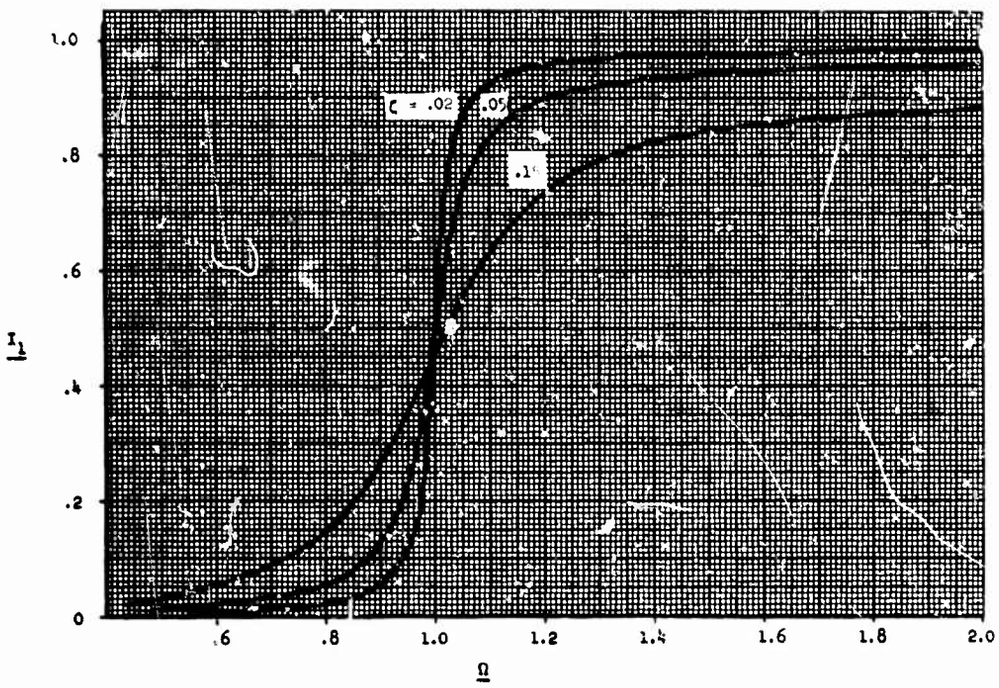


Figure 5 I_1 vs Ω

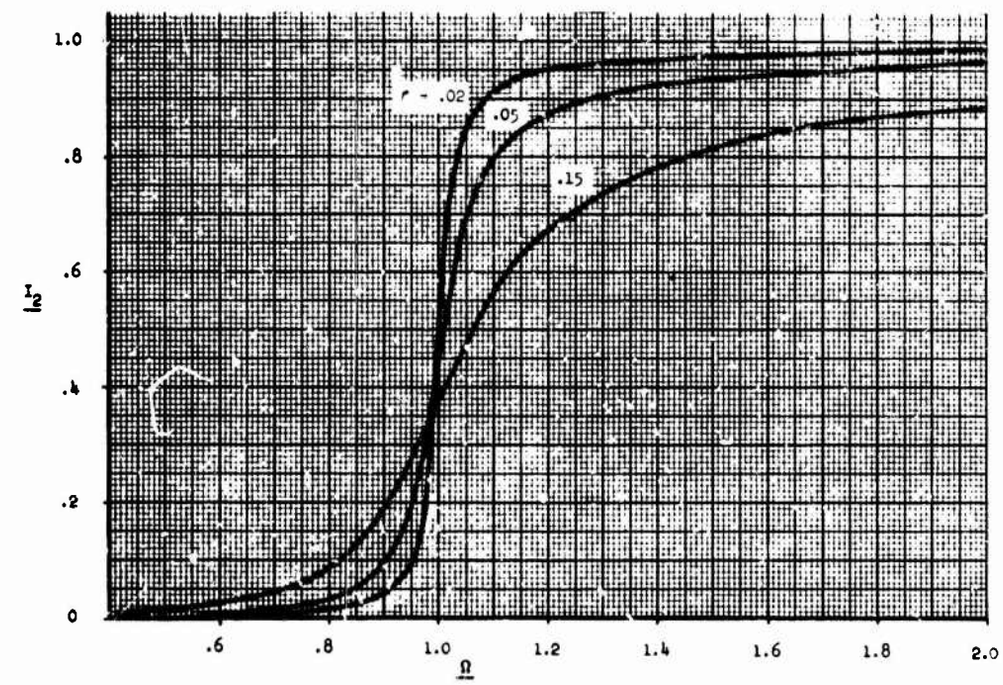


Figure 6 I_2 vs Ω

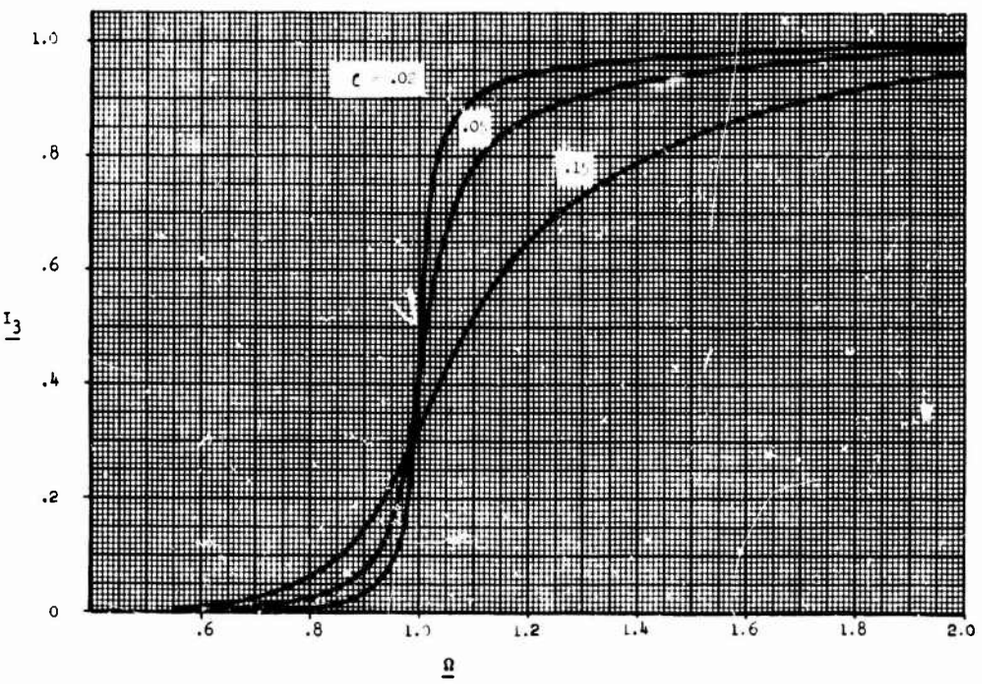


Figure 7 I_3 vs Ω

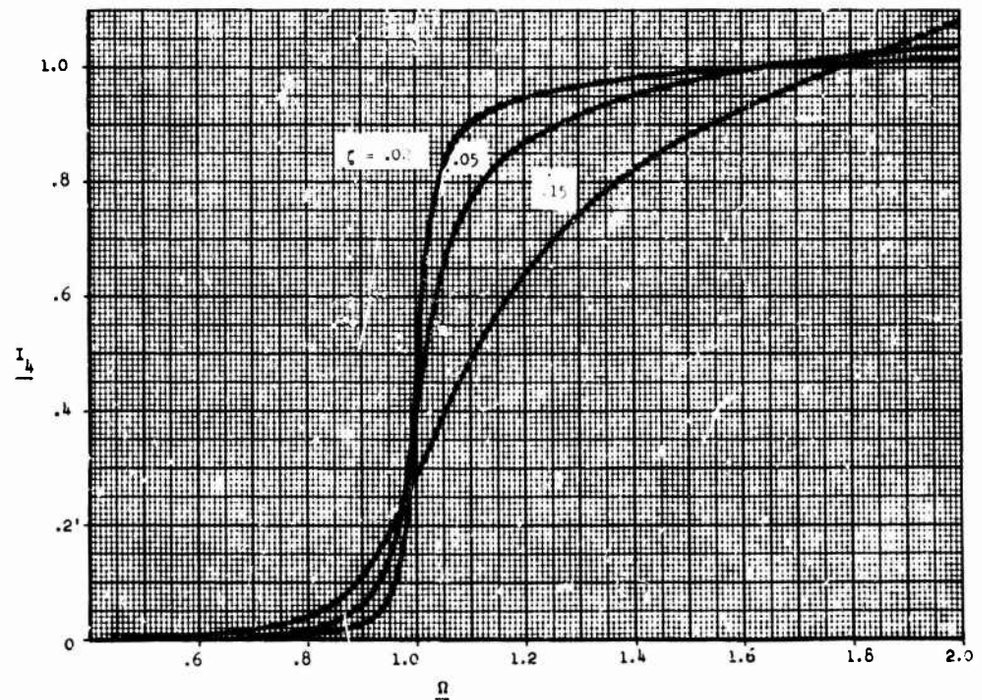


Figure 8 I_4 vs Ω

The curves are plotted over a range of Ω's between .5 and 2, but accurate reading of the difference between two I_b values well above or well below resonance is not possible. Thus, if a nonresonant band of excitation appears important it will be necessary to evaluate the basic equations (36) to (39) directly, or to use an approximation of the type discussed in the next section.

APPROXIMATE SOLUTIONS FOR NONRESONANT EXCITATION

Outside the resonant range the influence of damping becomes quite small and can be neglected with good approximation. The function I_b can then be written

$$I_b = \frac{4\zeta}{\pi}\int \frac{\Omega^b}{(1-\Omega^2)^2 + 4\zeta^2\Omega^2}\, d\Omega$$

$$\simeq \frac{4\zeta}{\pi}\int \frac{\Omega^b}{(1-\Omega^2)^2}\, d\Omega \qquad (40)$$

provided $4\zeta^2\,\Omega^2 \ll (1-\Omega^2)^2$. Thus, for ζ = .15 the approximation will be useful in the range below Ω = .6 or above Ω = 1.6. For smaller damping the useful range will be larger. The integrand in (40) can be expanded into a series in Ω^2:

$$\frac{\Omega^b}{(1-\Omega^2)^2} \simeq \Omega^b\,(1 + 2\,\Omega^2 + 3\,\Omega^4 + 4\,\Omega^6 + ..) \qquad (41)$$

for $\Omega < 1$, or

$$\frac{\Omega^b}{(1-\Omega^2)^2} \simeq \Omega^b\left(1 + \frac{2}{\Omega^2} + \frac{3}{\Omega^4} + \frac{4}{\Omega^6} + \ldots\right) \qquad (42)$$

for $\Omega > 1$. These expressions can be substituted into (40), which can then be readily integrated to obtain

$$I_b \simeq \frac{4\zeta}{\pi}\left(\frac{\Omega^{b+1}}{b+1} + \frac{2\Omega^{b+3}}{b+3} + \frac{3\Omega^{b+5}}{b+5} + \ldots\right) \qquad (43)$$

for $\Omega < 1$, and

$$I_b \simeq \frac{4\zeta}{\pi}\left(\frac{\Omega^{b-1}}{b-1} + \frac{2\Omega^{b-3}}{b-3} + \frac{3\Omega^{b-5}}{b-5} + \ldots\right) \qquad (44)$$

for $\Omega > 1$, as long as none of the denominators equal zero. If a denominator equals zero that term in the series becomes a log term; thus, if $b \pm M = 0$ the corresponding term becomes

$$\frac{M+1}{2}\,\frac{\Omega^{b\pm M}}{b \pm M} \qquad \frac{M+1}{2}\ln\Omega \qquad (45)$$

in equation (43) or (44).

In using either the high frequency or low frequency nonresonant approximation, it is important to remember that the entire band of excitation running from Ω = .2 to 3 cannot be determined by using the high frequency approximation to determine I_b (3) and low frequency approximation for I_b (.2), and then taking the difference. It is necessary instead, to use the low frequency approximation to evaluate the range from .2 to say .6 and the high frequency approximation for 1.6 to 3. The plotted results can then be used to determine the response in the resonant range. (This restriction is due to the fact that the constants of integration are not included in the evaluation of the indefinite integrals leading to the approximations for I_b).

The primary use of the approximate solutions will not be for the case cited, however, since in such a case it probably would be easier to use the exact relations given in Table II, or it would be sufficiently accurate to use only the plotted results. The approximations will be most useful for excitation spectra having discontinuities (which requires that they be divided into segments before analysis) or for cases in which the excitation is primarily nonresonant.

ILLUSTRATIVE EXAMPLE

A base-excited spring-mass system is subjected to an acceleration input with maximum spectral density of 1.0 g^2/cps and a spectrum shape as shown in Figure 9. The system has a 45 cps natural frequency and a damping ratio of ζ = .05. The problem is to find the mean square acceleration response.

Begin by dividing the excitation into regions within which the spectral density is a straight line on a log-log plot. The total mean square response will then be the sum of the contributions of the individual regions. Three regions are required for this problem. They are designated I, II, and III in Figure 9. The slopes of the three regions are 12, 0, and -12 db/octave corresponding to b values of 4, 0, and -4 (from equation 18). From Table I the appropriate transfer function is seen to be H_2. The mean square response can be expressed, with the use of (23), as

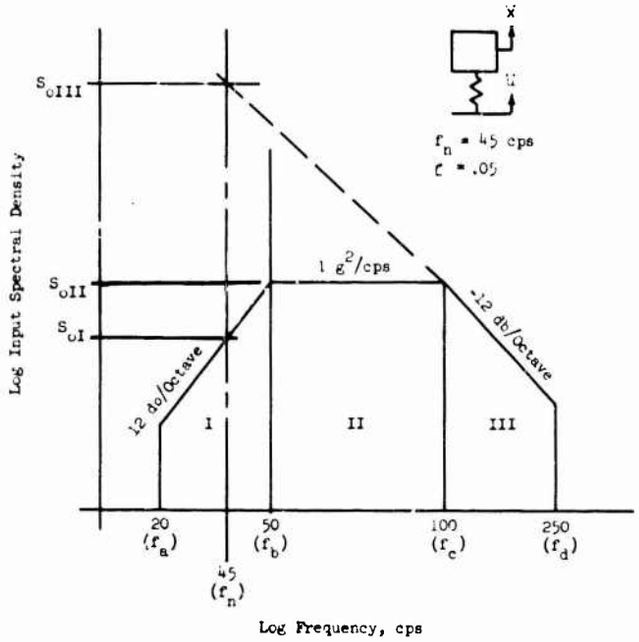


Figure 9 Excitation Spectral Density for Illustrative Example

$$\langle \ddot{x}^2 \rangle = \langle \ddot{x}_I^2 \rangle + \langle \ddot{x}_{II}^2 \rangle + \langle \ddot{x}_{III}^2 \rangle$$

$$= \frac{\pi \omega_n S_{oI}}{4\zeta} \left[I_4 + 4\zeta^2 I_6 \right]_{\Omega_a}^{\Omega_b}$$

$$+ \frac{\pi \omega_n S_{oII}}{4\zeta} \left[I_0 + 4\zeta^2 I_2 \right]_{\Omega_b}^{\Omega_c}$$

$$+ \frac{\pi \omega_n S_{oIII}}{4\zeta} \left[I_{-4} + 4\zeta^2 I_{-2} \right]_{\Omega_c}^{\Omega_d}$$

The normalized frequencies are

$\Omega_a = 20/45 = .445$

$\Omega_b = 50/45 = 1.11$

$\Omega_c = 100/45 = 2.22$

$\Omega_d = 250/45 = 5.56$

Since $4\zeta^2 = .01$ and the term multiplied by $4\zeta^2$ is of the order of the first term in brackets in the range of interest (see the general behavior shown in Figure 3), the following approximation is valid:

$$\left[I_4 + 4\zeta^2 I_6 \right]_{.445}^{1.11} \doteq I_4(1.11) - I_4(.445)$$

$$\left[I_0 + 4\zeta^2 I_2 \right]_{1.11}^{2.22} \doteq I_0(2.22) - I_0(1.11)$$

$$\left[I_{-4} + 4\zeta^2 I_{-2} \right]_{2.22}^{5.56} \doteq I_{-4}(5.56) - I_{-4}(2.22)$$

From equation (19) the spectral densities at $\Omega = 1$ are

$$S_{oI} = S_{oII} \left(\frac{45}{50}\right)^4 = .656\, S_{oII}$$

$$S_{oIII} = S_{oII} \left(\frac{45}{100}\right)^{-4} = 24.5\, S_{oII}$$

The mean square response becomes

$$\langle \ddot{x}^2 \rangle \doteq \frac{\pi w_n S_{oII}}{4\zeta} \Big\{ .656[I_4(1.11) - I_4(.445)] + I_0(2.22) - I_0(1.11) + 24.5[I_{-4}(5.56) - I_{-4}(2.22)] \Big\}$$

From Figure 8:

$$I_4(1.11) = .78$$

$$I_4(.445) = 0$$

From Figure 4

$$I_0(2.22) = 1.00$$

$$I_0(1.11) = .90$$

The series approximation of equation (43) can be used for region III:

$$I_{-4}(5.56) \doteq \frac{4(.05)}{\pi}\left[\frac{(5.56)^{-5}}{-5} + \frac{2(5.56)^{-7}}{-7}\right] = -2.5 \times 10^{-6}$$

$$I_{-4}(2.22) = \frac{4(.05)}{\pi}\left[\frac{(2.22)^{-5}}{-5} + \frac{2(22.22)^{-7}}{-7} + \frac{3(2.22)^{-9}}{-9}\right] = -3.20 \times 10^{-4}$$

(I_{-4} can also be found by using the recursion relations of Table II, but the series approximation is much simpler when applicable).

The mean square response is

$$\langle \ddot{x}^2 \rangle = \frac{\pi w_n S_{oII}}{4\zeta}\left[.656(.78-0) + (1.00-.90) + 24.5\,(-.025 + 3.20)\,10^{-4}\right] = .619\,\frac{\pi w_n S_{oII}}{4\zeta}$$

The contribution from region III is seen to be negligible. This could have been inferred at the outset, but the calculations were carried through in order to demonstrate the approach. It is of interest to compare this result with that obtained by using a white noise approximation. The white noise result is given by (24) as

$$\langle \ddot{x}^2 \rangle_{WN} = \frac{\pi w_n S_{oI}}{4\zeta}(1 + 4\zeta^2) = .664\,\frac{\pi w_n S_{oII}}{4\zeta}$$

Thus, the error in using a white noise approximation in this case is only 7.3%.

The problem is completed by converting the excitation spectral density into appropriate units and substituting into the above result:

$$S_{oII} = 1.0\,\frac{g^2}{cps} \times \frac{cps}{2\pi\ rad/sec} \times \frac{(386)^2(in/sec^2)^2}{g^2} = 2.38 \times 10^4\,\frac{(in/sec^2)^2}{rad/sec}$$

$$\langle \ddot{x}^2 \rangle = .619\,\frac{\pi w_n S_{oII}}{4\zeta} = 6.54 \times 10^7\,(in/sec^2)^2 = 439\ g^2$$

The rms acceleration is

$$\ddot{x}_{rms} = 20.9\ g$$

CONCLUSIONS

A method has been developed for evaluating the response of linear single-degree-of-freedom systems to bands of random excitation. Any integral db/octave variation in level may exist within the excitation band, and no restrictions are made on the amount of damping in the vibrating system. Exact analytical expressions are given for computing the response directly for slopes ranging from -24 to +36 db/octave. The basic functions required for computations are presented graphically for the range of greatest interest, and approximate expressions are given to facilitate the calculations in many practical cases.

REFERENCES

1. Random Vibration in Mechanical Systems, Crandall and Mark, Academic Press, 1963.

2. An Introduction to Random Vibration, Robson, American Elsevier, 1963.

PREDICTION OF STRESS AND FATIGUE LIFE OF ACOUSTICALLY-EXCITED AIRCRAFT STRUCTURES*

Noe Arcas
Grumman Aircraft Engineering Corporation
Bethpage, New York

Recently, a technique for predicting the R.M.S. stress on aircraft structure excited by high intensity noise was proposed by Clarkson (3). The agreement he obtained in comparing predicted and measured stresses appears quite promising, particularly in view of the relatively simple form of his results. In this paper, Clarkson's work is extended in several areas:

1. Modal functions which provide improved boundary conditions are used.
2. Further data is included in the comparison of theory and experiment.
3. Statistical confidence limits are obtained for the predicted stresses.
4. Fatigue life predictions are made and the results are compared with experimental data.

INTRODUCTION

In recent years, the need has existed for a method to predict stress levels and fatigue life of aircraft structure excited by high intensity noise. The most widely used technique has been a series of design nomographs developed by Douglas under contract to the Air Force (1). Although these curves were, and still are, quite useful, they have been found to be relatively conservative and limited in the types of structure considered. General analytical solutions are also available (2), but these are too complex to be used in the early design stage of an aircraft.

Recently, Clarkson (3) proposed a simplified technique which could be used in the initial design phase, and which could be applied to various types of construction (rudders, stabilizers, fuselage panels, and others). The method proposed has been shown by comparison with experiment to provide estimates of overall R.M.S. stresses which lie generally within a factor of two of the actual values. This appears to be relatively good agreement in view of the simplifications made.

In this study, modifications are made to Clarkson's technique in order to improve the boundary conditions that are used in the analysis. The resulting frequency and stress predictions derived from this modified method are compared to Clarkson's version, and to a similar technique proposed by Ballentine (4). In addition, predictions made by using this revised technique are compared to actual stress data that has been accumulated from measurements made at Grumman and data presented in (3) and (4).

Predictions of the time to failure of some structure are also compared with actual test data; however, the limited amount of data available restricts the conclusions that can be made regarding the accuracy of these results.

*Paper not presented at Symposium.

CLARKSON METHOD

The method of stress prediction proposed in (3) assumes that the critical stress excited in the aircraft structure is due primarily to response in a single mode of vibration. The assumption is also made that this mode is excited by a uniform perfectly correlated random pressure field. Under these assumptions the R.M.S. stress can be written as

$$S_{RMS} = \left[\frac{\pi}{4\zeta} f_R G_P(f_R) \right]^{\frac{1}{2}} S_o \qquad (1)$$

where

S_{RMS} is the root mean square stress

ζ is the critical damping ratio

f_R is the fundamental resonant frequency of vibration

$G_P(f_R)$ is the spectral density of the pressure at the fundamental resonant frequency

S_o is the stress at the location of interest per unit static pressure

The value of the damping ratio for built-up aluminum structure is generally in the range of .01 to .02; Clarkson uses a value of .017. The spectral density of the pressure can be obtained from the octave band level. The required expression is:

$$G_P(f_R) = (.0002)^2 \left[10^{.1A}\right] \qquad (2)$$

where

$A = S_{PL} - 10 \text{ Log } (f_2 - f_1)$

S_{PL} is the octave band level in dB of the octave that contains the fundamental resonance.

$f_2 - f_1$ is the bandwidth of the octave

$G_P(f_R)$ is the spectral density in $\left[\frac{\text{Dynes}}{\text{cm}^2}\right]^2/\text{Hz}$

Eqs. (1) and (2) can be used to predict the stress response of one-sided surfaces such as flat plates or the panels of an aircraft fuselage due to incident acoustic energy. For structure constructed of two skins separated by ribs with significant excitation on one skin only, (e.g. horizontal stabilizer or elevator) a lower stress results. This occurs because the ribs and unexcited skin drain energy from the excited structure. A value of about one third of that obtained by the above equations is recommended by Clarkson (3). If a structure has two skins and is excited on both sides (e.g. a rudder) the stress will be higher than the value predicted for one sided excitation. An increase of 3 dB seems appropriate, based on Clarkson (3) and other experimental data (5). Thus the resulting stress will be about 1.4/3 of that obtained from Eq. (1).

The type of construction considered in (3) consists of aluminum skin-stringer panels whose ends are attached to frames. Two cases are analyzed: the first assumes that both the stringers and frames are infinitely stiff, and for this case the panels behave as flat plates with clamped boundaries; the second assumes the frames are infinitely stiff, but the stringers are flexible and undergo bending. The value of S_o and f_R required for Eq. (1) will depend on which of these cases is considered.

To obtain f_R for the fully fixed condition, the fundamental resonant frequency of a rectangular plate with clamped boundaries is used. The value of S_o is obtained by considering the stress that would result due to static deflection arising from a uniform constant pressure field acting on the plate. The procedure for obtaining S_o and f_R when stringer bending occurs is to assume a fundamental mode shape and then use energy equations to obtain expressions for the desired parameters.

MODIFIED METHOD

In using Ref. (3) a problem arises when the stiffness of the stringer is allowed to increase. In that case the stress parameter predicted by the equations based on the fully fixed case will differ from that predicted by the expressions that allow boundary deflection. By assuming a more complex mode shape, this situation can be corrected.

The mode shape used in this analysis is made up of the sum of two expressions. The first term accounts for panel deformation. It is taken as the product of the mode shapes of a clamped-clamped beam in the x and y directions and is given by

$$W_1 = [\cosh\theta x - \cos\theta x - M(\sinh\theta x - \sin\theta x)]$$
$$[\cosh\eta y - \cos\eta y - M(\sinh\eta y - \sin\eta y)] \qquad (3)$$

where η, θ, and M are constants dependent on the mode of vibration being considered. This mode shape differs from that of Clarkson, who used the static deflection shape of a plate under uniform pressure. The second term accounts for the additional deflection due to stringer flexibility. It consists of the static deformation shape of a clamped-clamped beam under a uniform load and is expressed by

$$W_2 = \left(\frac{y}{a}\right)^4 - 2\left(\frac{y}{a}\right)^3 + \left(\frac{y}{a}\right)^2 \qquad (4)$$

where

a is the beam length.

The entire expression consists of the sum of both terms or

$$W = kW_1 + W_2 \qquad (5)$$

where k is a constant dependent on the relative stiffness of the plate and supporting stringer. The coordinate system used is shown in Fig. 1.

An energy approach as outlined in Ref. (3) can be used to obtain an expression for the fundamental resonant frequency. By equating the expression for the maximum kinetic energy to the maximum strain energy one obtains

$$\omega_R^2 = (C_1 + C_2)/(C_3 + C_4) \qquad (6)$$

where

$$C_1 = 498.3Dk^2\left(\frac{a}{b^3} + \frac{b}{a^3}\right) + \frac{.8}{a^3}(bD + EI) \qquad (7)$$

$$C_2 = 301.9\frac{Dk^2}{ab} + 33.18\frac{Dkb}{a^3} \qquad (8)$$

$$C_3 = .0016\, a(\rho_B + \rho tb) + .996\, k^2 ab\rho t \qquad (9)$$

$$C_4 = .066\, \rho tkba \qquad (10)$$

$$D = Et^3/12(1-\nu^2) \qquad (11)$$

$$\omega_R = 2\pi f_R \qquad (12)$$

and

ρ is the mass density of the plate

E is the elastic modulus

I is the cross-sectional moment of inertia of the stringer

ν is Poisson's ratio

The constant k must now be evaluated. The correct value for k is that which minimizes the resonant frequency. Differentiating the frequency expression with respect to k and setting the result equal to zero results in the following quadratic equation.

$$mk^2 + nk + p = 0 \qquad (13)$$

where

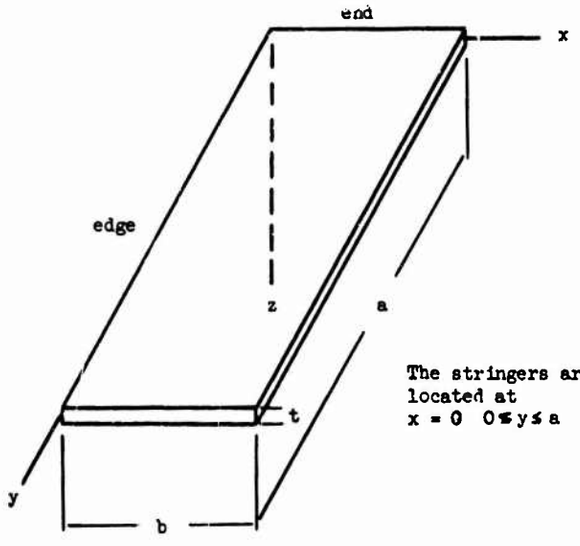
$$m = \rho tDa\left(33.1\frac{a}{b^2} + .0432\frac{b^2}{a^3} + \frac{20.0}{a}\right) \qquad (14)$$

$$n = Da(\rho_B + \rho tb)\left(1.585\left(\frac{a}{b^3} + \frac{b}{a^3}\right) + \frac{.96}{ab}\right) - 1.593\frac{\rho tb}{a^2}(bD + EI) \qquad (15)$$

$$p = \frac{b}{a^2}(.0528\rho_B D - .0531\rho tEI) \qquad (16)$$

and

ρ_B is the mass per unit length of the stringer.



The stringers are located at
x = 0 $0 \leq y \leq a$ x = b
$0 \leq y \leq a$

Fig. 1 Coordinate System

Solution of this equation gives the appropriate value of k for any particular problem.

The energy approach can also be used to obtain expressions for the stress parameter S_o. This is done by equating the work done by the static pressure to the maximum strain energy of the structure. The resulting equations are

Edge $x = 0,\ y = a/2,\ z = t/2$

$$S_x = Et\frac{G_1}{G_2}\left(39.88\,\frac{k}{b^2} - \frac{.185}{a^2}\right) \qquad (17)$$

Center $x = b/2,\ y = a/2,\ z = t/2$

$$S_x = -Et\frac{G_1}{G_2}\left(24.24k\left(\frac{1}{b^2} + \frac{.33}{a^2}\right) + \frac{.185}{a^2}\right) \qquad (18)$$

End $x = b/2,\ y = 0,\ z = t/2$

$$S_y = \frac{Et}{a^2}\frac{G_1}{G_2}\left(39.88k + 1.122\right) \qquad (19)$$

where

$$G_1 = \frac{ab}{60D} + \frac{.345kab}{D} \qquad (20)$$

$$G_2 = 249.2\,k^2\left(\frac{a}{b^3} + \frac{b}{a^3}\right) + \frac{.4}{a^3}\left(b+\frac{EI}{D}\right) + 150.95\,\frac{k^2}{ab} + 16.59\,\frac{kb}{a^3} \qquad (21)$$

It is of interest to compare the results of the modified approach with those of Ref. (3). Eqs. (6) through (21) were solved for a range of parameters using a digital computer program. Fig. 2 presents comparisons of frequency predictions using the two methods. The results are seen to be in close agreement.

The major difference between the two methods lies in the prediction of the stress parameter S. The stress parameter for the modified version will approach the fully fixed value as the stringer stiffness increases. The results of Ref. (3) do not show this effect. Figs. 3 and 4 present plots of the variation in stress parameter with increasing stringer stiffness.

Under conditions where the assumption that all the boundaries remain fully fixed is justifiable, Eqs. (6) through (21) can be simplified by letting EI approach infinity. The expression for the fundamental resonant frequency for the fully fixed case then becomes

$$f_R = 2.29(10^5)\frac{t}{b^2}\left(1+\left(\frac{b}{a}\right)^4 + .606\left(\frac{b}{a}\right)^2\right)^{\frac{1}{2}} \qquad (22)$$

where a, b, and t are expressed in inch units. The corresponding stress parameter expressions are

Center

$$S_x = -.5177\left(\frac{b}{t}\right)^2\left(1 + .33\left(\frac{b}{a}\right)^2\right)/B \qquad (23)$$

Edge

$$S_x = .8519\left(\frac{b}{t}\right)^2/B \qquad (24)$$

where

$$B = 1.442 + 1.442\left(\frac{b}{a}\right)^4 + .8737\left(\frac{b}{a}\right)^2 \qquad (25)$$

Comparisons between predictions from Eqs. (22) through (25) and curves presented in Ref. (3) are shown in Figs. 5, 6, and 7. Also shown are predicted results obtained from equations derived by Ballentine (4). His expressions were obtained by using

$$W = \left(1-\cos\frac{2\pi x}{b}\right)\left(1-\cos\frac{2\pi y}{a}\right) \qquad (26)$$

to represent the fundamental mode shape of a clamped-clamped plate. All three expressions yield similar results for the resonant frequency; however, significant differences occur in the prediction of the stress parameter. These differences are due to the different mode shapes used in the three analyses. The mode shape used herein appears to provide the best approximation of the three; for large aspect ratios it reduces to the correct shape for one dimensional bending.

COMPARISON WITH TEST RESULTS

Once the fundamental resonant frequency and stress parameter have been determined, Eq. (1) along with the required multiplying factor can be used to predict the R.M.S. stress for a known excitation. Such calculations have been performed for a large number of structural configurations for which test data is available. Three sets of test data were used:

1) Grumman data obtained from fatigue tests and field measurements

2) Data for various aircraft structures presented by Clarkson (3)

3) Laboratory data on simple stiffened panels reported by Ballentine (4).

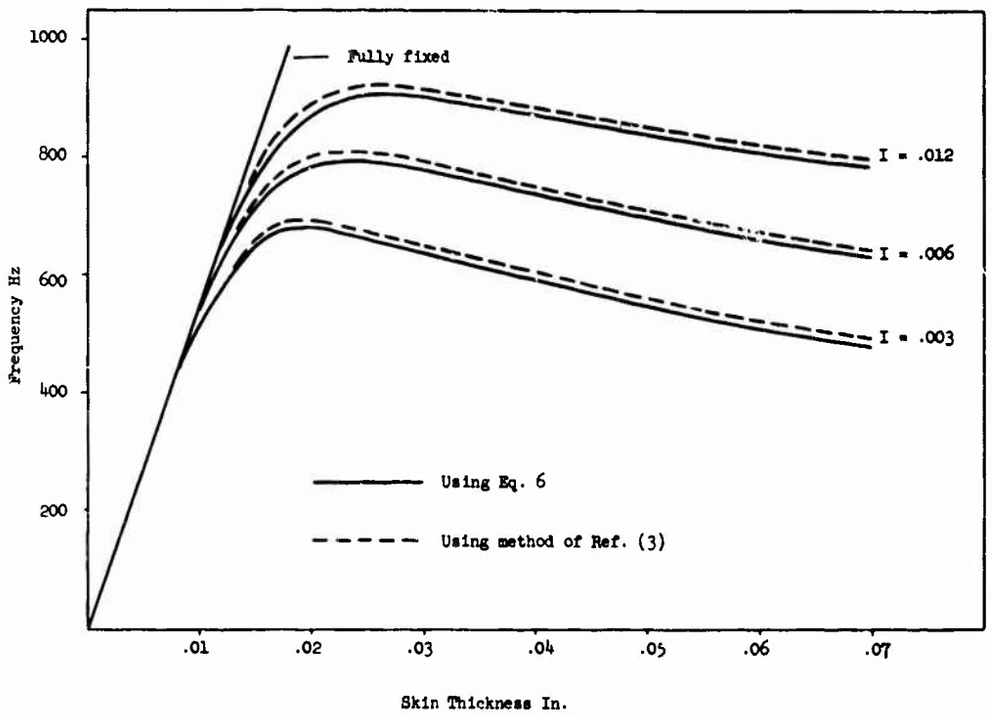


Fig. 2 Fundamental Resonant Frequency vs. Thickness for a 14" by 2" Aluminum Panel for Three Stringer Moments of Inertia

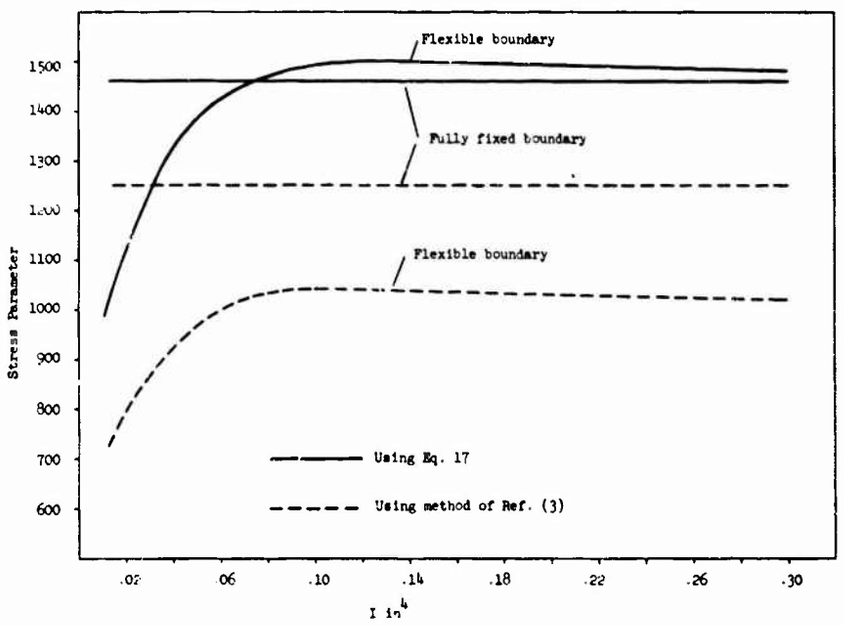


Fig. 3 Edge Stress Parameter vs. the Stringer Moment of Inertia for a 14" by 2" Aluminum Panel of .040" Thickness

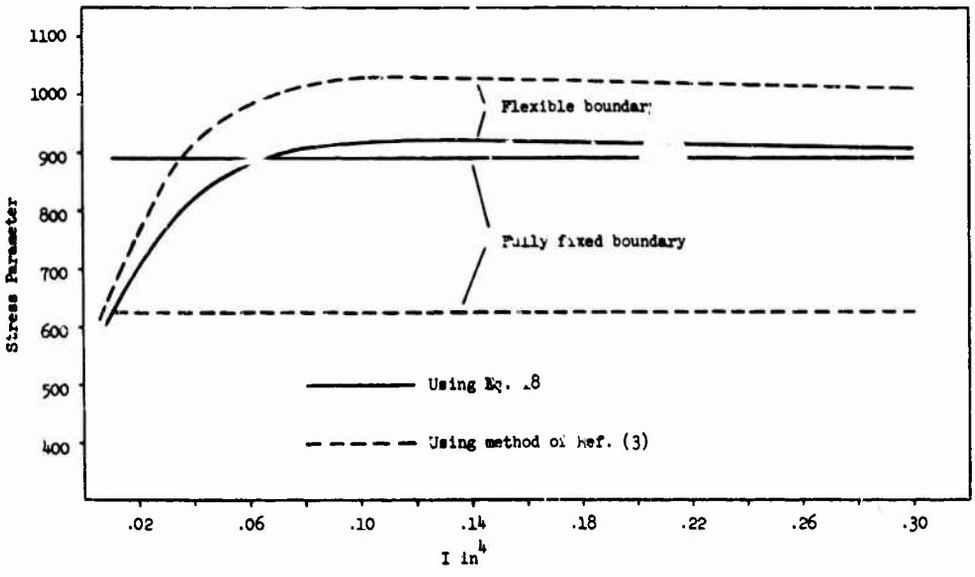


Fig. 4 Center Stress Parameter vs. the Stringer Moment of Inertia for a 14" by 2" Aluminum Panel of .040" Thickness

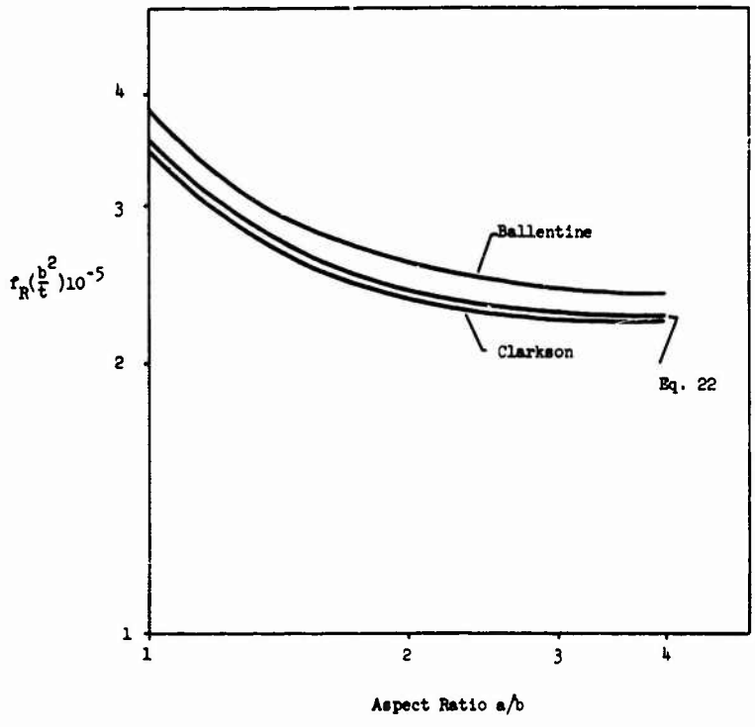


Fig. 5 Fundamental Resonant Frequency of a Fully Fixed Aluminum Plate vs. the Aspect Ratio

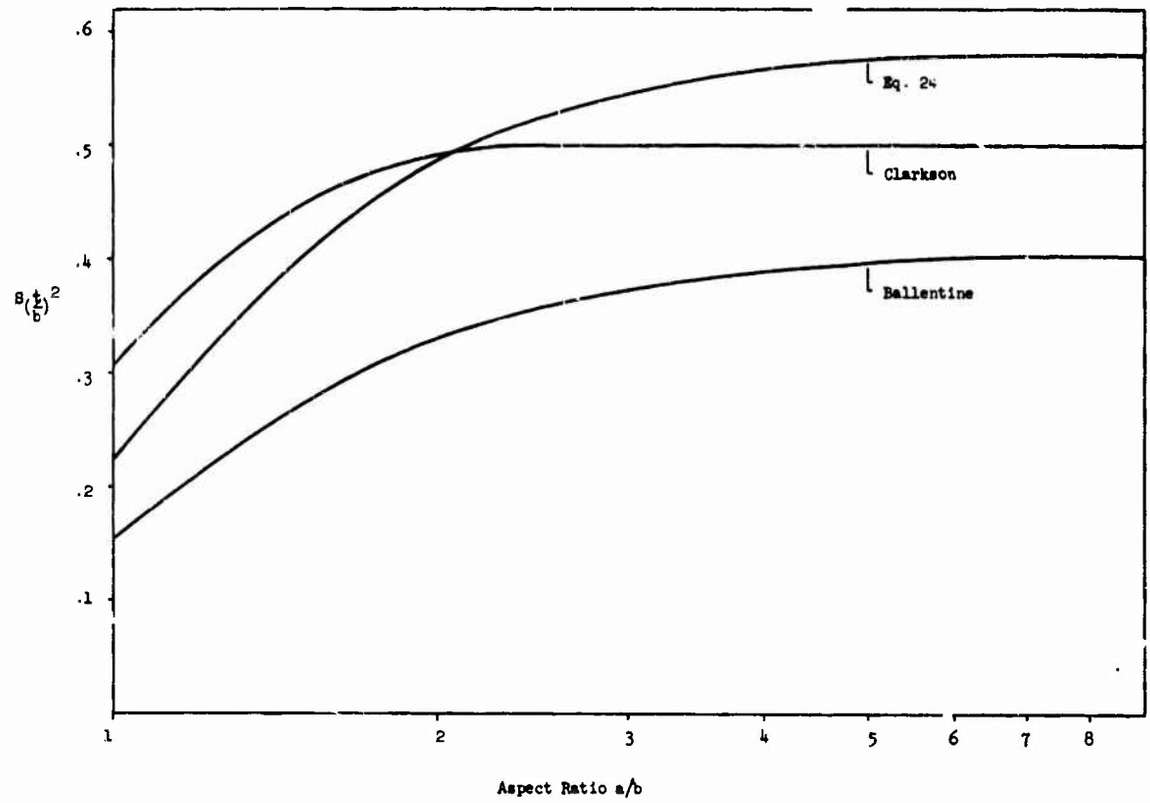


Fig. 6 Edge Stress Parameter of a Fully Fixed Aluminum Plate vs. the Aspect Ratio

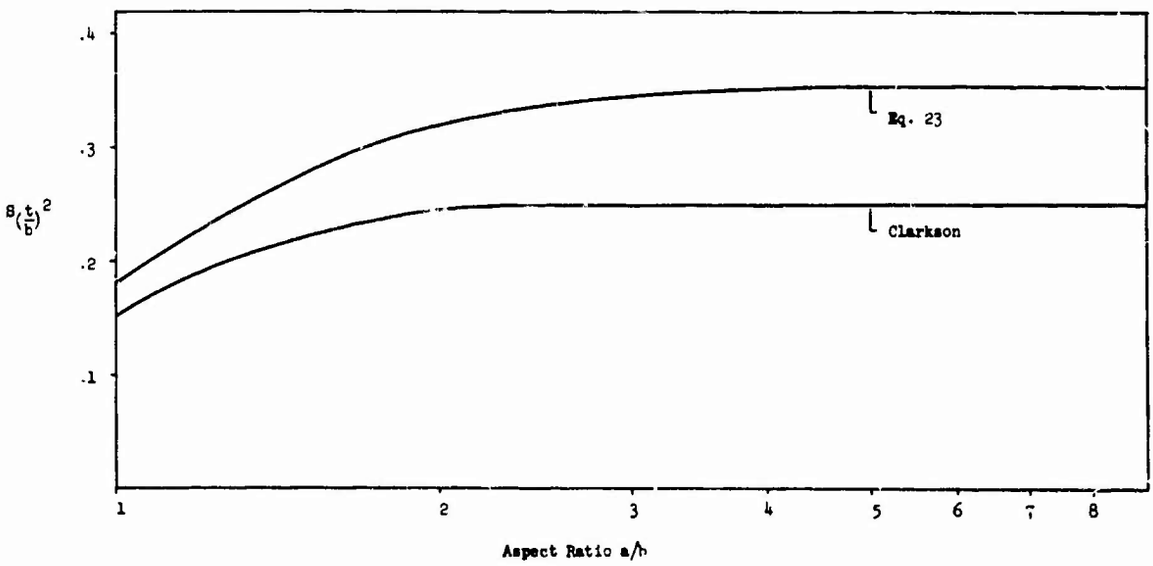


Fig. 7 Center Stress Parameter of a Fully Fixed Aluminum Plate vs. the Aspect Ratio

Fig. 8 shows a plot of the predicted vs. measured stress for all these collections. The prediction method reported herein was used to obtain the calculated values. A band showing a factor of two variation is also shown in the plot. Most of the data is seen to fall within this range.

In order to obtain further insight into the accuracy of the prediction method, a statistical analysis of the results was carried out for the data shown in Fig. 8. The mean and standard deviation of the ratios of measured to predicted stresses were determined for all three collections, and the results are presented in Table 1. In addition, probability distribution functions, based on an assumed normal density, have been plotted and are shown in Fig. 9. To use the results of this statistical analysis, a multiplier is selected based on the confidence desired The predicted results are then multiplied by this factor.

In looking at Fig. 9 it is apparent that the Grumman data showed the poorest agreement of the three. This is probably due to the fact that this collection includes specimens with flexible boundary conditions; but, the others do not. It is also apparent that the Ballentine data showed the best agreement. This is probably due to several factors:

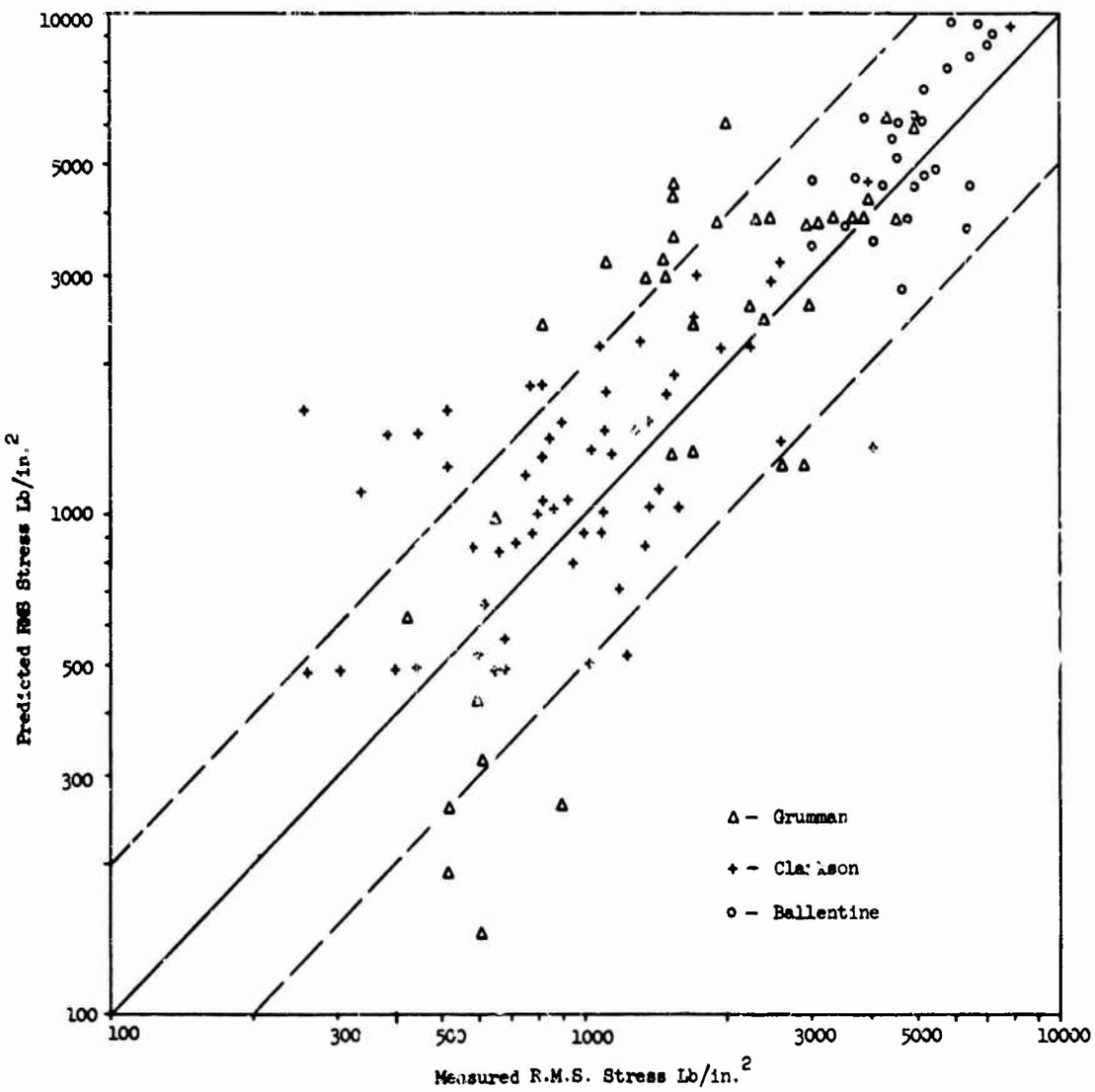


Fig. 8 Measured vs. Predicted Stress for all Three Collections of Data

TABLE 1

Mean and Standard Deviation of the Ratio of the Measured to Predicted Stress

Source of Measured Data	Sample Size	Mean	Standard Deviation	Boundary Conditions	Type Of Structure
Grumman	38	1.073	.886	Fully Fixed and Stringer Deflection	Collection of Rudder, Fuselage, Vertical Fin, Elevator, and Bonded-doubler Panels.
Clarkson (3)	59	.962	.530	Fully Fixed	Collection of Rudder, Fuselage, Elevator, and Stabilizer Panels.
Ballentine (4)	28	.923	.296	Fully Fixed	Single Skin Rib-Stringer Panels.

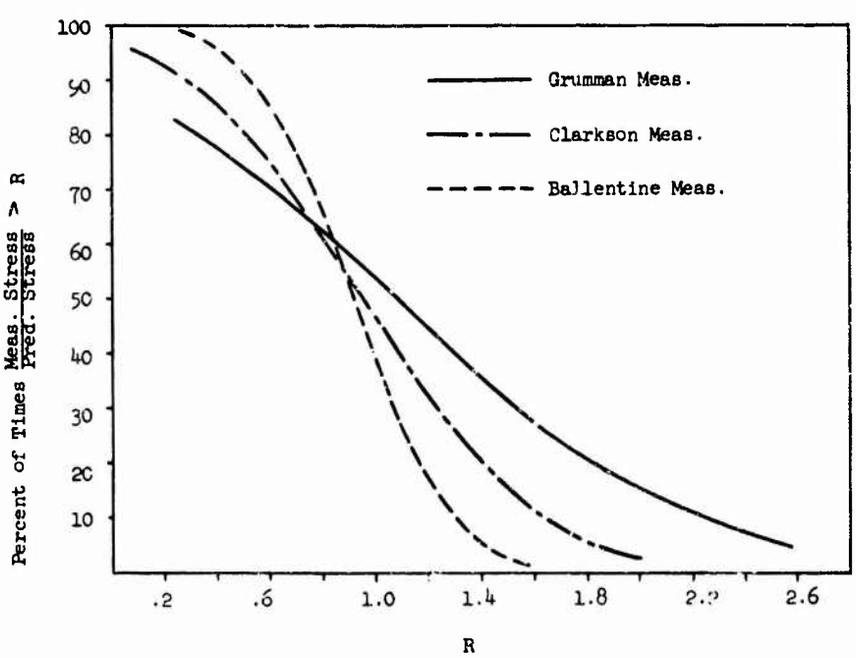


Fig. 9 Probability Distributions of the Ratio of Measured to Predicted Stress

1. Ballentine's test panels showed primarily single mode response, whereas much of the Grumman data showed multi-mode response.

2. The spectrum level was carefully controlled in Ballentine's tests, whereas the spectrum level had to be calculated from octave band measurements for other data.

3. Ballentine tested single skin rib-stringer panels; the other data consists of tests conducted on a greater variety of more complex structure.

FATIGUE LIFE PREDICTION

Life predictions were determined for four-test specimens which had experienced fatigue failures due to acoustic loading. Stresses and frequencies calculated by using the equations presented in this study, and S-N curves available in (4) were used to determine the fatigue life. The calculated and actual values are shown in Table 2. Examination of the results shows that the prediction of fatigue life is by no means accurate. At this point, the best one can hope for is that evidence of future problems can be detected in the early design phase. This would have been true in the four cases given in Table 2.

CONCLUSIONS

A technique which can provide reasonable estimates of stress and time to failure of aircraft structure excited by high intensity noise is presented. A comparison between predictions made on actual structure and test data has been used to obtain statistical information on the prediction method. This information provides the designer with some much needed data for designing safety factors into the aircraft structure without being extremely conservative.

The accuracy obtained in the stress predictions is rather surprising in view of the simplifications involved in the theory. However, to go beyond a simple analysis of this form and include some of

TABLE 2

Comparison of Predicted Fatigue Life
With Actual Values

Type Of Specimen	Predicted Resonant Freq. Hz	*Meas. Resonant Freq. Hz	Predicted R.M.S. Stress $Lb/In.^2$	Meas. R.M.S. Stress $Lb/In.^2$	Predicted Life -95% Conf. Level Hrs.	Predicted Life Mean Curve Hrs.	Actual Time To Failure Hrs.
Rudder	265	370	6110	5000	1.2	5.4	8
Rudder	353	350	3970	3200	6.3	28.4	8
Horizontal Stabilizer	399	500	3040	2900	21	94.5	12
Vertical Fin	224	-	4170	-	8.7	39.2	40

*Where multi-modal response occurred, a mean resonant frequency was estimated and used for the measured value.

the effects that were neglected (multi-mode response, non-uniform pressure field) would lead to more involved calculations. The results might also be of small benefit for design purposes.

A great deal of additional information on specimens that have undergone failure is required to check out the accuracy of fatigue life predictions. In addition, a good collection of life and stress data on identical panels tested in a similar noise environment would be helpful in establishing an ultimate goal that could be achieved by analytical procedures.

REFERENCES

1. Anderson, G. E., Et Al., Structural Design for Acoustic Fatigue, ASD-TDR-63-820, October 1963.

2. Powell, A., On the Fatigue Failure of Structures Due to Vibrations Excited by Random Pressure Fields, Journal of the Acoustical Society of America, Vol. 30, December 1958.

3. Clarkson, B. L., Stresses in Skin Panels Subjected to Random Acoustic Loading, A.F.M.L. Report TR-67-199, May 1967.

4. Ballentine, J. R., Et Al., Refinement of Sonic Fatigue Structural Design Criteria, A.F.F.D.L. Report TR-67-156, January 1968.

5. Unpublished Grumman Aircraft Engineering Corporation Test Data.

VIBRATION ANALYSIS OF COMPLEX STRUCTURAL SYSTEMS BY MODAL SUBSTITUTION

R. L. Bajan and C. C. Feng, University of Colorado
Boulder, Colorado

and

I. J. Jaszlics, Martin Marietta Corporation,
Denver, Colorado

An improved analytical method for the vibration analysis of complex structural systems is presented. The structure is divided into several subsystems, each of which is represented by its normal modes of vibration. The vibration modes of the complete system are obtained by either partial, or full modal coupling of the subsystem modes. The salient feature of the present method is that the resulting eigenvalue problem is kept relatively small by introducing the subsystem modes into the analysis in sequential groups, rather than simultaneously as is usual in conventional vibration analyses. The system modes thus obtained are convergent to the modes obtained through conventional solution of the complete eigenvalue problem. A modal error contribution algorithm is developed to optimize the sequence of introduction of the subsystem modes into the analysis. A simple example is presented which shows the rapid convergence of the method.

INTRODUCTION

Dynamic load and stability analyses of complex, flexible structures require the application of extensive mathematical models, incorporating a large number of discrete structural degrees of freedom. Present practice, especially in the aerospace industry, is to solve for the vibration modes of the structure first, and then to utilize a "modal," rather than a discrete-element mathematical simulation in the load and stability analyses. The displacements and loads then may be obtained by transformations from the modal coordinates to the discrete coordinates. The economy of this approach for undamped structures that can be represented by second-order linear differential equations is very inviting. The strongly coupled discrete system, whose inertial and stiffness properties are described in the form of large matrices, is replaced by an uncoupled system, with diagonal mass and stiffness matrices. The simplicity of the approach is retained for damped systems when the damping matrix in modal coordinates remains diagonal.

The computation of the vibration modes of an undamped structural system with n degrees of freedom requires the solution of a real eigenvalue problem of the order n. In the case of some complex structures, such as aircraft with external stores, or coupled space booster-payload systems, several hundred degrees of freedom may be necessary for adequate description of the structure. The direct solution of eigenvalue problems of this size presents considerable computational difficulty.

The current trend in computing the normal vibration modes of complex structures involves "modal coupling" of the vibration modes of conveniently defined subsystems. The subsystem modes are computed by utilizing the discrete-element analytical model available for each subsystem. The system model is then synthesized from the modal representations of several subsystems, rather than from a large number of discrete elements. When all available subsystem modes are utilized (full modal coupling), the number of degrees of freedom is not reduced in comparison with the discrete-element model. However, highly accurate system modes can be computed by utilizing only a relatively small number of modes from each subsystem, resulting in a reduced eigenvalue problem. This method (partial modal coupling) was first presented by Hunn [1, 2] for the free vibration analysis of aircraft. The method of partial modal coupling was defined in a systematic matrix presentation by Gladwell [3], and was extended to multiply

connected continuous systems by Hurty [4, 5]. Hurty [6] is also credited by the development of an error algorithm that can determine the difference between the eigenvalue of a mode obtained by partial modal coupling and the eigenvalue that would be obtained by full modal coupling.

A problem that is inherent to the partial modal coupling method lies in the selection of subsystem modes for inclusion in the system analysis. When only a few of the available modes are used, the resulting eigenvalue problem is small; however, the accuracy of the results may suffer. Using too many subsystem modes can result in the loss of computational economy that is one of the inviting features of the method. Generally, semi-empirical criteria, such as selection of subsystem modes below a specified natural frequency are employed in the attempt to optimize the formulation of the system equations.

The method of vibration analysis presented here is an extension of the partial modal coupling concept. In a manner analogous to partial model coupling, the homogeneous equations of motion are formulated by using some of the available subsystem modes. The resulting eigenvalue problem is solved for the approximate system modes. Some of these system modes, defined as the "object modes," are retained in the succeeding steps of the analysis. The approximate system modes not included in the group of object modes (the "deleted modes") are temporarily discarded. The eigenvalue error of the object modes is then defined as the difference between their computed eigenvalues and the eigenvalues of the corresponding system modes which could be obtained by full modal coupling. The objective is to "improve" the object modes until their eigenvalue errors decrease below a predetermined allowable error.

Following the initial step described above, a new group of thus far unused subsystem modes (the "replacement modes") is introduced into the system eigenvalue problem, replacing the deleted modes. The selection of the replacement modes is based on a modal eigenvalue error contribution algorithm. This algorithm determines the approximate contribution of each unused subsystem mode to the eigenvalue error of each object mode just computed. Since the eigenvalue error is caused by the absence of the unused subsystem modes, the logical candidates for inclusion in the group of replacement modes are the modes with the largest eigenvalue error contribution.

The new eigenvalue problem, defined by the object modes and the replacement modes is now solved. The computation cycle described above continues until the object modes are improved to a desired level of accuracy. At this point, a new group of object modes may be selected, or the analysis may be terminated. It must be noted that all of the available subsystem modes may be used up as replacement modes before satisfactory improvement of the object modes is achieved. In this case, groups of the previously deleted system modes may be reintroduced into the analysis. The process described above is convergent, and when the improved object modes are continually replaced by new object mode groups, it will result in all of the system modes that could have been obtained by full modal coupling. While the method thus may be used to solve the full modal coupling equations through successive small eigenvalue solutions, no economy of solution is claimed for its application in this manner. Its main applicability lies in the area of partial modal coupling, when only some of the system modes are desired. It will obtain these modes in a rapidly convergent process, to any desired degree of accuracy.

ANALYTICAL DEVELOPMENT

The system equations of motion for full modal coupling can be written in matrix notation:

$$[T]'[m][T]\{\ddot{q}\} + [T]'[k][T]\{q\} = \{0\} \qquad (1)$$

where [m] and [k] denote the discrete-element mass and stiffness matrices, respectively. The vector of discrete-coordinate displacements $\{x\}$ is related to the modal coordinates $\{q\}$ through the modal coupling transformation matrix [T]. The transformation can be partitioned as:

$$\{x\} = \left[\begin{array}{c|c} T_c & T_n \end{array}\right] \left\{\begin{array}{c} q_c \\ \hline q_n \end{array}\right\} \qquad (2)$$

In general, the sub-matrix $\left[T_n\right]$ contains all of the subsystem normal mode shape vectors, one subsystem mode in each column. The columns of the sub-matrix $\left[T_c\right]$ contain the connection transformations, which are a set of independent vectors forcing compatible displacements of the subsystems. A detailed derivation of the connection transformations and the modal coupling transformation matrix is presented in Ref. [7].

The stiffness and mass matrices formed by the triple matrix product in Equ. (1) can be partitioned in accord with Equ. (2):

$$[T]'[m][T] = [M] = \left[\begin{array}{c|c} M_{cc} & M_{cn} \\ \hline M_{nc} & M_{nn} \end{array}\right] \qquad (3)$$

and

$$[T]'[k][T] = [K] = \left[\begin{array}{c|c} K_{cc} & K_{cn} \\ \hline K_{nc} & K_{nn} \end{array}\right] \qquad (4)$$

and for energy-normalized subsystem modes,

$$K_{nn} = [\omega^2] \text{ (the diagonal of the natural frequencies squared), and} \qquad (5)$$

$$M_{nn} = [I] \text{ (the identity matrix)}$$

When the subsystem modes are defined as fixed-constraint normal modes [7],

$$\left[K_{cn}\right] = \left[K_{nc}\right] = [0] \qquad (6)$$

A special case of modal coupling is inertial coupling, where $\left[K_{cc}\right]$ is diagonal or zero and $\left[K_{cn}\right]$ and $\left[K_{nc}\right]$ are zero.

The equations of motion for partial modal coupling are similar to Equ. (1). The submatrix $\left[T_n\right]$ is further partitioned into "retained" and "unused" subsystem normal modes (indices nr and nu, respectively):

$$\left[T_n\right] = \left[T_{nr} \mid T_{nu}\right] \qquad (7)$$

The partial modal coupling transformation matrix $\left[T_o\right]$ will only include the partition $\left[T_{nr}\right]$, and the submatrix $\left[T_c\right]$. $\left[T_c\right]$ must be included in its entirety, since it contains the compatibility equations for all of the subsystems. The modally coupled system mass and stiffness matrices are formed exactly as those for full modal coupling (with the subscript o denoting partial modal coupling):

$$\left[M_o\right] = \left[T_c \mid T_{nr}\right]'[m]\left[T_c \mid T_{nr}\right] = \left[T_o\right]'[m]\left[T_o\right]$$

and (8)

$$\left[K_o\right] = \left[T_c \mid T_{nr}\right]'[k]\left[T_c \mid T_{nr}\right] = \left[T_o\right]'[k]\left[T_o\right]$$

In vibration analyses by partial modal coupling, the system equations of motion analogous to (1), but with the mass and stiffness matrices shown in (8), are solved for the mode shapes $\left[\varphi_o\right]$, and the frequencies $\left[\Omega_o\right]$. The matrix $\left[\varphi_o\right]$ is the matrix of eigenvectors for the characteristic value (eigenvalue) problem associated with the equations of motion, and the diagonal matrix $\left[\Omega^2_o\right]$ (or the diagonal matrix $\left[\Omega^{-2}_o\right]$, depending on the method of solution) is the matrix of the eigenvalues. The elements of $\left[\varphi_o\right]$ may be regarded as participation factors for the vectors in $\left[T_o\right]$ in each of the system mode shapes. The mode shapes in the discrete coordinates may be obtained by the transformation:

$$\left[X_o\right] = \left[T_o\right]\left[\varphi_o\right] \qquad (9)$$

Equations (7,8,9) are also used in the initial cycle of modal substitution analysis. The analysis, however, is not terminated after the modes $\left[X_o\right]$ are obtained. Instead, $\left[X_o\right]$ is now partitioned into the object modes (subscript $o\alpha$), and the deleted modes (subscript $o\beta$):

$$\left[X_o\right] = \left[X_{o\alpha} \mid X_{o\beta}\right] \qquad (10)$$

During subsequent cycles of the analysis, the number of object modes $\left(N_\alpha\right)$ will remain constant. The number of deleted modes $\left(N_\beta\right)$, and the number of degrees of freedom in the modally coupled system model $\left(N = N_\alpha + N_\beta\right)$ may vary from cycle to cycle, or they may stay constant.

Following the partitioning of $\left[X_o\right]$, the modes $\left[X_{o\beta}\right]$ are replaced by a new group of subsystem modes $\left[T_{nr1}\right]$, selected from the unused subsystem modes $\left[T_{nu}\right]$. The remaining, still unused columns of $\left[T_{nu}\right]$ are denoted as $\left[T_{nu1}\right]$. The new modal coupling transformation matrix is assembled for the next computational cycle:

$$[T_1] = \left[X_{o\alpha} \mid T_{nr1}\right] \qquad (11)$$

The modally coupled system mass and stiffness matrices $[M_1]$ and $[K_1]$ are formed in a manner analogous to Equations (8). Since the vectors in $\left[X_{o\alpha}\right]$ are orthogonal with respect to the discrete-coordinate mass and stiffness matrices, $[M_1]$ and $[K_1]$ will take the following form:

$$[M_1] = \left[X_{o\alpha} \mid T_{nr1}\right]'[m]\left[X_{o\alpha} \mid T_{nr1}\right] = \left[\begin{array}{c|c} I & M_{\alpha n1} \\ \hline M_{n\alpha 1} & I \end{array}\right]$$

and (12)

$$[K_1] = \left[X_{o\alpha} \mid T_{nr1}\right]'[k]\left[X_{o\alpha} \mid T_{nr1}\right] = \left[\begin{array}{c|c} \Omega^2_{o\alpha} & K_{\alpha n1} \\ \hline K_{n\alpha 1} & \omega^2_{nr1} \end{array}\right]$$

where it has been assumed that the modes $\left[X_o\right]$ are energy-normalized. For fixed-constraint subsystem modes the partition $\left[K_{\alpha n1}\right]$, and its transpose $\left[K_{n\alpha 1}\right]$ become null matrices, thus, in all subsequent steps of modal substitution the coupling remains purely inertial. The symbol $\Omega_{o\alpha}$ denotes the natural frequencies of the system modes $\left[X_{o\alpha}\right]$, and ω_{nr1} denotes the natural frequencies of the subsystem modes $\left[T_{nr1}\right]$. The solution of the eigenvalue problem resulting from the system equations of motion written for the mass matrix $[M_1]$ and stiffness matrix $[K_1]$ will result in the "modal" mode shapes $[\varphi_1]$, which may be transformed into the discrete-coordinate mode shapes $[X_1]$ through the transformation matrix $[T_1]$. $[X_1]$ is then partitioned into the retained modes $[X_{1\alpha}]$ and the deleted modes $[X_{1\beta}]$. The next cycle of modal substitution is initiated by the introduction of the subsystem modes $\left[T_{nr_2}\right]$ from the unused modes $\left[T_{nu1}\right]$ into the modal coupling transformation matrix $[T_2]$. This process continues until the eigenvalue error of the object modes $\left[X_{i\alpha}\right]$ becomes less than the predetermined allowable eigenvalue error. The replacement

modes introduced into the modal coupling transformation matrix $[T_i]$ do not necessarily have to belong to the set of unused modes $[T_{nu(i-1)}]$. Instead, some of the previously deleted system modes $[X_\beta]$ may be re-introduced as replacement modes. Indeed, when all of the unused subsystem modes $[T_{nu}]$ have been introduced into the analysis, the substitution cycles must continue with reintroduction of the modes $[X_\beta]$. The stiffness and mass matrices resulting from the reintroduction of the modes $[X_\beta]$ are similar to those shown in Equ. (12). The lower right-hand partitions, however, may contain off-diagonal elements, as only those vectors of $[X_\beta]$ computed in the same substitution cycle are orthorgonal through the mass and stiffness matrices. The decision as to which modes to introduce into the next cycle as replacement modes can be automatized through a modal selection algorithm. This algorithm is a logical extension of the computation of the approximate eigenvalue error for the object modes.

ERROR ANALYSIS AND MODAL SELECTION ALGORITHM

The homogeneous equations of motion for full modal coupling can be partitioned in the following form, when written for a single system mode:

$$\left[\begin{array}{c|c} K_i & K_{iu} \\ \hline K_{ui} & K_u \end{array}\right]\left\{\begin{array}{c} \varphi_r \\ \hline \varphi_u \end{array}\right\}_j = \Omega_j^2 \left[\begin{array}{c|c} M_i & M_{iu} \\ \hline M_{ui} & M_u \end{array}\right]\left\{\begin{array}{c} \varphi_r \\ \hline \varphi_u \end{array}\right\}_j \qquad (13)$$

In Equ. (13), $[K_i]$ and $[M_i]$ denote the stiffness and mass matrices respectively, for partial modal coupling in modal substitution cycle i. The remaining partitions correspond to the unused modes, and their coupling terms with the retained modes. Ω_j^2 is the exact eigenvalue that can be obtained from solving the complete system equations, and $\{\varphi_r\}_j$ and $\{\varphi_u\}$ are partitions of the exact energy-normalized eigenvector, for system mode j.

An equation analogous to (13) can be written for partial model coupling in modal substitution cycle i:

$$[K_i]\{\varphi_i\}_j = \Omega_{ij}^2 [M_i]\{\varphi_i\}_j \qquad (14)$$

where Ω_{ij}^2 is an approximate system eigenvalue for mode j, and $\{\varphi_i\}_j$ is an approximate system eigenvector, corresponding to $\{\varphi_r\}_j$ in the exact system mode. Ω_{ij}^2 and $\{\varphi_i\}_j$ are solutions of the partial system eigenvalue problem resulting from the equation of motion in cycle i.

The eigenvalue error $\delta\Omega_j^2$ for the mode j is now defined:

$$\delta\Omega_j^2 = \Omega_j^2 - \Omega_j^2 \qquad (15)$$

In order to compute $\delta\Omega_j^2$ for the modes resulting from partial modal coupling, the vector $\{\varphi_u\}_j$ is expressed as a function of $\{\varphi_r\}_j$, making use of the lower partitions of Equ. (13):

$$\{\varphi_u\}_j = \left[[K_u] - \Omega_j^2 [M_u]\right]^{-1}\left[\Omega_j^2 [M_{ui}] - [K_{ui}]\right]\{\varphi_r\}_j \qquad (16)$$

The upper partitions of (13), then can be arranged in the form:

$$[K_i]\{\varphi_r\}_j = \Omega_j^2\left[[M_i] + [N_i]_j\right]\{\varphi_r\}_j \qquad (17)$$

where the incremental mass matrix $[N_i]_j$ is defined as:

$$[N_i]_j = \frac{1}{\Omega_j^2}\left[\Omega_{ij}^2[M_{iu}] - [K_{iu}]\right]\left[[K_u] - \Omega_j^2 [M_u]\right]^{-1}\left[\Omega_j^2 [M_{ui}] - [K_{ui}]\right] \qquad (18)$$

Equation (16) is now premultiplied by the transpose of $\{\varphi_i\}_j$, and rearranged:

$$L\varphi_i'J_j\left[[K_i] - \Omega_{ij}^2 [M_i]\right]\left\{\{\varphi_i\}_j - \{\varphi_r\}_j\right\} = \delta\Omega_j^2 L\varphi_i'J_j [M_i]\{\varphi_r\}_j - \Omega_j^2 L\varphi_i'J_j [N_i]_j \{\varphi_r\}_j \qquad (19)$$

Equation (14) indicates that the left side of (19) is identically zero. The error vector $\{f_r\}_j$ is now defined:

$$\{f_r\}_j = \{\varphi_i\}_j - \{\varphi_r\}_j \qquad (20)$$

and noting that $\{\varphi_i\}_j$ is an energy-normalized mode shape vector, the eigenvalue error is expressed from Equ. (19):

$$\delta\Omega_j^2 = \Omega_j^2 \frac{L\varphi_i'J_j [N_i]_j \{\varphi_i\}_j - L\varphi_i'J_j [N_i]_j \{f_r\}_j}{1 - L\varphi_i'J_j [N_i]_j \{f_r\}_j} \qquad (21)$$

Equation (21) is an exact expression for the eigenvalue error. It assumes that the error vector $\{f_r\}_j$ is known. For further derivation of the approximate error expression, the following initial assumptions are made:

$$\delta\Omega_j^2 \ll \Omega_j^2 \qquad (22a)$$

$$\left|\{f_r\}_j\right| \ll \left|\{\varphi_i\}_j\right| \qquad (22b)$$

and, as logical extensions uf (22b):

$$\left[\varphi_i'\right]_j \left[N_i\right]_j \left\{f_r\right\}_j \ll \left[\varphi_i'\right]_j \left[N_i\right] \left\{\varphi_i\right\}_j \qquad (22c)$$

and

$$\left[\varphi_i'\right]_j \left[N_i\right]_j \left\{f_r\right\}_j \ll 1 \qquad (22d)$$

Equation (17) is also replaced by an approximate expression. Since the unused modes are either approximately or completely orthogonal through the discrete-coordinate mass and stiffness matrices,

$$\left[\bar{N}_i\right]_j \approx \left[\left[M_{iu}\right] - \frac{1}{\Omega_j^2}\left[K_{iu}\right]\right]\left[\frac{\Omega_j^2}{\omega_u^2 - \Omega_j^2}\right]\left[\left[M_{ui}\right] - \frac{1}{\Omega_j^2}\left[K_{ui}\right]\right] \qquad (23)$$

where the notation ω_u is used to denote the natural frequencies of the unused modes. Equation (23) is the exact expression for $\left[N_i\right]_j$ in the initial modal substitution cycle, when all of the unused modes are subsystem normal modes.

Using the assumptions of Equations (22), and replacing $\left[N_i\right]_j$ by $\left[\bar{N}_i\right]_j$ in Equ. (21), the approximate relative error measure is obtained:

$$e_j = \left[\varphi_i'\right]_j \left[\left[M_{iu}\right] - \frac{1}{\Omega_{ij}^2}\left[K_{iu}\right]\right]\left[\frac{\Omega_{ij}^2}{\omega_u^2 - \Omega_{ij}^2}\right]\left[\left[M_{ui}\right] - \frac{1}{\Omega_{ij}^2}\left[K_{ui}\right]\right]\left\{\varphi_i\right\}_j \qquad (24)$$

and the relative eigenvalue error is

$$S_j = \frac{e_j}{1+2e_j} \approx \frac{\delta\Omega_j^2}{\Omega_j^2} \qquad (25)$$

Equation (24) is further simplified when the subsystem normal modes are fixed-constraint modes, in which case $\left[K_{iu}\right]$ and $\left[K_{ui}\right]$ are zero.

In order to determine the contribution of the individual unused modes to the relative error, e_j is decomposed into components e_{jk} associated with each of the unused modes:

$$e_j = \sum_{k=1}^{k=u} e_{jk} = \sum_{k=1}^{k=u} \left[\varphi_i'\right]_j \left[U\right]' \left\{T_u\right\}_k \left(\frac{\Omega_{ij}^2}{\omega_{uk}^2 - \Omega_{ij}^2}\right) \left[T_u'\right]_k \left[U\right] \left\{\varphi_i\right\}_j \qquad (26)$$

The following notation is introduced in Equ. (26):

u = number of unused modes

$$\left[U\right] = \left[\left[m\right] - \frac{1}{\Omega_{ij}^2}\left[k\right]\right]\left[T_r\right]$$

$\left\{T_u\right\}_k$ = mode shape of the k-th unused mode

$\left[T_r\right]$ = matrix of mode shapes included in the partial modal coupling

ω_{uk} = natural frequency of the k-th unused mode

For small values of the eigenvalue error, e_j is nearly equal to the approximate error S_j (25). Thus, e_{jk} is an approximation of the eigenvalue error in the j-th system mode, due to omission of the k-th unused mode. [E] is now defined as the matrix of the coefficients e_{ij} for the object modes. The introduction sequence of the unused modes may be optimized then in the following manner: let $\{W\}$ be a weighting vector of N_α elements proportional to the relative importance of the N_α object modes. The introduction preference vector $\{P\}$ is defined as:

$$\{P\} = [E]' \{W\} \qquad (27)$$

Each element in $\{P\}$ corresponds to one unused mode awaiting introduction into the problem in the next modal coupling cycle. The magnitude of the elements in $\{P\}$ is a measure of significance of the corresponding mode for improviding the object modes. Thus, if the number of replacement modes is N_β, the N_β modes with the largest corresponding elements in $\{P\}$ are selected for introduction.

NUMERICAL EXAMPLE

Application of the method is illustrated for a simply connected 11-degree of freedom system, subdivided into three subsystems (Figure 1). The eigenvalue solution was limited to five degrees of freedom, and the lowest three system modes were selected as object modes. The value of $k/m = 100/sec^2$ was assumed for the discrete parameters shown in Figure 1. The nine subsystem modes have the eigenvalues shown in Table 1. In addition, to the nine subsystem modes there are two connection vectors corresponding to displacement between Subsystems 1 and 2 (x_{12} and x_{21}), and displacement between Subsystems 2 and 3 (x_{23} and x_{32}).

Table 1.

Subsystem Normal Mode Eigenvalues

Mode	Subsystem 1	Subsystem 2	Subsystem 3
1	3.675	71.15	20.83
2	65.57	128.9	100.00
3	111.7	--	179.2
4	185.7	--	--

The initial modal coupling analysis was performed by solving a 5-degree of freedom eigenvalue problem. The 5 degrees of freedom included the two connection vectors and the first two

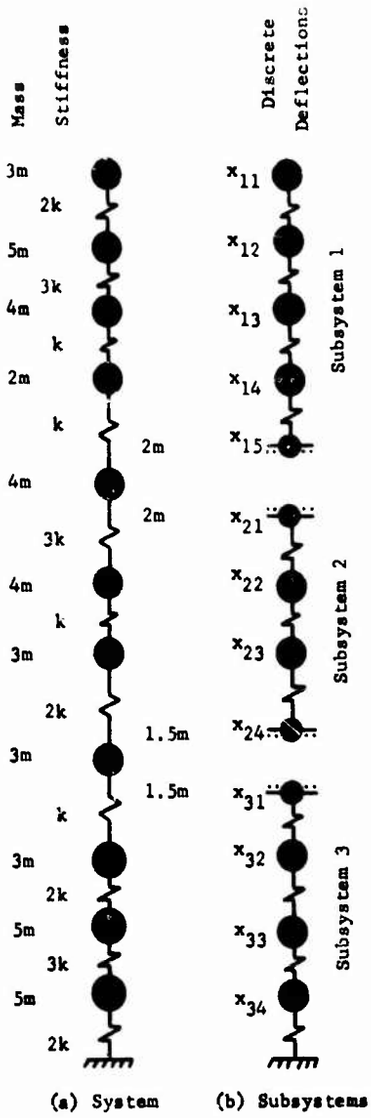


Fig. 1 Simply Connected 11-Degree of Freedom System

modes of Subsystem 1 and the first mode of Subsystem 3. Subsequently, three additional modal substitution cycles were performed, in which all of the subsystem modes were introduced. The exact system eigenvalues for the object modes, and the eigenvalues obtained by modal substitution are shown in Table 2 for each computation cycle.

Table 2.

Eigenvalues for the Object Modes

Mode	Exact	Modal Substitution			
		Cycle 0	Cycle 1	Cycle 2	Cycle 3
1	0.8399	0.8414	0.8399	0.8399	0.8399
2	7.238	7.438	7.242	7.239	7.238
3	17.85	18.38	18.02	17.99	17.85

The percent of error in the object mode frequencies is plotted vs. the modal substitution cycle number in Figure 2.

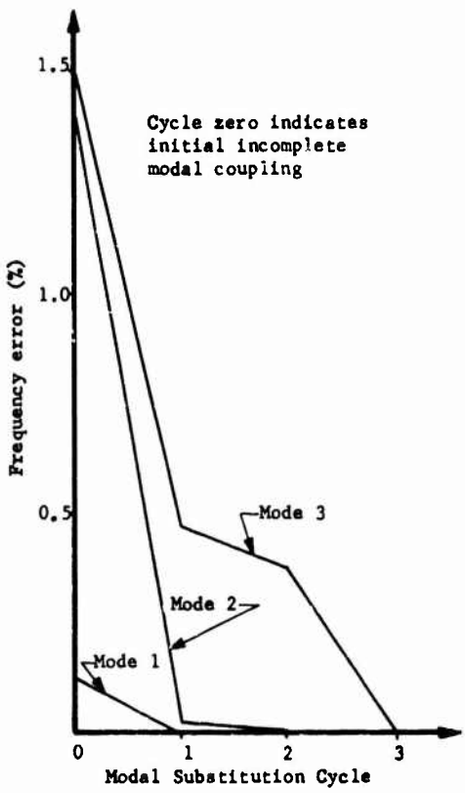


Fig. 2 Frequency Error History

CONCLUSIONS

The modal substitution method has been shown to be applicable to the vibration analysis of complex systems. No advantage of the method is claimed for analysis of systems that can be represented by relatively simple mathematical models. Frequently, however, mathematical models using several hundred degrees of freedom are required. While the equations of motion for dynamic response analysis of such systems may be limited to a relatively small number of degrees of freedom describing overall system motion in modal coordinates, the mode shapes must represent the accurate local deformations. It is in problems of this nature that partial modal coupling, and modal substitution in particular, presents an optimum method for vibration analysis.

Use of the modal substitution method to analyze a system with several hundred degrees of freedom may typically result in 50 object modes with four- or five-digit accuracy in three or four cycles, solving a 100 x 100 or smaller eigenvalue problem each time. From the view point of a dynamic analysis employing 50 system modes, the results obtained are equivalent to full modal coupling, while using only a small fraction of the fully coupled solution time.

An interesting aspect of modal substitution is that very small eigenvalue solutions in the modal substitution cycles may be used to solve very large eigenvalue problems. Ultimately, when limited to successive 2 x 2 eigenvalue solutions, the method becomes analogous to Jacobi's method for eigenvalue solutions of symmetric matrices. Thus, while not discussed in the present paper, proof of convergence of the modal substitution method can be reduced to proof of the Jacobi method [8].

Modal substitution, until the present time, has been tried only on an experimental basis for relatively small systems (less than 100 degrees of freedom). Convergence to four or five digits in the object mode eigenvalues has been achieved consistently within two to five cycles, independently of problem size.

The method may be regarded as a general method for solving large eigenvalue problems. It is not fundamentally dependent on the use of subsystem normal modes, but rather, other displacement functions, such as columns of the flexibility influence matrix, etc. may be used. The natural future extension of the development presented here is in the exploration of more general applications of the principle of sequential iterative substitution of assumed modes.

REFERENCES

1. Hunn, B. A., "A Method of Calculating the Space Free Resonant Modes of an Aircraft", J. R. Aero. Soc., Vol. 57, June, 1953, pp. 420-422.

2. Hunn, B. A., "A Method of Calculating the Normal Modes of an Aircraft", Quart. J. Mech., Vol 8, Pt. 1, 1955, pp. 38-58.

3. Gladwell, G. M. L., "Branch Mode Analysis of Vibrating Systems", J. Sound Vib., I, 1964, pp. 41-59.

4. Hurty, W. C., "Vibrations of Structural Systems by Component Mode Synthesis", Proc. Amer. Soc. Civ. Engrs., Vol. 86, No. EM4, August, 1960, pp. 51-69.

5. Hurty, W. C., Dynamic Analysis of Structural Systems by Component Mode Synthesis, Technical Report 32-350. Jet Propulsion Laboratory, Pasadena, Calif., Jan. 15, 1964.

6. Hurty, W. C., A Criterion For Selecting Realistic Natural Modes of a Structure, Technical Memorandum 33-364. Jet Propulsion Laboratory, Pasadena, Calif., Nov., 1967.

7. Bajan, R., and Feng, C. C., "Free Vibration Analysis by the Modal Substitution Method", AAS Symposium, Space Projections from the Rocky Mountain Region, Denver, Colorado, July 1968.

8. Kogbetliantz, E. G., "Solution of Linear Equations by Diagonalization of Coefficient Matrices", Quarterly of Applied Mathematics, Vol. 13, No. 2, 1955, pp. 123-132.

THE APPLICATION OF THE KENNEDY-PANCU METHOD TO EXPERIMENTAL VIBRATION STUDIES OF COMPLEX SHELL STRUCTURES

John D. Ray,† Charles W. Bert, and Davis M. Egle
School of Aerospace and Mechanical Engineering
University of Oklahoma
Norman, Oklahoma

The theoretical basis for the Kennedy-Pancu (K-P) technique is outlined briefly. This vibration data analysis technique, which uses both amplitude and phase data, is much more reliable than the usual amplitude method in separating nearly equal natural frequencies and extraneous modes from the pure resonant mode. Application of the K-P technique to two different kinds of shell structures is described. This is believed to be the first reported use of the technique for shell structures.

The first example is a cylindrical shell with a small number of longitudinal stiffeners. The physical quantity used here for the K-P plot was the output of an electromagnetic velocity pickup. The second example is a truncated conical shell of sandwich construction, with glass-fiber reinforced plastic facings and an aluminum hexagonal honeycomb core. In this example, the quantity used in the K-P plot was the output of a metallic foil strain gage. Here the use of the K-P technique resulted in the discovery of a vibrational mode unidentified in previous research on free-free truncated conical shells.

INTRODUCTION

The Kennedy-Pancu (K-P) vibration data analysis technique was introduced in 1947 (Ref. [1]) in connection with ground vibration tests on aircraft. Subsequently, Bishop and his associates (Ref. [2-6]) studied this technique (along with several others) in detail both analytically and experimentally. The application of the technique has been limited to beam-type structures and aircraft ground and in-flight vibration testing. Although the technique is well suited for shell-type structures because of their numerous nearly equal frequencies, to the authors' knowledge, there have been no successful applications to shell vibration.

The Kennedy-Pancu method requires the measurement of both the amplitude and phase of the response of the structure relative to the excitation. These measurements are taken at several closely incremented frequencies. Because of the rapid change in phase with respect to frequency, this measurement is difficult to make with sufficient accuracy. In the present work, this was overcome by using highly accurate digital phase and frequency meters. In addition, the phase was used as the controlled parameter (instead of frequency) to allow rapid data collection and a more uniform distribution of points in the K-P plot.

The main limitation in using the technique in vibration testing is the accuracy to which the phase, amplitude, and frequency may be measured. Even with accurate digital instrumentation, the accuracy is limited because of noise and distortion in the response and excitation signals. For amplitude and frequency measurement, these effects may be minimized by filtering the signals. However, because the phase shift in an electronic filter is usually present over a much wider range of frequencies than the amplitude attenuation, the use of filters in phase-measuring circuits has more disadvantages than advantages and is generally not

*The work reported here was sponsored in part by the U. S. Army Aviation Materiel Laboratories, Fort Eustis, Virginia, monitored by Mr. J. P. Waller, and in part by the National Science Foundation under research grant GK-1490.

†Presently associated with Memphis State University, Memphis, Tennessee.

a satisfactory solution to the noise problem. This limits use of the method to cases in which the signal-to-noise ratio is high relative to that which would yield acceptable results for peak-amplitude measurement.

Harmonic distortion in the signals is another source of error which may be minimized by filtering in amplitude and frequency measurements but not in phase measurements. However, because the phase meter used in this research utilized only the zero crossing points for phase information, a reasonable amount of harmonic distortion could be tolerated. Nonetheless, this type of distortion was minimized in the present tests by maintaining a constant response by varying the excitation level. Holding the output constant established the same peak response of the shell throughout the frequency range and thus minimized the effect of nonlinearities, whether they be geometric (large deflections) or material (nonlinear stress-strain and nonlinear damping).

REVIEW OF THE KENNEDY-PANCU METHOD

In applying their technique to a multi-degree-of-freedom system (as applicable to this case), Kennedy and Pancu made the assumption that each mode acts independently of the others, i.e. each mode responds to the applied force like a single-degree-of-freedom system. Also they assumed that the system is linear and that superposition of modes holds. In other words, they assumed the existence of normal modes, which is a widely accepted assumption in multi-degree-of-freedom vibrational analysis.

The response of a single-degree-of-freedom linear system, with Kimball-Lowell-type material damping and excited by a simple harmonic force of amplitude F and frequency ω, can be expressed as follows:

$$X = [(k - m\omega^2)^2 + b^2]^{-1/2} \qquad (1)$$

$$\tan \phi = b/(k - m\omega^2) \qquad (2)$$

where

$X = X_o/F$

$X_o = x/\sin(\omega t - \phi)$

x = displacement

ϕ = phase relation between the displacement and forcing function

b = material damping factor*

k = spring rate

m = mass

If a complex-plane plot is made of the complex receptance, α, given by:

$$\alpha = Xe^{i\phi} \qquad (3)$$

with the mass, damping factor, and spring rate fixed and the frequency varied, the result is as shown in Fig. 1.

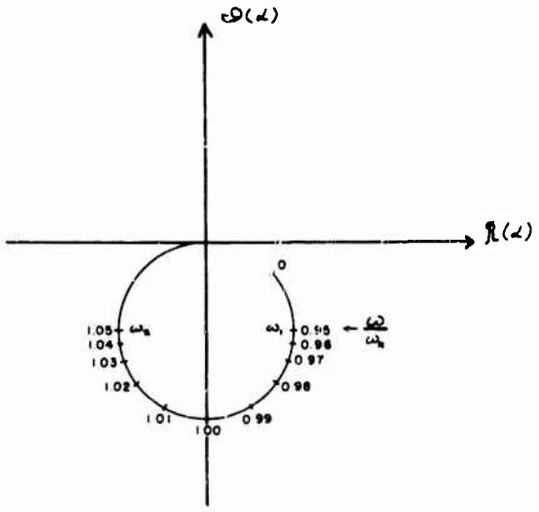


Fig. 1 - Kennedy-Pancu plot for single-degree-of-freedom system

The complex receptance traces out almost a complete circle on the complex plane. Kennedy and Pancu noted the following three observations about the graph:

(1) At resonance ($\omega^2 = k/m$), the displacement vector lies on the imaginary axis and hence, is 90 deg. out of phase with the applied force,

(2) The change in arc length(s) along the curve per unit change in frequency ($ds/d\omega$) is a maximum at resonance, and

(3) The diameter of the circle is inversely proportional to the damping factor.

The procedure for obtaining the damping factor from the Argand plot can be simplified by eliminating the necessity of making absolute calibrations of the excitation and response transducers. This is accomplished by expressing the damping coefficient in terms of frequency as follows:

$$\delta = (\omega_1 - \omega_2)/\omega_n \qquad (4)$$

*The material damping factor is not to be confused with the viscous damping coefficient, which is equal to b/ω.

where $\delta = b/k$ is a dimensionless damping factor, and ω_1 and ω_2 are the frequencies at the half-power points on the response curve. Further assuming that the response curve is symmetrical about the resonant frequency, ω_n, then Eq. (4) becomes:

$$\delta = 2 [1 - (\omega_1/\omega_n)] \qquad (5)$$

The half-power-point frequency can be determined readily from the Argand plots by drawing a line parallel to the real axis through the center of the circle; the point of intersection of this line with the circle is the half-power-point frequency, ω_1. Application of these values to Eq. (5) gives the value of the uncoupled damping coefficient for the system.

For a multiple-degree-of-freedom system, the complex receptance will consist of a number of terms, each of which has the form of Eq. (3). A typical Kennedy-Pancu plot for a two-degree-of-freedom system is shown in Fig. 2.

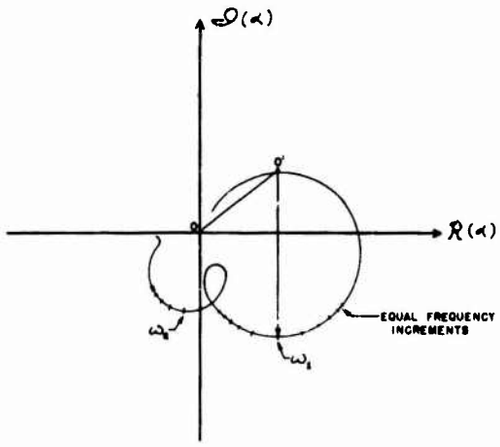


Fig. 2 - Kennedy-Pancu plot for two-degree-of-freedom system

It is evident that there are two natural frequencies because of the presence of two circular arcs and because the change in arc length per unit change in frequency has two maxima. The characteristics of this plot are strongly dependent on the closeness of the two frequencies and the location of the excitation force and the response pickup. Several Kennedy-Pancu plots for systems with two and three degrees of freedom may be found in Refs. [1-6].

In analyzing the Kennedy-Pancu plot, the resonant frequencies are determined by the maximum of the change in arc length per unit frequency change. Circles are then fitted to the points in the neighborhood of these resonant frequencies. The vector O'C represents the resonant component of the receptance and OO' is the off-resonant component. The damping factor may be calculated with Eqs. (4) or (5).

APPLICATION TO A STRINGER STIFFENED CYLINDRICAL SHELL

Specimen. The Kennedy-Pancu technique was used to assist in analyzing the vibration data on a thin cylindrical shell stiffened with two unequally spaced longitudinal stiffeners. The shell and stiffener geometry are indicated in Fig. 3. The shell is supported on both ends by

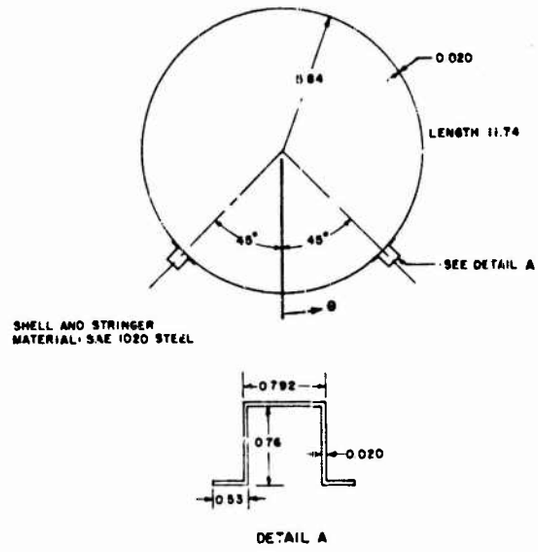


Fig. 3 - Geometry of stringer stiffened shell. All dimensions in inches except as noted

internal discs with a knife edge contacting the shell. The radius of the knife edge support was adjusted to permit longitudinal motion of the shell but restrict motion normal to the shell surface. This simulates the ideal freely supported end condition (i.e. simply supported without axial constraint).

Instrumentation. A schematic diagram of the instrumentation is shown in Fig. 4. Both the exciter and the response pickup were small electromagnets with a permanent magnet for bias. When the device is subjected to a simple harmonic current, the force exerted on the steel shell is of the same frequency as the current but the waveform contains some second and third harmonic distortion. When the device is placed close to a vibrating steel surface, the voltage produced is proportional to surface velocity for small displacements. Thus, in this appli-

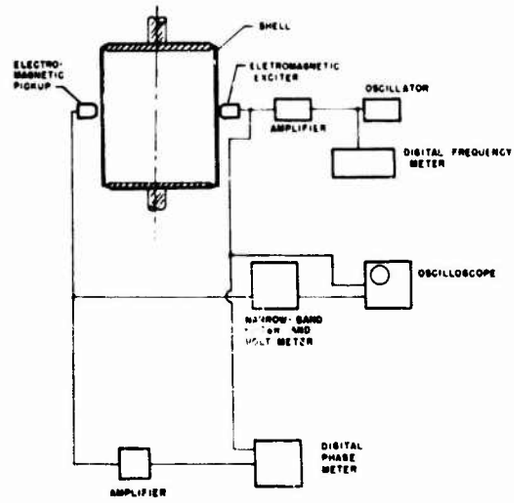


Fig. 4 - Instrumentation for stringer stiffened shell vibration experiments

cation, the Kennedy-Pancu plots are graphs of the complex impedance instead of receptance. The only detail which this affects is that, at resonance, the phase of the impedance vector relative to the force is either 0 or 180 deg. instead of 90 or 270 deg. Other than this, there is no difference in the application of this technique.

Experimental Procedure. In determining the natural frequencies, the test procedure involved choosing the exciter or pickup locations and locating several resonances by the peak amplitude method. A Kennedy-Pancu plot was then constructed for a range of frequencies including those that were detectable by peak amplitude. The natural frequencies were determined from the K-P plot as described earlier in this paper. At this stage, the exciter and/or the pickup location is changed slightly, and a new K-P plot is drawn. If this process is repeated several times, moving the exciter and the pickup each time, the chances of missing a vibration mode are greatly reduced. It should be noted that moving the exciter location is an essential part of the procedure.

The amplitude, phase and frequency data were collected by varying the phase in 10-deg. increments (or 5-deg. increments in regions of high frequency change per unit phase change). This was found to be much easier and faster to do than changing the frequency in equal increments. In regions near a resonance, the phase changes quite rapidly with frequency, thus requiring precise control on the frequency. Actually, in this application, the period, rather than the frequency, was measured. This was desirable because of the increased accuracy in the period for the frequency range and the type of instrument used.

Results. A plot of the natural frequencies of the stiffened cylinder for the lowest axial mode (m = 1) and several circumferential modes is shown in Fig.5. The Kennedy-Pancu technique

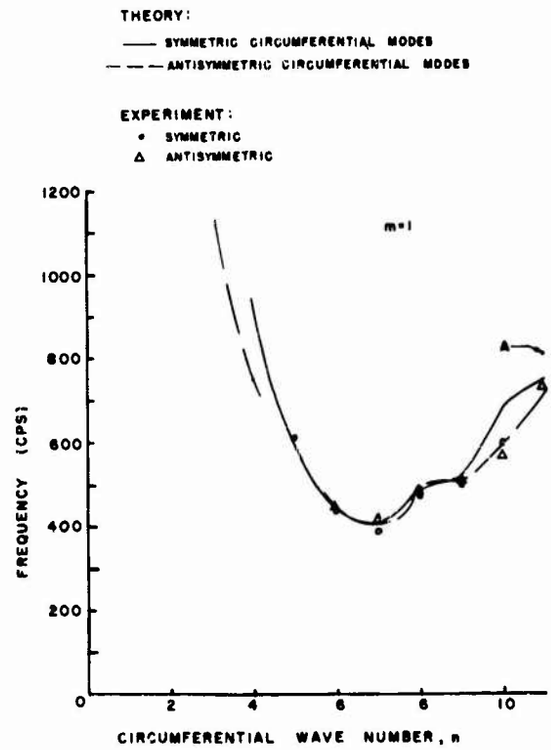


Fig. 5 - Frequency versus circumferential wave number for the stringer stiffened shell

is especially suited to this type of structure because the frequency density is up to twice as high as that of an axisymmetric shell structure. The reason for this, as was noted in Ref. [7], is that the frequencies associated with the symmetric and antisymmetric circumferential modes are usually different for the nonaxisymmetric structure, whereas they are equal for the axisymmetric shell. The theoretical frequencies shown in Fig. 5 were calculated with the analysis of Ref. [7]. It is noted that the theory does not predict an antisymmetric frequency for n = 5 and there are two antisymmetric frequencies for n = 11. The higher of these two frequencies is denoted by the point A in the figure.

With the exception of the symmetric mode frequency at n = 10, the agreement between the theoretical and experimental results is very good. The one discrepancy is possibly due to misidentification of the n value, since these modes are very irregular and difficult to identify. Although one would expect the lowest natural frequency to be associated with a mode that is easily excited, considerable difficulty was encountered in this application. The symmetric mode at 384 cps was undetectable in several peak-amplitude surveys with different locations of exciter and/or pickup. After this mode had been detected, it became immediately obvious that, regardless of which vibration data analysis technique is employed, repositioning of the exciter and pickup (or using multiple exciters and pickups) should be a part of a thorough vibration analysis.

A Kennedy-Pancu plot of the complex impedance for an exciter located at θ = 180 deg. (see Fig. 3) and the pickup located at θ = 100 deg., with both the exciter and pickup axial locations midway between the ends of the shell, is shown in Fig. 6. The frequency range of

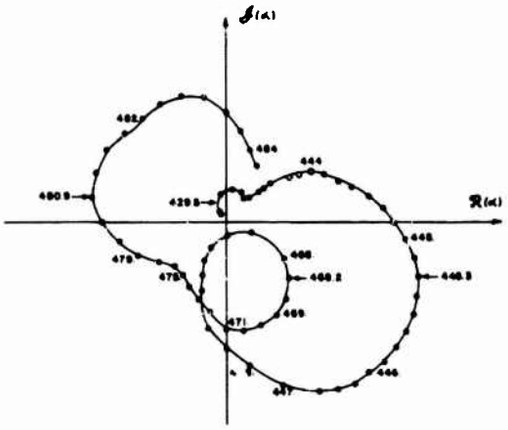


Fig. 6 - Typical Kennedy-Pancu plot showing four natural frequencies of the stringer stiffened shell

this plot covers four of the lowest five natural frequencies, the lowest frequency being omitted. The data were taken at equal phase increments for most of the points shown. The resonant frequencies, which were determined by the maximum change in arc length per unit change in frequency, are denoted by the four arrows in the figure. Although it appears that there may be another resonance between 482 and 484 cps, $ds/d\omega$ steadily decreases from 480.0 to 484 cps. Other K-P plots for different exciter and pickup locations substantiated this.

APPLICATION TO SANDWICH CONICAL SHELL

Specimen. The shell investigated was of truncated conical configuration (see Fig. 7). It was constructed of 5052 aluminum hexagonal-cell honeycomb core bonded by a film adhesive to E-glass, 181-style glass-cloth facings impregnated with 828-Z epoxy resin. Detailed material property data for the constituent materials are given in Ref. [8].

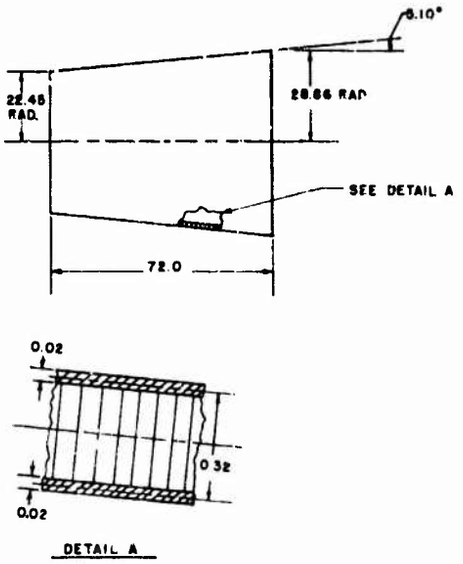


Fig. 7 - Geometry of sandwich shell. All dimensions in inches except as noted

To achieve free end conditions as closely as possible, the shell was suspended vertically from a steel frame by six soft springs equally spaced around the shell circumference. Suspension resonant frequency was below 1 cps.

Instrumentation. An electrodynamic exciter (MB, Model C11) was attached to the shell by a force link specially designed to reduce shell/exciter coupling. The excitation force was applied between the shell and the frame.

The shell response instrumentation consisted of 600 metallic-foil, electrical-resistance strain gages (Budd, Model C6-141B) oriented circumferentially and axially at various grid locations on the outer facing of the shell. The electronic circuitry used to monitor and measure the dynamic strain signals is shown schematically in Fig. 8.

Each strain-gage system was calibrated separately by applying a known sinusoidal signal. Frequencies covered ranges from 5-500 cps, while the instrumentation components had flat responses to 20,000 cps and more.

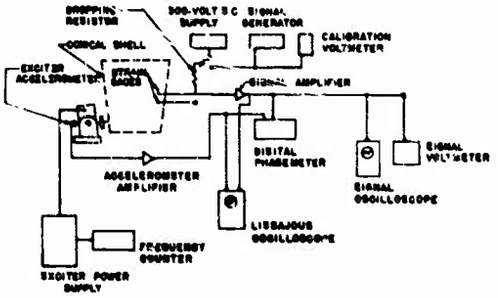


Fig. 8 - Schematic diagram of strain-gage instrumentation for sandwich-shell vibration experiments

An accelerometer (Endevco, Model FA-72) was attached to the armature of the vibration exciter to provide a measure of the input force applied to the shell. The output of the accelerometer was amplified (Endevco, Model 2016) and then fed into a readout system, as indicated on Fig. 8. The voltmeter gave an indication of the output level and the oscilloscope was used to monitor the signal to assure that there was no distortion.

The outputs of the strain-gage system and the accelerometer were applied to each side of the digital phase meter (AD-YU Digital Phase Meter, Model 524A and EAI Digital Voltmeter, Model 5002A) that indicated the relative phase between the input and strain distribution.

The system indicated on Fig. 8 is for the output amplitude and phase of a single strain gage. Only one gage could be monitored at a time since only one data acquisition system was available. A telephone switchboard was used to change gage locations. The switchboard was found to give the best signal-to-noise ratio at the lowest cost; other faster switching arrangements were tried but each increased the noise level. The strain-gage signals were on the order of 100 microvolts, which made the noise level of prime importance.

A stroboscope (General Radio Model 1531-AB) was used sometimes to help define the modal shape of the shell under excitation.

A second oscilloscope was used to display a Lissajous pattern as an indication of the phase between the input and strain. This was used as a check on the phase-angle quadrant obtained from the phase meter.

A band-pass filter (SKL Model 302) was used sometimes to help eliminate the noise in the strain-gage signals. The filter was used sparingly, since it introduced a phase shift that was dependent on frequency. When the phase data were of prime importance, the filter was not used.

Experimental Procedure. The procedure used to acquire the resonant-frequency and modal-strain-distribution data at each resonance was to first locate the resonant frequency using the Kennedy-Pancu technique and then define the modal shape at this frequency.

The resonant frequency was located by monitoring a series of gages while the system was excited throughout the frequency range of interest. In this first survey, the peak amplitude method was used to locate the approximate range of the resonant frequency. The phase between the input and gage was not needed in this survey. The gages for the final Kennedy-Pancu measurements were selected by exciting the shell and noting the anti-nodal points. Inherently certain portions of the shell were excited at most of the resonant frequencies. In the survey, the input acceleration, strain outputs, and frequencies were monitored. Frequency intervals were taken at 5 cps across the entire band, with 1 cps near resonance. Closer intervals were taken to completely define the resonant point. Once the resonant frequencies were located, data were taken at these frequencies to make the Kennedy-Pancu plot.

The K-P data were taken by varying the excitation frequency and monitoring the phase angle between the input acceleration and the strain-gage signal. The gage selected for these data was the one that gave the largest output in the preliminary peak-amplitude survey. The excitation frequency was varied from a point below resonance that indicated near zero phase to a point above resonance that indicated the phase was returning to zero. Since the phase meter would not function below a threshold input voltage (0.35 volts), data were taken only in the general vicinity of resonances. These data were sufficient to define the uncoupled resonances by means of the characteristic circular arcs on the K-P plots. To minimize the nonlinear effects of the shell, the strain level applied to the shell was varied. The excitation frequency was changed until approximately 10-deg variation in phase was noted. The input force was varied until the gages exhibited a predetermined output; then the input acceleration, output gage signal, phase relation, and frequency were recorded.* This same procedure was repeated until the output signal became too small.

The Kennedy-Pancu plot was drawn from these data, and the uncoupled resonant frequencies determined. The excitation frequency of the

*At times the phase meter would not give an accurate reading in relation to the phase-angle quadrant. The Lissajous pattern was used as a check to make sure that the quadrant was correct.

shell was set at the uncoupled resonant frequency and the excitation level was not changed from the previous data. Each strain-gage output and the corresponding phase relation were read. From these data the modal strain distribution was determined. Once the data were acquired, the shell nodal points were investigated and checked by locating the points by feel and also be sight using a stroboscope.

The same procedure was repeated for each resonant frequency throughout the frequency range. Resonant frequencies were investigated from 5 cps to 400 cps. The lower limit was below the first resonant frequency and was the lowest frequency of the exciter and the upper limit was reached when the strain signal-to-noise ratio was too low to obtain reliable data.

Results. The experimentally measured values of resonant frequencies and associated strain distributions and damping are presented in this section.

Resonant frequencies for various meridional modes are shown in Fig. 9 as a function of

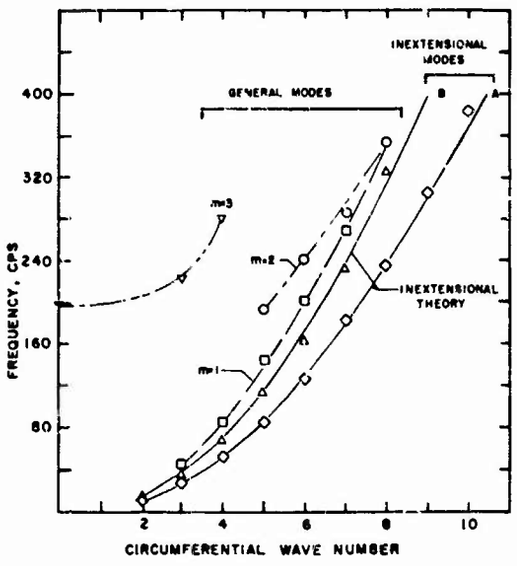


Fig. 9 - Resonant frequency versus circumferential wave number for sandwich shell

circumferential mode number. On this figure the two curves that were derived from an inextensional analysis [8] are shown along with the experimental resonant frequency points. Each resonant point was obtained from a Kennedy-Pancu plot. Fig. 10 shows two typical plots that were used to separate the resonant frequencies. As can be seen from the plots, the

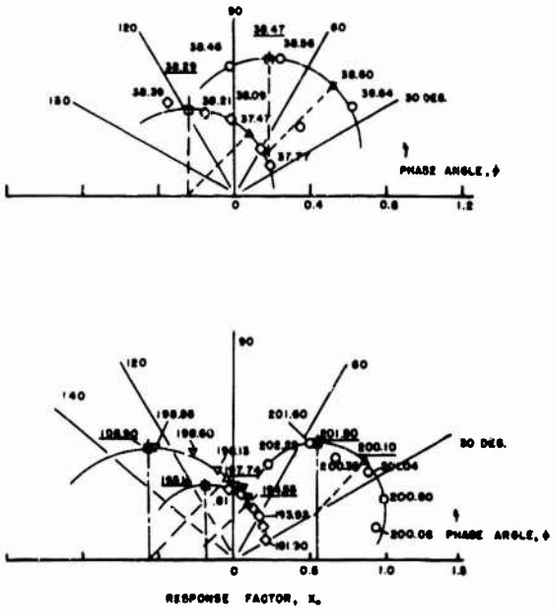


Fig. 10 - Typical Kennedy-Pancu plots showing separation of pure modes for the sandwich shell

separation of the resonant frequencies which were very close together was accomplished quite adequately by means of the K-P technique. Damping factors were determined from these figures using the technique outlined previously.

It can be seen in Fig. 9 that the experimentally measured resonant-frequency points associated with the two lowest unsymmetric modes agree quite closely with the frequencies calculated by the inextensional analysis over the entire range of circumferential wave numbers covered.

The resonant-frequency curves for the higher modes indicate the same trend as those of the two lowest modes. In the region of low circumferential wave numbers, n, the higher modes were difficult to detect because the resonant frequency coincided with the resonant frequency of another mode. At these lower resonant frequencies the response of the mode having a higher n would dominate that of the lower-n mode. This problem was one of the major difficulties encountered in applying the Kennedy-Pancu technique in this investigation. It was beyond the scope of this investigation because of the limitation of equipment, but a solution to this problem would be to introduce additional excitation systems. By placing the exciters near a point that is a node of the strong mode, the system would exhibit a larger response in the weak mode.

Shown in Fig. 11 are typical plots of

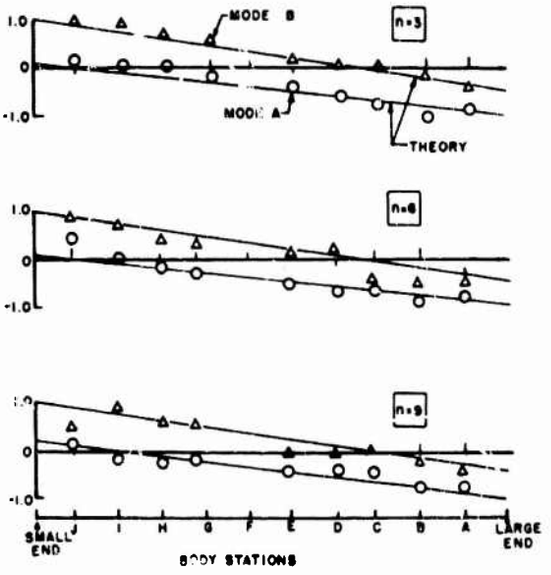


Fig. 11 - Meridional distributions of circumferential strain on the sandwich shell for the two lowest modes for three typical circumferential wave numbers (n)

circumferential strain associated with the two lowest meridional modes. Also included in Fig. 11 are the analytical results derived from the inextensional analysis presented in Ref. [8]. In general, there is very good agreement between the analytical and experimental strain distributions for these modes. It can be seen that increasing the circumferential wave number shifts the location of the node, as was observed by Mixson [9].

The circumferential modal shapes were symmetrical about the exciter location. Moving the exciter to a new circumferential location on the shell resulted in the same modal shape but with the nodal lines shifted circumferentially.

Since the agreement between the experimental data and the values derived by the inextensional analysis are in close agreement, it is assumed that the lowest experimental unsymmetrical modes are the inextensional modes. Hereafter, these two lowest experimental modes will be referred to as the inextensional modes. The other modes which have higher resonant frequencies will be referred to as general modes, since they exhibit both extensional and inextensional deformation.

It can be noted on Fig. 9 that the resonant frequency for the m = 1 general mode is close to inextensional mode B at the low circumferential wave numbers, but as the wave number increases the curves separate and the m = 1 mode converges to the m = 2 general mode. Also it can be noted on this figure that all of the general modes tend to converge at the higher frequencies. This convergence is characteristic of the dynamics of both cylindrical and conical shells.

The resonant frequency data and the associated strain distributions indicated that some coupling between modes occurred. These coupled modes were a combination of two circumferential modes having the same meridional mode when the resonant frequencies were close. Similar phenomena have been reported by Koval [10] for cylindrical shells and by Watkins and Clary [11] and Mixson [9] for conical shells. Pronounced coupling phenomena were observed at resonant frequencies of 33 cps, 64 cps, and 94 cps. In all of these cases, the strain distributions were typically the same except for the difference in circumferential wave numbers and the nodal patterns were symmetrical about the exciter, but not evenly spaced. The coupling observed was probably caused by the presence of four equally spaced, 3-inch-wide, longitudinal lap jounts on the inside and outside facing (i.e. a total of eight lap joints; one every 45 deg.). However, it is interesting to note that the only modes which coupled were inextensional modes (A and B). There was no observed coupling of the general modes (m = 1, 2, 3) with each other or with the inextensional modes. This may have been because for the particular shell construction and geometry, the inextensional modes were the only ones sufficiently close together (in frequency as well as in circumferential wave number) to couple.

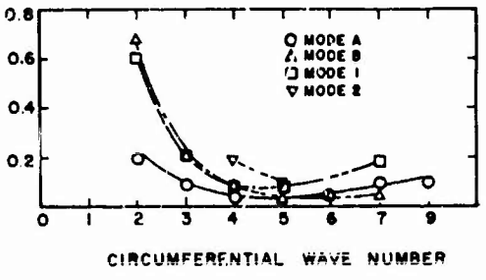


Fig. 12 - Logarithmic decrement versus circumferential wave number for the four lowest modes of the sandwich shell

Fig. 12 shows a plot of the damping logarithmic decrement as a function of circumferen-

tial wave number. The values for this figure were obtained from the Kennedy-Pancu plots and converted to logarithmic decrements. As pointed out previously, the damping coefficient of the system can be obtained from the Kennedy-Pancu plots. The damping coefficient is converted to logarithmic decrement by multiplying the coefficient by 2π.

CONCLUDING REMARKS

When used in conjunction with instrumentation having sufficient accuracy, the Kennedy-Pancu vibration data analysis technique has been proven to be a powerful tool for experimental investigations of shell-type structures. It has been useful both in separating natural frequencies which are very close together and in separating pure modal shapes.

REFERENCES

1. C.C. Kennedy and C.D.P. Pancu, "Use of Vectors in Vibration Measurement and Analysis", Jour. Aeronaut. Sci., Vol 37, pp. 603-625, 1947.

2. R.E.D. Bishop and G.M.L. Gladwell, "An Investigation into the Theory of Resonance Testing", Philosophical Trans. Royal Society (London), Series A, Vol 255, pp. 243-244, 1963.

3. R.E.D. Bishop and J.W. Pendered, "Note on Resonance Testing", Jour. Mech. Eng. Sci., Vol. 5, pp. 243-244, 1963.

4. J.W. Pendered and R.E.D. Bishop, "The Determination of Modal Shapes in Resonance Testing", Jour. Mech. Eng. Sci., Vol. 5, pp. 379-385, 1963.

5. J.W. Pendered and R.E.D. Bishop, "A Critical Introduction to Some Industrial Resonance Testing Techniques", Jour. Mech. Eng. Sci., Vol. 5, pp. 345-367, 1963.

6. J.W. Pendered, "Theoretical Investigation into the Effects of Close Natural Frequencies in Resonance Testing", Jour. Mech. Eng. Sci., Vol. 7, pp. 372-279, 1965.

7. D.M. Egle and J.L. Sewall, "An Analysis of Free Vibration of Orthogonally Stiffened Cylindrical Shells with Stiffeners Treated as Discrete Elements", AIAA Jour., Vol. 6, pp. 518-526, Mar. 1968.

8. C.W. Bert, B.L. Mayberry, and J.D. Ray, "Vibration Evaluation of Sandwich Conical Shells with Fiber-Reinforced Composite Facings" to be published by U.S. Army Aviation Materiel Laboratories, Fort Eustis, Virginia.

9. J.S. Mixson, "Experimental Modes of Vibration of 14° Conical-Frustum Shells with Free Ends", NASA TN D-4428, Apr. 1968.

10. L.R. Koval, "Note of Effect on Dynamic Asymmetry on the Vibration of Cylindrical Shells", J. Acoust. Soc. Amer., Vol. 35, pp. 252-253, Feb. 1963.

11. J.D. Watkins and R.R. Clary, "Vibrational Characteristics of Some Thin-Walled Cylindrical and Conical Frustum Shells," NASA TN D-2729, Mar. 1965.

DISCUSSION

Mr. Forlifer (NASA, Goddard): Are you familiar with the work of Clyde Stahle, formerly of Martin Baltimore, in the late 50's and early 60's in mechanizing this technique as far as giving experimental data directly in terms of real and imaginary components and applying this to modal surveys on everything but shell structures, I guess.

Mr. Bert: No, I'm not – I would be quite appreciative of getting that reference.

Mr. Forlifer: He reported it at a Shock and Vibration Symposium in the early 60's. (Shock and Vibration Bull. No. 34, Part 4, pp. 30-42, June 1961. Ed.)

Mr. Bert: I might add that we did look into the possibilities of mechanizing this but we did have trouble. For example, in trying one approach we made was to try to fit a circle. With a given number of points one can fit a circle – then if some more points are added – the circle that fits is different. We never did get it to converge very satisfactorily – so that approach was not successful. I do not like to say that it can not succeed because next week some one will make it work like a charm. Other people have tried this method and it has not worked for shell structures. I believe the reason is in connection with the accuracy of the measurements. It does require highly accurate phase and frequency measurements.

NORMAL MODE STRUCTURAL ANALYSIS CALCULATIONS VERSUS RESULTS*

Culver J. Floyd
Raytheon Company
Submarine Signal Division
Portsmouth, Rhode Island

Acceleration data from the MIL-S-901C medium weight machine has been used as inputs to a computer-aided normal mode analysis for new sonar cabinet chassis design. The same data has been used as inputs to a more conventional hand calculation method. Cabinets and chassis analyzed by these two methods have now been tested. This paper compares the results of the two calculation methods.

INTRODUCTION

For several years we have been concerned with the advantages, if any, which a computer-aided analysis would have over a hand analysis method. In the design of the AN/BQS-13 sonar system we had the opportunity to compare both systems on a fairly large scale. Either computer-aided analysis or hand analysis can produce equipment capable of passing MIL-S-901C shock tests. The computer-aided analysis seems to be faster. Either method is very dependent on the analyst's assumptions or the best math model of the structure.

SOURCE OF TEST DATA

During 1965, the AN/BQS-6B sonar system was shock and vibration tested to MIL-S-901C and MIL-STD-167. Figure 1 shows this system. Collection of data from testing the eighteen units gave a good picture of the acceleration of different weight and size units which have different internal structures. [1]

The contract called for a special deck simulation fixture to be used since the locations of the cabinets aboard ship were known. This fixture was required to have a 25-30 Hz resonant frequency. As in the conventional MIL-S-901C tests, the hammer height for the six blows was determined by the weight on the anvil. An accelerometer was located inside the bottom of each cabinet. A typical waveform is shown in Figure 2. A 30 Hz-50g sine wave has been superimposed for comparison. Summation of this data from the eighteen units showed that 50g was the average acceleration with the spread from 40 to 60g.

SHOCK DESIGN NUMBER COMPARISON

In the course of developing the 50g-30 Hz number, comparison was made with design shock factors in other military publications.

Table 1 tabulates this comparison. Although MIL-E-16400E, Figure 3 is specified for equipments over 4500 pounds, the number shown was selected for comparison. NavShips 900-185 gives a range for equipment rigidly mounted on the shock table.

NavShips 250-660-30 gives a shock factor range dependent on material yielding. Most electronic equipment will tolerate some yielding so long as function is not impaired and mechanical features operate smoothly.

NavShips 250-423-31 also presents a range of numbers depending on foundation frequency and permitted yielding. For example, a dynamic conversion number of 24 could be used on a structure which could function with large yielding. Forty-nine would be required for a non-yielding structure.

*Paper not presented at Symposium.

The vibration requirements of MIL-STD-167 are shown for reference. The levels for exploratory vibration were established as a means of determining resonant frequency and modes of chassis along three orthogonal axes.

HAND ANALYSIS

Conventional hand calculations used these design numbers as inputs. Two limits were imposed on the static designs. First, the resonant frequency of any spring mass system or subsystem must be higher than 47 Hz to eliminate large transmissibilities from the basic 30 Hz forcing frequency and from the 33 Hz test frequency of MIL-STD-167.

The spring mass system was usually a shelf or a drawer. The subsystem occasionally appeared as a smaller chassis.

Second, the static stress of cabinet parts was multiplied by 50. This stress was required to be smaller than the yield stress for the material used. For stress purposes, all subsystems were calculated as if their resonant frequency was 47 Hz and their damping was 0.1 of critical. A shock design number of 85 was then used for stress calculation for these chassis. This calculated stress also was required to be smaller than the yield stress of the material used.

The eleven cross hatched cabinets in Figure 3 were stress analyzed in this manner. The interior design covered a wide range from PC boards to power supplies.

COMPUTER-AIDED ANALYSIS

The same waveform was also used to produce the design shock spectrum in Figure 2. The upper curve is for zero damping. The lower curve is for 0.05 damping. Experience and test data have shown that 0.15 or 0.20 damping is probably more realistic in a composite assembly.

This shock spectrum was used as inputs to a normal mode program. [2, 3] The results were plotted in normal mode diagrams similar to Figure 4. Calculated joint accelerations were used to calculate member stresses both at the cabinet level and at the chassis level.

Ten cabinets were dynamically analyzed using this method (Reference, Figure 3). The size and weight of these cabinets again cover a wide range. The interior construction varied from printed circuit boards to analog gear trains and high power amplifiers and switching devices.

EXPLORATORY TEST PROGRAM

An exploratory test program for the subassembly levels was established to confirm structural design early in the project.

Each chassis, drawer, or subassembly was mounted on the vibration table in a normal manner and vibrated at .020 inch DA along each of three orthogonal axes through the frequency range of 5-100 Hz. The subassembly was deemed adequate if no resonances appeared below 47 Hz.

Exploratory shock was also a part of the program. The subassembly normally mounted to the test fixture was subjected to one 50g drop along each of three orthogonal axes. High-speed movies were taken to record behavior. A single accelerometer on the table recorded the shock input.

A special fixture was made and attached to a Barry Vari Shock Machine modifying the 1/2 sine 11 Ms pulse to approximately the waveform which we had measured on the MIL-S-901C medium weight machine. Figure 5 shows this spring bed type fixture with an 18-inch square cathode ray tube mounted.

The fixture consists of an upper and lower plate separated by spring cartridges. The number of cartridges used was determined by the weight of the test specimen. A test frequency of 30 Hz was desired but the exploratory nature of the test was not affected if the actual frequency was between 25 and 35 Hz.

Large low frequency rocking modes were encountered but could usually be brought under control by redistributing the spring cartridge and shifting the test specimen CG. Some assemblies tested on this device ran less than a pound, while the largest was a power supply weighing 90 pounds not including the mounting. Some assemblies were only tested to 50g as measured by the accelerometer above the springs.

Others such as the picture tube shown in Figure 5 were shocked several times to 85g or more.

EXPLORATORY TEST RESULTS

The original plan called for 185 chassis, drawers, or shelves to be done in this manner. However, as the project developed the number dropped to 148 due to similarities.

Three types of inadequate designs plagued us during these tests:

1. Wiring and cable were poorly clamped.

2. Cold solder joints and wires kept appearing.

3. Hardware not large enough and not locked in place kept loosening.

Although modes were essentially as predicted, analytical frequencies invariably turned out to be higher. Although some had been predicted as low as 50 Hz during the exploratory tests, no chassis was less than 60 Hz.

Occasionally second or third modes would be visible with these inputs. Behavior under this exploratory vibration test was visually examined and later found to be indicative of performance under shock. The higher the resonant frequency, the less motion in shock. The modes observed in the high speed motion pictures were comparable.

The structural results were very satisfying and indicated that it is possible to design adequately for shock tests. This assumption has now been borne out in cabinet level tests.

CABINET LEVEL TESTS AND RESULTS

The cabinets shown in Figure 3 have now been tested to MIL-STD-167 and to MIL-S-901C. Problems were encountered at the cabinet level during these tests since no exploratory testing was done at the cabinet level. These problems were of three types.

In the first type, failure occurred in a detailed part because some change had taken place between the time of the structural analysis and the hardware assembly.

The second failure type occurred because the tested part knowingly was not like the one analyzed. Schedules and procurement times prevented getting the ideal. Usually the part ended up looking like the ideal before the test was over.

The third failure type was wiring associated. With perhaps only two exceptions, every cabinet sooner or later developed broken wires to a greater or lesser degree. Usually this was at a connector or terminal post. Proper lacing or clamping always corrected the problem.

Captive screws which typically hold chassis in place gave constant trouble. Although the screw was strong enough for shock tests, the strong arm of the test mechanic often twisted these screws off as he loosened or tightened them during the inspection processes.

Figure 7 shows one of these cabinets mounted on the 30 degree inclined fixture. This cabinet was analyzed by computer methods. [2, 3] This unit consists of 28 amplifiers mounted on water panels and weighing 1320 pounds. Figure 4 is the predicted mode shape for this cabinet. The worst predicted acceleration was for the center water panel in a vertical down direction. The high speed movies taken of this test dramatically show two or three of the lower bending modes.

The input waveform to this cabinet is shown in Figure 6. Note again the basic 30 Hz frequencies with the higher frequencies superimposed.

CONCLUSION

1. It is possible to design electronic equipment which has a reasonable chance of passing MIL-STD-167 and MIL-S-901C tests the first time.

2. The design number used from the various military manuals gave a good agreement for the weight of equipment we supply.

3. The computer aids the analyst in determining interaction of chassis and cabinet. The computer does not necessarily eliminate hand calculation at the detail level. Good judgement of the analyst is essential for the

assumptions required with both computer and hand calculation methods.

4. Exploratory vibration and shock testing of the type described here is adequate to give complete confidence that the parts and assemblies will pass the vigorous requirements of MIL-STD-167 and MIL-S-901C.

5. The first six normal modes provide adequate acceleration and load data to satisfy these particular tests.

REFERENCES

1. "A Guide for Design of Shock Resistant Naval Equipment," Bureau of Ships, NavShips 250-660-30

2. "Guide for the Design of Shock and Vibration Resistant Electronic Equipment," Bureau of Ships, NavShips 900-185

3. "Shock Design of Shipboard Equipment, Dynamic Analysis Method," Bureau of Ships, NavShips 250-423-30

BIBLIOGRAPHY

1. "Military Specification Shock Tests, H.I. (High Impact); Shipboard Machinery, Equipment and Systems, Requirements for," U.S. Navy, MIL-S-901C, 15 January 1963

2. "Military Specification Electronic Equipment, Naval Ship and Shore: General Description," U.S. Navy, MIL-E-16400E, 15 June 1962

3. "Shock Design of Shipboard Equipment, Interim Design Inputs for Submarine and Surface Ship Equipment," Bureau of Ships, NavShips 250-423-31

4. J. Putukrian, "Dynamic Analysis of a Typical Electronic Equipment Subjected to Nuclear Weapon Induced Shock," Shock and Vibration Bull. No. 37, Part 4, January, 1968

5. T.K. Hasselman, and C.M. Hwang, "Shock Response of Electronic Equipment Cabinet by Normal Mode Method," Shock and Vibration Bull. No. 36, Part 7, January, 1967

6. C.J. Floyd, "A Simulated 25-30 CPS Deck for Shock Testing," Shock and Vibration Bull. No. 35, Part 1, March, 1966

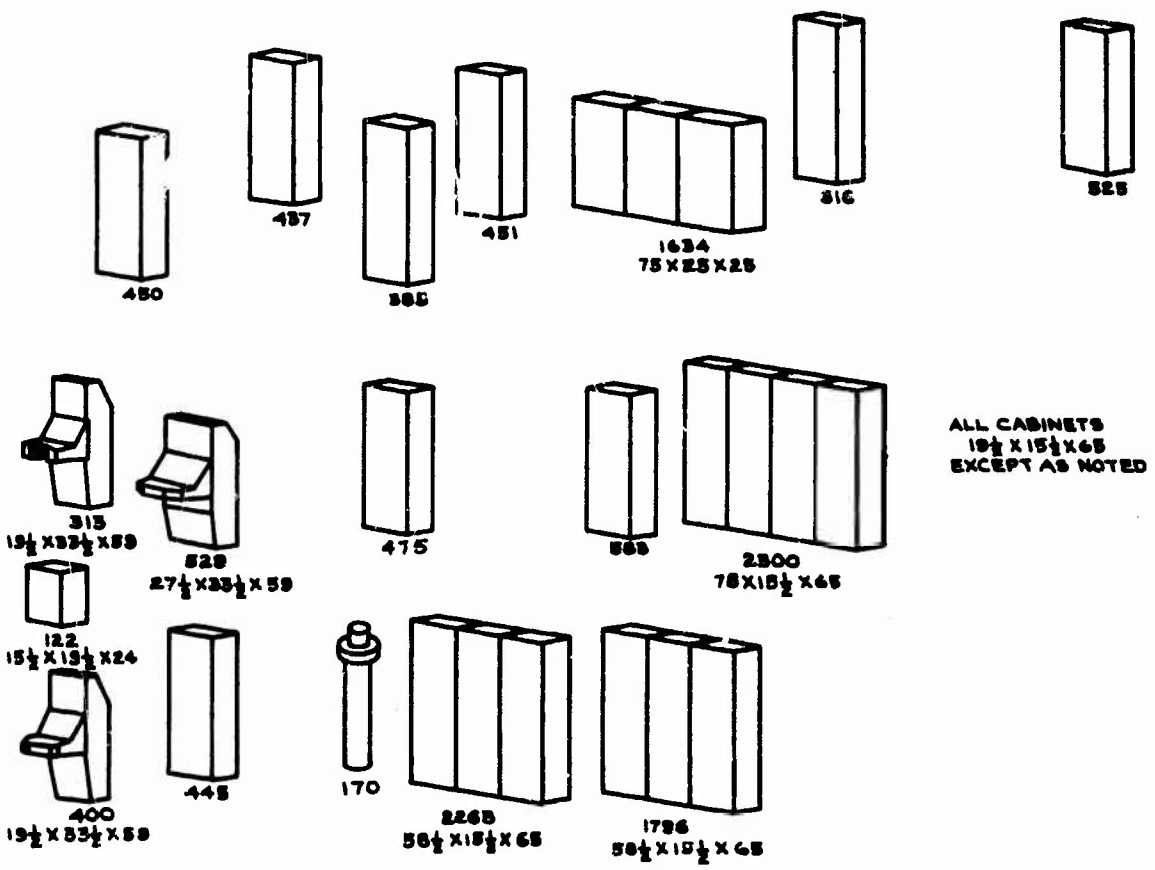


Fig. 1 - Types and Weights of Cabinets (1965 Tests)

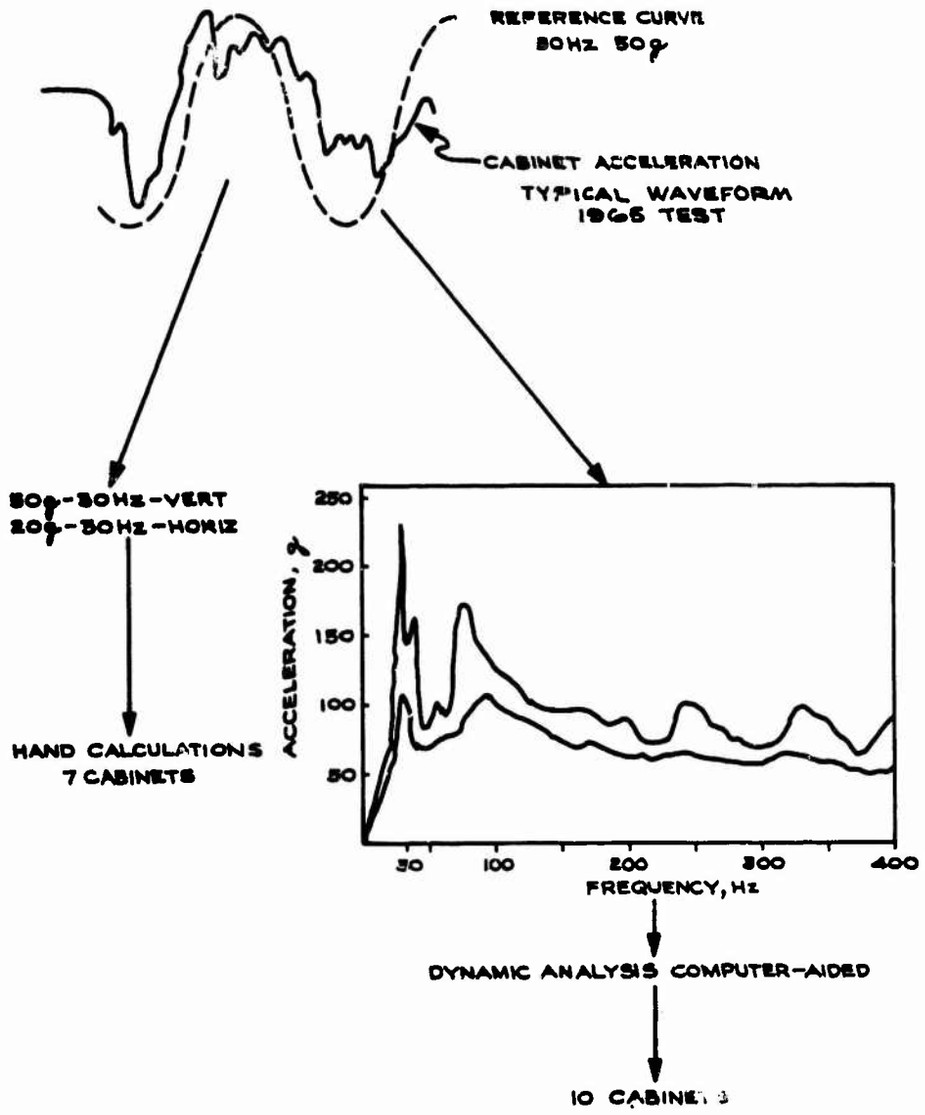


Fig. 2 - Derivation of Inputs

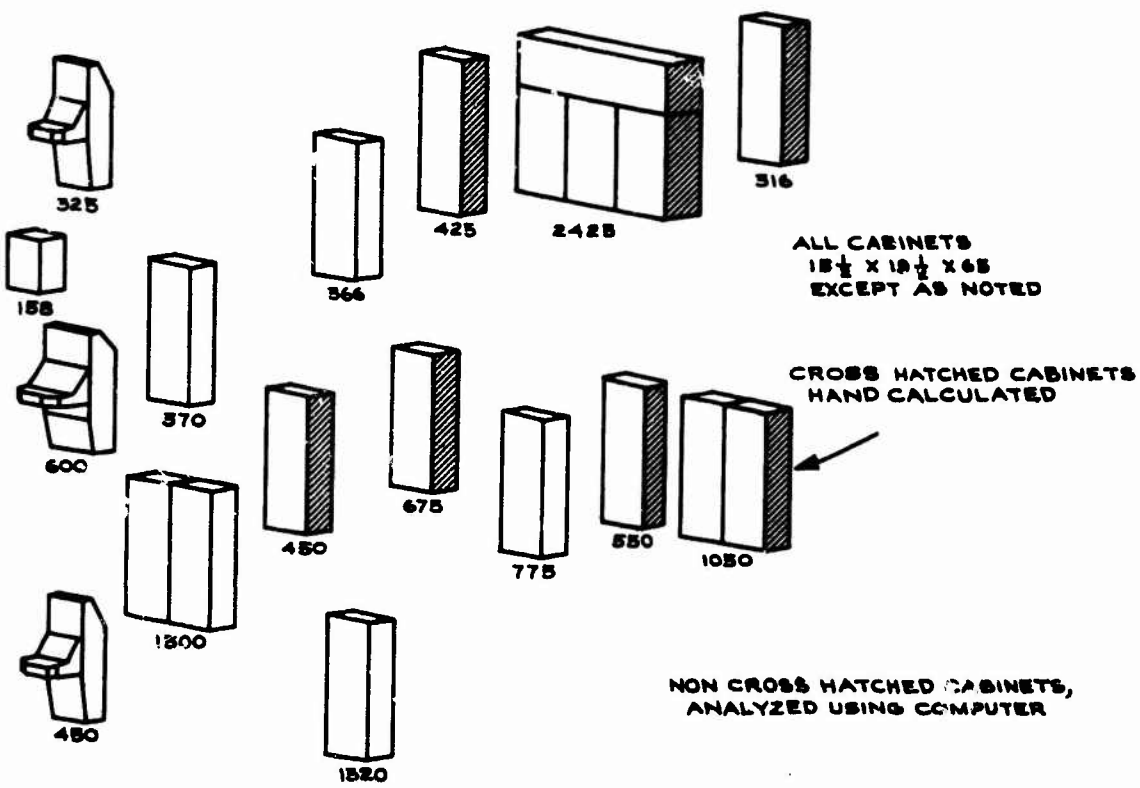


Fig. 3 - Types and Weights of Cabinets (1968 Tests)

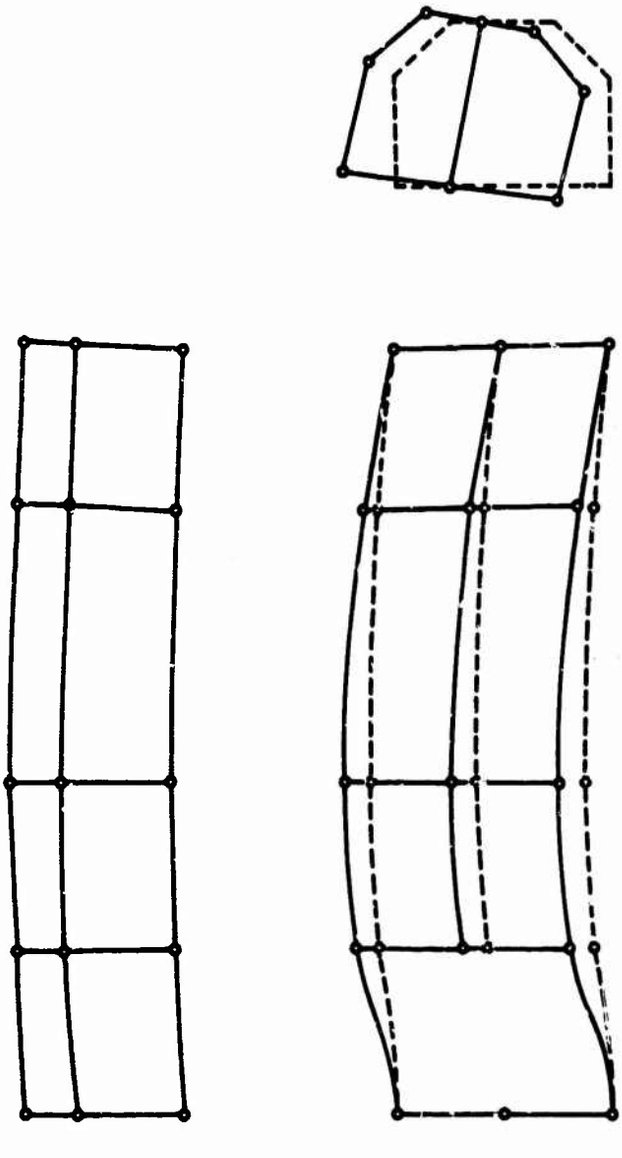


Fig. 4 - Typical Cabinet Mode Shape



Fig. 5 - Drop Test Fixture

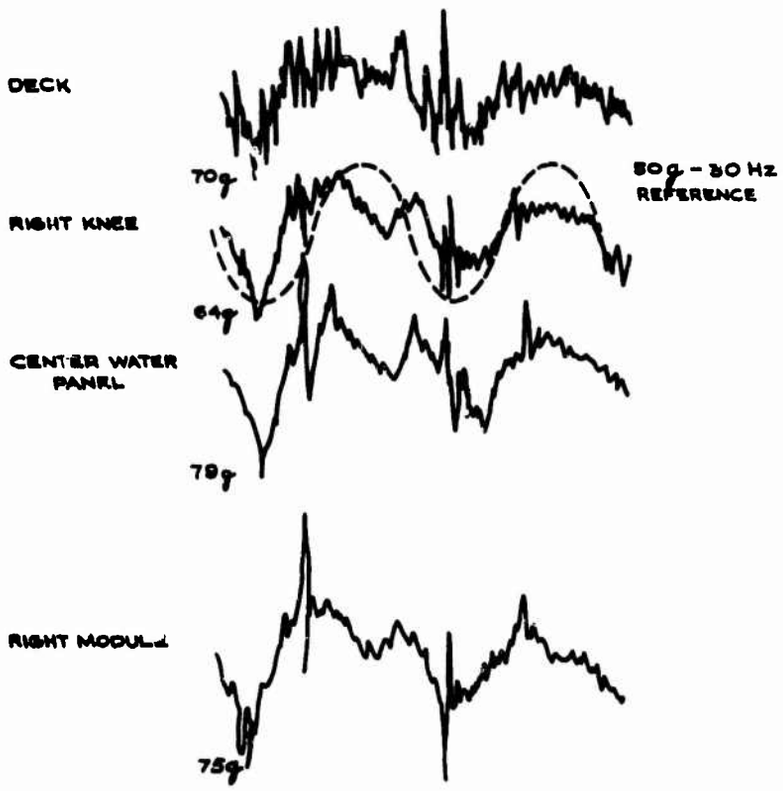


Fig. 6 - Typical Waveforms (1968 Tests)

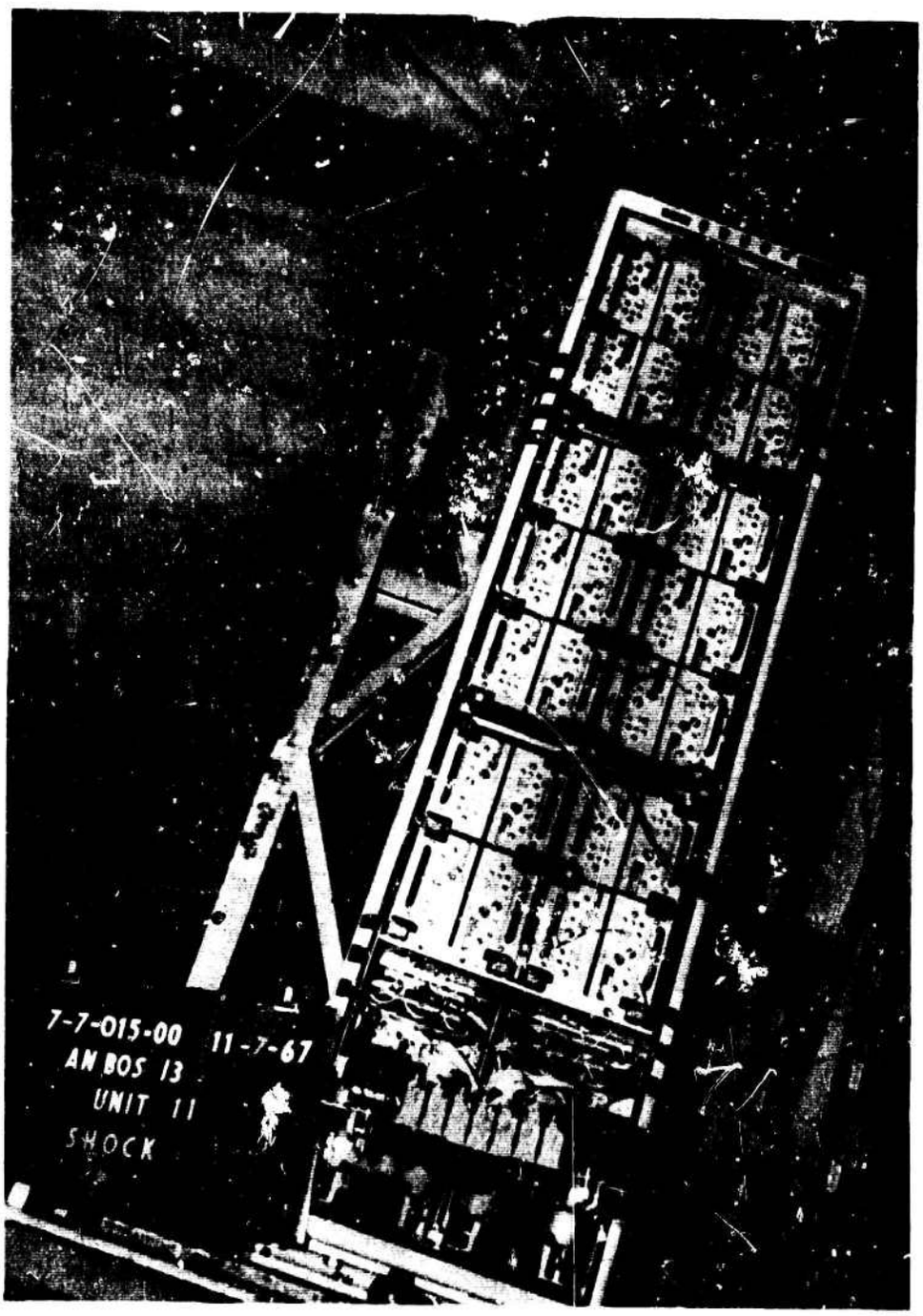


Fig. 7 - Typical Cabinet Mounted on an Inclined Fixture

Table 1
Comparison of Shock Design Numbers, 500-Pound Cabinet

Type of Test/ Requirement	Vertical	Horizontal	
		Athwartships	Fore & Aft
MIL-E-16400E Figure 3	42	42	42
NavShips 9[illegible]-185	50 to 100g 55-70 Hz	50-100g 55-70 Hz	50-100g 55-70 Hz
NavShips 250-660-30	25-80g Deperdent on Allowable Yielding	25-80	10-32
NavShips 250-423-31	24-49 at 30 Hz 46-92 at 60 Hz	24-49 at 30 Hz 46-92 at 60 Hz	10-20 at 30 Hz 18-36 at 60 Hz
AN/BQS-6B Tests (1965)	50-30 Hz	20-30 Hz	
MIL-STD-167	Three Orthogonal Axes 5-15 Hz — .060 DA 16-25 Hz — .040 DA 26-33 Hz — .020 DA		
Exploratory Vibration	Three Orthogonal Axes 50g-30 Hz		
Exploratory Shock	Three Orthogonal Axes 5-100 Hz — .020 DA Note: 100 Hz — .020 DA = 10g		
AN/BQS-13 Tests (1968)	55-30 Hz	25-30 Hz	25-30 Hz

COMPARISONS OF CONSISTENT MASS MATRIX SCHEMES

R. M. Mains
Department of Civil and Environmental Engineering
Washington University
St. Louis, Missouri

It has become popular to use one or another "consistent" mass matrix scheme in dynamic analysis with finite elements. Such schemes have the claimed advantage of transferring to the computer some of the calculations previously done by hand, and of producing greater accuracy in the calculation of natural frequencies and mode shapes. These schemes have a distinct disadvantage in calculations because they produce non-diagonal mass matrices which require either: (1) two eigenvalue problems to be solved, one for the mass alone and one for the mass together with the stiffness; (2) the eigenvalues of the unsymmetric product of KM must be solved. In either case computation time and complexity are at least doubled.

In order to develop some judgement on whether the extra effort is worth-while or not, the author has compared the masses, frequencies, and mode shapes for 7 different versions of mass with the same stiffness for a cantilever beam. There seems to be little to gain from the consistent mass schemes.

I SUMMARY AND CONCLUSIONS

A cantilever beam divided into 20 segments and represented by 40 coordinates has been solved for its natural frequencies and normal mode shapes for seven different cases of mass or coordinate combinations. The resulting frequencies have been studied and compared, with the following conclusions:

1. The rotational coordinates must be included in the solution, or the frequencies of the modes will be significantly reduced, and calculated responses to shock will be increased. (See Table 3.)

2. Within the range of frequencies for which the mode shapes bear some semblance of reality, the exact form or magnitude of the rotational mass inertia does not seem to be critical. (See Table 6.)

3. The two "consistent" mass schemes produce frequencies which stay close together through 15 of 40 modes, but the mode shapes are close only through mode 6 (and mode 3 is excepted here). (Tables 3 and 6.)

4. There is little reason to conclude, on the basis of the lowest 6 mode frequencies and mode shapes, that the consistent mass matrices produce any better result than the author's diagonal mass matrix with pro-rated masses and eyeballed radii of gyration.

5. There is little reason, within the lowest 6 modes, for concluding that the extra complication of the consistent mass schemes in computing masses and requiring two eigenvalue solutions provides anything worth the cost and effort.

6. The number of modes to be considered valid in a solution should be related to the number of coordinate stations, and not to the total number of coordinates. e.g. 1/3 of 20 $\approx$ 6 rather than 1/3 of 40 $\approx$ 13.

II INTRODUCTION

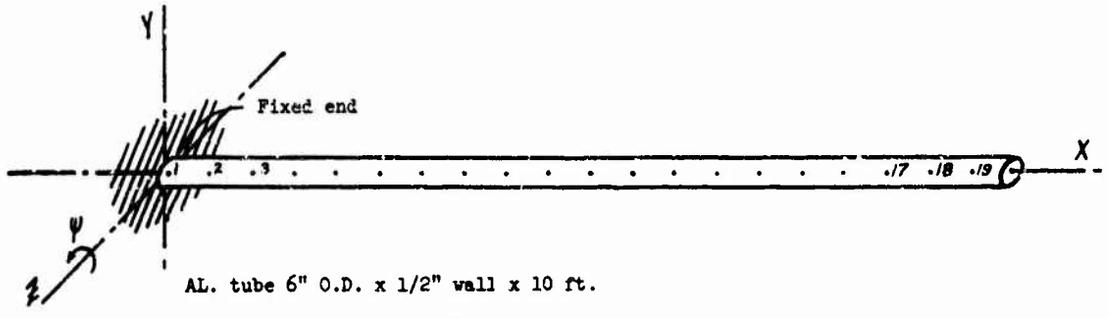
For some time there has been a growing interest in "finite element" techniques for the solution of practical problems. This has been demonstrated by a number of technical

papers, of which reference 1 is an example; by recent books, such as reference 2; and by short courses and summer institutes of which reference 3 is an example. The finite element idea is not new, since the technique was used in the early work with photoelasticity, flow nets and field theory. The availability of high-speed computers has led to the development of more complex finite elements in the attempt to refine solutions and achieve answers which agree more closely with either theoretical or measured values.

In structural dynamics, the refinement of finite elements has led to a more complicated representation of the masses,[4],[5]* sometimes called "consistent" mass because it is presumably more in conformance with reality. The work reported in this paper was undertaken in order to develop some data from which one could form some judgement as to what to do in various cases.

III SCOPE OF PROBLEM

In order to form a basis for comparison, a simple cantilever beam of constant cross-section was chosen, as shown in Fig. 1. The calculation



AL. tube 6" O.D. x 1/2" wall x 10 ft.

20 stations along length

y and Ψ coordinates

Fig. 1

CANTILEVER BEAM SYSTEM

of normal mode frequencies (eigenvalues) and normal mode shapes (eigenvectors) for this beam was then undertaken, with the beam divided into 20 equal finite elements along its length. The stiffness matrix for the solutions was developed in the usual way,[6] with allowance made for shear deformation and with both translational and rotational coordinates. The mass matrices were different for each of seven cases, as follows:

A. With both translation and rotation

1. Diagonal mass matrix, according to the author's usual way.

2. Non-diagonal mass matrix, according to Archer.[4]

3. Non-diagonal mass matrix, according to McCalley.[5]

4. Diagonal mass matrix, as no. 1, but with modified rotational inertia.

B. With translation only

5. Same as 1 with rotational inertias removed.

6. Same as 2 with rotational inertias removed.

7. Same as 3 with rotational inertias removed.

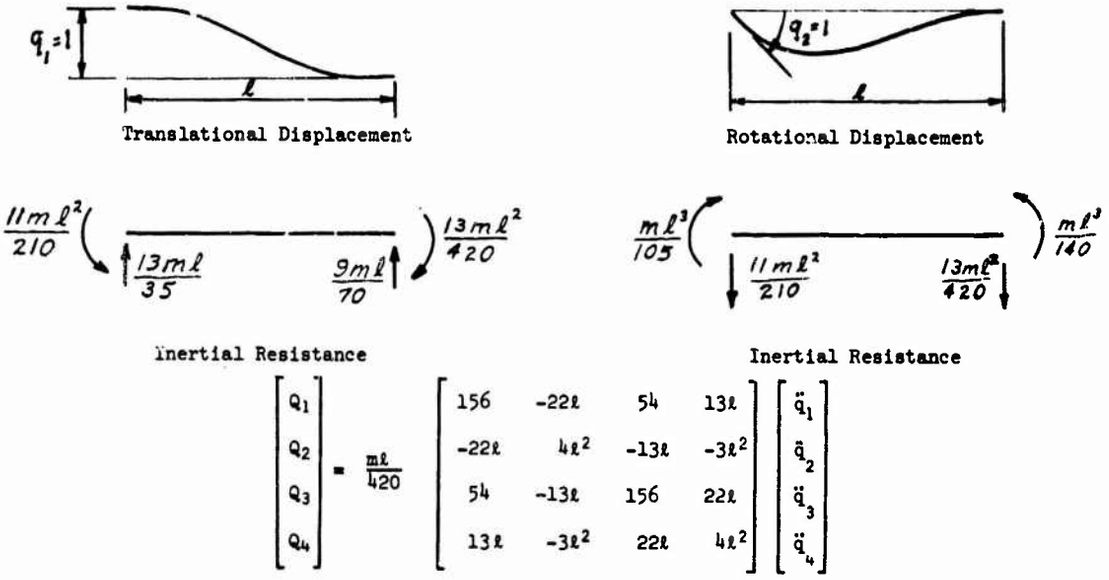
The comparison of the results of these different solutions of the same problem should be useful in determining what should be explored next.

IV COMPUTATIONS

The element stiffness matrix, including the effect of shear deformation, was computed with the results shown in Table 1, in the coordinate system shown in Fig. 1. It is of interest to note the negative sign on the carry-over elements, 2-4 and 4-2, resulting from the large contribution of shear flexibility. The system stiffness matrix was assembled by successive additions of this element stiffness matrix to the appropriate locations in the system matrix.

The mass matrix according to the author's usual way, was computed as a diagonal matrix, with translational masses pro-rated between coordinate points, and the rotational mass inertia taken as the (radius of gyration)^2 x (translational mass). This matrix for the element is shown in Table 2(a).

*Superscripts refer to items in the list of references.



$$\begin{bmatrix} Q_1 \\ Q_2 \\ Q_3 \\ Q_4 \end{bmatrix} = \frac{m\ell}{420} \begin{bmatrix} 156 & -22\ell & 54 & 13\ell \\ -22\ell & 4\ell^2 & -13\ell & -3\ell^2 \\ 54 & -13\ell & 156 & 22\ell \\ 13\ell & -3\ell^2 & 22\ell & 4\ell^2 \end{bmatrix} \begin{bmatrix} \ddot{q}_1 \\ \ddot{q}_2 \\ \ddot{q}_3 \\ \ddot{q}_4 \end{bmatrix}$$

Fig. 2

CONSISTENT MASS ACCORDING TO ARCHER

The mass matrix according to Archer [4] was computed according to his eq.(12), which is shown on Fig. 2. The numerical results are given in Table 2(b). It should be noted that the translational masses, 1-1 and 1-3, add to the 1-1 mass of Table 2(a), as they should do. The rotational mass inertias, 2-2 and 2-4, add to less than 5 percent of the 2-2 inertia in Table 2(a).

The mass matrices according to McCalley[5] were computed according to Figures 3(a) and 3(b) which are taken from his Figures 6 and 7. The numerical values are given in Tables 2(d), (e) and (f). As with Archer's version of mass, the translational masses, 1-1 and 1-3, add to the 1-1 mass of Table 2(a) as they should. The rotational mass inertias, 2-2 and 2-4 add to 75 percent of the 2-2 inertia in Table 2(a) and 140 percent of the 2-2 inertia in Table 2(c). This is interesting to observe, but its significance may be low.

The author's mass matrix was altered by changing the rotational mass inertia in an effort to make the higher frequencies come closer to those obtained with McCalley's masses, as an example. These altered values are the ones shown in Table 2(c).

The system mass matrices for the calculations with both translational and rotational coordinates were assembled by successive additions of the element mass matrices to the appropriate locations in the system mass matrix. The system mass matrices for the calculations with translational coordinates only were then obtained by eliminating the rows and columns corresponding to the rotational coordinates.

The system stiffness matrix for translational coordinates only can be obtained in at least three ways. First, the system stiffness with both translation and rotation can be inverted, the rotational coordinate rows and columns eliminated, and the reduced matrix again inverted to get the translational system stiffness. This was done on an IBM 360/50 at double precision, but it did not work properly. The system stiffness (at 40 x 40) inverted without error signal and the inverse was symmetric to 14 digits. The product of the inverse and the original gave unity down the diagonal, and the largest off diagonal element was 10^{-12}. The elimination of rows and columns checked properly and produced a 20 x 20 matrix, but the reduced matrix failed on inversion because of a zero determinant part way through the process. This was no great surprise, since it has happened many times before when a system matrix is used in its natural state.

The second technique consists of arranging the matrix to be reduced as follows:

$$\begin{bmatrix} K_{11} & K_{12} \\ K_{21} & K_{22} \end{bmatrix} \qquad (1)$$

such that the coordinates to be retained are contained in K_{11}, while the coordinates to be eliminated are contained in K_{22}. Then the

$$M_t = \frac{\mu L}{(1+12\beta)^2}\begin{bmatrix} (\frac{13}{35}+\frac{42}{5}\beta+48\beta^2) & (\frac{11}{210}+\frac{11}{10}\beta+6\beta^2)L & \frac{9}{70}+\frac{18}{5}\beta+24\beta^2 & -(\frac{13}{420}+\frac{9}{10}\beta+6\beta^2)L \\ (\frac{11}{210}+\frac{11}{10}\beta+6\beta^2)L & (\frac{1}{105}+\frac{1}{5}\beta+\frac{6}{5}\beta^2)L^2 & (\frac{13}{420}+\frac{9}{10}\beta+6\beta^2)L & -(\frac{1}{140}+\frac{1}{5}\beta+\frac{6}{5}\beta^2)L^2 \\ \frac{9}{70}+\frac{18}{5}\beta+24\beta^2 & (\frac{13}{420}+\frac{9}{10}\beta+6\beta^2)L & \frac{13}{35}+\frac{42}{5}\beta+48\beta^2 & -(\frac{11}{210}+\frac{11}{10}\beta+6\beta^2)L \\ -(\frac{13}{420}+\frac{9}{10}\beta+6\beta^2)L & -(\frac{1}{140}+\frac{1}{5}\beta+\frac{6}{5}\beta^2)L^2 & -(\frac{11}{210}+\frac{11}{10}\beta+6\beta^2)L & (\frac{1}{105}+\frac{1}{5}\beta+\frac{6}{5}\beta^2)L^2 \end{bmatrix}$$

Order of Coordinates: $y_1\ \theta_1\ y_2\ \theta_2$

Notation:

A = cross sectional area, in.^{2}

E = Young's modulus, lbf/in.^{2}

G = shear modulus, lbf/in.^{2}

L = length, in.

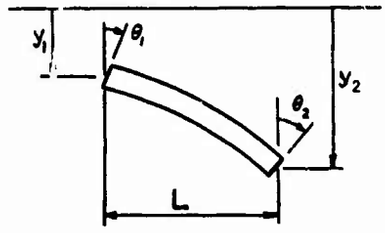
α = shear form factor, numeric

$\beta = EI\alpha/GAL^2$, numeric

$\mu = \rho_m A$, mass per unit length, lbf sec^2/in.^{2}

ρ_m = mass density, lbf sec^2/in.^{4}

Coordinate System



Total Mass Matrix $M = M_r + M_t$

Fig. 3(a)

TRANSLATIONAL MASS MATRIX ACCORDING TO McCALLEY

$$M_r = \frac{\mu L(r_g/L)^2}{(1+12\beta)^2}\begin{bmatrix} \frac{6}{5} & (\frac{1}{10}-6\beta)L & -\frac{6}{5} & (\frac{1}{10}-6\beta)L \\ (\frac{1}{10}-6\beta)L & (\frac{2}{15}+2\beta+48\beta^2)L^2 & -(\frac{1}{10}-6\beta)L & -(\frac{1}{30}+2\beta-24\beta^2)L^2 \\ -\frac{6}{5} & -(\frac{1}{10}-6\beta)L & \frac{6}{5} & -(\frac{1}{10}-6\beta)L \\ (\frac{1}{10}-6\beta)L & -(\frac{1}{30}+2\beta-24\beta^2)L^2 & -(\frac{1}{10}-6\beta)L & (\frac{2}{15}+2\beta+48\beta^2)L^2 \end{bmatrix}$$

Order of Variables: $y_1\ \theta_1\ y_2\ \theta_2$

Notation:

A = cross sectional area, in.^{2}

E = Young's modulus, lbf/in.^{2}

G = shear modulus, lbf/in.^{2}

I = planar moment of inertia, in.^{4}

L = length, in.

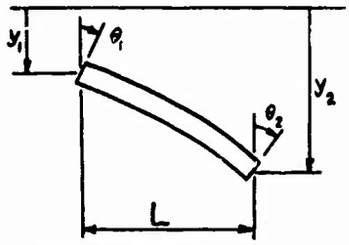
$r_g = (I/A)^{1/2}$, radius of gyration, in.

α = shear form factor, numeric

$\beta = EI\alpha/GAL^2$, numeric

μ = mass per unit length, lbf sec^2/in.^{2}

Coordinate System



Total Mass Matrix $M = M_r + M_t$

Fig. 3(b)

ROTATIONAL MASS ACCORDING TO McCALLEY

reduced stiffness, K_{11}^{*} is

$$K_{11}^{*} = K_{11} - K_{12} K_{22}^{-1} K_{21} \qquad (2)$$

This scheme has worked well before, and it would probably have worked well in this case. However, the 360 time allocation was spent, and the third alternative was necessary.

The third technique (and the one used herein) consists of generating the deflection influence coefficient matrix for the system with shear flexibility included and rotational coordinates eliminated. The inversion of this matrix then produces the reduced system stiffness matrix. The deflection influence coefficient matrix was generated on an IBM 7072 computer, and the plots of the results were good. The inversion failed, however, again because of a zero determinant. The matrix was then condiditoned by pre- and post-multiplying by the inverse square root of its diagonal (as a diagonal matrix) to produce a matrix with unit diagonals and the off-diagonal terms less than unity. This matrix inverted successfully with a product check showing the largest off-diagonal term at 10^{-4}. The inverse was then restored by the same pre- and post-multiplication to produce the reduced system stiffness matrix. When this matrix was multiplied against the original deflection influence coefficient matrix, the largest off-diagonal term was 4×10^{-4}. A higher precision computation might have been better, but the 7072 cannot do this. Since an accuracy of 4 parts in 10,000 is not really poor compared to the accuracy of physical input data, the remainder of the computations were made with this reduced system stiffness matrix.

The eigenvalues and eigenvectors for the various solutions were calculated with a program which used the Given's method of tri-diagonalization, with an upper- and lower-bound trapping of eigenvalues. Eigenvectors are found for the tri-diagonalized matrix, and then restored to the full matrix. The arithmetic is as follows:

Given $\quad -M X \omega^2 + K X = 0 \qquad (3)$

in which

M = mass matrix (diagonal)

K = stiffness matrix

X = displacement vector

ω^2 = matrix of eigenvalues (diagonal)

let $X = M^{-\frac{1}{2}} Y \qquad (4)$

and premultiply by $M^{-\frac{1}{2}}$ to get

$$(M^{-\frac{1}{2}} K M^{-\frac{1}{2}}) Y = Y\omega^2 \qquad (5)$$

This equation is the one for which $(M^{-\frac{1}{2}} K M^{-\frac{1}{2}})$ is tri-diagonalized to solve for Y and ω^2, and then rotated back to the original system coordinates. When this process has been completed, the solution requires that

$$Y^T Y = I \qquad (6)$$

from which

$$X^T M X = I \qquad (7)$$

and

$$X^T K X = \omega^2 \qquad (8)$$

When the mass matrix is not diagonal, as with Archer's and McCalley's versions, the eigenvalue program proceeds as follows:

The mass matrix is first diagonalized by solving the eigenvalue problem

$$MU = IU\lambda^2 \qquad (9)$$

This solution produces U vectors such that

$$U^T U = I \qquad (10)$$

and $\quad U^T M U = \lambda^2 \qquad (11)$

Now eq. (3) is rearranged to give:

$$KX = M X \omega^2 \qquad (12)$$

Let $\quad X = U\lambda^{-1} V \qquad (13)$

and premultiply by U^T to give

$$U^T K U \lambda^{-1} V = U^T M U \lambda^{-1} V \omega^2 \qquad (14)$$

then

$$[U^T K U]\lambda^{-1} V = \lambda V \omega^2$$

Premultiplication by λ^{-1} then gives

$$[\lambda^{-1} U^T K U \lambda^{-1}] V = V \omega^2 \qquad (15)$$

This is the eigenvalue problem again, for which

$$V^T V = I \qquad (16)$$

As a consequence of eq. (16) and (15)

$$V^T \lambda^{-1} U^T K U \lambda^{-1} V = \omega^2 \qquad (17)$$

and eq. (13) reduces this to

$$X^T K X = \omega^2 \qquad (18)$$

Equations (16) with (13) and (11) give

$$X^T M X = V^T V = I \qquad (19)$$

so long as $X = U\lambda^{-1} V \qquad (13)$

The remainder of the computstions consisted of listings of frequencies and their ratios, and mode shapes and their ratios, for the purpose of making comparisons and forming judgements.

A search was made for a theoretical solution against which to compare the results. Timoshenko's solution [7] for the simple beam with shear and rotational inertia is acknowledged to be the first such paper, and numerical values for the frequencies can be found or calculated. The same was not true for the cantilever beam with shear and rotational inertia, because the frequency equation does not reduce to anything tracteble. A numerical solution is no doubt possible, but that would be another study in itself. Consequently, the theoretical frequencies for a cantilever beam without shear and rotational inertia were calculated, and they appear in the tabulations of results as the theoretical frequencies.

V RESULTS AND DISCUSSION

The object of the calculations was to be able to compare the various frequencies with each other, and also the various mode shapes. The frequency comparison can be done in one table of reasonable size, but the comparison of 4 sets of mode shapes at 40 x 40 each and 3 at 20 x 20 each would need a sizeable publication all by itself. The full mode shape sets are available, and can be supplied to anyone needing to examine them in detail. Only selected sample sets are included in this paper in the interest of conserving space.

Table 3 lists the normal mode frequencies for each of the seven cases solved. These frequencies were also plotted (semi-logarithmically), and the plots showed that the theoretical frequencies and the ones found with McCalley's mass were smooth curves. For the cases with both linear and rotational coordinates, the frequencies found with the other masses showed a jump in the curve at the 19th to 21st mode. This jump is quite noticeable in the tabulated data, as is the smoothness of the frequencies from McCalley's mass. The frequency plots for the solutions with only translational coordinates were all smooth, and this is easily seen in the tabulated data. One could argue that the jumps in the frequencies are a result of the rotational mass inertias not being included properly, but the author contends that after about mode 6, the solutions have no physical meaning in any case. This point is further argued below.

In order to have a basis for comparison, the frequencies calculated with McCalley's mass were divided into the other frequencies, with the results listed in Table 4. An examination of both Tables 3 and 4 can produce any of several mode numbers as the limit of agreement, according to the tolerance allowed. A more significant observation, however, is that mode 5 from the linear-only solutions is lower in frequency than mode 4 of the linear-plus-rotation solutions. Similarly, mode 9 is less than 6, mode 12 is less than mode 7, and mode 20 is less than mode 9. Whichever kind of solution is taken as correct, the linear-only solutions have produced a significantly lower set of frequencies than the linear-plus-rotation solutions did. This would affect shock response calculations since they contain a factor of 1/frequency.

It is interesting to note that if one sums the frequencies for each case through modes 5 and 6, the result is:

	sum through 5	sum through 6
THEOR	1944	3367
RMM	1714	2845
ARCH	1769	2970
MCCY	1746	2926
RMOD	1725	2867
RMMLIN	1080	1664
ARCHLIN	1142	1777
MCCYLIN	1136	1762

On this basis, there is little reason to argue for or against any particular method, except that the linear-only cases all seem far out of line with the others.

With regard to the mode shapes, a theoretical solution was not feasible within the scope of this investigation, so the mode shapes found with McCalley's mass were used for a base. Table 5(a) lists the linear coordinates for the first 8 modes with McCalley's mass, and Table 5(b) lists the rotational coordinates for the same 8 modes. It is the author's contention that at least three coordinates are needed in each loop of a mode to define it properly. Examination of Table 5 shows that mode 6 clearly satisfies this requirement, while modes 7 and 8 do not (and the higher modes were progressively worse, of course).

In order to form some basis for comparison of modes the following scheme was used:

$$\text{AVG.MODE RATIO}=\left[\Sigma\frac{\text{MODE COORDINATE}}{\text{MCCY COORDINATE}}\right]\div[\text{NO.OF COORD.}] \qquad (20)$$

When this calculation was made, the resulting numbers conveyed the same impression of relative quality that a study of the detailed mode ratios produced. The mode details are available and can be supplied if needed for study, but in the interest of conciseness, only the average mode ratios are given herein.

Table 6 lists these average mode ratios as defined by eq. (20) for the first 12 modes The column heading code translates as:

LRMM=linear coordinates, RMM mass, 40x40

LARC=linear coordinates, ARCH mass, 40x40

LRMD=linear coordinates, RMMOD mass, 40x40

MCC =linear coordinates, MCCY mass, 40x40

RMML=linear coordinates, RMLIN mass, 20x20

ARCL=linear coordinates, ARCHLIN mass, 20x20

MCCL=linear coordinates, MCCYLIN mass, 20x20

RRMM=rotational coordinates, RMM mass, 40x40

RARC=rotational coordinates, ARCH mass, 40x40

RRMD=rotational coordinates, RMMOD mass, 40x40

MCCR=rotational coordinates, MCCY mass, 40x40

The first three columns show good agreement (number near 1.0) for modes 1,2,4,5, with mode 3 off for each. Columns 4 and 5 show their best agreement in modes 1 and 2, with poor agreement elsewhere. The last three columns show the best agreement of all for modes 1 through 6 except mode 5. It is of interest to note the signs of the average mode ratios. A negative sign means that the mode happened (by chance) to come out of the eigenvector routine with signs opposite to the reference mode. This is a normal fact of life since all normal modes are subject to an arbitrary multiplier of ± 1.

If the conclusion had been reached, on the basis of frequency comparisons, that the first 6 modes were valid for the 40x40 cases, for any of the mass schemes, how would the comparisons of Table 6 modify that conclusion? If it is recalled that usually a dynamic analysis is carried to a *stress answer*, and that the *stresses depend* directly upon the *relative deformations* of the ends of the element, one must conclude that *the details of the mode shape are critical*. Indeed, seemingly minor variations in the mode shapes make important differences in the stresses calculated therefrom. Direct supporting evidence for this statement is not yet available in terms of the set of solutions herein reported. The statement is therefore made on the basis of opinion, with the full intent to support it later by translating these mode shapes into stresses and making similar comparisons.

In order that checks or comparisons can be made by the reader, the deflection influence coefficient matrix for linear coordinates only is given in Table 7.

LIST OF REFERENCES

1. Mallett, Robert H. and Marcal, Pedro V., "Finite Element Analysis of Non-Linear Structures," Jour. of Struct. Div., ASCE, v 94,ST9, Sept. 1968.

2. Zienkiewicz, O.C. and Cheung, Y.K., *The Finite Element in Structural and Continuum Mechanics*, McGraw Hill, 1967.

3. Special Summer Program - "Finite Element Methods in Solid Mechanics," Mass. Inst. of Tech., June 1968.

4. Archer, John S., "Consistent Mass Matrix for Distributed Mass Systems," Jour. of Struct. Div., ASCE, v 89, ST4, Aug. 1963.

5. McCalley, Robert B., Jr., "Mass Matrix for a Prismatic Beam Segment," Rept. no. KAPL-M-6913, Knolls Atomic Power Lab, General Electric Co., Schenectady, N.Y., Mar. 1968.

6. Maine, R.M., "The Practical Problems of Generating Large Stiffness or Flexibility Matrices," ASME paper no. 63WA268, Nov. 1963.

7. Timoshenko, S.P., "On the Correction for Shear of the Differential Equation for Transverse Vibration of Prismatic Bars," Phil. Mag. v 41, p 744, 1921.

TABLE 1. NUMERICAL VALUES OF STIFFNESS FOR ELEMENTS

	1	2	3	4	
1	0.28861E 07	0.86583E 07	-0.28861E 07	0.86583E 07	Y_1
2	0.86583E 07	0.91850E 08	-0.86583E 07	-0.39900E 08	ϕ_1
3	-0.28861E 07	-0.86583E 07	0.28861E 07	-0.86583E 07	Y_2
4	0.86583E 07	-0.39900E 08	-0.86583E 07	0.91850E 08	ϕ_2

TABLE 2. NUMERICAL VALUES OF MASS FOR ELEMENTS

(A) ACCORDING TO AUTHOR'S USUAL PRACTICE

	1	2	3	4
1	0.63788E-02	0.00000E 00	0.00000E 00	0.00000E 00
2	0.00000E 00	0.24319E-01	0.00000E 00	0.00000E 00
3	0.00000E 00	0.00000E 00	0.63788E-02	0.00000E 00
4	0.00000E 00	0.00000E 00	0.00000E 00	0.24319E-01

(B) ACCORDING TO ARCHER

	1	2	3	4
1	0.47385E-02	0.40095E-02	0.16403E-02	-0.23693E-02
2	0.40095E-02	0.43740E-02	0.23693E-02	-0.32805E-02
3	0.16403E-02	0.23693E-02	0.47385E-02	-0.40095E-02
4	-0.23693E-02	-0.32805E-02	-0.40095E-02	0.43740E-02

(C) AUTHOR'S PRACTICE MODIFIED TO PRODUCE McCALLEY FREQUENCIES

	1	2	3	4
1	0.63788E-02	0.00000E 00	0.00000E 00	0.00000E 00
2	0.00000E 00	0.13176E-01	0.00000E 00	0.00000E 00
3	0.00000E 00	0.00000E 00	0.63788E-02	0.00000E 00
4	0.00000E 00	0.00000E 00	0.00000E 00	0.13176E-01

(Table II continues)

(Table II continued)

(D) McCALLEY TRANSLATIONAL MASS

	1	2	3	4	
1	0.43095E-02	0.32764E-02	0.20693E-02	-0.31024E-02	Y_1
2	0.32764E-02	0.38367E-02	0.31024E-02	-0.38178E-02	θ_1
3	0.20693E-02	0.31024E-02	0.43095E-02	-0.32764E-02	Y_2
4	-0.31024E-02	-0.38178E-02	-0.32764E-02	0.38367E-02	θ_2

(E) McCALLEY ROTATIONAL MASS

	1	2	3	4
1	0.28008E-04	-0.44871E-03	-0.28008E-04	-0.44871E-03
2	-0.44871E-03	0.13268E-01	0.44871E-03	0.51621E-02
3	-0.28008E-04	0.44871E-03	0.28008E-04	0.44871E-03
4	-0.44871E-03	0.51621E-02	0.44871E-03	0.13268E-01

(F) SUM OF (D) AND (E)

	1	2	3	4
1	0.43375E-02	0.28277E-02	0.20413E-02	-0.35511E-02
2	0.28277E-02	0.17105E-01	0.35511E-02	0.13442E-02
3	0.20413E-02	0.35511E-02	0.43375E-02	-0.28277E-02
4	-0.35511E-02	0.13442E-02	-0.28277E-02	0.17105E-01

TABLE 3. LIST OF NATURAL FREQUENCIES

	THEOR FREQ	AMM FREQ	ARCH FREQ	MCCY FREQ	AHMOD FREQ	AMLIN FREQ	ARCHLIN FR	MCCYLIN FR	
1	0.16753E 02	0.16676E 02	0.16920E 02	0.16700E 02	0.16673E 02	0.15427E 02	0.16247E 02	0.16260E 02	1
2	0.10500E 03	0.10192E 03	0.10292E 03	0.10235E 03	0.10211E 03	0.83754E 02	0.87440E 02	0.87345E 02	2
3	0.29402E 03	0.27536E 03	0.27998E 03	0.27757E 03	0.27643E 03	0.19823E 03	0.20736E 03	0.20682E 03	3
4	0.57611E 03	0.51464E 03	0.52909E 03	0.52242E 03	0.51784E 03	0.32583E 03	0.34343E 03	0.34173E 03	4
5	0.95238E 03	0.80501E 03	0.83986E 03	0.82648E 03	0.81170E 03	0.45451E 03	0.48735E 03	0.48337E 03	5
6	0.14227E 04	0.11314E 04	0.12014E 04	0.11803E 04	0.11426E 04	0.58432E 03	0.63471E 03	0.62692E 03	6
7	0.19871E 04	0.14806E 04	0.16037E 04	0.15761E 04	0.14968E 04	0.70717E 03	0.78489E 03	0.77129E 03	7
8	0.26455E 04	0.18416E 04	0.20377E 04	0.20077E 04	0.18626E 04	0.82397E 03	0.93816E 03	0.91623E 03	8
9	0.33980E 04	0.22050E 04	0.24938E 04	0.24697E 04	0.22300E 04	0.93419E 03	0.10952E 04	0.10618E 04	9
10	0.42445E 04	0.25630E 04	0.29605E 04	0.29555E 04	0.25908E 04	0.10374E 04	0.12564E 04	0.12078E 04	10
11	0.51852E 04	0.29089E 04	0.34153E 04	0.34496E 04	0.29379E 04	0.11332E 04	0.14221E 04	0.13537E 04	11
12	0.62199E 04	0.32370E 04	0.38176E 04	0.38886E 04	0.32657E 04	0.12213E 04	0.15918E 04	0.14986E 04	12
13	0.73486E 04	0.35424E 04	0.41980E 04	0.42476E 04	0.35692E 04	0.13012E 04	0.17643E 04	0.16410E 04	13
14	0.85714E 04	0.38209E 04	0.46396E 04	0.47303E 04	0.38446E 04	0.13727E 04	0.19374E 04	0.17786E 04	14
15	0.98883E 04	0.40690E 04	0.51133E 04	0.52993E 04	0.40887E 04	0.14353E 04	0.21074E 04	0.19083E 04	15
16	0.11299E 05	0.42837E 04	0.55786E 04	0.58943E 04	0.42988E 04	0.14888E 04	0.22687E 04	0.20265E 04	16
17	0.12804E 05	0.44626E 04	0.60072E 04	0.64861E 04	0.44731E 04	0.15330E 04	0.24142E 04	0.21200E 04	17
18	0.14403E 05	0.46037E 04	0.63720E 04	0.70426E 04	0.46100E 04	0.15676E 04	0.25352E 04	0.22114E 04	18
19	0.16096E 05	0.47055E 04	0.66472E 04	0.75192E 04	0.47085E 04	0.15924E 04	0.26234E 04	0.22701E 04	19
20	0.17884E 05	0.47671E 04	0.68145E 04	0.78552E 04	0.47678E 04	0.16074E 04	0.26730E 04	0.23034E 04	20
21	0.19765E 05	0.73948E 04	0.20966E 05	0.85160E 04	0.10035E 05				
22	0.21740E 05	0.79078E 04	0.21242E 05	0.87221E 04	0.10162E 05				
23	0.23809E 05	0.76859E 04	0.21720E 05	0.90502E 04	0.10372E 05				
24	0.25973E 05	0.79172E 04	0.22360E 05	0.94472E 04	0.10657E 05				
25	0.28230E 05	0.81899E 04	0.23183E 05	0.10021E 05	0.11006E 05				
26	0.30582E 05	0.84925E 04	0.24090E 05	0.10645E 05	0.11404E 05				
27	0.33028E 05	0.88145E 04	0.25065E 05	0.11343E 05	0.11839E 05				
28	0.35567E 05	0.91463E 04	0.26076E 05	0.12094E 05	0.12285E 05				
29	0.38201E 05	0.94793E 04	0.27101E 05	0.12865E 05	0.12743E 05				
30	0.40929E 05	0.98058E 04	0.28123E 05	0.13604E 05	0.13195E 05				
31	0.43751E 05	0.10119E 05	0.29129E 05	0.14214E 05	0.13634E 05				
32	0.46667E 05	0.10415E 05	0.30105E 05	0.14578E 05	0.14050E 05				
33	0.49677E 05	0.10687E 05	0.31036E 05	0.14746E 05	0.14436E 05				
34	0.52781E 05	0.10933E 05	0.31903E 05	0.14693E 05	0.14787E 05				
35	0.55979E 05	0.11149E 05	0.32686E 05	0.15181E 05	0.15097E 05				
36	0.59271E 05	0.11333E 05	0.33367E 05	0.15544E 05	0.15361E 05				
37	0.62657E 05	0.11482E 05	0.33926E 05	0.15577E 05	0.15577E 05				
38	0.66137E 05	0.11595E 05	0.34343E 05	0.15[illegible]E 05	0.15741E 05				
39	0.69712E 05	0.11671E 05	0.34602E 05	0.15[illegible]E 05	0.15852E 05				
40	0.73380E 05	0.11710E 05	0.34830E 05	0.16531E 05	0.15908E 05				
	7	9	10	11	12	13	50	14	

TABLE 4. LIST OF RATIOS OF FREQUENCIES

	THEOR/MCCV	RMM /MCCV	ARCH/MCCV	MCCV/MCCV	RMOO/MCCV	RMLN/MCCV	ARCL/MCCV	MCCL/MCCV	
1	0.10032E 01	0.99656E 00	0.10132E 01	0.10000E 01	0.99838E 00	0.95492E 00	0.99920E 00	0.10000E 01	1
2	0.10259E 01	0.99580E 00	0.10056E 01	0.10000E 01	0.99766E 00	0.95889E 00	0.10001E 01	0.10000E 01	2
3	0.10593E 01	0.99204E 00	0.10087E 01	0.10000E 01	0.99589E 00	0.95847E 00	0.10026E 01	0.10000E 01	3
4	0.11029E 01	0.98511E 00	0.10128E 01	0.10000E 01	0.99123E 00	0.95347E 00	0.10050E 01	0.10000E 01	4
5	0.11523E 01	0.97402E 00	0.10162E 01	0.10000E 01	0.98212E 00	0.94443E 00	0.10082E 01	0.10000E 01	5
6	0.12054E 01	0.95857E 00	0.10179E 01	0.10000E 01	0.96806E 00	0.93205E 00	0.10124E 01	0.10000E 01	6
7	0.12607E 01	0.93941E 00	0.10175E 01	0.10000E 01	0.94969E 00	0.91687E 00	0.10176E 01	0.10000E 01	7
8	0.13177E 01	0.91727E 00	0.10149E 01	0.10000E 01	0.92773E 00	0.89930E 00	0.10239E 01	0.10000E 01	8
9	0.13759E 01	0.89282E 00	0.10098E 01	0.10000E 01	0.90294E 00	0.87982E 00	0.10315E 01	0.10000E 01	9
10	0.14362E 01	0.86720E 00	0.10017E 01	0.10000E 01	0.87660E 00	0.85892E 00	0.10402E 01	0.10000E 01	10
11	0.15031E 01	0.84326E 00	0.99006E 00	0.10000E 01	0.85166E 00	0.83711E 00	0.10505E 01	0.10000E 01	11
12	0.15995E 01	0.83243E 00	0.98174E 00	0.10000E 01	0.83981E 00	0.82496E 00	0.10622E 01	0.10000E 01	12
13	0.17301E 01	0.83398E 00	0.98832E 00	0.10000E 01	0.84029E 00	0.79293E 00	0.10751E 01	0.10000E 01	13
14	0.18120E 01	0.80775E 00	0.98083E 00	0.10000E 01	0.81276E 00	0.77179E 00	0.10893E 01	0.10000E 01	14
15	0.18660E 01	0.76784E 00	0.96490E 00	0.10000E 01	0.77155E 00	0.75214E 00	0.11043E 01	0.10000E 01	15
16	0.19170E 01	0.72675E 00	0.94644E 00	0.10000E 01	0.72931E 00	0.73467E 00	0.11195E 01	0.10000E 01	16
17	0.19741E 01	0.68803E 00	0.92617E 00	0.10000E 01	0.68964E 00	0.72006E 00	0.11340E 01	0.10000E 01	17
18	0.20452E 01	0.65369E 00	0.90478E 00	0.10000E 01	0.65459E 00	0.70887E 00	0.11464E 01	0.10000E 01	18
19	0.21407E 01	0.62580E 00	0.88403E 00	0.10000E 01	0.62620E 00	0.70147E 00	0.11556E 01	0.10000E 01	19
20	0.22767E 01	0.60687E 00	0.86751E 00	0.10000E 01	0.60696E 00	0.69784E 00	0.11605E 01	0.10000E 01	20
21	0.23209E 01	0.86834E 00	0.24620E 01	0.10000E 01	0.11784E 01				
22	0.24925E 01	0.86078E 00	0.24354E 01	0.10000E 01	0.11651E 01				
23	0.26308E 01	0.84925E 00	0.23999E 01	0.10000E 01	0.11461E 01				
24	0.27377E 01	0.83451E 00	0.23590E 01	0.10000E 01	0.11233E 01				
25	0.28171E 01	0.81727E 00	0.23134E 01	0.10000E 01	0.10983E 01				
26	0.28729E 01	0.79779E 00	0.22630E 01	0.10000E 01	0.10713E 01				
27	0.29117E 01	0.77709E 00	0.22097E 01	0.10000E 01	0.10434E 01				
28	0.29409E 01	0.75627E 00	0.21561E 01	0.10000E 01	0.10158E 01				
29	0.29694E 01	0.73683E 00	0.21066E 01	0.10000E 01	0.99052E 00				
30	0.30086E 01	0.72080E 00	0.20673E 01	0.10000E 01	0.96994E 00				
31	0.30780E 01	0.71190E 00	0.20493E 01	0.10000E 01	0.95920E 00				
32	0.32012E 01	0.71443E 00	0.20651E 01	0.10000E 01	0.96378E 00				
33	0.33688E 01	0.72474E 00	0.21047E 01	0.10000E 01	0.97898E 00				
34	0.35203E 01	0.72921E 00	0.21279E 01	0.10000E 01	0.98626E 00				
35	0.36874E 01	0.73440E 00	0.21531E 01	0.10000E 01	0.99447E 00				
36	0.38385E 01	0.73396E 00	0.21609E 01	0.10000E 01	0.99482E 00				
37	0.40224E 01	0.73711E 00	0.21780E 01	0.10000E 01	0.10000E 01				
38	0.41904E 01	0.73465E 00	0.21759E 01	0.10000E 01	0.99734E 00				
39	0.44038E 01	0.73727E 00	0.21858E 01	0.10000E 01	0.10014E 01				
40	0.44389E 01	0.70837E 00	0.33180E 01	0.10000E 01	0.96231E 00				
	15	16	17	18	19	20	22	21	

TABLE 5. SAMPLE MODAL MATRIX (LOWEST 8 MODES)

(A) LINEAR COORDINATES

	1	2	3	4	5	6	7	8
1	0.18192E-01	0.12212E 00	0.34521E 00	0.64978E 00	-0.98821E 00	-0.13226E 01	0.16462E 01	-0.19860E 01
2	0.68566E-01	0.40094E 00	0.10110E 01	0.17032E 01	-0.23268E 01	-0.27906E 01	0.30807E 01	-0.32209E 01
3	0.14874E 00	0.78657E 00	0.17824E 01	0.26257E 01	-0.30244E 01	-0.28938E 01	0.23092E 01	-0.14123E 01
4	0.25635E 00	0.12301E 01	0.24626E 01	0.29997E 01	-0.25252E 01	-0.12234E 01	-0.41487E 00	0.18834E 01
5	0.34902E 00	0.16847E 01	0.28948E 01	0.26311E 01	-0.95326E 00	0.11788E 01	-0.26227E 01	0.27132E 01
6	0.54440E 00	0.21073E 01	0.29766E 01	0.15751E 01	0.10014E 01	0.26969E 01	-0.22638E 01	0.10968E 00
7	0.72019E 00	0.24595E 01	0.26707E 01	0.10791E 00	0.24424E 01	0.23014E 01	0.28849E 00	-0.26526E 01
8	0.91411E 00	0.27092E 01	0.20065E 01	-0.13628E 01	0.27024E 01	0.78363E 00	0.25759E 01	-0.21177E 01
9	0.11239E 01	0.28315E 01	0.10735E 01	-0.24211E 01	0.16670E 01	-0.19392E 01	0.24013E 01	0.10531E 01
10	0.13479E 01	0.28096E 01	0.67369E-02	-0.27672E 01	-0.16787E 00	-0.28104E 01	-0.70608E-01	0.29096E 01
11	0.15828E 01	0.24349E 01	-0.10351E 01	-0.23071E 01	-0.19295E 01	-0.17186E 01	-0.24728E 01	0.11389E 01
12	0.18277E 01	0.23072E 01	-0.18931E 01	-0.11816E 01	-0.27825E 01	0.57606E 00	-0.25037E 01	-0.20504E 01
13	0.20806E 01	0.18340E 01	-0.24323E 01	0.72783E 00	-0.23260E 01	0.24748E 01	-0.13145E 00	-0.26805E 01
14	0.23397E 01	0.12297E 01	-0.25612E 01	0.16201E 01	-0.78536E 00	0.26585E 01	0.23768E 01	0.38553E-01
15	0.26033E 01	0.51431E 00	-0.22435E 01	0.24483E 01	0.10911E 01	0.10131E 01	0.26302E 01	0.27275E 01
16	0.28703E 01	-0.28859E 00	-0.15022E 01	0.24846E 01	0.23816E 01	-0.12836E 01	0.41180E 00	0.20578E 01
17	0.31394E 01	-0.11533E 01	-0.41169E 00	0.16659E 01	0.24165E 01	-0.25696E 01	-0.20973E 01	-0.10811E 01
18	0.34096E 01	-0.20170E 01	0.91804E 00	0.14882E 00	0.10745E 01	-0.18302E 01	-0.23708E 01	-0.26503E 01
19	0.36803E 01	-0.29769E 01	0.23659E 01	-0.17669E 01	-0.11999E 01	0.65378E 00	0.12099E 00	-0.40170E 00
20	0.39510E 01	-0.39582E 01	0.38290E 01	-0.37517E 01	-0.36816E 01	0.36233E 01	0.35755E 01	0.35370E 01

(B) ROTATIONAL COORDINATES

	1	2	3	4	5	6	7	8
1	0.55618E-02	0.30253E-01	0.71065E-01	0.11081E 00	-0.13987E 00	-0.15504E 00	0.15846E 00	-0.15352E 00
2	0.10727E-01	0.52254E-01	0.10732E 00	0.13786E 00	-0.13013E 00	-0.87130E-01	0.20778E-01	0.58364E-01
3	0.15497E-01	0.66084E-01	0.11032E 00	0.90638E-01	-0.42058E-02	0.11961E 00	-0.24267E 00	0.33693E 00
4	0.19873E-01	0.72020E-01	0.84890E-01	-0.40296E-02	0.15437E 00	0.28408E 00	-0.32756E 00	0.26521E 00
5	0.23856E-01	0.70544E-01	0.38586E-01	-0.11031E 00	0.25628E 00	0.27053E 00	-0.12339E 00	-0.10629E 00
6	0.27451E-01	0.62357E-01	-0.19030E-01	-0.19225E 00	0.24552E 00	0.78120E-01	0.18764E 00	-0.33280E 00
7	0.30665E-01	0.48372E-01	-0.77466E-01	-0.22296E 00	0.12304E 00	-0.16385E 00	0.31376E 00	-0.13812E 00
8	0.33505E-01	0.29691E-01	-0.12662E 00	-0.19172E 00	-0.55265E-01	-0.28887E 00	0.13697E 00	0.23118E 00
9	0.35982E-01	0.79620E-02	-0.15813E 00	-0.10658E 00	-0.20600E 00	-0.21082E 00	-0.17206E 00	0.31337E 00
10	0.38108E-01	-0.16678E-01	-0.16648E 00	0.81722E-02	-0.23834E 00	0.15224E-01	-0.31668E 00	0.54408E-02
11	0.39900E-01	-0.41667E-01	-0.14976E 00	0.11928E 00	-0.18799E 00	0.23122E 00	-0.15798E 00	-0.30892E 00
12	0.41375E-01	-0.66091E-01	-0.10980E 00	0.19420E 00	-0.28898E-01	0.28642E 00	0.15238E 00	-0.23773E 00
13	0.42556E-01	-0.88756E-01	-0.51880E-01	0.21061E 00	0.14263E 00	0.14277E 00	0.31766E 00	0.13070E 00
14	0.43448E-01	-0.10866E 00	0.16246E-01	0.16269E 00	0.24390E 00	-0.98273E-01	0.18074E 00	0.33819E 00
15	0.44140E-01	-0.12506E 00	0.85607E-01	0.62619E-01	0.22462E 00	-0.26601E 00	-0.12481E 00	0.12868E 00
16	0.44601E-01	-0.13753E 00	0.14757E 00	-0.63422E-01	0.89911E-01	-0.23854E 00	-0.30091E 00	-0.23067E 00
17	0.44889E-01	-0.14602E 00	0.19537E 00	-0.18368E 00	-0.10364E 00	-0.25464E-01	-0.16718E 00	-0.27800E 00
18	0.45040E-01	-0.15086E 00	0.22554E 00	-0.27139E 00	-0.27771E 00	0.24377E 00	0.17389E 00	0.77844E-01
19	0.45097E-01	-0.15284E 00	0.23890E 00	-0.31427E 00	-0.37467E 00	0.42029E 00	0.45107E 00	0.46769E 00
20	0.45105E-01	-0.15316E 00	0.24121E 00	-0.32234E 00	-0.39452E 00	0.46002E 00	0.52049E 00	0.57781E 00

TABLE 6. AVERAGE RATIO [MODAL MATRIX/COMPARISON MATRIX] EACH MODE

	LRMP/PCC	LARC/MCC	LRMO/MCC	RMPL/MCCL	ARCL/MCCL	RRMM/MCCR	RARC/MCCR	RRMO/MCCR	
1	0.99866E 00	0.99661E 00	0.99898E 00	0.94811E 00	-0.99979E 00	0.99893E 00	0.10008E 01	0.99920E 00	1
2	-0.99438E 00	0.10047E 01	0.99663E 00	-0.96693E 00	-0.99890E 00	-0.99865E 00	0.10035E 01	0.99814E 00	2
3	0.12049E 01	0.84185E 00	-0.11251E 01	-0.11779E 01	-0.10021E 01	0.98765E 00	0.10117E 01	-0.98836E 00	3
4	0.10112E 01	0.98764E 00	-0.10077E 01	0.[illegible]87E 00	0.99505E 00	0.98718E 00	0.10625E 01	-0.10110E 01	4
5	-0.97856E 00	-0.10390E 01	0.99449E 00	-0.[illegible]373E 00	0.98751E 00	-0.84403E 00	-0.93310E 00	0.82778E 00	5
6	-0.92575E 00	-0.10126E 01	0.93426E 00	-0.34697E 00	-0.97001E 00	-0.98016E 00	-0.10121E 01	0.98515E 00	6
7	-0.10934E 01	0.11745E 01	-0.11458E 01	-0.80201E 00	-0.98123E 00	-0.73794E 00	0.94486E 00	-0.75093E 00	7
8	0.68794E 00	-0.12184E 01	0.76198E 00	0.71192E 00	0.97330E 00	0.56845E 00	-0.73216E 00	0.51002E 00	8
9	0.60384E 00	0.78929E 00	-0.56554E 00	0.33992E 01	-0.10511E 01	0.87531E 00	0.94857E 00	-0.85926E 00	9
10	-0.88516E 00	-0.89972E 00	0.86734E 00	-0.19457E 01	0.99581E 00	-0.17591E 01	-0.13916E 01	0.17617E 01	10
11	0.71088E 00	0.96872E 00	-0.72625E 00	0.76186E 00	-0.95266E 00	-0.24508E 00	-0.22034E 00	0.35293E 00	11
12	0.95852E 00	-0.69448E 00	0.93273E 00	0.20891E 01	-0.10138E 01	0.49922E 00	-0.95184E 00	0.51677E 00	12
	61	62	63	64	65	66	67	68	

TABLE 7. DEFLECTION INFLUENCE COEFFICIENT MATRIX-LINEAR ONLY

	1	2	3	4	5	6	7	8
1	0.31916E-05	0.34649E-05	0.37381E-05	0.40114E-05	0.42846E-05	0.45579E-05	0.48311E-05	0.51043E-05
2	0.34649E-05	0.74763E-05	0.85692E-05	0.96622E-05	0.10755E-04	0.11848E-04	0.12941E-04	0.14034E-04
3	0.37381E-05	0.85692E-05	0.13947E-04	0.16406E-04	0.18865E-04	0.21324E-04	0.23784E-04	0.26243E-04
4	0.40114E-05	0.96622E-05	0.16406E-04	0.23696E-04	0.28068E-04	0.32440E-04	0.36812E-04	0.41184E-04
5	0.42846E-05	0.10755E-04	0.18865E-04	0.28068E-04	0.37818E-04	0.44649E-04	0.51480E-04	0.58311E-04
6	0.45579E-05	0.11848E-04	0.21324E-04	0.32440E-04	0.44649E-04	0.57404E-04	0.67241E-04	0.77078E-04
7	0.48311E-05	0.12941E-04	0.23784E-04	0.36812E-04	0.51480E-04	0.67241E-04	0.83548E-04	0.96937E-04
8	0.51043E-05	0.14034E-04	0.26243E-04	0.41184E-04	0.58311E-04	0.77078E-04	0.96937E-04	0.11734E-03
9	0.53776E-05	0.15127E-04	0.28702E-04	0.45556E-04	0.65142E-04	0.86914E-04	0.11033E-03	0.13483E-03
10	0.56508E-05	0.16220E-04	0.31161E-04	0.49928E-04	0.71973E-04	0.96751E-04	0.12371E-03	0.15232E-03
11	0.59241E-05	0.17313E-04	0.33620E-04	0.54300E-04	0.78804E-04	0.10659E-03	0.13710E-03	0.16981E-03
12	0.61973E-05	0.18406E-04	0.36080E-04	0.58672E-04	0.85635E-04	0.11642E-03	0.15049E-03	0.18729E-03
13	0.64706E-05	0.19499E-04	0.38539E-04	0.63043E-04	0.92466E-04	0.12626E-03	0.16388E-03	0.20478E-03
14	0.67438E-05	0.20592E-04	0.40998E-04	0.67415E-04	0.99298E-04	0.13610E-03	0.17727E-03	0.22227E-03
15	0.70171E-05	0.21685E-04	0.43457E-04	0.71787E-04	0.10613E-03	0.14594E-03	0.19066E-03	0.23976E-03
16	0.72903E-05	0.22778E-04	0.45916E-04	0.76159E-04	0.11296E-03	0.15577E-03	0.20405E-03	0.25724E-03
17	0.75635E-05	0.23871E-04	0.48376E-04	0.80531E-04	0.11979E-03	0.16561E-03	0.21744E-03	0.27473E-03
18	0.78368E-05	0.24964E-04	0.50835E-04	0.84903E-04	0.12662E-03	0.17545E-03	0.23083E-03	0.29222E-03
19	0.81100E-05	0.26057E-04	0.53294E-04	0.89275E-04	0.13345E-03	0.18528E-03	0.24422E-03	0.30971E-03
20	0.83833E-05	0.27150E-04	0.55753E-04	0.93647E-04	0.14028E-03	0.19512E-03	0.25760E-03	0.32719E-03

	9	10	11	12	13	14	15	16
1	0.53776E-05	0.56508E-05	0.59241E-05	0.61973E-05	0.64706E-05	0.67438E-05	0.70171E-05	0.72903E-05
2	0.15127E-04	0.16220E-04	0.17313E-04	0.18406E-04	0.19499E-04	0.20592E-04	0.21685E-04	0.22778E-04
3	0.28702E-04	0.31161E-04	0.33620E-04	0.36080E-04	0.38539E-04	0.40998E-04	0.43457E-04	0.45916E-04
4	0.45556E-04	0.49928E-04	0.54300E-04	0.58672E-04	0.63043E-04	0.67415E-04	0.71787E-04	0.76159E-04
5	0.65142E-04	0.71973E-04	0.78804E-04	0.85635E-04	0.92466E-04	0.99298E-04	0.10613E-03	0.11296E-03
6	0.86914E-04	0.96751E-04	0.10659E-03	0.11642E-03	0.12626E-03	0.13610E-03	0.14594E-03	0.15577E-03
7	0.11033E-03	0.12371E-03	0.13710E-03	0.15049E-03	0.16388E-03	0.17727E-03	0.19066E-03	0.20405E-03
8	0.13483E-03	0.15232E-03	0.16981E-03	0.18729E-03	0.20478E-03	0.22227E-03	0.23976E-03	0.25724E-03
9	0.15988E-03	0.18201E-03	0.20415E-03	0.22628E-03	0.24841E-03	0.27055E-03	0.29268E-03	0.31481E-03
10	0.18201E-03	0.21226E-03	0.23958E-03	0.26691E-03	0.29423E-03	0.32155E-03	0.34888E-03	0.37620E-03
11	0.20415E-03	0.23958E-03	0.27556E-03	0.30863E-03	0.34169E-03	0.37475E-03	0.40781E-03	0.44088E-03
12	0.22628E-03	0.26691E-03	0.30863E-03	0.35089E-03	0.39024E-03	0.42958E-03	0.46893E-03	0.50828E-03
13	0.24841E-03	0.29423E-03	0.34169E-03	0.39024E-03	0.43933E-03	0.48551E-03	0.53169E-03	0.57787E-03
14	0.27055E-03	0.32155E-03	0.37475E-03	0.42958E-03	0.48551E-03	0.54199E-03	0.59554E-03	0.64910E-03
15	0.29268E-03	0.34888E-03	0.40781E-03	0.46893E-03	0.53169E-03	0.59554E-03	0.65994E-03	0.72142E-03
16	0.31481E-03	0.37620E-03	0.44088E-03	0.50828E-03	0.57787E-03	0.64910E-03	0.72142E-03	0.79429E-03
17	0.33694E-03	0.40353E-03	0.47394E-03	0.54763E-03	0.62405E-03	0.70265E-03	0.78290E-03	0.86424E-03
18	0.35908E-03	0.43085E-03	0.50700E-03	0.58697E-03	0.67023E-03	0.75621E-03	0.84438E-03	0.93419E-03
19	0.38121E-03	0.45818E-03	0.54006E-03	0.62632E-03	0.71640E-03	0.80977E-03	0.90586E-03	0.10041E-02
20	0.40334E-03	0.48550E-03	0.57313E-03	0.66567E-03	0.76258E-03	0.86332E-03	0.96734E-03	0.10741E-02

	17	18	19	20
1	0.75635E-05	0.78368E-05	0.81100E-05	0.83833E-05
2	0.23871E-04	0.24964E-04	0.26057E-04	0.27150E-04
3	0.48376E-04	0.50835E-04	0.53294E-04	0.55753E-04
4	0.80531E-04	0.84903E-04	0.89275E-04	0.93647E-04
5	0.11479E-03	0.12662E-03	0.13345E-03	0.14028E-03
6	0.16561E-03	0.17545E-03	0.18528E-03	0.19512E-03
7	0.21744E-03	0.23083E-03	0.24422E-03	0.25760E-03
8	0.27473E-03	0.29222E-03	0.30971E-03	0.32719E-03
9	0.33694E-03	0.35906E-03	0.38121E-03	0.40334E-03
10	0.40353E-03	0.43085E-03	0.45818E-03	0.48550E-03
11	0.47394E-03	0.50700E-03	0.54006E-03	0.57313E-03
12	0.54763E-03	0.58697E-03	0.62632E-03	0.66567E-03
13	0.62405E-03	0.67023E-03	0.71640E-03	0.76258E-03
14	0.70265E-03	0.75621E-03	0.80977E-03	0.86332E-03
15	0.78290E-03	0.84438E-03	0.90586E-03	0.96734E-03
16	0.86424E-03	0.93419E-03	0.10041E-02	0.10741E-02
17	0.94613E-03	0.10251E-02	0.11041E-02	0.11830E-02
18	0.10251E-02	0.11165E-02	0.12051E-02	0.12936E-02
19	0.11041E-02	0.12051E-02	0.13066E-02	0.14053E-02
20	0.11830E-02	0.12936E-02	0.14053E-02	0.15175E-02

Voice: You mentioned that there is no accurate solution for the Timoshenko beam. Actually, R.A. Anderson in 1958 in the Journal of Applied Mechanics published a solution for a cantilever beam, simply supported and fixed at two ends. The solution is absolutely accurate in the sense that he has gone to complete energy formulation and by the variational approach he obtained the boundary conditions. When you take into consideration the shear and rotary inertia effects you have to be very careful about the boundary conditions. What Anderson did was to divide the displacement into two parts, one was the shear displacement and the other was the bending displacement. From them in the case of the cantilever beam at the fixed end, the slope due to the shear displacement is not zero, the bending slope is zero. So this will give you a different kind of solution. Recently, in 1968 Kapur published a paper where he obtained a consistent mass matrix dividing a displacement into two different parts, the shear displacement and the bending displacement. The results corroborate the work of Anderson exactly. It would be very interesting if you could look into the solutions obtained by Anderson and Kapur to get a more accurate comparison, because that is much more accurate than what Timoshenko did almost 20 years ago.

Dr. Mains: My lack of search through the literature sufficiently is showing. I thought I had it with Timoshenko's paper but apparently not. I will check it and see how the comparison does come out.

Mr. Bert (University of Oklahoma): I would like to mention that the paper by R.A. Anderson is dated about 1953 and it was exact in the sense that it was a series solution. However, the problem was actually solved in closed form by T.C. Huang – I believe about 1963 or 64. There have been about 20 or 30 papers on the Timoshenko beam equations since Timoshenko's work, so it is one of the manifestations of the information explosion, I believe.

Dr. Mains: Are they in such form that you can translate them into numerical answers?

Mr. Bert: Yes. Huang's work is in very nice form and it is just a question of very simple transcendental equation which depends on the particular boundary conditions. But the problem that you have was for the cantilever boundary conditions so it is in rather simple form to get numerical results. He actually gives some tabulations of it, there are some typographical errors in the paper so you had best work it through carefully following his method because it is exact and in closed form.

MEASUREMENT OF A STRUCTURE'S MODAL EFFECTIVE MASS

G. J. O'Hara* and G. M. Remmers†

An important parameter in the shock design and analysis of response of shipboard equipment is Modal Effective Mass. This paper describes the experimental determination of the modal effective masses of symmetric double cantilever beams when they are suspended by a long cable to simulate a free-free condition. Several special techniques and instrumentation modifications were employed to improve the measurements obtained so that a statistical best fit approach could be applied to find the first three modal effective masses. The partial differential beam equation including shear and rotary inertia was solved for approximate mode shapes by the Second Method of Ritz where advantage was taken of the experimentally determined fixed base natural frequencies. They were used to estimate the values of the first mode's effective mass for comparison with the measured value. The results obtained and reported show consistent agreement well within reasonably expected bounds of experimental and mathematical resolution.

INTRODUCTION

Mechanical shock induced by underwater explosion during combat operations is a vital consideration in design of naval equipment. The Navy's Dynamic Design Analysis Method (DDAM) [1] based upon normal mode theory, is one of the techniques employed for this problem. The DDAM inputs are specified in terms of type of ship, location aboard, direction of shock, equipment classification, and the equipment's fixed base natural frequencies and modal effective masses. The shock design value data has been developed from realistic shock measurements of ship shock trials and other special experiments and tests. Since fixed base frequencies (FBNF) and modal effective mass values directly affect the shock design value prescriptions, efforts have been made to obtain these by measurement.

A paper [2] presented to the 38th Shock and Vibration Symposium described the successful measurement of fixed-base natural frequencies of structures attached to a single non-rigid base. This present paper concerns itself with the experimental determination of the modal effective mass of these same model equipments when they are suspended by long cable to approximate a free-free condition.

DESCRIPTION OF MODAL EFFECTIVE MASS

Consider a structure S which is attached to a vehicle V at one base point as is shown in Fig. 1(a). For simplicity and for the purposes of this paper assume that both undamped structures have only unidirectional motions. We may now ask and answer the question: "Can the structure S be replaced by a set of independent linear single degree of freedom oscillators, as shown in Fig. 1(b), such that by observations at the base point, and/or any point on V, we cannot tell whether S or the oscillators are present?" The answer is, "Yes."

Normal mode theory [3] shows that each such oscillator must have a fixed base frequency corresponding to a fixed base natural frequency of S. In addition, each of the oscillator masses must have a value of

*Naval Research Laboratory, Washington, D.C.
†Now at Naval Ship Research and Development Center, Carderock, Maryland.

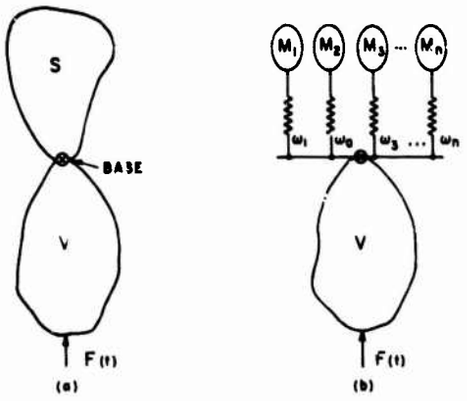


Fig. 1 - (a) Vehicle (V) with structural (S) attached, (b) vehicle with effective mass model of S attached

$$M_a = \frac{\left[\sum_k m_k \bar{X}_{ka}\right]^2}{\sum_k m_k \bar{X}_{ka}^2} \quad . \qquad (1)$$

Then M_a is the modal effective mass in the ath mode of the structure S where the m_k's are the component masses of S, and the $\bar{X}_{ka}$ is the corresponding ath mode shape value.

The net result of this is that the forces transmitted through the base and the motion of the base are identical in both cases, if the set of oscillators is complete. It is of interest to note that the sum of the modal effective masses of S equals the mass of S.

MATHEMATICAL BACKGROUND

Consider the structure S to be in the free-free condition as shown in Fig. 2(a). Then by virtue of the modal mass concept it can be considered to be of the type of Fig. 2(b), when forced and measured at its usual base. In Fig. 2(a) M_n is the nth modal effective mass, ω_m is the mth fixed base natural frequency of S, and M_0 is the local unsprung mass at the base plus the mass acting in ultra high frequency modes which may not be totally accounted for in the model.

In this paper the ratio of force to acceleration (F/A) at the base point will be used as it stands to avoid confusion with terms like "apparent mass," "dynamic mass," and sometimes "effective mass." It should be easily seen, however, that this ratio (F/A) is very closely allied with the ordinary concept of mechanical

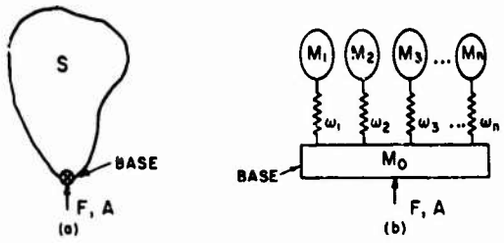


Fig. 2 - Effective mass model of S with unsprung mass

impedance when driving and measuring at only one point.

Mathematical analysis of Fig. 2(b) reveals three forms of the same equation for the F/A ratio at the base.

$$F/A = M_t \frac{\pi\left[1 - \frac{\omega^2}{\omega_r^2}\right]}{\pi\left[1 - \frac{\omega^2}{\omega_a^2}\right]} \quad , \qquad (2a)$$

$$F/A = M_0 \frac{\pi\left[\omega_r^2 - \omega^2\right]}{\pi\left[\omega_a^2 - \omega^2\right]} \quad , \qquad (2b)$$

and

$$F/A = M_0 + \sum_{a=1}^{n} \frac{M_a \omega_a^2}{\omega_a^2 - \omega^2} \quad . \qquad (2c)$$

In these equations, M_t is the total mass of S, M_0 the "base" or local mass, M_a the modal effective mass, $\omega_r]_1^m$ the free-free resonant frequencies, $\omega_a]_1^m$ the fixed-base or antiresonant frequencies, ω is the driving frequency, and M_a the modal effective mass which is to be sought. Therefore Eq. (2c), which is the partial fraction expansion of Eq. (2b), is the equation we shall deal with.

To explore the possibility of finding the first few modal masses for simple structures the same symmetric double cantilever beams from the fixed-base natural frequency experiment [2] were used. They were suspended by a long cable to simulate the free-free condition and their F/A ratios were measured.

As always it is desirable to have an idea as to the magnitudes of the expected values to compare with the experimental results. Therefore the modal effective mass of the first mode

of each beam was calculated using the Second Method of Ritz, where advantage was taken of the previous experimental determination of the fixed base frequencies. The equation for vibration of prismatic bars including shear and rotary inertia is

$$\frac{\partial^4 y}{\partial x^4} + \frac{m}{EI}\frac{\partial^2 y}{\partial x^2} - \frac{\rho}{E}\left(1 + \frac{E}{K'G}\right)\frac{\partial^4 y}{\partial x^2 \partial t^2} + \frac{\rho^2}{K'EG}\frac{\partial^4 y}{\partial t^4} = 0, \tag{3}$$

where

m = mass per unit run,

E = modulus of elasticity,

G = shear modulus,

I = moment of inertia of area,

ρ = mass per unit volume,

K' = shear distortion factor,

y = deflection,

x = distance along beam, and

t = time.

For this study

$$E = 29.6 \times 10^6 \text{ psi},$$

$$K' = 5/6,$$

$$E/K'G = 3.2,$$

$$G = 11.1 \times 10^6 \text{ psi},$$

$$E/G = 8/3.$$

Assuming $y = y(x) \sin \omega t$ yields

$$\frac{d^4 y}{dx^4} - \frac{m\omega^2}{EI} y + \frac{\omega^2 \rho}{E}\left[1 + \frac{E}{K'G}\right]\frac{d^2 y}{dx^2} + \frac{\rho^2 \omega^4}{K'EG} y = 0, \tag{4}$$

where ω is the frequency of vibration which has already been determined [2]. To proceed let

$$y_1 = \phi_b + C\phi_s, \tag{5}$$

where ϕ_b is the first mode shape of a cantilever deflecting by bending, ϕ_s the mode shape of a shear beam, and C a constant for each beam to be found to give the best fit in the sense of Ritz. This approximation for y_1 is substituted for y in the original differential equation; it was multiplied by ϕ_b and then integrated from 0 to ℓ, with the result being set equal to zero. This produced the following equation for C:

$$C = -\frac{\int_0^\ell \left[\phi_b^{iv}\phi_b - \frac{m\omega^2}{EI}\phi_b^2 + \frac{\omega^2\rho}{E}\left[1 + \frac{E}{K'G}\right]\phi_b''\phi_b + \frac{\rho^2\omega^4}{K'EG}\phi_b^2\right] dx}{\int_0^\ell \left[\phi_s^{iv}\phi_b - \frac{m\omega^2}{EI}\phi_s\phi_b + \frac{\omega^2\rho}{E}\left[1 + \frac{E}{K'G}\right]\phi_s^{iv}\phi_b + \frac{\rho^2\omega^4}{K'EG}\phi_s\phi_b\right] dx}. \tag{6}$$

In the actual calculation ℓ was taken to be an effective length, that of the overhanging beam length, plus one third of the clamping distance.

The equation for y_1 was also substituted into Eq. (1) to find the modal effective mass for the first mode. This yielded:

$$M_1 = m \times \frac{\left[\int_0^\ell \phi_b dx\right]^2 + 2C\left[\int_0^\ell \phi_b dx\right]\left[\int_0^\ell \phi_s dx\right] + C^2\left[\int_0^\ell \phi_s dx\right]^2}{\int_0^\ell \phi_b^2 dx + 2C\int_0^\ell \phi_b\phi_s ds + C^2\int_0^\ell \phi_s^2 dx}. \tag{7}$$

Thus a calculated approximate modal effective mass for the first mode of each beam was available for comparison with experimental values.

TEST STRUCTURES AND APPARATUS

Twelve double-cantilever beams were built so that each in turn would represent a different system with several modes of vibration. The dimensions of these steel test specimens were such that each beam weighed approximately 200 lb while the fundamental frequencies varied between 32 and 921 Hz. Thus the frequency range usually considered in shock design was covered while each beam represented a lightweight structure S. The beam lengths varied from 28-1/4 to 92 in. while the thickness varied from 6 to 2 in. All beams were 4 in. wide. Each beam was machined from rectangular bar stock and had bolt holes drilled in the center of the length and 4-in. width. Dimensions and weights of the beams, which are numbered 1 through 12, are given in Table 1.

TABLE 1
Nominal Beam and Clamping Block Specifications

Beam No.	Weight (lb)	Total Length (in.)	Width (in.)	Height (in.)
1	209.75	92	4	2
2	207.5	77.5	4	2.375
3	206.5	66.25	4	2.75
4	207.5	61	4	3
5	209	56.75	4	3.25
6	202	49.5	4	3.625
7	199	44.25	4	4
8	198	39	4	4.5
9	197	37	4	4.75
10	196	35	4	5
11	195.5	31.5	4	5.5
12	190.5	28.25	4	6
Upper clamping block	29.75	9.5	4	3
Lower clamping block	29.75	9.5	4	3

A pair of clamping blocks was attached to each beam's center. These clamping blocks had been attached to these beams when their fixed-base natural frequencies had been determined by another means in earlier experiments [2]. Furthermore they provided a convenient attachment point for the driver, force gage, and accelerometer. The arrangement of the six 1/2 in. diameter bolts, beam, clamping blocks, and the suspension line is shown in Fig. 3.

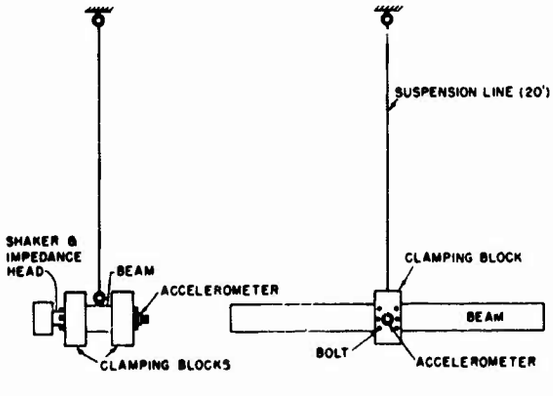


Fig. 3 - Arrangement of beam specimen, suspension, shaker, impedance head, and external accelerometer

Sinusoidal force was applied to one clamping block with a Wilcoxon Model F-4 electrodynamic shaker. This exciting force from the shaker was transmitted to the specimen through a Wilcoxon Model 820 mobility head. The force was measured by the head's force transducer. The acceleration was measured on the opposite clamping block with a Wilcoxon Model 720 accelerometer.

The accelerometer contained in the mobility head was not used for these experiments because of limitations imposed by the local stiffness of the surface being driven as well as the stiffness of the impedance head [4]. With 200-lb steel specimen the useful range goes up to the neighborhood of about 400 Hz. By measuring the beam center's acceleration with the accelerometer on the clamping block opposite the driven one, local stiffness effects at the driving point were reduced and the useful data range was extended to about 1k Hz.

General requirements of the electronic apparatus were to generate sinusoidal current to drive the shaker over the required range (10 to 1000 Hz), detect wide variations in acceleration signal levels, filter each signal through a narrow band-pass, and compute the ratio of the force to acceleration. It was desirable that all these functions be performed synchronously while under the control of a single local oscillator. Commercially available dual channel wave analyzing and recording systems that meet these requirements are made specifically for mobility/impedance measurements of this type.

In these experiments an early model Ad-Yu Type 1010 mechanical mobility plotting system was used. Several modifications were made prior to these tests, and one during these tests. The most noteworthy prior modification was the addition of a frequency synthesizer for use as an optional local oscillator. It not only allowed the driving frequency to be controlled better than 0.1 Hz, but its stable characteristics allowed a more accurate mixer balance adjustment, provided a more stable driving frequency, and more accurate tracking by the filters. The original devices which produced a dc-voltage proportional to the logarithm of each signal magnitude were replaced with devices of NRL design. A summing circuit was added so the ratio of force signal magnitude to acceleration signal magnitude could be plotted on the phase recorder. Thus with a digital voltmeter in parallel with the ratio magnitude plotter, the recording system as used for the first six beams was capable of either continuous sweep or intermittent digital operation. The circuit

block diagram is shown in Fig. 4. Earlier modal effective mass measurements with this system were published in Ref. [5].

Midway in the series of tests this system was modified so as to convert it to intermittent digital operation only. The accuracy of the F/A ratio was improved by substituting decade attenuators (calibrated in steps of 0.1 db) in place of the log potentiometers. These attenuators were adjusted by hand until the output of each crystal filter was the same reference value. In this manner the summer, the ratio plotter, the digital voltmeter, and the detector and servo of the recorders were eliminated. The ratios were found from the db values of the settings of the attenuators when both outputs were the same. This modified circuit is shown in Fig. 5.

PROCEDURE

After aligning the beam and clamping blocks to form a symmetric double cantilever configuration, the 1/2-in. diameter bolts were torqued to 40 lb-ft except for the middle bolt in each row of three. They were torqued to only 35 lb-ft because parts of their heads were cut away to make room for the mobility head. A 3/8-16 stud attached the external accelerometer inside the array of bolt heads to the far clamping block while another 3/8-16 stud similarly attached the head and driver to the near clamping block.

Electronic components were adjusted during preliminary observations on the frequency spectrum. Figure 6 shows traces of automatic plots obtained by sweeping first Beam 1 and then a 200-lb calibration block. The frequencies of the peaks of the F/A ratio (indicating the FBNF) were carefully determined. Fifty suitable data frequencies were then chosen on the positive (F and A in phase) portions of the ratio plots. These data frequencies were chosen so that the well behaved portions of the F/A plot preceding each FBNF was represented. More data points were allocated to the lower frequencies.

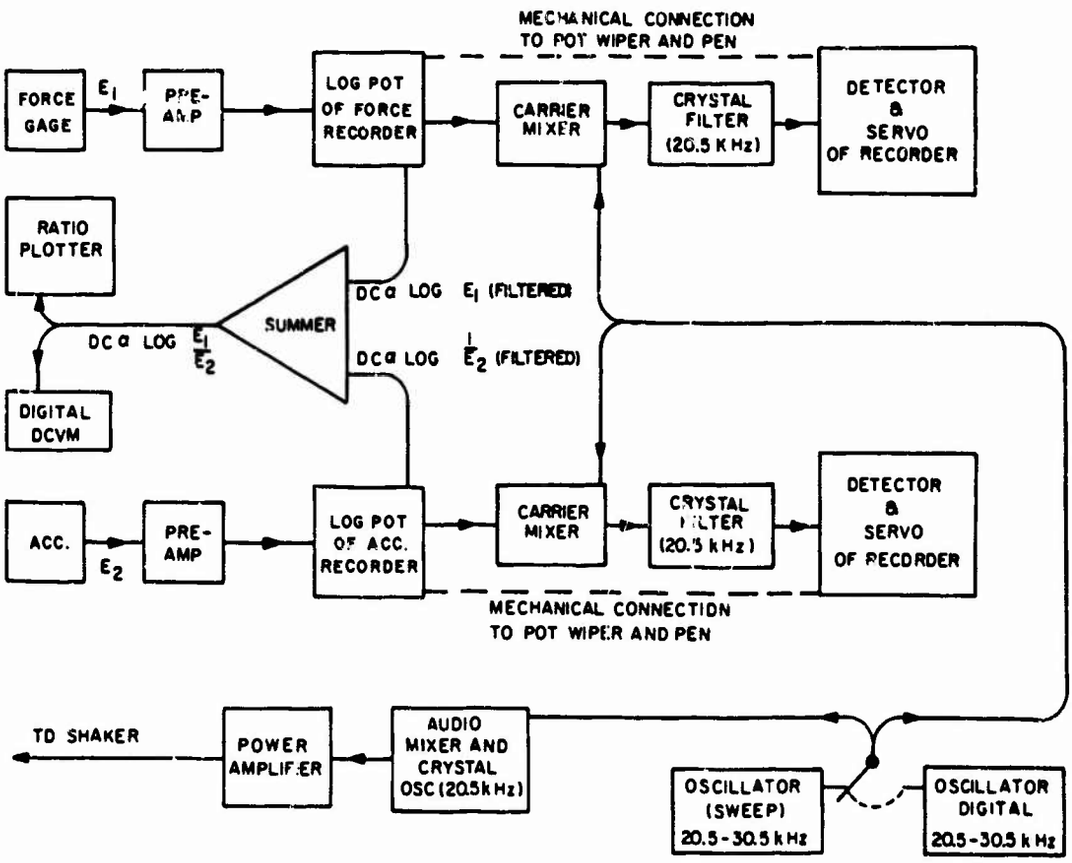


Fig. 4 - Block diagram of recording system

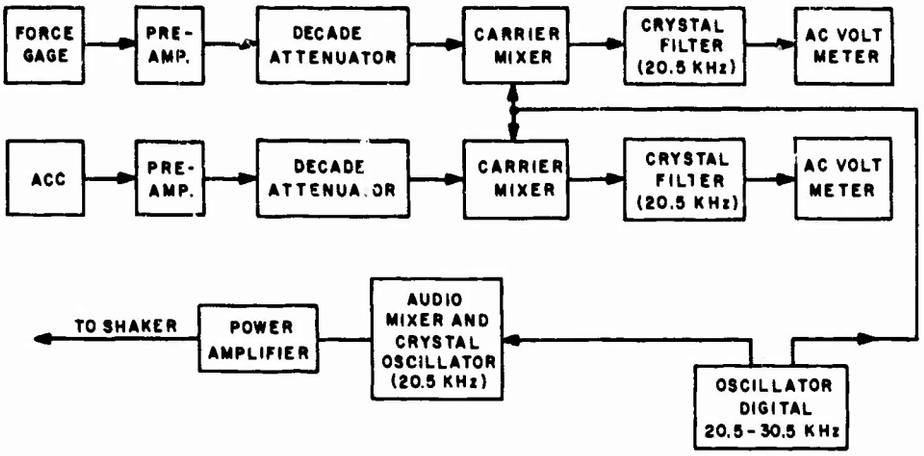


Fig. 5 - Block diagram of modified recording system

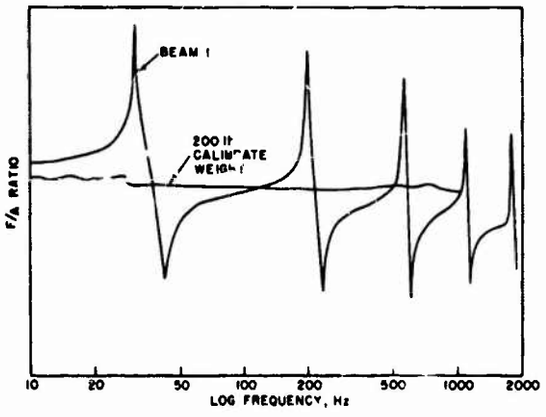


Fig. 6 - Sample of automatically obtained data, used to decide where accurate points to be measured

After recording the ratio values of the test specimen in terms of the db settings of the attenuators (force signal level in db minus the acceleration signal level in db) the shaker, mobility head, and external accelerometer were again affixed to a suspended solid steel cylinder. The F/A ratios in db for the same frequencies were recorded for the 200-lb weight while maintaining the same gains in the system. In this manner the db values representing the beam could be compared with those db values of the calibration weight and a direct value of each beam's F/A × g in db relative to 200 lb was recorded for computation. A digital computer program used these data points to find a least squares "best" fit of modal masses for the 50 points of F/A and the FBNF. The program printed out the static weight of the specimens as measured by the F/A data; also it computed the residual or unsprung weight, that of the clamping blocks bolts, and the higher modes whose frequencies were not determined.

RESULTS

Table 2 presents the averaged results of this experiment. Note that the experimentally determined modal effective weights agree well with the approximate calculations except in the case of Beam 12 which is the shortest stiffest beam with a fundamental fixed base frequency of 921.4 Hz.

Figure 7 is a plot of the ratio of the measured to the calculated first mode weight for each of the three separate runs used. Each run is denoted by an X. The encircled points connected by straight lines (for clarity) show the average values which were used in Table 2. There are two auxiliary scales on the graph. That on the abscissa associates the frequency with the fundamental fixed base frequency of

TABLE 2
Measured Values of Modal Effective Weights for Twelve Different Beam Specimens with Scale Weights and Calculated First Mode Weights for Comparison

Frequency of First Mode (Hz)	Value of Ritz "C"	Beam No.	Effective Weight in First Mode		Weight in		Residual Weight	Static Weight	
			Measured	Calculated	Second Mode	Third Mode		Experimental	Scale
32.1	—	1	128.1	126.1	39.0	13.7	100.5	281.3	273.1
55.3	0.018462	2	127.0	126.4	39.6	19.4	90.0	276.0	271.6
84.9	0.044616	3	124.9	125.6	38.4	17.2	92.6	273.1	270.7
108.1	0.080850	4	126.9	127.0	43.9	21.1	104.6	296.6	271.3
135.5	0.092104	5	130.1	128.2	36.0	—	113.4	279.5	272.5
197.4	0.217933	6	137.2	127.5	69.6	—	85.9	292.7	265.8
197.4	0.217933	6	127.3	127.5	48.9	—	99.4	275.6	265.8
264.2	0.343874	7	128.4	127.4	48.0	—	100.7	277.1	263.0
388.2	0.344381	8	137.7	126.5	—	—	140.4	278.1	262.1
446.0	0.441701	9	121.5	128.3	—	—	153.1	274.6	261.3
529.9	0.443482	10	134.0	127.5	—	—	153.0	287.0	260.1
692.0	0.513305	11	130.2	126.8	—	—	168.9	299.1	259.6
921.4	0.883812	12	94.9	128.1	—	—	202.2	297.1	254.6

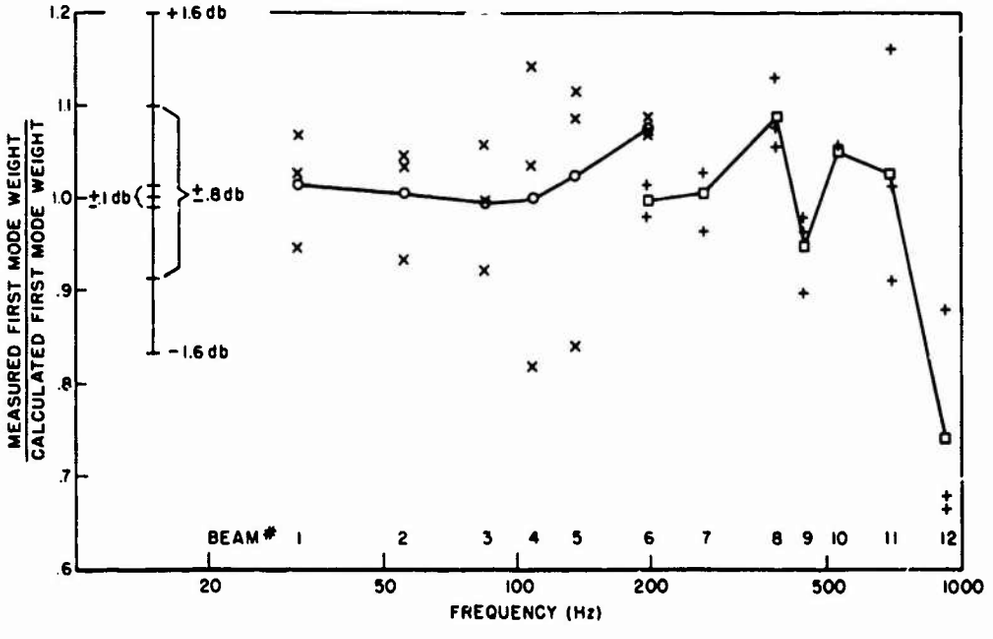


Fig. 7 - First mode results

each beam, and the other on the ordinate expresses the ratio in db to show the scatter in those terms for those familiar with electronic measurement. Note that Beam 6 was measured twice. Beams 1 to 6 were measured and then certain modifications were made to the electronics in an attempt to improve resolution. Beams 6 through 12 were then measured with the modifications included.

Figure 8 plots the ratio of experimentally determined weight to platform balance weight. The experimentally determined weight is the sum of the modal weights and the residual weight as given in Table 2. Scales and plotting are otherwise the same as in Fig. 7.

The comparison between the averaged measured and approximately calculated values of the first mode effective mass is better than anticipated for the present state of the art of mechanical impedance measurements [4]. These values are within ±10 percent (except for Beam 12) or ±0.6 db where db is 20 $\log_{10}$ F/A.

Great care was taken to make these measurements as accurate as possible with the equipment used. Several factors served to limit this accuracy: (1) the electronic system accuracy of about ±0.8 db, which was the reason for using the average of three runs, and (2) because of the frequency range limitations only the first two or three normal modes were used in the least squares solutions.

Consider again Eq. (2c), and rewrite as

$$F/A = M_0 + \sum_{s=1}^{2} \frac{M_s}{1 - \frac{\omega^2}{\omega_s^2}} + \sum_{s=3}^{\infty} \frac{M_s}{1 - \frac{\omega^2}{\omega_s^2}} ,$$

for Beams 5 through 7 as an example. Now the third term of this equation has a denominator which is always positive and less than one since $\omega < \omega_s$ for all $s \geq 3$. This helps to account for the differences in the summed experimental weight. A similar argument can be advanced for Beams 8 through 12.

CONCLUDING REMARKS

The accuracy of these modal effective mass measurements makes them entirely suitable for use on simple structures. The approach used herein is limited by the requirement that the structure under test be free. However, this is a natural first step toward development of a technique for measuring the modal masses while the structure remains attached, in place, on the vehicle.

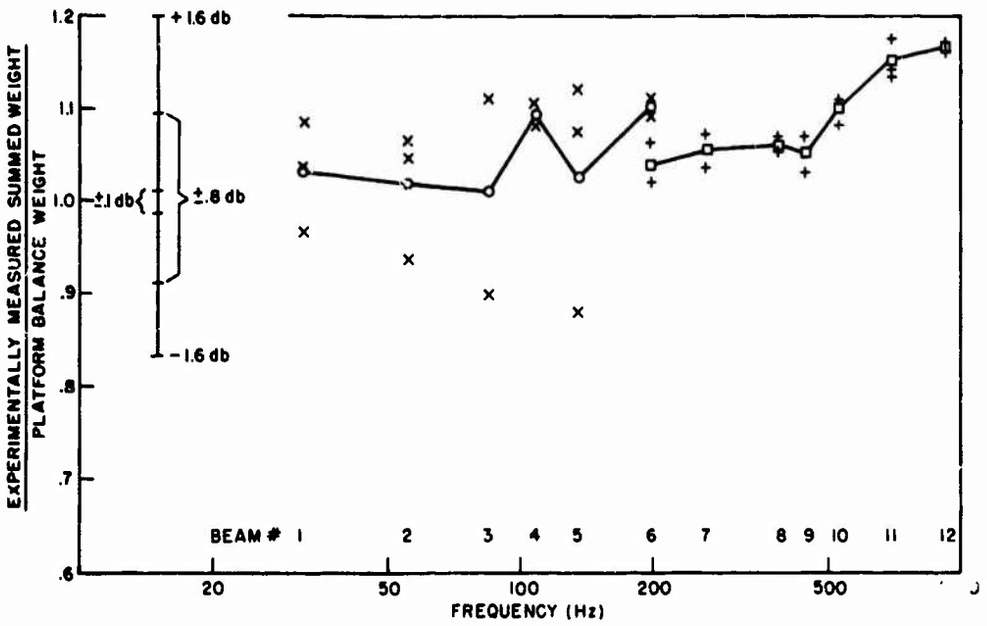


Fig. 8 - Ratio of experimentally measured static weight to scale weight for all beams. A db scale is included to show that the scatter is small in terms of db.

These are among the most useful and accurate mechanical impedance measurements that the authors have made to date. Greater accuracy and resolution are possible but at a high cost – for it would require special development in three areas: (1) electronics, (2) transducers, and (3) calibration techniques.

REFERENCES

1. R.O. Belsheim and G.J. O'Hara, "Shock Design of Shipboard Equipment, Part I – Dynamic Design Analysis Method (DDAM)," NRL Report 5545, Sept. 16, 1960

2. G.M. Remmers and H.C. Mayo, "Experimental Technique for Determining Fixed Base Natural Frequencies of Structures on Single Nonrigid Attachment Points," NRL Memorandum Report 1800, Aug. 31, 1967, Shock and Vibration Bull. 38, Part 2, Oct. 1968

3. G.J. O'Hara and P.F. Cunniff, "Elements of Normal Mode Theory," NRL Report 6002, Nov. 15, 1962

4. F. Schloss, "Recent Advances in the Measurement of Structural Impedance," DTMB Report 1584, Jan. 1963

5. G.M. Remmers and G.J. O'Hara, "Experimental Measurement of a Structure's Modal Mass," NRL Progress Report, Dec. 1967

SIMPLIFYING A LUMPED PARAMETER MODEL

Martin T. Soifer and Arlen W. Bell
Dynamic Science, a Division of Marshall Industries
Monrovia, California

This work constitutes an extension of work previously presented by the authors. A method for simplifying a lumped parameter model by reducing the number of mass points is derived. Two degrees of freedom per mass point are allowed for, and the basis for the reduction procedure is that the work done on the reduced system is equal to the work done on the original system by the inertia forces during a free vibration. The procedure is applied to the in-plane deformation of a truss, and a dynamic equivalence between the reduced and original systems is established.

INTRODUCTION

A procedure for reducing the number of mass points in a lumped parameter system was presented recently by the authors [1]. Although the procedure was successfully applied to several problems, a drawback was that it restricted each mass point of a given system to a single degree of freedom. This work is an extension of the work contained in the previous paper in that it allows two degrees of freedom per mass point.

The lumped parameter method of analysis, a method commonly employed for studying the dynamics of complex elastic structures, usually yields reliable results for the first "n" modes of the real structure if at least "2 n" mass points are introduced. Reduction of the real structure to the lumped parameter model depends on such considerations as: the physical appearance of the structure, the number of modes desired, the effects of rotary inertia, shear, and the lumping of appendage masses with main masses (see references [2] through [4]).

In a number of problems, although the first "n" modes of the real structure are desired, it is necessary, in view of the considerations mentioned above, to introduce a number of mass points far in excess of the "2 n" required. Solution of this system, will, in most cases, only slightly improve the accuracy of the results for the first "n" modal characteristics, and it would therefore, be more desirable to deal with a system consisting of less mass points. An example is the dynamics of a truss type structure. For the formulation it is advantageous to locate a mass point at each truss joint. However, depending on the size of the truss, the number of modes desired, and the possible interaction of the truss with an adjoining structure, locating a mass point at each truss joint may make the dynamic problem too cumbersome to handle efficiently. Consequently, a technique is desired which will simplify a given lumped parameter model by reducing the number of mass points.

As in the previous paper, the basis of the reduction procedure is that the work done on the reduced system is equal to the work done on the original system by the inertia forces during a free vibration. The procedure is applied to the in-plane deformation of a truss, and a dynamic equivalence is established between the original and reduced lumped parameter models. Dynamic equivalence is defined here as demonstrating a "closeness" in natural frequencies and summed effective (modal) weights between the reduced and original systems. Consideration of effective weight is of importance for problems in which a base acceleration is the input since it is the 1 g base reaction, reference [2].

REDUCTION PROCEDURE

Consider an undamped, linear, elastic system consisting of "n" discrete mass points connected by springs. Each mass point is allowed two degrees of freedom; corresponding to displacements in the x and y directions.

Let δ_i; $1 \le i \le n$, denote the displacement of the i th mass point in the x-direction, and δ_i; $(n+1) \le i \le 2n$, the displacement of the $(i-n)$ th mass point in the y-direction. Similarly, let P_j; $1 \le j \le n$, denote the force acting on the j th mass point in the x-direction, and P_j; $(n+1) \le j \le 2n$, the force acting on the $(j-n)$ th mass point in the y-direction.

For such a system, the displacements and forces are related through the influence coefficient matrix, α_{ij}, by the equations

$$\delta_i = \sum_{j=1}^{2n} \alpha_{ij} P_j \; ; \; i = 1, 2, \ldots, 2n \qquad (1)$$

For a free vibration, the forces, P_j, acting on the system, are inertia forces. That is

$$P_j = \begin{cases} -m_j \ddot{x}_j \; ; \; 1 \le j \le n \\ -m_{(j-n)} \ddot{y}_{(j-n)} \; ; \; (n+1) \le j \le 2n \end{cases} \qquad (2)$$

where $\ddot{x}_j$; $1 \le j \le n$, denotes the x-component of acceleration of the j th mass point, and $\ddot{y}_{(j-n)}$; $(n+1) \le j \le 2n$, the y-component of acceleration of the $(j-n)$ th mass point.

Using equation (2), equation (1) may be rewritten in the form

$$\delta_i = -\left\{ \sum_{j=1}^{n} \alpha_{ij} m_j \ddot{x}_j + \sum_{j=(n+1)}^{2n} \alpha_{ij} m_{(j-n)} \ddot{y}_{(j-n)} \right\} \qquad (3)$$

The work, W_k, done on the system of "n" mass points during a free vibration is given by

$$W_k = \frac{1}{2} \sum_{i=1}^{2n} P_i \delta_i \qquad (4)$$

Replacing j by i in equation (2), and making use of equation (3), equation (4) may be written in the expanded form

$$W_k = \frac{1}{2} \left\{ \sum_{i=1}^{n} \sum_{j=1}^{n} m_i m_j \alpha_{ij} \ddot{x}_i \ddot{x}_j + \sum_{i=1}^{n} \sum_{j=(n+1)}^{2n} m_i m_{(j-n)} \alpha_{ij} \ddot{x}_i \ddot{y}_{(j-n)} + \sum_{i=(n+1)}^{2n} \sum_{j=1}^{n} m_{(i-n)} m_j \alpha_{ij} \ddot{y}_{(i-n)} \ddot{x}_j + \sum_{i=(n+1)}^{2n} \sum_{j=(n+1)}^{2n} m_{(i-n)} m_{(j-n)} \alpha_{ij} \ddot{y}_{(i-n)} \ddot{y}_{(j-n)} \right\} \qquad (5)$$

Interchanging i and j in the third summation, and noting that $\alpha_{ij} = \alpha_{ji}$, equation (5) becomes

$$W_k = \frac{1}{2} \left\{ \sum_{i=1}^{n} \sum_{j=1}^{n} m_i m_j \alpha_{ij} \ddot{x}_i \ddot{x}_j + 2 \sum_{i=1}^{n} \sum_{j=(n+1)}^{2n} m_i m_{(j-n)} \alpha_{ij} \ddot{x}_i \ddot{y}_{(j-n)} + \sum_{i=(n+1)}^{2n} \sum_{j=(n+1)}^{2n} m_{(i-n)} m_{(j-n)} \alpha_{ij} \ddot{y}_{(i-n)} \ddot{y}_{(j-n)} \right\} \qquad (6)$$

Equation (6) may be further simplified by replacing j by $(j+n)$ in the second and third summations, and i by $(i+n)$ in the third summation. The resulting expression is

$$W_k = \frac{1}{2} \sum_{i=1}^{n} \sum_{j=1}^{n} \left\{ \alpha_{ij} m_i m_j \ddot{x}_i \ddot{x}_j + 2 \alpha_{i(j+n)} m_i m_j \ddot{x}_i \ddot{y}_j + \alpha_{(i+n)(j+n)} m_i m_j \ddot{y}_i \ddot{y}_j \right\} \qquad (7)$$

Consider next dividing the "n" mass points into "r" groups. Each group may or may not contain the same number of mass points. The subdivision process is assumed to be arbitrary. For each group, replace the mass points of the original system entering the group by a single mass point located at the center of mass of the group, and equal to the sum of the masses entering the group. For example, for the i th group, introduce the mass M_i, defined as

$$M_i = \sum_{j=(k+1)}^{\ell} m_j \; ; \; i = 1, 2, \ldots, r \qquad (8)$$

where $(\ell - k)$ denotes the number of mass points of the original system entering the group. The "r" M_i's defined by equation (8) are the mass points of the reduced system. A method for connecting these mass points is required such that the reduced system is dynamically equivalent (as previously defined) to the original system.

Considering the reduced system, the work, $\bar{W}_k$, done on the system during a free vibration

is given by

$$\bar{W}_k = \frac{1}{2} \sum_{i=1}^{r} \sum_{j=1}^{r} \left\{ \bar{\alpha}_{ij} M_i M_j \ddot{X}_i \ddot{X}_j + 2\bar{\alpha}_{i(j+r)} M_i M_j \ddot{X}_i \ddot{Y}_j + \bar{\alpha}_{(i+r)(j+r)} M_i M_j \ddot{Y}_i \ddot{Y}_j \right\} \quad (9)$$

where $\bar{\alpha}_{ij}$ denotes the as yet unknown influence coefficients for the reduced system. $\ddot{X}_i$ and $\ddot{Y}_i$ denote respectively, x and y acceleration components of the i th mass point, M_i.

The criterion to be used for determining $\bar{\alpha}_{ij}$ is that the work done on any mass point, M_p, of the reduced system during a free vibration is equal to the work done on all the mass points of the original system which make up the mass M_p. This implies that the total work done on each system is the same (the converse would not necessarily be true). Assume that there are "a" mass points in the first of the "r" groups, "(b - a)" in the second, ..., "(ℓ - k)" in the p th, ..., and finally, "(n - m)" in the r th. The work, w_p, done on the "(ℓ - k)" mass points which make the p th group is obtained from equation (7) as

$$w_p = \frac{1}{2} \sum_{i=(k+1)}^{\ell} \sum_{j=1}^{n} \left[\lambda_{ij} + 2\bar{\lambda}_{ij} + \bar{\bar{\lambda}}_{ij} \right]$$

which may also be written in the form

$$w_p = \frac{1}{2} \sum_{i=(k+1)}^{\ell} \left\{ \sum_{j=1}^{a} \gamma_{ij} + \sum_{j=(a+1)}^{b} \gamma_{ij} + \cdots + \sum_{j=(k+1)}^{\ell} \gamma_{ij} + \cdots + \sum_{j=(m+1)}^{n} \gamma_{ij} \right\} \quad (10)$$

where,

$$\begin{aligned} \gamma_{ij} &= \left(\lambda_{ij} + 2\bar{\lambda}_{ij} + \bar{\bar{\lambda}}_{ij} \right) \\ \lambda_{ij} &= \alpha_{ij} m_i m_j \ddot{x}_i \ddot{x}_j \\ \bar{\lambda}_{ij} &= \alpha_{i(j+n)} m_i m_j \ddot{x}_i \ddot{y}_j \\ \bar{\bar{\lambda}}_{ij} &= \alpha_{(i+n)(j+n)} m_i m_j \ddot{y}_i \ddot{y}_j \end{aligned} \quad (11)$$

The work, $\bar{w}_p$, done on the p th mass point, M_p, of the reduced system is obtained from equation (9) as

$$\bar{w}_p = \frac{1}{2} \sum_{j=1}^{r} \left\{ \bar{\alpha}_{pj} M_p M_j \ddot{X}_p \ddot{X}_j + 2\bar{\alpha}_{p(j+r)} M_p M_j \ddot{X}_p \ddot{Y}_j + \bar{\alpha}_{(p+r)(j+r)} M_p M_j \ddot{Y}_p \ddot{Y}_j \right\} \quad (12)$$

Assume that the accelerations of the mass points of the reduced system are such that the inertia forces of the reduced system are related to the inertia forces of the original system through the relations

$$\begin{aligned} M_\ell M_k \ddot{X}_\ell \ddot{X}_k &= \frac{n_i n_j \sum\sum \lambda_{ij}}{\sum\sum \alpha_{ij}} \\ M_\ell M_k \ddot{X}_\ell \ddot{Y}_k &= \frac{n_i n_j \sum\sum \bar{\lambda}_{ij}}{\sum\sum \alpha_{i(j+n)}} \\ M_\ell M_k \ddot{Y}_\ell \ddot{Y}_k &= \frac{n_i n_j \sum\sum \bar{\bar{\lambda}}_{ij}}{\sum\sum \alpha_{(i+n)(j+n)}} \end{aligned} \quad (13)$$

where the sums on i and j are extended over the number of mass points of the original system which make up M_ℓ and M_k, and n_i and n_j denote the number of original mass points associated with each of these sums.

Substituting equation (13) into (10), and expanding, yields

$$w_p = \frac{1}{2} \left\{ \left[\frac{\sum_{i=(k+1)}^{\ell} \sum_{j=1}^{a} \alpha_{ij}}{a(\ell - k)} \right] M_p M_1 \ddot{X}_p \ddot{X}_1 + 2 \left[\frac{\sum_{i=(k+1)}^{\ell} \sum_{j=1}^{a} \alpha_{i(j+n)}}{a(\ell - k)} \right] M_p M_1 \ddot{X}_p \ddot{Y}_1 + \left[\frac{\sum_{i=(k+1)}^{\ell} \sum_{j=1}^{a} \alpha_{(i+n)(j+n)}}{\alpha(\ell - k)} \right] M_p M_1 Y_p \ddot{Y}_1 \right] + \left[\frac{\sum_{i=(k+1)}^{\ell} \sum_{j=(a+1)}^{b} \alpha_{ij}}{(b-a)(\ell - k)} \right] M_p M_2 \ddot{X}_p \ddot{X}_2$$

$$+\frac{2\sum_{i=(k+1)}^{\ell}\sum_{j=(a+1)}^{b}\alpha_{i(j+n)}}{(b-a)(\ell-k)}M_pM_2\ddot{X}_p\ddot{Y}_2$$

$$+\frac{\sum_{i=(k+1)}^{\ell}\sum_{j=(a+1)}^{b}\alpha_{(i+n)(j+n)}}{(b-a)(\ell-k)}M_pM_2\ddot{Y}_p\ddot{Y}_2\Bigg]+\dots$$

$$+\Bigg[\frac{\sum_{i,j=(k+1)}^{\ell}\alpha_{ij}}{(\ell-k)^2}M_p^2\ddot{X}_p^2$$

$$+\frac{2\sum_{i,j=(k+1)}^{\ell}\alpha_{i(j+n)}}{(\ell-k)^2}M_p^2\ddot{X}_p\ddot{Y}_p$$

$$+\frac{\sum_{i,j=(k+1)}^{\ell}\alpha_{(i+n)(j+n)}}{(\ell-k)^2}M_p^2\ddot{Y}_p^2\Bigg]+\dots$$

$$+\Bigg[\frac{\sum_{i=(k+1)}^{\ell}\sum_{j=(m+1)}^{n}\alpha_{ij}}{(\ell-k)(n-m)}M_pM_r\ddot{X}_p\ddot{X}_r$$

$$+\frac{2\sum_{i=(k+1)}^{\ell}\sum_{j=(m+1)}^{n}\alpha_{i(j+n)}}{(\ell-k)(n-m)}M_pM_r\ddot{X}_p\ddot{Y}_r$$

$$+\frac{\sum_{i=(k+1)}^{\ell}\sum_{j=(m+1)}^{n}\alpha_{(i+n)(j+n)}}{(\ell-k)(n-m)}M_pM_r\ddot{Y}_p\ddot{Y}_r\Bigg]\Bigg\} \tag{14}$$

A schematic of the $\bar{\alpha}_{ij}$ matrix is as follows:

$$\left[\begin{array}{c|c} \alpha_{ij} & \bar{\alpha}_{i(j+r)} \\ \hline \bar{\alpha}_{(i+r)j} & \bar{\alpha}_{(i+r)(j+r)} \end{array}\right] \tag{15}$$

where $1 \le i, j \le r$, and in accordance with Maxwell's reciprocal relation $\bar{\alpha}_{i(j+r)} = \bar{\alpha}_{(i+r)j}$.

To obtain the elements of each of the sub-matrices associated with the p th mass point, expand the right hand side of equation (12), and equate the result to the right hand side of equation (14). Noting the linear independence of the $\ddot{X}_i$'s and $\ddot{Y}_i$'s yields the following results:

$\underline{\bar{\alpha}_{pj} \; ; \; 1 \le j \le r}$

$$\bar{\alpha}_{p1} = \frac{1}{a(\ell-k)}\sum_{i=(k+1)}^{\ell}\sum_{j=1}^{a}\alpha_{ij}$$

$$\bar{\alpha}_{p2} = \frac{1}{(b-a)(\ell-k)}\sum_{i=(k+1)}^{\ell}\sum_{j=(a+1)}^{b}\alpha_{ij}$$

$$\vdots$$

$$\bar{\alpha}_{pp} = \frac{1}{(\ell-k)^2}\sum_{i,j=(k+1)}^{\ell}\alpha_{ij}$$

$$\vdots$$

$$\bar{\alpha}_{pr} = \frac{1}{(n-m)(\ell-k)}\sum_{i=(k+1)}^{\ell}\sum_{j=(m+1)}^{n}\alpha_{ij} \tag{16a}$$

$\underline{\bar{\alpha}_{p(j+r)} = \bar{\alpha}_{(p+r)j} \; ; \; 1 \le j \le r}$

$$\bar{\alpha}_{p(1+r)} = \frac{1}{a(\ell-k)}\sum_{i=(k+1)}^{\ell}\sum_{j=1}^{a}\alpha_{i(j+n)}$$

$$\bar{\alpha}_{p(2+r)} = \frac{1}{(b-a)(\ell-k)}\sum_{i=(k+1)}^{\ell}\sum_{j=(a+1)}^{b}\alpha_{i(j+n)}$$

$$\vdots$$

$$\bar{\alpha}_{p(p+r)} = \frac{1}{(\ell-k)^2}\sum_{i,j(k+1)}^{\ell}\alpha_{i(j+n)}$$

$$\vdots$$

$$\bar{\alpha}_{p(2r)} = \frac{1}{(n-m)(\ell-k)}\sum_{i=(k+1)}^{\ell}\sum_{j=(m+1)}^{n}\alpha_{i(j+n)} \tag{16b}$$

$\underline{\bar{\alpha}_{(p+r)(i+r)} \; ; \; 1 \le j \le r}$

$$\bar{\alpha}_{(p+r)(1+r)} = \frac{1}{a(\ell-k)}\sum_{i=(k+1)}^{\ell}\sum_{j=1}^{a}\alpha_{(n+i)(n+j)}$$

$$\bar{\alpha}_{(p+r)(2+r)} = \frac{1}{(b-a)(\ell-k)}\sum_{i=(k+1)}^{\ell}\sum_{j=(a+1)}^{b}\alpha_{(n+i)(n+j)}$$

$$\bar{\alpha}_{(p+r)(p+r)} = \frac{1}{(\ell-k)^2} \sum_{i,j=(k+1)}^{\ell} \alpha_{(n+i)(n+j)}$$

$$\bar{\alpha}_{(p+r)(2r)} = \frac{1}{(n-m)(\ell-k)} \sum_{i=(k+1)}^{\ell} \sum_{j=(m+1)}^{n} \alpha_{(n+i)(n+j)} \qquad (16c)$$

By varying the subscript p ($1 \le p \le r$) in equations (16a) through (16c), and appropriately adjusting the summation limits for the subscript i, each element of each submatrix is obtained.

Hence, equations (16a) through (16c), in conjunction with equation (8), completely specifies the reduced system in terms of the physical properties of the original system.

It should be noted that if each mass point is restricted to a single degree of freedom, corresponding, for example, to motion in the x-direction, then equations (16b) and (16c) would no longer be applicable; only equation (16a) would apply. If equation (16a) is compared with equation (11) of reference [1], it is seen that they are identical; as would be expected.

To demonstrate the validity of the use of the reduction procedure presented, it is necessary to demonstrate that a dynamic equivalence is established between the original and reduced systems. That is, it is necessary to show, in a given problem, that for the first "k" modes of interest, the natural frequencies, $\bar{f}_i$; $i = 1, 2, \ldots, k$, and summed effective weight, $\sum_{i=1}^{k} \bar{\mu}_i$, of the reduced system are "close" to the natural frequencies, f_i ; $i = 1, 2, \ldots, k$, and summed effective weight, $\sum_{i=1}^{k} \mu_i$, of the original system. The k th mode effective weight is defined as

$$\mu_k = g \frac{\left[\sum_i m_i \varphi_i^{(k)}\right]^2}{\sum_i m_i \left[\varphi_i^{(k)}\right]^2} \qquad (17)$$

where g denotes the gravitational acceleration, and $\varphi_i^{(k)}$ the k th mode shape associated with the i th mass point, m_i.

Use of the reduction procedure is demonstrated next in the example.

EXAMPLE

The truss shown in Figure 1a has a span to height ratio of ten, and was proportioned such that each of its elements would be equally stressed to 20,000 psi when a 30,000 lb. vertical load is placed at each joint. Using a material density $\rho = 0.283$ lb/in^3, and a weight distribution obtained by assigning to each mass point (truss joint) one half the sum of the weights of the truss members entering each joint, a diagonal weight matrix is obtained. Allowing for in-plane (x, y) deformation of the truss, a stiffness matrix is generated and inverted; yielding the influence coefficient matrix, α_{ij}.

Using the DTMB Program 2262, reference [5], with the weight matrix and the influence coefficient matrix, the natural frequencies, f_i, and summed effective weights for both x and y motions, $\sum_i \mu_i^x$ and $\sum_i \mu_i^y$, were obtained for the system's thirty-six modes. These results are presented for the first eighteen modes in Tables 1, 2, and 3.

Replacing the mass points lying on the same truss vertical (see Figure 1a) by a single mass point, and using equation (8), the reduced system shown in Figure 1b is obtained. Using equations (16a) through (16c) and the influence coefficient matrix, α_{ij}, the influence coefficient matrix for the reduced system, $\bar{\alpha}_{ij}$, is obtained.

With the reduced system's weight and influence coefficient matrices as input to the DTMB program, the parameters of interest $\left(\bar{f}_i, \sum_i \bar{\mu}_i^x, \sum_i \bar{\mu}_i^y\right)$ were obtained. For the purpose of comparison, these results are also presented in Tables 1 through 3 for the system's eighteen modes.

Examination of Table 1 shows that using the reduced system reproduces the original system's natural frequencies to within 9.0% accuracy for the first eight modes. The higher modes demonstrate a marked loss in accuracy. From Table 2 it is seen that for all modes considered, with the exception of the second and third modes, the x-direction modal weight is reproduced to within 9.6% accuracy. The second and third modes demonstrate a 15.6% error. From Table 3 it is seen that the y-direction modal weights are reproduced for all modes to within 2.9% accuracy.

CONCLUSION

The two-dimensional reduction procedure developed in this paper gives a dynamic equivalence of sufficient accuracy for stowage shock analysis for the example problem considered. Thus for a typical truss structure, a halving of mass points can be accomplished.

The application of this method is most useful for truss and plane frame structures composing portions of larger structures. For a truss type structure it is relatively easy to obtain the flexibility matrix of all the joints by inversion of the joint stiffness matrix. However, if the truss is merely a portion of a more complex, and less well defined structure, then usually far too many mass points have been used in the truss definition. Thus, the mass point reduction procedure allows the entire structure to be dynamically analyzed with the same level of accuracy, and more nearly equal mass sizes. Since the effort required in dynamic analysis is approximately proportional to the square of the total degrees of freedom, it is usually worthwhile to simplify the lumped parameter model to the fullest extent possible.

This method is useful to obtain greater dynamic accuracy when restricted to a limited number of mass points. Similar to other methods for accomplishing this result, many problems must be examined in order to properly define the applicability of the technique. When a sufficient number of problems have been examined, then generalized guidelines and rules may be formulated.

REFERENCES

1. Soifer, M. T., and Bell, A. W., "Reducing the Number of Mass Points in a Lumped Parameter System," Presented at the 38th Symposium on Shock and Vibration, held in St. Louis, Missouri, May 1-2, 1968.

2. Belsheim, R. O., and O'Hara, G. J., "Shock Design of Shipboard Equipment, Dynamic Design - Analysis Method," NavShips 250-423-30, May 1961.

3. Harrington, R. L., and Vorus, W. S., "Dynamic Shock Analysis of Shipboard Equipment," Marine Technology, pp. 331-354, Oct. 1967.

4. Fisher, E. G., "Theory of Equipment Design," Shock and Vibration Handbook, Vol. 3, Chapter 42, McGraw-Hill, 1961.

5. Avila, J. H., "Normal Mode Computer Analysis of Structures," David Taylor Model Basin Report 2262, Jan. 1967.

Table 1. Frequency Comparison

Mode (i)	f_i (cycles/sec.)	$\bar{f}_i$ (cycles/sec.)	% Error[a]
1	3.76	3.80	0.5
2	6.85	6.86	0.4
3	10.72	11.24	4.9
4	15.51	15.64	0.6
5	16.03	17.47	9.0
6	19.20	19.26	0.4
7	21.08	25.54	6.1
8	25.51	26.16	2.5
9	26.42	36.24	23.2
10	29.73	36.41	22.5
11	35.17	41.46	17.9
12	25.83	62.66	75.4
13	41.42	90.72	119.0
14	42.43	106.45	155.6
15	42.62	114.15	167.8
16	46.15	142.62	196.6
17	54.54	189.48	247.4
18	58.14	191.72	340.5

Table 2. Effective Weight Comparison (x-direction)

Mode (i)	$\sum_1 u_i^x$ (lbs.)	$\sum_1 \bar{u}_i^x$ (lbs.)	% Error[a]
1	0	0	0
2	3,972	4,581	15.6
3	3,972	4,582	15.8
4	25,844	26,313	9.6
5	25,844	28,319	9.6
6	67,174	69,355	3.3
7	67,174	69,389	3.3
8	68,690	71,200	3.2
9	70,266	71,200	1.3
10	70,266	71,258	1.4
11	70,296	71,256	1.4
12	70,555	73,234	3.8
13	70,555	73,234	3.6
14	70,560	73,474	4.1
15	70,560	73,474	4.1
16	70,560	73,546	4.2
17	70,663	73,556	4.1
18	70,663	73,675[b]	4.2

[a] to nearest tenth of a percent

[b] total truss weight = 73,675 lbs.

Table 3. Effective Weight Comparison (y-direction)

Mode (i)	$\sum_1 u_i^y$ (lbs.)	$\sum_1 \bar{u}_i^y$ (lbs.)	% Error[a]
1	62,008	62,228	0.4
2	62,008	62,228	0.4
3	66,577	67,551	1.5
4	66,577	67,552	1.5
5	66,337	66,686	0.6
6	69,337	66,966	0.6
7	70,830	71,428	0.8
8	70,830	71,439	0.6
9	70,830	72,011	1.7
10	70,947	72,012	1.5
11	71,310	73,171	2.6
12	71,310	73,171	2.6
13	71,435	73,509	2.9
14	71,435	73,509	2.8
15	73,047	73,520	0.6
16	73,047	73,520	0.6
17	73,047	73,667	0.8
18	73,142	73,675[b]	0.7

[a] to nearest tenth of a percent

[b] total truss weight = 73,675 lbs.

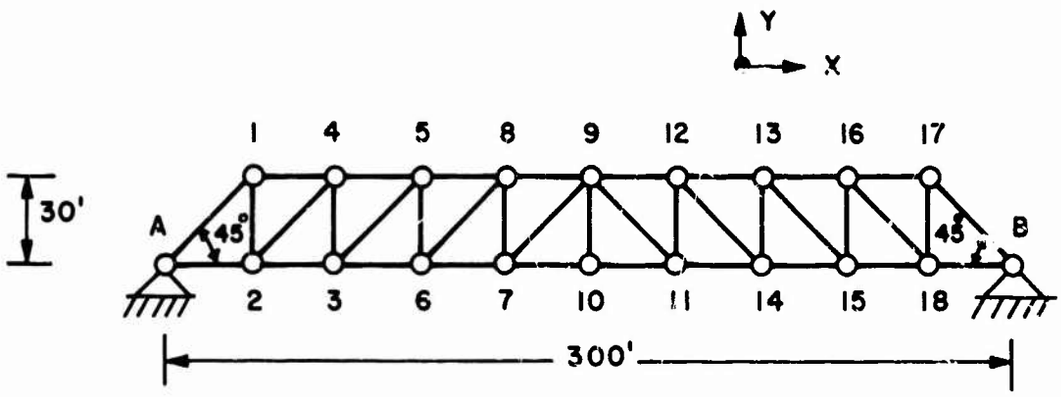


Figure 1a. Truss (Original System)

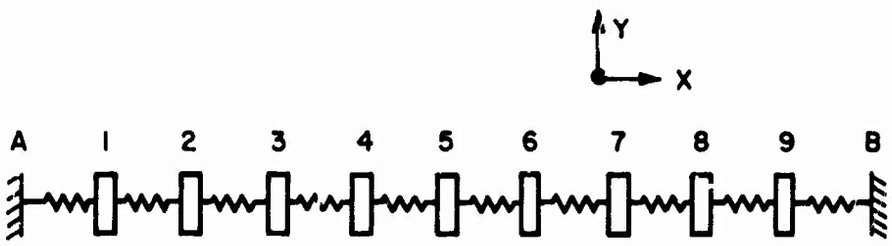


Figure 1b. Reduced System

DISCUSSION

Dr. Mains (Washington University): You were speaking of getting the reduced system flexibility matrix from the system stiffness matrix. This implies that you are going to do some inverting. Do you have any difficulty with this?

Mr. Bell: None on the scale of the problems we have tried to date.

Dr. Mains: How big have you gone?

Mr. Bell: This was a 36 by 36 for the paper, and we have done up close to an 80 by 80.

Dr. Mains: In the work that I reported a little earlier I had a 40 by 40. I inverted it, multiplied the inverse against the original, and the off diagonal elements were 10^{-12} or lower. And yet when you plot it up, what would be the deflection influence coefficient matrix, it was much too ragged to use so I had to generate the deflection influence coefficient matrix from scratch in order to have something useable in the reduced system. This happens often. These things do not invert, cross out and reinvert nicely.

Mr. Bell: Right – this is a function of the particular program being used and also the computer. The computer we were using was the CDC 6600 which has a 60 bit word length.

Dr. Mains: I was using the 360-50 at double precision which is pretty close to the same, so that we have a comparable base there. But I have had trouble also on the CDC in the same way.

Mr. Bell: We have had some problems with inversion and this is often just a peculiarity of the physical system with which you are working.

Voice: Have you compared these stresses from 1 model to the other? and these calculations?

Mr. Bell: No, we have not. To obtain the stresses you put the modal loads generated back on the original structure not back onto the model.

Mr. Kapur (Aerospace Corp.): I noticed that your frequencies were quite a bit off, especially after the 10th mode. Doesn't it affect your response calculations – the stresses and displacements? Won't they be quite different?

Mr. Bell: For a vibration problem that would be true. We developed this method primarily for shock analysis, where only the modes of the higher modal effective weights are included in the analysis. Under the Dynamic Design Analysis Method (DDAM) the requirement is that either half the modes be taken, or 80% of the summed effective modal weights. A lot of these large frequency errors are associated with modes that are essentially insignificant.

Mr. McCalley (General Electric Co.): I might mention that it is possible to take these systems and eliminate some of the coordinates and if you do a specific trick you can keep any specific frequencies you want. Without going into the details, the secret is to make the amplitudes of the coordinates you eliminate a linear combination of the mode shapes in the reduced system. By this means, you can keep any of the first n frequencies you want – there is one complication that you won't like – you'll get a non-diagonal mass matrix.

Mr. Pakstys (General Dynamics/Electric Boat): I would like to comment on this business of differences in frequency. In the DDAM method, depending on the frequency range, the inputs might be dependent on the frequency. If the frequencies are way off, the inputs would be affected.

Mr. Bell: This is true. The high frequencies are associated with high shock input levels. But since the effective weight is generally quite small the total loads introduced are small.

STEADY STATE BEHAVIOR OF TWO DEGREE OF FREEDOM NONLINEAR SYSTEMS

J. A. Padovan, J. R. Curreri
Polytechnic Institute of Brooklyn
Brooklyn, New York

and

M. B. Electronics
New Haven, Connecticut

The Ritz averaging method is used in obtaining approximate solutions to the response of a two degree of freedom nonlinear system. The general equations are derived for linear damping with cubic nonlinearities in both springs. Frequency response curves are plotted for various values of a hardening spring characteristic in either of the two springs. The response is shown for both masses. Similar to the single degree of freedom system, the two degree system has either 1, 2 or 3 solutions, not all of which are stable. A study of the nonlinear response curves make it easy to postulate the nature of the spring nonlinearities that would result in more simultaneous solutions.

INTRODUCTION

The environmental vibration test of structures frequently results in response curves that are, to say the least, confusing. We apply to the structure a sinusoidal input and measure responses on various points of the structure that are periodic, but not harmonic. Obviously, in these cases something has gone nonlinear. The proper interpretation of response magnitudes that are obtained from tests requires a knowledge of what happens when nonlinearities are introduced into the system.

This paper is intended to shed a little more light on the response characteristics of two degree of freedom systems with nonlinear springs.

Previous investigators have reported on various aspects of the more than one degree of freedom vibration problem. Several papers (1) were concerned with the normal mode vibrations of nonlinear systems. Several others (2), (3), (4) dealt with the steady state behavior of nonlinear dynamic vibration absorbers. In particular, Roberson and Arnold made a study of the effects of making a dynamic absorber spring nonlinear. Carter and Liu investigated the improved dynamic absorber action by making both springs nonlinear. An exact result by geometrical methods for strongly nonlinear two degree of freedom systems was discussed in Reference 5.

This paper extends the previous investigations by considering the problem generally as a two degree of freedom system, not necessarily as a dynamic absorber. The nonlinearity is introduced separately in each of the springs to study the overall characteristics on the response of each of the masses in the system. A wide range of system parameters is introduced to follow the changing response patterns. The purpose of the paper is basically to develop an understanding of what happens when nonlinearities appear in either spring of the system. Both hardening and sofetning cubic nonlinearities are considered for each spring, although only hardening characteristics are plotted. Mass ratios and linear frequency ratios are altered to examine a wide range of possible responses. The results are discussed to show the differences that are introduced by the nonlinear spring characteristics.

The Ritz averaging method using one term approximations is used in solving for the responses of the two degree of freedom nonlinear system. No absolute measure of the solution accuracy is afforded by the Ritz procedure. Only in the limit as the nonlinear spring approaches the linear spring coefficient does the approximate response expression converge to the exact linear response.

Thus, for small nonlinearities the epproximate solution is feirly accurate. The present paper does not limit the investigetion to small nonlinearities.

Interesting results are shown by the epproximate solution. Similar to the single degree of freedom system, the two degree system has either 1, 2 or 3 simulteneous solutions. For certein velues of the paremeters used, however, the two degree system with cubic nonlineerity could have as many es 5 simulteneous solutions, not all of which ere steble. A study of the shape the nonlineer response curves makes it easy to postulate the neture of the spring nonlinearity that would result in even more simulteneous solutions.

Another interesting result is that the second mode resonence is primarily affected in e herdening spring cherecteristic. The term resonence in the nonlineer system is used here to describe the growth without bound of the system response with increesed frequency. This occurs whether the nonlineerities are introduced into either the upper or the lower spring. On the other hend, it is the first mode cherecteristic thet is primarily effected by e softening spring cherecteristic. Again, this occurs whether the softening spring feeture is introduced into the upper or the lower spring.

RITZ PROCEDURE FOR MULTI-DEGREE OF FREEDOM SYSTEMS

For an n degree of freedom system, the X1, X2,---Xk---Xn es functions of time maybe supplied. Whet is sought is the behevior of the system under the ection of a periodic disturbing force. For e differential equation of the type

$$E_k\left[X_1, X_2, - - -, X_n\right] = 0 \qquad (1)$$

The solution would give the sesired co-ordinetes es functions of time. In the sbsence of e procedure yielding en exact solution, en epproximate solution cen be obteined by the following procedure.

1. Replece eech of the co-ordinetes of type $X_k(t)$ by e corresponding function of the form

$$X_k(t) = \sum_{i=1}^{N} A_{ki}\,\phi_i(t) \qquad k = 1,2,---n \qquad (2)$$

The coefficients ki constitute e set of nN unknown constents. The functions $\phi i(t)$ ere selected functions of time which epproximate the system's motions.

2. Substitute equations 2 into the differentiel expressions of equstion 1 so thet a set of functions of time

$$E_k\left[X_1(t), X_2(t), - - -, X_n(t)\right] \neq 0 \qquad k = 1,2,- - -n \qquad (3)$$

will be obtained, non of which will in general be equal to zero.

3. Perform all of the integrations of the type

$$\int_0^{\frac{2\pi}{\omega}} E_k\left[X_1(t), X_2(t) - - - X_n(t)\right]\phi_i\,dt \qquad k = 1,2,---n \quad i = 1,2,---N \qquad (4)$$

Equations 4 constitute a set of nN algebraic equations in nN unknowns of the type ϕ_i

4. Solve the algebraic equations of equation 4 for the coefficients A_{ki} and insert them into the series of equation 2 to obtain the approximate solution sought.

GENERAL SYSTEM EQUATIONS

A schemetic diagram for the system under consideration is shown in Figure 1. For the initiel steady state solution of the system

$$F_1(X_1) = \alpha_1 X_1 + \beta_1 X_1^3 \qquad (5)$$

$$F_2(X_3) = \alpha_2 X_3 + \beta_2 X_3^3 \qquad (6)$$

where

$$X_3 = X_2 - X_1 \qquad (7)$$

From Newton's second law applied to masses M_1 and M_2 gives the following differential equations of motion for the system

$$M_1\frac{d^2X_1}{dt^2} + (C_1+C_2)\frac{dX_1}{dt} - C_1\frac{dX_2}{dt} + \alpha_1 X_1 + \beta_1 X_1^3 - \alpha_2 X_3 - \beta_2 X_3^3 = f(t) + M_1 g \qquad (8)$$

$$M_2\frac{d^2X_2}{dt^2} + C_2\frac{dX_2}{dt} - C_2\frac{dX_1}{dt} + \alpha_2 X_3 + \beta_2 X_3^3 = M_2 g \qquad (9)$$

The Ritz averaging method when applied to equations 8 and 9 gives the following

$$E_1\left[X_1, X_2, X_3\right] = M_1\frac{d^2X_1}{dt^2} + (C_1+C_2)\frac{dX_1}{dt} - C_2\frac{dX_2}{dt} + \alpha_1 X_1 + \beta_1 X_1^3 - \alpha_2 X_3 - \beta_2 X_3^3 - f(t) - M_1 g \qquad (10)$$

$$E_2\left[X_1, X_2, X_3\right] = M_2\frac{d^2X_2}{dt^2} + C_2\frac{dX_2}{dt} - C_2\frac{dX_1}{dt} + \alpha_2 X_3 + \beta_2 X_3^3 - M_2 g \qquad (11)$$

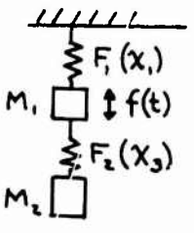


Figure 1

As initial approximating functions for the steady state response of the nonlinear system shown in Figure 1 the following relations will be used

$$x_1 = A_{11}\sin\omega t + A_{12}\cos\omega t \tag{12}$$

$$x_2 = A_{21}\sin\omega t + A_{22}\cos\omega t \tag{13}$$

If the damping is omitted then the cosine terms in equations 12 and 13 can be neglected for simplicity. The resulting approximating equations would then be

$$x_1 = A_{11}\sin\omega t \tag{14}$$

$$x_2 = A_{21}\sin\omega t \tag{15}$$

To apply the Ritz averaging procedure, the following relations must be satisfied

$$\int_0^{2\pi}\Big\{M_1\omega^2A_{11}\sin^2\theta - M_1\omega^2A_{12}\sin\theta\cos\theta + (C_1+C_2)\omega A_{11}\cos\theta\sin\theta - (C_1+C_2)\omega A_{12}\sin^2\theta - C_1\omega A_{21}\cos\theta\sin\theta + C_2\omega A_{22}\sin^2\theta + \alpha_1A_{11}\sin^2\theta + \alpha_1A_{12}\cos\theta\sin\theta + B_1A_{11}(\sin\theta+A_{12}\cos\theta)^3\sin\theta + \alpha_2(A_{11}-A_{21})\sin^2\theta + \alpha_2(A_{12}-A_{22})\cos\theta\sin\theta + B_2\big[(A_{11}-A_{21})\sin\theta + (A_{12}-A_{22}\cos\theta\big]^3\sin\theta - F_0\sin^2\theta - M_1g\sin\theta\Big\}\,d\theta = 0 \tag{16}$$

$$\int_0^{2\pi}\Big\{-M_1\omega^2A_{11}\sin\theta\cos\theta - M_1\omega^2A_{12}\cos^2\theta + (C_1+C_2)\omega A_{11}\cos^2\theta - (C_1+C_2)\omega A_{12}\sin\theta\cos\theta - C_2\omega A_{21}\cos^2\theta + C_2\omega A_{22}\sin\theta\cos\theta + \alpha_1A_{12}\cos^2\theta + \alpha_1A_{11}\sin\theta\cos\theta + B_1(A_{11}\sin\theta+A_{12}\cos\theta)^3\cos\theta + \alpha_2(A_{11}-A_{21})\sin\theta\cos\theta + \alpha_2(A_{12}-A_{21})\cos^2\theta + B_2(A_{11}-A_{21})\sin\theta + (A_{12}-A_{22})\cos^3\theta\cdot\cos\theta - F_0\sin\theta\cos\theta - M_1g\cos\theta\Big\}\,d\theta = 0 \tag{17}$$

$$\int_0^{2\pi}\Big\{-M_2\omega^2A_{21}\sin^2\theta - M_2\omega^2A_{22}\cos\theta\sin\theta + C_2\omega A_{21}\cos\theta\sin\theta - C_2\omega A_{22}\sin^2\theta - C_2\omega A_{11}\cos\theta\sin\theta + C_2\omega A_{12}\sin^2\theta + \alpha_2(A_{21}-A_{11})\sin^2\theta + \alpha_2(A_{22}-A_{11})\cos\theta\sin\theta + B_2\big[(A_{21}-A_{11})\sin\theta + (A_{22}-A_{12})\cos\theta\big]^3\sin\theta - M_2g\sin\theta\Big\}\,d\theta = 0 \tag{18}$$

$$\int_0^{2\pi}\Big\{-M_2\omega^2A_{21}\sin\theta\cos\theta - M_2\omega^2A_{22}\cos^2\theta + C_2\omega A_{21}\cos^2\theta - C_2\omega A_{22}\sin\theta\cos\theta - C_2\omega A_{11}\cos^2\theta + C_2\omega A_{12}\sin\theta\cos\theta + \alpha_2(A_{21}-A_{11})\sin\theta\cos\theta + \alpha_2(A_{22}-A_{11})\cos^2\theta + B_2\big[(A_{21}-A_{11})\sin\theta + (A_{22}-A_{12})\cos\theta\big]^3\cos\theta - M_2g\cos\theta\Big\}\,d\theta = 0 \tag{19}$$

Performing the integrations gives the four equations

$$-M_1\omega^2A_{11} + \alpha_1A_{11} + \alpha_2(A_{11}-A_{21}) + \tfrac{3}{4}B_1A_{11}^3 + \tfrac{3}{4}B_1A_{11}A_{12}^2 + \tfrac{3}{4}B_2(A_{11}-A_{21})^3 + \tfrac{3}{4}B_2(A_{11}-A_{21})(A_{12}-A_{22})^2 + C_2\omega A_{22} - (C_1+C_2)\omega A_{12} - F_0 = 0 \tag{20}$$

$$-M_1\omega^2A_{12} + \alpha_1A_{12} + \alpha_2(A_{12}-A_{22}) + \tfrac{3}{4}B_1A_{11}^2A_{12} + \tfrac{5}{16}B_1A_{12}^3 + \tfrac{3}{4}B_2(A_{11}-A_{21})^2(A_{12}-A_{22}) + \tfrac{5}{16}B_2(A_{12}-A_{22})^3 + (C_1+C_2)\omega A_{11} - C_2\omega A_{21} = 0 \tag{21}$$

$$-M_2\omega^2A_{21} - C_2\omega A_{22} + C_2\omega A_{12} + \alpha_2(A_{21}-A_{11}) + \tfrac{3}{4}B_2(A_{21}-A_{11})^3 + \tfrac{3}{4}B_2(A_{21}-A_{11})(A_{22}-A_{11})^2 = 0 \tag{22}$$

$$-M_2\omega^2A_{22} + C_2\omega A_{21} - C_2\omega A_{11} + \alpha_2(A_{22}-A_{11}) + \tfrac{3}{4}B_2(A_{21}-A_{11})^2(A_{22}-A_{12}) + \tfrac{3}{16}B_2(A_{12}-A_{22})^3 = 0 \tag{23}$$

Special cases involving equations 20 through 23 will be solved.

Case 1. For this case the terms C_1, C_2 and B_2 will be assumed zero. One term approximations given by equations 14 and 15 will be considered. This gives rise to the following equations

$$-M_1\omega^2A_{11} + \alpha_1A_{11} + \tfrac{3}{4}B_1A_{11}^3 + \alpha_2(A_{11}-A_{21}) - F_0 = 0 \tag{24}$$

$$-M_2\omega^2A_{21} + \alpha_2(A_{21}-A_{11}) = 0 \tag{25}$$

Solving equations 24 and 25 simultaneously will yield relations for the unknown amplitudes A_{11} and A_{21}. A relation for A_{21} in terms of A_{11} and the system properties can be obtained by adding equations 24 and 25.

$$A_{21} = \frac{\alpha_2}{\alpha_2 - M_2\omega^2}A_{11} \tag{26}$$

Now substituting equation 26 into equation 24 gives

$$-M_1\omega^2 A_{11} + \alpha_1 A_{11} + \frac{3}{4}B_1 A_{11}^3 - F_0 + \alpha_2 A_{11} - \alpha_2^2 \frac{1}{(\alpha_2 - M_2\omega^2)} = 0 \quad (27)$$

Combining like terms in equation 27 yields

$$A_{11}^3 + \frac{4}{3B_1}\left[-M_1\omega^2 + \alpha_1 + \alpha_2\left(1 - \frac{\alpha_2}{\alpha_2 - M_2\omega^2}\right)\right]A_{11} - \frac{4}{3B_1}F_0 = 0 \quad (28)$$

The solution of equation 27 for A_{11} as a function of w was obtained with the aid of a computer. The results of the solution are given in the curves, Figures 2, 3, 4, 6 and 8.

Case 2 C_1, C_2 and B_1 will be assumed zero for this case. Again for the same reasons as before the cosine terms will be neglected. Under the latter conditions equations 20, 21, 22 and 23 reduce to the following algebraic equations

$$-M_1\omega^2 A_{11} + \alpha_1 A_{11} + \frac{3}{4}B_2(A_{11} - A_{21})^3 + \alpha_2(A_{11} - A_{21}) - F_0 = 0 \quad (29)$$

$$-M_2\omega^2 A_{21} + \alpha_2(A_{21} - A_{11}) + \frac{3}{4}B_2(A_{11} - A_{21})^3 = 0 \quad (30)$$

As in Case 1, a relation for A_{21} in terms of A_{11} and the system parameters can be obtained by adding equations 29 and 30.

$$A_{21} = \frac{(\alpha_1 - M_1\omega^2)A_{11} - F_0}{M_2\omega^2} \quad (31)$$

To simplify the future algebraic manipulations the following relations are introduced

$$\Phi_1 = \frac{\alpha_1 - M_1\omega^2}{M_2\omega^2} \quad (32)$$

$$\Phi_2 = \frac{F_0}{M_2\omega^2} \quad (33)$$

Substituting relations 32 through 33 into equation 29 yields

$$A_{11}\left[-M_1\omega^2 + \alpha_1 + \alpha_2(1 - \Phi_1)\right] + \alpha_2\Phi_2 + \frac{3}{4}B_2\left[A_{11}(1 - \Phi_1) + \Phi_2\right]^3 - F_0 = 0 \quad (34)$$

To obtain equation 33 in its final form, the higher order terms can be expanded and the like terms combined to give

$$A_{11}^3 + A_{11}^2\left(\frac{3\Phi_2}{1 - \Phi_1}\right) + A_{11}\left\{\frac{4}{3}\left[\frac{-M_1\omega^2 + \alpha_1}{B_2(1 - \Phi_1)^3}\right] + \frac{4\alpha_2}{3B_2(1 - \Phi_1)^2} + \frac{3\Phi_2^2}{(1 - \Phi_1)^2}\right\} - \frac{4}{3}\frac{\alpha_2\Phi_2 + F_0}{B_2(1 - \Phi_1)^3} + \frac{\Phi_2^3}{(1 - \Phi_1)^3} = 0 \quad (35)$$

Equation 35 is also solved by a computer program. The results are shown in the curves.

RESULTS

Figure 2 shows the response X_1 for Case 1 as the frequency increases. Both masses are equal. For Case 1, the upper spring $F_1(X_1)$ is non linear while $F_2(X_2)$ is linear. Notice that the nonlinearity of the response appears essentially in the second mode and not in the first mode. Also, with $F_1(X_1)$ linear and $F_2(X_2)$ non linear, the same effect appears - that is the non linear response appears in the second mode. This is shown in the set of curves in Figure 3.

Figures 4 and 5 compares the responses at X_1 and X_2 for the same conditions depicted in Figure 2. Of the three roots of a non-linear response, the middle one is not stable. This means that mass M_2 undergoes essentially only one resonance. The response for X_2 (from Figure 5) shows that beyond a frequency of 1, the lower root is essentially the only solution. This is because the upper root (mathematically stable) is so close to the unstable root that it becomes unstable. Of course this plot is for the particular values of forcing function (F_0=1). Nevertheless, X_1 shows an expected response for the same value

An examination of Figures 6, 7, 8 and 9 shows how the conclusions are modified by a reduction of the mass ratio of $\frac{M_2}{M_1}$ from unity to 0.1.

REFERENCES

1. Rosenberg, Kuo "Nonsimilar Normal Mode Vibrations of Nonlinear Systems Having Two Degrees of Freedom", Journal of Applied Mechanics, June 1964.

2. Roberson, "Synthesis of a Nonlinear Vibration Absorber", J. of Franklin Inst. 1952.

3. Arnold, "Steady State Behavior of Systems Provided with Nonlinear Dynamic Vibration Absorbers", Journal of Applied Mechanics, December, 1955.

4. Carter, Liu, "Steady-State Behavior of Nonlinear Dynamic Vibration Absorber," Journal of Applied Mechanics, March 1961.

5. Finney, Rosenberg, "On Steady-State Forced Vibrations in Strongly Nonlinear Systems Having Two Degrees of Freedom", Colloques Internationaux, Marseille, 1964.

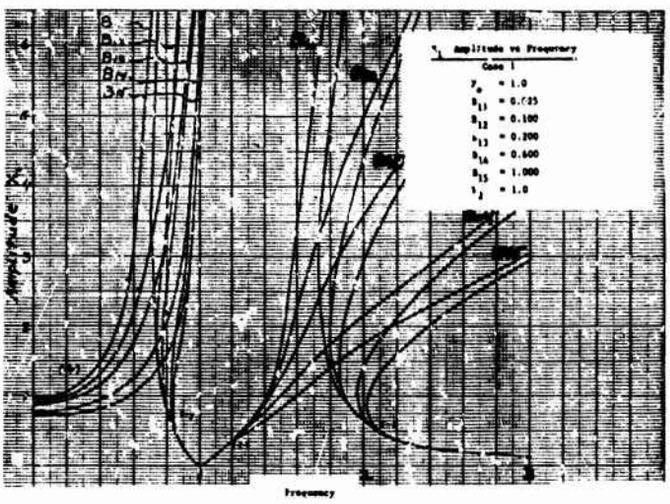


Figure 2

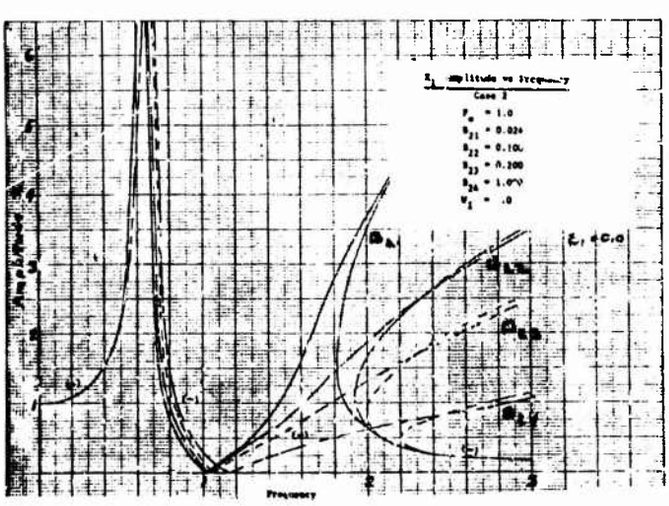


Figure 3

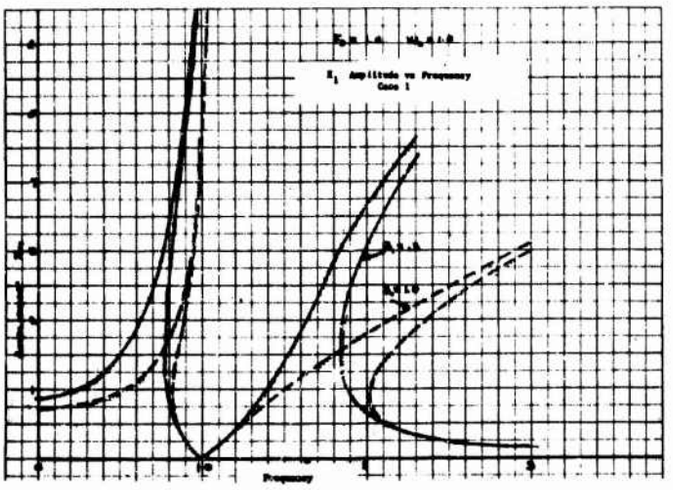


Figure 4

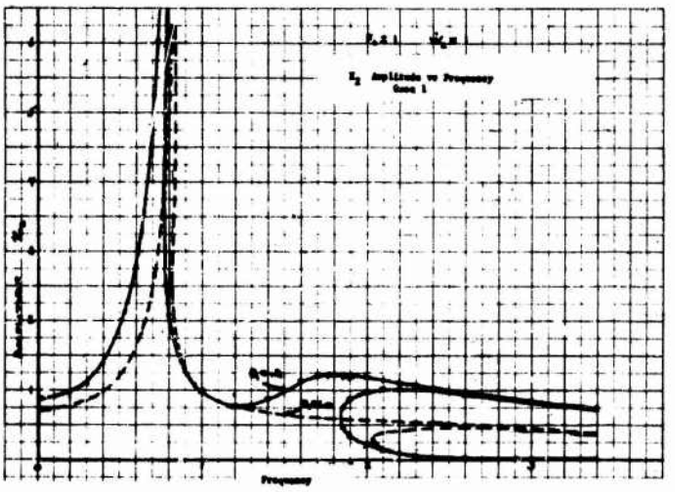


Figure 5

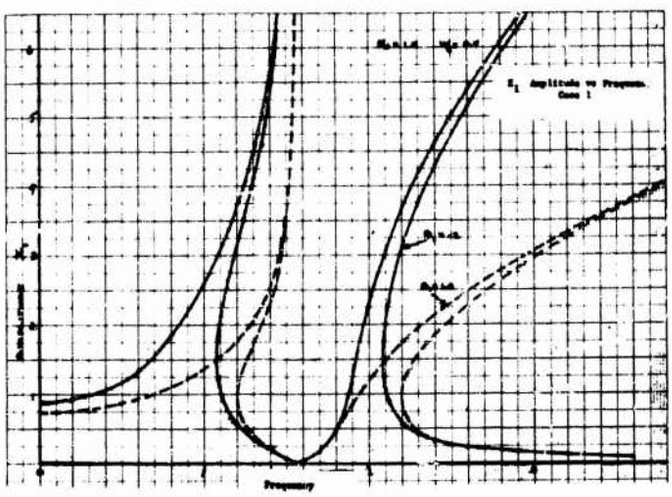


Figure 6

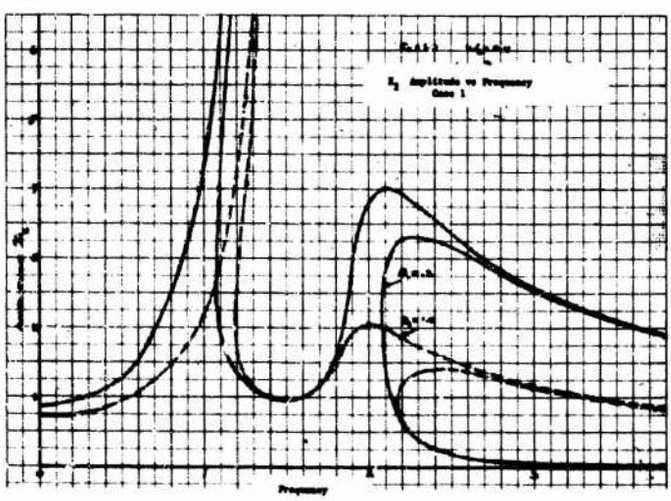


Figure 7

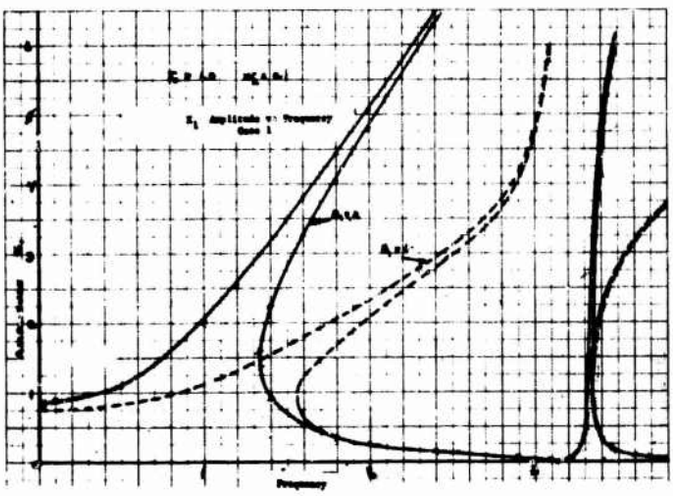


Figure 8

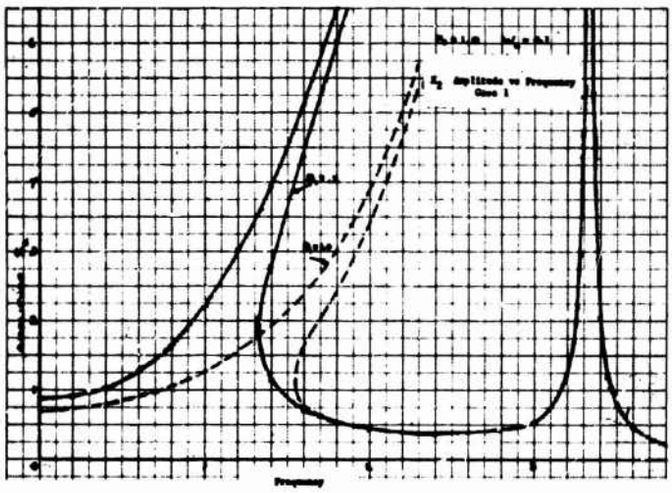


Figure 9

Mr. Matthews (Naval Missile Center): Have your students attempted any experimental work in this area?

Mr. Curreri: I have also a graduate thesis student involved in that very problem. One is trying to construct such a system. This is rather difficult. The other is trying to solve the problem by analog.

Mr. Hanks (NASA, Langley): Have you given any thought as to the effect of the position of the driving force, on the first mass rather than the second mass, considering that it will be a point of different impedance in the second mode than in the first mode? Will that have any effect on the results?

Mr. Curreri: Need I add that I have a graduate student on that?

THE FLUTTER OR GALLOPING OF CERTAIN STRUCTURES IN A FLUID STREAM

Raymond C. Binder
University of Southern California
Los Angeles, California

This paper presents a first-order analysis for one case that has not been presented in the literature. A two-degree-of-freedom system (torsion and translation) in a fluid stream is first analyzed for the general case. The basic equations of motion are set up and the characteristic equation found. The particular case is taken in which the center of gravity coincides with the elastic axis. There are indications that this case is involved in various applications. A closed form solution is obtained as a function of pertinent system parameters including approach fluid velocity.

In a range of velocities the motion of the system is bounded and no dangerous torsional or translational displacement amplitude is involved. At one particular velocity, however, the characteristic roots are equal, and the vibration amplitude increases with time; this condition might be classed as a critical flutter or gallop. At this critical condition the flutter frequency equals the natural translation frequency. At a higher approach velocity the characteristic equation gives at least one positive root, which means an amplitude build-up, and an unstable condition.

Under certain weather conditions, an overhead electrical transmission line may accumulate sleet or ice to form an unsymmetrical section; such a line may gallop during certain winds. The galloping data reported by several different investigators check the main features of the foregoing analysis very closely.

The closed form analysis and the independent experimental checks of the analysis give an illustration of what might happen in dynamically similar systems, as aircraft, missiles, and other bodies in a fluid stream. The closed form solution helps to identify the cause and to suggest possible cures of the dangerous vibration.

INTRODUCTION

There are various problems in which a structure or body in a fluid stream may have an undesirable dangerous vibration, flutter or gallop. In approaching problems of this sort it is helpful to have available information about certain basic types or cases. Also, it would help to have a rational analysis stressing physical insight or the main physical mechanism involved. Frequently a first-order analytical approach, with some physical insight, can help considerably in interpretation and in devising possible cures. After a study of the first-order phase, if desirable, a more sophisticated second-order analysis may be considered. Zimmerman [1], [2] has presented an analysis of certain basic types; his approach has real value in handling many applications.

The following presents a first-order analysis for one case that has not been detailed in the literature. For this case experimental data are available to give a check on the analysis. In the following a discussion will be given first of the basic equations; then the particular case will be detailed and the analysis compared with experimental observations.

GENERAL ANALYTICAL RELATIONS

Figure 1 shows a schematic of the system.

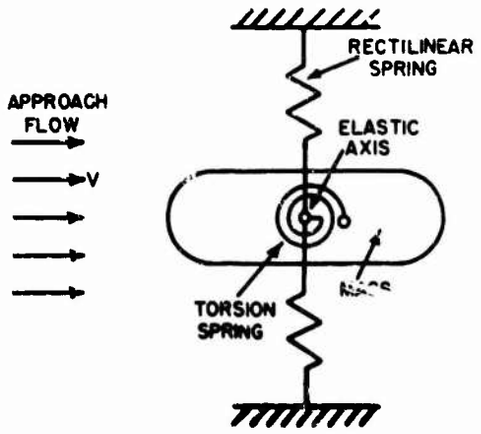


Fig. 1 - Schematic of System

The mass in the fluid stream can rotate about an axis and can move in a vertical direction; there is a linear vertical spring and a linear torsion spring; one end of each is fastened to the elastic axis. The mass can execute independent freedom of motion in either torsional pitch or rectilinear plunge. Figure 2 illustrates the notation. The lift force is perpendicular to the approach flow. The lift force is at the aerodynamic center; the aerodynamic center is that point about which the pitch moment does not change with angle of attack. The distance between the aerodynamic center and the elastic axis is a; the distance between the elastic axis and the center of gravity is b; the rectilinear displacement from the equilibrium position is z; and the angular displacement is α. Let M represent mass, K_z the equivalent rectilinear vertical spring rate, let K_α represent the equivalent torsion spring rate and let R be the effective radius of gyration. The equations of motion for the lumped-element system are

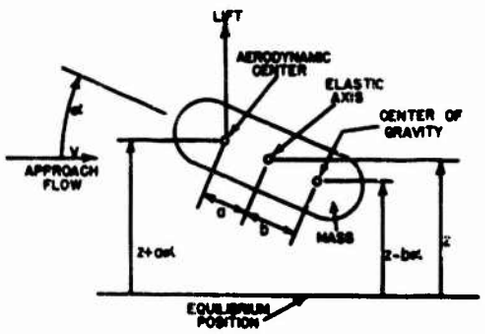


Fig. 2 - Notation

$$M\ddot{z} - Mb\ddot{\alpha} + K_z z = \text{Force} \qquad (1)$$

$$R^2 M\ddot{\alpha} - Mb\ddot{z} + K_\alpha \alpha = \text{Moment} \qquad (2)$$

where the double dot over a variable represents the second time derivative.

Let L represent lift force, A represent a reference area, V approach velocity, ρ fluid density, q the approach stream dynamic pressure $\frac{1}{2}\rho V^2$ and C_L the dimensionless lift coefficient defined as

$$C_L = \frac{L}{qA} \quad . \qquad (3)$$

We assume a linear relation between lift coefficient and angle of attack. Then the net lift force and the net pitch moment become

$$\text{Force} = C_L qA = qA\left(\frac{\partial C_L}{\partial \alpha}\right)\alpha \qquad (4)$$

$$\text{Moment} = C_L Aa\left(\frac{\partial C_L}{\partial \alpha}\right)\alpha q \quad . \qquad (5)$$

Let

$$C_{L\alpha} = \frac{\partial C_L}{\partial \alpha} \quad . \qquad (6)$$

We define the uncoupled natural frequencies, one rectilinear (or translational) and one torsional, by the relations

$$\omega_z^2 = \frac{K_z}{M} \qquad \omega_\alpha^2 = \frac{K_\alpha}{MR^2} \quad . \qquad (7)$$

Then the differential equations of motion can be expressed in the form

$$\ddot{z} - b\ddot{\alpha} + \omega_z^2 z - \frac{qA}{M} C_{L\alpha}\alpha = 0 \qquad (8)$$

$$\ddot{\alpha} - \frac{b}{R^2}\ddot{z} + \omega_\alpha^2 \alpha - \frac{qAa}{MR^2} C_{L\alpha}\alpha = 0 \quad . \qquad (9)$$

Let each displacement be expressed in the general form

$$z = De^{st} \qquad \alpha = Ee^{st} \qquad (10)$$

where t is time and s is a root. Let

$$s = p + i\omega \qquad (11)$$

where p is the real part, $i = \sqrt{-1}$, and ω is the magnitude of the imaginary component. Setting the determinant of the D and E coefficients equal to zero, gives the characteristic equation in the two forms

$$\left[s^2 + \omega_z^2\right]\left[s^2 + \omega_\alpha^2 - \frac{qAaC_{L\alpha}}{MR^2}\right]$$

$$- \frac{b}{R^2} s^2 \left[bs^2 + \frac{qAC_{L\alpha}}{M}\right] = 0 \qquad (12)$$

$$s^4 + s^2\left[\frac{R^2(\omega_\alpha^2 + \omega_z^2)}{R^2 - b^2} - \frac{qAC_{L\alpha}(a+b)}{M(R^2-b^2)}\right]$$

$$+ \left[\frac{\omega_\alpha^2 \omega_z^2 R^2}{R^2-b^2} - \frac{\omega_z^2 qAaC_{L\alpha}}{M(R^2-b^2)}\right] = 0 \ . \qquad (13)$$

The characteristic Eq. (13) has the general form

$$s^4 + s^2 B_1 + B_2 = 0 \qquad (14)$$

with four roots.

PARTICULAR CASE

A variety of basic types or cases could be studied, depending on the values of a, b, M and R. Certain types have been detailed to some extent [1]. In applications it is sometimes very difficult to establish directly and clearly the influence of such factors as a, b, M and R.

For the particular case in which b = 0 (center of gravity coincides with the elastic axis), Eq. (12) gives a relatively simple form with roots clearly defined

$$\left[s^2 + \omega_z^2\right]\left[s^2 + \omega_\alpha^2 - \frac{qAaC_{L\alpha}}{MR^2}\right] = 0 \ . \qquad (15)$$

There are indications that this particular case is involved in various applications.

In flutter analysis a prime interest is the influence of the approach flow velocity V. It is helpful to use a plot of components of the roots each as a function of a parameter y, where y is defined as

$$y = \sqrt{\frac{qAaC_{L\alpha}}{MR^2}} \ . \qquad (16)$$

The parameter y is proportional to the velocity V.

Equation (15) can be written as two separate relations, each equal to zero,

$$s^2 + \omega_z^2 = 0 \qquad (17A)$$

$$s^2 + \omega_\alpha^2 - y^2 = 0 \ . \qquad (17B)$$

Equation (17A) gives a pair of roots

$$s = \pm i\omega_z \qquad (18)$$

which are purely imaginary with no real components. Figure 3 shows a plot of the positive

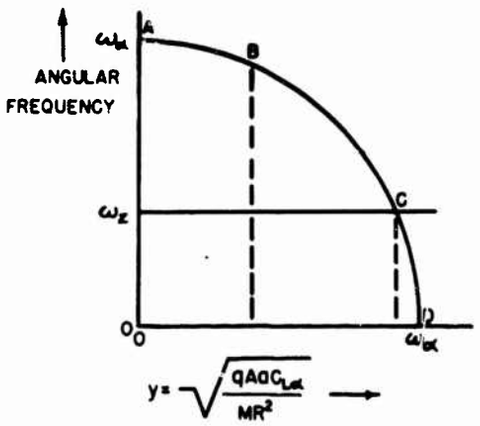


Fig. 3 - Imaginary components of roots versus y.

variable imaginary component ω as a function of y. In Fig. 3 the line through $\omega = \omega_z$ represents the constant natural undamped vertical frequency over a range of y values (which are proportional to velocity V).

Next consider only values of y equal to or less than ω_α. Then Eq. (17B) can be recast in the forms

$$s^2 = y^2 - \omega_\alpha^2 = -\omega^2$$

$$y^2 + \omega^2 = \omega_\alpha^2 \qquad (19)$$

$$s = \pm i\sqrt{\omega_\alpha^2 - y^2} \ . \qquad (19A)$$

The roots are purely imaginary with no real components. Equation (19) is the equation of a circle. For only positive values of y and ω, in Fig. 3 the curve ABCD represents one-quarter of a circle. At $\omega = 0$ the value of y is ω_α.

Imagine next the range in which y is equal to or greater than ω_α. Then Eq. (17B)

gives

$$(p + i\omega)^2 = y^2 - \omega_\alpha^2$$

$$p^2 = y^2 - \omega_\alpha^2 \qquad (20)$$

$$s = \pm p = \pm\sqrt{y^2 - \omega_\alpha^2} \ . \qquad (20A)$$

The roots are purely real, positive and negative, with no imaginary components. Equation (20) is the equation of an equilateral hyperbola. Referring only to positive values of the variable y and the variable p, the curve DEF in Fig. 4 indicates part of the hyperbola.

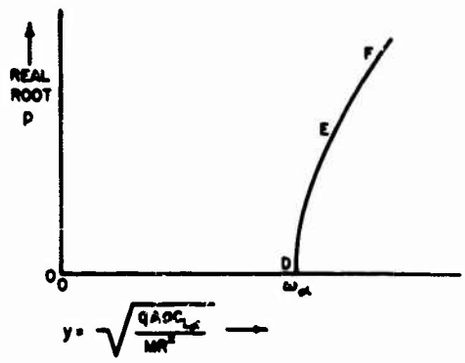


Fig. 4 - Real components of roots versus y.

Consider first solutions of the differential equations of motion for different values of y in the range from y = 0 to y less than ω_α. This range is indicated in Fig. 3. With the exception of point C, the solution can be expressed in the form

$$z = A_1 \sin\left[\sqrt{\omega_\alpha^2 - y^2}\,t + \phi_1\right] + A_2 \sin\left[\omega_z t + \phi_2\right] \qquad (21A)$$

$$\alpha = A_3 \sin\left[\sqrt{\omega_\alpha^2 - y^2}\,t + \phi_1\right] + A_4 \sin\left[\omega_z t + \phi_2\right] \qquad (21B)$$

where the A's are coefficients, and ϕ_1 and ϕ_2 are phase angles. As an example, at y = 0, no flow, (point A in Fig. 3) these equations become

$$z = A_1 \sin\left[\omega_\alpha t + \phi_1\right] + A_2 \sin\left[\omega_z t + \phi_2\right] \qquad (22A)$$

$$\alpha = A_3 \sin\left[\omega_\alpha t + \phi_1\right] + A_4 \sin\left[\omega_z t + \phi_2\right] \ . \qquad (22B)$$

At point C there are two identical roots and thus the solution has the form

$$z = A_1 \sin\left[\omega_z t + \phi_1\right] + A_2 t \sin\left[\omega_z t + \phi_2\right] \qquad (23A)$$

$$\alpha = A_3 \sin\left[\omega_z t + \phi_1\right] + A_4 t \sin\left[\omega_z t + \phi_z\right] \ . \qquad (23B)$$

Because of the t term there is an amplitude build-up with time. This case might be called a particular type of flutter; in some cases (as for overhead electrical transmission lines and other structures such as suspension bridges) this condition could be called "galloping." The term galloping has the implication of a relatively low frequency (as contrasted with the high frequency, small amplitude, wind induced aoelian vibration). The basic differential equations of motion do not include frictional damping. In a practical case some damping could restrict the rectilinear displacement amplitude to a finite limit.

Next let us examine solutions for the differential equations of motion for values of y in the range from $y = \omega_\alpha$ to y greater than ω_α; this range is indicated in Fig. 4. The solutions to the differential equations can be expressed in the form

$$z = A_1 \sin(\omega_z t + \phi_1) + D_3 e^{pt} + D_4 e^{-pt} \qquad (24A)$$

$$\alpha = A_2 \sin(\omega_z t + \phi_1) + E_3 e^{pt} + E_4 e^{-pt} \qquad (24B)$$

where D_3, D_4, E_3 and E_4 are coefficients. Since one p root is real and positive, there is an amplitude build-up and the motion is unstable.

As the approach fluid velocity V increases from zero to some higher value, an important question is the velocity at which galloping starts. Referring to Fig. 3, galloping starts at point C, with the y value

$$y = \sqrt{\omega_\alpha^2 - \omega_z^2} = \sqrt{\frac{qAsC_{L\alpha}}{MR^2}} \ . \qquad (25)$$

Since $q = \frac{1}{2}\rho V^2$, the corresponding galloping velocity V_G (at point C) is given by the relation

$$V_G = \sqrt{\frac{2MR^2(\omega_\alpha^2 - \omega_z^2)}{\rho A a C_{L\alpha}}} \quad . \qquad (26)$$

The simple closed form solution given by Eq. (26) points out the factors to consider in studies of possible undesirable vibrations. To develop a high V_G, attention could be given to increasing the torsional frequency ω_α, to increasing the radius of gyration R, to reducing the area A and to reducing the distance a. In an analysis there is a question as to the possible values of the lift-coefficient slope $C_{L\alpha}$. In order to be on the safe side and calculate for the lowest V_G, one might select a high value for $C_{L\alpha}$. For example, for a flat plate $C_{L\alpha}$ is about 2π.

EXPERIMENTAL OBSERVATIONS

Probably there are various cases, as aircraft, missiles, marine craft, and other structures in a fluid stream, in which the center of gravity is at or is close to the elastic axis. Lack of complete data in various applications prevents a comprehensive check of theory and data now. Some pertinent data, however, are available for overhead electrical transmission lines. Thus these data will be discussed briefly to provide a check on the main features of the foregoing analysis, and to illustrate what might happen in dynamically similar systems.

Under certain conditions the symmetrical circular section of an overhead transmission line may accumulate sleet or ice to provide an unsymmetrical section to the wind. The line can vibrate in torsion and it can vibrate vertically in translation. In certain winds the line may gallop. Evidence indicates that the center of gravity is very close to the elastic axis.

Madeyski [3] reported measurements of a particular energized transmission line in Burlington, Ontario, Canada. During a freezing rain, with wind, ice was deposited on the conductor and the line galloped. Later, measurements were made of the vibration characteristics of the line. The natural frequency in torsion ω_α was measured as 15.7 radians per second, and the natural translational frequency ω_z was measured as 7.8 radians per second. Observations showed that the line galloped at the natural frequency in translation. The motion was simple harmonic. The torsional motion had the same frequency as the translational; the torsional vibration was in phase with the translational vibration. This matching of frequencies checks point C in Fig. 3 and Eqs. (23A) and (23B). The line galloped in winds varying from 20 to 30 feet per second. A value of 2π was taken for $C_{L\alpha}$ and the aerodynamic center was taken at the quarter-chord point (aft from the leading edge). From the data listed by Madeyski it is difficult to make a precise calculation of the radius of gyration R due to the ice formation. Making some reasonable calculations as to the ice formation, the use of Eq. (26) indicates a galloping velocity in the region from 25 to 32 feet per second; this theoretical calculation checks closely with the measurements.

For a series of tests with another transmission line, Madeyski [4] gave the following conclusions: (a) galloping took place at the natural frequency of the conductor in translation; (b) both the torsional and the translation motion at any point of a galloping conductor are basically simple harmonic; (c) galloping is a phenomenon of an extremely critical nature; and (d) the fundamental frequency of the torsional motion during galloping is the same as that of the translation motion.

A number of investigations, laboratory, wind tunnel and field were conducted under the author's direction [5]. Different prototype field test lines were erected near Purdue University, West Lafayette, Indiana. Semicircular wooden foils were fastened along the length of each conductor to provide an unsymmetrical sectio . normal to a horizontal wind. Small scale models of a transmission line, with similar unsymmetrical sections along an elastic line, were arranged in a laboratory wind tunnel.

Field prototype tests, with natural winds, showed that the galloping action was very critical. Galloping started only at a certain wind velocity. For example, one field test line galloped only when the normal wind reached 12 feet per second. One field line originally did not gallop with the normal prevailing wind velocities. Referring to Fig. 3, the torsional frequency ω_α was so high that the condition at point C was not reached. Torsional inertia was added to the lines by means of cross bars; this lowered the torsional natural frequency so that the line galloped with normal winds. This checked the indication given in Fig. 3.

It may be possible that a transmission line without ice could have a very high natural torsional frequency. An accumulation of ice may add enough torsional inertia to lower the torsional frequency sufficiently so that the line would gallop with prevailing winds.

At different times, over twenty cases of natural galloping, first mode, were observed with the Purdue prototype field test lines. The natural frequency in translation was measured during periods of no galloping. In each case of natural galloping the frequency of galloping equaled the natural translational

frequency (about 2.1 radians per second for one set of spans). In some cases the vertical double displacement of the line was about 12 feet. For each case of natural galloping the natural torsional frequency was definitely hi er than the natural translational frequency.

Observations of both field test lines and wind tunnel models showed two distinct stages in the galloping action: a small displacement irregular vertical random motion at the start; and a fully developed large vertical displacement periodic motion following the irregular random start. The initial start resembles a motion due to random excitation from vertical fluctuations in the approach stream; in some respects this action is similar to an aoelian vibration. Lumley and Panofsky [6] give data regarding vertical velocity fluctuations in horizontal winds. Measurements by Hard [7] on field lines showed a beat phenomena in the aoelian vibrations. Thus a mode or modes of the transmission line can be excited by the random vertical fluctuations in the approach horizontal flow; the vertical displacement may be small. If the unsymmetrical conductor is displaced sufficiently in a vertical direction, it will start to twist. Sooner or later a significant twisting of the line develops and the galloping starts.

An example of a measured fully developed orbit of field line galloping is indicated in Fig. 5; the double vertical displacement amplitude was about 10 feet. Various modifications of this orbit have been observed. The line twists back and forth as it moves up and down. There is a sharp twist or snap at the top and bottom of the orbit. If the conductor starts and continues in an orbit of the type shown in Fig. 5, it can build up to a high steady state vertical displacement amplitude.

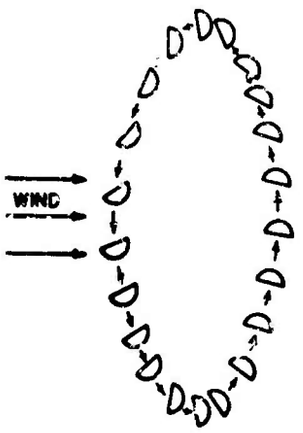


Fig. 5 - Orbit of natural gallop

Let z_0 represent the vertical displacement amplitude; z is the instantaneous vertical displacement. Figure 6 shows a typical plot of the measured vertical displacement ratio z/z_0 versus time. The plot was drawn for a case in which the double vertical displacement amplitude was about 6 feet. The motion is close to simple harmonic. Figure 7 shows the corresponding angular displacement α versus time; the motion is close to simple harmonic. The phase angle difference between the vertical displacement and the angular displacement is small.

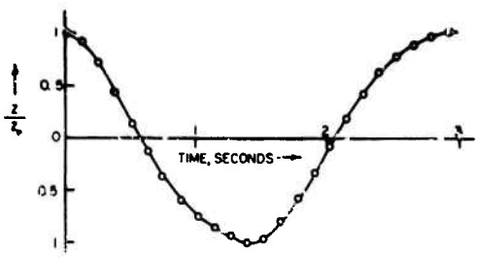


Fig. 6 - Vertical displacement versus time. z_0 is displacement amplitude.

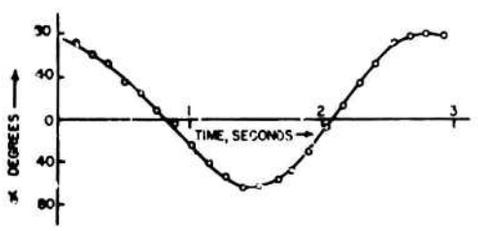


Fig. 7 - Angular displacement versus time.

Frequently a field line would start in a higher mode and then drop to a lower mode. For example, a line would start to move in a fifth or sixth mode, and then drop to a second or first mode. The lower modes give higher vertical displacement amplitudes.

FLOW ACTION IN GALLOPING

At times the suggestion has been made that the vortex shedding behind the structure is the one and only cause of galloping. Care should be taken in reaching conclusions regarding the role of vortex shedding. A distinction should be made between turbulent flow and a stable, precise periodic vortex trail behind a body. A distinction should be made between the flow around a fixed body in a stream and the flow around a dynamically suspended body that is capable of movement. For a fixed cylinder in a stream, the stable

precise periodic vortex shedding may take place only in a narrow range of relatively low Reynolds numbers. A galloping transmission line, on the other hand, may involve a range of relatively high Reynolds numbers.

The prospect of the vortex shedding as the sole exciter raises questions as to the precise matching of the vortex shedding with the particular characteristics of the mechanical elements in a system. This matching may require a certain unobtainable precision of the vortex shedding.

Studies with smoke on field lines and models in the laboratory wind tunnel show that the fully developed rocking motion of the conductor itself sheds the vortex. The vortex shedding itself is not the sole cause of the system galloping. The dynamics of the system (as shown by the equations of motion) determines the galloping; the galloping, in turn, causes an alternate shedding in the downstream flow.

A study of the work per cycle may help explain the flutter or galloping action. Let W represent the total work per cycle done by the flow on the mass in the stream. The increment of work dW for the time interval dt can be expressed in the form

$$\frac{dW}{dt} = L\frac{dz}{dt} \quad . \tag{27}$$

Let the variable vertical velocity $\dot{z}$ ($=dz/dt$) and the variable lift L be represented by the simple harmonic relations

$$\dot{z} = \dot{z}_0 \cos \omega t \tag{28}$$

$$L = L_0 \cos[\omega t + \theta] \tag{29}$$

where $\dot{z}_0$ is vertical velocity amplitude, L_0 is lift amplitude, ω is angular frequency and θ is the phase angle between lift and velocity. The total work per cycle W can be expressed in the form

$$W = L_0 \dot{z}_0 \int_0^{\frac{2\pi}{\omega}} \cos \omega t \cos[\omega t + \theta] dt$$

$$W = L_0 \dot{z}_0 \frac{\pi}{\omega} \cos \theta \quad . \tag{30}$$

Figure 8 shows plots of the vectors z, $\dot{z}$ and and L with different values of the phase angle θ. If $\cos \theta$ is positive, there is a lift component in the direction of the velocity and the net work W is added to the system by the flow. This case is illustrated in Fig. 8a and could be classed as an unstable build-up process or flutter. If $\cos \theta$ is negative there is a lift component in a direction opposite to the velocity and net work W is removed from the system. This case is illustrated in Fig. 8b

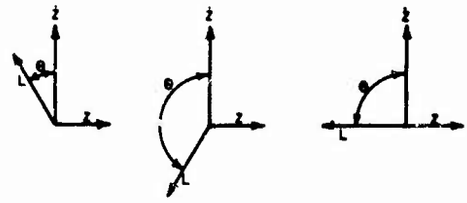


Fig. 8 - Plots with different phase angles

and could be classed as a stable process in which the vibration is damped or decreased. If $\cos \theta$ is zero, the net work W is zero. This case is illustrated in Fig. 8c and could be classed as a neutral stable case.

CONCLUDING REMARKS

The closed form analysis and the independent experimental checks of the analysis give an illustration of what might happen in dynamically similar systems, as aircraft, missiles, and other bodies in a fluid stream. The closed form solution helps to identify the cause and to suggest possible cures for the dangerous vibration.

REFERENCES

1. N. H. Zimmerman, "Elementary Static Aerodynamics Adds Significance and Scope in Flutter Analysis," Symposium Proceedings, Structural Dynamics of High Speed Flight, Aerospace Association, Office of Naval Research, ACR-62 Vol. 1, April 1961, p. 28.

2. N. H. Zimmerman, M. A. Ferman and R. L Turner, "A Basic Approach to Flutter of Primary Surfaces," Seventh U. S. Navy Symposium on Aeroballistics, Point Mugu, Calif., Miscellaneous Publication No. M.P.-66-10, Vol. 2, June 1966, p. 935.

3. A. Madeyski, "Vibration Characteristics of a Conductor Which Had Previously Galloped," Research Division Report No. 57-317, Hydro-Electric Power Commission of Ontario, Canada, August 1957.

4. A. Madeyski, "Galloping Conductor Test on the Experimental Line," Research Division Report No. 57-325, Hydro-Electric Commission of Ontario, Canada, August 1957.

5. R. C. Binder, "Galloping of Conductors Can Be Supressed," Electric Light and Power, Vol. 40, No. 9, May 1962, p. 56.

6. J. J. Lumley and N. A. Panofsky, The Structure of Atmospheric Turbulence (Interscience Publishers, New York, N. Y., 1964).

7. A. R. Hard, "Studies of Conductor Vibration in Laboratory Span, Outdoor Test Span and Actual Transmission Lines," Conference Internationale des Grands Reseaux Electriques a Haute Tension, Paris, France, June 1958.

DISCUSSION

R. J. Fritz (General Electric Co.): Would it have been reasonable to use the Hurwitz root-stability method to determine the unstable points?

Mr. Binder: You could do that. This just happened to come out without much trouble. If you have a more complicated system this would be a good way to do it.

Mr. Fritz: The lift coefficient which you assume to be constant – did you try to estimate the lift coefficient using airfoil theory?

Mr. Binder: Yes. In this case it turned out pretty close to flat plate analysis of the order of two pi. When you have motion you change the lift coefficient slope, but it is of that general order, surprisingly.

Mr. Galef (TRW): In your equation 15 it seems to me that if you let the omega z be zero the equation reduces to the simple expression for torsional divergence, which would not be surprising except that we get torsional divergence with an infinite omega z.

Mr. Binder: We got divergence at the numerical value of y equal to omega sub alpha and thereon out. Physically we normally observed that even though the velocities get beyond this critical velocity, the lines do not change very much from this lower value. Often they will fracture or there will be damage to the lines before they get any higher. We do not have any experimental data to indicate what would happen at the higher values of y, but it indicates there is divergence. All the indications and observations are that we get this first double root business and if it gets pretty violent the line breaks. We have not had any experimental data to answer this correctly.

Mr. Galef: The term galloping is usually reserved for a single degree of freedom in stability associated with the negative slope of the lift curve. This would seem to explain some of the experimental results as well as the flutter that you have been talking about.

Mr. Binder: No, the word galloping has not been restricted to that sense. The implication of the word galloping is that there is a relatively high amplitude and a relatively low frequency. I checked all the experts and that is the general conclusion. The galloping process as we have defined it here is quite similar to flutter, only galloping has the implication of a much larger amplitude and a lower frequency. Now these cases involve a two degree of freedom system – that seems to be essential.

Mr. Galef: You always have positive slope on your lift curve?

Mr. Binder: Yes.

Mr. Paul (Sikorsky Aircraft): Are you referring to the classical galloping line system described many years ago by Den Hartog relating drag and lift? When the stall area is reached it can be shown that the negative damping with respect to the plunging motion gives an oscillation at the flapping frequency of the single degree of freedom system.

Mr. Binder: That is another area of activity – the so-called stall flutter.

Mr. Paul: No, that's not stall flutter. Stall flutter is usually associated with the torsional degree of freedom.

Mr. Binder: No, the term stall refers to conditions beyond the peak of the curve, and this is a different story. In the aerodynamic literature there is a great deal of study of stall flutter. The observation we have made with this type of structure is that you can have all of this below the stall condition.

Mr. Paul: That is the fundamental question: is the Den Hartog simple theory incorrect for the system which he analysed? Have you looked at that and determined that that system is a category all by itself not necessarily related to your present analysis.

Mr. Binder: Yes.

AIRCRAFT LANDING GEAR BRAKE SQUEAL AND STRUT CHATTER INVESTIGATION*

by

F. A. Biehl
McDonnell Douglas Corporation
Long Beach, California

Aircraft landing gear squeal and chatter vibration problems were investigated to determine their effects on passenger compartment vibrations, landing gear damage and brake wear. A digital computer program was used to simulate an aircraft braking stop and has demonstrated that the brake torque function is responsible for the excitation of both vibration modes. Vibration absorbers are suggested as effective attenuation devices.

INTRODUCTION

Sources and attenuation of aircraft main landing gear squeal and chatter vibration modes were investigated to determine the possible effects of these vibrations on the landing gear loads, brake lining deterioration, and passenger comfort. The term "squeal mode" refers to the rotational oscillation of the brake stator assembly and the "chatter mode" refers to a fore and aft landing gear motion. For the landing gear analyzed in this paper, the squeal frequency will be near 200 Hz and the chatter frequency near 15 Hz. It is quite possible that the chatter mode could excite one or more aircraft elastic structural modes and result in relatively large vibration amplitudes.

Utilization of new cermetallic brake lining mixes has introduced irregular brake torque characteristics that are conducive to squeal and chatter excitation. The mixes affect the relationship of brake friction coefficient to the relative brake stator-rotor angular velocity. An effective negative damping is imposed by the brake torque function, creating a temporary divergence to some limiting value for a given aircraft velocity.

Any solution must consider each mode separately since, in some instances, elimination of squeal does not imply the elimination or attenuation of chatter. Reduction or elimination of these vibrations can be approached from two viewpoints: (1) remove the cause, i.e., development of a brake mix with flat brake torque capability, and (2) attenuate the vibration responses with special devices.

The IBM-CSMP (Continuous Systems Modeling Program) simulation language was employed to develop a digital computer program (shown in Appendix A) that analytically exhibits the squeal and chatter vibration modes. The program simulates an aircraft rolling to a braking stop due to the induced tire drag load. The following paragraphs describe the data sources and the development and results of the program.

*Paper not presented at Symposium.

NOMENCLATURE

a	flexibility coefficient
BT	brake torque
BTP	brake torque peak
BTS	brake torque steady value
c	damping coefficient
D	drag force
RF	restoring force
RT	restoring torque
F	force
I	mass moment of inertia
k	stiffness coefficient
L	strut length
M	moment
m	mass
q	generalized coordinate
R	wheel radius
SR	slip ratio
T	torque
V	aircraft velocity

W	aircraft weight
$X, \dot{X}, \ddot{X}$	axle linear displacement, velocity and acceleration
a	friction curve slope
ζ	critical damping ratio
$\theta, \dot{\theta}, \ddot{\theta}$	stator angular displacement, velocity and acceleration
$\rho, \dot{\rho}, \ddot{\rho}$	squeal absorber anbular displacement, velocity and acceleration
σ	angular sectionalized wing displacement
ϕ	modal amplitude
$\psi, \dot{\psi}, \ddot{\psi}$	wheel angular displacement, velocity and acceleration
ω	angular frequency

Subscripts

A	squeal vibration absorber
B	break
CA	chatter vibration absorber
DS	dead space
FP	free play
i	initial
K	kinetic
n	natural frequency
S	static or stator
T	total
TK	tire
W	wheel

CHATTER PHENOMENON

Chatter response is discussed in detail in References 1 and 2. The important highlights are reviewed here to illustrate some effects that appear in the computed landing gear response histories.

A block resting on a moving belt as shown in Figure 1 provides a simple mechanical model. The block is accelerated by the sliding friction force ($\mu_K W$) generated between it and the belt. When the block velocity equals the belt velocity, the block and belt will stick together. The block will continue forward at the constant belt velocity until the static friction force ($\mu_S W$) is overcome by the combined spring damper force. The driving force then returns to sliding friction and the block, now governed by simple harmonic motion, returns to the initial position and repeats the entire cycle.

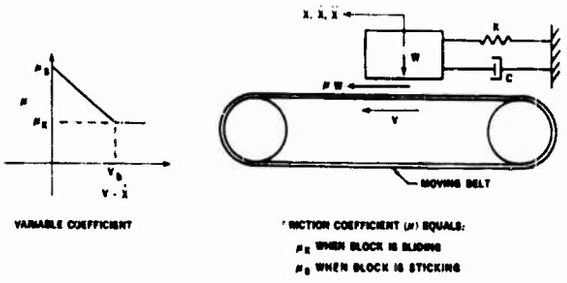


FIGURE 1. CHATTER MODEL

Figure 2 illustrates the displacements, velocities, and accelerations of a block in the "chatter" mode (i.e., $\mu_K < \mu_S$) with the same variables superimposed for a block with a constant friction coefficient (i.e., $\mu_K = \mu_S$). Several distinctive features are apparent:

1. The period of vibration increases due to chatter (frequency decrease)
2. Chatter motion tends to change the vibration amplitude
3. Chatter acceleration response is interrupted by abrupt discontinuities. This may explain the somewhat annoying motions aircraft passengers frequently experience.

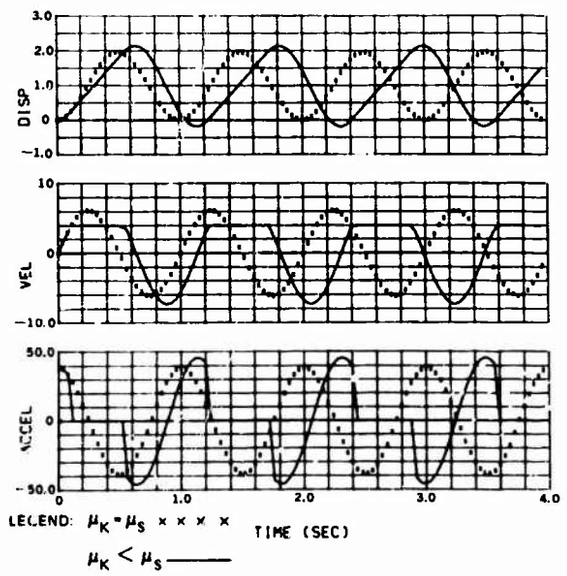


FIGURE 2. COMPUTED RESPONSES – CHATTER MODEL

The sliding block is employed to illustrate another aspect of the gear chatter excitation. For most mechanical systems a gradual change from sliding to sticking friction coefficients is a more plausible transition than the sudden change described previously. If the relative velocity ($V - \dot{x}$) is less than V (see left-hand side of Figure 1), then the equation of motion for the block is

$$m\ddot{X} + c\dot{X} + kX = \mu W \qquad (1)$$

where

$$\mu = \mu_s - a\,(V - \dot{X}) \qquad (2)$$

Hence, from (1) and (2)

$$m\ddot{X} + (c - aW)\,\dot{X} + kX = (\mu_s - aV)\,W \qquad (3)$$

In Equation 2, a is the friction coefficient slope. If aW is greater than c, negative damping will be effectively produced and the solution will tend to diverge. The motion will attain a limit since during some time periods other forces will govern the motion when the relative velocity reaches zero or exceeds the sloping region.

STRUT FREE VIBRATION FREQUENCIES

Free vibration frequencies of the landing gear were computed using theoretical stiffness data and measured mass and inertia data. The gear model consisted of a zero-mass cantilevered beam with a concentrated mass attached to the free end. The weight of this concentrated (unsprung) mass was defined as the weight of one-third of the strut plus the weight of the brake stators, axle, and rolling assemblies. The natural frequency of the strut in the fore and aft direction calculated on the basis of perfect elastic resistance to motion is accurate when the strut motions are large relative to the free-play movement or inherent gear slop. Free play in gear fore-and-aft motion is usually small and will significantly affect free vibration frequencies only when the amplitude of vibration is slightly larger than the free play. The effect of initial vibration amplitude on free vibration frequency in the presence of free play is shown in Figure 3. The level portion of the diagram indicates that sufficiently large amplitudes result in predominantly elastic gear resistance. The specific gear plotted (Figure 3) can be seen to have a natural frequency of 18 Hz for pure elastic resistance. Subsequent analyses allow for the possibility of free play in the gear design.

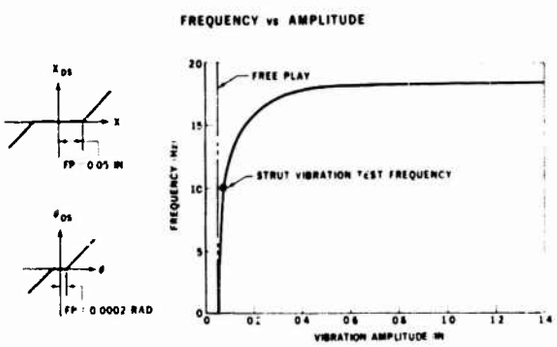


FIGURE 3. LANDING GEAR FREE VIBRATION FREQUENCY

BRAKE TORQUE FUNCTION

As stated previously, the brake torque function is dependent on the brake lining materials; or, more specifically, the brake lining material mixes control the friction coefficient between the brake rotor and stator interfaces. Figure 4 shows an idealized brake torque curve. Brake torque is shown as a smooth function of brake stator and rotor relative angular velocity. Measurements of actual hardware functions show irregularities in the curve and variations with subsequent stops of the same brake assembly. The essential feature, however, of an increasing brake torque at slow aircraft forward velocities (small values of $\dot{\psi}$) is indicated and is reasonably representative of measured data. In the analysis, the initial conditions simulate the gear in a statically deflected rearward position ($\dot{\theta} = 0$ and $\dot{\psi} = V/R$). Thus, for the initial state, the abscissa (Figure 4) can be specified in terms of the forward velocity V of the aircraft cg and the breakpoint in the plot can be associated with a particular aircraft velocity. The analysis is started at $V_i > V_B$, where V_B is the prescribed velocity at the breakpoint. At the start of the simulation, while V_i is greater than V_B, a period of non-vibratory motion precedes the eventual excitation of squeal vibrations that may occur when the aircraft is decelerated by the drag forces through the break-velocity region.

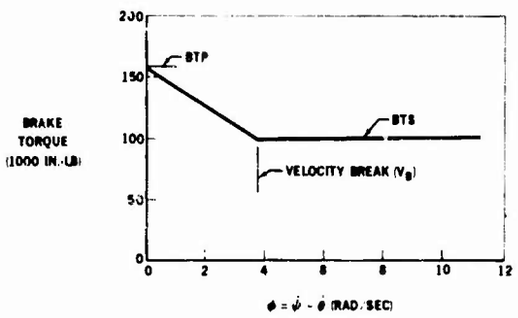


FIGURE 4. BRAKE TORQUE FUNCTION

The idealized curve (Figure 4) was used for the numerical analysis. A value of ϕ equal to 3.8 rad/sec was selected as the point separating the two distinct straight line portions of the brake torque curve.

The brake torque peak value (BTP) and the flat brake torque value (BTS) must be selected with some caution to achieve compatibility with the drag force generated at the tire contact point. Excessive brake torque will tend to decrease the wheel angular velocity too severely while large drag forces increase the wheel angular velocity. The analysis revealed that when these conditions prevail, the resulting responses will be erratic and inconsistent with measured data.

SLIP RATIO AND DRAG CALCULATIONS

Drag force is obtained from the product of tire friction coefficient and tire normal force. The normal force is equal to the aircraft weight per gear and any vertical dynamic

forces are ignored. The friction coefficient is dependent on wheel slip ratio and the computed drag force direction is determined by the logic shown in Figure 5. An aft drag force (see ①, ④, and ⑥ in Figure 5) is the most probable condition during braking while a forward drag force would seem unlikely. There is, however, no definite evidence that a forward drag force is impossible. If V denotes the aircraft forward velocity and $\dot{x}$ is the velocity of the wheel center relative to the aircraft cg, the velocity $V-\dot{x}$ is then the axle velocity with respect to the ground. Equation 4 indicates that for the slip ratio, SR, tire slipping will be measured by the difference between the wheel translational velocity and the tire tangential velocity, $R\dot{\psi}$.

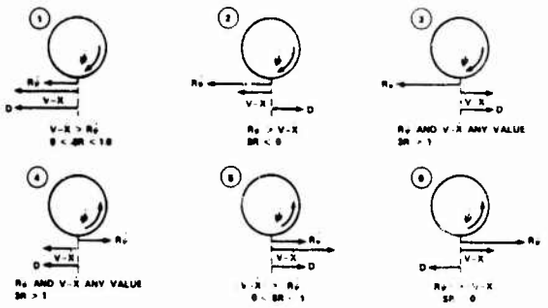


FIGURE 5. SLIP RATIO CONFIGURATIONS

$$SR = 1.0 - \frac{R\dot{\psi}}{V - \dot{X}} \qquad (4)$$

The tire-ground friction coefficient (μ) is a function of the slip ratio. The specific ralationship for this function used in the numerical anlysis in this report is shown in Figure 6 and was obtained from Reference 3.

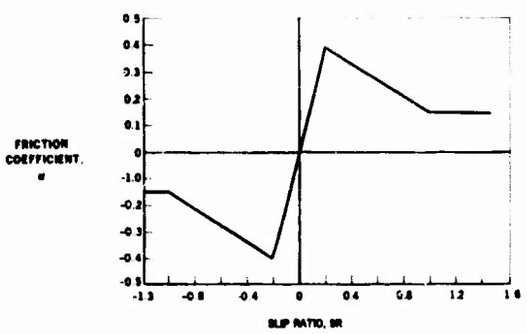


FIGURE 6. TIRE FRICTION COEFFICIENT VS SLIP RATIO

EQUATIONS OF MOTION

The equations of motion are categorized by the component to which they apply. In the right-hand diagram of Figure 7, the reversed effective inertia, ground drag, and brake torque forces are shown applied to the gear rotating assembly. Each force is considered as a sum of forces

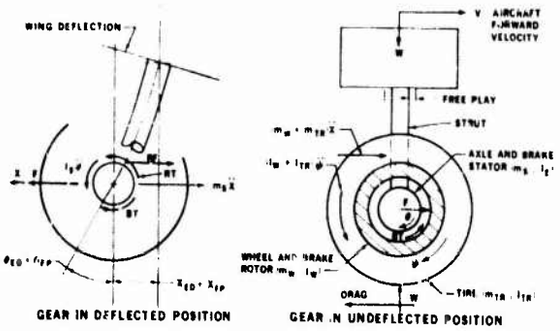


FIGURE 7. GEAR SCHEMATIC

contributed by all wheels on the gear. Using D'Alembert's approach the dynamic equations of equilibrium for the rotating wheel, tire and brake rotor assembly are:

$$(m_W + m_{TR})\,\ddot{X} + F = D \qquad (5)$$

$$(I_W + I_{TR})\,\ddot{\psi} + BT = R \cdot D \qquad (6)$$

In Equation 5, F is the fore and aft force applied through the brake and, in Equation 6, BT is the torque resistance developed by the brake. The angle ψ in Equation 6 refers to the angular rotation of the wheel.

In the left diagram (Figure 7) the reversed effective inertia, strut and brake resistance forces are shown applied to the brake stator. The dynamic equations for the brake stator and axle assembly are as follows:

$$m_S\,\ddot{X} + RF = F \qquad (7)$$

$$I_S\,\ddot{\theta} + RT = BT \qquad (8)$$

Replacing the quantity F in Equation 5 with the left side of Equation 7 the following equation is obtained:

$$m_T\,\ddot{X} + RF = D \qquad (9)$$

The angular rotation θ in the above equations refers to the rotation of the stator and essentially results from the angular rotation incurred at the bottom of the strut (at the junction of strut and axle) when the strut is deflected fore and aft. The strut forces RF and RT resisting translational and rotational displacement of the stator and axle assemblies are given by

$$\begin{Bmatrix} RF \\ RT \end{Bmatrix} = \begin{bmatrix} K_{XX} & K_{X\theta} \\ K_{\theta X} & K_{\theta\theta} \end{bmatrix} \begin{Bmatrix} X_{DS} \\ \theta_{DS} \end{Bmatrix} + \begin{bmatrix} C_{XX} & C_{X\theta} \\ C_{\theta X} & C_{\theta\theta} \end{bmatrix} \begin{Bmatrix} \dot{X} \\ \dot{\theta} \end{Bmatrix} \qquad (10)$$

The relationship of X_{DS} and θ_{DS} to X and θ, respectively, has been shown previously (Figure 3). The quantities X_{DS} and θ_{DS} are introduced to account for free

play or slop in gear fore-and-aft motion. The displacements X and θ are composed of two parts: namely an elastic contribution (X_{ED} and θ_{ED} in Figure 7) and a contribution from free play (X_{FP} and θ_{FP} in Figure 7). The elements of the first matrix on the right-hand side of Equation 10 constitute the combined strut-wing stiffness matrix with respect to fore-and-aft elastic deflection. The matrix which follows the plus sign in Equation 10 constitutes the strut structural damping matrix with respect to fore-and-aft motion.

Sticking Logic

As the wheel angular velocity is reduced with brake application, the stator angular velocity increases due to squeal excitation and eventually these rates are equal. When "sticking" occurs (i.e., $\dot{\psi} = \dot{\theta}$) Equation 6 is replaced by

$$I_T \ddot{\theta} + RT = R \cdot D \tag{11}$$

Conceivably, the two parts remain stuck together until the strut develops a sufficient restoring torque (RT) equal to the brake torque peak (BTP) minus the stator inertia torque ($I_S \ddot{\theta}$). Typically during the sticking condition $RT \leq BTP - I_S\ddot{\theta}$. Sticking appears to be primarily of rotational origin and when occurring will cause the squeal mode to vanish because the stator is no longer free to oscillate independent of the wheel. The consequence of sticking can be seen in measured brake pressure responses and is exhibited in the numerical results obtained from the mathematical model developed in this paper. The brake torque value must also be modified during sticking. Under these circumstances, the BT developed is dependent on the drag and inertia forces and not on the relative angular velocity ϕ. The magnitude of BT may vary from zero to the brake torque peak (BTP) during sticking. When sticking occurs, the value of the brake torque is computed from

$$BT = I_S \ddot{\theta} + RT \tag{12}$$

Aircraft Equations

The aircraft equations used in the analysis are

$$\dot{V} = -D \cdot \frac{g}{W} \tag{13}$$

$$V = \int \dot{V}\, dt \tag{14}$$

In the program an initial velocity is selected that is slightly greater than the break velocity in the brake torque curve.

Initial Conditions

The mathematical simulation is started with the brake applied. To avoid elastic transients due to the step input in brake torque, starting values are computed for the several variables and employed as initial conditions when integrating the equations of motion. The required initial drag force, drag friction, slip ratio, wheel rotating velocity, gear elastic displacement and rotation are expressed by the following equations:

$$D_i = \frac{BTS}{R} \tag{15}$$

$$\mu_i = \frac{D_i}{W} \tag{16}$$

$$SR_i = \frac{\mu_i}{2} \tag{17}$$

$$\dot{\psi}_i = (1 - SR_i)\frac{V_i}{R} \tag{18}$$

$$\begin{bmatrix} X_i \\ \theta_i \end{bmatrix} = \begin{bmatrix} a \end{bmatrix} \begin{bmatrix} D_i \\ BTS \end{bmatrix} + \begin{bmatrix} X_{FP} \\ \theta_{FP} \end{bmatrix} \tag{19}$$

In Equation 19, the matrix [a] is the strut flexibility matrix and is the inverse of the stiffness matrix given in Equation 10.

Airplane Elastic Mode Equations

An assumed elastic airplane wing torsion mode was simulated with the expectation that a considerable increase in axle displacement would be realized. The formulation takes the form of the excitation of an equivalent simple resonator in the modal coordinate. The equations involving one elastic mode are:

$$\bar{m}\ddot{q} + \bar{c}\dot{q} + \bar{k}q = \phi \cdot M(t) \tag{20}$$

Where:

- $\bar{m}, \bar{c}, \bar{k}$ = generalized mass, damping, and stiffness
- q = generalized coordinate
- ϕ = the modal amplitude at the gear attachment location
- $M(t)$ = torsional moment applied to the wing at the gear attachment

$$\bar{c} = 2\zeta \bar{m} \omega_n \tag{21}$$

$$\bar{k} = \omega_n^2 \bar{m} \tag{22}$$

where:

- ζ = structural mode critical damping
- ω_n = structural mode natural frequency

$$\sigma = \phi \cdot q \tag{23}$$

where:

- σ is the actual wing pitch displacement (wing torsional rotation)

The torsional moment is given by:

$$M = RT + L \cdot RF \tag{24}$$

The elastic forces at the stator become:

$$\begin{bmatrix} RF \\ RT \end{bmatrix} = \begin{bmatrix} k_{xx} & k_{x\theta} \\ k_{\theta x} & k_{\theta\theta} \end{bmatrix} \begin{bmatrix} X_{DS} - L \cdot \sigma \\ \theta_{DS} - \sigma \end{bmatrix} \tag{25}$$

The forces and deflections may be visualized from Figure 8.

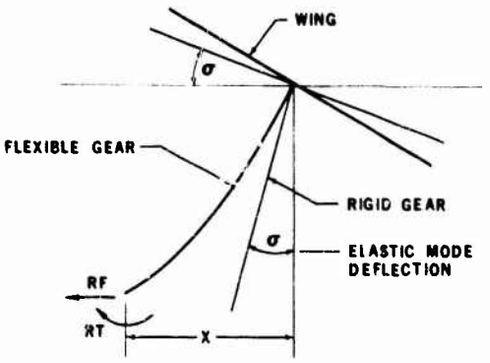


FIGURE 8. ELASTIC MODE DEFLECTIONS

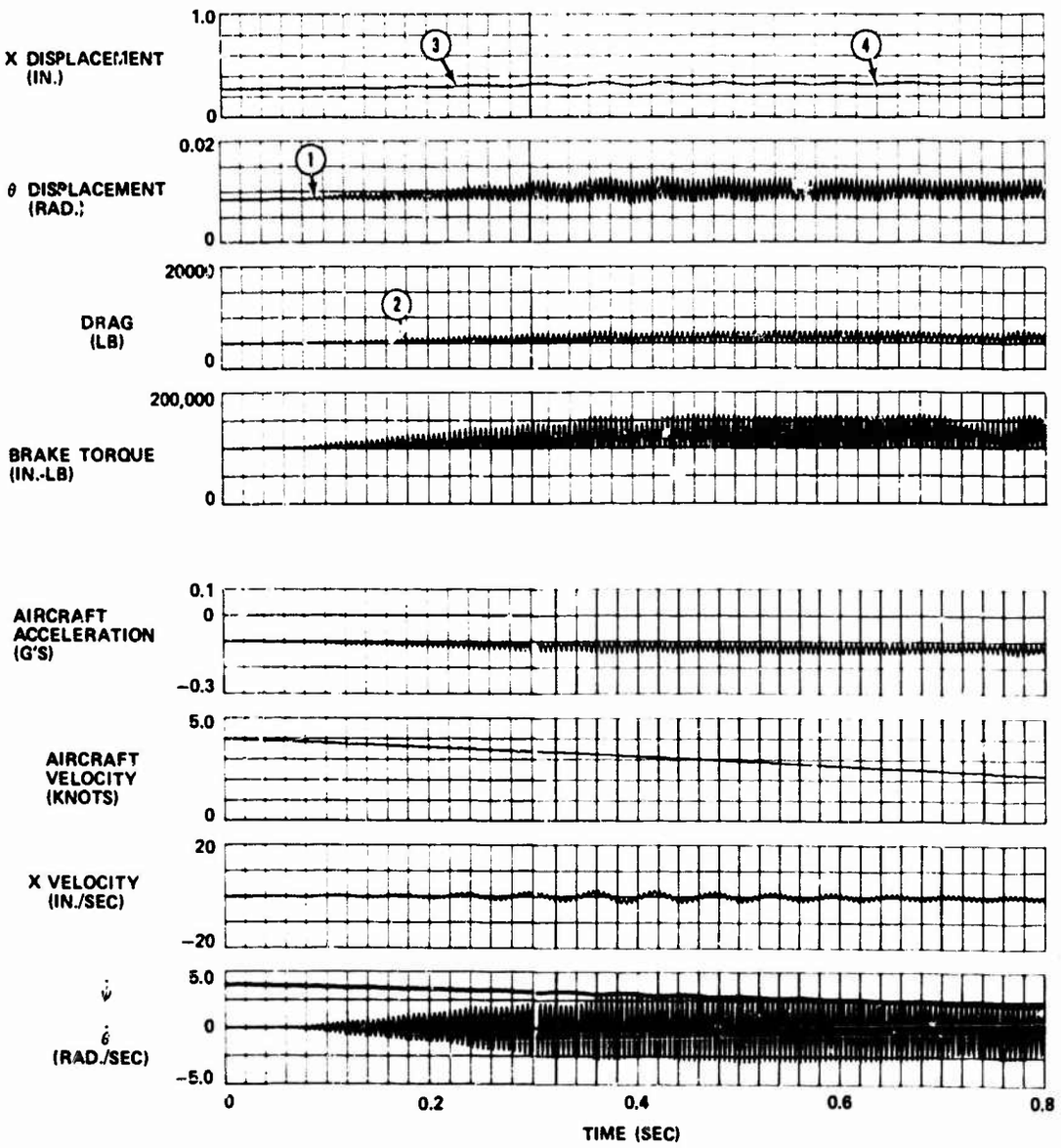


FIGURE 9. COMPUTED RESPONSES

Inclusion of an elastic mode required initial conditions for the coordinate associated with the mode. In the analysis, the initial values of X and θ are calculated using the following set of equations:

$$M_i = D_i \cdot L + BTS \tag{26}$$

$$q_i = \phi \cdot \frac{M_i}{\bar{k}} \tag{27}$$

$$\sigma_i = \phi \cdot q_i \tag{28}$$

$$\begin{bmatrix} X_i \\ \theta_i \end{bmatrix} = \begin{bmatrix} \quad a \quad \end{bmatrix} \begin{bmatrix} D_i \\ BTS \end{bmatrix} + \begin{bmatrix} X_{FP} \\ \theta_{FP} \end{bmatrix} + \begin{bmatrix} L \cdot q_i \\ \sigma_i \end{bmatrix} \tag{29}$$

The values of $\dot{q}$, $\dot{X}$ and $\dot{\theta}$ are all taken initially to be of zero magnitude.

ANALYSIS AND COMPUTED RESPONSES

The computed responses of a simulated aircraft braking stop are shown in Figure 9. The brake torque function (Figure 4) and the applied tire friction coefficient versus slip ratio (Figure 6) used in this analysis are specifically the functions shown. Aircraft elastic mode effects are not included in the calculated responses. The magnitudes of the physical parameters employed in the analysis are representative of the Douglas DC-9 aircraft.

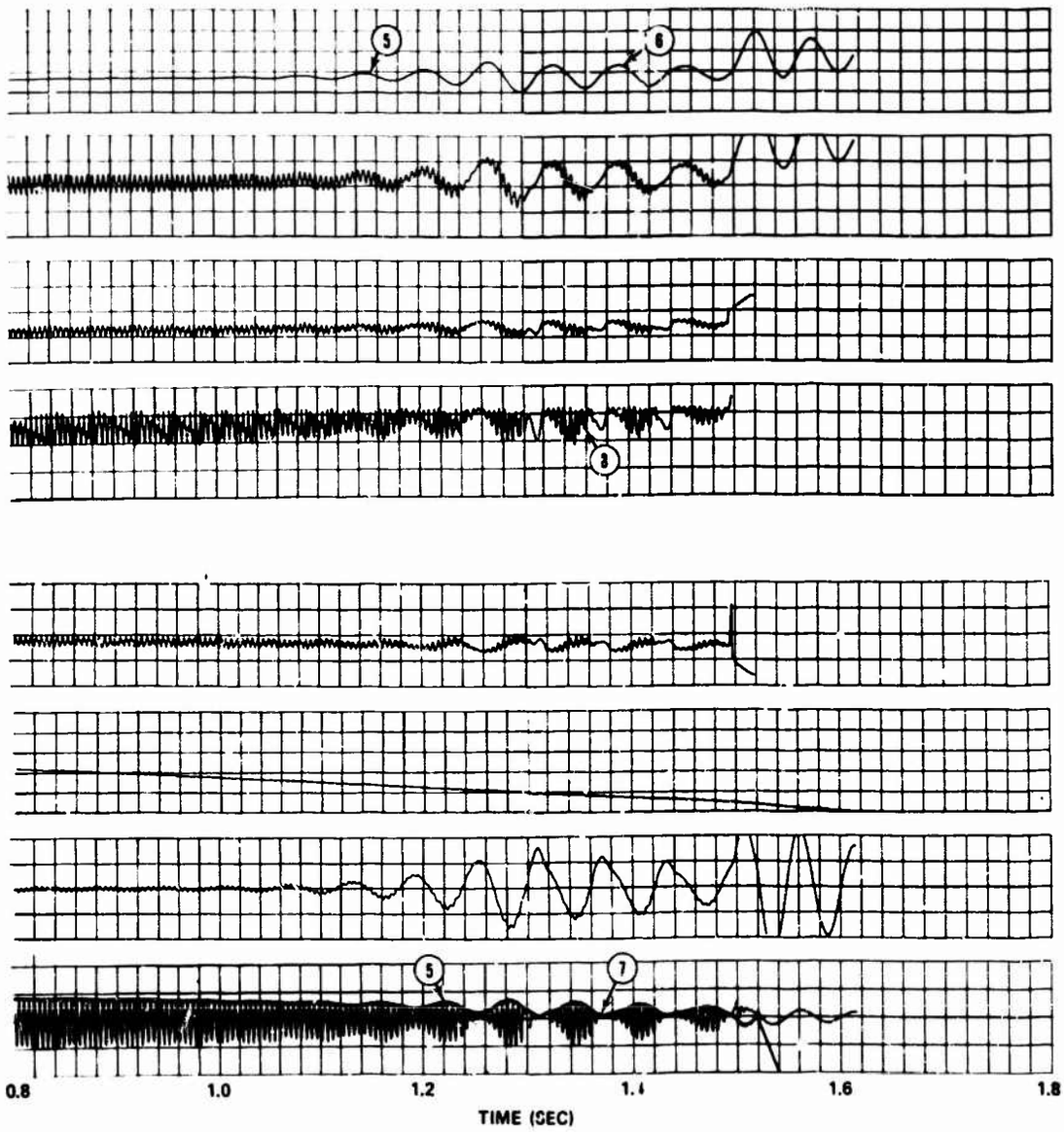


FIGURE 9. (CONTINUED)

The aircraft braking simulation was started at an aircraft velocity of 4 knots. For the parameters chosen in the model, the velocity decreased below the break velocity in 0.1 seconds. At this instant, the brake torque took on values on the negative sloping portion of the brake torque curve. At this point a sequence of events, which are numerically indicated (see Figure 9), occurred in the following order: (1) squeal mode appears, (2) irregularities occur in the brake torque, (3) chatter vibrations are initiated and (4) chatter vibrations decay to a steady amplitude due to structural damping forces. The functions ψ and $\dot{\theta}$ are plotted together so that the effect of sticking between the rotor and stator can be exhibited. Subsequent events shown and numerically marked (Figure 9) are: (5) first appearance of sticking and the actual inauguration of the chatter mode, (6) increase in sticking in chatter amplitude, (7) increase in sticking duration and the disappearance of the squeal mode and (8) the beat-like growth and decay of the brake torque with each chatter cycle. This beat-like behavior has been observed in recorded brake hydraulic pressures during chatter excitations.

The calculated response also indicates that the gear fore and aft displacement, X, is always aft of the neutral position and never decreases to an amplitude within the freeplay region. Therefore, the total gear stiffness is effective during a complete chatter vibration cycle and the expected forced vibration frequency would be 18 Hz (Figure 4). The average calculated chatter frequency is approximately 16 Hz, the discrepancy apparently resulting from the slip-stick phenomenon previously described.

As the velocity approaches one-third knot or less, the developed program tends to produce questionable results. An explanation may be found in examining the constraint of the tire degree-of-freedom in the simulation. At very slow velocities tire rotational deformations might be expected and conceivably should be included. The additional vibration mode, termed wheel chatter, would be introduced corresponding to a frequency governed by the tire rotational restoring spring and the wheel rim plus brake rotor mass. This frequency has not been observed in the limited measure data obtained on the DC-9 aircraft.

The simulation was modified to examine the effect of tire dynamics upon response characteristics. The results were unsatisfactory because the response was dominated by the wheel chatter mode while the gear chatter mode vanished. A redundancy may be implied by the simultaneous definition of drag force through a measured slip ratio function and the inclusion of a tire degree-of-freedom. The tire deformations might be implicit in the slip ratio function as the measurements are obtained relative to the landing gear axle. Apparently, a slip ratio function relative to the tire contact point is required.

METHODS OF ATTENUATION

The most direct and effective method of providing attenuation of both the squeal and chatter modes is to employ the proper mixes in the brake lining material. The expression "proper mixes" refers to those mixes that influence a constant brake torque amplitude at all relative angular velocities, i.e., a flat brake torque function. Brake lining suppliers are presently developing various mixes to solve this problem.

The squeal condition, intimate with the brake stator rotation, can be attenuated by physically attaching to the brake stator a vibration absorber tuned near to the squeal frequency. Since fore and aft motion of the strut, in general, accompanies the rotational motion at the bottom of the strut, chatter will usually occur in conjunction with brake squeal. However, the analytical studies revealed that squeal removal did not necessarily eliminate chatter. Chatter can be effectively attenuated by a vibration absorber intimate with the fore and aft motion of the strut. Analysis indicates that the chatter absorber weight will be excessive.

VIBRATION ABSORBER EQUATIONS

The vibration absorber can be characterized by a mounting-base-excited simple oscillator. The absorber produces a large force reaction at the mounting base when the forcing function coincides with the resonant frequency. The opposing reaction force on the structure attenuates the motion. Two new resonant frequencies are generated, thus the selection of absorber mass and critical damping ratio is important. The selection of a squeal vibration absorber is discussed in Reference 4 along with appropriate design charts. Calculated results for several design conditions tended to confirm the curves presented in Reference 1. Schematics of the absorbers are shown in Figure 10.

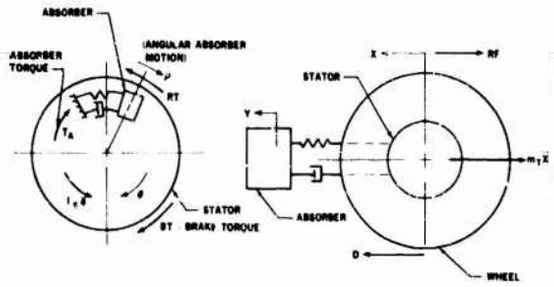


FIGURE 10. VIBRATION ABSORBER SCHEMATICS

Squeal vibration absorbor equations are:

$$I_A\ddot{\rho} + c_{\rho\rho}(\dot{\rho} - \dot{\theta}) + k_{\rho\rho}(\rho - \theta) = 0 \qquad (30)$$

where

$I_A = m_A R_A^2$; effective absorber rotating inertia

$C_{\rho\rho} = 2\zeta_A I_A \omega_{nA}$; absorber rotational damping coefficient

$K_{\rho\rho} = \omega_{nA}^2 I_A$; absorber rotational stiffness

The stator rotational equation of motion must be modified to include the absorber torque reaction (T_A):

$$I_S\ddot{\theta} + RT - BT - T_A = 0 \qquad (31)$$

$$T_A = c_{\rho\rho}(\dot{\rho} - \dot{\theta}) + k_{\rho\rho}(\rho - \theta) \qquad (32)$$

The applicable chatter vibration absorber equations are:

$$m_{CA}\ddot{Y} + c_{CA}(\dot{Y} - \dot{X}) + k_{CA}(Y - X) = 0 \qquad (33)$$

where:

m_{CA} = chatter absorber mass

$C_{CA} = 2\zeta_{CA} m_{CA} \omega_{nCA}$; chatter absorber damping coefficient

$k_{CA} = \omega_{nCA}^2 m_{CA}$; chatter absorber spring stiffness

The equation of motion of the stator assembly must be modified to include the absorber applied force (F_A).

$$m_T \ddot{X} + RF - F_A - D = 0 \qquad (34)$$

A simulation that employs a vibration absorber necessitates initial displacements on the absorbers. For initial displacement of the absorber take

$$\rho_i = \theta_i \quad \text{squeal absorber} \qquad (35a)$$

$$Y_i = X_i \quad \text{chatter absorber} \qquad (35b)$$

The initial velocities are given

$$\dot{\rho}_i = 0 \quad \text{squeal absorber} \qquad (36a)$$

$$\dot{Y}_i = 0 \quad \text{chatter absorber} \qquad (36b)$$

SELECTION OF ABSORBER PARAMETERS

A squeal vibration absorber was analytically added to the simulation employing the equations of the previous section. The properties of this absorber were established on the basis of the work in Reference 4 utilizing the plot in Figure 3 in this reference. The addition of the absorber to the stator results essentially in a two-degree-of-freedom system. The magnitudes of the absorber's damping level and tuning frequency should be carefully selected such that both of the modes in the two-degree-of-freedom system are suppressed. The cases studied in this paper corroborated the results in Reference 4 concerning the proper parameters of a vibration absorber to attentuate a squeal mode. For the particular gear and brake torque curve used in this investigation an effective squeal vibration absorber might weigh 5 to 8 pounds and require 15 percent critical damping.

A schematic representation of a chatter vibration absorber considered in this study is shown previously (Figure 10). An absorber weighing 100 lb and having 10 percent critical damping was found to appreciably attenuate the chatter vibration. This result does not constitute an optimum set of properties and with further study a lesser weight chatter absorber may be obtained.

SUMMARY AND CONCLUSION

The paper discusses aircraft landing gear chatter and brake squeal vibrations. Transmission of disturbing vibrations into the aircraft passenger compartment and the possibility of accumulated landing gear damage and brake wear prompted an investigation into these phenomena. A digital program was prepared to simulate the DC-9 aircraft main landing gear slowing to a braking stop. The mathematical model represented the fore and aft motion of the gear with the accompanying rotational motion at the gear axle. Comparison of computed responses and measured data indicated a reasonably appropriate simulation.

The analysis confirmed the supposition that the brake torque function characteristic was the primary contributor to chatter and squeal excitation. Specifically, the increasing brake torque amplitude in relation to a diminishing relative brake rotor-to-stator angular velocity instigated the self-excited condition. This function effectively produced a negative damping that sustained and/or increased the vibration amplitudes. An intermittent, periodic slip-stick action that appeared as the chatter motion increased is essential in explaining a chatter frequency that is lower than the measured free vibration gear fore and aft frequency.

Several vibration attenuation methods are detailed; the most effective and direct is to use a mix in the brake lining that ensures a flat brake torque function. Vibration absorbers can be employed to eliminate squeal and chatter. A squeal vibration absorber could be utilized without a substantial weight penalty; however, a chatter vibration absorber would require an excessive weight.

The excitation of an elastic vibration mode, particularly a wing torsion mode, would substantially increase the chatter motion and amplify the vibrations perceived by the passengers. Equations are presented that include a wing torsion mode in the equations of motion for the complete system.

REFERENCES

1. C. M. Harris and C. E. Crede, "Shock and Vibration Handbook," Chapter 40 (Author S. A. Tobias), McGraw-Hill Book Co., Inc., New York, 1961.

2. F. L. Ryder, "Creative Engineering Analysis," Prentice-Hall, Inc., Englewood Cliffs, N. J., 1961.

3. S. A. Batterson, "A Study of the Dynamics of Airplane Braking Systems as Affected by Tire Elasticity and Brake Response," NASA TN D-3081, October 1965.

4. A. K. Abu-Akeel, "Damping of High Frequency Brake Vibrations in Aircraft Landing Gear," AIAA Paper No. 68-312, Presented at AIAA/ASME 9th Structures, Structural Dynamics and Materials Conference, Palm Springs, California, April 1-3, 1968.

APPENDIX A

COMPUTER PROGRAM

A listing of the digital program simulating brake squeal and strut chatter is presented in Figure A-1. This program was used to obtain the numerical results presented in this report. The program is written in the IBM-CSMP (Continuous Systems Modeling Program) language.

```
INIT
*
*  CALCULATE STRUT RESONANT FREQUENCIES
*
      STX = SXT
      TM  = SM + WM + TMS
      TI  = SI + WI + TIR
      B = STT/TI+ SXX/TM
      C = ( SXX * STT - SXT * STX ) / ( TM* TI)
      RF12 =(B - SQRT ( B**2 - 4.0*C ) )/2.0
      RF1 = SQRT (RF12)
      FF1 = RF1 / 6.2832
      RF22 =(B + SQRT ( B**2 - 4.0 * C ) )/2.0
      RF2 = SQRT (RF22)
      FF2 = RF2 / 6.2832
      B1 = STT/SI + SXX/TM
      C1 = (SXX * STT - SXT *STX) / (TM * SI )
      SQ = SQRT (B1**2 - 4.0*C1)
      F1 = SQRT (( B1-SQ )/2.0) / 6.2832
      F2 = SQRT (( B1+SQ )/2.0) / 6.2832
*
*  CALCULATE STRUT DAMPING MATRIX
*
      T1 = ( RF12 *TM - SXX ) / SXT
      T2 = ( RF22 *TM - SXX ) / SXT
      BM1 = TM + TI* ( T1**2 )
      BM2 = TM + TI * ( T2**2 )
      GC1 = 2.0 * BM1 * CRD1 * RF1
      GC2 = 2.0 * BM2 * CRD2 * RF2
      CXX = ((T2**2)*GC1 + (T1**2)*GC2) / DETR
      DETR = ( T2 - T1 )**2
      CXT = (-T2* GC1 - T1 * GC2) / DETR
      CTX = CXT
      CTT =  ( GC1 + GC2 ) / DETR
*
*  CALCULATE FLEXIBILITY MATRIX
*
      DET = SXX*STT - STX*SXT
      A11 = STT / DET
      A12 = - STX / DET
      A21 = - SXT / DET
      A22 = SXX / DET
*
NOSORT
      DT   = BTP
      CALL PRNT
SORT
*
*  CALCULATE INITIAL CONDITIONS TO ELIMINATE STARTING TRANSIENTS
*
      BEIT = BTS / RST
      OIT  = BTS / R
      FUIT = OIT / W
      SRIT = FUIT / 2.0
      PSIT = ( 1.0 - SRIT ) * VLIT / R
      XIT  = A11 * OIT + A12 * BTS * FPX
      THIT = A21 * OIT + A22 * BTS * FPTH
      BT = BTS
      X    = XIT
      TH   = THIT
      O    = OIT
      PSIID= PSIT
*
CONST  SXX = 63300.0,  SXT = -1134000.0,  STT = 43100000.0,...
       SI = 26.88,  WI = 47.4,  TIR = 161.8,...
       SM = 0.632,  WM = 1.032,  TMS = 0.676,...
       CRD1 = 0.05,  CRD2 = 0.05,  VLK = 4.0,  BTS = 100000.0, ...
       R = 20.0,  W = 50000.0,  CT = 21.6, ST = 25400.0, WR = 11.0
CONST FPX = 0.05  , FPTH = 0.0002, VLIT = 81.0720, BTP = 160000.0
```

FIGURE A-1. CSMP COMPUTER PROGRAM

```
DYNAM
*
*  AIRPLANE  DECELERATION  EQUATIONS
*
      VL10 = -G * ( 386.4 / W )
      VL = INTGRL ( VLIT   , VL10 )
      KV  = VL / 20.268
*
*  ELASTIC  RESTORING FORCES
*
        XOS  = DEADSP ( -FPX, FPX, X )
        THOS = DEADSP ( -FPTH, FPTH, TH )
        ERT  = STT*THOS + STX*XOS + CTT*TH10 + CTX*X10
        ERF  = SXX*XOS + SXT*THOS + CXX*X10 + CXT*TH10
*
*  INTEGRATING EQUATIONS
*
        X20 = ( 0 - ERF ) / TM
        X10 = INTGRL ( IC2, X20 )
        X   = INTGRL ( XIT, X10 )
      TH10 = INTGRL ( IC1, TH20 )
        TH  = INTGRL (THIT, TH10 )
      PS110 = INTGRL (PSIT, PS120 )
*
*  DRAG FORCE CALCULATION
*
      SR = 1.0 - ( R*PSI10 ) / ( VL-X10 )
      FU = AFGEN ( FRICT, ABS(SR) )
AFGEN FRICT = 0.0, 0.0, 0.2, 0.4, 1.0, 0.2, 10000.0, 0.2
NOSORT
      IF ( ( VL-X10 ) - R*PS110 ) 5, 6, 6
    5 MU = -FU
      GO TO 7
    6 MU = FU
    7 D = MU * W
SORT
*
      DTS = BTP - ST * PSI20
      PHI = PS110 - TH10
AFGEN  FUNCT = -100.0, 160000.0, 0.0, 160000.0, 3.8, 100000.0, ...
                1000.0, 100000.0
*
*  LOGIC  TO  PERMIT  LOCKING  OF  WHEEL  AND  HUB
*
PROCED  PSI20, TH20 = CAL ( R, D, BT, ERT, PHI, DT )
      IF ( PHI .LE. 0.0 .AND. ERT .LE. DT ) GO TO 10
      PSI20 = ( R*D - BT ) / ( W1 + TIR )
      TH20 = ( BT - ERF ) / ST
      GO TO 15
   10 PSI20 = ( R*D - ERT ) / T1
      TH20  = PSI20
   15 CONTINUE
ENDPRO
*
*  BRAKE TORQUE EQUATIONS
*
NOSORT
      IF ( PHI .GE. 0.0 ) GO TO 100
      BT = S1 * TH20 + ERT
      GO TO 200
  100 CONTINUE
      BT = AFGEN ( FUNCT, PHI )
  200 CONTINUE
      DT = DTS
      IF ( VL ) 1, 2, 2
    1 TIME = FINTIM
    2 CONTINUE
SORT
*
LABEL     STRUT CHATTER
INCON IC1 = 0.0, IC2 = 0.0
RANGE  X, TH
TIMER  DELT = .00005, FINTIM = 3.00, OUTDEL = 0.001, PRDEL = 0.001
PRINT SR, D, VL, X10, BT, TH10, VL10, PS110
METHOD  RKSFX
END
STOP
```

FIGURE A-1. (CONTINUED)

APPENDIX B

GEAR STIFFNESS MATRIX CALCULATION

The gear stiffness matrix was obtained from the inversion of the flexibility matrix representing deflections in X and θ at the axle end of the strut. The elements of the flexibility matrix are derived from the theoretical flexibility at the gear attachment location and the theoretical cantilevered gear flexibility matrix.

A diagram of the wing chord section at the gear – wing joint is shown in Figure B-1. The forces and displacements involved in describing the attachment flexibilities are shown in the figure. The forces D and M which are the gear reactions acting on the wing are replaced by the forces F_1 and F_2 when performing the Redundant Force Analysis on the wing box. The forces F_1 and F_2 produce the displacements X_1, X_2, Z_3, and Z_4 shown in the figure. Deflections are related to unit applied loads by the flexibility matrix [A]. Thus, it can be written that

$$\begin{bmatrix} X_1 \\ X_2 \\ Z_3 \\ Z_4 \end{bmatrix} = [A] \begin{bmatrix} F_1 \\ F_2 \end{bmatrix} \qquad (B1)$$

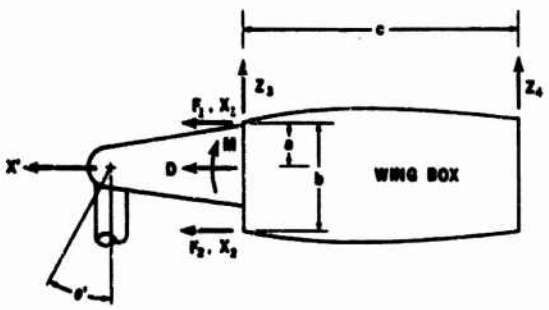


FIGURE B-1. GEAR ATTACH FLEXIBILITY

The forces F_1 and F_2 are related to the forces D and M by a matrix [B] of geometric elements. This relationship is given by

$$\begin{bmatrix} F_1 \\ F_2 \end{bmatrix} = [B] \begin{bmatrix} D \\ M \end{bmatrix} \qquad (B2)$$

where

$$[B] = \begin{bmatrix} \frac{b-a}{b} & \frac{-1}{b} \\ \frac{a}{b} & \frac{1}{b} \end{bmatrix} \qquad (B3)$$

and the distances a and b are as shown (Figure B-1). The deflection and rotation, X' and θ' of the strut at the wing-joint are expressed in terms of the vector matrix of the wing box deflections by the geometric matrix [C] as follows

$$\begin{bmatrix} X' \\ \theta' \end{bmatrix} = [C] \begin{bmatrix} X_1 \\ X_2 \\ Z_3 \\ Z_4 \end{bmatrix} \qquad (B4)$$

where

$$[C] = \begin{bmatrix} \frac{b-a}{b} & \frac{a}{b} & 0 & 0 \\ 0 & 0 & \frac{1}{c} & \frac{-1}{c} \end{bmatrix} \qquad (B5)$$

Combining Equations B1, B2 and B3 the gear deflections are given as functions of the gear forces by

$$\begin{bmatrix} X' \\ \theta' \end{bmatrix} = [F] \begin{bmatrix} D \\ M \end{bmatrix} \qquad (B6)$$

where

$$[F] = [C] \quad [A] \quad [B] \qquad (B7)$$

The strut displacement X and rotation θ at the axle are given by

$$\begin{bmatrix} X \\ \theta \end{bmatrix} = [H] \begin{bmatrix} X' \\ \theta' \end{bmatrix} + [E] \begin{bmatrix} D \\ T \end{bmatrix} \qquad (B8)$$

In Equation B8, [E] is the strut cantilevered flexibility matrix, D is the force at the axle in the X direction, T is the axle torque and [H] is the following geometric matrix

$$[H] = \begin{bmatrix} 1 & L \\ 0 & 1 \end{bmatrix} \qquad (B9)$$

D and M are related to D and T as

$$\begin{bmatrix} D \\ M \end{bmatrix} = [H]^T \begin{bmatrix} D \\ T \end{bmatrix} \qquad (B10)$$

where the superscript T indicates matrix transpose. The complete flexibility relationship is

$$\begin{bmatrix} X \\ \theta \end{bmatrix} = \left[[H] [F] [H]^T + [E] \right] \begin{bmatrix} D \\ T \end{bmatrix} \qquad (B11)$$

The stiffness matrix [K] is obtained by inverting the first matrix on the right-hand side of Equation B11; thus

$$[K] = \left[[H] [F] [H]^T + [E] \right]^{-1} \qquad (B12)$$

Therefore, the flexibility matrix [a] referred to in the main body of this paper is equal to $[K]^{-1}$.

EXPERIMENTAL INVESTIGATION OF NONLINEAR VIBRATIONS OF LAMINATED ANISOTROPIC PANELS

Bryon L. Mayberry* and Charles W. Bert
School of Aerospace and Mechanical Engineering
University of Oklahoma
Norman, Oklahoma

Steady-state vibrational experiments were performed to determine experimentally the resonant frequencies of different clamped rectangular plates made of various composite-material laminates under large deflections. The panels were fabricated from a glass-fiber reinforced plastic consisting of glass fabric (E-glass with S-920 finish, Style 909) impregnated with epoxy (Epon 828, curing agent Z). Lamination arrangements were: (a) Two parallel plies oriented at 0° (parallel to longest edge of plate), (b) Two parallel plies at 45°, (c) Four-ply 0°/90° cross ply, and (d) Four-ply +45°/-45° cross ply.

Base excitation of the rigid clamping fixture was accomplished with an electrodynamic shaker. Resonance was determined by the peak amplitude response of a small metallic-foil strain gage at the plate center and stroboscopic observation of a grid pattern on the plate surface was used for mode identification. As the exciting force (and thus the plate deflection) was increased, the resonance frequencies associated with the various vibrational modes increased. This indicated that the nonlinearity was a geometric one of the hardening-spring type, in qualitative agreement with various theoretical analyses of large-amplitude vibration of rectangular plates.

INTRODUCTION

Composite materials, especially those consisting of laminations of fiber-reinforced plastics, are coming into widespread use in various types of vehicle structures. A basic structural configuration present in many different kinds of vehicle structures is the rectangular panel. Thus, information on the static strength, buckling and vibrational characteristics of such panels constructed of laminated composite material is of considerable importance in the design of such vehicles.

Very recent composite-material research has been devoted to static strength under multiaxial tension [1], static plate buckling under uniaxial compression [2], and small-deflection plate vibration [3, 4]. However, in many important applications, the dynamic excitations encountered are large enough to produce deflections which are in the large-deflection regime. Thus, the purpose of the present experimental investigation was to study large-deflection vibration of clamped rectangular plates composed of laminated composite material.

SPECIMENS AND MATERIALS

The specimen configuration was a thin plate of rectangular planform. The plates were clamped on all four edges to active dimensions of 9 in. by 6 in.

Four plates were fabricated of laminated anisotropic material, with a different lamination arrangement being used for each plate. Each layer was made of rectangularly orthotropic material in the form of glass-fiber reinforced plastic (GFRP). The GFRP consisted of E-glass/S-920 finish, 909 style fabric impregnated with Epon 828 epoxy resin and curing agent Z.

The material properties of a composite material are highly dependent upon the resin content. The specimens had an average resin content of 46 percent by weight. The basic composite material properties obtained from two-ply, parallel-laminated specimens were as follows:

Major Young's modulus, $E_{11} = 2.70 \times 10^6$ psi

*Presently 2d Lt., USAF, Pilot Training, Webb AFB, Texas.

Minor Young's modulus, $E_{22} = 2.56 \times 10^6$ psi

Major Poisson's ratio, $\nu_{12} = 0.242$

Minor Poisson's ratio, $\nu_{21} = 0.230$

Shear modulus, $G = 0.6 \times 10^6$ psi*

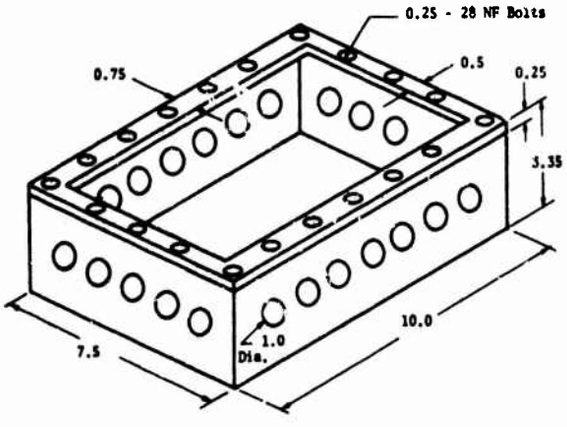
Density, $\rho = 0.000197$ lb-sec^2/in^4

The four lamination arrangements used are listed in Table 1. Curing was carried out in a large autoclave to assure uniform properties.

EXPERIMENTAL APPARATUS

The experimental apparatus was designed to give the most accurate results for the most practical boundary conditions. Thus, the boundary conditions of all edges clamped, essentially completely restrained from both planar and rotational movements, were selected. These boundary conditions are most commonly encountered in aerospace structures, are easiest to approximate experimentally, and minimize extraneous side effects.

A specially designed test fixture was used to clamp the edges of the plate and to attach the plate to the electrodynamic shaker (MB Model C-10). Fig. 1 shows a sketch of the fixture, the base of which was machined from a solid



Note: All dimensions in inches

Fig. 1 - Test Fixture

block of aluminum. The bottom of the fixture base is bolted to the shaker head and the plate is clamped to the top of the base by a heavy rectangular frame with 18 bolts at a 1.5-in. spacing. The base, frame, bolts and bolt spacing were all designed to be sufficiently rigid to assure that the lowest natural frequencies were well above the panel frequency ranges of interest. Fig. 2 is a photograph showing the specimen mounted in the fixture.

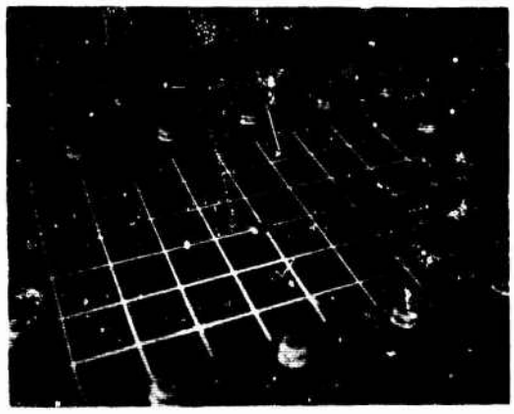


Fig. 2 - Specimen mounted in test fixture

The purpose of the 1-in.-diameter holes in the fixture base (see Fig. 1) was to eliminate air spring and damping effects due to pumping action.

INSTRUMENTATION

Metallic-foil, electrical-resistance strain gages located along the center lines of each plate were the transducers used to determine the natural frequencies.

The electronic circuitry of the instrumentation package that was used to monitor, measure, and record the dynamic signals from the strain gages is shown schematically in Fig. 3 and a photograph is shown in Fig. 4. A voltage of 7 volts D.C. was applied to the gage from a 300-volt D.C. power supply through a variable 10 k-ohm dropping resistor. The resistor also acted as a high-impedance source to the A.C. signal from the strain gage. The signal was applied as input to the A.C. amplifier, which had a high impedance to the D.C. portion of the signal and thus allowed only the A.C. component to be amplified. The voltmeter and oscilloscope were used to monitor amplitude and waveform of only one strain gage. After amplification by the oscillograph amplifier, the signals from all of the strain gages were recorded on an

*Estimated.

oscillograph for a permanent re...

A stroboscope (General Radio Strobotac, Type 1531-AB) was used to observe closely the different modal patterns encountered at various resonant frequencies, as described in the next section.

After the main test series was completed, an additional series was conducted using the same plates as before, but with a small hole drilled through the center of each plate. A finely graduated scale protruding through the hole was used to measure the deflection amplitude.

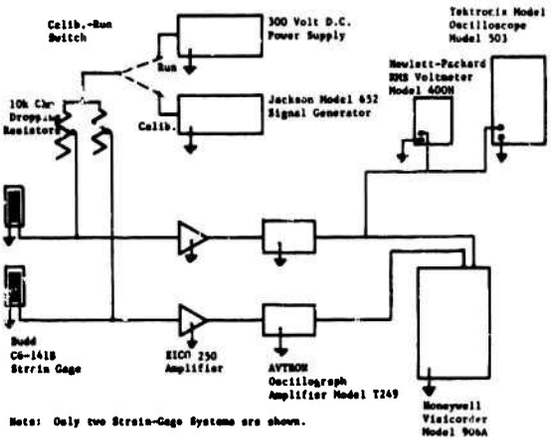


Fig. 3 - Strain-gage electronic schematic diagram

EXPERIMENTAL PROCEDURE

Two different versions of the peak-amplitude method were used to determine the resonant frequencies with very good results. Since the resonant frequencies of a clamped plate are not nearly so closely spaced as those of a shell structure, it was decided that it was unnecessary to use the more refined Kennedy-Pancu method, which requires both amplitude and phase data [5].

The first version used the peak amplitude of metallic-foil strain gages. Since base excitation was used to excite the specimen symmetrically, only one strain gage, located at the center of the plate, was adequate.

As the frequency was increased until the specimen entered a resonant frequency range, the strain-gage signal steadily increased, until it reached a peak value, and then decreased as the frequency was increased further. After the initial sweep, the procedure was repeated and the frequency held at the point at which the peak signal amplitude was obtained. This frequency at which the peak amplitude response was obtained was recorded as the resonant frequency for the particular amplitude.



A. M-B ELECTRODYNAMIC EXCITER TABLE POWER SUPPLY: MODEL C-10

B. M-B ELECTRODYNAMIC EXCITER TABLE: MODEL C-10

C. CMC FREQUENCY COUNTER: MODEL 225B

D. GENERAL RADIO STROBOSCOPE: MODEL 1531-B

E. A.C. AMPLIFIERS: MODEL 250

F. TEKTRONIX OSCILLOSCOPE: MODEL 503

G. 300 VOLTS D.C. POWER SUPPLY

H. AVTRON OSCILLOGRAPH AMPLIFIER: MODEL T249

I. BUDD STRAIN GAGE INDICATOR: MODEL HW-1

J. JACKSON SIGNAL GENERATOR: MODEL 652

K. HONEYWELL VISICORDER: MODEL 906A

Fig. 4 - Photograph of instrumentation

The major disadvantage of the procedure just described is that it is difficult to clearly identify the particular type of mode of the vibration taking place. This problem of uncertainty in identification of modal type led to the use of a second version of the peak-amplitude method.

The second version used stroboscopic light synchronized to the excitation frequency to slow or stop the motion. To facilitate observation of modal patterns, a square grid-line

pattern was painted on the specimen. The paint was a color of high contrast with respect to the color of the plate. Examples of the modal patterns obtained in this way are shown in Figs. 5-7.* The three-dimensional effect of modal



Fig. 5 - Modal Pattern (m = 1, n = 1)



Fig. 6 - Modal Pattern (m = 3, n = 1)

shapes taken by various grid lines as well as locations of the nodes are shown quite clearly. The stroboscopic technique allows the experimenter to detect such localized phenomena as buckling (static or dynamic) of very thin sheets, material flaws, etc.

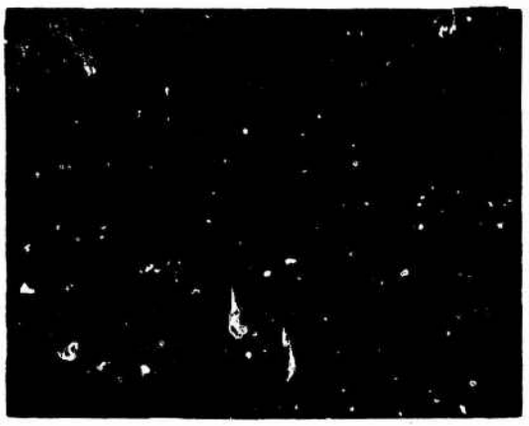


Fig. 7 - Modal Pattern (m = 5, n = 3)

Using each version of the peak-amplitude method as a check on the other, the experimental resonant frequencies can be obtained very accurately.

EXPERIMENTAL RESULTS AND DISCUSSION

The resonant frequencies, associated with various modes and extrapolated to zero amplitude, are summarized in Table 2. These results agree reasonably well with the results of a linear free-vibrational analysis taking into account layered anisotropic coupling effects [4]. Generally, the experimental results were higher than the results of the Rayleigh-Ritz analysis. This discrepancy may be due to an erroneous value of the shear modulus, an erroneous extrapolation to zero amplitude, initial buckles or other plate imperfections, or an error in the analysis.

In contrast, a series of experiments reported recently by Ashton and Anderson [3] on boron-fiber reinforced plastic plates generally resulted in experimental frequencies about 10 percent lower than the ones predicted by their linear analysis. However, their lower values may be attributed to the flexibility of their test fixture in comparison to the rigidity of the boron plate. In unidirectional form (i.e., a single layer), their composite material has a Young's modulus slightly higher than that of steel.

When the plates were excited at large excitation amplitudes, there was a noticeable in-

*Due to the intolerable noise level associated with very large amplitude vibration of the GFRP plates, the photographs shown in Figs. 5-7 were taken on rubber membranes stretched and clamped in the plate test fixture.

crease in resonant frequency with increasing amplitude. This hardening-type nonlinear-spring effect was due to the development of membrane forces as a result of end restraint and geometric nonlinearity, i.e., the nonlinearity in the strain-displacement relations. In other words, at large normal deflections the edge restraints induce membrane forces which tend to stiffen the plate.

The results of theoretical analyses of the nonlinear vibrational behavior of plates are usually presented in terms of dimensionless resonant frequency (frequency divided by the linear frequency) versus amplitude ratio (maximum plate deflection amplitude divided by the plate thickness). Thus, in the second series of experiments, resonant frequency was determined as a function of plate center deflection amplitude, instead of excitation amplitude. The results for the lowest mode of each of the four plates is shown in Fig. 8.

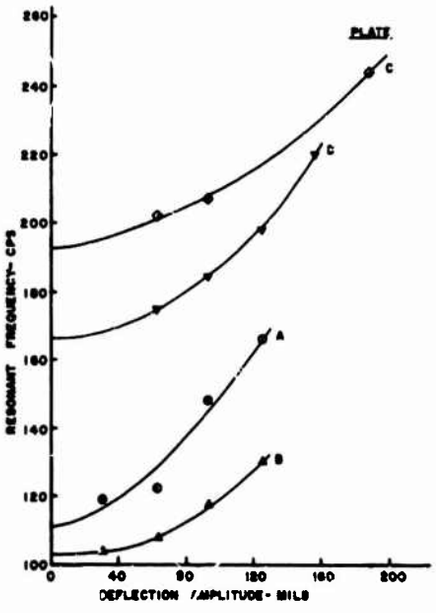


Fig. 8 - Effects of deflection amplitude on the fundamental resonant frequencies

Fig. 9 compares the same experimental results (in dimensionless form) for two of the plates with those predicted by the nonlinear free-vibrational analysis of an orthotropic plate presented in Appendix A.

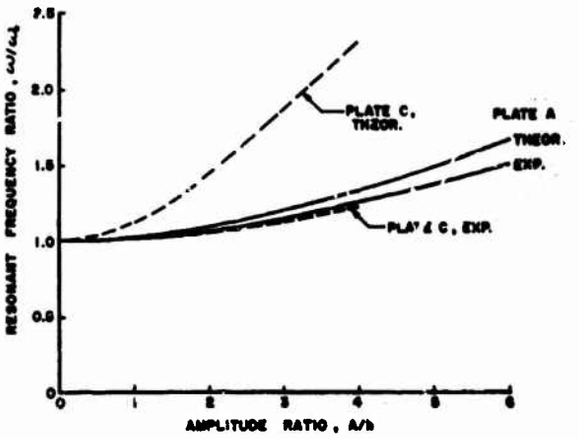


Fig. 9 - Comparison between theory and experiment for the fundamental mode

As can be seen in Fig. 9, there is very good agreement between theory and experiment for Plate A, which is simple orthotropic. However, there is very poor agreement for Plate C. This discrepancy is apparently due to the effect of bending/stretching coupling in decreasing the plate stiffness; this coupling effect is not included in the theoretical analysis.

No comparison is made between theoretical and experimental results for Plates B and D. The reason for this is that they have material-symmetry axes which are at an acute angle with the plate edges and thus have strong in-plane normal/shear coupling and bending/twisting coupling, which are not included in the analysis presented.

It should be mentioned that the agreement achieved between theory and experiment for Plate A is considerably better than that obtained by others for nonlinear vibration of isotropic rectangular plates [6, 7].

Also, it is interesting to note that since the ratio of the major and minor Young's moduli is nearly unity for the plate material used, the effect of orthotropic behavior was small in the case of Plate A.

CONCLUDING REMARKS

The successful use of stroboscopic light for mode identification and a single strain gage for accurate resonant frequency determination by the peak-amplitude method was demonstrated very clearly.

There was very good agreement between the frequency versus amplitude relation measured and that predicted by an approximate perturbation analysis presented in Appendix A for the case of a simple aligned-orthotropic plate. However, since the analysis did not include any nonaligned-orthotropic coupling or laminated anisotropic coupling effects, it overestimated the increase in frequency with amplitude for the more complicated orientations or lamination arrangements.

TABLE 1

LAMINATION ARRANGEMENTS

Plate Designation	No. of 0.0105-In. Plies	Lamination Arrangement & Orientation of Major Material-Symmetry Axis with Respect to Plate Axis
A	2	Parallel ply, 0°
B	2	Parallel ply, 45°
C	4	Cross ply (2 plies at 0° & 2 at 90°)
D	4	Angle ply (2 plies at - 45° & 2 at 45°)

TABLE 2

EXPERIMENTAL RESONANT FREQUENCIES AT SMALL AMPLITUDES

Plate	Mode		Resonant Frequency, cps
	Axial (m)	Lateral (n)	
A	1	1	111
	3	1	346
	1	3	461
B	1	1	103
	3	1	310
	1	3	427
C	1	1	192
	3	1	493
	1	3	867
D	1	1	166
	3	1	499
	1	3	795

APPENDIX A

AN APPROXIMATE PERTURBATION ANALYSIS OF NONLINEAR VIBRATION OF AN ORTHOTROPIC RECTANGULAR PLATE

This analysis is a perturbation analysis analogous to Evensen's recent analysis of nonlinear beam vibration [8]. The point of departure is a set of dynamic equations analogous to those formulated (but not solved for this configuration) by Iwinski and Nowinski [9] for a statically loaded, rectangularly orthotropic plate.

Nowinski's equations, with the inclusion of the inertia term, can be written as follows:

$$L_4(w)-(12C/h^2)L_2(w)+(\rho h/D_1)w_{,tt} = 0 \qquad (1)$$

$$C = u_{,x}+kv_{,y}+(1/2)w^2_{,x}+(1/2)kw^2_{,y} \qquad (2)$$

where a subscript comma denotes differentiation with respect to the variable following the comma in the subscript, and

$C = \epsilon_x+k\epsilon_y$ = a function of t only

D_1 = flexural rigidity in the x direction

E_1, E_2 = Young's moduli in the x and y directions

h = plate thickness

$k = (D_2/D_1)^{1/2} = (E_2/E_1)^{1/2}$

$\ell^2 = (2G_{12}/E_1)(1-k^2\nu_{12}^2) + \nu_{21}$

$L_2(w) = w_{,xx}+kw_{,yy}$

$L_4(w) = w_{,xxxx}+2\ell^2 w_{,xxyy}+k^2 w_{,yyyy}$

t = time

u, v = displacements in the x and y directions

w = normal deflection

x, y = rectangular coordinates measured in directions parallel and perpendicular to the edges of the plate

ν_{12} = Poisson's ratio (ratio of contraction in y direction to elongation in x direction, due to loading in x direction)

ϵ_x, ϵ_y = midplane strains in the x and y directions

ρ = density of plate material

Since C is independent of x and y, Eq. (2) may be multiplied by the differential area dxdy and integrated to obtain the following expression:

$$\int_0^b \int_0^a C\,dxdy = \int_0^b u|_{x=0}^{x=a}\,dy+k\int_0^a v|_{y=0}^{y=b}\,dx + (1/2)\int_0^b \int_0^a (w^2_{,x}+w^2_{,y})\,dxdy \qquad (3)$$

where a and b are the plate dimensions in the x and y directions, respectively.

For a plate which has planar restraint on all four edges, planar displacements u and v vanish at the boundaries and Eq. (3) reduces to the following:

$$2abC = \int_0^b \int_0^a (w^2_{,x}+w^2_{,y})\,dxdy \qquad (4)$$

Integrating the right-hand side of Eq. (4) by parts gives:

$$2abC = \int_0^b w\,|_{x=0}^{x=a} w_{,x}dy+k\int_0^a w\,|_{y=0}^{y=b} w_{,y}dx - \int_0^b \int_0^a w(w_{,xx}+kw_{,yy})\,dxdy \qquad (5)$$

For a plate which is supported (simply or clamped) on all four edges, normal deflection w vanishes at the boundaries and Eq. (5) simplifies as follows:

$$2abC = -\int_0^b \int_0^a w(w_{,xx}+kw_{,yy})\,dxdy \qquad (6)$$

Now the problem has been reduced to the integration of Eq. (1) subject to Eq. (6) and the boundary conditions. This intermediate result may be regarded as a generalization of Nash's formulation [10] for the isotropic case to the orthotropic case.

The method of solution used here is the perturbation technique. Initially the following relations are used:

$$\tau = \omega t \qquad (7)$$

$$w(x,y,t) = w[x,y,t+(2\pi/\omega)] = \epsilon w_1+\theta(\epsilon^3) \qquad (8)$$

$$C(t) = \epsilon^2 C_2 + \theta(\epsilon^4) \qquad (9)$$

$$\omega^2(\epsilon) = \omega_0^2[1+\epsilon^2\Omega_2+\theta(\epsilon^4)] \qquad (10)$$

where $\theta(\ )$ denotes terms of the order of the quantity inside the parentheses, ϵ is the perturbative parameter, and ω_0 is the linear natural frequency. The application of the perturbation procedure to Eqs. (1) and (6) and collecting terms of the various orders yields the following results:

$$\theta(\epsilon): L_4(w_1)+(\rho h\omega_0^2/D_1)w_{1,\tau\tau} = 0 \qquad (11)$$

$$\theta(\epsilon^2):\ 2abC_2(\tau) = -\int_0^b \int_0^a w_1(w_{1,xx}+kw_{1,yy})\ dxdy \quad (12)$$

$$\theta(\epsilon^3):\ L_4(w_3)+(\rho h\omega_o^2/D_1)w_{3,\tau\tau}$$

$$= (12C_2/h^2)L_2(w_1)-(\rho h\omega_o^2\Omega_2/D_1)w_{1,\tau\tau} \quad (13)$$

Eq. (11) is the equation governing the linear (small-deflection) motion of an orthotropic rectangular plate. Thus, the following one-term solution is assumed:

$$w_1(x,y,\tau) = \phi_m(x)\phi_n(y)\cos\tau \quad (14)$$

where $\phi_m(x)$ and $\phi_n(y)$ are the following clamped-clamped beam vibration functions tabulated by Young and Felgar [11]:

$$\phi_m = \cosh \beta_m x - \cos \beta_m x - \alpha_m(\sinh \beta_m x - \sin \beta_m x) \quad (15)$$

$$\phi_n = \cosh \beta_n' y - \cos \beta_n' y - \alpha_n'(\sinh \beta_n' y - \sin \beta_n' y) \quad (16)$$

where m, n denote the longitudinal and lateral modal numbers, respectively.

Then Eq. (12) becomes:

$$2abC_2(\tau) = I_{mn}(a,b) \quad (17)$$

where

$$I_{mn}(a,b) = \int_0^b \int_0^a \phi_m\phi_n(\phi_{m,xx}\phi_n+k\phi_m\phi_{n,yy})\ dxdy$$

$$= (\int_0^a \phi_m\phi_{m,xx}dx)(\int_0^b \phi_n^2\ dy)$$

$$+ k(\int_0^a \phi_m^2\ dx)(\int_0^b \phi_n\phi_{n,yy}\ dy) \quad (18)$$

The integrals appearing in parentheses in Eq. (18) were tabulated by Felgar [12]; thus, Eq. (18) becomes:

$$I_{mn}(a,b) = (\alpha_m\beta_m a)(2-\alpha_m\beta_m a)(b/a)$$

$$+ (\alpha_n'\beta_n' b)(2-\alpha_n'\beta_n' b)(a/b) \quad (19)$$

Since Eq. (11) has a nontrivial solution, Eq. (13) can have a solution only if its right-hand side satisfies the following orthogonality condition:

$$\int_0^b \int_0^a \int_0^{2\pi} [(12C_2/h^2)L_2(w_1)-(\rho h\omega_o^2\Omega_2/D_1)w_{1,\tau\tau}]$$

$$w_1 d\tau\ dxdy = 0 \quad (20)$$

or

$$\int_0^b \int_0^a \int_0^{2\pi} [(6/abh^2)I_{mn}(a,b)\phi_m\phi_n\ (\phi_{m,xx}\phi_n$$

$$+ k\phi_m\phi_{n,yy})\cos^4\tau+(\rho h\omega_o^2\Omega_2/D_1)\ \phi_m^2\phi_n^2\cos^2\tau]$$

$$d\tau\ dxdy = 0 \quad (21)$$

Integrating Eq. (21) and rearranging, one obtains the following result:

$$\Omega_2 = (9/2)(D_1/\rho h\omega_o^2)\ I_{mn}(a,b) \quad (22)$$

Inserting Eq. (22) into Eq. (10) yields:

$$\omega^2 = \omega_o^2\ [1+(9/2)(D_1/\rho h\omega_o^2)I_{mn}^2\ (a,b)\epsilon^2] \quad (23)$$

It is now necessary to relate the perturbative parameter, ϵ, to the plate deflection amplitude, A, at a specific point on the plate. Since the plate deflection was measured at the center of the experimental plates, the center is selected as the point at which A is defined. Thus,

$$A = \epsilon\ \phi_m(a/2)\ \phi_n(b/2) \quad (24)$$

Then Eq. (23) can be rewritten as follows:

$$\omega^2 = \omega_o^2+(9/2)(D_1h/\rho)[I_{mn}(a,b)/\phi_m(a/2)\phi_n(b/2)]^2$$

$$(A/h)^2 \quad (25)$$

For the case of the fundamental mode (m = n = 1), for example, [11] gives:

$$\phi_m(a/2) = \phi_n(b/2) = 1588$$

$$\alpha_m = \alpha_n' = 0.9825$$

$$\beta_m a = \beta_n' b = 4.7300$$

Thus for the plate dimensions, a = 9 in., b = 6 in., Eq. (25) becomes

$$\omega^2 = \omega_o^2+(9/2)(D_1h/\rho)(26.2)^2(1.588)^{-4}(A/h)^2$$

REFERENCES

1. C.W. Bert, B.L. Mayberry, and J.D. Ray, "Behavior of Fiber-Reinforced Plastic Laminates Under Uniaxial, Biaxial, and Shear Loadings", University of Oklahoma Research Institute, Contract DAAJ 02-67-C-0111, Final Report to U.S. Army Aviation Materiel Laboratories, Ft. Eustis, Va., Aug. 1968.

2. J.E. Ashton and J.D. Anderson, "Dynamic Response of Anisotropic Plates", General Dynamics Corp., Fort Worth, Texas, Report No. FZM-5008, Mar. 1968.

4. B.L. Mayberry, "Vibration of Layered Anisotropic Panels", unpublished master's thesis, University of Oklahoma, Norman, Okla., June 1968.

5. J.D. Ray, C.W. Bert, and D.M. Egle, "The Application of the Kennedy-Pancu Method to Experimental Vibration Studies of Complex Shell Structures", supplementary paper presented at the 39th Shock and Vibra-

tion Symposium, Monterey, California, Oct. 1968.

6. E.J. Kirchman and J.E. Greenspon, "Nonlinear Response of Aircraft Panels in Acoustic Noise", J. Acoust. Soc. Amer., Vol. 29, pp. 854-857, 1957.

7. P.W. Smith, Jr., C.I. Malme, and C.M. Gogos, "Nonlinear Response of a Simple Clamped Panel", J. Acoust. Soc. Amer., Vol. 33, pp. 1476-1480, 1961.

8. D.A. Evensen, "Nonlinear Vibrations of Beams with Various Boundary Conditions", AIAA J., Vol. 6, pp. 370-372, 1968.

9. T. Iwinski and J. Nowinski, "The Problem of Large Deflections of Orthotropic Plates (I)", Archiwum Mechaniki Stosowanej, Vol. 9, pp. 593-603, 1957.

10. T. Wah, "Large Amplitude Flexural Vibration of Rectangular Plates", I.J. Mech. Sci., Vol. 5, pp. 425-438, 1963.

11. D. Young and R.P. Felgar, Jr., "Tables of Characteristic Functions Representing Normal Modes of Vibration of a Beam," Engineering Research Series No. 44, Bureau of Engineering Research, University of Texas, Austin, Texas, Jul. 1949.

12. R.P. Felgar, Jr., "Formulas for Integrals Containing Characteristic Functions of a Vibrating Beam", Circular No. 14, Bureau of Engineering Research, University of Texas, Austin, Texas, 1950.

DISCUSSION

Dr. Ashton (General Dynamics/Fort Worth): How did you, – or did you keep the unsymmetrical plate flat when you made it?

Mr. Bert: It was not absolutely flat. There was a small amount of warping. It was maintained in flatness by being clamped at the edges. Other than the possibility of local wrinkling I think it would be satisfactory.

Mr. Ashton: Let me just give you the reason for the question. We have done a little work on unsymmetrical plates, in particular both Jim Whitney at AF and John Mandel and some one else at Case Western Reserve University have been doing some work along these lines and have obtained some solutions. The fact you show your theory and experiment converging at low amplitude to the same number does not seem quite in line with some of the results they have found – that is the reason for my question.

Mr. Bert: This plot was aligned to converge. In this paper we are not trying to verify the linear theory – we are looking at the nonlinear aspect. So that I essentially faired it in to be exact. Now some of ours were high and some were low, we had about 10 percent maximum variation in our linear theory. That is a subject of another investigation.

STRUCTURAL DYNAMICS ANALYSIS OF AN ANISOTROPIC MATERIAL *

S. K. Lee
General Electric Company
Syracuse, New York

A theoretical study is presented on the propagation of a plane wave through an anisotropic material -- a linear elastic material which is reinforced with parallel fibers in one direction. Other than the Young's modulus along the direction of the fiber, the property of the reinforced material is assumed to remain unchanged. Fourier method is used and the frequency equation, analytical expressions of the displacements, stresses are obtained. The numerical results can then be computed. This theoretical analysis may be used to improve the performance of systems incorporating a reinforcement member.

INTRODUCTION

The intensive use of light weight high tensile stress fiberglass as a strength member in space vehicle, jet engine, sonar equipment, and numerous other industrial applications requires accurate knowledge of their dynamic response. In this paper the effect of reinforcement due to fiberglass or other strength member is included to derive the equations of motion. The boundary conditions are obtained by matching the geometrical form of the system and the initial velocities are zero. The initial displacements are resulted from loading the system statically at t = 0, then the static load is taken away and the body is set into motion.

The solution of the problem can be divided into two parts, the static one and the dynamic one. In the former we find the stresses and displacements due to static loading. Then we use these static results as the inital conditions for the dynamic problem. The complete solution is given in infinite series form and the numerical results can be computed by using high speed computers.

NOMENCLATURE

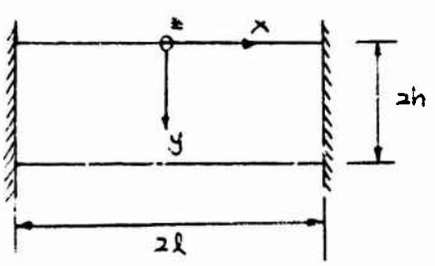
x, y, z	rectangular coordinate system
σ	normal stress
τ	shear stress
G	modulues of rigidity
E	Young's modulus
μ	Poisson's ratio
u, v, w	displacement components
ρ	density

NOMENCLATURE (Continued)

c^2	G/ρ
β^2	E_x/G
ϵ	longitudinal strain
γ	shear strain
t	time
ω	natural frequency
ℓ, h	dimensions along the x and y direction respectively
p_0	applied pressure
α, ζ	chosen constants
p, λ	characteristic constants

ANALYTICAL MODEL

The particular model we consider here is a thin rectangular slab symmetrical in both loading and material properties with respect to the y axis.



*Paper not presented at Symposium.

ANALYTICAL MODEL (Continued)

The slab is so reinforced along the y-direction that the overall Young's modulus is very large, say

$$E_y \doteq \infty \text{ , thus } \mu_{xy} = \mu_{yz} \doteq 0 \qquad (1)$$

The thickness in the z direction is so thin that $\sigma_z \doteq 0$, i.e., a plane stress problem. Note that similar problem in plane strain can also be solved.

The following relationship can be readily obtained, [1]

for the displacement,

$$u = u(x,y,t),\ v = v(x,y,t),\ w = 0 \qquad (2)$$

for the strain - displacement,

$$\epsilon_x = \frac{\partial u}{\partial x},\ \epsilon_y = \frac{\partial v}{\partial y}$$
$$\gamma_{xy} = \frac{\partial v}{\partial x} + \frac{\partial u}{\partial y} \qquad (3)$$

for the strain - stress,

$$\epsilon_x = \frac{\sigma_x}{E_x},\ \epsilon_y = 0$$
$$\gamma_{xy} = \frac{\tau_{xy}}{G} \qquad (4)$$

From Eqs. (3) and (4) we obtain

$$\sigma_x = E_x \frac{\partial u}{\partial x},\ \tau_{xy} = G\left(\frac{\partial v}{\partial x} + \frac{\partial u}{\partial y}\right) \qquad (5)$$

$$v = v(x,t), \quad \text{independent of } y \qquad (6)$$

The equations of motion are

$$\frac{\partial \sigma_x}{\partial x} + \frac{\partial \tau_{xy}}{\partial y} = \rho \frac{\partial^2 u}{\partial t^2}$$
$$\frac{\partial \tau_{xy}}{\partial x} + \frac{\partial \sigma_y}{\partial y} = \rho \frac{\partial^2 v}{\partial t^2} \qquad (7)$$

Combination of Eqs. (5) and (7) gives,

$$\beta^2 \frac{\partial^2 u}{\partial x^2} + \frac{\partial^2 u}{\partial y^2} = \frac{1}{c^2} \frac{\partial^2 u}{\partial t^2} \qquad (8)$$

$$\frac{1}{G} \frac{\partial \sigma_y}{\partial y} = \frac{1}{c^2} \frac{\partial^2 v}{\partial t^2} - \left(\frac{\partial^2 u}{\partial x \partial y} + \frac{\partial^2 v}{\partial x^2}\right)$$

We are interested in solving Eq. (8) with a zero initial velocity. The initial displacement is resulted from loading the slab statically and then taking away the load at t = 0.

The boundary conditions are

$$\begin{aligned}
&u(x,y,t) = -u(-x,y,t)\\
&u(l,y,t) = 0\\
&\tau_{xy}(x,0,t) = 0\\
&\tau_{xy}(x,2h,t) = 0\\
&\tau_{xy}(c,y,t) = 0\\
&v(l,t) = 0\\
&\tau_y(x,c,t) = 0\\
&\tau_y(x,2h,t) = 0\\
&\frac{\partial u}{\partial y}\Big|_{x=l} = 0
\end{aligned} \qquad (9)$$

The problem is therefore completely defined.

STATIC ANALYSIS

We want to find the statically deformed shape of the slab, due to a certain system of load. Here we choose to apply along x axis

$$\tau_y(x,0) = \begin{cases} p_c, & \text{for } c \le x \le a \\ 0, & a \le x \le l-\delta \\ \frac{-a}{\delta}, & l-\delta \le x \le l \end{cases} \qquad (10)$$

Since the independent variable t disappears we can obtain other corresponding equations by simply crossing out t.

The equations of motions reduce to two equations of equilibrium:

$$\beta^2 \frac{\partial^2 u}{\partial x^2} + \frac{\partial^2 u}{\partial y^2} = 0$$
$$\frac{\partial \sigma_y}{\partial y} = -G\left(\frac{\partial^2 u}{\partial x \partial y} + \frac{d^2 v}{dx^2}\right) \qquad (11)$$

Together with Eq. (11), the boundary conditions are:

$$\begin{aligned} &u(x,y) = -u(-x,y) \\ &u(\ell,y) = 0 \\ &\tau_{xy}(x,0) = 0 \\ &\tau_{xy}(x,h) = 0 \\ &\tau_{xy}(0,y) = 0 \\ &v(\ell) = 0 \\ &\sigma_y(x,h) = 0\,, \quad \left.\frac{\partial u}{\partial y}\right|_{x=\ell} = 0 \end{aligned} \tag{12}$$

By Fourier method [2], we assume

$$u(x,y) = \sum_{n=0}^{\infty} \left(C_n \sin K_n \frac{x}{\beta} + D_n \cos K_n \frac{x}{\beta}\right) \left(A_n' \sinh K_n y + B_n' \cosh K_n y\right) \tag{13}$$

where K_n, C_n, D_n, A_n', B_n' are constants to be determined.

With Eqs (10) and (12), it can be shown that

$$u(x,y) = \sum_{n=1}^{\infty} A_n \sin\frac{n\pi}{\ell}x \, \frac{\sinh(y-h)\frac{n\pi\beta}{\ell}}{\cosh\frac{n\pi\beta}{\ell}h} \tag{14}$$

$$v(x) = \sum_{n=1}^{\infty} A_n \beta \left(\cos\frac{n\pi}{\ell}x - \cos n\pi\right) \tag{15}$$

$$\sigma_y(x,y) = G\sum_{n=1}^{\infty} A_n \left(\frac{n\pi}{\ell}\right)^2 \beta \cos\frac{n\pi x}{\ell} \left\{(y-h) - \frac{\ell}{n\pi\beta}\left[\sinh\frac{n\pi\beta}{\ell}y - \left(1+\cosh\frac{n\pi\beta}{\ell}y\right)\tanh\frac{n\pi\beta}{\ell}h\right]\right\} \tag{16}$$

where

$$A_n = -p_0\ell^2\left[\sin\frac{n\pi a}{\ell} + (-1)^{n-1}\frac{n\pi a}{\ell}\right] \Big/ \left[G n^3\pi^3\beta\left(1 - \frac{\ell}{n\pi\beta}\tanh\frac{n\pi\beta}{\ell}h\right)\right] \tag{17}$$

DYNAMIC ANALYSIS

We now want to solve Eq. (8) with Eq. (9)- the boundary conditions. The initial conditions may be written as [3]

$$\begin{aligned} &u(x,y,t)\Big|_{t=0} = u(x,y) \\ &v(x,t)\Big|_{t=0} = v(x) \\ &\sigma_y(x,y,t)\Big|_{t=0} = \sigma_y(x,y) \\ &\left.\frac{\partial u}{\partial t}\right|_{t=0} = 0 \\ &\left.\frac{\partial v}{\partial t}\right|_{t=0} = 0 \\ &\left.\frac{\partial \sigma_y}{\partial t}\right|_{t=0} = 0 \end{aligned} \tag{18}$$

Let us assume that

$$\begin{aligned} u(x,y,t) &= \sum_{n=0}^{\infty} U_n(x,y)\cos c\lambda_n t \\ v(x,t) &= \sum_{n=0}^{\infty} V_n(x)\cos c\lambda_n t \\ \sigma_y(x,y,t) &= \sum_{n=0}^{\infty} S_n(x,y)\cos c\lambda_n t \end{aligned} \tag{19}$$

where the constant λ_n, functions U_n, V_n, S_n are to be determined.

Using Eqs. (9) and (18), after some algebra, we obtain

$$u = \sum_{n=1}^{\infty}\sum_{r=1}^{\infty} A_{nr} \sin\frac{n\pi x}{\ell} \, \frac{\sin\rho_{nr}(y-h)}{\cos\rho_{nr}h} \cos c\lambda_{nr} t \tag{20}$$

$$v = -\sum_{n=1}^{\infty} A_n \beta \cos n\pi + \sum_{n=1}^{\infty}\sum_{r=1}^{\infty} \frac{\ell}{n\pi} \cdot \rho_{nr} A_{nr} \cos\frac{n\pi x}{\ell} \cos c\lambda_{nr} t \tag{21}$$

$$\sigma_x = E_x \sum_{n=1}^{\infty}\sum_{r=1}^{\infty} A_{nr} \frac{n\pi}{\ell} \cos\frac{n\pi x}{\ell} \sin\rho_{nr}(y-h) \cdot \cos c\lambda_{nr} t / \cos\rho_{nr}h \tag{22}$$

$$\sigma_y = G\sum_{n=1}^{\infty}\sum_{r=1}^{\infty} A_{nr} \frac{n\pi}{\ell} \cos\frac{n\pi x}{\ell} \left\{y\rho_{nr}\left[1 + \beta^2 + \left(\frac{\ell}{n\pi}\right)^2\rho_{nr}^2\right] - \tan\rho_{nr}h - \frac{\sin\rho_{nr}(y-h)}{\cos\rho_{nr}h}\right\} \cos c\lambda_{nr} t \tag{23}$$

where

$$A_{nr} = -p_0\ell^2\left[\sin\frac{n\pi a}{\ell} + (-1)^{n-1}\frac{n\pi a}{\ell}\right] \cdot \left\{2\left(\frac{n\pi\beta}{\ell}\tan\rho_{nr}h - \rho_{nr}\tanh\frac{n\pi\beta}{\ell}h\right) \Big/ \left[\beta\rho_{nr}^2 + \beta\left(\frac{n\pi\beta}{\ell}\right)^2\right] + \frac{\ell}{n\pi}2h\rho_{nr}\right\} \Big/ \left\{G\pi^3 n^3\left(1 - \frac{\ell}{n\pi\beta}\tanh\frac{n\pi\beta}{\ell}h\right)\left[\left(2h - \frac{\sin 2\rho_{nr}h}{\rho_{nr}}\right) \Big/ (2\cos^2\rho_{nr}h) + \left(\frac{\ell}{n\pi}\right)^2\rho_{nr}^2 2h\right]\right\} \tag{24}$$

and

$$\tan\rho_{nr}h + h\left(\frac{\ell}{n\pi}\right)^2\rho_{nr}^3 + h\left(\beta^2 - 1\right)\rho_{nr} = 0 \tag{25}$$

$n = 1, 2, 3, \ldots$
$r = 1, 2, 3, \ldots$

$$\rho_{nr}^2 = \lambda_{nr}^2 - \left(\frac{n\pi}{\ell}\right)^2 \tag{26}$$

Therefore the problem is analytically solved.

CONCLUSIONS

1. The natural frequencies are given by

$$\omega_{nr}^2 = c^2\left[\beta_{nr}^2 + \left(\frac{2n\pi}{\lambda}\right)^2\right]$$

Where β's are the roots of

$$\tan \beta_{nr} h + h\left(\frac{\zeta}{n\pi}\right)^2 \beta_{nr}^3 + h(\beta^2 - 1)\beta_{nr} = 0$$

Note that for every n we have an infinite number of β's.

2. The analytical proof of the uniform convergence of the series solution is very difficult. Future analysis may be extended to include the proof numerically.

3. The same approach can be used to solve the plane strain problem. The geometrical shape of the material is not very important, for example, a circular plate reinforced axially, a circular cylinder reinforced in the longitudinal direction, etc., can be readily solved.

REFERENCES

1. A. E. H. Love, A Treatise On The Mathematical Theory of Elasticity, Chapter 1, 2, Dover Publications, New York, New York, 1944

2. R. Courant and D. Hilbert, Methods of Mathematical Physics, Vol. 1, Chapter 2, 5, Interscience Publishers, New York, New York 1953

3. K. C. Valanis, "Exact and Variational Solutions to a General Viscoelasto-Kinetic Problem", Journal of Applied Mechanics, Vol. 33, No. 4, PP. 888-892, Dec. 1966

EXPERIMENTS ON THE LARGE AMPLITUDE PARAMETRIC RESPONSE OF RECTANGULAR PLATES UNDER IN-PLANE RANDOM LOADS*†

R. L. Silver
Graduate Assistant
Department of Mechanical and Aerospace Engineering
Syracuse University
Syracuse, New York

and

J. H. Somerset
Assistant Professor
Department of Mechanical and Aerospace Engineering
Syracuse University
Syracuse, New York

Experiments have been performed to determine the large amplitude lateral vibration of a simply supported rectangular plate subjected to a distributed in-plane load of the form $P = P_0 + P_1\phi(t)$, where $\phi(t)$ is a narrow band random process. Power spectral densities of load and response are obtained and the effects of transaction mechanisms are evaluated. Typical sample functions are obtained. An analysis is presented which shows that certain frequency shifts occur in the spectrum of the response, with the result that the mean frequency of the response is not an integral fraction of the load mean frequency, and the spectrum of the response is shifted along the frequency axis. The experimental results are compared to the theory presented in this paper and with analytical results previously obtained by Shyu and Somerset [5]. The agreement between theory and experiment is good.

INTRODUCTION

In recent years, there has been a significant amount of interest in the parametric vibration of systems and structures. In general, a parametric vibration of a structure is governed by a differential equation of the form:

$$\ddot{f}(t) + \zeta[1 - \mu\phi(t)]f(t) + \psi(f,\dot{f},\ddot{f},t) = 0 \qquad (1)$$

where $\ddot{f}(t)$ is the response of the system, $\psi(f,\dot{f},\ddot{f},t)$ is some nonlinear function, and $\phi(t)$ is some function of time, t. (See Table III for notation.)

The earliest investigations of the parametric instability of structures[1,2,3]‡ were concerned with the linear form of Equation (1), wherein $\phi(t)$ was taken to be a periodic function with period T. The results of those linear investigations showed that a parametric instability could be manifest over a countably infinite number of continuous regions of the (ζ,μ,T) parameter space.

In order to determine the amplitude of the response, it is necessary to include the nonlinearities attendant to the system under consideration. In 1956, Bolotin [4] presented solutions to some nonlinear problems concerned with columns and plates; in those investigations equation (1) was nonlinear, with $\phi(t) = \cos \omega t$. In 1963, Berazovskii and Shulezhko[5] calculated some corrections for the instability zone boundaries. In 1967, Somerset and Evan-Iwanowski [6] presented a solution for the large amplitude parametric vibration of plates, in which the influence of nonlinear inertia was included. Experiments by Bolotin [4] and by Somerset and Evan-Iwanowski[7,8] and by Evensen and Evan-Iwanowski[9] and by Somerset[10] have shown that the theoretical results apply to the parametric vibration of plate and column structures.

The analyses and experiments show that many types of structures may exhibit a parametric instability. Usually, the instability occurs for dynamic loads which are applied in such a manner that if the load were static and sufficiently large, buckling would occur. The period of a parametric oscillation is some multiple of the load frequency; the frequency of the load is not, in general, equal to the natural frequency of the structure.

*This paper not presented at Symposium.
†This work supported by NSF Grants GK-919 & 2868.
‡Bracketed numbers refer to Bibliography.

If $\phi(t)$ is a random function of time, the problem becomes more complicated. Some analytical results have been published concerning the stability of linear systems (Eq. 1) with $\phi(t)$ a random function, and some analogue computer results have been given[11, 12,13,14]. Again, the linear results can only be used to estimate the stability of the zero solution. Nonlinearities must be included if the amplitude of the parametric response is to be calculated. Although it is common industrial practice to test the performance of assembled structures, such as rockets and associated equipment, under random loads, no experiments concerning the parametric response of structural elements under stochastic loads has been found in the literature.

Shyu and Somerset[15] have developed a solution for the nonlinear response of a rectangular plate subjected to an in-plane load of the form

$$P = P_0 + P_1\phi(t)$$

where $\phi(t)$ is a random function of time. The experiments presented in this paper were conducted to evaluate the applicability of the theory, and to examine directly the parametric response of a structure under a random load. In this paper, a summary of their analyses is presented and their results are used as the basis for an additional analysis. Physical limitations are discussed and the experimental results are compared with the analysis by Shyu and Somerset and with the additional analyses.

ANALYTICAL CONSIDERATIONS

Outline of the Theory

The analysis was concerned with a simply supported rectangular plate sustaining an in-plane load of the form $P = P_0 + P_1\phi(t)$, where $\phi(t)$ was a random function of time, t. A normalizing condition was imposed on $\phi(t)$, namely, $\sqrt{\phi^2(t)} = 1$. Figure 1 depicts the problem.

The in-plane forces were given by

$$N_x = \frac{Eh}{1 - \nu^2}(\epsilon_{xx} + \nu\epsilon_{yy})$$

$$N_y = \frac{Eh}{1 - \nu^2}(\epsilon_{yy} + \nu\epsilon_{xx})$$

$$N_{xy} = \frac{Eh}{2(1 + \nu)}\epsilon_{xy}$$

where

$$\epsilon_{xx} = \frac{\partial u}{\partial x} + \frac{1}{2}\left(\frac{\partial w}{\partial x}\right)^2$$

$$\epsilon_{yy} = \frac{\partial v}{\partial y} + \frac{1}{2}\left(\frac{\partial w}{\partial y}\right)^2$$

$$\epsilon_{xy} = \frac{\partial u}{\partial y} + \frac{\partial v}{\partial x} + \frac{\partial w}{\partial x}\frac{\partial w}{\partial y}$$

and $u(x,y,t)$, $v(x,y,t)$ and $w(x,y,t)$ were the x, y, and z displacements respectively.

The boundary conditions on the lateral displacements along the edges of the plate and on the edge moments were those of a simply supported plate, namely,

$$\frac{\partial^2 w(0,y,t)}{\partial x^2} = \frac{\partial^2 w(a,y,t)}{\partial x^2}$$

$$= \frac{\partial^2 w(x,0,t)}{\partial y^2} = \frac{\partial^2 w(x,b,t)}{\partial y^2} = 0$$

$$w(0,y,t) = w(a,y,t) = w(x,0,t) = w(x,b,t) = 0$$

The boundary conditions on the in-plane displacements were

$$u(0,y,t) = u(a,y,t) = 0$$

$$v(x,0,t) = 0$$

$$v(x,b,t) = V(t)$$

The load was assumed to be a narrow band random process. The method of slowly varying phase and amplitude was applied, for which

$$P_1\phi(t) = \phi_1(t)\cos[\gamma t + \beta(t)]$$

where $\phi_1(t)$ and $\beta(t)$ were slowly varying, and γ was the center frequency of the load.

A lateral response was assumed of the form

$$w(x,y,t) = A(t)\sin(\pi x/a)\sin(\pi y/b)$$

with the assumption that $A(t)$ was also a narrow band random process. An $A(t)$ was assumed of the form

$$A(t) = A_1(t)\cos[\omega t + \theta(t)]$$

where $A_1(t)$ and $\theta(t)$ were assumed to be slowly varying.

The rms amplitude of the deflection of the center of the plate was found to be

$$A_{rms} = \sqrt{\overline{A^2(t)}}$$

$$= \sqrt{\frac{2}{3\alpha}\left(\frac{\gamma^2}{4} - \bar{\omega}^2 + \frac{0.82\,\pi^2}{m}\left(\frac{\nu}{a^2} + \frac{1}{b^2}\right)\overline{\phi_1}\right)}$$

where

$$\alpha = \frac{Eh\,\pi^4}{16\,m}\left(\frac{3}{a^4} + \frac{1}{b^4}\right)$$

$$\varpi^2 = \frac{D\,\pi^4}{m}\left(\frac{1}{a^2} + \frac{1}{b^2}\right)^2 - \frac{\pi^2}{m}\left(\frac{\nu}{a^2} + \frac{1}{b^2}\right) P_0$$

$$D = \frac{Eh^3}{12(1 - \nu^2)}$$

When the response of the plate was assumed to be

$$w(x,y,t) = B(t)\,\sin(\pi x/a)\,\sin(\pi y/b)$$

with $B(t)$ a narrow band process given by

$$B(t) = B_1(t)\,\sin[\omega t + E(t)]$$

the solution for the rms amplitude was found to be

$$B_{rms} = \sqrt{\overline{B^2(t)}}$$

$$= \sqrt{\frac{2}{3\alpha}\left(\frac{\gamma^2}{4} - \varpi^2\right) - \frac{0.82\,\pi^2}{m}\left(\frac{\nu}{a^2} + \frac{1}{b^2}\right)\overline{\phi_1}}$$

Figure 2 is a sketch of the values of A_{rms} vs. P_1/P_E. The presence of the solution corresponding to $B(t)$ implies that the plate exhibits a lateral vibration only if the center frequency, γ, lies between γ_1 and γ_2, as shown in Figure 3. The analysis predicts that the responee of the plate will be governed by the solid line in Figure 3.

Phyeical Limitations of the Analytical Results

It has been shown by Somerset and Evan-Iwanowski[6,7] and Somereet[10] that transition mechanisms exist between the "idling"† vibratione and the parametric reeponse of the plate.

For periodic loads it has been possible to study the transition phenomena and the parametric responee separately[7,10]. However, if the dynamic part of the load is random, it would be expected that the transition mechanisms would strongly affect the response of the plate. One would expect the traneition mechanisms to cauee the response curve of Figure 2 to be limited by the jump phenomena, ae sketched in Figure 3.

†As defined in the theoretical inveetigations [6], the "idling" vibrations are the forced vibratione of period, T, caueed by a periodic in-plane load of period T. They are present whether or not a parametric oecillation is manifest.

Spectral Shifte of the Response

It hae been found, experimentally, that a spectral ahift between response and load occurs for conetant frequency einueoidal loads. The parametric response occurs at a frequency which is one-half that of the load frequency. This analysis will show an additional epectral ehift owing to the fact that the frequency of the load is randomly distributed about a particular mean frequency.

The previous analysie as conducted by Shyu and Somerset[15] relates the root mean square value of the center deflection, A_{rms}, of a rectangular, simply eupported plate, to the root mean square value of the dynamic portion of the in-plane random load, $\overline{\phi_1}$. The result can be written in the following form:

$$A_{rms}^2 = \frac{1}{C_1}\left[2(\gamma^2/4 - \varpi^2) + C_2\overline{\phi_1}\right] \qquad (2)$$

where the in-plane load has the form

$$P = P_0 + P_1\phi(t) \quad , \text{ and } \quad \overline{\phi_1} = 1.25\,P_1$$

because

$$\sqrt{\lim_{T\to\infty}\frac{1}{T}\int_0^T P_1^2\phi^2(t)\,dt}$$

$$= P_1\sqrt{\overline{\phi^2(t)}} = P_1$$

The analysis by Shyu and Somerset predicts the second momente of the reeponee (A_{rms}^2). Experiments have been conducted to verify those results (see Experimental Reeults and Conclusions) but the analysis by Shyu and Somerset does not predict directly the power spectral density of the response. In this paper an approximate analysis of the power spectral densities is given.

It has been shown[15] that a random load of a specific RMS magnitude and a specific load frequency dietribution, when imposed on the plate, will give a particular RMS magnitude of response. If, now, an infinite number of thought experimente were performed in which a different load center frequency were chosen for each experiment with a specific load magnitude attached to each center frequency, the outcome of each experiment could be considered to be the magnitude of reeponse of the plate. If it is desired to determine the load frequency for which the response magnitude is maximum it would be neceesary to chooee the load frequency of each experiment infinitesimally close to the frequency of the previous experiment, until the maximum response ie obtained. This method is similar to the method of euperposition.

For a eyetem which is nonlinear the accuracy of euch a representation is not clear

at the outset, but it should be appropriate for prediction of spectral shifts.

In the experiment the distribution of load magnitude vs. load frequency is that of a bell-shaped curve, symmetric with respect to its center frequency, γ_0 (see Experimental Results and Conclusions). Thus it is reasonable to use a normal distibution as a mathematical representation of the load distribution. By this choice it is hoped that an analysis can be carried out to determine the load frequency for which A_{rms} is maximum.

If in Equation 2 a narrow band random distribution is substituted for $\overline{\phi_1}$, it should be possible to differentiate A_{rms} with respect to γ and determine the value of γ for which A_{rms} is maximum.

Mathematically it is possible to approximate the experimentally determined load power spectral density shapes by the normal distribution

$$\overline{\phi_1} = \frac{1}{\sqrt{2\pi}\,\sigma} e^{-z^2/2\sigma^2}$$

where σ is the standard deviation, essentially determining the bandwidth of the load function $\phi(t)$ and z is a variable proportional to the frequency γ. If z is replaced by $\gamma-\gamma_0$, $\overline{\phi_1}$ will be centered at the mean frequency γ_0 which is then, of course, the center frequency of the load. Therefore

$$\overline{\phi_1}(\gamma) = \frac{1}{\sqrt{2\pi}\,\sigma} e^{-(\gamma - \gamma_0)^2/2\sigma^2} \qquad (3)$$

In order to find the maximum of A_{rms} it is necessary to differentiate Equation 2 to obtain

$$2 A_{rms} \frac{dA_{rms}}{d\gamma} = \frac{1}{C_1}\left[2[2(\frac{\gamma}{t}) - 0] + C_2 \frac{d\overline{\phi_1}}{d\gamma}\right] \qquad (4)$$

The condition for A_{rms} to be maximum or minimum is that $dA_{rms}/d\gamma = 0$ and since A_{rms} is non-zero and finite in the region being considered the following condition is imposed on Equation 4:

$$\gamma + C_2 \frac{d\overline{\phi_1}}{d\gamma} = 0 \qquad (5)$$

Now it is desired to determine if the value of γ which satisfies this equation corresponds to maximum A_{rms} or minimum A_{rms}. It is therefore necessary to examine the second derivative of A_{rms} with respect to γ:

$$2 A_{rms} \frac{d^2 A_{rms}}{d\gamma^2} + 2\left(\frac{dA_{rms}}{d\gamma}\right)^2 = \frac{1}{C_1}\left[1 + C_2 \frac{d^2\overline{\phi_1}}{d\gamma^2}\right] \qquad (6a)$$

Since $dA_{rms}/d\gamma = 0$ at the points being considered:

$$2 C_1 A_{rms} \frac{d^2 A_{rms}}{d\gamma^2} = 1 + C_2 \frac{d^2\overline{\phi_1}}{d\gamma^2} \qquad (6b)$$

Differentiating Equation 3 twice:

$$\frac{d\overline{\phi_1}}{d\gamma} = -\frac{(\gamma - \gamma_0)}{\sqrt{2\pi}\,\sigma^3} e^{-(\gamma - \gamma_0)^2/2\sigma^2} \qquad (7a)$$

$$\frac{d^2\overline{\phi_1}}{d\gamma^2} = \frac{(\gamma - \gamma_0)^2 - \sigma^2}{\sqrt{2\pi}\,\sigma^5} e^{-(\gamma - \gamma_0)^2/2\sigma^2} \qquad (7b)$$

From Equation 4 it is seen that A_{rms} is increasing with increasing γ in the region $\gamma < \gamma_0$ (see Equation 7a). Thus as γ is increased from zero the first value of γ, γ_m, for which $dA_{rms}/d\gamma = 0$ must be a maximum or an inflection point; it cannot be a minimum. If γ_m were a point of inflection the second derivative, $d^2A_{rms}/d\gamma^2$ would be zero. From Equation 6b it is seen that only a very special case, $d^2\overline{\phi_1}/d\gamma^2 = -1/C_2$, will make γ_m correspond to a point of inflection and so γ_m corresponds to a maximum of the response.

From Equation 6b it is seen that a necessary condition for $d^2A_{rms}/d\gamma^2$ to be less than zero is $d^2\overline{\phi_1}/d\gamma^2 < 0$. From Equation 7b it is seen that $d^2\overline{\phi_1}/d\gamma^2 < 0$ implies that $(\gamma - \gamma_0)^2 < \sigma^2$. And since this implies that $\sigma > |\gamma - \gamma_0|$, the following condition is a bound on γ_m: $\gamma_0 - \sigma < \gamma_m < \gamma_0 + \sigma$.

The value of γ, γ_n, corresponding to a minimum value of A_{rms} (where it has been shown above that $\gamma_n > \gamma_m$), occurs when $d^2A_{rms}/d\gamma^2 > 0$.

From Equation 6b it is seen that $d^2\overline{\phi_1}/d\gamma^2 > 0$ is a sufficient condition for $d^2A_{rms}/d\gamma^2$ to be greater than zero. Thus if $(\gamma - \gamma_0)^2 > \sigma^2$ or rewriting, $|\gamma - \gamma_0| > \sigma$, then the regions of possible values of γ_n are $\gamma_0 - \sigma > \gamma_n$ or $\gamma_n > \gamma_0 + \sigma$. Since it has been shown that $\gamma_m < \gamma_n$ the region where γ_n can occur is $\gamma_n > \gamma_0 + \sigma$.

If Equation 7a is substituted into Equation 5 an implicit function of γ results, defining the two values of γ, γ_m, γ_n.

$$\gamma = -C_2 \frac{d\overline{\phi_1}}{d\gamma}$$

$$\gamma = \frac{(\gamma - \gamma_0)\, C_2}{\sqrt{2\pi}\,\sigma^3} e^{-(\gamma - \gamma_0)^2/2\sigma^2} \qquad (8)$$

It is well to examine qualitatively the following: $\gamma - \gamma_0 = 0$, $\gamma - \gamma_0 < 0$, $\gamma - \gamma_0 > 0$:

$\gamma - \gamma_0 = 0$

It is seen that if $\gamma = \gamma_0$ is substituted in Equation 8 then $\gamma = 0$ results and there is a contradiction. This value of γ does not, therefore, satisfy Equation 8. That is, neither γ_m or γ_n can equal γ_0 .

$\gamma - \gamma_0 < 0$

In this region

$$\gamma = \frac{(\gamma - \gamma_0)\, C_2}{\sqrt{2\pi}\,\sigma^3} e^{-(\gamma - \gamma_0)^2/2\sigma^2} < 0$$

and γ is a negative frequency which is, of course, in contradiction with the starting condition. Thus

$$0 < \gamma_0 - \sigma < \gamma_m$$

$\gamma - \gamma_0 > 0$

This condition, $\gamma > \gamma_0$ gives the only reasonable region for maximum and minimum A_{rms} to exist. Thus it is seen that the theory predicts that the load frequency for which A_{rms} is maximum, γ_m , will lie in the region $0 < \gamma - \gamma_0 < \sigma$ and that the load frequency for which A_{rms} is minimum will lie in the region $\gamma - \gamma_0 > \sigma$.

As a consequence of the above considerations it is seen that the theory predicts that the load frequency, γ_m , corresponding to maximum lateral plate response, will be shifted a relatively small amount "to the right" of the load center frequency, γ_0 . This prediction is substantiated in the experimental results.

Upon further examination Equation 8 yields additional predictions of the experimental results. Rewriting Equation 8:

$$\left(\frac{\gamma}{\gamma - \gamma_0}\right) e^{(\gamma - \gamma_0)^2/2\sigma^2} = C_2/\sqrt{2\pi}\,\sigma^3 \qquad (9)$$

Increasing C_2 is equivalent to increasing the magnitude of ϕ_1 (that is P_1). If this is done, one or both factors on the left side of Equation 9 must increase. Therefore, $\gamma/(\gamma - \gamma_0) = 1/[1 - (\gamma_0/\gamma)]$ must increase and/or $e^{(\gamma - \gamma_0)^2/2\sigma^2}$ must increase. If $\gamma/(\gamma - \gamma_0)$ increases γ_0/γ must decrease or γ must increase. Obviously, also, if $e^{(\gamma - \gamma_0)^2/2\sigma^2}$ increases, γ must increase. Thus an increase in P_1 must cause an increase in γ , the load frequency corresponding to maximum lateral plate response. This observation agrees with the experimental results.

It is also possible for Equation 8 to be rewritten so that the effect of the bandwidth of ϕ_1 on the value of γ for which A_{rms} is maximum can be considered.

$$e^{(\gamma - \gamma_0)^2/2\sigma^2} = (1 - \gamma_0/\gamma)\, C_2/\sqrt{2\pi} \qquad (10)$$

Now if σ increases and if it is assumed that γ increases also, the left hand factor increases since changes in $\gamma - \gamma_0$ and σ in the exponent of e tend to cancel out. If the left side increases then $1 - \gamma_0/\gamma$ must increase, ie. γ must increase. This conclusion is entirely consistent with the original assumption that γ increases when σ increases and so increased bandwidth (increased σ) implies increased load center frequency for maximum A_{rms}. This observation also agrees with the experimental results.

APPARATUS

The apparatus permitted an experimental investigation of the parametric response of a simply supported rectangular plate subjected to an in-plane load of the form

$$P = P_0 + P_1\phi(t)$$

where $P_1\phi(t)$ was a narrow band random load, with $\sqrt{\overline{\phi^2(t)}} = 1$. The load parameters P_0 , P_1 , the bandwidth, Γ , and the center frequency, γ , could be varied independently. The load and the displacement of the center of the plate could be measured simultaneously.

The apparatus is shown in Figure 4a and Figure 4b. The specimen plate (1), an electrodynamic shaker (2), and other attendant apparatus were mounted in a frame (3). The dynamic portion of the load was generated by the electrodynamic shaker in conjunction with a loading device (4). A sine-noise generator (5) and a power amplifier constituted the input to the shaker. The vibration of the center of the plate was measured by a strain gage arrangement on a displacement transducer (6). The load was measured by strain gage arrangement of a load transducer (7). Carrier amplifiers (8) were used to monitor the strain gage circuits; the output from each carrier amplifier was recorded on an instrument tape recorder (9), and each output was monitored by a four-trace oscilloscope. Subsequent analysis of the recorded data was performed using a true rms voltmeter (10), an operational amplifier (11), and a frequency analyzer (12). A summary of the equipment is given in Table I.

Figures 5a and 5b show the plate and associated apparatus. The loading device consisted a linear spring, an adjustable head, a ball joint, and a loading truss. The loading truss was constrained to move in a vertical plane by a wire suspension. The spring was secured between the ball joint on the truss and

the adjustable head on the shaker. Owing to the vibratory displacement of the shaker head, in conjunction with the initial compression of the spring, a load of the form $P = P_0 + P_1 (t)$ was applied to the plate.

The boundary conditions were maintained along the vertical edges of the plate by wire suspensions. The horizontal edges of the plate were fitted into V-grooves machined in the load truss and in the load cell.

The plate was fabricated from rigid vinyl plastic. The dimensions and properties of the specimen are given in Table II. A special fixture was fabricated to machine the edges of the plate, in order to assure uniform contact between the plate and the V-grooves.

The displacement transducer is shown in Figure 5a. The transducer was calibrated statically and the calibration was verified for dynamic accuracy by comparison with the displacement recorded by a capacitive displacement transducer.

EXPERIMENTAL PROCEDURE

At the outset of experimentation, the plate was "calibrated" to determine the natural frequency of lateral vibration for each load. From Figure 6, it may be seen that the agreement between theory and experiment was quite good over a range of values of the in-plane load. It has been shown that for small in-plane static loads, the boundary conditions at the V-grooves cannot be maintained, and the theory cannot be applied[10].

The experiments were conducted as follows. The static portion of the load, P_0, was applied by compressing the linear spring with the adjustable head. A narrow band random signal was impressed on the moving coil of the shaker, and the subsequent motion of the shaker head was manifest as a narrow band random load applied in the plane of the plate. The load was measured by the load cell; the signal from the load cell was stored on magnetic tape for subsequent analysis.

The lateral displacement of the center of the plate was recorded by the displacement transducer; the signal from the displacement transducer was also stored on magnetic tape.

The experiments were conducted for various values of P_0, P_1, Γ, and γ. Two classes of experiments were conducted:

(A) experiments in which γ, Γ, and P_0 were constant, and P_1 varied,

(B) experiments in which Γ, P_0, and P_1 were constant, and γ varied.

In addition, observations were made on the load and displacement sample functions, to verify some of the assumptions made in the theory concerning the nature of the response.

Experiments of type (A) were conducted to investigate the applicability of the theory. Experiments of Type (B) were conducted to demonstrate more clearly the effects of the transition mechanisms.

After the load parameters P_0, P_1, γ and Γ were set, the load and the response were recorded on magnetic tape. The tape recordings constituted sample functions of the random processes defined by the load and by the response of the plate. The load parameters P_0, P_1, γ, and Γ defined a point in the load parameter space. Each sample function of the load had associated with it a sample function of the plate response; the functions were considered as input-output pairs corresponding to a particular point in the load parameter space.

The rms average of each sample function was obtained, and the power spectral density of each sample function was obtained. Because the load and response were stationary, the parameters (P_0, P_1, γ, Γ, A_{rms}) defined a point in a load-response parameter space with which were associated the power spectral densities $\phi_L^{ijkm}(F)$ and $\phi_R^{ijkm}(F)$ where

$i = P_0$,

$j = P_1$,

$k = \gamma$,

$m = \Gamma$,

$\phi_L^{ijkm}(F)$ Load power spectral density

$\phi_R^{ijkm}(F)$ Response power spectral density.

Any sample function was available by reproducing the appropriate section of magnetic tape. An arbitrary zero time was established for each section of tape, and any analysis of a particular sample function was initiated at the "zero time". The rms value of a sample function was obtained by measuring the signal with a true rms voltmeter. Because the time constant of the voltmeter was not sufficiently large, the output from the voltmeter was integrated using an electrometer connected as an operational amplifier. The resulting rms value was therefore an "average rms". In order to substantiate the accuracy of the "average rms" value, comparisons between the voltmeter-integration method and measurements using a quasi rms meter with sufficiently long time constants (3 sec. to 100 sec.) were made. The two methods were found to agree within 4%. The voltmeter-integration method was chosen for its simplicity, and because it solved some other problems as well.

The power spectral density of a sample function was determined by passing the signal from the tape through a narrow band filter. The output from the filter was analyzed by the

voltmeter-integration technique. By varying the center frequency of the filter for successive reproductions of the same sample function, the power spectral density was obtained. Figure 7 is a schematic drawing of the measurement techniques.

In the use of the instrument tape recorder were found two advantages:

1. input-output sample function pairs were obtained,
2. the assumption of quasi-stationarity of the sample functions was realized experimentally.

EXPERIMENTAL RESULTS AND CONCLUSIONS

The experimental data are presented in Figures 8 through 20. Figures 8 and 9, which indicate the lateral response in $(A_{rms}/h, P_1/P_E)$ space, verify the applicability of the theory. The theory predicts that the rms amplitude of the plate response should be identical for load bandwidths of 10 Hz. and 3 Hz. The response under 10 Hz. bandwidth loads show good agreement with the response under 3 Hz. bandwidth loads. The experimentally determined response curves also show good agreement with the curves predicted by the theory. It is to be noted that the experimental curves approach the abscissa for slightly higher values of P_1/P_E than predicted by the theory owing to the influence of damping and transition mechanisms.

Each point in the $(P_0, P_1, \gamma, \Gamma, A_{rms})$ parameter space had associated with it two power spectral densities: one for the load, $\Phi_L^{ijkm}(F)$, and one for the response $\Phi_R^{ijkm}(F)$. Some experimentally determined power spectral density load-response pairs are plotted in Figures 10 through 17. The ordinate for each set of power spectral density curves is arbitrarily scaled so that, for any point in the load-response parameter space, the maximum value of $\Phi_L^{ijkm}(F)$ or $\Phi_R^{ijkm}(F)$ is unity. A great amount of information is available from a perusal of the power spectral density curves.

In Figure 10, the power spectral density of two load-response pairs associated with two values of P_1 is plotted on the same abscissa. The theory predicts that the center frequency of the response should be nearly equal to $\gamma/2$; the experiments again verify the analysis. From a designer's point of view, it is quite significant that the power spectral density of the load is removed from the power spectral density of the response.

In Figures 11 through 17, a dual abscissa is employed, resulting in an artificial "overlap" between the load and response power spectral densities. F_L denotes the abscissa for the load power spectral density, whereas F_R denotes the abscissa for the response. This method of plotting demonstrates a significant experimental generality: the center frequency of the response is nearly equal to, and somewhat greater than, $\gamma/2$. Moreover, by comparing Figures 11 and 12, 14 and 15, and by perusal of Figures 13, 16, and 17, it may be seen that as P_1 increases, the center frequency of the response also increases. The amount of shift increases as the bandwidth of the load increases. Figure 17 probably provides the best illustration of the shift in center frequency of the response with increasing load. In that figure, the shift of the center frequency of the response is quite evident. The shift in center frequency of the response admits an explanation.

Owing to the fact that the amplitude of the lateral response increases as γ increases, other load parameters being constant, the amplitudes corresponding to frequencies at the "edges" of the load bandwidth are not equal. Rather, the amplitude of the response is greater near the high frequency "edge" of the bandwidth.

It is also to be noted that for a given range of the variable P_1, a greater shift is associated with a greater bandwidth of the load. This result is entirely expected. As the load bandwidth is increased, a greater portion of the frequency-response curve is included in the "bandwidth", and a greater center frequency shift is manifest.

Figures 10 through 17 also demonstrate the degree to which the dynamic portion of the load corresponds to an ideal narrow band load. In Figures 10, 11, 12, 14, 15, 16, 17, the power spectral density of the load corresponds well with the idealized case. Figures 13 and 15 (top) show some distortion of the load power spectral density. It is the opinion of the authors that very satisfactory power spectral densities were realized during experimentation. One always encounters physical limitations on the frequency distribution of the load during any experimentation.

Figures 18 and 19 show the effects of the transition mechanisms quite clearly. In the experiments associated with Figures 18 and 19, the load parameters P_0, P_1 and Γ, were fixed, and γ was varied. Whereas the theory predicted that a response would be manifest between γ_1 and γ_2, the experimental results show that the lateral response was manifest over a smaller range of frequencies. It is readily seen that the jump phenomena would account for the limitation on the values of γ over which a response would result. It is to be noted that good agreement between theory and experiment is realized for values of γ near 2ω.

Figure 20 substantiates an important theoretical result. Figures 20a and 20b are tracings of some load-response sample functions obtained from pictures taken with an oscilloscope camera. In the theory, a load was

assumed of the form

$$P_1\phi(t) = \phi_1(t)\cos[\gamma t + \beta(t)]$$

and a response was assumed of the form

$$A(t) = A_1(t)\cos[\omega t + \theta(t)]$$

where

$$\omega = \frac{\gamma}{2}$$

and

$$\theta(t) = \frac{\beta(t)}{2} + \delta(t)$$

The theory indicates that $\delta(t)$ is small, the implication being that the maxima of the response sample functions should occur near maxima of the load sample functions. Figure 20b clearly shows that the maxima of the response sample function occur near maxima of the load sample function.

TABLE I EQUIPMENT

Tape Recorder:	Sanborn - Model 2000
Voltmeter:	Hewlett-Packard Model 3400A, true mean square voltmeter
Frequency Analyzer:	Bruel and Kjaer Frequency Analyzer type 2107
Random Signal Generator:	MB Sine-Random generator, Model N670
Operational Amplifier:	Keithley Electrometer Model 601
Carrier Amplifier:	Textronix type 3C66
Vibration Meter:	MB Vibration meter Model 550

TABLE II SPECIMEN PROPERTIES

Dimensions	10 × 10 × 0.05 in.
Modulus of elasticity, E	4.7×10^6 psi
Density	0.048 lb/cu in.
Poisson's ratio	0.3
Buckling load(theoretical)	2.12 lb/in.
Frequency of free lateral Vibrations(theoretical	27.5 Hz

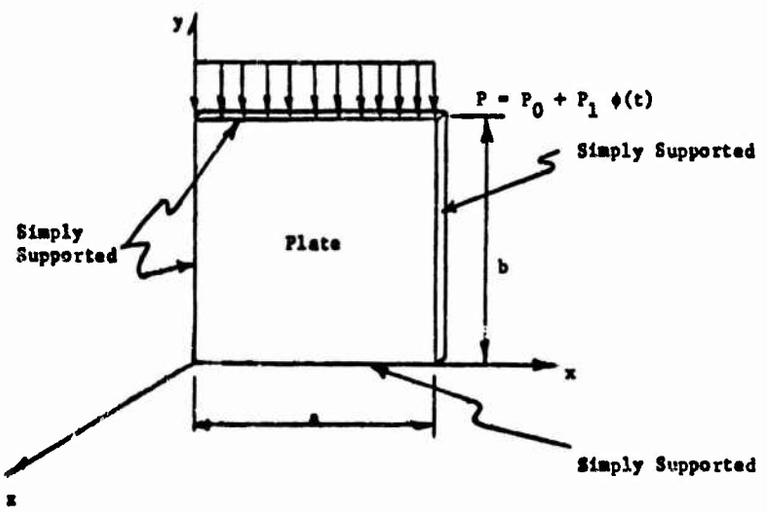


Figure 1

Plate and Load Configuration

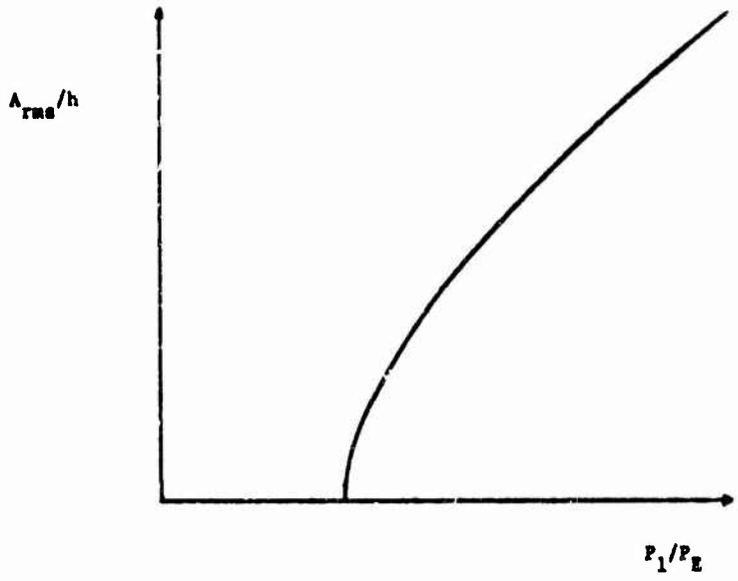


Figure 2

Sketch of Theoretical Results in (A_{rms}/h, P_1/P_E) Parameter Space

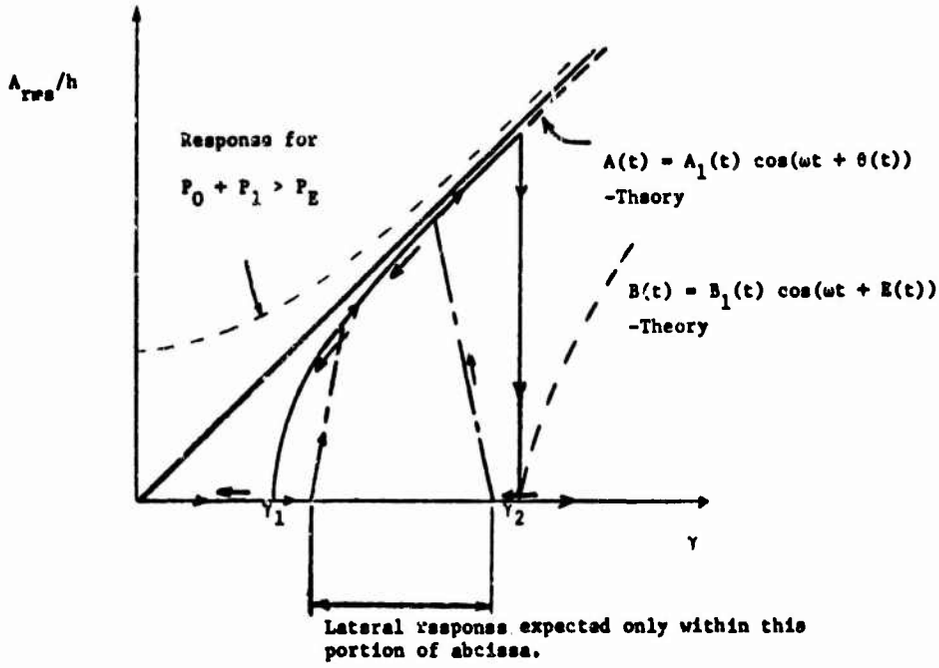


Figure 3

Influence of Transition Mechanisms on Plate Response

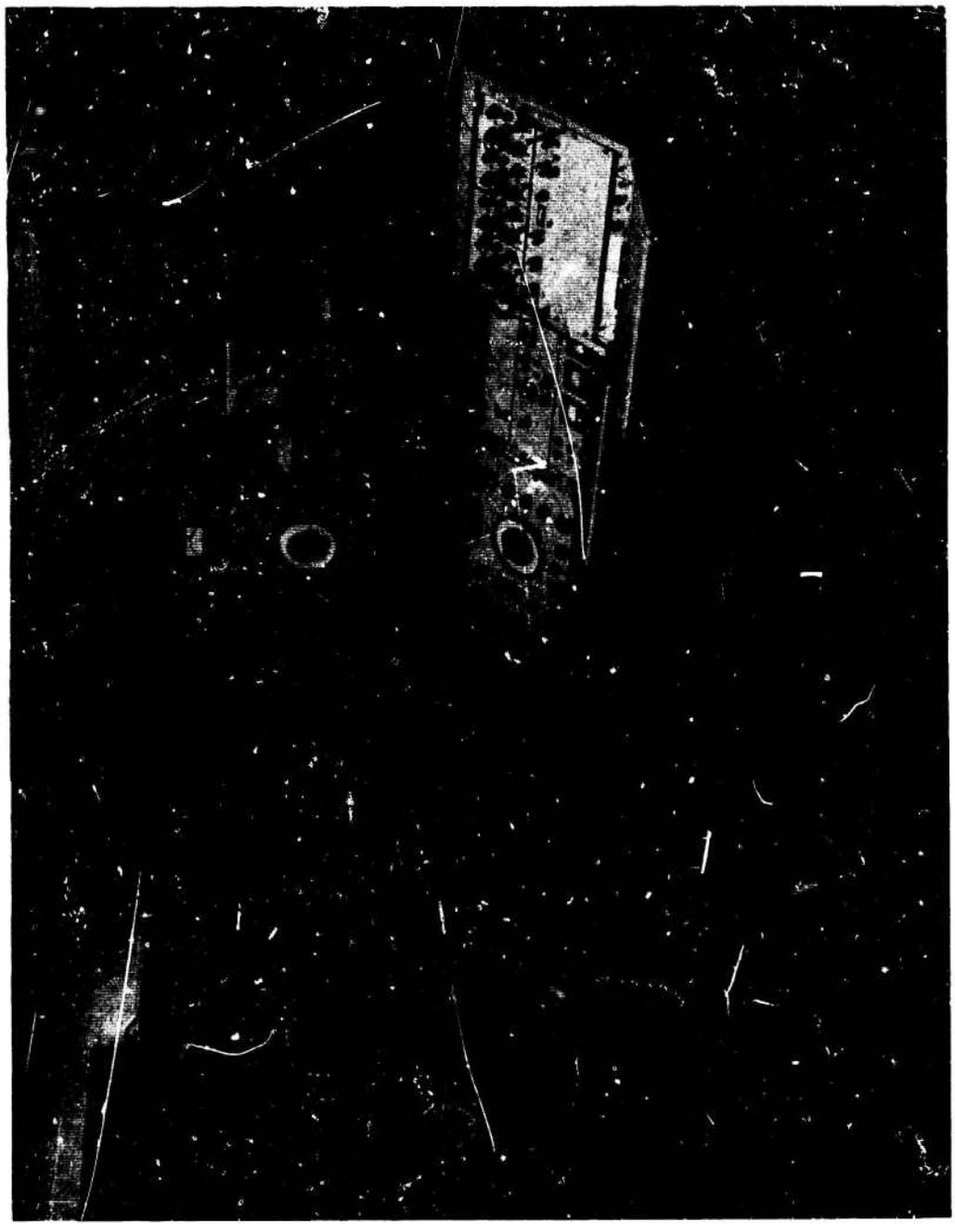
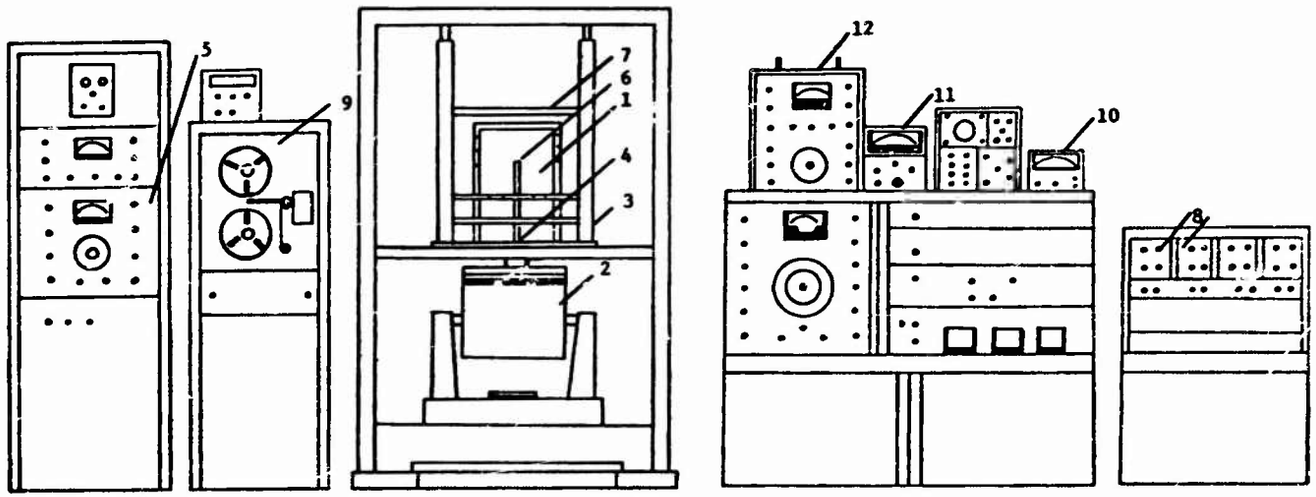


Figure 4a. Experimental Apparatus



1. Specimen Plate
2. Electrodynamic Shaker
3. Mounting Frame
4. Loading Device
5. Sine-Noise Generator
6. Displacement Transducer
7. Load Transducer
8. Carrier Amplifiers
9. Instrument Tape Recorder
10. RMS Voltmeter
11. Operational Amplifier
12. Frequency Analyzer

Figure 4b

Line Drawing - Apparatus

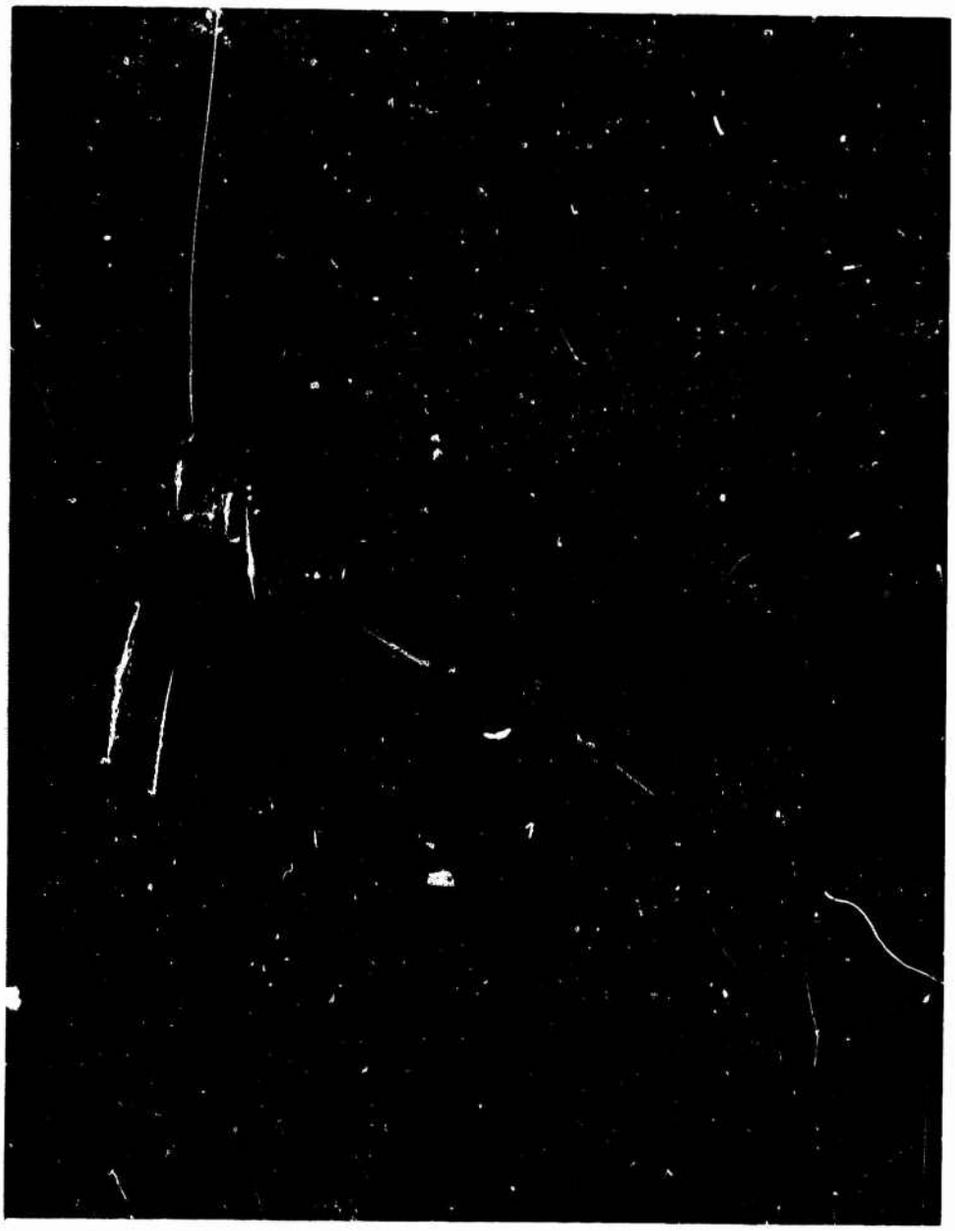
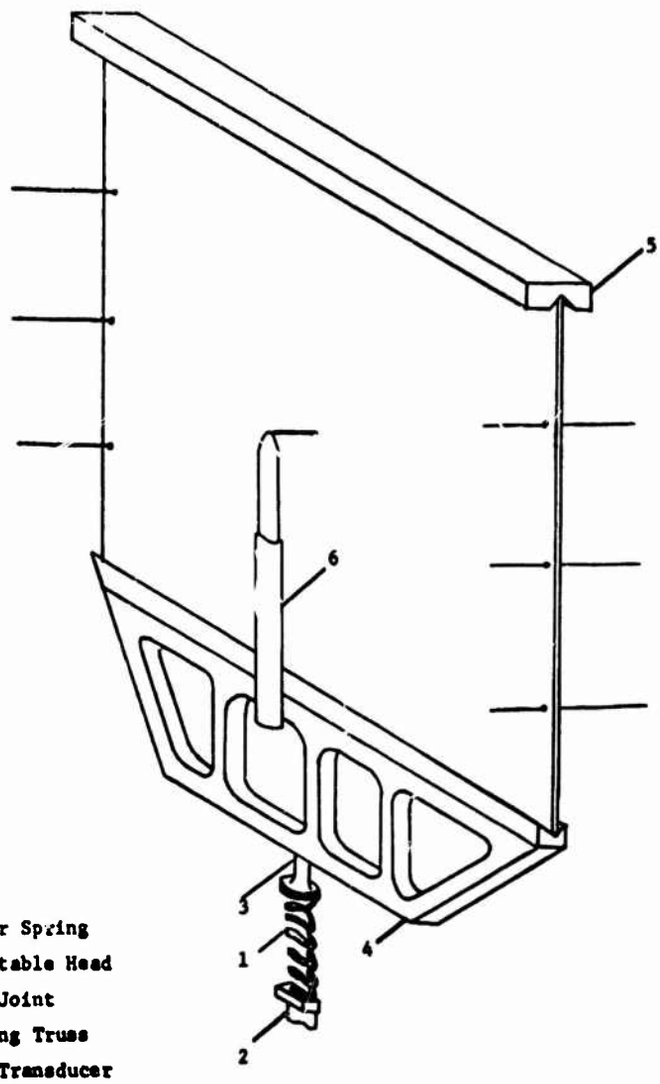


Figure 5a

Specimen and Attendant Apparatus



1. Linear Spring
2. Adjustable Head
3. Ball Joint
4. Loading Truss
5. Load Transducer
6. Displacement Transducer

Figure 5b

Line Drawing - Specimen Arrangement

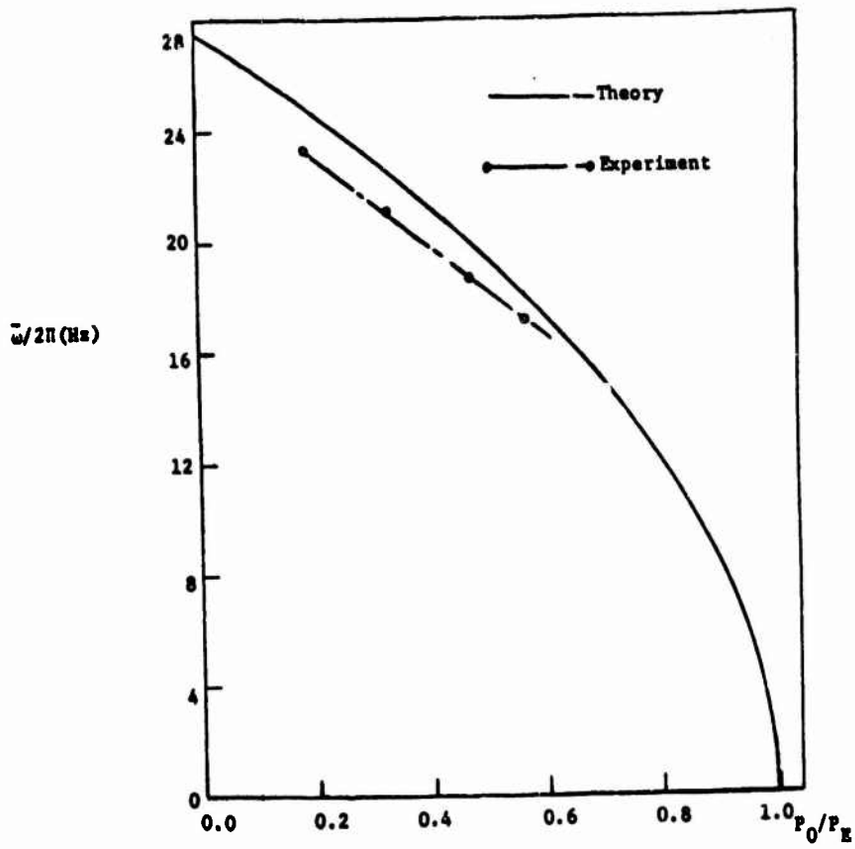


Figure 6

Plate Calibration

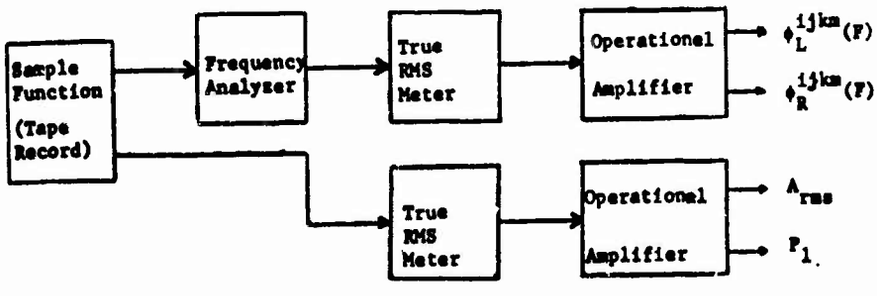


Figure 7

Flow Chart-Analysis of Sample Functions

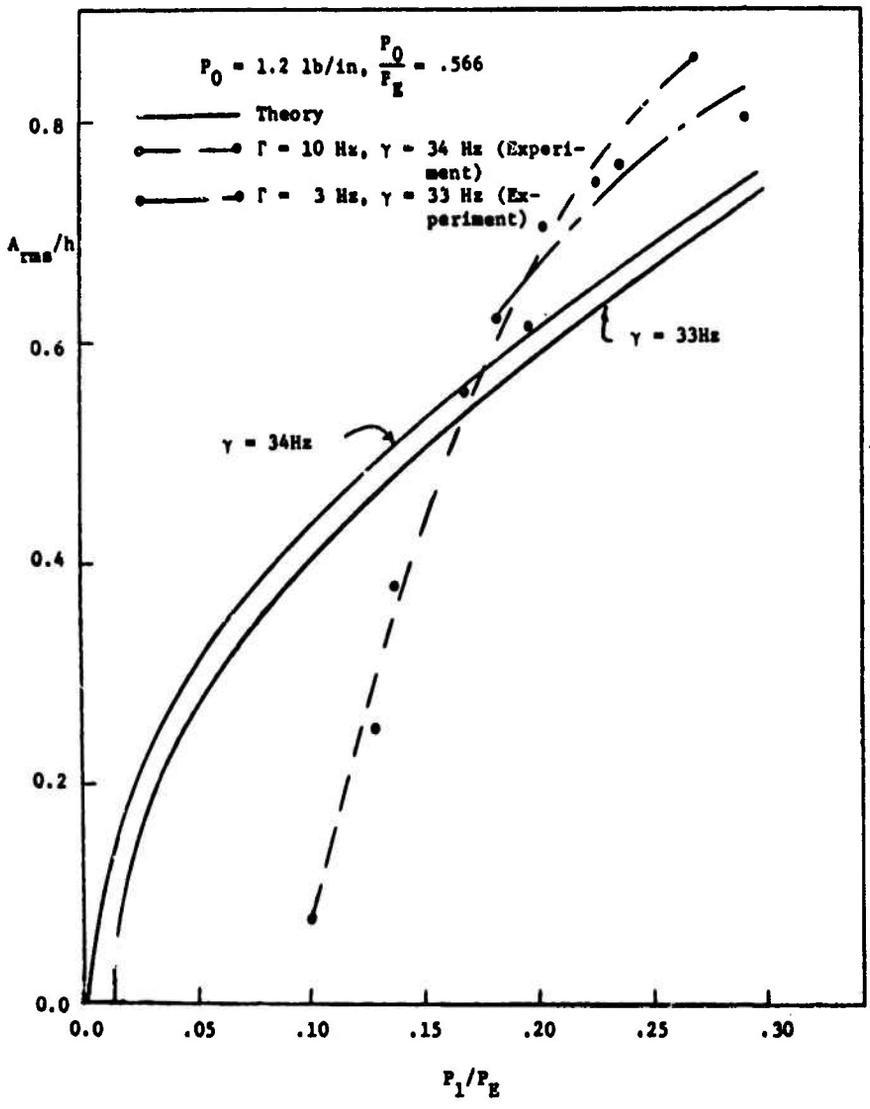


Figure 8

Load-Response Curve in (P_1P_E, A_{rms}/h) Parameter Space

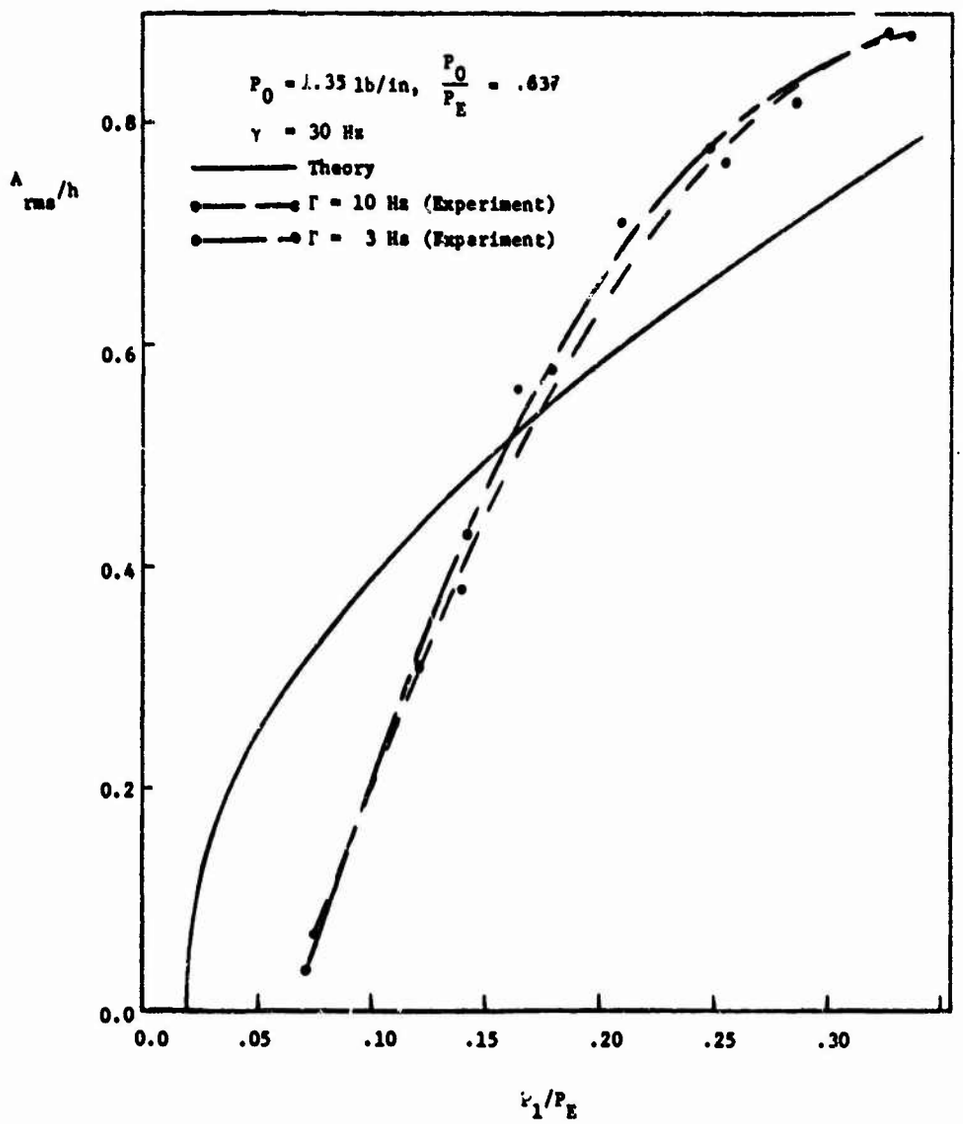


Figure 9

Load-Response Curve in (P_1/P_E, A_{rms}/h) Parameter Space

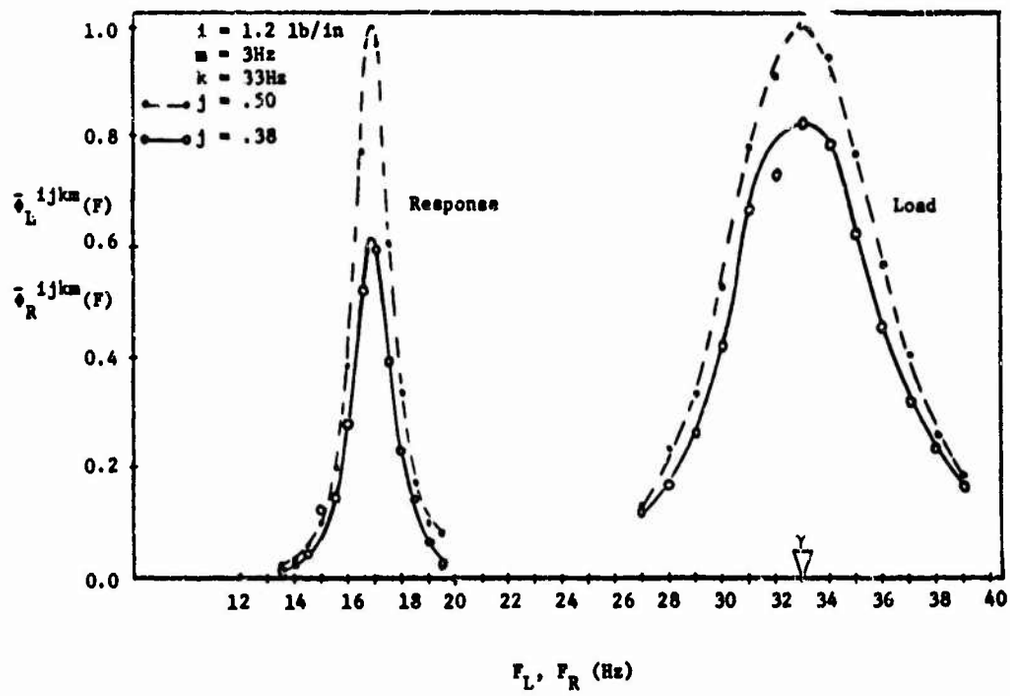


Figure 10

Power Spectral Density of Load and Response
(Experimental Results)

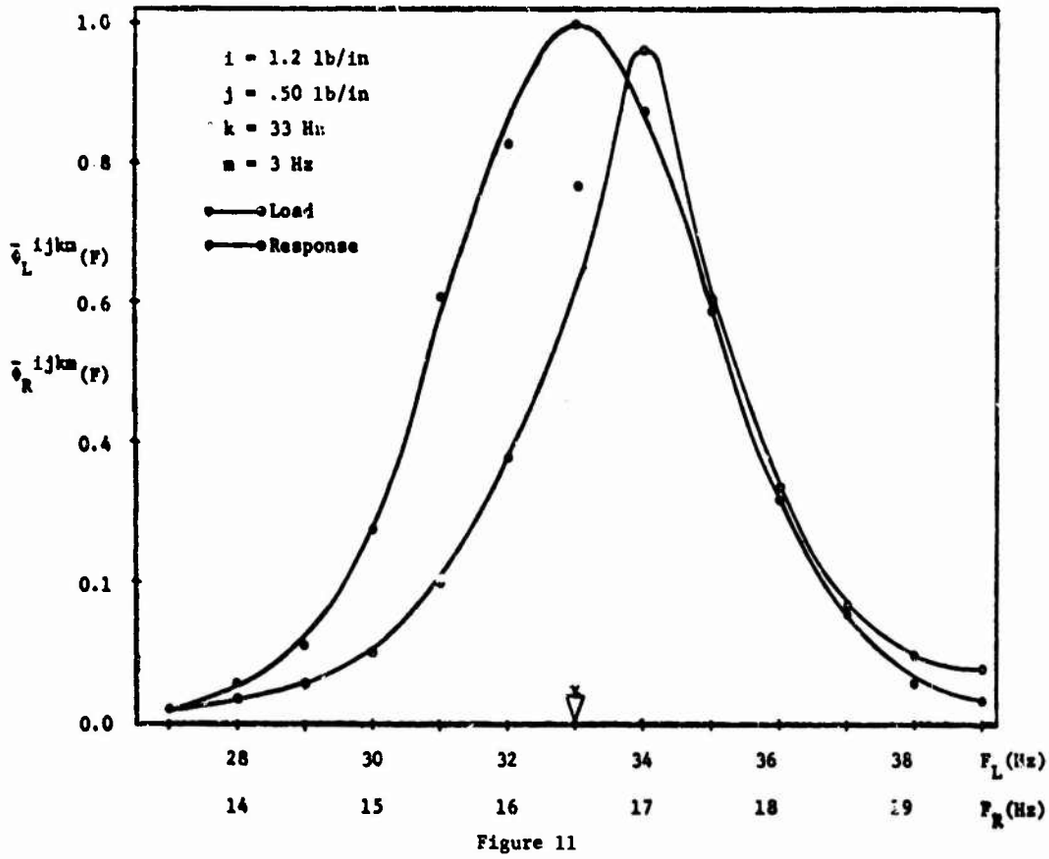


Figure 11

Power Spectral Density of Load and Response (Experimental Results)

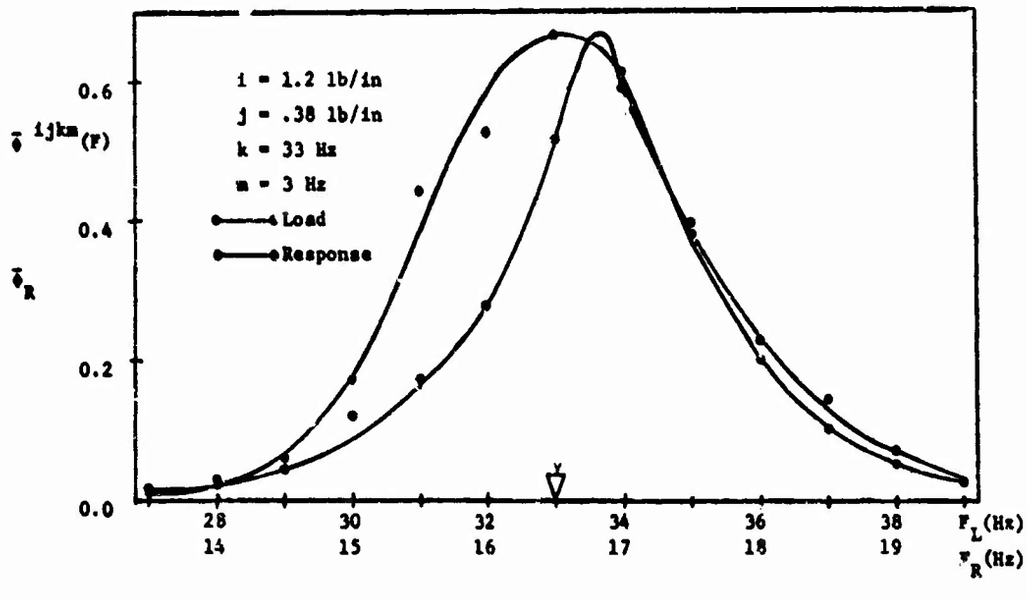


Figure 12

Power Spectral Density of Load and Response (Experimental Results)

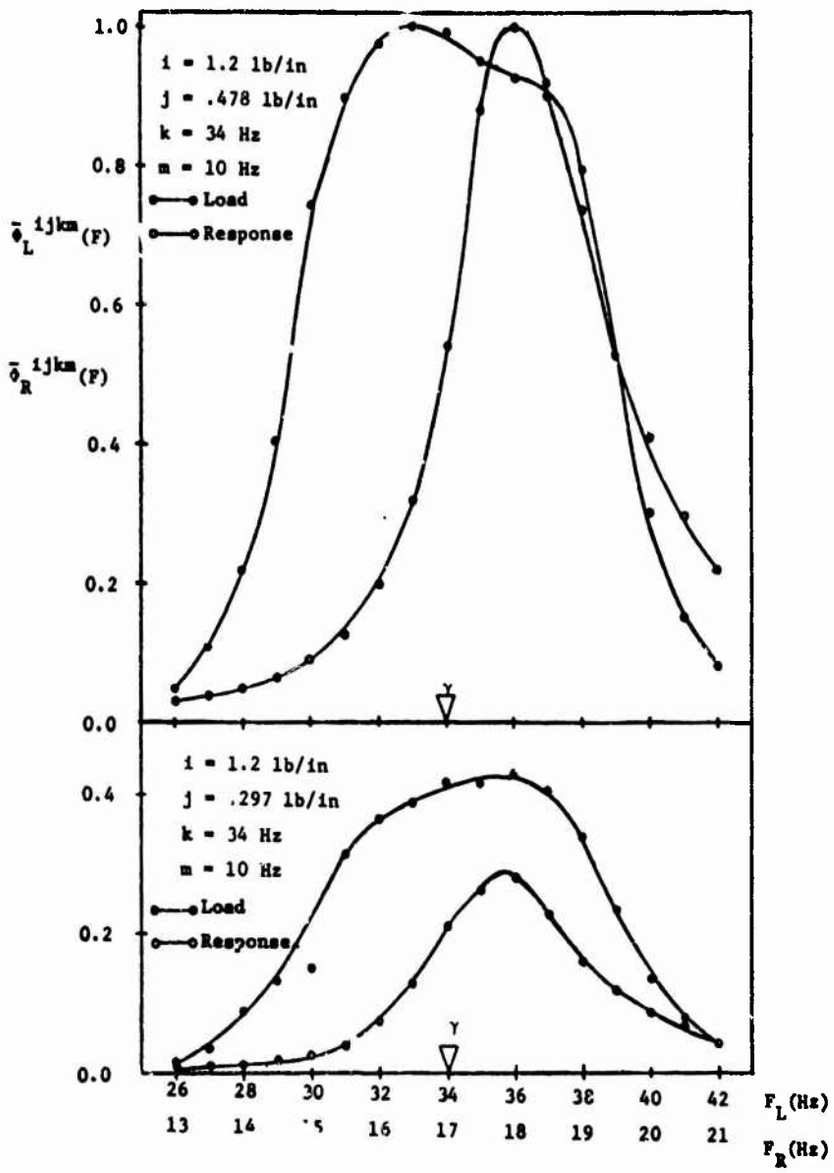


Figure 13

Power Spectral Density of Load and Response
(Experimental Results)

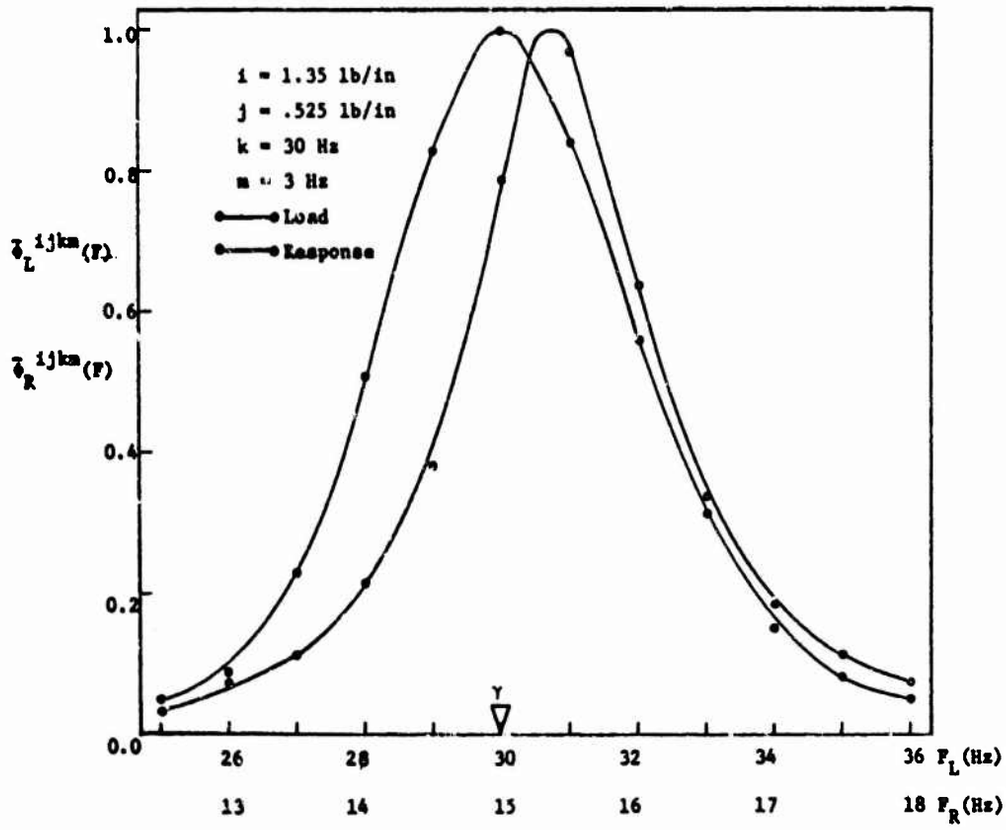


Figure 14

Power Spectral Density of Load and Response

(Experimental Results)

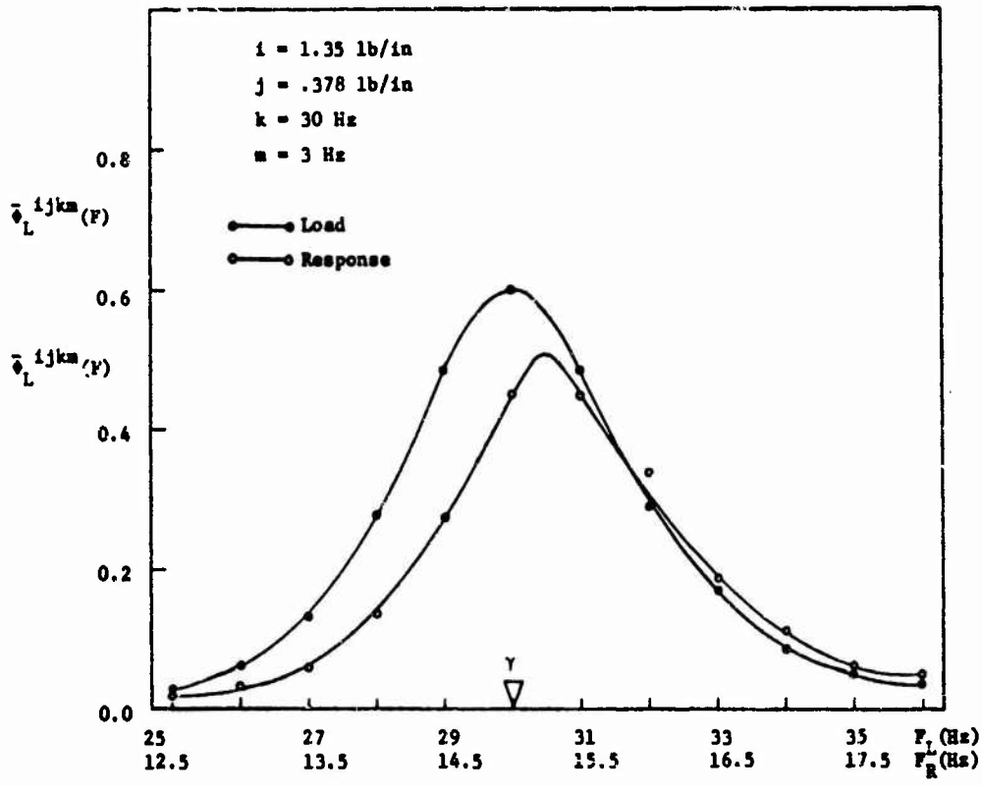


Figure 15

Power Spectral Density of Load and Response
(Experimental Results)

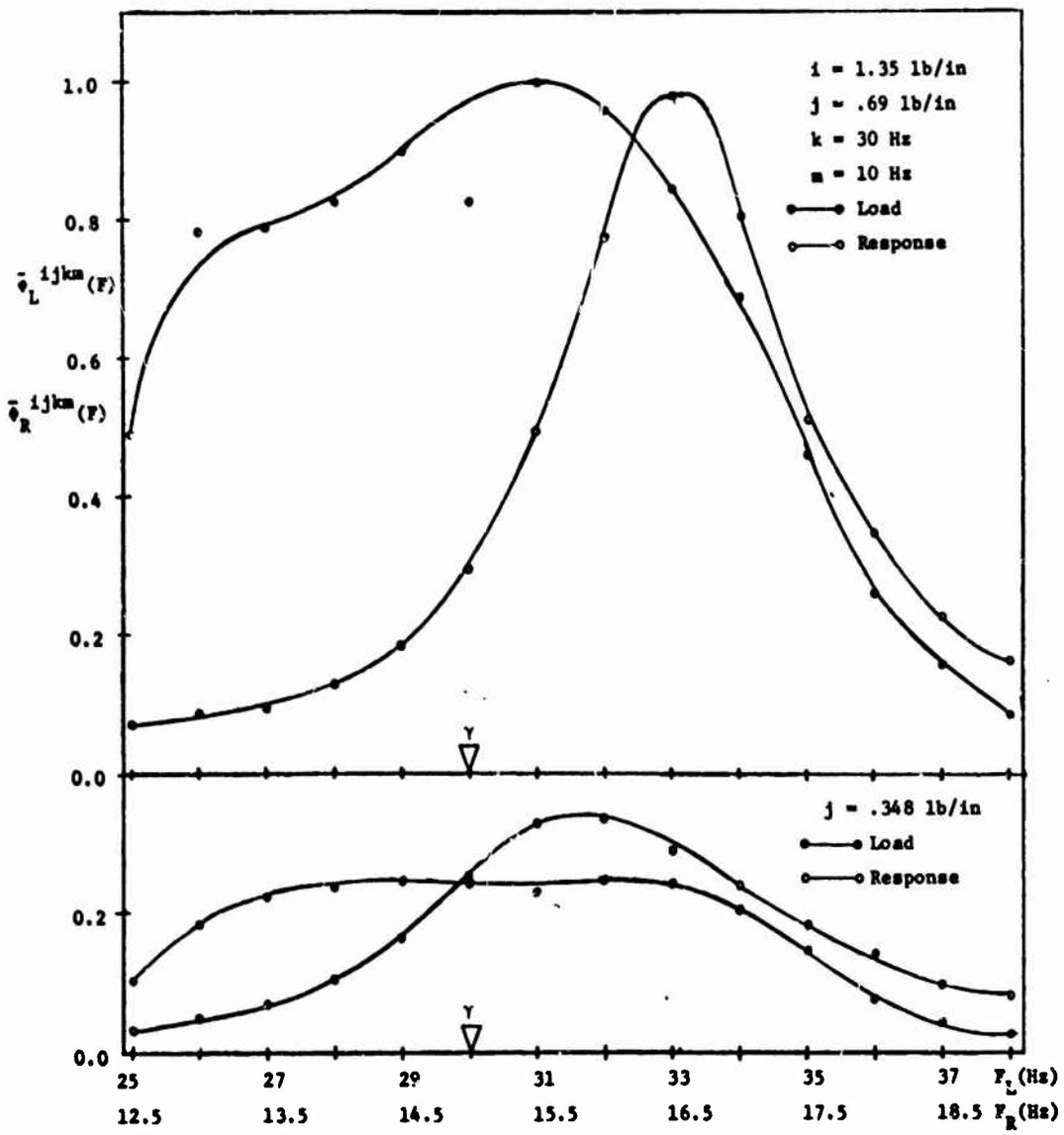


Figure 16

Power Spectral Density of Load and Response
(Experimental Results)

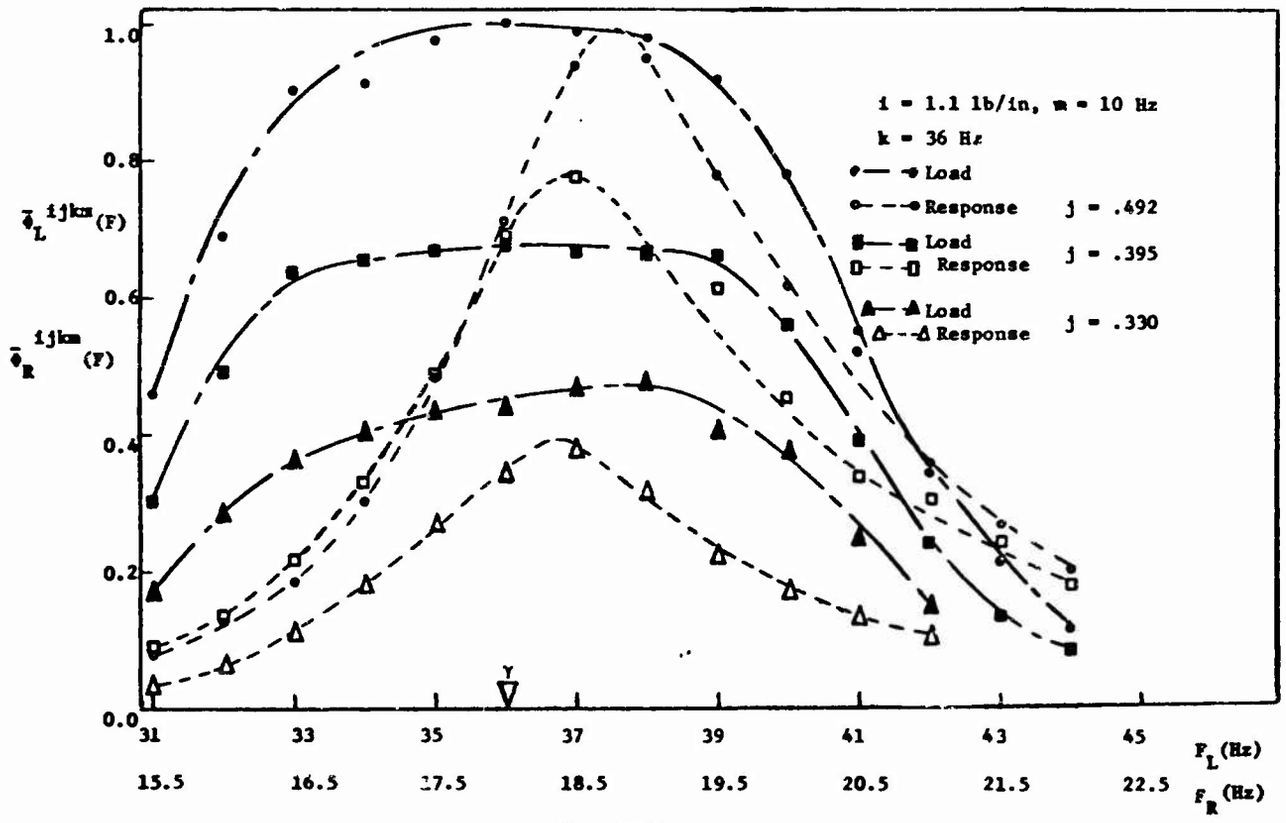


Figure 17

Power Spectral Density of Load and Response (Experimental Results)

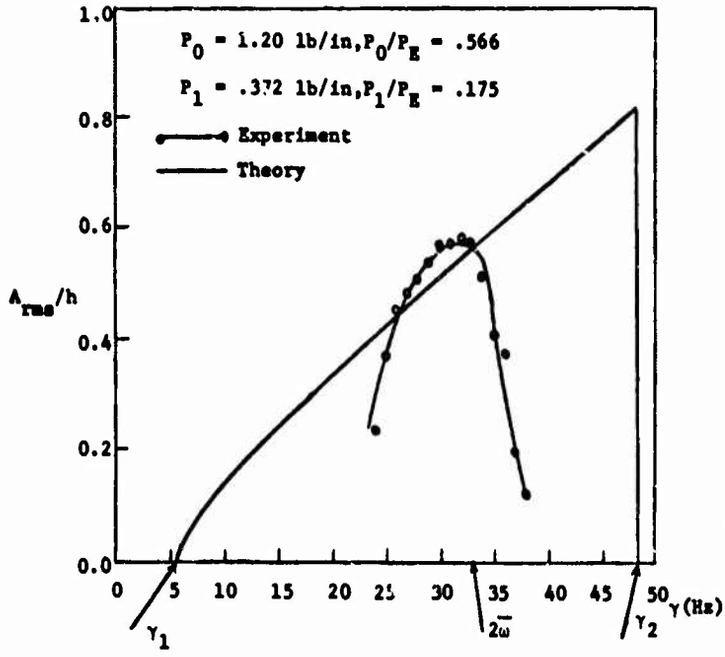


Figure 18

Response Curve in (A_{rms}/h, γ) Parameter Space.

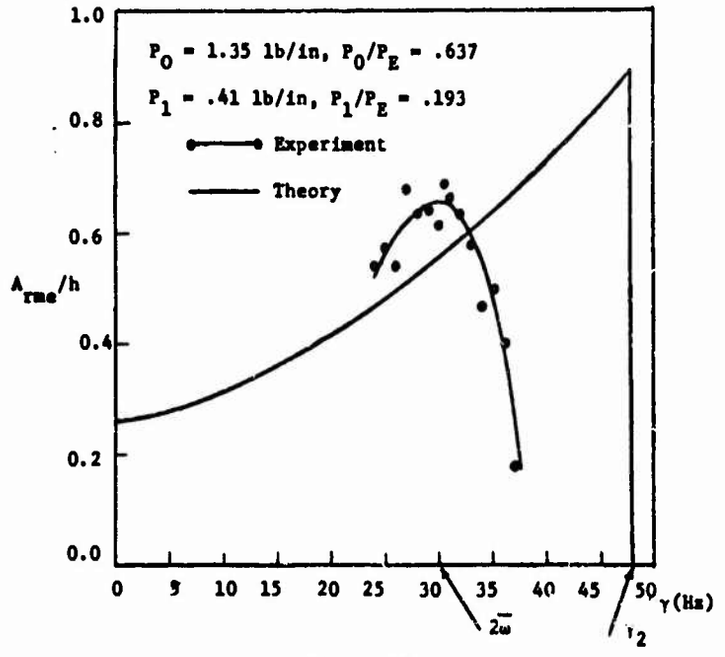


Figure 19

Response Curve in (A_{rms}/h, γ) Parameter Space

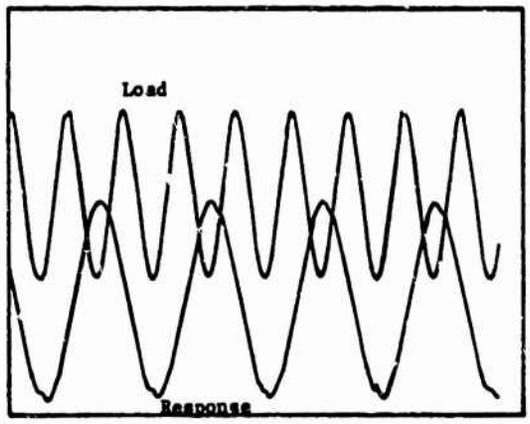


Figure 20a

Load-Response Sample Functions for
39 Hz Sinusoidal Input.

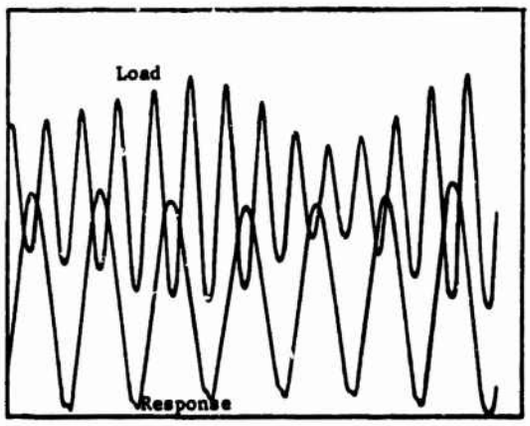


Figure 20b

Load-Response Sample Functions for
3 Hz Bandwidth Random Input.

TABLE III LIST OF SYMBOLS

A_{rms}	Root mean square value-response	γ_0	Mean frequency of random load power spectral density
B_{rms}	Root mean square value-response	γ_1	Increasing jump frequency
C_1	Conetant	γ_2	Decreasing jump frequency
C_2	Constant	Γ	Bandwidth of $\phi(t)$
$f(t)$	Response of System	$\delta(t)$	Function of time
F_L	Filter center frequency-load power epectral deneity	ζ	Independent parameter
F_R	Filter center frequency-response power spectral density	$\theta(t)$	Phase angle of response function
h	Plate thickness	ϑ	Independent parameter
m	Mass per equare inch of plate	ν	Poisson's ratio
$P(t)$	Total in-plane load	σ	Standerd deviation
P_E	Classical buckling load	$\phi(t)$	Function of time
P_0	Static in-plane load	$\phi_1(t)$	Envelope of narrow band process defined by $\phi(t)$
$P_1(t)$	Amplitude of dynamic in-plane load	$\overline{\phi_1}$	Vslue proportional to RMS of load
t	Time	$\phi_L^{ijkm}(F)$	Power spectrel density-load
T	Period of load parameter	$\phi_R^{ijkm}(F)$	Power apectral density-response
x	Frequency variable	$\phi_L^{ijkm}(F)$	Normalized power spectral density-losd
$\beta(t)$	Phase angle of load function	$\phi_R^{ijkm}(F)$	Normalized power spectral density-response
γ	Load frequency	ψ	Nonlinear function
γ_m	Load frequency of maximum of plete reeponee	ω	Frequency perameter
γ_n	Load frequency of minimum of plete reeponse	$\overline{\omega}$	Natural frequency of lateral vibretion of the plate-function of P_0

BIBLIOGRAPHY

1. Einaudi, R., "Sulle configurazioni di equilibrio instabili di una piastra sollecitate da sforzi tangerziale puleanti," Atti Accad Gioenia J. Memoria XX(1-5), 1935-1936.

2. Chelomei, V. K., "The Dynamic Stability of Plates," Trudy Kiev. Avista 8, 1938.

3. Bodner, V. A., "Stability of Plates Subjected to Longit dinal Periodic Forces," Prikl. Mat. Mekh. 2. 87, 1938.

4. Bolotin, V. V., Dynamic Stability of Eleetic Syetems, Gos. Izdst. ech-Teor, Lit Moscow, 1956.

5. Berenovskii, A. A. and L. F. Shulezko, "Nonlinear Formuletion of the Problem of e Parametric Instability of Plates." Ukran. Aced. of Scien. Izveet., pp. 889-993, 1963.

6. Somereet, J. H. and R. M. Evan-Iwanowski, "Influence of Nonlinear Inertie on the Perametric Response of Rectanguler Plates," Int. Jour. Nonlinesr Mech., V. 2, no. 3, 1967.

7. Somerset, J. H. and R. M. Evan-Iwanowski, "Experiments on Large Amplitude Parametric Vibration of Rectangular Plates," Developments in Theoretical and Applied Mechanics, V. 3, Proc. 3rd Southeastern Conf. on Theor. and Appl. Mech., 1966.

8. Somerset, J. H. and R. M. Evan-Iwanowski, "Experiments on the Parametric Instability of Elastic Columns," Developments in Theoretical and Applied Mechanics, V. 2, Pergamon Press, 1965.

9. Evensen, H. A. and R. M. Iwanowski, "Effects on Longitudinal Inertia upon the Parametric Response of Elastic Columns," Jour. of Applied Mechanics, Paper no. 65-WA/APM - 13, 1965.

10. Somerset, J. H., "Transition Mechanisms Attendant to Large Amplitude Parametric Vibrations of Rectangular Plates," Journal of Engineering for Industry, paper no. 67-Vibr-5, 1967.

11. Caughey, T. K. and J. K. Dienes, "The Behavior of Linear Systems with Random Parametric Excitation," Journal of Mathematics and Physics, Vol. XLI, no. 4, Dec. 1962.

12. Leibowitz, M. A., "Statistical Behavior of Linear Systems with Randomly Varying Parameters," Journal of Mathematical Physics, Vol. 4, no. 6, June 1963.

13. Caughey, T. K. and A. H. Gray, Jr., "On the Almost Sure Stability of Linear Dynamic Systems with Stochastic Coefficients," Journal of Applied Mechanics, Paper no. 64-APM-46, 1964.

14. Wang, P. K. C., "On the Almost Sure Stability of Linear Stochastic Distributed-Parameter Dynamical Systems," Journal of Applied Mechanics, Paper no. 65-WA/APM-12, 1965.

15. Shyu, T. P. and J. H. Somerset, "Nonlinear Parametric Response of Rectangular Plates under In-Plane Random Loads," to be published.

RESPONSE OF STIFFENED PLATES TO MOVING SPRUNG MASS LOADS*

Ganpat M. Singhvi
Schutte Mochon, Inc.
Milwaukee, Wisconsin

and

Larry J. Feeser
University of Colorado
Boulder, Colorado

An analytical procedure to predict the behavior of orthogonally stiffened plates subjected to a moving sprung mass system is developed. The loading considered consists of a damped spring borne mass supported by an unsprung wheel mass subjected to a pulsating driving force moving with a constant velocity in an arbitrary straight path across the plate. The general solution in the form of a triple infinite series is obtained to represent the dynamic deflection of a rectangular stiffened plate simply supported on all four sides. Numerical solutions obtaining dynamic deflections and dynamic bending moments at the center of the plate and under the load are presented for a rectangular stiffened plate and are compared with constant force and crawl load solutions. The results of the study indicate that the inertia of the moving mass has a significant effect upon the deflections and moments in stiffened plates and must be included to obtain good designs.

INTRODUCTION

The dynamic behavior of beams and deck systems subjected to moving and pulsating loads has been the subject of numerous mathematical and experimental studies during the past century. A good description of the early work is found in papers by Licari, Wilson and Cappelli [1, 2].

In recent years, the design of deck systems with closely spaced stiffeners has received considerable attention. Generally, these deck systems are made up of stiffeners placed perpendicular to each other and welded to one side of a deck plate. The plate stiffener system with rigid connections is assumed to act as a monolithic unit. Because the stiffnesses of the system are generally different in two principal directions, the system is occasionally referred to as an orthotropic plate. The behavior of a plate with stiffeners placed symmetrically with respect to the middle surface of the plate can be described by the Huber [3] equation. For eccentrically stiffened plates Giencke [4] and others [5] have tried to determine the rigidities which can be used in Huber's equation.

In 1964, Feeser and Au [6, 7, 8] derived the governing differential equations of the Pflüger [9] type for the dynamic behavior of eccentrically stiffened plates. Analytical solutions were presented for the free vibration behavior and the dynamic response to moving pure force loads.

In this paper, a procedure is developed for obtaining solutions to the differential equations governing the dynamic response of stiffened plates subjected to moving sprung mass loads. The loading considered consists of a damped spring borne mass supported by an unsprung wheel mass which is subjected to a pulsating driving force moving with a constant velocity in an arbitrary straight path across the plate. The Huber equation, modified to consider geometric anisotropy of the plate, and D'Alembert's principle were used to formulate the governing coupled differential equations of motion.

A general solution for the equations is obtained as functions of space and time coordinates and certain undetermined coefficients. These coefficients result from the assumed sine series expansion for the unknown acceleration under the moving load. By means of known relationships, a recurrence formula is derived from which an infinite system of linear algebraic equations is obtained for an infinite set of undetermined coefficients. The general solution in the form of triple infinite series, represents the dynamic deflection of the stiffened plate.

MATHEMATICAL FORMULATION

Consider a simply supported rectangular stiffened plate with torsionally soft stiffeners shown in Fig. 1. The differential equation giv-

*Paper not presented at Symposium.

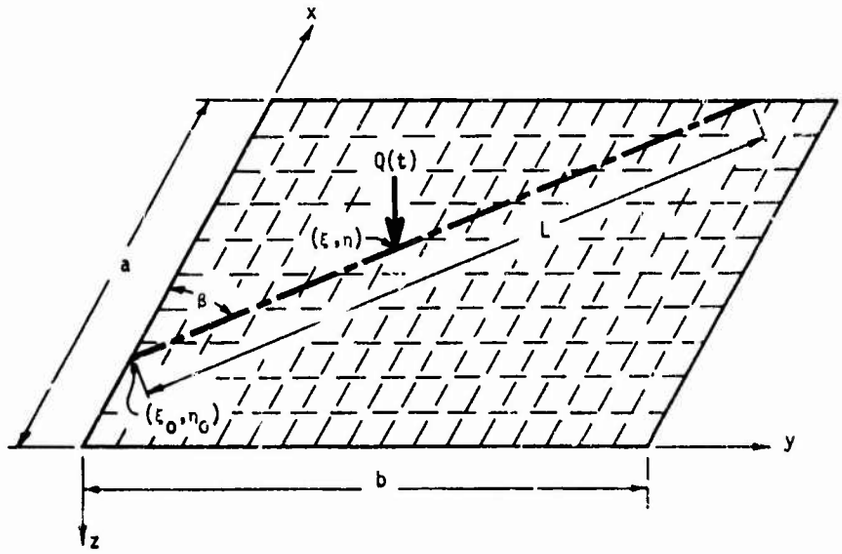


FIG. 1 - Rectangular Stiffened Plate

ing the relationship between the deflection and the static loading of a constant thickness orthotropic plate, often referred to as Huber's equation is

$$D_x \frac{\partial^4 w}{\partial x^4} + 2H \frac{\partial^4 w}{\partial x^2 \partial y^2} + D_y \frac{\partial^4 w}{\partial y^4} = q(x,y) \qquad (1)$$

where w is the deflection of the middle surface of the plate, D_x and D_y represent the bending stiffnesses in the x and y directions respectively, the coefficient H is computed from the torsional rigidity and Poisson's ratio of the plate, and q(x,y) is the loading intensity at any point, expressed as the function of the coordinates x and y. For a plate with eccentric stiffeners, H is also a function of the eccentricity and the torsional rigidity of the stiffeners. Various approximations have been suggested by assuming different values for H. One of the most widely accepted approximate methods for determining H for orthotropic plates with torsionally soft stiffeners makes use of the concept of effective stiffness introduced by Giencke [4]. This concept is based on the assumption that the horizontal strain is zero at the adjusted centroid of the cross section in each direction. The adjusted centroids in the x and y directions are located at distances e_x^* and e_y^* respectively, below the middle surface of the deck plate. The distances e_x^* and e_y^* are defined as follows:

$$e_x^* = \frac{e_x A_x}{A_x + \frac{h}{(1-\nu^2)}}$$

$$e_y^* = \frac{e_y A_y}{A_y + \frac{h}{(1-\nu^2)}} \qquad (2)$$

in which h is the thickness of the deck plate; A_x and A_y are cross sectional areas of the stiffeners in the x and y direction per unit length along the y and x axes, respectively; e_x and e_y are distances from the middle surface of the deck plate to the centroid of the stiffeners in the x and y directions, respectively, and ν is Poisson's ratio. Writing the equations of equilibrium for a typical plate element shown in Fig. 2 and making use of the concept of effective stiffness, the governing differential equation describing the dynamic equilibrium of a stiffened plate can be obtained as [5]

$$D_x \frac{\partial^4 w}{\partial x^4} + 2H^* \frac{\partial^4 w}{\partial x^2 \partial y^2} + D_y \frac{\partial^4 w}{\partial y^4} +$$

$$m_o \frac{\partial^2 w}{\partial t^2} + c_o \frac{\partial w}{\partial t} = q(x,y,t)$$

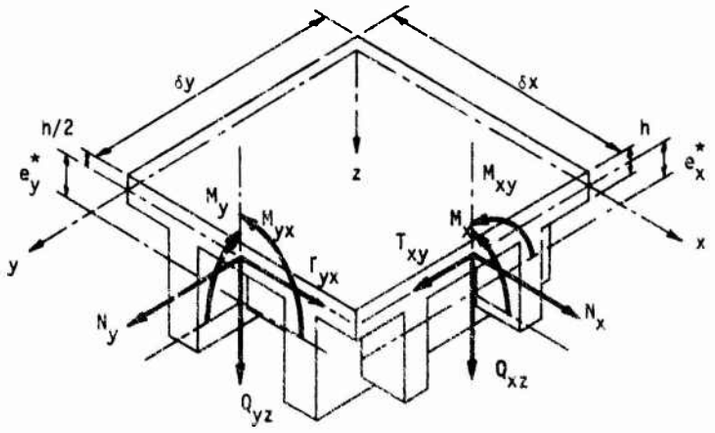


FIG. 2 - Typical Element of Stiffened Plate

where

$$D_x = E \int_{A_x} (z - e_x^*)^2 \, dA_x + \frac{E}{(1 - \nu^2)} \int_{-h/2}^{h/2} (z - e_x^*)^2 dz$$

$$D_y = E \int_{A_y} (z - e_y^*)^2 \, dA_y + \frac{E}{(1 - \nu^2)} \int_{-h/2}^{h/2} (z - e_y^*)^2 dz$$

$$H^* = D + \nu B \left[e_x^* \, e_y^* + \frac{(1 - \nu)}{4\nu} (e_x^* + e_y^*)^2 \right]$$

$$D = \frac{Eh^3}{(1 - \nu^2)}$$

$$B = \frac{Eh}{(1 - \nu^2)}$$

E = Modulus of elasticity

m_o = mass per unit projected area of the element of the plate stiffener combination

c_o = coefficient of viscous damping

Consider a pulsating type of loading as shown in Fig. 3 moving with a constant velocity in an arbitrary straight path across the plate. Let the vertical displacement of the plate be $w(x,y,t)$ for $0 \leq x \leq a$, $0 \leq y \leq b$ and $0 \leq t \leq L/v$. The vertical displacement of the sprung mass M_s and the unsprung wheel mass M_u are $w_1(t)$ and $w_o(t)$, respectively. Positive directions are as indicated in Fig. 3.

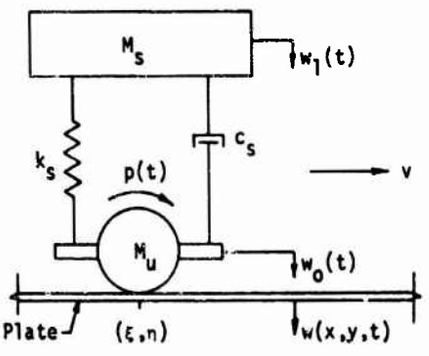


FIG. 3 - Forcing System

At any time t the concentrated reaction force Q(t) resulting from the combined effects of the pulsating, inertia and gravity force acting at the point of contact between the plate and unsprung mass is

$$Q(t) = (p_o \sin 2\pi\omega t + gM_u - M_u \frac{d^2w_o}{dt^2} - M_s \frac{d^2w_1}{dt^2} + gM_s)$$

in which p_o = pulsating force, ω = forcing frequency, and g = acceleration due to gravity.

The transverse forcing function q(x,y,t) for the concentrated variable force Q(t) applied at (ξ,η) on the plate can be represented as a function of the load position coordinates by the following double infinite series:

$$q\left[x,y,t,\frac{d^2w_o}{dt^2},\frac{d^2w_1}{dt^2}\right] = \frac{4Q(t)}{ab} \sum_{m=1}^{\infty}\sum_{n=1}^{\infty} (\sin\theta_n\xi \sin\theta_m\eta \sin\theta_n x \sin\theta_m y)$$

in which

$$\theta_n = \frac{n\pi}{a}$$

$$\theta_m = \frac{m\pi}{b}$$

Using d'Alembert's principle the differential equations defining the system's dynamic response can be written as

$$M_s \frac{d^2w_1}{dt^2} + c_s \frac{dw_1}{dt} + k_s w_1 = c_s \frac{dw_o}{dt} + k_s w_o \qquad (3)$$

$$D_x \frac{\partial^4 w}{\partial x^4} + 2H^* \frac{\partial^4 w}{\partial x^2 \partial y^2} + D_y \frac{\partial^4 w}{\partial y^4} + m_o \frac{\partial^2 w}{\partial t^2} + c_o \frac{\partial w}{\partial t} = \frac{4}{ab}\left[p_o \sin 2\pi\omega t + gM_u + gM_s - M_s \frac{d^2w_1}{dt^2} - M_u \frac{d^2w_o}{dt^2}\right] \sum_{m=1}^{\infty}\sum_{n=1}^{\infty} (\sin\theta_n\xi \sin\theta_m\eta \sin\theta_n x \sin\theta_m y) \qquad (4)$$

subjected to the following initial and boundary conditions:

Initial displacement and velocity conditions:

$$w_o(0) =) \; ; \quad \frac{dw_o(0)}{dt} = 0 \; ;$$

$$w_1(0) = 0 \; ; \quad \frac{dw_1(0)}{dt} = 0 \; ;$$

$$w(x,y,0) = 0 \; ; \quad \frac{\partial w(x,y,0)}{\partial t} = 0.$$

Boundary conditions:

$$w(0,y,t) = 0 \; ; \quad \frac{\partial^2 w(0,y,t)}{\partial x^2} = 0 \; ;$$

$$w(a,y,t) = 0 \; ; \quad \frac{\partial^2 w(a,y,t)}{\partial x^2} = 0 \; ;$$

$$w(x,0,t) = 0 \; ; \quad \frac{\partial^2 w(x,0,t)}{\partial y^2} = 0 \; ;$$

$$w(x,b,t) = 0 \; ; \quad \frac{\partial^2 w(x,b,t)}{\partial y^2} = 0 \; .$$

General solutions of Eqs. (3) and (4), subjected to the initial and boundary conditions, describe the dynamic response of the stiffened plate to a moving sprung mass system. The inertia effects due to the moving mass have created particular mathematical difficulties in the past because the moving forcing function in this case becomes a function of the dependent variable in the differential equations and therefore requires the solution of a partial differential equation with variable coefficients. The solutions to such equations usually are difficult to obtain, and so past efforts have either searched for approximate solutions or have neglected inertia effects entirely.

Let $\frac{d^2w_o}{dt^2}$ be a continuous function defined in the interval $0 \leq t \leq L/v$ and represented by a Fourier sine series expansion with undetermined a_j coefficients given by

$$\frac{d^2w_o}{dt^2} = \sum_{j=1}^{\infty} a_j \sin\phi_j t \qquad (5)$$

in which $\phi_j = \frac{j\pi V}{L}$. Integrating Eq. (5) and substituting into Eq. (3) gives

$$M_s \frac{d^2 w_1}{dt^2} + c_s \frac{dw_1}{dt} + k_s w_1 = - \sum_{j=1}^{\infty} a_j \left[\frac{c_s \cos \phi_j t}{\phi_j} + \frac{k_s \sin \phi_j t}{\phi_j^2} - \frac{c_s}{\phi_j} - \frac{k_s t}{\phi_j} \right] \qquad (6)$$

The general solution of Eq. (6) in terms of the a_j coefficients can be written as [5]

$$w_1(t) = C_1 \sum_{j=1}^{\infty} a_j \lambda_j(t) \qquad (7)$$

where

$$\lambda_j(t) = K_{j_1} \cos \phi_j t - K_{j_2} \sin \phi_j t + \frac{t}{\phi_j} + e^{-\gamma t} \left[K_{j_3} \sin \psi t - K_{j_1} \cos \psi t \right]$$

in which

$$K_{j_1} = \frac{\mu_j D_s}{(1 - \mu_j^2)^2 + \mu_j^2 D_s^2} ;$$

$$K_{j_2} = \frac{D_s^2}{(1 - \mu_j^2)^2 + \mu_j^2 D_s^2} + \frac{(1 - \mu_j^2)}{(1 - \mu_j^2)^2 \mu_j^2 + \mu_j^4 D_s^2} ;$$

$$K_{j_3} = \frac{(2\mu_j^2 K_{j_2} - D_s \mu_j K_{j_1} - 2)}{\mu_j (\sqrt{4 - D_s^2})} ;$$

$$\gamma = 2\pi g_c ; \qquad \mu_j = \frac{jf}{g_o} ;$$

$$g_o = \frac{1}{2\pi} \sqrt{\frac{k_s}{M_s}} ; \qquad g_c = \frac{c_s}{4\pi M_s} ;$$

$$D_s = \frac{2g_c}{g_o} ; \qquad f = \frac{V}{2L} ;$$

$$\psi = 2\pi \sqrt{g_o^2 - g_c^2} ; \qquad C_1 = \frac{1}{4\pi^2 g_o^2} .$$

Differentiating Eq. (7) twice yields

$$\frac{d^2 w_1}{dt^2} = \sum_{j=1}^{\infty} a_j \Omega_j(t) \qquad (8)$$

where

$$\Omega_j(t) = K_{j_2}^* \sin \phi_j t - K_{j_1} \cos \phi_j t + e^{-\gamma t} \left[K_{j_1}^{**} \cos \psi t - K_{j_3}^* \sin \psi t \right]$$

in which

$$K_{j_1}^{**} = (K_{j_1} - D_s \mu_j K_{j_2}) + \frac{D_s}{\mu_j} ;$$

$$K_{j_2}^* = \mu_j^2 K_{j_2} ;$$

$$K_{j_3}^* = \frac{(2 - D_s^2) \mu_j K_{j_2} - D_s K_{j_1}}{\sqrt{4 - D_s^2}} - \frac{(2 - D_s^2)}{\mu_j (\sqrt{4 - D_s^2})} .$$

Substituting the acceleration functions, Eqs. (5) and (8), into Eq. (4) gives

$$\bar{D}_x \frac{\partial^4 w}{\partial x^4} + 2\bar{H}^* \frac{\partial^4 w}{\partial x^2 \partial y^2} + \bar{D}_y \frac{\partial^4 w}{\partial y^4} + \frac{\partial^2 w}{\partial t^2} + \bar{c} \frac{\partial w}{\partial t} = \left[4 \sum_{m=1}^{\infty} \sum_{n=1}^{\infty} \left[g R_f \sin 2\pi\omega t + g R_m - R_u \sum_{j=1}^{\infty} a_j \sin \phi_j t - R_s \sum_{j=1}^{\infty} a_j \Omega_j(t) \right] (\sin \theta_n \xi \sin \theta_m \eta \sin \theta_n x \sin \theta_m y) \right] \qquad (9)$$

in which

$$\bar{D}_x = \frac{D_x}{m_o} ; \qquad \bar{H}^* = \frac{H^*}{m_o} ;$$

$$\bar{D}_y = \frac{D_y}{m_o} ; \qquad \bar{c} = \frac{c_o}{m_o} ;$$

$$R_u = \frac{M_u}{M_o} \; ; \qquad R_m = R_u + R_s \; ;$$

$$R_s = \frac{M_s}{M_o} \; ; \qquad R_f = \frac{P_o}{M_o g} \; ;$$

$$M_o = \eta_o ab$$

The general solution of Eq. (9) is obtained by the method of separation of variables, in terms of undetermined a_j coefficients, and the solution can be written as

$$w(x,y,t) = \sum_{m=1}^{\infty} \sum_{n=1}^{\infty} \left[g\, X_{mn}(t) + \sum_{j=1}^{\infty} a_j\, X_{mn_j}(t) \right] \Theta_{mn}(x,y) \qquad (10)$$

in which

$$X_{mn}(t) = M_{mn}(t) - e^{-ct}\left[M_{mn}(0) \cos \lambda_{mn} t + \frac{\{c\, M_{mn}(0) + \dot{M}_{mn}(0)\}}{\lambda_{mn}} \sin \lambda_{mn} t \right] \; ;$$

$$X_{mn_j}(t) = M_{mn_j}(t) - e^{-ct}\left[M_{mn_j}(0) \cos \lambda_{mn} t + \frac{\{c\, M_{mn_j}(0) + \dot{M}_{mn_j}(0)\}}{\lambda_{mn}} \sin \lambda_{mn} t \right] \; ;$$

$$\Theta_{mn}(x,y) = \sin \theta_n x \sin \theta_m y \; ;$$

$$c = \bar{c}/2 \; ; \quad \lambda_{mn} = \sqrt{p_{mn}^2 - c^2} \quad \text{for } p_{mn}^2 > c^2 \; ;$$

$$p_{mn}^2 = \left[\bar{D}_x\, \theta_n^4 + 2\bar{H}^*\, \theta_n^2\, \theta_m^2 + \bar{D}_y\, \theta_m^4 \right] \; ;$$

$$M_{mn}(t) = \sum_{i=1}^{6} (A_{mn_i} \sin \rho_{mn_i} t + B_{mn_i} \cos \rho_{mn_i} t) \; ;$$

$$M_{mn_j}(t) = \sum_{i=1}^{4} \left[(A_{mn_{ij}} \sin \rho_{mn_{ij}} t + B_{mn_{ij}} \cos \rho_{mn_{ij}} t) + e^{-\gamma t} (\bar{A}_{mn_{ij}} \sin \epsilon_{mn_i} t + \bar{B}_{mn_{ij}} \cos \epsilon_{mn_i} t) \right] \; ;$$

$$\rho_{mn_5} = -\theta_n v \cos\beta - \theta_m v \sin\beta \; ;$$

$$\rho_{mn_6} = -\theta_n v \cos\beta + \theta_m v \sin\beta \; ;$$

$$\rho_{mn_1} = 2\pi\omega + \rho_{mn_5} \; ; \quad \rho_{mn_3} = 2\pi\omega - \rho_{mn_5} \; ;$$

$$\epsilon_{mn_1} = \psi + \rho_{mn_6} \; ; \quad \rho_{mn_{1j}} = \phi_j + \rho_{mn_5} \; ;$$

$$\epsilon_{mn_2} = \psi + \rho_{mn_5} \; ; \quad \rho_{mn_{2j}} = \phi_j + \rho_{mn_6} \; ;$$

$$\epsilon_{mn_3} = \psi - \rho_{mn_5} \; ; \quad \rho_{mn_{3j}} = \phi_j - \rho_{mn_5} \; ;$$

$$\epsilon_{mn_4} = \psi - \rho_{mn_6} \; ; \quad \rho_{mn_{4j}} = \phi_j - \rho_{mn_6} \; ;$$

$$\rho_{mn_2} = 2\pi\omega + \rho_{mn_6} \; ; \quad \rho_{mn_4} = 2\pi\omega - \rho_{mn_6} \; ;$$

$$\left.\begin{aligned} A_{mn_i} &= R_f\, R_{mn_i} \\ B_{mn_i} &= R_f\, R^*_{mn_i} \end{aligned}\right\} \; i = 1,2,3,4$$

$$\left.\begin{aligned} A_{mn_i} &= 2\, R_m\, \bar{R}^*_{mn_i} \\ B_{mn_i} &= 2\, R_m\, \bar{R}^*_{mn_i} \end{aligned}\right\} \; i = 5,6 \; ;$$

$$\left.\begin{aligned} \bar{A}_{mn_{ij}} &= R_s \left[K^{**}_{j_1}\, G^*_{mn_i} + K^*_{j_3}\, \bar{G}_{mn_i} \right] \\ \bar{B}_{mn_{ij}} &= R_s \left[K^*_{j_3}\, G^*_{mn_i} - K^{**}_{j_1}\, \bar{G}_{mn_i} \right] \end{aligned}\right\} \; i = 1,2,3,4 \; ;$$

$$\left.\begin{aligned} A_{mn_{ij}} &= -R_s K^*_{j_1} R^*_{mn_{ij}} - R_{mn_{ij}} K^{**}_{j_2} \\ B_{mn_{ij}} &= +R_s K^*_{j_1} R_{mn_{ij}} - R^*_{mn\ j} K^{**}_{j_2} \end{aligned}\right\} i = 1, 2,3,4;$$

$$K^*_{j_1} = \mu_j^2 K_{j_1} \quad ; \quad K^{**}_{j_2} = (R_u + R_s K^*_{j_2}) \ ;$$

$$R_{mn_i} = S_{mn_i}\left[(p_{mn}^2 - \rho_{mn_i}^2)\cos\alpha_{mn_i} + \bar{c}\rho_{mn_i}\sin\alpha_{mn_i}\right]$$

$$\bar{R}_{mn_i} = S_{mn_i}\left[(p_{mn}^2 - \rho_{mn_i}^2)\cos\alpha_{mn_i} - \bar{c}\rho_{mn_i}\sin\alpha_{mn_i}\right]$$

$$R^*_{mn_i} = S_{mn_i}\left[(p_{mn}^2 - \rho_{mn_i}^2)\sin\alpha_{mn_i} - \bar{c}\rho_{mn_i}\cos\alpha_{mn_i}\right]$$

$$\bar{R}^*_{mn_i} = S_{mn_i}\left[(p_{mn}^2 - \rho_{mn_i}^2)\sin\alpha_{mn_i} + \bar{c}\rho_{mn_i}\sin\alpha_{mn_i}\right]$$

$$R_{mn_{ij}} = S_{mn_{ij}}\left[(p_{mn}^2 - \rho_{mn_{ij}}^2)\cos\alpha_{mn_i} + \bar{c}\,\rho_{mn_{ij}}\sin\alpha_{mn_i}\right]$$

$$R^*_{mn_{ij}} = S_{mn_{ij}}\left[(p_{mn}^2 - \rho_{mn_{ij}}^2)\sin\alpha_{mn_i} - \bar{c}\rho_{mn_{ij}}\cos\alpha_{mn_i}\right]$$

$$G^*_{mn_i} = Q_{mn_i}\left[\beta_{mn_{i1}}\sin\alpha_{mn_i} + \beta_{mn_{i2}}\cos\alpha_{mn_i}\right]$$

$$\bar{G}_{mn_i} = Q_{mn_i}\left[\beta_{mn_{i1}}\cos\alpha_{mn_i} - \beta_{mn_{i2}}\sin\alpha_{mn_i}\right]$$

$$S_{mn_i} = \frac{(-1)^i}{\left[(p_{mn}^2 - \rho_{mn_i}^2)^2 + (\bar{c}\rho_{mn_i})^2\right]}$$

$$S_{mn_{ij}} = \frac{(-1)^i}{\left[(p_{mn}^2 - \rho_{mn_{ij}}^2)^2 + (\bar{c}\,\rho_{mn_{ij}})^2\right]}$$

$$Q_{mn_i} = \frac{(-1)^i}{(\beta_{mn_{i1}}^2 + \beta_{mn_{i2}}^2)}$$

$$\alpha_{mn_1} = -\theta_n \xi_o - \theta_m \eta_o$$

$$\alpha_{mn_2} = +\theta_m \eta_o - \theta_n \xi_o$$

$$\alpha_{mn_3} = \alpha_{mn_5} = -\alpha_{mn_1}$$

$$\alpha_{mn_4} = \alpha_{mn_6} = -\alpha_{mn_2}$$

$$\beta_{mn_{i1}} = (p_{mn}^2 + \gamma^2 - \epsilon_{mn_i}^2) - \bar{c}\gamma$$

$$\beta_{mn_{i2}} = (2\gamma - \bar{c})\,\epsilon_{mn_i}$$

The undetermined coefficients, a_j, will be found by matching the assumed acceleration function under the load with the acceleration obtained by solving the differential equations. The following relationships exist between the dependent variables $w_o(t)$ and $w(x,y,t)$

$$\frac{d^2 w_o(t)}{dt^2} = \frac{d^2 w(x,y,t)}{dt^2}\Bigg|_{\substack{x=\xi \\ y=\eta}} \qquad (11)$$

Differentiating Eq. (10) according to Eq. (11) gives

$$\sum_{j=1}^{\infty} a_j \sin\phi_j t = \sum_{m=1}^{\infty}\sum_{n=1}^{\infty}\sum_{j=1}^{\infty}\left[a_j \Lambda_{mn_j}(t) + g\,\Lambda_{mn}(t)\right]$$

Application of the Fourier-Euler inversion formula gives the following recurrence relation-

ship for the undetermined a_j coefficients

$$- a_k \frac{\pi k}{2\phi_k} = \int_0^{t_1} \sum_{m=1}^{\infty} \sum_{n=1}^{\infty} \left[g \Lambda_{mn}(t) + \sum_{j=1}^{\infty} a_j \Lambda_{mn_j}(t) \right] \sin \phi_k t \, dt \quad (12)$$

where

$$\Lambda_{mn}(t) = \Big[\Big[\ddot{X}_{mn}(t) - v^2(\theta_n^2 \cos^2\beta + \theta_m^2 \sin^2\beta) X_{mn}(t) \Big] \Theta_{mn}(x,y) + v^2 \sin 2\beta \, \theta_n \theta_m X_{mn}(t) \, \Theta_{mn_1}(x,y) + 2v \Big[\theta_n \cos\beta \, \Theta_{mn_2}(x,y) + \theta_m \sin\beta \, \Theta_{mn_3}(x,y) \Big] \dot{X}_{mn}(t) \Big]_{\substack{x = \xi(t) \\ y = \eta(t)}}$$

and

$$\Lambda_{mn_j}(t) = \Big[\Big[\ddot{X}_{mn_j}(t) - v^2(\theta_n^2 \cos^2\beta + \theta_m^2 \sin^2\beta) X_{mn_j}(t) \Big] \Theta_{mn}(x,y) + v^2 \sin 2\beta \, \theta_n \theta_m X_{mn_j}(t) \, \Theta_{mn_1}(x,y) + 2v \Big[\theta_n \cos\beta \, \Theta_{mn_2}(x,y) + \theta_m \sin\beta \, \Theta_{mn_3}(x,y) \Big] \dot{X}_{mn_j}(t) \Big]_{\substack{x = \xi(t) \\ y = \eta(t)}}$$

In performing the above integrations this recurrence formula defines an infinite system of linear algebraic equations in the infinite set of unknown a_j coefficients. This infinite system of equations may be written in the following form:

$$- a_k \bar{\phi}_k = \sum_{m=1}^{\infty} \sum_{n=1}^{\infty} \sum_{j=1}^{\infty} a_j U_{kjmn} + \sum_{m=1}^{\infty} \sum_{n=1}^{\infty} S_{kmn} \quad (13)$$

where the U_{kjmn} and S_{kmn} coefficients are evaluated from Eq. (12). Simultaneous solution of Eq. (13) yields the infinite set of a_j coefficients. With the coefficients known Eq. (10) describes the behavior of a stiffened plate under the moving mass system.

NUMERICAL RESULTS

To illustrate the analytical procedure developed in this paper a numerical example is presented.

A rectangular stiffened plate of dimension a = 12 ft. and b = 9 ft., simply supported on all four edges is considered. The thickness of the deck plate is 3/16 inch. Open stiffeners are spaced 6 inches on centers in the x and y directions. The stiffeners in the x and y directions consist of 3/4 inch deep by 1/8 inch thick vertical bars respectively as shown in Fig. 4. The system is made of aluminum having a modulus of elasticity, $E = 10 \times 10^6$ psi, and Poisson's ratio, $\nu = 0.30$.

The force system, as shown in Fig. 3, having an unsprung mass ratio, $R_u = 0.25$, sprung mass ratio, $R_s = 0.25$ and force ratio, $R_f = 0$, is considered to move across the middle of the plate parallel to the x direction ($\beta = 0$) with a constant velocity of 30 ft./sec. The load enters the plate at x = 0 and y = b/2.

Solutions for deflections and moments, neglecting the effects of flexural plate damping ($c_o = 0$) and spring damping ($c_s = 0$) were calculated. A computer program for determining the dynamic deflection at the center of the stiffened plate, the deflection under the moving mass, dynamic bending moments at the center of the plate and bending moments under the moving mass was developed. The static influence lines for deflection and moments at the center of the plate as well as the influence lines for the deflection and moments at the center of the plate due to a moving pure force are also calculated by the program. The inertia effects due to the moving mass are neglected and the spring stiffness is considered infinite to obtain the influence lines due to the moving pure force from the general solution given by Eq.(10).

Fig. 5 shows the influence line for deflection at the center of the stiffened plate ob-

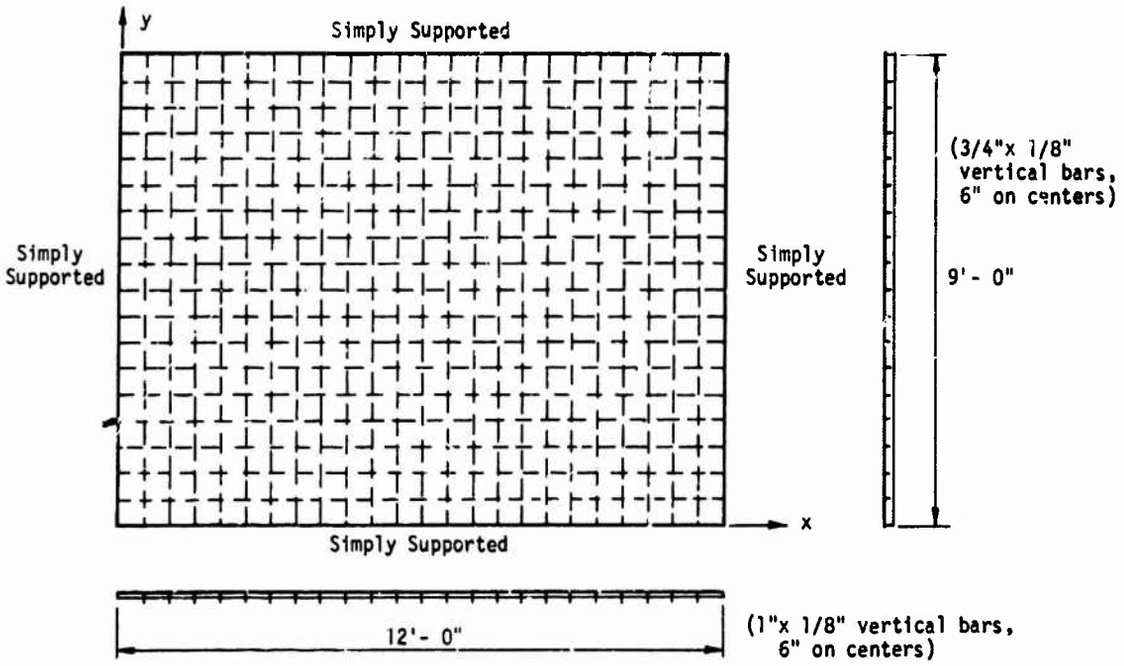


FIG. 4 - Stiffened Plate Dimensions for Numerical Example

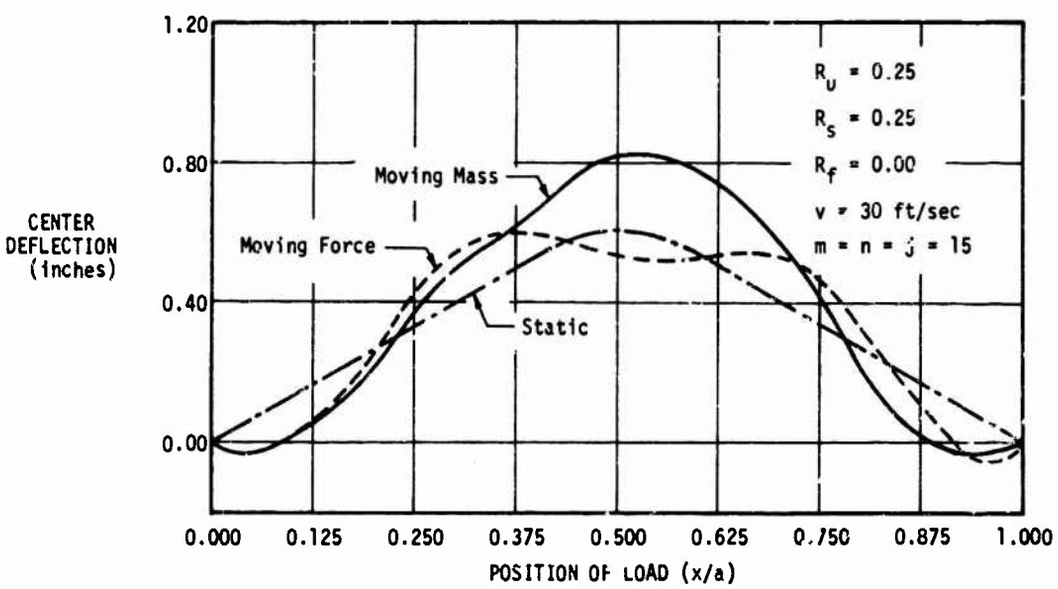


FIG. 5 - Deflection at the Center Versus Position of the Moving Mass

tained from the general solution given by Eq. 10. The maximum values of the indices m=n=j were set at 15. Also indicated on the plot are the static influence line for deflection at the center of the plate due to the moving pure force. For the example considered, the maximum deflection considering the inertia of the moving mass is about 36% larger than maximum static deflection and 39% larger than the deflection due to the moving force at the center of the plate. Figs. 6 and 7 show the influence lines for moment due to the moving mass, moving pure force and static load. Fig. 8 shows the deflection curves for various values of the indices. It also shows an indication of rate of convergence of infinite series solution.

Figures 9 and 10 are plots of deflection and moments under the moving mass versus the position of the moving mass.

CONCLUSIONS

Equations describing the response of stiffened plates to moving sprung mass loads are derived and solved for the general case. One numerical example is presented to illustrate the results. Obviously, no general conclusions can be drawn from the results of one numerical solution since a relatively large group of problems with varying parameters must be solved to obtain such conclusions.

The example demonstrates that the inertia of the moving mass can have a significant effect upon the deflection and moments.

Superposition of the solutions for multiple moving sprung masses cannot be made from various single solutions but rather the governing differential equations must be derived for the multiple configuration. Solutions can then be obtained by procedures similar to those presented here.

ACKNOWLEDGMENT

Early preliminary work leading to these results was supported by the National Science Foundation.

REFERENCES

1. J. S. Licari and E. N. Wilson, "Dynamic Response of a Beam Subjected to a Moving Forcing System," Proceedings of the Fourth U.S. National Congress of Applied Mechanics, Vol. 1, pp. 419-425, 1962.

2. A. P. Cappelli, J. S. Licari and E.N.Wilson, "Dynamic Response of a Rectangular Plate Subjected to a Moving Mass and Pulsating Load," Presented at the ASCE-EMD Specialty Conference, Los Angeles, April, 1965.

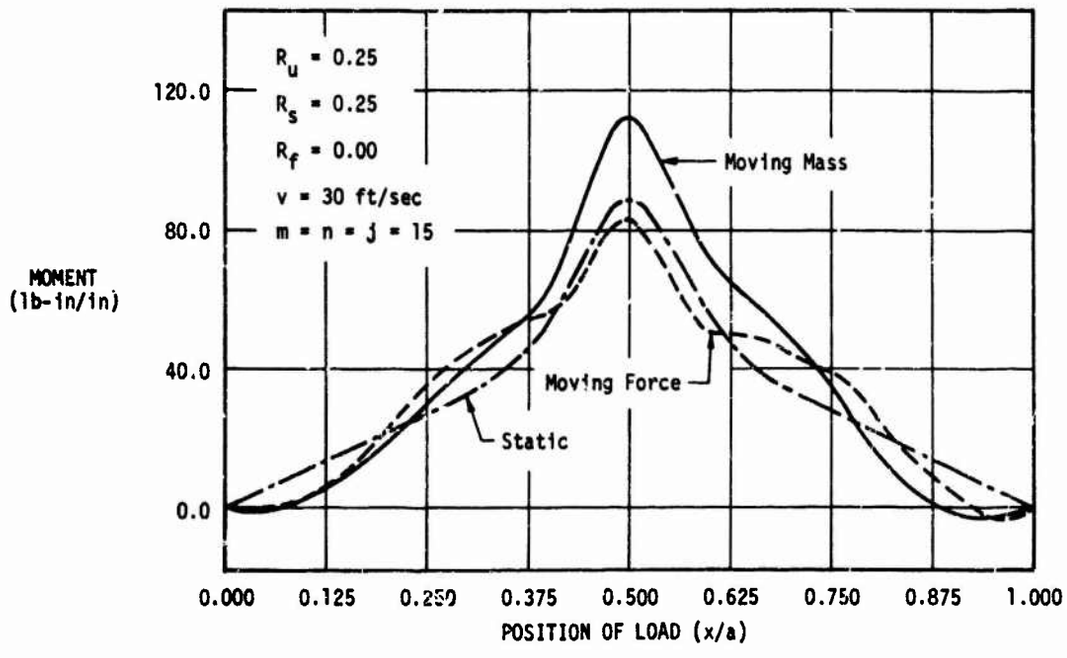


FIG. 6 - Moment M_y at the Center Versus Position of the Moving Mass

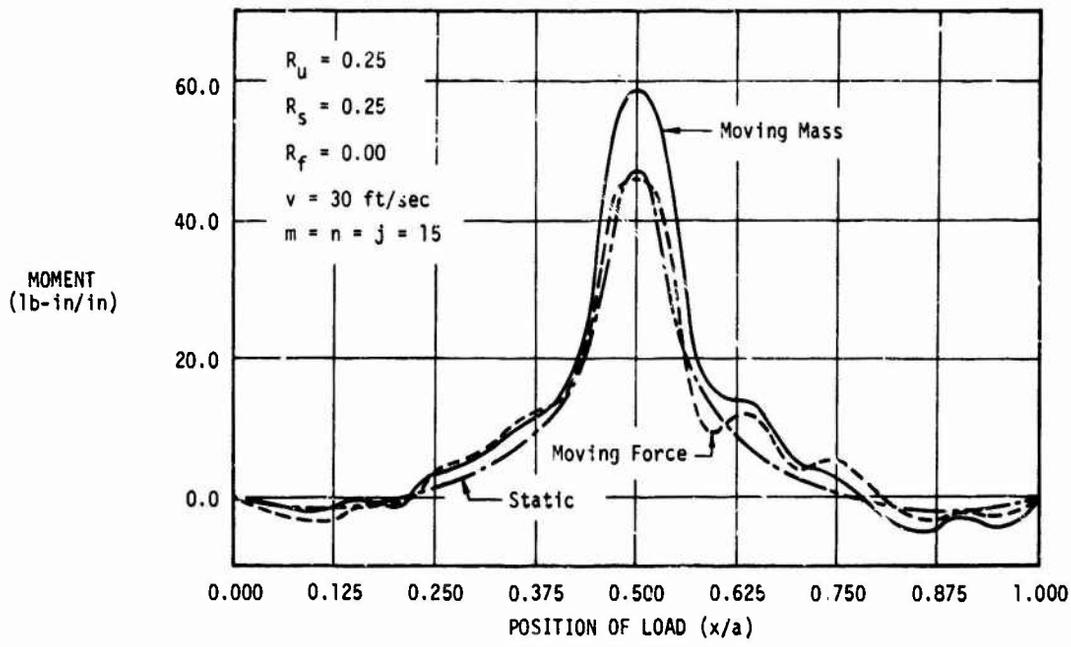


FIG. 7 - Moment M_x at the Center Versus Position of the Moving Mass

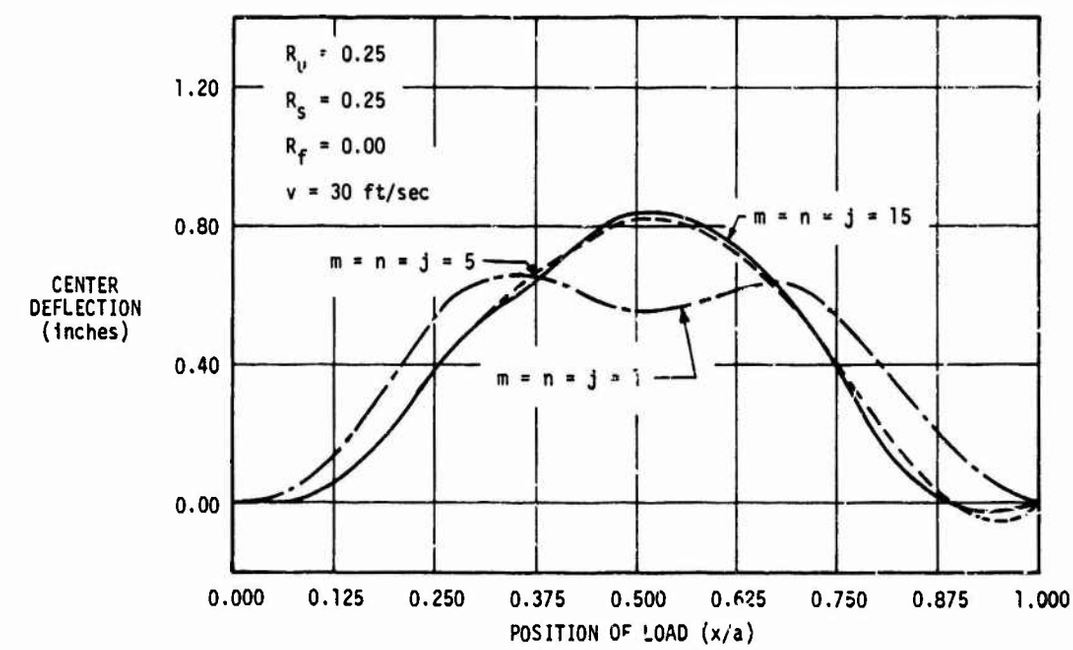


FIG. 8 - Deflection at the Center Versus Position of the Moving Mass

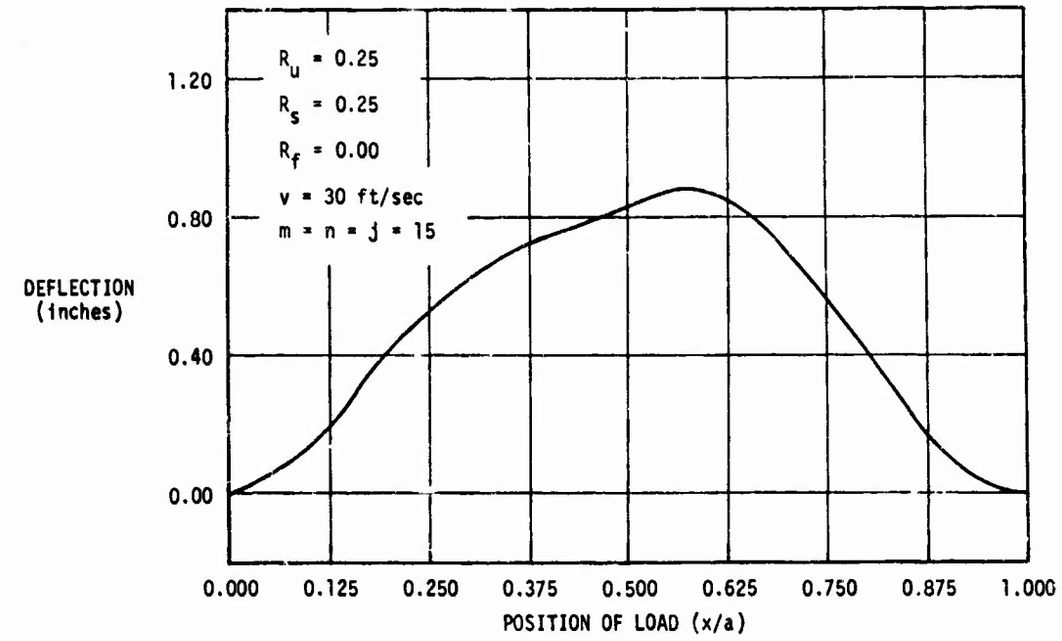


FIG. 9 - Deflection Under the Mass Versus Position of the Moving Mass

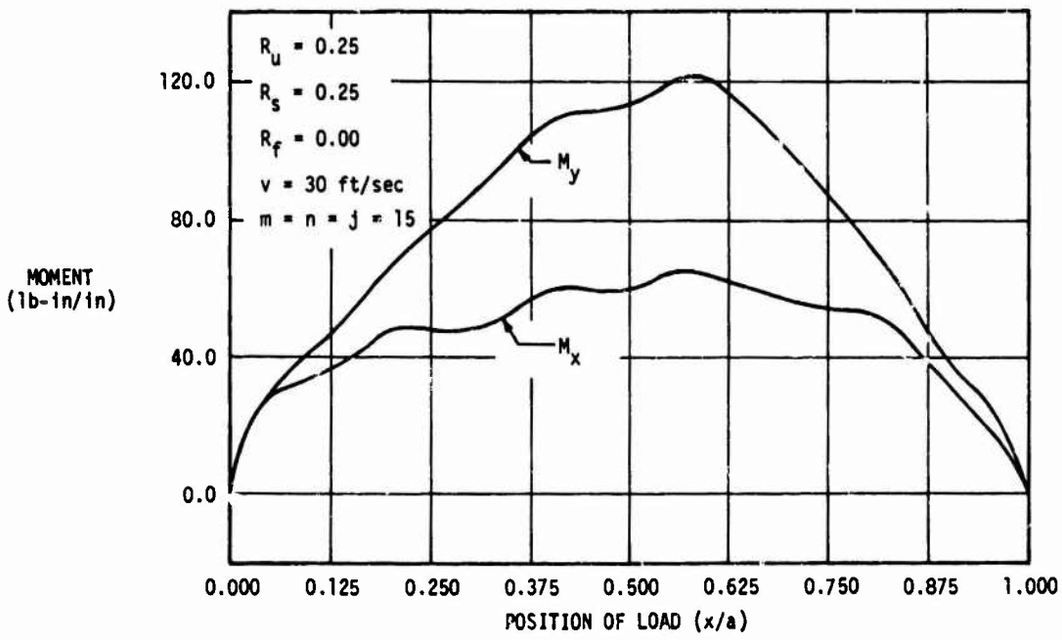


FIG. 10 - Moments Under the Mass Versus Position of the Moving Mass

3. M. T. Huber, "Die Theorie der Kreuzweise bewehrten Eisenbetonplatten, "Der Bauingenieur, Vol. 4, p. 354, 1923.

4. E. Giencke, "Die Grundgleichungen fur die orthotrope Platte mit exzentrischen Steifen," Der Stahlbau, Vol. 24, pp. 128-129, 1955.

5. G. M. Singhvi, "Response of Rectangular Stiffened Plates Subjected to a Moving Sprung Mass Load," Ph.D. Thesis, Department of Civil Engineering, University of Colorado, Boulder, Colorado, 1968.

6. L. J. Feeser, "Dynamic Behavior of Eccentrically Stiffened Orthotropic Plates," Ph.D. Thesis, Department of Civil Engineering, Carnegie-Melion University, Pittsburgh, Pennsylvania, 1964.

7. L. J. Feeser and Tung Au, "Dynamic Response of Eccentrically Stiffened Plates," Conference Preprint 103, ASCE Structural Engineering Conference, New York, Oct., 1964.

8. L. J. Feeser and Tung Au, "Vibration of Eccentrically Stiffened Plates by Ritz Method," Presented at the ASCE-EMD Specialty Conference, Los Angeles, April, 1965.

9. A. Pflüger, "Zum Beulproblem der anisotropen Rechteckplatte," Ingenieur Archiv, Vol. 16, p. 111, 1947.

PARAMETRIC RESPONSE SPECTRA FOR IMPERFECT COLUMNS*

Martin L. Moody
University of Colorado
Boulder, Colorado

Response spectra for the maximum amplitude of mid-span deflection for a simply supported column subjected to 20 cycles of harmonically varying axial force are presented. The nonlinear effects of inertia and large deflections are included in the investigation, and typical linear steady state solutions are shown for comparison.

INTRODUCTION

Parametric column response has been a problem of considerable interest to the engineering profession for many years. This paper is concerned with the maximum amplitude of lateral deflection of imperfect (i.e. not straight) columns subjected to harmonically varying axial force. The response of imperfect columns subjected to harmonically varying axial force was first investigated by Mettler [1] in 1941. He determined steady state responses for the case of the linear undamped column. Weidenhammer [2] later solved for the steady state response of imperfect columns including the effects of linear damping and nonlinear longitudinal inertia. Bolotin [3] has also solved this problem including the nonlinear effects of damping, elasticity, and inertia. These previous investigations have been concerned with steady state solutions which are of limited value, since a steady state solution, in which the period of response is equal to the period of the forcing function, simply does not exist for most values of the parameters which are of interest to structural engineers. A summary of the published works on parametric vibrations through 1965 has been compiled by Evan-Iwanowski [4]. A recent study by Anderson and Moody [5] has resulted in the development of response spectra for a linear column with linear damping. Their results were obtained by analog computation.

In this investigation, the effects of nonlinear longitudinal inertia and nonlinear elasticity are included in the defining differential equation, and numerical solutions are obtained using a Runge-Kutta method. Linear solutions and nonlinear solutions for different values of the longitudinal inertia parameter are investigated, and typical amplitude-time response curves are shown. Response spectra for the maximum amplitude of lateral vibration are presented for values of the parameters which are considered to be of practical interest, and the results are compared with steady state solutions.

BASIC EQUATIONS

The basic equation which defines the lateral displacements of an axially loaded column has been developed previously [3, 6], therefore a rigorous development of the defining differential equation will not be repeated herein. However, a brief description of the source of the nonlinear terms is in order. The system to be analysed is a slender column subjected to a periodic axial force, as shown in Fig. 1, and supporting an end mass.

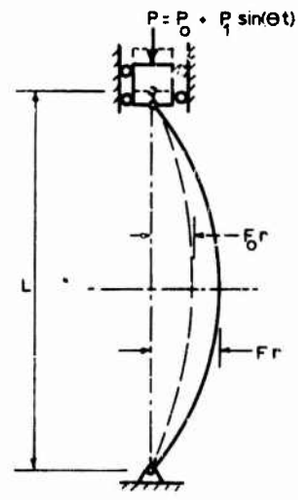


Fig. 1 - Imperfect Column with Simple Supports

*Paper not presented at Symposium.

Considering a one mode solution and neglecting the nonlinear effects leads to a non-homogeneous Mathieu equation, thus*

$$\ddot{F} + \frac{(1-P_o^*)}{\Omega^2}\left[1 - \frac{P_1^*}{(1-P_o^*)}\sin(T)\right]F = \frac{F_o}{\Omega^2} \qquad (1)$$

or $$\ddot{F} + \frac{1}{4\alpha^2}\left[1 - 2\beta\sin(T)\right]F = \frac{F_o}{\Omega^2} \qquad (2)$$

Solutions for Eq. 2 are unstable in certain regions of the α-β plane. Boundaries for these regions have been determined by others [3,7] and are shown, in part, in Fig. 2 for values of the parameters considered to be of interest to structural engineers. There are higher unstable regions, however, these higher regions have been found to be relatively unimportant [5] and are not shown. Considering the inertia effect of the end mass on the axial force in the column results in the following additional term for Eq. 2:

$$\frac{\pi^4 W}{2S^2}\left[\ddot{F}F + (\dot{F})^2\right]F \qquad (3)$$

If the effect of large deflections is to be considered, then the following term which is an approximation may be added to Eq. 2:

$$\frac{\pi^4}{8\Omega^2 S^2}F^3 \qquad (4)$$

Bolotin [3] has discussed the development of the above terms in detail. By adding Terms 3 and 4 to Eq. 2, the following differential equation is obtained:

$$\ddot{F} + \frac{1}{\Omega^2}\left[(1 - P_o^*) - P_1^*\sin(T)\right]F + \frac{\pi^4 W}{2S^2}\left[\ddot{F}F + (\dot{F})^2\right]F + \frac{\pi^2}{8\Omega^2 S^2}F^3 = \frac{F_o}{\Omega^2} \qquad (5)$$

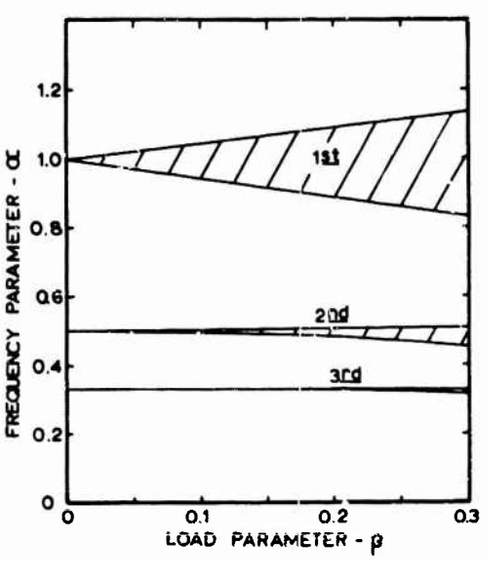


Fig. 2 - Unstable Regions (shaded) for Mathieu Equation

Initial Conditions - The column is assumed to be at rest, initially, under the influence of an initial static axial force P_o. Therefore, the initial displacement is given by

$$F(0) = \frac{F_o}{1 - P_o^*} \qquad (6)$$

and the initial velocity is $\dot{F}(0) = 0$. For this investigation, a value of $F_o = 0.25$ is used for the initial imperfection, and a value of $P_o^* = 0.51$ is used for the initial axial force. This results in an initial displacement of $F(0) = 0.51$ for all example solutions considered herein. The initial imperfection, which is one-fourth the radius of gyration of the column, was selected as a practical upper bound value. Similarly, an initial axial force which is 51% of the fundamental Euler load was selected.

SOLUTIONS

Transient solutions are obtained using a Runge-Kutta method for a period which is equivalent to 20 cycles of overloading. Typical solutions near the primary unstable region are available [6] for the nonlinear case presented herein. This investigation is extended to include solutions near the second and third unstable regions. It is found that solutions which display a beat are always found near the unstable regions. Examples of such solutions near the second unstable region are shown in Fig. 3. These solutions which display a beat are found to be typical of both the linear and the nonlinear equations.

During the investigation, it was found that the effect of nonlinear elasticity was negligible except for excessively large deflections. Therefore, only one value of the slenderness ratio (S = 120) is used in this investigation. All solutions presented include the effect of S = 120, however for W = 0 the solutions are equivalent to linear solutions. The nonlinear elasticity is not considered to be of practical importance by the author.

Large values of the weight ratio W, which defines the magnitude of the longitudinal inertia, tend to eliminate the lateral vibrations of the column. This decrease in maximum

*All mathematical symbols are defined under NOTATION at the end of this paper.

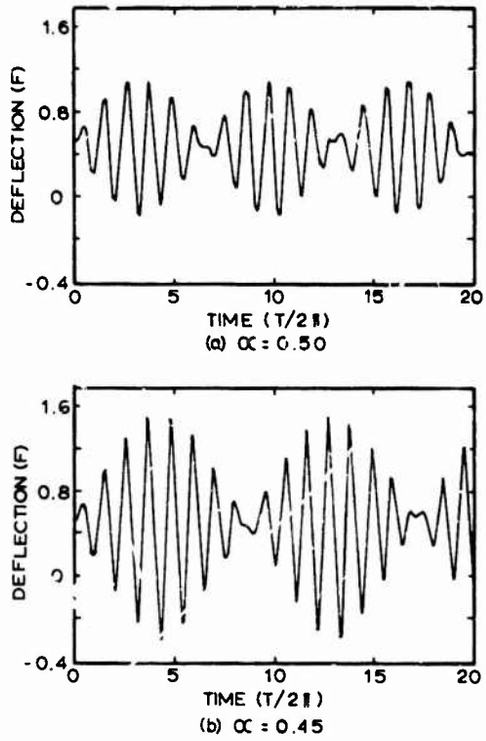


Fig. 3 - Nonlineer Solutions Neer Second Unsteble Region - β=0.10, P_o^*=0.51, P_1^*=0.098, F_o=0.25, S=120 & W=310

amplitude of vibretion as the weight retio increeses is shown in Fig. 4 for two different positions in the α-β plane. Ona of thase curves is inside the primary unsteble region (α = 1.00), and the other is between the first and second unstable region (α = 0.80). It is possible that the weight ratio W may be quite large for practicel problems. However, since large values of W (in excess of 1000) appeer to prevent large deflections from developing, en intermediete value of W = 310 is used herein for the example solutions. The solutions for W=0 ere found to be equivalent to lineer solutions for the renge of deflections presented.

Response spectre for the absolute maximum deflection have been plotted for three different velues of the loed perameter β. These plots ere shown in Fig. 5, 6, end 7, and include both the linear and the nonlineer solutions for comperison. The locetion of the first three unsteble regions (linear) ere also shown so the spectra mey be relsted to the α-β plane as shown in Fig. 2. The fourth unsteble region is near e velue of α = 0.25, which is reflected in the lerge deflections at this point for the lineer (W = 0) solutions. Since these are trensient solutions, the response values ere plotted into

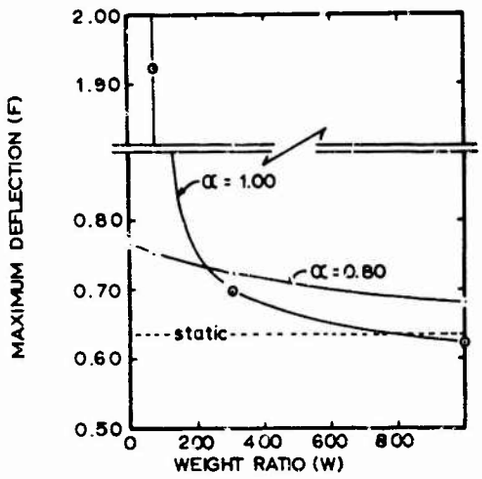


Fig. 4 - Effect of Nonlineer Inertia on Deflection - β = 0.20, P_o^* = 0.510 P_1^* = 0.196, F_o = 0.25, S = 120, W = 310

the unstable regions es fine broken lines. It should also be pointed out that in the steble regions the transient solutions for twenty cycles of overload are very close to maximum deflections which occur after many more cycles of loeding. In tha stabla regions, the solutions ere generally found to repeat themselves within twenty cyclee of loading.

With the eddition of nonlinear inertia, the regions of maximum deflection seem to be moved toward smaller values of α(i.e. to the left in Fig. 5, 6, & 7). It may eleo be observed in Fig. 5, 6, and 7 thet the odd numbered unstable regions seem to ba the regions most affected by nonlinear inertia. In general, the nonlinear inertia causes e decrease in maximum leterel deflection, however, this is not alweys true due to the shift of the maximum zones to the left.

The steady state solutions which have been determined by others [1, 2, & 3] assumes that the response of the column is identical to the frequency of the dynamic overloed, and is only valid near the second unsteble region. This type of solution does not admit e solution with e beet, as shown in Fig. 3. For purposes of comparison, steady state solutions for the lineer case have been plotted on aech of the response spectrs.

ACKNOWLEDGEMENT

This research wes conducted under Research Grent Number GK 950 from the National Science Foundation.

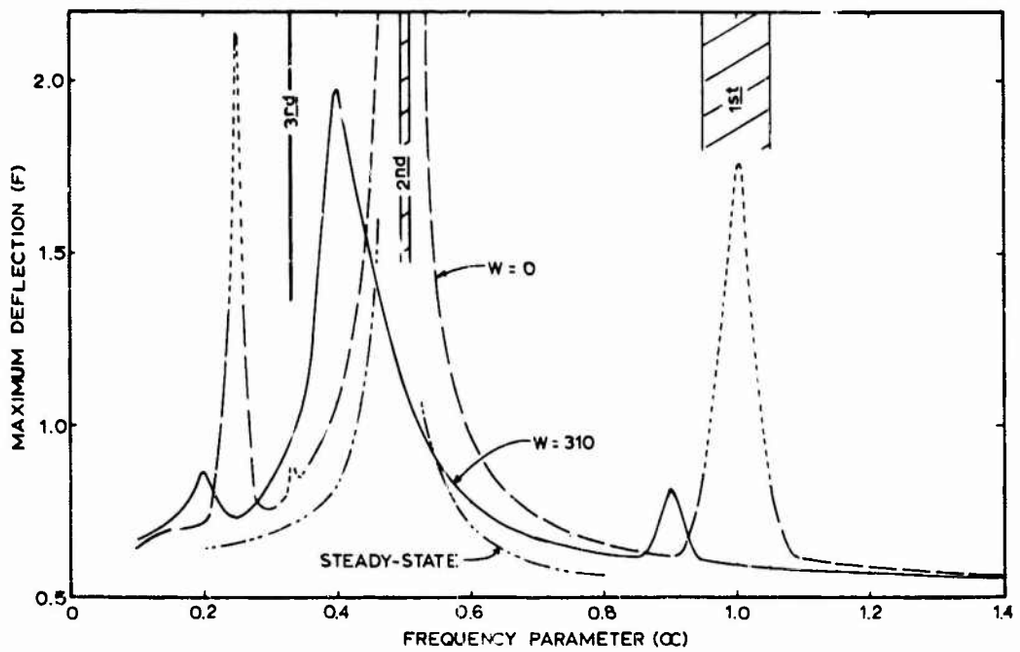


Fig. 5 - Transient Response Spectra for Maximum Deflection - β=0.10, P_o^*=0.51, P_1^*=0.098, F_o=0.25, S=12

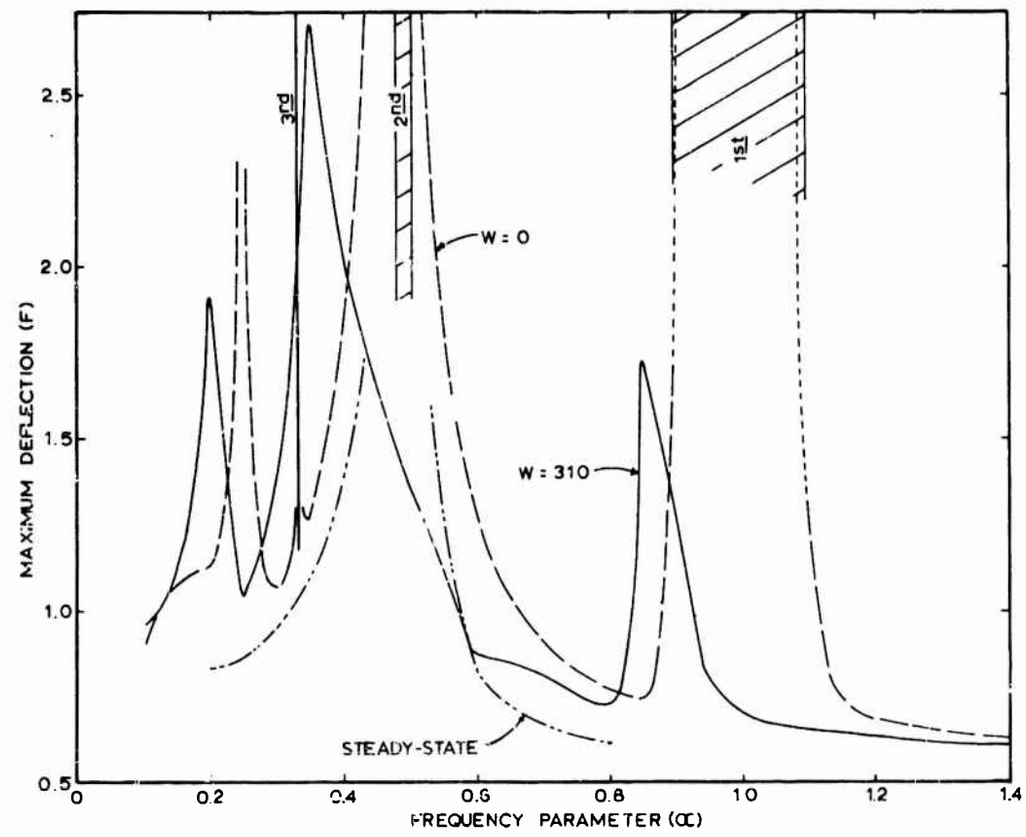


Fig. 6 - Transient Response Spectra for Maximum Deflection - β=0.10, P_o^*=0.51, P_1^*=0.196, F_o=0.25, S=120

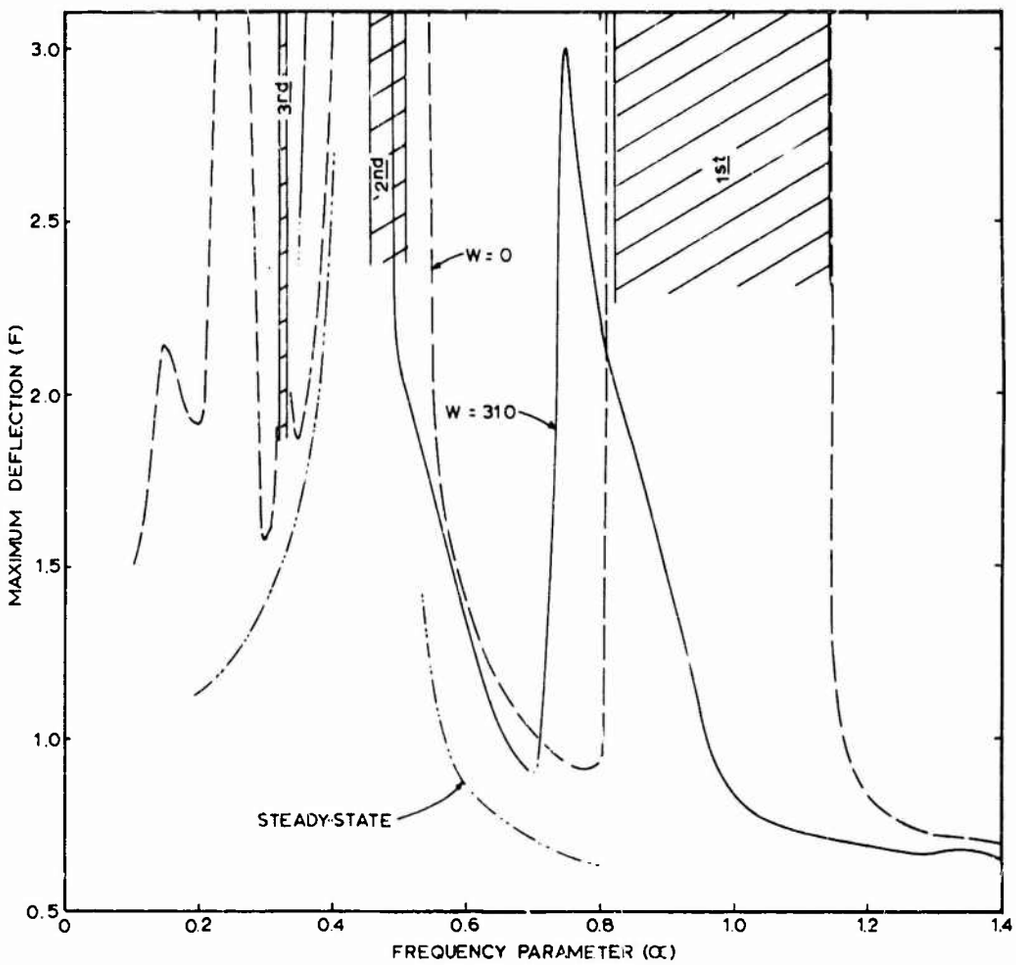


Fig. 7 - Transient Response Spectra for Maximum Deflection - β=0.30, P_o^*=0.51, P_1^*=0.294, Γ_o=0.25, and S=120

NOTATION

F = dimensionless mid-span displacement for fundamental mode (half sine wave) or ratio of mid-span deflection to radius of gyration of the section

$\dot{F}$ = derivative of F with respect to T

$\ddot{F}$ = second derivative of F with respect to T

F_o = initial dimensionless mid-span deflection in unstressed state

L = length of column

M = end mass on column

P = time dependent axial force on column

P_o = initial axial static force on column

P_1 = maximum magnitude of harmonic overload on column

P_o^* = dimensionless static axial force on column or ratio of P_o to fundamental Euler buckling load

P_1^* = dimensionless dynamic overload on column or ratio of P_1 to fundamental Euler buckling load

r = radius of gyration of section

S = slenderness ratio (L/r)

T = dimensionless time (Θt)

t = real time

W = weight ratio or ratio of static axial load to weight of column

α = frequency parameter or one-half the ratio of the loading frequency Θ to the fundamental frequency of the loaded column $\omega\sqrt{1 - P_1^*}$

β = loading parameter or $\frac{1}{4} P_1^*/(1 - P_o^*)$

Θ = frequency of harmonic overload

Ω = dimensionless loading frequency (Θ/ω)

ω = fundamental frequency of lateral vibration for simple column

REFERENCES

1. E. Mettler, "Biegeschwingungen eines Stabes mit kleiner Vorkrummung, exzentrisch angreifender pulsierender Axiallast und statischer Querbelastung," Forshungshafte aus d. Geb. d. Stahlbaues 4, pp. 1-23, 1941

2. F. Weidenhammer, "Nichtlineare Biegeschwingungen des axial-pulsierend belasteten Stabes," Ingenieur-Archiv, Vol. 20, pp. 315-330, 1952

3. V. V. Bolotin, The Dynamic Stability of Elastic Systems, translation by V.I. Weingarten, L. B. Grezczuk, K. N. Trirogoff, and K. D. Gallegos, Holden-Day, Inc., San Francisco, 1964

4. R. M. Evan-Iwanowski, "On the Parametric Response of Structures," Appl. Mech. Rev., Vol. 18, No. 9, pp. 699-702, Sept. 1965

5. T. L. Anderson and M. L. Moody, "Parametric Vibration Response of Columns," Journal of the Structural Division, ASCE, submitted March 1968

6. M. L. Moody, "The Parametric Response of Imperfect Columns," Developments in Mechanics, Vol. 4, Proceedings of the Tenth Midwestern Mechanics Conference, Fort Collins, Colo., pp. 329-346, 1968

7. S. Lubkin and J. J. Stoker, "Stability of Columns and Strings Under Periodically Varying Forces," Quar. Appl. Math., Vol. 1, pp. 215-236, 1943

GPO 867-704